

Les étoiles pulsantes et les binaires à éclipses comme indicateurs de distances dans l'univers

N. Nardetto

▶ **To cite this version:**

N. Nardetto. Les étoiles pulsantes et les binaires à éclipses comme indicateurs de distances dans l'univers. Astrophysique stellaire et solaire [astro-ph.SR]. Université Côte d'Azur, 2017. ⟨tel-03540545⟩

HAL Id: tel-03540545

https://hal.science/tel-03540545v1

Submitted on 24 Jan 2022

HAL is a multi-disciplinary open access archive for the deposit and dissemination of scientific research documents, whether they are published or not. The documents may come from teaching and research institutions in France or abroad, or from public or private research centers.

L'archive ouverte pluridisciplinaire **HAL**, est destinée au dépôt et à la diffusion de documents scientifiques de niveau recherche, publiés ou non, émanant des établissements d'enseignement et de recherche français ou étrangers, des laboratoires publics ou privés.



HAL Authorization

Université Côte d'Azur - UFR Sciences
Ecole Doctorale Sciences Fondamentales et Appliquées

Thèse d'Habilitation à Diriger des Recherches

Les étoiles pulsantes et les binaires à éclipses comme indicateurs de distances dans l'univers

par
Nicolas NARDETTO

soutenue le mercredi 20 Décembre 2017

Jury :

M. Xavier DELFOSSE	Université Grenoble-Alpes	*Rapporteur*
M. Pascal FOUQUE	Université Paul Sabatier - Toulouse 3	*Rapporteur*
Mme Agnès LEBRE	Université de Montpellier	*Rapportrice*
Mme Yveline LEBRETON	Observatoire de Paris-Site de Meudon	*Examinatrice*
Mme Karine PERRAUT	Université Grenoble-Alpes	*Examinatrice*
M. Ennio PORETTI	Osservatorio Astronomico di Brera	*Examinateur*

Université Côte d'Azur, Observatoire de la Côte d'Azur, CNRS, Laboratoire Lagrange, France
Nicolas.Nardetto@oca.eu

arXiv:1801.04158v1 [astro-ph.SR] 12 Jan 2018

Table des matières

1 Introduction **7**
- 1.1 Un peu de cosmogonie : Notre vision de l'univers au XXIe siècle . . . 7
- 1.2 Un peu de cosmologie . . . 9

2 Les différents moyens de déterminer la constante de Hubble (Ho) **13**
- 2.1 L'étalonnage des échelles de distance dans l'univers . . . 15
- 2.2 Les méthodes liées au rayonnement de fond cosmologique . . . 17
- 2.3 Les méthodes liées aux quasars . . . 20
- 2.4 Comment dépasser la tension sur H_0 ? . . . 22

3 La relation *PL* des Céphéides et les distances dans le Groupe Local **25**
- 3.1 L'impact de la métallicité sur la relation *PL* . . . 34
- 3.2 Les binaires à éclipses et la distance du LMC . . . 37
- 3.3 Impact de la binarité et de l'environnement des Céphéides sur la relation *PL* . . . 40
- 3.4 La méthode de BW appliquée aux Céphéides . . . 44

4 La méthode de Baade-Wesselink appliquée aux Céphéides : trois problématiques **47**
- 4.1 Le *p*-facteur . . . 48
- 4.2 Le *k*-facteur . . . 58
- 4.3 L'environnement des Céphéides . . . 61
- 4.4 Une piste de recherche : la comparaison avec les autres types d'étoiles pulsantes . . . 64

5 Les binaires à éclipses et l'interférométrie **71**
- 5.1 Les mesures de diamètre angulaire par interférométrie et l'instrument VEGA/CHARA . . . 72
- 5.2 La relation brillance de surface - couleur des étoiles . . . 76
- 5.3 L'impact de la rotation sur la relation brillance de surface - couleur . . . 86
- 5.4 Contraindre le p-facteur et le k-facteur des Céphéides à l'aide des binaires à éclipses . . . 88

6 Synthèse et perspectives **93**

bibliographie **95**

A Tableau récapitulatif des valeurs de la constante de Hubble depuis 2000. **117**

B L'étalonnage des échelles de distance dans l'univers. **121**

C Distance des galaxies déterminées dans le cadre du projet Araucaria **123**

D Le cas particulier de Polaris **125**

E La modélisation des Céphéides **127**

F La relation brillance de surface - couleur **129**

G *Calibrating the Cepheid period-luminosity relation from the infrared surface brightness technique. I. The p-factor, the Milky Way relations, and a universal K-band relation* **133**

H *Calibrating the Cepheid period-luminosity relation from the infrared surface brightness technique. II. The effect of metallicity and the distance to the LMC* **149**

I *An eclipsing-binary distance to the Large Magellanic Cloud accurate to two per cent* **161**

J *High-resolution spectroscopy for Cepheids distance determination. II. A period-projection factor relation* **185**

K *High-resolution spectroscopy for Cepheids distance determination. V. Impact of the cross-correlation method on the p-factor and the γ-velocities* **197**

L *The Baade-Wesselink p-factor applicable to LMC Cepheids* **205**

M *HARPS-N high spectral resolution observations of Cepheids I. The Baade-Wesselink projection factor of δ Cep revisited* **211**

N *High-resolution spectroscopy for Cepheids distance determination. III. A relation between γ-velocities and γ-asymmetries* **223**

O *High-resolution spectroscopy for Cepheids distance determination. IV. Time series of Hα line profiles* **233**

P *VEGA/CHARA interferometric observations of Cepheids. I. A resolved structure around the prototype classical Cepheid δ Cep in the visible spectral range* **241**

Q *Understanding the dynamical structure of pulsating stars : The center-of-mass velocity and the Baade-Wesselink projection factor of the β Cephei star α Lupi* **259**

R *Understanding the dynamical structure of pulsating stars : The Baade-Wesselink projection factor of the δ Scuti stars AI Velorum and β Cassiopeiae* **271**

S *Understanding the dynamical structure of pulsating stars. HARPS spectroscopy of the δ Scuti stars ρ Puppis and DX Ceti* **277**

T *An investigation of the close environment of β Cephei with the VEGA/CHARA interferometer* **289**

U *Improving the surface brightness-color relation for early-type stars using optical interferometry* **297**

V *Theoretical impact of fast rotation on calibrating the surface brightness-color relation for early-type stars* **311**

W *The Surface Brightness–Color Relations Based on Eclipsing Binary Stars : Toward Precision Better than 1% in Angular Diameter Predictions* **321**

X *RR-Lyrae-type pulsations from a 0.26-solar-mass star in a binary system* **341**

Y *Physical parameters and the projection factor of the classical Cepheid in the binary system OGLE-LMC-CEP-0227* **347**

Chapitre 1

Introduction

Depuis l'aube de l'humanité, nous cherchons à comprendre et à caractériser notre univers. La question de la détermination des distances dans l'univers a toujours été centrale, et a plusieurs fois amené à des changements de paradigmes.

1.1 Un peu de cosmogonie : Notre vision de l'univers au XXIe siècle

La vision de l'univers à l'époque de la Grèce antique se résumait à une Terre plate, placée au centre, un monde supra-lunaire parfait, appartenant au domaine des dieux, comprenant le Soleil, les 5 planètes (Mercure, Vénus, Mars, Jupiter, Saturne) et, au delà, la "sphère des fixes" sur laquelle se trouvaient les étoiles. En 300 avant JC, Aristote observe les éclipses de Lune et remarque la courbure de l'ombre de la Terre sur la Lune, ce qui donne la première preuve que la Terre est ronde. Magellan l'expérimentera presque 2 millénaires plus tard. A partir de la taille de l'ombre, Aristarque de Samos établira que la Terre a un diamètre trois fois plus important que la Lune et que sa distance à la lune est de 64 rayons terrestres. A la même époque, Eratosthène utilise les positions relatives des ombres à Syène (aujourd'hui Assouan) et à Alexandrie pour en déduire la circonférence de la Terre. Alors qu'il n'y pas d'ombre dans les puits de Syène, les gnomons indiquent un angle de 7.2° à Alexandrie, soit $1/50$ d'un tour complet (360°). La distance entre Syène et Alexandrie étant de 5000 stades, la circonférence de la Terre est 50 fois plus importante, soit environ 250000 stades ($\simeq$ 40000 km). Cette mesure permet à Aristarque de Samos d'en déduire la distance de la Terre à la Lune. Ce dernier, par une mesure d'angle liée au premier quartier de Lune, estime alors pour la première fois la distance entre la Terre et le Soleil. Malgré Héraclite qui propose que la Terre tourne sur elle-même, et Pythéas, le Marseillais, qui mesure son inclinaison, notre planète semble indiscutablement immobile sous nos pieds et finalement le modèle géocentrique de Ptolémée (IIe siècle avant JC) s'impose avec la Terre immobile et ronde au centre de l'univers et le Soleil et les planètes autour. Ce modèle, complexe, qui nécessite des épicycles pour reproduire le mouvement des planètes, va perdurer pendant 1700 ans.

En 1543, Copernic revient à un modèle héliocentrique (car Aristarque de Samos l'avait déjà proposé bien avant lui), mais celui ci ne reproduit toujours pas les observations et des épicycles restent nécessaires. Le changement de paradigme va finalement trouver son origine dans les observations minutieuses (à 1 minute de précision) de Tycho Brahé à Uraniborg sur l'île de Ven, dans le détroit du Sund (cette île aujourd'hui suédoise appartenait à l'époque au Danemark). Tycho Brahé est contre le modèle héliocentrique et ce n'est qu'à sa mort que son disciple, Kepler, va étudier en détail les données pour en déduire le mouvement ellip-

tique des planètes. Grâce à ces ellipses, le modèle héliocentrique reproduit alors bien mieux les observations. Ainsi, la troisième loi de Kepler permet de déduire la distance au Soleil de toutes les planètes (à partir de la distance Terre-Soleil). En 1610, Galilée observe les phases de Vénus, ce qui valide indubitablement le modèle héliocentrique. Il montre également que le monde supra-lunaire n'est pas parfait ; il observe effectivement les cratères sur la Lune, les taches du Soleil, les anneaux de Saturne (même s'il ne sait pas encore qu'il s'agit d'anneaux). Il découvre également les 4 plus gros satellites de Jupiter, illustrant le fait qu'un astre peut tourner autour d'une autre planète que la Terre. Mais une question demeure : pourquoi ne sent-on pas la Terre bouger sous nos pieds ? Galilée pose alors les principes de ce qui deviendra plus tard le "référentiel Galiléen" : un individu enfermé dans la cale d'un bateau naviguant sur une mer calme, ne peut faire aucune expérience pour prouver que le bateau est en mouvement rectiligne uniforme. Notre vision du système solaire est alors complétée par la découverte d'Uranus (Herschel ; 1778) et, par le calcul d'abord, de Neptune (Le Verrier ; 1846). Mais une chose demeure : la sphère des fixes.

Il y a 3000 ans, les Egyptiens avaient tout de même repéré une étoile variable sur la sphère des fixes, Algol. Un objet dont l'éclat varie dans le ciel parfait supra-lunaire ne pouvait être pour les Grecs que l'oeil de la Méduse, qui deviendra ensuite chez les Arabes *Ras El Ghul*, c'est-à-dire la tête du démon. Bien plus tard, en 1596, une autre variable est découverte, Mira Ceti, par Fabricius, dont le nom même signifiant "La merveilleuse" montre bien le changement de vision par rapport aux étoiles et à la sphère des fixes. En 1784, Goodrick découvre la première Céphéide, δ Cep. C'est également lui qui proposera le concept de "binaire à éclipses" pour expliquer la variabilité d'Algol. A son époque, Tycho Brahé tenta de mesurer la parallaxe d'une nova dans la constellation de Cassiopée en 1572, mais la tentative fut infructueuse. C'est bien Bessel (1838) qui mesure pour la première fois la parallaxe annuelle d'une étoile, 61 Cyg ($\pi = 0.314$) et en déduit une distance correspondant à 3.18 parsecs. La sphère des fixes est donc bien plus éloignée que ce que l'on imaginait alors. Un nouveau changement de paradigme se prépare alors avec les théories de la relativité restreinte (Einstein 1905) et générale (Einstein 1916). Ces théories permettent d'abord de comprendre l'avance du périhélie de Mercure (43 seconde d'arc par siècle de plus que la valeur prédite par la théorie Newtonienne). Mais elles seront également très utiles pour décrire l'univers dans son ensemble, comme nous le verrons plus loin. En 1908, Henrietta Leavitt (Leavitt 1908) dénombre 1777 Céphéides dans les nuages de Magellan, des étoiles supergéantes jaunes très brillantes. Puis en 1912, Leavitt & Pickering (1912) étudient 25 d'entre elles dans le petit nuage de Magellan et découvrent alors une propriété très particulière : leur période de pulsation (typiquement de quelques jours à quelques mois) est reliée à la moyenne de leur luminosité intrinsèque (relation *PL*), ce qui en fait des indicateurs de distance uniques. Nous reviendrons sur les propriétés qui font que les Céphéides pulsent. En déterminant la distance de ces étoiles dans les amas globulaires, Shapley (1918) montre que le Soleil ne se trouve pas au centre de la Voie Lactée mais sur le bord (du fait de la distribution non isotrope des amas). A cette époque, il y a donc environ un siècle seulement, un débat fait rage entre les partisans d'un univers qui se réduit à la Voie Lactée (Shapley 1919) et ceux qui pensent qu'il est bien plus grand et constitué d'"univers îles" (i.e. de galaxies) comme l'avait imaginé le philosophe Kant un peu plus tôt (Curtis 1920). De 1926 à 1929, Hubble détermine ainsi la distance de la galaxie du triangle (Hubble 1926) et de la galaxie d'Andromède (Hubble 1929b), que l'on pense être alors simplement des nébuleuses spirales (classées M33 et M31 par Messier), et trouve une distance bien au delà des limites de la Voie Lactée. Hubble détermine également la distance de la galaxie de Barnard (NGC 6822) (Hubble 1925). On comprend alors que ces “nébuleuses spirales” sont des "univers îles", ce qui met fin au débat Shapley-Curtis. Hubble trouvera néanmoins une distance pour ces galaxies deux fois trop petite, du fait d'une confusion entre les Céphéides de type I (qu'il a effectivement observées dans M31 et M33) et les Céphéides de type II (W Virginis, moins métalliques et moins brillantes de 1.5 magnitude environ), et sur lesquelles repose effectivement l'étalonnage de la relation *PL* effectué

par Shapley. Hubble mesure ainsi la distance de 46 galaxies. Un peu plus tôt, dès 1914, Vesto Slipher avait observé ces "nébuleuses spirales" à l'aide d'un spectroscope et avait trouvé un décalage vers le rouge des raies spectrales pour 11 nébuleuses parmi les 15 observées (Slipher 1914, 1917). Par définition, si une raie spectrale de longueur d'onde d'émission λ_0 est observée à une longueur d'onde de λ, alors le décalage vers le rouge (ou *redshift*) est :

$$z = \frac{\lambda}{\lambda_0} - 1 \tag{1.1}$$

Pour les objets proches (< 2 milliards d'années-lumière, < 600 Mpc ou encore $z < 0.15$), le décalage vers le rouge peut être assimilé à une vitesse de récession dont la formule est simplement donnée par l'effet Doppler $v = cz$. Survient alors une découverte incroyable dont la paternité fait toujours débat [1]. En 1927, Georges Lemaître rédige un article en Français dans la revue *Annales de la Société scientifique de Bruxelles*, établissant que l'univers est en expansion (Lemaître 1927). Il montre en effet que plus une galaxie est éloignée de nous, plus elle s'éloigne rapidement. Hubble (1929a) établit alors à son tour une valeur de la pente de cette relation, ou *constante de Hubble*, H_0, où l'indice 0 indique que c'est l'expansion actuelle de l'univers. Si l'univers accélère ou décélère avec le temps, H peut varier selon l'époque de l'univers considérée. Commence alors l'ère de la cosmologie.

1.2 Un peu de cosmologie

L'expansion de l'univers découle naturellement de la relativité générale couplée avec l'hypothèse d'un univers homogène (c'est-à-dire ayant la même densité de matière en tout point, à un instant donné) et isotrope (identique dans toutes les directions). Pour décrire les équations de la dynamique de l'univers, nous devons également supposer que le contenu de l'univers se comporte comme un fluide parfait, c'est-à-dire dont toutes les propriétés intéressantes (du point de vue de la dynamique cosmique) sont décrites par sa densité de masse-énergie ρ et sa pression moyenne p. Dans ce cas, le tenseur d'énergie-impulsion prend une forme simple et les équations d'Einstein se réduisent à un ensemble de deux équations différentielles, les équations de Friedmann :

$$\dot{a}^2 - \frac{1}{3}(8\pi G\rho + \Lambda)a^2 = -k \tag{1.2}$$

$$\frac{\ddot{a}}{a} = -\frac{4}{3}\pi G(\rho + 3p/c^2) + \frac{1}{3}\Lambda \tag{1.3}$$

Dans ces équations, $a = a(t)$ est le facteur d'échelle de l'univers. Celui-ci est fondamentalement relié au décalage vers le rouge (mesuré par exemple par la position d'une raie en émission dans une galaxie) du fait que la quantité $z+1$ est égale au rapport entre la taille de l'univers maintenant (a_0) et la taille de l'univers au moment de l'émission de la lumière (a). Λ est la constante cosmologique. Elle correspond à une répulsion universelle et a été introduite à l'origine par Einstein pour forcer l'univers à être statique, en accord avec la vision de Newton qui imaginait un univers homogène, statique et infini. A la découverte de l'expansion de l'univers par Hubble, la constante a été enlevée, pour ensuite être ré-introduite avec la découverte de l'expansion accélérée. k est le terme de courbure de l'univers et vaut -1, 0 ou 1 selon que l'univers est

1. Lire http ://www.nature.com/news/2011/110627/full/news.2011.385.html et l'introduction de "L'invention du big bang", Jean-Pierre Luminet (Le Seuil, 1997).

courbé négativement, spatialement plat, ou courbé positivement [2]. Afin de résoudre ces équations, nous devons introduire une relation entre la pression et la densité :

$$p = \omega\rho \tag{1.4}$$

pour chacun des composants de l'univers, c'est-à-dire la matière et le rayonnement essentiellement. Ces composantes de densité varient avec le facteur d'échelle a lorsque l'univers est en expansion et donc varient avec le temps. Au temps t, on peut définir le paramètre de Hubble :

$$H(t) = \frac{\dot{a}}{a} \tag{1.5}$$

et la constante de Hubbleqw H_0 est la valeur du paramètre de Hubble prise à l'instant $t = 0$. Si $\Lambda = 0$, on peut décrire la cinématique de l'univers simplement en utilisant la première équation de Friedman (Eq. 1.2). Si on ajoute l'hypothèse que l'univers est plat ($k = 0$), alors on obtient :

$$\rho = \rho_c = \frac{3H^2}{8\pi G} \tag{1.6}$$

où ρ_c est la densité critique. Ainsi, plusieurs cas peuvent se présenter. Si l'univers a une densité $\rho < \rho_c$, alors $k < 0$ et l'univers est courbé négativement, ce qui implique $\dot{a} > 0$ et donc une expansion éternelle. Si à l'inverse $\rho > \rho_c$, alors $k > 0$ et l'univers est courbé positivement, ce qui implique qu'il existe un instant t pour lequel $\dot{a} = 0$. A ce point, l'expansion va s'arrêter et l'univers va commencer à se contracter. Si la constante cosmologique Λ est positive, alors l'univers est quasiment contraint de s'expandre indéfiniment, à moins que la densité de matière soit bien plus grande que Λ et dans ce cas l'univers peut se recontracter avant que l'expansion domine.

On peut introduire des quantités sans dimensions pour décrire la densité d'énergie associée à la constante cosmologique $\Omega_\Lambda = \Lambda/3H_0^2$ et la courbure de l'espace temps, $\Omega_k = k/H_0^2$. En réarrangeant l'Eq. 1.2, on obtient alors :

$$\frac{H^2}{H_0^2} = \frac{\rho}{\rho_c} - \Omega_k a^{-2} + \Omega_\Lambda \tag{1.7}$$

La densité pour une composante particulière de l'univers (matière ou rayonnement) X peut être exprimée comme une fraction de la densité critique sous la forme :

$$\frac{\rho_X}{\rho_c} = \Omega_X a^\alpha \tag{1.8}$$

où l'exposant α représente la dilution de la composante avec l'expansion de l'univers et est reliée au paramètre ω (Eq. 1.4) par l'équation $\alpha = -3(1+\omega)$. L'équation 1.8 est valable seulement si ω est constant. Ainsi, pour la matière ordinaire, $\alpha = -3$: la densité diminue comme $\frac{1}{R^3}$ lorsque l'univers se dilate, ce qui est intuitif. Pour le rayonnement, on a $\alpha = -4$, car en plus de la dilatation géométrique, il y a une perte d'énergie liée au décalage vers le rouge au fur et à mesure que l'univers se dilate. Ce décalage vers le rouge n'est pas lié à l'effet Doppler (mais assimilable à un effet Doppler en deçà de $z = 0.15$) mais bien à un effet relativiste gravitationnel. Enfin, la densité d'énergie associée à la constante cosmologique reste la même quelle que soit la taille de l'univers, ainsi on $\alpha = 0$ et $\omega = -1$. Une solution avec $\omega < -\frac{1}{3}$ (appelée quintessence) peut également produire de l'expansion. Par ailleurs, il n'y a aucune raison pour que ω reste constant avec z, et

2. k est ici le terme de courbure de l'univers à ne pas confondre avec le k-facteur des Céphéides discuté plus loin

les observations futures pourront probablement contraindre des modèles du type $\omega = \omega_0 + \omega_1 z$. Le terme d'énergie noire regroupe tous ces types de modèles.

Finalement, on obtient la variation du *paramètre* de Hubble en fonction de la *constante* de Hubble :

$$H^2 = H_0^2(\Omega_\Lambda + \Omega_m a^{-3} + \Omega_r a^{-4} - \Omega_k a^{-2}) \tag{1.9}$$

où Ω_r est la densité d'énergie de radiation et Ω_m est la densité d'énergie de matière. Cette équation indique que le rayonnement dominait en terme d'énergie lorsque l'univers était de petite taille (a petit). De son côté, Ω_Λ implique une force répulsive responsable de l'expansion de l'univers comme nous l'avons vu, *mais elle correspond également à une densité d'énergie qui affecte la courbure de l'univers*. Ainsi, on a :

$$\Omega_\Lambda + \Omega_m + \Omega_r - \Omega_k = 1 \tag{1.10}$$

Dans cette équation, si $\Omega_k = 0$, l'univers est plat, et la somme totale de l'énergie de densité de la matière et du rayonnement ajoutée à la densité d'énergie liée à la constante cosmologique doit correspondre à la densité critique dont la formulation est alors plus complexe que l'Eq. 1.6. Il est à noter que les univers proches de $\Omega_k = 0$ ont tendance à s'éloigner de ce point d'équilibre, ce qui pose le problème de la "platitude de l'univers". La période d'inflation dans l'histoire de l'univers permet de résoudre ou disons contourner ce problème. L'univers observable, plat ou quasi-plat, n'est qu'une partie d'un univers plus grand courbé ou pas, fini sans bord ou infini, un peu comme l'horizon sur Terre. Ces quelques rappels de cosmologie nous ont permis de replacer la constante de Hubble dans son contexte, et nous allons voir maintenant comment cette quantité peut être mesurée concrètement de nos jours.

Chapitre 2

Les différents moyens de déterminer la constante de Hubble (Ho)

En moins d'un siècle, nous sommes donc passés d'un univers statique de la taille d'une galaxie à la vision d'un univers observable en expansion, d'un âge d'environ 13.6 milliards d'années et contenant 100 milliards de galaxies. Pour mesurer l'expansion de l'univers (i.e. H_0), il faut une vitesse d'éloignement et une distance. Mesurer des vitesses d'éloignement est relativement aisé : il suffit d'observer avec un spectrographe un objet présentant une raie d'émission. En revanche, la question des distances est extrêmement délicate. Il faut soit une chandelle standard (i.e. un objet dont la luminosité est connue), soit une règle standard (i.e. un objet dont la longueur est connue), et ensuite nous pouvons utiliser la magnitude apparente ou le diamètre angulaire pour estimer la distance. Ce qui veut dire que comprendre la physique de ces objets est incontournable si l'on cherche à estimer sans équivoque leur luminosité intrinsèque ou leur taille réelle. Hubble trouva une valeur autour de 500 km/s/Mpc, soit environ dix fois plus grande que les estimations actuelles. Cette valeur initialement trop élevée et les révisions progressives vers de plus basses valeurs (*cf* Trimble (1996); Tammann (2006)) s'expliquent d'abord par un biais dans les échantillons de départ (Behr 1951), puis par une confusion entre des étoiles brillantes et certaines régions HII (Humason et al. 1956; Sandage 1958) et enfin, entre les Céphéides de type I et II (Baade 1956).

Par ailleurs, pour mesurer H_0, il faut que les objets en question soient suffisamment loins pour que leur vitesse soit essentiellement due à l'expansion générale de l'univers (ce que l'on appelle dans la littérature, "The Hubble flow"). On sait par exemple que le système solaire se déplace à 390 km s^{-1}vers la constellation du Lion, tandis que la Voie Lactée dans son ensemble, se déplace à 600 km s^{-1}dans la direction de l'amas du Centaure (lieu connu sous le nom de grand attracteur ou concentration de Shapley). Ainsi, il faut sortir du Superamas de l'Hydre et du Centaure pour s'affranchir des vitesses liées au potentiel gravitationnel local et donc atteindre quelques dizaines de Mpc, soit autour de $z \simeq 0.01$. Pour les distances autour de $z = 0.15$, la relation entre le décalage vers le rouge z et la luminosité (ou le diamètre angulaire) n'est plus linéaire et dépend de la densité de matière Ω_m et d'énergie noire Ω_Λ, et aussi de la constante de Hubble elle-même. D'ailleurs, on définit en cosmologie des distances particulières. Les deux plus importantes sont la distance de diamètre angulaire D_A qui fait le lien entre le diamètre angulaire apparent et la taille réelle d'un objet (comme une galaxie), et la distance de luminosité $D_L = (1+z)^2 D_A$, qui relie le flux observé d'un objet à sa luminosité intrinsèque.

Malheureusement, il n'existe pas d'objet dont on connaisse la luminosité (ou la taille) en une seule étape, sans ambiguité, et pouvant être observé jusqu'à quelques dizaines de Mpc. L'approche utilisée est donc de

déterminer la distance d'objets proches pour ensuite étalonner la luminosité des objets plus lointains. Le processus peut se répéter plusieurs fois et on obtient finalement ce que l'on pourrait appeler un véritable échafaudage des échelles de distances dans l'univers, tel que celui représenté sur la Figure B.1. Chaque avancée dans ce domaine a permis de comprendre la physique des objets utilisés. Le contenu astrophysique des méthodes utilisées est clairement un désavantage pour l'estimation de la constante de Hubble, mais il est incontournable. Le nombre d'étapes utilisées l'est également car chacune d'entre elle apporte son lot d'incertitudes statistiques et systématiques. Ainsi, si l'on regarde les valeurs de la constante de Hubble obtenues depuis l'an 2000 par les différentes méthodes que nous allons maintenant décrire, on obtient un intervalle de valeur entre typiquement 60 et 75 km/s/Mpc (Fig. 2.1).

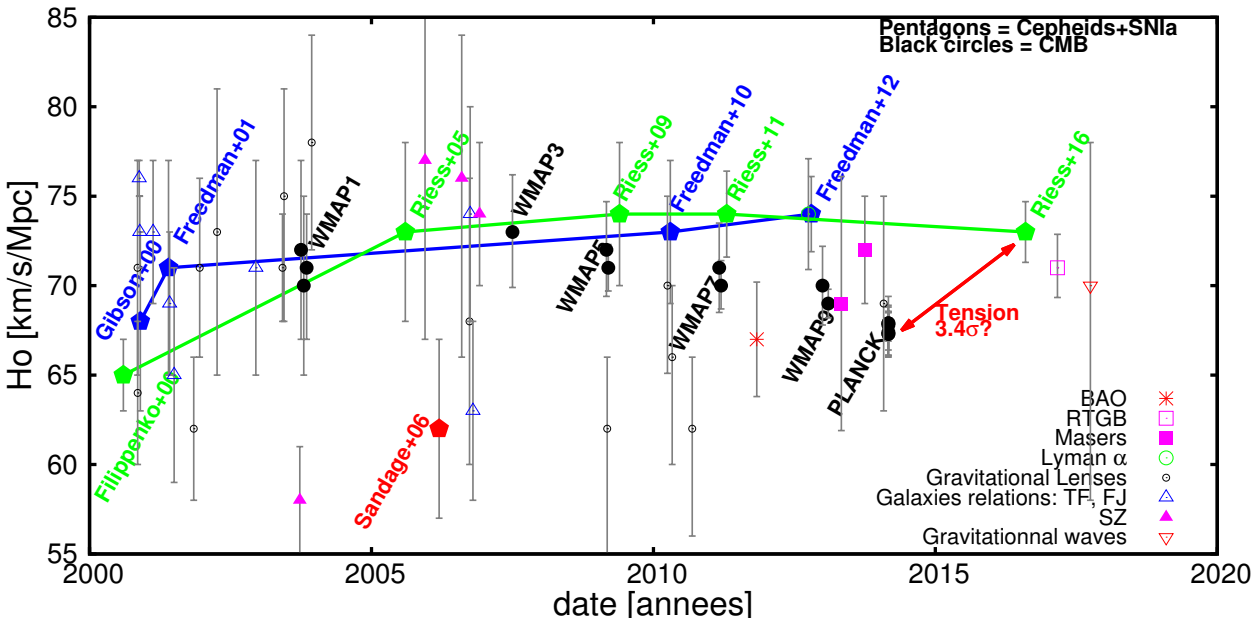


FIGURE 2.1 – Evolution de la détermination de la constante de Hubble depuis l'an 2000. Les différentes méthodes sont indiquées. Les deux groupes qui utilisent les Céphéides et les supernova de type Ia ont des résultats compatibles : d'une part le *Carnegie Hubble Project* de Wendy Freedman (en bleu) et d'autre part, le projet SHOES d'Adam Riess (en vert). Seule la valeur de Sandage et al. (2006), autour de 61,km/s/Mpc, est significativement plus faible. Cette incohérence est discutée dans la revue de Jackson (2015), et est attribuée à la façon de gérer l'impact de la métallicité sur la relation *PL* des Céphéides (voir Sect. 3.1). Les valeurs issues des observations du rayonnement de fond cosmologique (WMAP 1, 3, 5, 7, 9 et Planck) diminuent progressivement au cours des études et des analyses pour finalement se situer autour de 3.4σ en dessous des valeurs basées sur les SN Ia. La littérature scientifique se réfère à cette incohérence sous le terme de *tension*. Les autres méthodes qui permettent d'étalonner la relation entre z et la luminosité des SNIa à savoir les masers et les relations liées aux Galaxies, Tully-Fisher (TF) et Faber-Jackson (FB), ne sont pas encore assez précises et exactes pour espérer lever la tension. Seule la valeur récente liée au *Red Tip of Giants Branch* RTGB donne une précision de 2% compatible avec les projets CHP et SHOES. On note également que les méthodes de détermination de distance à 1 étage : *Baryonic Acoutic Oscillatio* (BAO), Lyman α, les lentilles gravitationnelles et la méthode de Sunyaev-Zeldovitch (SZ) présentent des incertitudes qui ne permettent pas actuellement de résoudre la tension et il en est de même de la méthode récente basée sur les ondes gravitationnelles.

2.1 L'étalonnage des échelles de distance dans l'univers

Si on considère d'abord l'approche liée à l'échafaudage des distances, on constate que le chemin le plus court pour atteindre la constante de Hubble nécessite au minimum deux objets astrophysiques : les Céphéides et les supernova de type Ia. En effet, comme nous l'avons déjà mentionné dans la Sect. 1.1, les Céphéides possèdent la propriété particulière que leur période de pulsation est reliée à leur luminosité moyenne intrinsèque. Cependant, pour utiliser la relation période-luminosité (*PL*), il faut l'étalonner, ce qui constitue véritablement la base de l'"échafaudage" des échelles de distance dans l'Univers. La relation a été étalonnée pour la première fois par Hertzsprung (1913) en utilisant des parallaxes statistiques, mais le moyen le plus direct est d'utiliser la méthode de la parallaxe trigonométrique : du fait du mouvement de la Terre autour du Soleil, les Céphéides proches se déplacent de manière apparente par rapport aux étoiles lointaines, ce qui donne leur distance. La combinaison de la distance et de la magnitude apparente fournit la magnitude absolue (module de distance) et donc la luminosité intrinsèque. Il est alors aisé de combiner la période et la luminosité pour en déduire la relation *PL*. Cependant, actuellement (i.e. fin 2017), il n'existe que 7 Céphéides pour lesquelles nous avons une mesure de parallaxe à mieux que 10% (Benedict et al. 2007). Aussi, une autre approche consiste à mesurer la distance du LMC (ou SMC) par une méthode indépendante (par exemple les binaires à éclipses) pour en déduire la relation *PL*. Le LMC se trouve à environ 50 kpc, soit 2 à 3 ordres de grandeur plus proche que les galaxies intéressantes pour mesurer la constante de Hubble, qui sont effectivement situées entre 5 et 40 Mpc. Les Céphéides, avec les géantes rouges, sont les seuls objets observables à la fois dans le LMC et dans ces galaxies. L'arrivée du *Hubble Space Telescope* (HST) a été très importante pour que ceci soit possible. Les instruments futurs comme l'E-ELT le seront également. On ne saurait donc trop souligner l'importance des Céphéides pour l'étalonnage des échelles de distance, car sans ces étoiles, il serait très difficile de faire le lien entre la Voie Lactée, le LMC et les galaxies externes. Mais même l'observation des Céphéides avec le HST ne permet pas d'atteindre des distances suffisantes pour établir la constante de Hubble directement (i.e. hors du "Hubble flow"). La dernière étape consiste donc à utiliser des objets astrophysiques encore plus brillants, c'est-à-dire les supernovae de type Ia (SNIa). Il s'agit de binaires dont l'une des composantes (une géante rouge) transfère de la masse vers une naine blanche, une étoile dont la stabilité provient de la dégénérescence des électrons. Lorsque la masse de la naine blanche dépasse la masse limite de Chandrasekhar, celle-ci explose. Bien que la magnitude absolue de l'explosion ne soit pas tout à fait constante, les SNIa ont des courbes de lumière similaires (Pskovskii 1967; Barbon et al. 1973; Tammann 1982), et il existe en particulier une très bonne corrélation entre le pic de brillance et la chute de luminosité 15 jours après le pic, une quantité que l'on note Δm_{15} (Phillips 1993; Hamuy et al. 1996). Le point clef pour contraindre la constante de Hubble consiste donc à observer jusqu'à 40 Mpc (i.e z 0.01) avec le Hubble Space Telescope des galaxies qui contiennent à la fois des Céphéides et des SNIa. On dispose à ce jour d'une vingtaine de galaxies qui répondent à ce critère. Ces SNIa permettent alors de fixer le point zéro de la relation entre z et la distance de luminosité des SNIa, ces dernières étant observables jusqu'à environ $z = 6$.

Cette approche est ainsi utilisée par deux groupes indépendants, le groupe du "Canergie Hubble Program" (CHP [1]) mené par Wendy Freedman, dont les valeurs de H_0 sont indiquées en bleu sur la Fig. 2.1 et le groupe "Supernova H_0 for the Equation of State" (SHOES) dirigé par Adam Riess, le co-récipiendaire du Prix Nobel de physique 2011 (en vert sur la Fig. 2.1). Les deux groupes s'accordent (dans les barres d'erreur) sur la constante de Hubble. Les méthodes sont assez similaires et pas totalement déconnectées :

1. Freedman et al. (2012) ont utilisé des observations uniques du satellite *Spitzer* à 3.6 μm et les

1. http://chp.obs.carnegiescience.edu/wiki/Main_Page

distances de 10 Céphéides Galactiques obtenues par des mesures de parallaxes trigonométriques avec le *Hubble Space Telescope* (Benedict et al. 2007) pour contraindre le point-zéro de la relation *PL*. La pente de la relation *PL* fut quant à elle déduite de l'observation *Spitzer* de 90 Céphéides dans le LMC. Cette relation *PL* fut ensuite utilisée pour étalonner la relation des supernovae Ia obtenue par Riess et al. (2011).

2. Riess et al. (2016) ont utilisé 4 indicateurs de distances géométriques pour étalonner la relation PL des céphéides : (1) les mégamasers de NGC 4258, (2) 8 binaires à éclipses du Grand Nuage de Magellan (LMC), (3) 15 parallaxes HST de Céphéides Galactiques [2] et enfin (4) 2 binaires à éclipses situées dans la galaxie M31 [3]. Leur meilleure estimation de la constante de Hubble est ainsi de $H_0 = 73.24 \pm 1.74$ km s^{-1} Mpc^{-1}, ce qui donne une incertitude de 2.4% (en incluant les incertitudes statistiques et systématiques).

Dans cette démarche, Riess et al. (2016) utilisent un mégamaser dans NGC 4258 pour étalonner la relation *PL*, la seule alternative au LMC (Claussen et al. 1984). Cette galaxie présente une coquille de masers qui sont orientés quasiment selon la tranche ("edge-on") (Miyoshi et al. 1995; Greenhill et al. 1995) et apparemment en rotation circulaire Képlerienne. La mesure des vitesses des masers individuels et de leur accélération permet de calculer la taille réelle de la coquille de masers, et donc la distance de la galaxie à 3%, soit une précision légèrement moins bonne que la précision actuellement obtenue sur le LMC (environ 2%). La méthode a subi quelques améliorations avant d'atteindre cette précision (Herrnstein et al. 1999; Humphreys et al. 2005; Argon et al. 2007). Néanmoins, des études indiquent que la distance à NGC 4258 pourrait être biaisée par un problème de dégénérescence dans la procédure d'ajustement des paramètres du maser (Reid et al. 2013). Par ailleurs, les valeurs de H_0 issues uniquement de cette méthode sont moins précises que celles obtenues dans le cadre des projets CHP ou de SHOES (carrés magenta sur la Fig. 2.1). Ainsi, le LMC (150 fois plus proche que NGC 4258) reste une référence pour construire l'échafaudage des échelles de distances dans l'univers. L'approche de Riess et al. (2016) basée sur ces 4 objets astrophysiques est représentée sur la Fig. 2.2 par des flèches rouges. Dans la suite, nous aborderons différentes façons d'améliorer ce "chemin" vers la constante de Hubble.

Il existe néanmoins une alternative aux SNIa pour la détermination de H_0. Toutes ces méthodes reposent sur une corrélation entre une propriété facilement observable de ces galaxies et leur luminosité. Ainsi, la vitesse de rotation des galaxies spirales vues par la tranche v est proportionnelle à la luminosité de la galaxie ($L \propto v^4$). En effet, le nombre d'étoiles contenues dans la galaxie détermine à la fois sa masse et donc sa vitesse de rotation, mais aussi son éclat. Il s'agit de la relation de Tully-Fisher (Tully & Fisher 1977). Cette relation nécessite néanmoins d'être étalonnée, notamment par les Céphéides. Le même type de relation peut être établie pour les galaxies elliptiques ; il s'agit alors de la relation de Faber-Jackson (Faber & Jackson 1976). Les galaxies elliptiques étant plus âgées dans l'histoire de l'univers, elles sont aussi moins métalliques et ne contiennent en général pas ou peu de Céphéides. Il faut alors utiliser des étoiles pulsantes de type II pour étalonner leur relation (RR Lyrae, W Vir), mais ces étoiles étant moins brillantes que les Céphéides, la méthode reste moins favorable. Enfin, il est possible de trouver des combinaisons plus complexes, comme le paramètre D_n (Dressler et al. 1987; Lynden-Bell et al. 1988) que l'on peut lier à la luminosité, ou la méthode type "fundamental plane" (Dressler et al. 1987; Djorgovski & Davis 1987) qui

2. Ces 15 parallaxes correspondent aux dix de Benedict et al. (2007) dont la précision s'échelonne entre 5% et 12%, trois d'Hipparcos (Perryman & ESA 1997; van Leeuwen et al. 2007a) et deux autres observées par l'équipe SHOES en utilisant un nouveau mode d'observation sur le HST (Casertano et al. 2016).

3. Il est intéressant de noter que ces estimations de distance n'utilisent pas la version purement observationnelle de la méthode de détermination de distance des binaires à éclipses (comme c'est le cas pour le LMC), mais sont basées sur des modèles stellaires. Nous reviendrons sur ce point dans la Sect. 5

relie quant à elle trois propriétés : la luminosité à l'intérieur d'un rayon effectif (en deçà duquel la moitié de la luminosité de la galaxie est émise), le rayon effectif et la dispersion de vitesse des étoiles. Enfin, le degré de résolution des étoiles dans une galaxie dépend de sa distance. Une dernière méthode repose donc sur la distribution de brillance de la galaxie (Tonry & Schneider 1988). Les valeurs de H_0 déduites des méthodes Tully-Fischer et Faber Jackson sont indiquées sur la Figure 2.1 par les triangles bleus. La précision et la dispersion des mesures laissent penser que ces approches ne sont pas au même point de maturité que la méthode SNIa. La conclusion est la même si l'on considère les autres méthodes liées aux propriétés des galaxies.

2.2 Les méthodes liées au rayonnement de fond cosmologique

Les indicateurs de distance sont des objets astrophysiques complexes, résultats d'une longue évolution de l'univers vers la complexité. Loin dans le passé n'existaient ni galaxies, ni étoiles. Par ailleurs, nous avons vu avec l'Eq. 1.9 qu'à une époque reculée, la densité de rayonnement dominait sur la densité de matière. Le rayonnement présent était en étroite interaction avec la matière. L'univers primordial était opaque. Ce n'est qu'à la fin de l'ère primordiale, après environ 300000 ans, que la matière de l'univers est devenue transparente : les électrons alors libres dans l'univers se sont combinés avec les protons pour former de l'hydrogène neutre. A partir de ce moment s'est également initié un processus de contraction locale (comparée à l'expansion globale) qui aboutira, des centaines de millions d'années plus tard, à l'apparition des premières étoiles et galaxies. Le rayonnement qui prédominait à l'époque de la (re)combinaison était à une température d'environ 3000K, donc essentiellement composé de photons du domaine de la lumière visible ou ultraviolette. Aujourd'hui, ce rayonnement, du fait de l'expansion de l'univers, est beaucoup moins énergétique, avec un pic d'émission dans le domaine des micro-ondes (0.001mm). Le caractère thermique du rayonnement se traduit par la forme du spectre : une loi de corps noir. La satellite Planck a mesuré une température de 2.728K, avec une incertitude extrêmement faible. Ce rayonnement fossile ("Cosmic Background Microwave", CMB) correspondant à $z_{\rm rec} = 3000/2.7 \simeq 1100$, représente la trace la plus ancienne que l'on ait jamais enregistrée. L'univers était alors environ 1100 fois plus petit que maintenant.

Au début de l'univers, des structures existaient sous la forme de légères fluctuations de densité ($\delta\rho \simeq 0.01$) dans un fluide constitué de photons et de baryons. Les gradients de pression associés à la force de rappel gravitationnelle ont conduit à des oscillations, très similaires à des ondes acoustiques, que l'on appelle "Baryonic Acoustic Oscillations (BAO)". Ce motif s'est alors figé au moment de la recombinaison alors même que l'univers était encore en expansion. Le pic le plus significatif que l'on obtient dans le CMB correspond ainsi à ce pic acoustique. La taille des structures angulaires dans le CMB est donc relié à la taille de "l'horizon acoustique" au moment de la recombinaison et à la distance angulaire entre nous et $z_{\rm rec}$, qui dépend justement des paramètres cosmologiques et de la courbure de l'univers. Plus l'univers est courbé négativement, plus la distance angulaire est grande et plus le pic acoustique dans le CMB se déplace vers une taille caractéristique plus petite. Ainsi, le satellite Planck et les missions précédentes ont montré que l'univers est spatialement plat ($k = 0$ ou $\Omega_{\rm k} = 0$ dans l'Eq. 1.10), c'est à dire que l'on a $\Omega_{\rm r} + \Omega_{\rm m} + \Omega_\Lambda \simeq 1$. Il faut noter que l'on ne pourra jamais montrer que l'univers est absolument plat, seulement qu'il est plat dans un certain domaine de confiance.

Mais la structure géométrique globale de l'univers n'est pas la seule propriété que l'on peut déduire du spectre de fluctuation du CMB. Le second pic permet de contraindre $\Omega_{\rm b}H^2$, c'est la densité de matière des baryons, alors que le troisième pic est sensible à la densité de matière totale (incluant la matière noire) $\Omega_m H^2$. Ainsi, H_0 peut être déterminée à partir du spectre du CMB, bien que cette quantité reste dégénérée

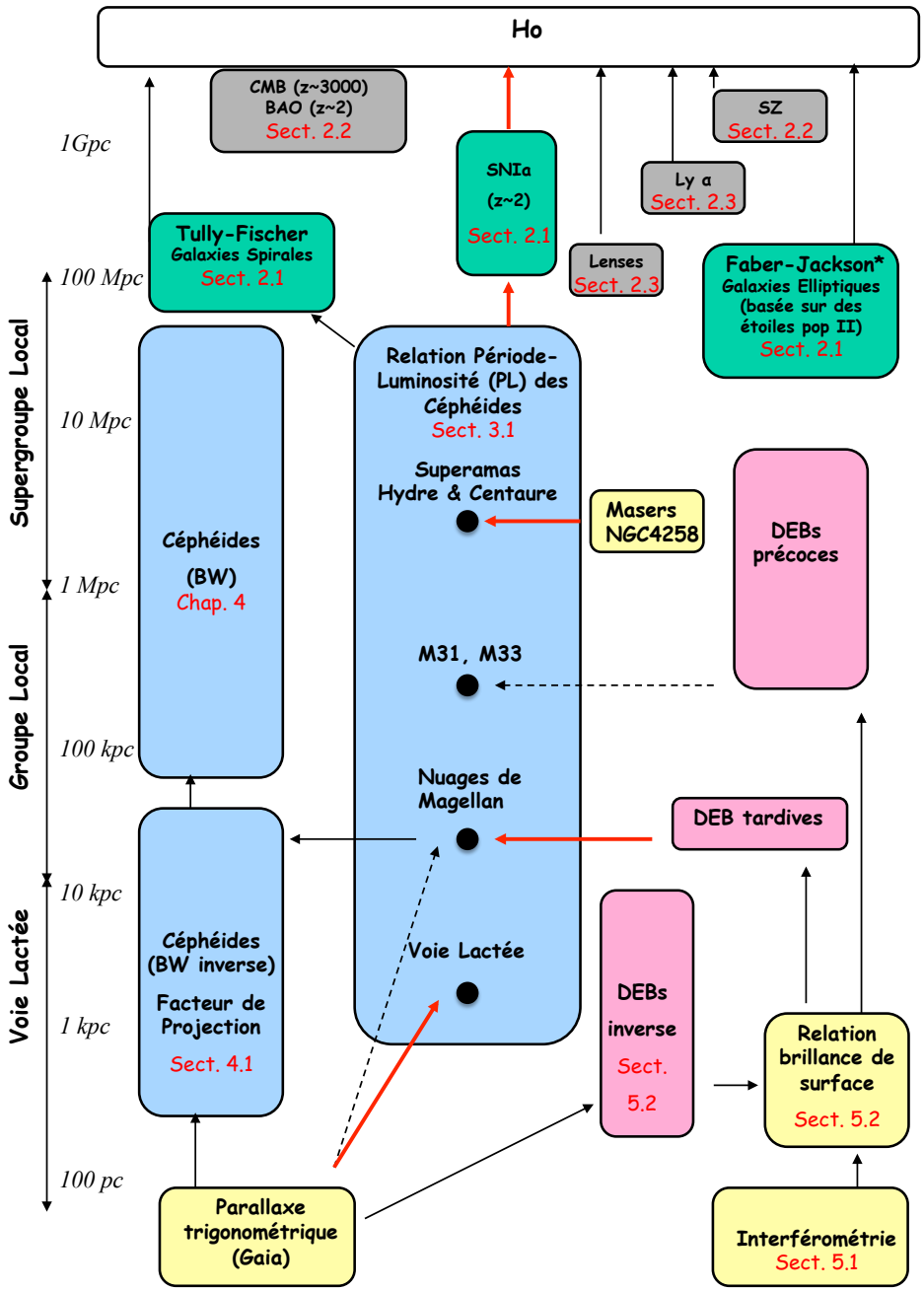


FIGURE 2.2 – Organigramme des méthodes de détermination de distances dans l'univers. Les flèches rouges indiquent le "chemin" suivi par Riess et al. (2016) pour contraindre H_0 : les parallaxes trigonométriques des céphéides Galactiques, la distance du LMC déduite des binaires à éclipses détachées tardives (DEB) et la distance au maser de NGC 4258. Ces distances de référence permettent de contraindre la relation PL des Céphéides et d'étalonner la relation des supernova de type Ia. Les différentes parties de ce diagramme sont explicitées dans les sections indiquées.

essentiellement avec w, le paramètre de l'Eq.1.4 qui définit l'équation d'état de l'énergie noire. En effet, le CMB nous indique que l'univers est quasi-plat et nous donne la densité d'énergie liée à la matière, ce qui permet d'en déduire la densité d'énergie liée à l'énergie noire. Il faut alors faire une hypothèse sur l'équation d'état de l'énergie noire (w) pour déterminer la pression répulsive qui sera justement à l'origine de l'expansion de l'univers et donc H_0. Sur la Figure 2.1, j'ai indiqué les valeurs de H_0 déduites du rayonnement de fond cosmologique avec WMAP puis Planck. Les valeurs de H_0 ainsi que les références utilisées dans ce graphique se trouvent dans le tableau de l'annexe A.2. WMAP a publié des résultats de manière régulière après 1, 3, 5, 7 et 9 observations respectivement. On constate une diminution progressive et assez curieuse des valeurs de H_0 dans le cas de WMAP au fil des années. Mais, on peut finalement noter que les résultats WMAP-9 et Planck sont compatibles.

La valeur de Riess et al. (2016) est 3.4σ plus élevée que celle déduite du rayonnement de fond cosmologique établie par le satellite Planck, $H_0 = 66.93 \pm 0.62$ km s^{-1} Mpc^{-1} (Planck Collaboration et al. 2016). La "tension" ainsi obtenue est aujourd'hui extrêmement débattue : soit elle provient d'erreurs systématiques, soit elle implique une nouvelle physique. Il faut voir effectivement que la valeur de H_0 déduite à partir de l'échafaudage des échelles de distance (Céphéides, supernova de type Ia) est déterminée à $z \simeq< 0.15$, alors que la valeur déduite à partir du rayonnement de fond cosmologique correspond à $z = 1100$.

Il existe néanmoins un moyen remonter les échelles de distance depuis le CMB dans ce qu'on pourrait appeler un étalonnage des échelles de distance *inverse*. En effet, les BAO (du fait de la vitesse du son qui est connue dans le plasma) fournissent une règle (ou distance) de référence caractéristique à l'époque du CMB, qui va conditionner la structure et l'évolution des amas de galaxies. Ainsi, si l'on mesure les corrélations dans la distribution des galaxies à grande échelle avec par exemple le *"Sloan Digital Sky Survey"* (SDSS), on trouve des distances typiques de l'ordre de 100 Mpc. En comparant cette échelle de distance obtenue autour de $z = 0.35$ avec celle du CMB correspondant à $z = 1100$, on obtient un moyen de contraindre les paramètres cosmologiques et donc H_0. Une valeur récente obtenue par cette méthode (BAO) est indiquée sur la Fig. 2.1 et est compatible avec les résultats du CMB. Il est à noter que les analyses données par WMAP ou Planck prennent cette contraindre additionnelle en compte dans leur analyse.

La dernière méthode liée au rayonnement de fond cosmologique est la méthode Sunyaev-Zel'dovich (S-Z). Le principe de la méthode (Sunyaev & Zeldovich 1972), ainsi que la façon dont elle est utilisée pour déduire la constante de Hubble (Silk & White 1978) ont fait l'objet de quelques revues (Birkinshaw 1999; Carlstrom et al. 2002). La méthode repose sur la physique de gaz chaud (10^8K) dans des amas, qui émettent du rayonnement X en émission par l'effet bremsstrahlung, générant une brillance de surface dont la formule dépend de la densité d'électrons et de leur température. Par ailleurs, les électrons du gaz chaud interagissent avec les photons du CMB (diffusion par effet Compton) et les décalent en fréquence. Apparaissent ainsi des "trous" dans l'émission radio du CMB (car les photons ont été retirés de ces fréquences pour être décalés vers les hautes fréquences). La combinaison des rayonnements X et radio permet de déterminer la distance du nuage. Cette estimation reposent sur quelques hypothèses concernant le nuage mais ne dépend d'aucune chandelle stellaire. En mesurant le décalage vers le rouge du nuage z, on obtient une contrainte sur H_0. Cette méthode s'applique autour de $z = 0.15$ à 1. Reese et al. (2002) a néanmoins identifié un budget d'erreur de l'ordre de 20 à 30% pour la détermination de distance d'un amas, ce qui explique la grande dispersion des mesures de H_0 par cette méthode indiquées sur la Fig. 2.1.

2.3 Les méthodes liées aux quasars

La théorie de la relativité générale exprime l'effet de la gravitation comme une courbure de l'espace-temps. Ainsi, le rayonnement issu d'une source lointaine, comme un quasar, est dévié par le champ gravitationnel d'un objet massif (une galaxie ou un amas de galaxies) situé entre la source et l'observateur. Ceci peut générer plusieurs sortes d'effets : déplacement de l'image, amplification, déformation ou même la création d'images multiples. Refsdal (1964) a montré que si la source d'arrière-plan est variable, alors il est possible de déterminer une distance absolue et donc la constante de Hubble. En effet, si le quasar devient subitement plus brillant, l'observateur, du fait de la lentille gravitationnelle, le percevra à des instants différents pour les différentes images du quasar. Le décalage temporel ainsi mesuré dépend essentiellement de la distance des objets, i.e. de la lentille et de la source, ainsi que du potentiel gravitationnel. Si le décalage vers le rouge z peut être mesuré pour ces objets, alors la constante de Hubble peut être déterminée directement. La première lentille gravitationnelle fut découverte par Walsh et al. (1979) et depuis lors, la méthode a été appliquée à de nombreuses occasions (voir Fig. 2.1). La principale difficulté provient de la dégénérescence entre le potentiel gravitationnel considéré et la constante de Hubble.

Une autre façon de procéder est d'utiliser le rayonnement issu de quasars, dont les raies en absorption (forêt de Lyman α) sont le résultat d'un long processus d'absorption de la matière le long de la ligne de visée. La distribution de ces raies donne une information sur la distribution de matière et donc contiennent des informations cosmologiques intéressantes dont H_0 peut être déduite (Tytler et al. 2004; McDonald et al. 2005; Font-Ribera et al. 2013; Delubac et al. 2014). Cette méthode a donné récemment (Chávez et al. 2012) une valeur de H_0 très proche du résultat de (Freedman et al. 2012) (voir figure 2.1).

Enfin, depuis deux jours [4] nous savons qu'il existe une autre méthode de détermination de la constante de Hubble basée sur la détection des ondes gravitationnelles ! On ne parle plus de chandelles stellaires pour déterminer la constante de Hubble mais de sirènes car la fréquence des ondes gravitationnelles est audible. La détection des ondes gravitationnelles générées par GW170817 (la collision de deux étoiles à neutrons) par Virgo et Ligo le 17 Août 2017 (The LIGO Scientific Collaboration et al. 2017) ainsi que sa contrepartie électromagnétique ont permis de définir la galaxie hôte du phénomène, il s'agit de NGC 4993. La distance de la galaxie est déduite directement à partir du signal gravitationnel (42.9 ± 3.2 Mpc), tandis que le décalage vers le rouge est mesuré de la façon habituelle à partir des ondes électromagnétiques. La valeur obtenue est $H_0 = 70.0^{+12.0}_{-8.0}$ km s^{-1}Mpc^{-1} (Abbott et al. 2017) [5]. La précision obtenue (environ 15%) n'est pas suffisante pour résoudre la tension sur la constante de Hubble, mais ouvre une nouvelle voie fort intéressante.

L'ensemble des méthodes que nous avons vues sont décrites schématiquement dans la Figure 2.3.

4. Ces lignes ont été écrites le 18 octobre 2017

5. Cette valeur est fortement corrélée à l'inclinaison du système binaire. Guidorzi et al. (2017) ont affiné ce résultat à partir d'observations X et ont obtenu $H_0 = 75.5^{+14.0}_{-7.3}$ km s^{-1}Mpc^{-1}.

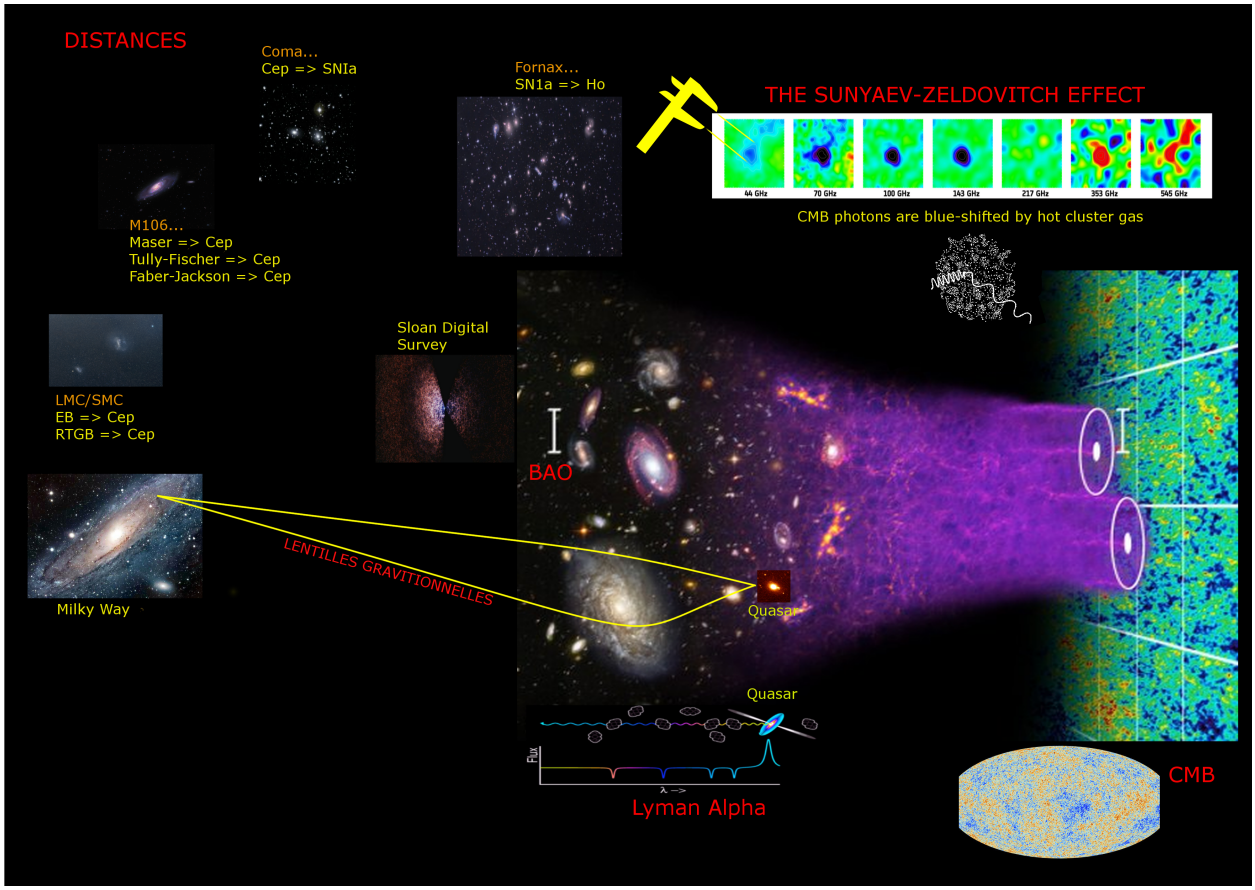


FIGURE 2.3 – Montage représentant les différentes méthodes de détermination de la constante de Hubble discutées dans ce manuscrit. Outre la méthode liée à l'étalonnage des échelles de distances dans l'univers basée essentiellement sur les Céphéides et supernova de type Ia (Sect. 2.1), on peut étudier le rayonnement de fond cosmologique (CMB), ou l'effet Sunyaev-Zeldovitch qui repose lui aussi sur les propriétés des photons du CMB (Sect. 2.2). D'autres méthodes reposent essentiellement sur les quasars, telles les lentilles gravitationnelles et les forêts Lyman α (Sect. 2.3). Enfin, les oscillations baryoniques acoustiques (BAO) dans le CMB fournissent une règle de référence à partir de laquelle les structures, et en particulier les amas de galaxies, vont se former à grande échelle. Ainsi, l'étude de la position des galaxies par les grands *surveys* photométriques et spectroscopiques (par exemple le "Sloan Digital Sky Survey" SDSS), permettent de contraindre H(z) (Reid et al. 2010, 2012).

2.4 Comment dépasser la tension sur H_0 ?

Parmi les différentes approches que nous avons vues pour contraindre la constante de Hubble H_0, il apparaît clairement sur la Fig. 2.1 que les plus précises reposent sur l'étalonnage des échelles de distance dans l'univers et sur le rayonnement de fond cosmologique (incluant la contrainte supplémentaire des oscillations acoustiques baryoniques, BAO). Les méthodes totalement indépendantes telles que S-Z, les lentilles gravitationnelles et les forêts de Lyman α restent relativement imprécises, et ne permettent pas, actuellement, de résoudre la tension obtenue entre les méthodes reposant sur les SNIa (Riess et al. 2016) et le satellite Planck (Planck Collaboration et al. 2016). Par ailleurs, concernant les distances, le chemin le plus robuste reste celui des Céphéides et des SNIa. Les mégamasers sont prometteurs, tandis que les méthodes liées aux propriétés des galaxies (Tully-Fisher et Faber-Jackson) donnent des résultats plutôt imprécis par rapport aux SNIa. Ainsi que peut-on dire à propos de cette tension ?

D'abord, le problème de la tension dépasse le "simple" problème de la mesure de la constante de Hubble H_0. Le modèle ΛCDM qui décrit l'univers dont la dynamique est décrite par les Equations 1.9 et 1.10 fait intervenir 6 paramètres. Mais finalement, lorsque l'on regarde les différentes façons de contraindre H_0, on s'aperçoit que le jeu de paramètres clefs peut se résumer, de manière simpliste, à Ω_k, Ω_m, w et H_0. L'approche CMB contraint *effectivement* ces 4 paramètres, et ce d'autant mieux si les BAO sont observées à bas décalage vers le rouge. Cependant, la contrainte est bien plus robuste pour les 2 premiers que pour les 2 derniers. Planck Collaboration et al. (2016) ont bien précisé dans leur papier : *"CMB experiments provide indirect and highly model-dependent estimates of the Hubble constant. It is therefore important to compare CMB estimates with direct estimates of H0, since any significant evidence of a tension could indicate the need for new physics."*. Cette dégénérescence explique-t-elle pourquoi les valeurs de H_0 décroissent progressivement lorsque l'on considère successivement WMAP-1 à 9, puis les résultats du satellite Planck ? Ces études donnent effectivement des tables de résultats avec de l'ordre de 10 à 20 paramètres ajustés, ce qui implique un travail complexe au niveau de la gestion de la dégénérescence entre les paramètres.

De l'autre côté, l'échafaudage des échelles basé sur les Céphéides et les SNIa permet avant tout de mesurer le taux d'expansion de l'univers maintenant, c'est à dire à $z = 0$, H_0, mais aussi en fonction de z (i.e. $H(z)$, et donc w) si des SNIa sont détectées suffisamment loin (autour de $z = 2$). Cette approche a elle aussi ses difficultés :

1. Les périodes des Céphéides de la Voie Lactée sont courtes ($P < 10$ jours) en comparaison des périodes des Céphéides dans les galaxies contenant des SNIa, et le recouvrement est finalement faible. Ainsi, la solution qui consiste à utiliser uniquement les parallaxes HST des Céphéides Galactiques pour contraindre la relation des SNIa paraît instable à elle seule (cf. l'annexe A de Efstathiou (2014)). La situation changera sensiblement avec l'arrivée de *Gaia* et la détermination de distances de Céphéides Galactiques à longues périodes.
2. Ensuite, la solution qui consiste à utiliser le LMC pour étalonner la relation *PL* est sensible à la métallicité, étant donné que le LMC a une métallicité un peu plus faible que les galaxies lointaines. Ainsi, la relation *PL* est-elle dépendante de la métallicité ? Si oui, comment cette correction doit-elle être prise en compte ? Sur la Figure 2.1 la valeur de H_0 déduite par Sandage et al. (2006), autour de 61 km/s/Mpc est significativement plus faible que celle de Riess et al. (2016). Cette incohérence est discutée dans la revue de Jackson (2015) et est attribuée à la façon de gérer l'impact de la métallicité sur la relation *PL* des Céphéides. Nous y reviendrons dans la Sect. 3.1.
3. Enfin, il a été noté récemment que le pic des SNIa peut être corrélé au taux de formation des étoiles (Rigault et al. 2015). Les auteurs avancent qu'un biais de +1.8km $s^{-1}Mpc^{-1}$ est possible dans la

valeur de H_0 déduite à partir des Céphéides et des SNIa.

Un dernier point à considérer est que l'approche CMB utilise d'abord des données (i.e. le rayonnement de fond cosmologique) dont les propriétés sont liées à l'époque où l'univers était beaucoup plus petit (i.e. à $z = 1100$), pour ensuite "remonter" en quelque sorte l'échafaudage des échelles de distances *en sens inverse*, et utiliser les BAO, et même les SNIa, ce qui fournit finalement une valeur de H_0. De manière opposée, la méthode liée à l'échafaudage des échelles de distances dans l'univers, basée sur les Céphéides et les SNIa, reposent sur des données à $z < 0.15$ et la mesure de H_0 est dans ce cas plus directe. Ainsi, comparer des valeurs de H_0 découlant de données obtenues d'une part à $z = 1100$ et, d'autre part, à $z < 0.15$ n'est pas forcément évident, et la tension pourrait tout aussi bien révéler la présence d'une "nouvelle physique" à prendre en compte.

Nous en arrivons donc à la conclusion que déterminer les distances dans l'univers à l'aide des Céphéides et des SNIa reste indispensable pour contraindre H_0 et, de manière indirecte, l'ensemble des paramètres du modèle ΛCDM. Les méthodes liées au CMB seul, bien que très puissantes, ne peuvent pas contraindre tous les paramètres du modèle sans introduire des dégénérescences. Aussi comment peut-on avancer et tenter de résoudre la "tension" liée à la détermination de H_0 ? Du côté de l'échafaudage des échelles de distances qui nous intéresse dans ce manuscrit, un des points clefs (outre les problématiques liées aux SNIa que nous n'aborderons pas ici) est d'étudier tout ce qui pourrait biaiser la relation *PL* des Céphéides, c'est-à-dire s'intéresser à toutes les propriétés physiques des Céphéides qui pourraient, à période égale, changer leur luminosité. Ainsi, Riess et al. (2016) indiquent que les plus grandes incertitudes sur H_0 proviennent pour 1.3% des distances des galaxies de référence (LMC, NGC 4258, M31), et pour 1.1% de notre connaissance de la relation PL : métallicité, dispersion, rougissement. En revanche, Riess et al. (2016) ne prennent pas en compte l'impact potentiel de l'environnement des Céphéides et de la binarité, qui peuvent, s'ils ne sont pas considérés, générer une dispersion dans la relation *PL*. Ainsi, les quatre principales questions sont en définitive :

1. La pente de la relation *PL* est-elle sensible à la métallicité et donc à la galaxie considérée ?
2. Quelle est la distance du LMC, de NGC 4258, de M31, et d'autres galaxies contenant des Céphéides, et donc le point-zéro de la relation *PL* ? Ce point-zéro est-il sensible à la métallicité ?
3. La dispersion de la relation PL peut-elle être améliorée dans l'infrarouge en considérant l'impact de l'environnement et de la binarité ?
4. Un autre point mérite l'attention. Serait-il possible de court-circuiter la relation PL des Céphéides et d'utiliser directement les méthodes dites de Baade-Wesselink pour déterminer la distance des Céphéides extragalactiques, de manière individuelle, sans passer par une relation statistique ?

Les points 1/ et 2/ sont des objectifs majeurs du projet international Araucaria [6] de détermination de distance dans le groupe local. Les points 3/ et 4/ sont étudiés dans le cadre de l'ANR "UnlockCepheids". Nous aborderons successivement ces quatres points dans les sections du chapitre suivant.

6. https://araucaria.camk.edu.pl/ ; https://en.wikipedia.org/wiki/Araucaria_Project

Chapitre 3

La relation *PL* des Céphéides et les distances dans le Groupe Local

Le groupe local est constitué d'environ 100 galaxies dans un volume d'environ 3 Mpc (McConnachie 2012). Les deux membres principaux de ce groupe sont la galaxie d'Andromède (M31) et la Voie Lactée, chacune d'elles possédant son propre système de galaxies satellites (voir Fig. 3.1a). Autour de la Voie Lactée, gravitent principalement les deux nuages de Magellan et les galaxies naines du Grand Chien, du Sagittaire, de la Petite Ourse, du Dragon, de la Carène, du Sextant, du Sculpteur, du Fourneau, du Lion I, du Lion II et du Toucan. Le système d'Andromède comprend M32, M33, M110, NGC 147, NGC 185, Andromeda I, Andromeda II, Andromeda III et Andromeda IV. La galaxie du Triangle (M33) est la troisième plus grande galaxie du groupe local. Les autres membres du groupe local sont gravitationnellement indépendants de ces larges sous-groupes. Le filament du Sculpteur (voir Fig. 3.1b), dont le membre le plus brillant et le plus massif est la galaxie du sculpteur située à 3.3 Mpc (à ne pas confondre avec la galaxie naine du Sculpteur qui est beaucoup plus proche), regroupe une vingtaine de galaxies situées au voisinage du pôle galactique sud, dans la constellation du Sculpteur (Karachentsev et al. 2003). La Table 3.1 est une compilation de plusieurs listes et de références qui indique, pour chaque galaxie du groupe local et du filament du sculpteur, une estimation de sa distance récente (jusqu'à 6.5 Mpc), la méthode utilisée pour déterminer cette distance, ainsi que sa métallicité *moyenne*, exprimée en [Fe/H]. A cette liste nous ajoutons M83 et NGC5253 liées gravitationnellement, ainsi que M82. Ces trois galaxies sont dirigées vers le centre de l'amas de la Vierge, un grand amas de galaxies situé entre 15 et 22 Mpc (voir Fig. 3.1b) et dans lequel on trouve effectivement des galaxies hôtes de SNIa. Le site web [1] du CBAT (*Central Bureau for Astronomical Telegrams*) liste l'ensemble des 6500 supernovae observées depuis 1885. Parmi celles-ci, on peut extraire environ 2800 SNIa dont la première référencée remonte à 1937. Parmi ces SNIa, quelles ont été les plus proches ? Historiquement d'abord (i.e. avant 1037), quatre ont été observées dans la Voie Lactée : (a) SN185, observée par les Chinois en 185 après JC et étudiée récemment par Zhao et al. (2006), (b) SN1006, également observée par les Chinois et étudiée par Winkler et al. (2003), (c) SN1572, observée par Tycho Brahé et (d) SN1604, observée par Kepler. Après 1937, les SNIa les plus proches observées sont SN1972E, SN2014J, SN1983N, et SN1937C, toutes situées à moins de 6.5 Mpc et repérées dans la Tab. 3.1. Il est à noter que SN1972E est le prototype des SNIa pour avoir été observée pendant 1 an (Ardeberg & de Groot 1973). Cependant, Riess et al. (2016) indiquent qu'une SNIa pourra être utilisée comme étalon de distance si elle répond à différents critères : 1) sa mesure photométrique doit être moderne, c'est à dire basée sur

1. http ://www.cbat.eps.harvard.edu/lists/Supernovae.html

des mesures CCD, 2) le début des observations doit commencer avant le maximum de brillance, 3) son rougissement doit être faible ($A_V < 0.5$ mag), 4) elle doit être typique d'un point de vue spectroscopique, et enfin 5) la galaxie hôte doit nécessairement contenir des Céphéides observées par le HST. Ce dernier point implique de considérer des galaxies de type Sa à Sd, dont la distance est inférieure à 40 Mpc, dont l'inclinaison est inférieure à 75° et dont la taille apparente est supérieure à 1'. Riess et al. (2016) ont trouvé seulement 19 SNIa qui répondent strictement à ces critères, indiquées dans la Tab. 3.1. J'ai rajouté dans la table des estimations de distance récentes de ces galaxies hôtes de SNIa, ainsi que leur métallicité (lorsque disponible). Ces SNIa sont d'une extrême importance vu qu'elle serviront à étalonner la relation des SNIa, qui elle contient plusieurs centaines de SNIa.

Le projet international et à long terme Araucaria[2] consiste à renforcer l'étalonnage des échelles de distance à l'aide de différents estimateurs : Céphéides, RR Lyrae, supergéantes rouges ou bleues et plus récemment, les binaires à éclipses. L'idée est de déterminer avec soin la distance d'un grand nombre de galaxies proches, dans le groupe local et dans le Sculpteur, et de tester la dépendance de ces estimateurs avec les paramètres des galaxies hôtes (métallicité, âge des populations stellaires). Ainsi, dans la Tab. 3.1, j'ai identifié les galaxies pour lesquelles le projet Araucaria a apporté une contribution significative. Les valeurs de distance indiquées correspondent alors à la moyenne des différentes estimations de distance issues de différentes méthodes utilisées dans le cadre du projet Araucaria, tandis que l'incertitude correspond à la dispersion des estimations. Le détail des distances obtenues dans le cadre du projet Araucaria sont indiquées dans la Table C.1 et représentées sous forme graphique en fonction de l'année de publication dans la Fig. 3.2. La Fig. 3.3 montre la distance des galaxies de la Table 3.1, en fonction de leur métallicité [Fe/H] (pour les galaxies du Groupe Local et du Sculpteur) et [O/H] pour les galaxies hôtes de SNIa. J'indique également sur cette figure les galaxies qui ont été étudiées jusqu'à présent dans le cadre du projet Araucaria. Cette figure montre clairement un point important : les galaxies hôtes de SNIa ont une métallicité très proche de celle de la Voie Lactée, alors que le LMC et le SMC sont clairement moins riches en métaux, ainsi que la majorité des galaxies situées à moins de 6.5 Mpc.

Ainsi, il est tentant de conclure qu'avec *Gaia*, il n'y aura pas lieu de s'inquiéter de l'impact de la métallicité sur la relation *PL* dans la mesure où la Voie Lactée et les galaxies hôtes de supernovae de type Ia ont environ la même abondance en métaux. Cependant, ce n'est pas si simple, car il est très difficile de mesurer la métallicité des Céphéides situées dans les galaxies hôtes de supernovae. Cette dernière est effectivement déduite *de manière indirecte* à partir de l'abondance de l'oxygène par rapport à l'hydrogène [O/H] dans les régions HII (zone de formation d'étoiles), et on fait ensuite l'hypothèse que ces régions HII et les Céphéides dans leur voisinage ont la même métallicité, ce qui n'est pas forcément le cas. En effet, l'abondance [O/H] est utilisée comme un diagnostic de l'évolution des galaxies du fait d'une relation entre l'abondance [O/H] des régions HII et la masse des galaxies (Lequeux et al. 1979). Cependant, cette relation n'est pas compatible pour les galaxies les plus proches, la Voie Lactée, le SMC et le LMC (Tremonti et al. 2004) probablement du fait de raies en émission H et O difficiles à étalonner dans les régions HII des galaxies lointaines (Kewley & Ellison 2008) avec des écarts de 0.9 dex selon les méthodes utilisées. Ainsi, la métallicité des galaxies hôtes de supernova n'est pas encore clairement établie. Par ailleurs, il est intéressant de noter que Rafelski et al. (2014), à une autre échelle, trouvent une relation (un peu dispersée certes) entre la métallicité et le décalage vers le rouge (une relation Zz), et ce jusqu'à environ $z = 6$. C'est pourquoi, R. Kudritzki, F. Bresolin et M. Urbaneja de l'équipe Araucaria visent à étalonner la relation [O/H]-masse des galaxies en utilisant les supergéantes bleues et rouges. Ces étoiles sont effectivement suffisamment brillantes

2. voir https ://araucaria.camk.edu.pl/ pour les objectifs, les participants, et la liste de publications. Je suis membre du projet Araucaria depuis 2008, date de mon arrivée à Concepcion du Chili pour mon post-doc.

pour une détermination spectroscopique de leur abondance. La méthode a été appliquée aux supergéantes de NGC 300 à 1.9 Mpc (Kudritzki et al. 2008) et NGC 3621 à 6.5 Mpc (Kudritzki et al. 2014). Pour aller plus loin, une méthode a été développée, s'appuyant non pas sur une supergéante individuelle, mais sur un nuage d'étoiles supergéantes : M83 à 4.3 Mpc (Gazak et al. 2014) et les galaxies des Antennes (NGC 4038 / NGC 4039) à 20 Mpc (Lardo et al. 2015). Des comparaisons entre l'abondance des supergéantes bleues et rouges, ainsi que les régions HII sont également en cours (Bresolin et al. 2016; Davies et al. 2017), et un projet SSC ("Super Stars Clusters") se met actuellement en place pour appliquer ces méthodes aux galaxies hôtes de SNIa utilisées dans le cadre du projet SHOES. Il est également important d'avoir à l'esprit que les supergéantes sont utilisées comme indicateurs de distance. Les rouges ont des phases d'évolution reconnaissables (où elles passent plus de temps), "red tip of giant branch" ou "red clump stars" (voir Table 3.1 pour des références récentes) ce qui en fait de bons indicateurs de distances (magnitude absolue visible comprise entre -8 et -11). Concernant les supergéantes bleues, après leur sortie de la séquence principale, elles suivent une ligne de magnitude absolue relativement constante pour une masse donnée. Il existe ainsi une relation entre la gravité de surface et la luminosité ("Flux Weighted Gravity - Luminosity Relationship (FGLR)", (Kudritzki et al. 2003)). Les supergéantes rouges permettent d'atteindre des distances de l'ordre de 30 Mpc (Jang & Lee 2015; Jang et al. 2017) tandis que les bleues (moins brillantes) permettent d'atteindre environ 6.5 Mpc. Dans ce contexte en permanente évolution, il semble ainsi toujours pertinent de se poser la question de l'impact de la métallicité sur la relation *PL*.

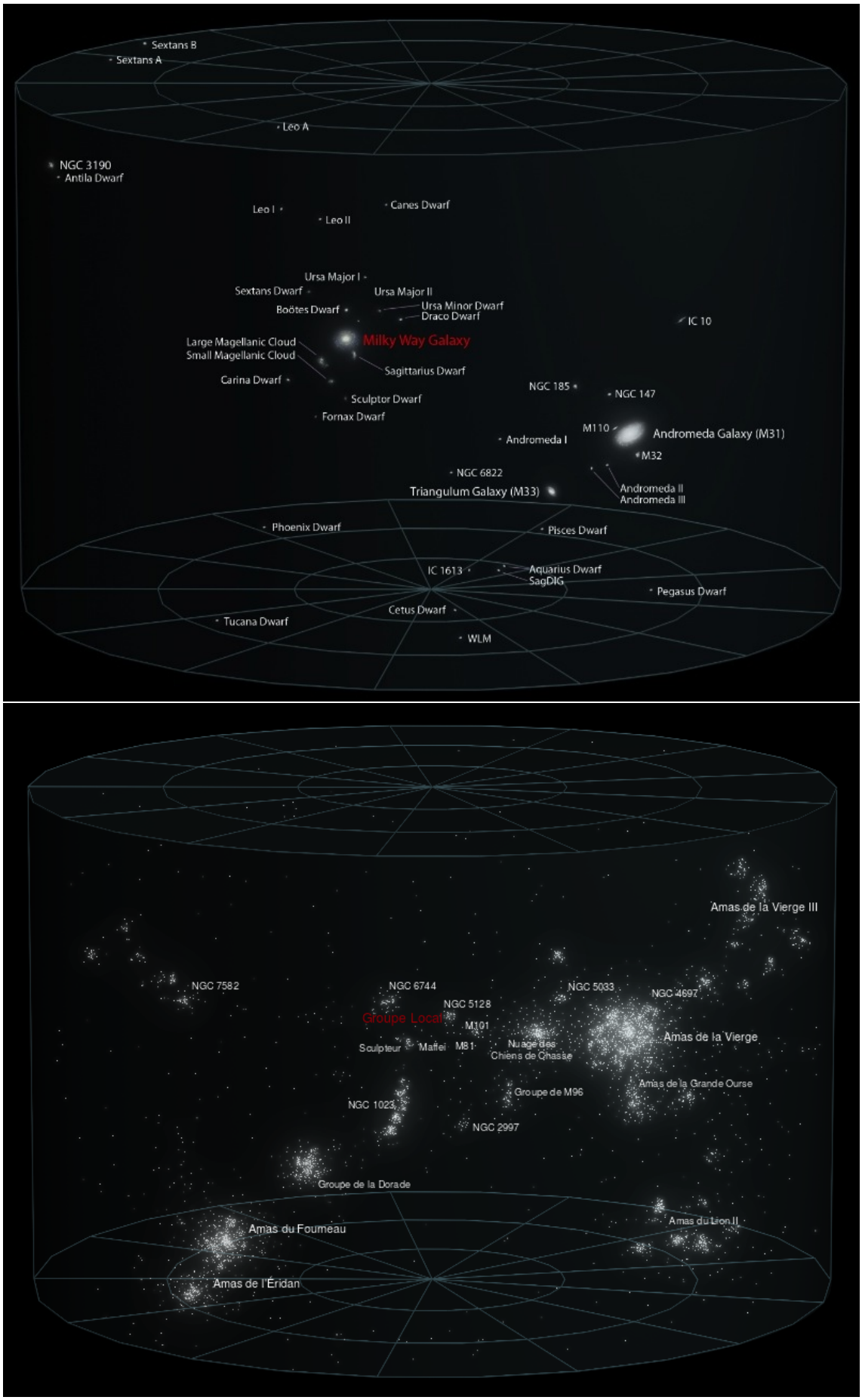


FIGURE 3.1 – Cartographie des galaxies du groupe local (en haut) et de l'Amas de la Vierge (en bas).

TABLE 3.1 – Liste des galaxies issues de McConnachie (2012) pour le groupe local, de Karachentsev et al. (2003) pour le filament du sculpteur, et de Riess et al. (2016) pour les galaxies hôtes de SNIa. La liste des SNIa a été également complétée à partir du site web du CBAT. [Gr] indique le groupe auquel la galaxie est gravitationnellement liée : [G] = Galaxy/Voie Lactée, [A] = M31, [L] = Local Group, [N] = nearby neighbors. [Type] indique le type de la galaxie : [S] = Spiral, [dSph] = dwarf Spheroidal, [Irr] = Irregular, [dIrr] = dwarf Irregular. La distance de la galaxie (D) est indiquée en kpc, ainsi que la méthode utilisée et la référence récente associée : rcs (Red Clump Stars), msf (Main Sequence Fitting), rtgb (Red Tip of Giant Branch), hbf (Horizontal Branch Fitting), rrl (RR Lyrae stars), tf (Tully-Fisher relation), cep (Cepheids), sbf (Surface Brightness Fluctuations), redshift pour les distances déduites à partir du décalage vers le rouge calculé sur le site web suivant https ://dso-browser.com/. Les métallicités moyennes des galaxies du Groupe Local sont par défaut issues de McConnachie (2012) . On trouvera les méthodes utilisées, ainsi que les références associées dans ce papier. Pour les autres galaxies, des recherches au cas par cas ont été nécessaires. Toutes les galaxies dont la distance est inférieure à 6410 kpc ont des métallicités exprimées en [Fe/H] (sauf si une note indique le contraire). Pour les galaxies avec $d > 6410$ kpc, c'est à dire les galaxies hôtes de SNIa, il n'est pas possible de déduire la métallicité à partir de Céphéides individuelles. Les déterminations de métallicité sont basées sur l'étude des régions HII et donne accès à l'abondance de l'oxygène par rapport à l'hydrogène, et sont ainsi exprimées en 12+[O/H]. Pour la cohérence de la Table, j'ai fait une conversion pour ces galaxies en [O/H] en utilisant 12 + log(O/H) = 8.69 pour le Soleil. On fait alors l'hypothèse que [O/H] est équivalent ou relativement proche de [Fe/H], ce qui n'est pas forcément le cas.

Name	Gr.	Type	D kpc		Ref	[Fe/H] [Sun]	Ref	SNIa
La Voie Lactée	G	S(B)bc	$0_{\pm 0}$			0	0	
Canis Major dSph	G	dSph	$7_{\pm 1}$	rcs	Bellazzini et al. (2006)	$-0.50_{\pm 0.20}$	McConnachie (2012)	
Segue (I)	G	dSph	$23_{\pm 2}$	msf	Belokurov et al. (2007)	$-2.72_{\pm 0.40}$	McConnachie (2012)	
Sagittarius dSph	G	dSph	$26_{\pm 2}$	rtgb	Monaco et al. (2004)	$-0.40_{\pm 0.20}$	McConnachie (2012)	
Ursa Major II	G	dSph	$32_{\pm 4}$	msf	Zucker et al. (2006)	$-2.47_{\pm 0.06}$	McConnachie (2012)	
Segue II	G	dSph	$35_{\pm 2}$	hbf	Belokurov et al. (2009)	$-2.00_{\pm 0.25}$	McConnachie (2012)	
Willman 1	G	dSph	$38_{\pm 7}$	msf	Willman et al. (2006)	-2.10	McConnachie (2012)	
Bootes II	G	dSph	$42_{\pm 1}$	msf	Walsh et al. (2008)	$-1.79_{\pm 0.05}$	McConnachie (2012)	
Coma Berenices	G	dSph	$44_{\pm 4}$	msf	Belokurov et al. (2007)	$-2.60_{\pm 0.05}$	McConnachie (2012)	
Bootes III	G	dSph ?	$47_{\pm 2}$	msf	Grillmair (2009)	$-2.10_{\pm 0.20}$	McConnachie (2012)	
LMC	G	Irr	$51_{\pm 2}$	*cf.* Tab. C.1	Araucaria Project	$-0.34_{\pm 0.15}$	Luck et al. (1998)	
SMC	G	dIrr	$64_{\pm 4}$	*cf.* Tab. C.1	Araucaria Project	$-0.68_{\pm 0.13}$	Luck et al. (1998)	
Bootes (I)	G	dSph	$66_{\pm 2}$	rrl	Dall'Ora et al. (2006)	$-2.55_{\pm 0.11}$	McConnachie (2012)	
Draco	G	dSph	$76_{\pm 6}$	rrl	Bonanos et al. (2004)	$-1.93_{\pm 0.01}$	McConnachie (2012)	
Ursa Minor	G	dSph	$76_{\pm 3}$	hbf	Carrera et al. (2002)	$-2.13_{\pm 0.01}$	McConnachie (2012)	
Sculptor	G	dSph	$86_{\pm 6}$	*cf.* Tab. C.1	Araucaria Project	$-1.68_{\pm 0.01}$	McConnachie (2012)	
Sextans (I)	G	dSph	$86_{\pm 4}$	sfh	Lee et al. (2009)	$-1.93_{\pm 0.01}$	McConnachie (2012)	
Ursa Major (I)	G	dSph	$97_{\pm 4}$	hbf	Okamoto et al. (2008)	$-2.18_{\pm 0.04}$	McConnachie (2012)	
Carina	G	dSph	$105_{\pm 6}$	*cf.* Tab. C.1	Araucaria Project	$-1.72_{\pm 0.01}$	McConnachie (2012)	
Hercules	G	dSph	$147_{\pm 8}$	hbf	Adén et al. (2009)	$-2.41_{\pm 0.04}$	McConnachie (2012)	
Fornax	G	dSph	$147_{\pm 12}$	*cf.* Tab. C.1	Araucaria Project	$-0.99_{\pm 0.01}$	McConnachie (2012)	
Leo IV	G	dSph	$154_{\pm 6}$	rrl/dscu	Moretti et al. (2009)	$-2.54_{\pm 0.07}$	McConnachie (2012)	
Canes Venatici II	G	dSph	$160_{\pm 4}$	rrl	Greco et al. (2008)	$-2.21_{\pm 0.05}$	McConnachie (2012)	
Leo V	G	dSph	$178_{\pm 10}$	hbf	Belokurov et al. (2008)	$-2.00_{\pm 0.20}$	McConnachie (2012)	
Pisces II	G	dSph	182	hbf	Belokurov et al. (2010)	-1.90	McConnachie (2012)	
Canes Venatici (I)	G	dSph	$218_{\pm 10}$	hbf	Martin et al. (2008)	$-1.98_{\pm 0.01}$	McConnachie (2012)	
Leo II	G	dSph	$233_{\pm 14}$	rtgb	Bellazzini et al. (2005)	$-1.62_{\pm 0.01}$	McConnachie (2012)	
Leo I	G,L	dSph	$254_{\pm 15}$	rtgb	Bellazzini et al. (2004)	$-1.43_{\pm 0.01}$	McConnachie (2012)	
Phoenix	L,G	dIrr/dSph	$415_{\pm 19}$	rtgb	Hidalgo et al. (2009)	$-1.37_{\pm 0.20}$	McConnachie (2012)	
Leo T	L,G	dIrr/dSph	$417_{\pm 19}$	hbf	Irwin et al. (2007)	$-1.99_{\pm 0.05}$	McConnachie (2012)	
NGC 6822 / Barnard	L,G	dIrr	$459_{\pm 17}$	*cf.* Tab. C.1	Araucaria Project	-0.5	Hosek et al. (2014) (a)	
Andromeda XVI	A,L	dSph	$525_{\pm 48}$	rtgb	Ibata et al. (2007)	$-2.10_{\pm 0.20}$	McConnachie (2012)	
Andromeda XXIV	A	dSph	$600_{\pm 33}$	hbf	Richardson et al. (2011)	$-1.80_{\pm 0.20}$	McConnachie (2012)	
NGC 185	A	dE/dSph	$617_{\pm 26}$	rtgb	McConnachie et al. (2005)	$-1.30_{\pm 0.10}$	McConnachie (2012)	
Andromeda XV	A	dSph	$631_{\pm 58}$	rtgb	Ibata et al. (2007)	$-1.80_{\pm 0.20}$	McConnachie (2012)	
Andromeda II	A	dSph	$652_{\pm 18}$	rtgb	McConnachie et al. (2005)	$-1.64_{\pm 0.04}$	McConnachie (2012)	
Andromeda XXVIII	A,L	dSph ?	$661_{\pm 152}$	rtgb	Slater et al. (2011)		McConnachie (2012)	
NGC 147	A	dE/dSph	$676_{\pm 28}$	rtgb	McConnachie et al. (2005)	$-1.10_{\pm 0.10}$	McConnachie (2012)	
Andromeda X	A	dSph	$701_{\pm 68}$	hbf	Zucker et al. (2007)	$-1.93_{\pm 0.11}$	McConnachie (2012)	
Andromeda XXIX	A	dSph	$731_{\pm 74}$	rtgb	Bell et al. (2011)	-1.80	McConnachie (2012)	
Andromeda XIV	A,L	dSph	$735_{\pm 112}$	rtgb	Majewski et al. (2007)	$-2.26_{\pm 0.05}$	McConnachie (2012)	
Andromeda I	A	dSph	$745_{\pm 24}$	rtgb	McConnachie et al. (2005)	$-1.45_{\pm 0.04}$	McConnachie (2012)	
Andromeda III	A	dSph	$748_{\pm 24}$	rtgb	McConnachie et al. (2005)	$-1.78_{\pm 0.04}$	McConnachie (2012)	
IC 1613	L	dIrr	$755_{\pm 42}$	*cf.* Tab. C.1	Araucaria Project	-0.79	Hosek et al. (2014) (a)	

TABLE 3.2 – Suite du Tableau.

Name	Gr.	Type	D kpc		Ref	[Fe/H] [Sun]	Ref	SNIa
Cetus	L	dSph	$755_{\pm 24}$	rtgb	McConnachie et al. (2005)	$-1.90_{\pm 0.10}$	McConnachie (2012)	
Andromeda XI	A	dSph	$759_{\pm 175}$	rtgb	Collins et al. (2010)	$-2.00_{\pm 0.20}$	McConnachie (2012)	
Andromeda XXVI	A	dSph	$762_{\pm 42}$	rtgb	Richardson et al. (2011)	$-1.90_{\pm 0.20}$	McConnachie (2012)	
Andromeda VII	A	dSph	$762_{\pm 35}$	rtgb	McConnachie et al. (2005)	$-1.40_{\pm 0.30}$	McConnachie (2012)	
Andromeda IX	A	dSph	$766_{\pm 25}$	rtgb	McConnachie et al. (2005)	$-2.20_{\pm 0.20}$	McConnachie (2012)	
Andromeda XXIII	A	dSph	$769_{\pm 46}$	rtgb	Richardson et al. (2011)	$-1.80_{\pm 0.20}$	McConnachie (2012)	
LGS 3 (b)	A	dIrr/dSph	$769_{\pm 25}$	rtgb	McConnachie et al. (2005)	$-2.10_{\pm 0.22}$	McConnachie (2012)	
Andromeda V	A	dSph	$773_{\pm 28}$	rtgb	McConnachie et al. (2005)	$-1.60_{\pm 0.30}$	McConnachie (2012)	
Andromeda /M31	A	Sb	$783_{\pm 25}$	rtgb	McConnachie et al. (2005)	-0.04	Hosek et al. (2014) (a)	
Andromeda VI	A	dSph	$783_{\pm 25}$	rtgb	McConnachie et al. (2005)	$-1.30_{\pm 0.14}$	McConnachie (2012)	
Andromeda XVII	A	dSph	$794_{\pm 37}$	rtgb	Irwin et al. (2008)	$-1.90_{\pm 0.20}$	McConnachie (2012)	
Andromeda XXII	A	dSph	794	rtgb	Martin et al. (2009)	-1.80	McConnachie (2012)	
IC 10	A	dIrr	$794_{\pm 44}$	tf	Tully et al. (2006)	-1.28	McConnachie (2012)	
Leo A	L	dIrr	$798_{\pm 44}$	rrl	Dolphin et al. (2002)	$-1.40_{\pm 0.20}$	McConnachie (2012)	
Andromeda XX	A	dSph	$802_{\pm 273}$	rtgb	McConnachie et al. (2008)	$-1.50_{\pm 0.10}$	McConnachie (2012)	
M32	A	cE	$805_{\pm 78}$	rrl	Fiorentino et al. (2010)	-0.25	McConnachie (2012)	
Triangulum / M33	A	Sc	$809_{\pm 22}$	*cf.* Tab. C.1	Araucaria Project	-0.15	Hosek et al. (2014) (a)	
Andromeda XXV	A	dSph	$813_{\pm 45}$	rtgb	Richardson et al. (2011)	$-1.80_{\pm 0.20}$	McConnachie (2012)	
NGC 205	A	dE/dSph	$824_{\pm 27}$	rtgb	McConnachie et al. (2005)	$-0.80_{\pm 0.20}$	McConnachie (2012)	
Andromeda XXVII	A	dSph	$828_{\pm 46}$	rtgb	Richardson et al. (2011)	$-1.70_{\pm 0.20}$	McConnachie (2012)	
Andromeda XXI	A	dSph	$859_{\pm 51}$	rtgb	Martin et al. (2009)	$-1.80_{\pm 0.20}$	McConnachie (2012)	
Andromeda XII	A,L	dSph	$871_{\pm 120}$	rtgb	Collins et al. (2010)	$-2.10_{\pm 0.20}$	McConnachie (2012)	
Tucana	L	dSph	$887_{\pm 49}$	rrl	Bernard et al. (2009)	$-1.95_{\pm 0.15}$	McConnachie (2012)	
Andromeda XIII	A	dSph	$912_{\pm 42}$	rtgb	Collins et al. (2010)	$-1.90_{\pm 0.20}$	McConnachie (2012)	
Pegasus dIrr	L,A	dIrr/dSph	$920_{\pm 30}$	rtgb	McConnachie et al. (2005)	$-1.40_{\pm 0.20}$	McConnachie (2012)	
Andromeda XIX	A	dSph	$933_{\pm 56}$	rtgb	McConnachie et al. (2008)	$-1.90_{\pm 0.10}$	McConnachie (2012)	
WLM (c)	L	dIrr	$933_{\pm 34}$	*cf.* Tab. C.1	Araucaria Project	-0.87	Hosek et al. (2014) (a)	
Sagittarius dIrr	L	dIrr	$1067_{\pm 88}$	rtgb	Momany et al. (2002)	$-2.10_{\pm 0.20}$	McConnachie (2012)	
Aquarius	L	dIrr/dSph	$1072_{\pm 39}$	rtgb	McConnachie et al. (2005)	$-1.30_{\pm 0.20}$	McConnachie (2012)	
NGC 3109	N	dIrr	$1300_{\pm 48}$	*cf.* Tab. C.1	Araucaria Project	$-0.67_{\pm 0.13}$	Hosek et al. (2014) (a)	
Antlia	N	dIrr	$1349_{\pm 62}$	tf	Tully et al. (2006)	$-1.60_{\pm 0.10}$	McConnachie (2012)	
Andromeda XVIII	L	dSph	$1355_{\pm 81}$	rtgb	McConnachie et al. (2008)	$-1.80_{\pm 0.10}$	McConnachie (2012)	
UGC 4879	L	dIrr/dSph	$1361_{\pm 25}$	rtgb	Kopylov et al. (2008)	$-1.50_{\pm 0.20}$	McConnachie (2012)	
Sextans B	N	dIrr	$1426_{\pm 20}$	tf	Tully et al. (2006)			
Sextans A	N	dIrr	$1432_{\pm 53}$	tf	Tully et al. (2006)	-1.00	Hosek et al. (2014) (a)	
HIZSS 3(A)	N	(d)Irr ?	$1675_{\pm 108}$	rtgb	Silva et al. (2005)			
HIZSS 3B	N	(d)Irr ?	$1675_{\pm 108}$	rtgb	Silva et al. (2005)			
KKR 25	N	dIrr/dSph	$1905_{\pm 61}$	tf	Tully et al. (2006)	$-2.10_{\pm 0.30}$	McConnachie (2012)	
E410-005 / KK3	S	?	1920	rtgb	Karachentsev et al. (2000)			
E294-010	S	?	1920	rtgb	Karachentsev et al. (2002)			
ESO 410 / G 005	N	dIrr/dSph	$1923_{\pm 35}$	tf	Tully et al. (2006)	$-1.93_{\pm 0.20}$	McConnachie (2012)	
NGC 55	S	Irr	$1932_{\pm 107}$	*cf.* Tab. C.1	Araucaria Project	$-0.37_{\pm 0.03}$	Kudritzki et al. (2016)	
IC 5152	S	dIrr	$1950_{\pm 45}$	tf	Tully et al. (2006)			
ESO 294 / G 010	N	dIrr/dSph	$2032_{\pm 37}$	tf	Tully et al. (2006)	$-1.48_{\pm 0.17}$	McConnachie (2012)	
NGC 300	N	Sc	$2080_{\pm 57}$	*cf.* Tab. C.1	Araucaria Project	-0.36	Kudritzki et al. (2008)	
GR 8	N	dIrr	$2178_{\pm 120}$	tf	Tully et al. (2006)			
KKR 3	N	dIrr	$2188_{\pm 121}$	tf	Tully et al. (2006)	$-2.02_{\pm 0.25}$	McConnachie (2012)	
UKS 2323-326	N	dIrr	$2208_{\pm 92}$	tf	Tully et al. (2006)	$-1.68_{\pm 0.19}$	McConnachie (2012)	
UA438	S		2230	rtgb	Karachentsev et al. (2002)			
IC 3104	N	dIrr	$2270_{\pm 188}$	rtgb	Karachentsev et al. (2002)			
UGC 9128	N	dIrr	$2291_{\pm 42}$	tf	Tully et al. (2006)	$-2.33_{\pm 0.24}$	McConnachie (2012)	
IC 4662	N	dIrr	$2443_{\pm 191}$	rtgb	Karachentsev et al. (2006)	$-1.34_{\pm 0.13}$	McConnachie (2012)	
KKH 98	N	dIrr	$2523_{\pm 105}$	tf	Tully et al. (2006)	$-1.94_{\pm 0.25}$	McConnachie (2012)	
UGC 8508	N	dIrr	$2582_{\pm 36}$	rtgb	Dalcanton et al. (2009)	$-1.91_{\pm 0.19}$	McConnachie (2012)	
DDO 125	N	dIrr	$2582_{\pm 59}$	rtgb	Dalcanton et al. (2009)	$-1.73_{\pm 0.17}$	McConnachie (2012)	
KKH 86	N	dIrr	$2582_{\pm 190}$	rtgb	Dalcanton et al. (2009)	$-2.33_{\pm 0.29}$	McConnachie (2012)	
DDO 99	N	dIrr	$2594_{\pm 167}$	rtgb	Dalcanton et al. (2009)	$-2.13_{\pm 0.22}$	McConnachie (2012)	
DDO 190	N	dIrr	$2793_{\pm 39}$	rtgb	Dalcanton et al. (2009)	$-2.00_{\pm 0.08}$	McConnachie (2012)	
NGC 4163	N	dIrr	$2858_{\pm 39}$	rtgb	Dalcanton et al. (2009)	$-1.65_{\pm 0.15}$	McConnachie (2012)	
DDO 113	N	dIrr	$2951_{\pm 82}$	rtgb	Dalcanton et al. (2009)	$-1.99_{\pm 0.21}$	McConnachie (2012)	
UGCA 86	N	dIrr	$2965_{\pm 232}$	rtgb	Karachentsev et al. (2006)			
DDO6	S	dIrr	3340	rtgb	Karachentsev et al. (2003)	-2.08	Karachentsev et al. (2003)	
KDG2,E540-030	S	dSph	3400	rtgb	Karachentsev et al. (2003)	-1.61	Karachentsev et al. (2003)	
M83	M83	S	$3420_{\pm 250}$	cep	Ferrarese et al. (2007)	0.30	Calzetti et al. (1999)	SN1983N (j)
E540-032 / FG24	S	dSph/dIrr	3420	rtgb	Karachentsev et al. (2003)	-1.45	Karachentsev et al. (2003)	
M81	M81	S	$3500_{\pm 200}$	*cf.* Tab. C.1	Araucaria Project	$0.06_{\pm 0.15}$ (d)	Kennicutt et al. (1998)	
M82 / NGC 3034	M81	Irr	3680, 981595	cep	Shappee & Stanek (2011)	$-1.15_{\pm 0.11}$ (e)	Durrell et al. (2010)	SN 2014J (j)
NGC 7793	S	S	3910	*cf.* Tab. C.1	Araucaria Project	-1.22	Karachentsev et al. (2003)	
NGC 253	S	Sc	3940	rtgb	Karachentsev et al. (2003)	-1.12	Karachentsev et al. (2003)	
N625	S	Irr	4070	tf	Tully et al. (2006)			
E349-031 / SDIG	S	dG	4100	tf	Tully et al. (2006)			
NGC 247	S	S	4100	*cf.* Tab. C.1	Araucaria Project	-1.0	García-Varela et al. (2008)	
NGC 5253	M83	dIrr ?	$4092_{\pm 115}$	cep	Sandage et al. (1994)	$-0.54(d)$	Kennicutt et al. (1998)	SN1972E (j)
Sc22	S	dSph	4210	rtgb	Karachentsev et al. (2003)	-1.51	Karachentsev et al. (2003)	
UA442	S	Im	4270	rtgb	Karachentsev et al. (2003)	-2.40	Karachentsev et al. (2003)	
E245-05	S	Irr	4430	rtgb	Karachentsev et al. (2003)	-2.08	Karachentsev et al. (2003)	
IC 4182	S	S	$4943_{\pm 185}$	cep	Sandage et al. (1992)	-1.96	Karachentsev et al. (2003)	SN1937C (j)
DDO226	S	dIrr	4920	sbf	Jerjen et al. (1998)			
NGC 59	S	S	5300	sbf	Jerjen et al. (1998)			
E149-003	S	?	6400	tf	Tully et al. (2006)			

TABLE 3.3 – Suite du Tableau.

Name	Gr.	Type	D kpc		Ref	[Fe/H] [Sun]	Ref	SNIa
M101			$6420_{\pm 550}$	cep	Shappee & Stanek (2011)	−0.05	Shappee & Stanek (2011)	SN2011fe
M66 (f) (g)		S	$10560_{\pm 600}$	rtgb	Lee & Jang (2013)			SN 1989B (j)
M96 (g)		S	$10710_{\pm 610}$	rtgb	Lee & Jang (2013)			SN 1998bu (j)
NGC 3972		S	12260	redshift	DSOB (i)			SN2011By
NGC 4536		S	14900	redshift	DSOB (i)	$0.16_{\pm 0.20}$	Macri et al. (2006)	SN1981B
NGC 3447		S	15000	redshift	DSOB (i)			SN2012ht
NGC 4526		S	15600	redshift	DSOB (i)			SN1994D (k)
NGC 1448		S	16260	redshift	DSOB (i)			SN2001el
NGC 4424		S	16260	redshift	DSOB (i)			SN2012cg
NGC 7250		Irr	16260	redshift	DSOB (i)			SN2013dy
NGC 1365		S	$18300_{\pm 1700}$	cep	Silbermann et al. (1999)	$0.27_{\pm 0.20}$	Kennicutt et al. (1998)	SN2012fr
Fornax A / NGC 1316		E	$20800_{\pm 500}$	sbf	Cantiello et al. (2013)			SN1980N, SN2006dd, SN1981D (k)
NGC 4753		S	19900	redshift	DSOB (i)	$0.07_{\pm 0.05}$	Macri et al. (2006)	SN 1983G (j)
NGC 3982		S	$20500_{\pm 1700}$	cep	Stetson & Gibson (2001)	0.07	Riess et al. (2009)	SN1998aq
NGC 2442		S ?	20900	redshift	DSOB (i)			SN2015F
NGC 4639		S	$25500_{\pm 2500}$	cep	Saha et al. (1997)	$0.31_{\pm 0.20}$	Macri et al. (2006)	SN1990N
NGC 4038 / NGC 4039 (h)		S	$21580_{\pm 1190}$	rtgb	Jang & Lee (2015)	$0.07_{\pm 0.03}$	Lardo et al. (2015)	SN2007sr
NGC 5584 (h)		S	$22490_{\pm 1240}$	rtgb	Jang & Lee (2015)			SN2007af
NGC 5917		?	26700	redshift	DSOB (i)			SN2005cf
NGC 3021		S	$27260_{\pm 420}$	rtgb	Jang & Lee (2017)	0.13	Riess et al. (2009)	SN1995al
NGC 3370		S	$28220_{\pm 540}$	rtgb	Jang & Lee (2017)	$0.11_{\pm 0.05}$	Macri et al. (2006)	SN1994ae
NGC 1309		S	$31200_{\pm 580}$	rtgb	Jang & Lee (2017)	0.18	Riess et al. (2009)	SN2002fk
UGC 9391		S	36100	redshift	DSOB (i)			SN2003du
NGC 1015		S	37100	redshift	DSOB (i)			SN2009ig

Notes :
(a) *cf.* Table 10 de Hosek et al. (2014) pour une liste de galaxies avec leur métallicité et les références associées.
(b) LGS 3 = Local Group Suspect 3
(c) WLM = Wolf-Lundmark-Melotte
(d) Pour M81 et NGC 5253, la métallicité est calculée à partir de l'abondance [O/H] donnée dans la Tab. 4 de Kennicutt et al. (1998)
(e) Pour M82, l'abondance correspond à [M/H] et non [Fe/H] (Durrell et al. 2010).
(f) M66 appartient au triplet du Lion avec M65 et NGC 3628
(g) Un résumé exhaustif et récent des estimations de distance de M66 et M96 se trouve dans Lee & Jang (2013), Tab. 3 et 4, respectivement.
(h) Un résumé exhaustif et récent des estimations de distance de NGC4038/39 et NGC 5584 se trouve dans Jang & Lee (2015), Tab. 4 et 5, respectivement.
(i) La distance des galaxies lointaines est difficile à trouver dans la littérature et est donc calculée à partir du redshift en utilisant le site web suivant : https ://dso-browser.com/.
(j) SNIa rejetées dans le cadre de l'étude de Riess et al. (2016) pour différentes raisons (voir l'introduction du Chapitre 3).
(k) les 4 SNIa (SN1994D, SN1980N, SN2006dd, SN1981D) sont de qualités suffisantes pour être utilisées pour l'étalonnage des échelles de distance dans l'univers, mais ne disposent pas de détermination de distance indépendante suffisamment précise.

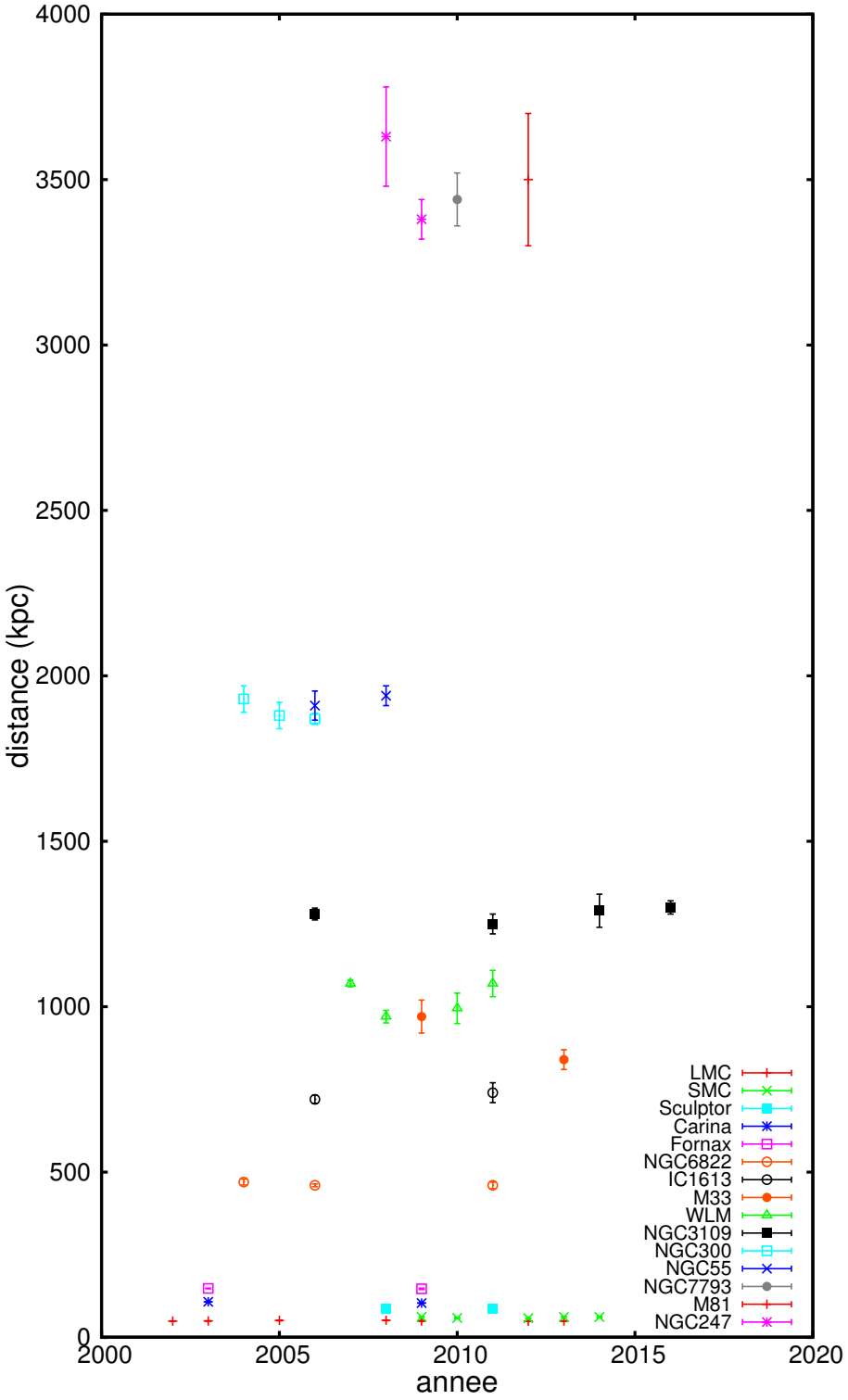


FIGURE 3.2 – Distances des différentes galaxies déterminées dans le cadre du projet Araucaria. Cette figure a été établie à partir de la Tab. C.1

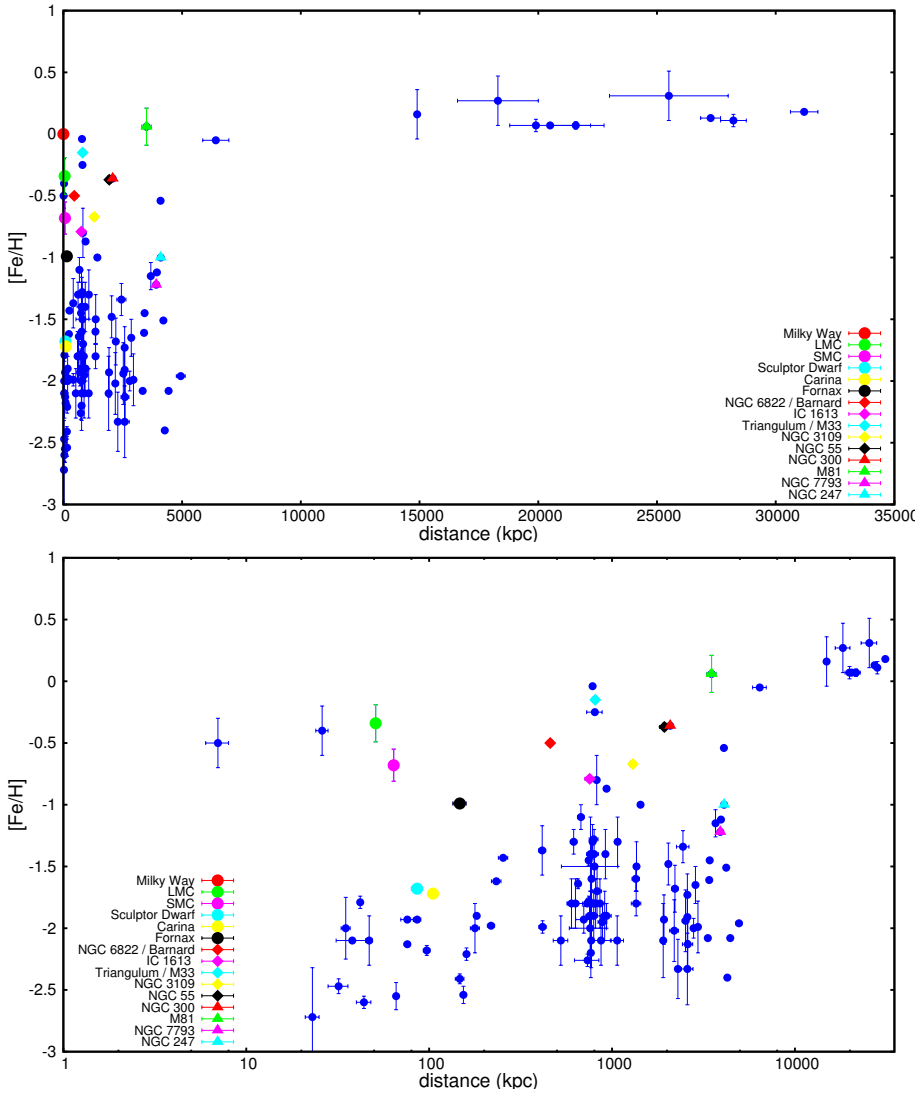


FIGURE 3.3 – Abondance en fer par rapport à l'hydrogène [Fe/H] en fonction de la distance des galaxies du groupe local (en log pour la figure du bas). Les galaxies qui ont fait l'objet d'étude dans le cadre du projet Araucaria sont indiquées par différentes couleurs.

3.1 L'impact de la métallicité sur la relation *PL*

Les propriétés physiques qui expliquent la relation entre la luminosité, la couleur d'une Céphéide et sa période sont bien comprises. En utilisant la loi de Stephan-Boltzmann,

$$L = 4\pi R^2 \sigma T_{\rm eff}^4 \tag{3.1}$$

la luminosité L peut être calculée pour toutes les étoiles incluant les Céphéides. Exprimée en magnitude cette relation devient :

$$M_{\rm bol} = -5\log R - 10\log T_{\rm eff} + C \tag{3.2}$$

Or, la température effective $\log T_{\rm eff}$ peut être physiquement reliée à la couleur intrinsèque de l'étoile (i.e. $(B\text{-}V)_0$), tandis le rayon dépend fondamentalement de la période de l'étoile, au travers d'une relation entre la période et la densité moyenne. Ainsi, dans sa forme linéaire pour les étoiles pulsantes, la relation de Stephan-Boltzmann peut prendre la forme d'une relation Période-Luminosité-Couleur *PLC* (Sandage 1958; Sandage & Tammann 1968) :

$$M_{\rm V} = \alpha \log P + \beta (B-V)_0 + \gamma \tag{3.3}$$

La pulsation de la Céphéide est possible du fait d'un changement d'opacité au niveau de la zone d'ionisation de l'hélium. Sur une portion du cycle de pulsation de l'étoile, cette couche d'ionisation est opaque aux radiations, ce qui génère une augmentation de chaleur et donc de pression, qui engendre à son tour une élévation des couches de gaz situées au dessus de la zone d'ionisation de l'hélium et finalement l'étoile se dilate. Puis, au fur et à mesure que le rayon de l'étoile augmente, la température de l'atmosphère diminue, et à un certain point, la couche d'hélium doublement ionisé se recombine et devient à nouveau transparente à la radiation, l'expansion s'arrête, l'étoile commence à se contracter et le cycle se répète. Ce cycle intervient seulement dans la bande d'instabilité (*IS* pour "Instability Strip") du diagramme HR. En effet, les étoiles les plus froides de la bande IS ont des cellules convectives qui s'enfoncent jusque dans la zone d'ionisation de l'hélium et qui perturbent le mécanisme d'opacité. A l'inverse, les Céphéides les plus chaudes de la bande IS ont une zone d'ionisation de l'hélium tellement haute dans l'atmosphère qu'elle ne permet pas de jouer le rôle de piston. De manière générale, les relations *PLC* observées et théoriques s'accordent assez bien (Caputo 2008). Cependant, l'atmosphère des Céphéides est affectée par un changement de l'abondance en métaux. Il en est de même de leur structure interne, ce qui affecte la relation entre la masse et le rayon. Ainsi on s'attend à ce que la relation entre la couleur et la magnitude des Céphéides, ainsi que la relation période-luminosité (*PL*) correspondante, dépende de la métallicité, que ce soit sa pente ou son point-zéro Sandage & Tammann (2008). Cependant, prédire l'effet de métallicité sur la magnitude (et même son signe) s'est avéré extrêmement compliqué. Des études théoriques ont été menées : Alibert et al. (1999); Sandage et al. (1999); Bono et al. (2008); Caputo (2008) et Romaniello et al. (2008, 2009). Nous nous concentrerons ici sur les aspects empiriques. Deux tests ont été proposés pour tester la sensibilité de la relation *PL* à la métallicité.

Le premier test consiste à observer des Céphéides situées respectivement dans la partie interne et externe du disque d'une galaxie individuelle, de mesurer leur métallicité (ce qui donne un gradient de métallicité dans le disque de la galaxie) et de comparer les relations *PL* obtenues (pente et point-zéro). Seulement, à un rayon donné de la galaxie, la métallicité est bien souvent déterminée à partir de l'abondance [O/H] et on fait alors l'hypothèse que les Céphéides ont la même métallicité, ce qui est loin d'être établi (Kudritzki et al.

2012; Bresolin et al. 2009). Par ailleurs, on considère que d'autres facteurs n'entrent pas en jeu, comme une dépendance radiale du "crowding", un changement de la loi d'extinction en fonction du rayon, etc... Cette approche a été adoptée pour M31 (Freedman & Madore 1990), M101 (Kennicutt et al. 1998), NGC 4258 (Macri et al. 2006) et M33 (Scowcroft et al. 2009).

Le second test consiste à comparer la distance d'une galaxie obtenue à l'aide de différents estimateurs (par exemple les Céphéides et les RTGB) pour ensuite chercher une corrélation avec la métallicité de la galaxie. Ainsi Udalski et al. (2001) ont comparé les distances des Céphéides et des RTGB dans la galaxie IC 1613 (de forte métallicité : [Fe/H]$=0.79$) et n'ont trouvé aucun effet de la métallicité : les distances obtenues étaient comparables. En revanche, en étudiant 10 galaxies contenant des Céphéides et des RTGB, Sakai et al. (2004) ont trouvé que la différence de distance entre les Céphéides et les RTGB décroit effectivement vers zéro lorsque la métallicité de la galaxie augmente (on retrouve bien zéro dans le cas de IC 1613), mais augmente lorsque l'on se rapproche de la métallicité solaire et que l'effet est de l'ordre de $\delta(m-M)/\delta[\mathrm{O/H}] = -0.24 \pm 0.05$ mag.dex^{-1}. Notons que Groenewegen et al. (2004a) ont trouvé un effet de $\delta(m-M)/\delta[\mathrm{Fe/H}] = -0.8 \pm 0.3$ mag.dex^{-1} en utilisant seulement les Céphéides de la Voie Lactée et son gradient de métallicité, et $\delta(m-M)/\delta[\mathrm{Fe/H}] = -0.27 \pm 0.8$ mag.dex^{-1} en considérant les Céphéides du LMC. Ceci dit, les choses ne sont pas si simples, car Romaniello et al. (2008), en se basant sur des mesures de métallicités spectroscopiques (i.e. sur des étoiles individuelles et non des régions HII), trouvent un effet de la métallicité sur la relation *PL* inverse à ce que nous venons de voir. Le tableau 3.4 tiré de Romaniello et al. (2008) et actualisé, fait une synthèse de l'impact de la métallicité sur la relation *PL*. Même si ce sujet fait l'objet d'intenses débats et recherches, la valeur qui fait actuellement référence est celle de Sakai et al. (2004). Cela veut dire que si l'on utilise la relation *PL* des Céphéides du LMC ([Fe/H]$= -0.34 \pm 0.15$, Luck et al. (1998) par exemple) pour déduire la distance d'une Céphéide se situant dans une galaxie hôte de SNIa de métallicité relativement élevée, similaire à celle de la Voie Lactée, alors son module de distance est diminué d'environ $\Delta\mu = [\mathrm{Fe/H}]_{\mathrm{LMC}}\Delta[\mathrm{O/H}] = 0.34 * 0.24 \simeq 0.08$ magnitude, i.e. que la galaxie paraît plus proche que ce qu'elle est en réalité.

Ce que nous venons de voir concerne l'impact de la métallicité sur le point-zéro de la relation *PL*, c'est-à-dire que la correction appliquée sur la magnitude est la même pour toutes les Céphéides, quelle que soit leur période. Mais on peut également se poser la question de l'impact de la métallicité sur la pente de la relation *PL*. Un exemple frappant se trouve dans la revue de Jackson (2015). Prenons le résultat de Riess et al. (2005) d'un côté avec $H_0 = 73 \pm 4 \pm 5$km s^{-1}et de l'autre, le résultat de Sandage et al. (2006) avec $H_0 = 63.3 \pm 1.9 \pm 5$km s^{-1}. Ces valeurs de H_0 sont clairement incompatibles (voir également Fig. 2.1), bien qu'elles reposent sur les mêmes galaxies de référence, c'est-à-dire : NGC 3370 (SN1994ae), NGC 3982 (SN1998aq), NGC 4639 (SN1990N) et NGC 4536 (SN1981B). Dans le pire des cas, i.e. SN 1990N dans NGC 4639, les auteurs trouvent une différence de 20-25% pour le module de distance : $\mu^0 =$ 31.74 pour Riess et al. (2005) et $\mu^0 = 32.20$ pour Sandage et al. (2006). Jackson (2015) indique que la différence ne vient pas de la relation *PL* utilisée pour déterminer la distance de cette galaxie, mais de la façon dont la correction de la métallicité est effectuée. D'un côté, Riess et al. (2005) appliquent une correction identique à toutes les Céphéides (comme nous l'avons expliqué plus haut) avec une valeur de correction en terme de magnitude qui s'exprime de la manière suivante : $\Delta\mu = -0.24\Delta[\mathrm{O/H}]$. De son côté, Sandage et al. (2006) considèrent une correction de la métallicité qui dépend de la période de la Céphéide : $\Delta\mu = 1.67(\log P - 0.933)\Delta[\mathrm{O/H}]$, où $\Delta[\mathrm{O/H}]$ est la métallicité des Céphéides observées dans NGC 4639 moins la métallicité du LMC. Macri et al. (2006) ont montré que l'approche de Riess et al. (2005) est probablement plus appropriée, mais la question reste épineuse et montre les difficultés liées à la métallicité [3].

3. A titre de comparaison, il est maintenant établi que les étoiles pulsantes de type RR Lyrae présentent une relation période

TABLE 3.4 – Impact de la métallicité sur le point zéro de la relation *PL*. Tableau 3.4 tiré de Romaniello et al. (2008) et actualisé.

$\frac{\delta\mu}{\delta[M/H]}$ (mag/dex)		Method	Référence
-0.32 ± 0.21	[Fe/H]	Analyse de Céphéides dans 3 champs de M31 (bandes *BVRI*)	Freedman & Madore (1990)
-0.88 ± 0.16	[Fe/H]	Comparaison de Céphéides dans 3 champs de M31 et du LMC (bandes *BVRI*)	Gould (1994)
-0.40 ± 020	[O/H]	Solution simultanée pour la distance pour 17 galaxies (bandes *UBVRIJHK*)	Kochanek (1997)
$-0.44^{0.10}_{-0.20}$	[O/H]	Comparaison des observations EROS des Céphéides du SMC et du LMC (bandes *VR*)	Sasselov et al. (1997)
-0.24 ± 0.16	[O/H]	Comparaison des observations du HST dans les champ interne et externe de M101	Kennicutt et al. (1998)
-0.12 ± 0.08	[O/H]	Comparaison de 10 Céphéides Galactiques par la méthode RTGB	Kennicutt et al. (1998)
-0.20 ± 0.20	[O/H]	Valeur utilisée lors du HST "Key Projet"	Freedman et al. (2001)
0	[Fe/H]	Comparaison OGLE des Céphéides dans IC 1613 et MC (bandes *VI*)	Udalski et al. (2001)
0	[O/H]	Comparaison des méthodes PNLF et SBF	Ciardullo et al. (2002)
-0.24 ± 0.05	[O/H]	Comparaison de la distance de 17 RTGB	Sakai et al. (2004)
-0.21 ± 0.19	[Fe/H]	Méthode BW des Céphéides de la Galaxie et du SMC (bandes *VK*)	Storm et al. (2004)
-0.23 ± 0.19	[Fe/H]	Méthode BW des Céphéides de la Galaxie et du SMC (bandes *I*)	Storm et al. (2004)
-0.29 ± 0.19	[Fe/H]	Méthode BW des Céphéides de la Galaxie et du SMC (indexe *W*)	Storm et al. (2004)
-0.27 ± 0.08	[Fe/H]	Compilation des distances et des métallicités de 53 Céphéides Galactiques et des nuages de Magellan	Groenewegen et al. (2004b)
-0.39 ± 0.03	[Fe/H]	Distance des galaxies hôtes de SNIa à l'aide des Céphéides	Saha et al. (2006)
-0.29 ± 0.09	[O/H]	Céphéides dans NGC 4258 et gradient [O/H] issu de Zaritsky et al. (1994)	Macri et al. (2006)
-0.10 ± 0.03	[Fe/H]	Moyenne pondérée de Kennicutt, Macri & Groenewegen	Benedict et al. (2007)
-0.017 ± 0.113	[O/H]	Comparaison de la distance de 18 galaxies (Céphéides et RTGB)	Tammann et al. (2008)
0	[Fe/H]	Comparaison des pentes entre les Céphéides Galactiques et du LMC	Fouqué et al. (2007)
0.05 ± 0.03	[Fe/H]	Relation théorique entre la période et l'index Wesenheit (V,I)	Bono et al. (2008)
-0.17 ± 0.31	[O/H]	Céphéides du LMC (0.45-8.0 μm)	Freedman & Madore (2011)
-0.23 ± 0.10	[Fe/H]	Distances BW des Céphéides de la Voie Lactée, du LMC et du SMC (Wesenheit (V,I))	Storm et al. (2011b)
0	[Fe/H]	Distances BW des Céphéides de la Voie Lactée, du LMC et du SMC (bandes *VJK*)	Storm et al. (2011b)
0	[Fe/H]	Distances des Céphéides Galactiques HST et du LMC/SMC (Wesenheit (V,I))	Majaess et al. (2011)
0	[Fe/H]	Distances des Céphéides Galactiques HST et du LMC/SMC (bande *K* & Wesenheit (V,K))	Groenewegen (2013)
-0.23 ± 0.11	[Fe/H]	Distances des Céphéides Galactiques HST et du LMC/SMC (bande *V*)	Groenewegen (2013)
-0.33 ± 0.12	[O/H]	Céphéides dans M31 (bandes *VI*)	Mager et al. (2013)

Dans le cadre du projet Araucaria, nous avons utilisée récemment la méthode de Baade-Wesselink, ainsi qu'un nouvel étalonnage du facteur de projection (nous y reviendrons dans la Sect. 4), pour déterminer la distance de 70 Céphéides Galactiques et en déduire une relation *PL* (Storm et al. 2011a) (voir l'annexe G). De la même manière, nous avons établi une relation *PL* basée sur l'observation de 36 Céphéides du LMC (Storm et al. 2011b) (voir l'annexe H). Il ressort de cette étude que 1) la pente de la relation *PL* n'est pas sensible à la métallicité, 2) le point-zéro de la relation *PL* n'est pas sensible à la métallicité dans les bandes *V*, *J* et *K*, mais 3) qu'un effet de 0.23 ± 0.10 mag/dex est obtenu lorsque l'on considère l'index de Wesenheit [4] (V, I). Ces résultats sont partiellement compatibles avec ceux obtenus par Groenewegen (2013).

Pour résumer, il semble admis actuellement par la plupart des chercheurs dans ce domaine que la pente de la relation *PL* ne dépend pas de la métallicité dans l'infrarouge. En revanche, concernant l'impact de la métallicité sur le point-zéro de la relation *PL*, la question reste ouverte et fait actuellement l'objet d'intenses recherches. Dans Riess et al. (2016), l'erreur sur H_0 due à la métallicité est estimée à 0.5% [5] (leur Table 7).

- métallicité - luminosité, qu'elle soit déterminée à partir d'amas globulaires (Sollima et al. 2006; Marengo et al. 2017) ou du SMC (Muraveva et al. 2015). Les RR Lyrae permettent de déterminer des distances dans le groupe local jusqu'à quelques Mpc (voir Table 3.1) ce qui n'en fait pas une méthode compétitive. Cependant, elles sont bien plus utiles pour faire de l'archéologie galactique avec des études montrant les interactions entre le Voie Lactée et les galaxies naines du sagittaire (Alcock et al. 1997; Sesar et al. 2017) ou encore la géométrie des nuages de Magellan Jacyszyn-Dobrzeniecka et al. (2016, 2017).

4. Si on adopte une loi d'extinction et qu'on l'applique à toutes les Céphéides, on peut utiliser les magnitudes et les couleurs observées pour en déduire l'extinction totale sur la ligne de visée. Ainsi, par exemple, si on a *V* et *I* (comme c'est souvent le cas pour les Céphéides observées par le HST) et qu'on fait l'hypothèse du rapport de l'absorption totale par rapport à une bande sélective $R_{VI} = \frac{A_V}{E(V-I)}$ (Cardelli et al. 1989), alors on obtient des magnitudes et couleurs corrigées de l'extinction, que l'on appelle magnitude Wesenheit (Madore 1982).

5. Il est intéressant de constater que dans leur dernière détermination de H_0, Riess et al. (2016) ont directement ajusté la correction de la magnitude liée à la métallicité : il s'agit du paramètre Z_W dans l'Eq. 2. Les valeurs obtenues de γ sont ainsi des *outputs* et sont indiqués dans leur Table 8.

Cette erreur tombe à zéro pour NGC4258, la galaxie hôte d'un mégamaser Humphreys et al. (2013) dont la métallicité est proche de celle de la Voie Lactée. De même, il est également important de mentionner que *Gaia* fournira prochainement une relation *PL* Galactique qui pourra être utilisée directement pour la détermination de distance des galaxies hôtes de SNIa, ce qui devrait réduire l'erreur liée à la métallicité sur H_0, même si le problème de la détermination de la métallicité de ces céphéides lointaines reste difficile. Il est aussi utile de rappeler que des galaxies comme M31, M33, M81, M83 (étudiées dans le cadre du projet Araucaria) ont une métallicité très proche de celle de la Voie Lactée, ce qui en fait des cibles prioritaires, très intéressantes pour l'avenir. A plus long terme, la stratégie du projet Araucaria d'observer des galaxies aux métallicités très différentes devrait également permettre de mieux contraindre l'impact de la métallicité sur la relation *PL* et ainsi fournir de nouvelles galaxies de références pour la détermination de H_0. En effet, la plus grosse contribution dans le budget d'erreur sur H_0 vient de l'incertitude sur la distance des galaxies de références : le LMC et M31 pour environ 1.3% (Riess et al. 2016).

3.2 Les binaires à éclipses et la distance du LMC

Déterminer avec précision la distance de certaines galaxies de référence *par une méthode indépendante des Céphéides et si possible indépendante de la métallicité* est l'une des priorités du projet Araucaria. Cela permet à la fois de contraindre la relation *PL* des Céphéides (utilisée ensuite pour la détermination de distance des SNIa) et d'estimer l'impact de la métallicité sur son point-zéro (voir section précédente). Les galaxies de référence utilisées par Riess et al. (2016) se résument au LMC et à M31. Et, très clairement, la distance du LMC est actuellement la source d'erreur la plus importante sur l'étalonnage des échelles de distances dans l'univers et sur la détermination de H_0 (1.3% d'après la Table 7 de Riess et al. (2016)). La Figure 3.4 montre les densités de probabilité correspondant à l'estimation du module de distance du LMC obtenues à partir de différentes méthodes jusqu'en 2010 (Freedman & Madore 2010a). Depuis 2010, la situation s'est bien améliorée grâce à la méthode des binaires à éclipses.

"The Optical Gravitionnal Lensing Experiment" OGLE [6] (Udalski et al. 1992) a observé environ 35 millions d'étoiles dans le champ du LMC pendant plus de 16 ans. En utilisant, ces données, notre groupe du projet Araucaria mené par G. Pietrzynski a détecté une douzaine de binaires à éclipses de masses intermédiaires avec des périodes orbitales s'échelonnant de 60 à 772 jours (Pietrzyński et al. 2013) (voir annexe I). La distance du LMC est alors basée sur une formule assez simple :

$$d[\mathrm{pc}] = 1.337.10^5 \frac{r[\mathrm{km}]}{\theta[\mathrm{mas}]} \tag{3.4}$$

Le diamètre linéaire (r) peut être déterminé pour une binaire à éclipses détachée à partir de l'analyse de sa courbe de lumière et de son orbite spectroscopique avec une précision de l'ordre de 1% (Andersen et al. 1991), tandis que le diamètre angulaire (θ) peut être calculé à partir d'une relation brillance de surface - couleur, i.e. $m_0 = S - 5\log(\phi)$ où S est la brillance de surface et m_0 est la magnitude intrinsèque dans une bande photométrique. La méthode fut décrite et utilisée pour la première fois par Lacy (1977). La principale source d'erreur de cette méthode provient quasi-totalement de notre méconnaissance de la relation brillance de surface - couleur. Celle-ci est relativement bien connue pour les étoiles tardives (à 2%), mais très incertaine pour les étoiles de type spectral ABO (à 6-8%). Nous reviendrons sur ce point dans le chapitre 5. Ainsi la méthode est affectée par les sources d'incertitudes suivantes (voir Pietrzyński et al. (2013)) : la précision

6. http ://ogle.astrouw.edu.pl/

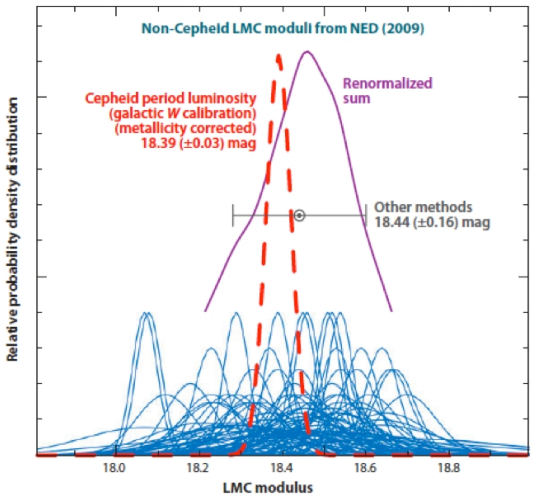


FIGURE 3.4 – Densités de probabilité correspondant à l'estimation du module de distance du LMC obtenues à partir de différentes méthodes. Le trait plein en violet correspond à la résultante (figure tirée de Freedman & Madore (2010a)). Toutes méthodes confondues, l'incertitude sur le module de distance du LMC est de 0.15 mag. La valeur retenue par les auteurs était de 18.5 $\pm$ 0.1 mag, ce qui entraînait alors une incertitude de 5% sur H_0. Actuellement, grâce à la distance du LMC déduite de la méthode des binaires à éclipses, la précision obtenue est de 2.2% (Pietrzyński et al. 2013) et l'impact sur H_0 de 1.3% (Riess et al. 2016).

sur l'amplitude des courbes de vitesses radiales (K_1 et K_2, environ 0.5%), la dimension absolue (0.5%), l'inclinaison (0.2%), le rayon relatif (1%), le point-zéro de la photométrie visible (0.6%) et infrarouge (0.8%), le rougissement (seulement 0.8%, puisque que la relation brillance de surface - couleur est quasi-parallèle aux effets liés au rougissement (Barnes & Evans 1976)), et enfin l'erreur liée à l'étalonnage de la relation brillance de surface - couleur (2%). Par ailleurs, la méthode est très peu sensible à la métallicité avec une correction de seulement 0.007 magnitude entre les binaires à éclipses de la Voie Lactée et du LMC (Thompson et al. 2001; Di Benedetto 2005). En combinant ces incertitudes quadratiquement, nous avons déterminé une distance au LMC à 2.2% de précision Pietrzyński et al. (2013). Cette distance a été utilisée par Riess et al. (2016) et a fortement contribué à obtenir une précision de 2.4% sur H_0.

Les binaires à éclipses ont jusqu'à présent été utilisées pour déterminer la distance de quelques galaxies jusqu'à environ 1 Mpc : LMC (2%), SMC (3%), M31 (4%) et M33 (6%). Afin d'obtenir de meilleures précisions et déterminer la distance de galaxies au-delà de 1 Mpc, il est nécessaire d'observer des binaires à éclipses de type précoces (plus brillantes) et donc d'étalonner la relation brillance de surface - couleur pour ces étoiles. Ce point est abordé dans le chapitre 5.

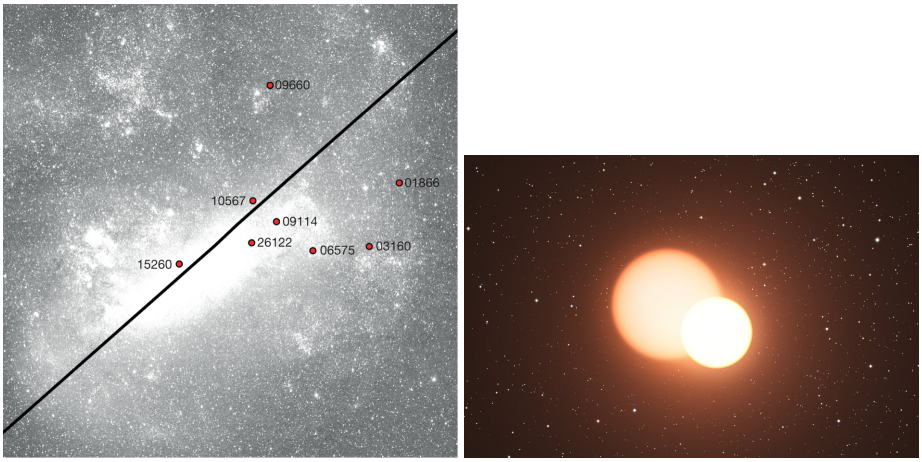


FIGURE 3.5 – A gauche, la position des binaires à éclipses observées dans le LMC par Pietrzyński et al. (2013). A droite, figure d'artiste d'un système double à éclipses. Plusieurs études ont montré que le LMC est incliné par rapport au plan du ciel d'environ 35 degrés (son inclinaison serait nulle s'il était vu de face) (Olsen & Salyk 2002; van der Marel et al. 2002; Nikolaev et al. 2004). Les binaires à éclipses observées étaient proches du centre du LMC et de la ligne des noeuds, ce qui n'affecte pas l'estimation de la distance. Cependant, la situation est maintenant plus complexe depuis l'étude détaillée de Jacyszyn-Dobrzeniecka et al. (2016, 2017) de la géométrie et de la profondeur du LMC déduite de l'observation des Céphéides et des RR Lyrae avec OGLE (Soszyński et al. 2015, 2016).

TABLE 3.5 – Les galaxies dont la distance a été déterminée par la méthode des binaires à éclipses (voir aussi Tab. C.1)

galaxie	distance kpc $\pm \sigma_{stat} \pm \sigma_{syst}$	reference
Sagittarus Arm	$2.14 \pm 0.06 \pm 0.05$	Suchomska et al. (2015)
LMC	50.30 ± 0.53	Elgueta et al. (2016)
LMC	$50.0 \pm 0.2 \pm 1.1$	Pietrzyński et al. (2013)
LMC	50.6 ± 1.6	Bonanos et al. (2011)
LMC	50.1 ± 1.4	Pietrzyński et al. (2009b)
LMC	43.2 ± 1.8	Fitzpatrick et al. (2003)
LMC	47.5 ± 1.8	Ribas et al. (2002)
LMC	50.7 ± 1.2	Fitzpatrick et al. (2002)
LMC	47.9 ± 1.6	Nelson et al. (2000)
LMC	45.7 ± 1.6	Guinan et al. (1998)
LMC	41.7 ± 6.2	Bell et al. (1991)
SMC	62.1 ± 1.9	Graczyk et al. (2014)
SMC	$58.3 \pm 0.5 \pm 1.3$	Graczyk et al. (2012)
SMC	$60.6 \pm 1.0 \pm 2.8$	Hilditch et al. (2005)
SMC	$60.0 \pm 1.1 \pm 2.8$	Harries et al. (2003)
SMC	52.5 ± 7.7	Bell et al. (1993)
M31	744 ± 33	Vilardell et al. (2010)
M31	772 ± 44	Ribas et al. (2005)
M33	964 ± 54	Bonanos et al. (2006)

3.3 Impact de la binarité et de l'environnement des Céphéides sur la relation *PL*

D'après Riess et al. (2016), la dispersion de la relation *PL* aurait un impact de 0.7% sur H_0. La figure 3.6 indique très clairement que la pente de la relation *PL* augmente avec la longueur d'onde, tandis que sa dispersion diminue. On passe ainsi d'une dispersion de 0.27 mag dans la bande V à une dispersion de 0.11 mag dans la bande K, tandis que la dispersion à 3.6μm, c'est-à-dire à la longueur d'onde de *Spitzer*, est également autour de 0.11 magnitude (Scowcroft et al. 2011; Freedman et al. 2012). Il est donc préférable en principe de se déplacer vers les hautes longueurs d'onde pour étalonner les échelles de distance dans l'univers à l'aide des Céphéides. Mais c'est sans prendre en compte l'impact de l'environnement des Céphéides et de la binarité.

En effet, la plupart des Céphéides observées par interférométrie ou par d'autres techniques présentent une coquille, ou plus généralement un environnement qui contribue pour environ 0.06 mag dans le visible (voir Sect. 4.3) et jusqu'à 0.3 mag ou plus dans l'infrarouge thermique (3-8μm). La table 3.6 fait la synthèse des mesures effectuées jusqu'à présent. L'environnement des Céphéides peut ainsi créer un biais positif sur la relation *PL* : sur le point-zéro, mais aussi sur la pente dans la mesure où une relation entre la période et la contribution en flux de l'enveloppe n'est pas exclue. Ceci ne serait pas nécessairement un problème si la contribution en flux de l'environnement était la même pour toutes les Céphéides d'une période donnée. Or, ce dernier point est loin d'être évident. L'environnement des Céphéides dépend très probablement de la perte de masse, de l'état évolutif de la Céphéide (premier, deuxième ou troisième passage) et peut-être aussi de la température effective, c'est-à-dire la position de la Céphéide sur le bord bleu ou rouge de la bande d'instabilité. Ainsi un des objectifs majeurs de l'ANR *UnlockCepheids* pilotée par Pierre Kervella vise à établir des corrections photométriques dans différentes bandes pour l'ensemble des Céphéides de la bande d'instabilité. Il est à noter également que l'environnement des Céphéides peut avoir un impact sur la relation brillance de surface - couleur et donc potentiellement sur la méthode de Baade-Wesselink que nous aborderons dans la prochaine Section 3.4. Nous parlerons de la découverte récente d'un environnement visible autour de δ Cep dans la Sect. 4.3.

Par ailleurs, 60% des Céphéides sont très probablement des binaires (Szabados 2003; Neilson et al. 2015). Au premier ordre, ces binaires n'ont pas d'impact sur la relation *PL* dans la mesure où les compagnons sont généralement des étoiles de la séquence principale ayant une luminosité plusieurs centaines de fois plus faible que celle de la Céphéide. Néanmoins, plusieurs études récentes montrent que ces compagnons peuvent être détectés par interférométrie et que leur contribution en flux n'est pas négligeable, que ce soit dans le visible (rapport de flux plus favorable) ou l'infrarouge (Gallenne et al. 2013b, 2014, 2016). Concernant V1334 Cyg, une contribution du compagnon en bande H de 3% a été obtenue (Gallenne et al. 2014). L'impact de la binarité sur la relation *PL* constitue également un objectif de l'ANR *UnlockCepheids*, mais nous ne détaillerons pas ce point dans ce manuscrit.

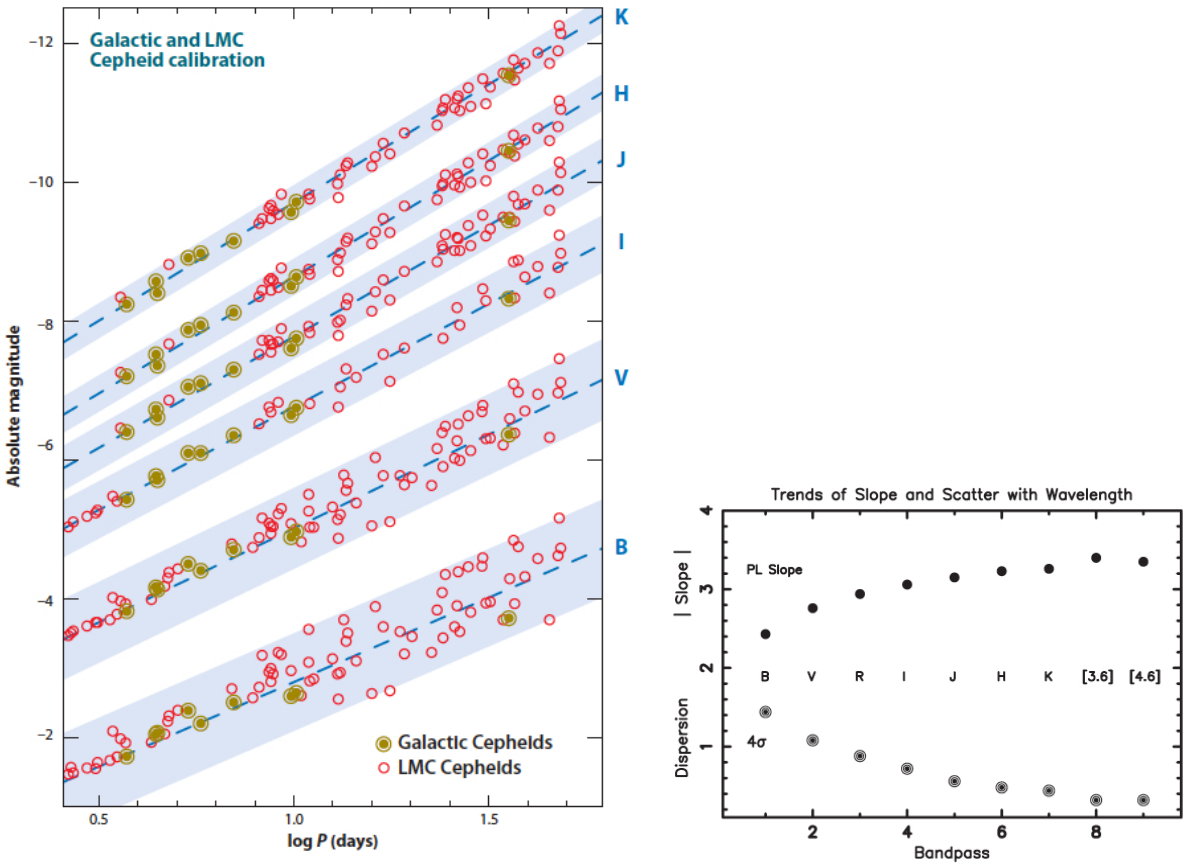


FIGURE 3.6 – A gauche, Figure extraite de Freedman & Madore (2010b) représentant la relation *PL* dans différentes bandes photométriques : B, V, I, J, H et K. On remarque que la pente augmente avec la longueur d'onde de référence de la bande photométrique, tandis que sa dispersion diminue, ce que l'on constate également sur la figure de droite tirée de Madore & Freedman (2012). Actuellement, la relation *PL* a une dispersion (mode fondamental) de 0.208, 0.146 et 0.077 magnitudes dans les bandes V, I et W_I de OGLE basé sur 4620 Céphéides (de différents modes de pulsation) des nuages de Magellan (Soszyński et al. 2015). Persson et al. (2004) obtiennent une dispersion de 0.11 magnitude en bande K, tandis que les observations Spitzer donnent 0.108 et 0.115 magnitude dans les bandes 3.6 et 4.5 μm, respectivement (Scowcroft et al. 2011).

TABLE 3.6 – Les enveloppes de Céphéides détectées par interférométrie (VEGA, FLUOR, MIDI), imagerie (VISIR, NACO, *Spitzer*) ou via le calcul de SEDs sont indiquées dans cette table avec la contribution en flux de l'enveloppe (comparée à la photosphère) et sa taille lorsqu'elle a été calculée. Concernant les SEDs, les excès infrarouge calculés à partir des données VISIR dans les PAH1 (à 8.6μm) et à différentes phases de pulsation sont assimilés à des rapports de flux entre enveloppe et photosphère (Gallenne et al. 2012). D'autres valeurs correspondant à d'autres domaines de longueur d'onde (PAH2, Si C) sont indiquées dans Gallenne et al. (2012), mais non reportées ici. Concernant les modèles géométriques ajustés dans les différentes études, on peut répertorier : des modèles de disque avec bord interne à partir de DUSTY (D), des modèle géométriques de gaussiennes (G), des modèles géométriques d'anneaux (A), ainsi que de simple disque (D). A ces informations, on peut rajouter que Marengo et al. (2010a) ont observé 29 Céphéides avec *Spitzer* et n'ont pas trouvé d'indice d'excès infrarouge causé par un environnement de poussière chaude ($\simeq$ 500K), excepté pour RS Pup, S Mus et δ Cep, tandis que sa présence est indiquée comme probable pour GH Lup, ℓ Car, T Mon, et X Cyg (Barmby et al. 2011). Il est intéressant de noter que l'excès infrarouge, pour certains auteurs, n'est pas dû à de la perte de masse (voir par exemple Schmidt 2015) et que les structures résolues autour de δ Cep, au lieu d'être des CSEs, seraient la contribution en flux d'une nébuleuse (dû au choc entre la perte de masse de l'étoile et le milieu interstellaire, telle que mise en évidence dans l'infrarouge par Marengo et al. (2010b) ou dans le domaine radio (Matthews et al. 2012). Enfin la complexité de l'environnement des Céphéides s'est encore accrue avec des observations XMM-Newton dans le domaine des rayons X (Engle et al. 2014; Ayres 2017). Polaris est également une céphéide très particulière (voir l'annexe D).

Céphéides	Période jours	instrument	λ μm	$\frac{f_{\rm cse}}{f_\star}$ %	$\frac{\theta_\star}{\theta_{\rm cse}}$	Référence
FF Aql	4.47	VISIR/SED	8.6	1.6 ± 2.8	-	Gallenne et al. (2012)
Polaris	3.97	FLUOR	2.2	1.5 ± 0.4	2.4 ± 0.1^A	Mérand et al. (2006)
AX Cir	5.27	VISIR/Image	8.6	13.8 ± 2.5	-	Gallenne et al. (2012)
		VISIR/SED	8.6	-0.8 ± 2.9	-	Gallenne et al. (2012)
δ Cep	5.36	VEGA	0.7	7 ± 1	6.3^{DI}	Nardetto et al. (2016)
		FLUOR	2.2	1.5 ± 0.4	2.4^A	Mérand et al. (2006)
X Sgr	7.01	MIDI	10.2	7	12.6 ± 3.8^D	Gallenne et al. (2013a)
		VISIR/Image	8.6	7.9 ± 1.4	-	Gallenne et al. (2012)
		VISIR/SED/ϕ_1	8.6	14.1 ± 5.4	-	Gallenne et al. (2012)
		VISIR/SED/ϕ_2	8.6	3.8 ± 9.8	-	Gallenne et al. (2012)
η Aql	7.18	VISIR/SED/ϕ_1	8.6	0.38 ± 3.6	-	Gallenne et al. (2012)
		VISIR/SED/ϕ_2	8.6	9.0 ± 4.1	-	Gallenne et al. (2012)
W Sgr	7.59	VISIR/Image	8.6	3.8 ± 0.6	-	Gallenne et al. (2012)
		VISIR/SED/ϕ_1	8.6	10.4 ± 4.6	-	Gallenne et al. (2012)
		VISIR/SED/ϕ_2	8.6	18.2 ± 3.3	-	Gallenne et al. (2012)
κ Pav	9.06	VISIR/SED	8.6	22.2 ± 3.2		Gallenne et al. (2012)
Y Oph	17.12	FLUOR	2.2	5.0 ± 2.0	-	Mérand et al. (2007)
		VISIR/Image	8.6	15.1 ± 1.4	-	Gallenne et al. (2012)
		VISIR/SED/ϕ_1	8.6	6.8 ± 2.7	-	Gallenne et al. (2012)
		VISIR/SED/ϕ_2	8.6	6.3 ± 2.7	-	Gallenne et al. (2012)
T Mon	27.02	MIDI	10.2	19	16.9 ± 3.8^D	Gallenne et al. (2013a)
ℓ Car	35.56	VINCI	2.2	4.2 ± 0.2	1.9 ± 1.5^G	Kervella et al. (2006)
		MIDI	10.2	10	3.0 ± 1.1^G	Kervella et al. (2006)
		Spitzer	70	50	-	Kervella et al. (2006)
U Car	38.81	VISIR/Image	8.6	16.3 ± 1.4	-	Gallenne et al. (2012)
		VISIR/Image	8.6	32.1 ± 2.5	-	Gallenne et al. (2012)
		VISIR/Image	8.6	30.9 ± 6.2	-	Gallenne et al. (2012)
RS Pup	41.44	NACO	1.6	38 ± 17	-	Gallenne et al. (2011)
		NACO	2.2	24 ± 11	-	Gallenne et al. (2011)
SV Vul	45.00	VISIR/SED	8.6	25.0 ± 2.5	-	Gallenne et al. (2012)

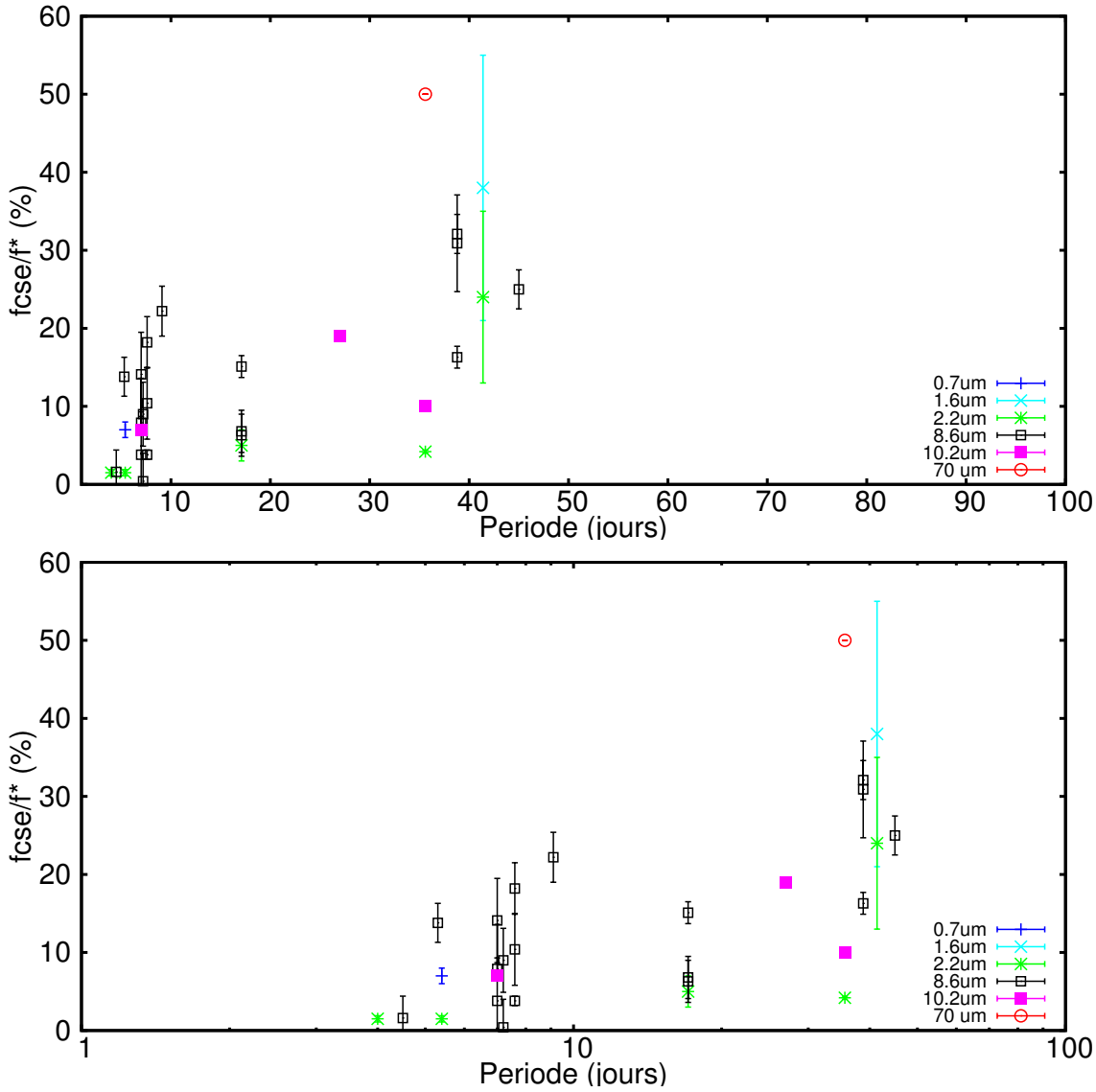


FIGURE 3.7 – Le rapport du flux de l'enveloppe à celui de la photosphère (exprimé en pourcentage) est représenté en fonction de la période (en haut) et de son logarithme (en bas). Cette figure utilise les données listées dans la table 3.6.

3.4 La méthode de BW appliquée aux Céphéides

Nous avons vu que Riess et al. (2016) se basent actuellement sur 15 Céphéides galactiques dont la distance a été déterminée par une mesure de parallaxe trigonométrique du *Hubble Space Telescope* pour contraindre H_0 (en plus du LMC, M31 et NGC 4258). Les incertitudes sur ces distances vont de 4% à 12% (Benedict et al. 2007). Dix-huit Céphéides longue-périodes supplémentaires situées à plus de 1kpc sont actuellement observées par le HST dans le cadre du projet SHOES (Riess et al. 2014). Il est également intéressant de noter qu'en comparaison, la précision sur les distances *Hipparcos* des Céphéides s'échelonne entre 5% et 29% (van Leeuwen et al. 2007a).

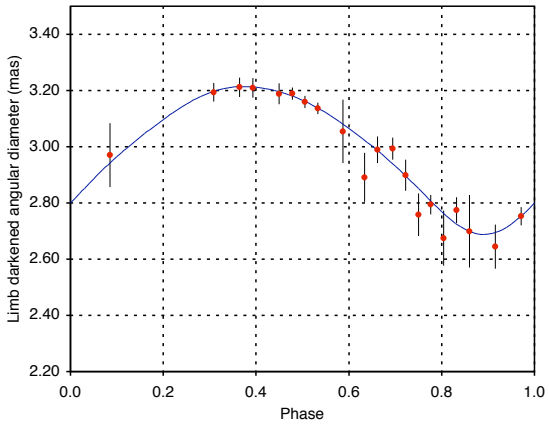
A côté de cela, la méthode de Baade-Wesselink (BW) a permis de déterminer la distance de 70 Céphéides galactiques (à moins de 4 kpc) et de 36 Céphéides du LMC avec une précision de quelques pourcents (Fouqué et al. 2007; Storm et al. 2011a,b). La méthode a été décrite pour la première fois par Lindemann (1918) [7], puis plus tard par Baade (1926); Wesselink (1946). Le principe est simple : il s'agit de comparer les dimensions linéaire et angulaire de la Céphéide afin de déterminer sa distance au moyen d'une simple division (voir Fig. 3.8). Les mesures photométriques (associées à une relation brillance de surface - couleur) fournissent la variation du diamètre angulaire *photosphérique* de l'étoile sur tout le cycle de pulsation, tandis que la variation du diamètre linéaire est déterminée par une intégration temporelle de la vitesse pulsante ($V_{\rm puls}$) de l'étoile. La détermination de cette dernière, à partir du décalage Doppler de la raie spectrale ($V_{\rm rad}$), est extrêmement délicate et fait intervenir ce que l'on appelle le facteur de projection, p, défini par $V_{\rm puls} = pV_{\rm rad}$. Ce nombre résume à lui seul toute la physique de l'atmosphère de la Céphéide (assombrissement centre-bord, gradient de vitesse, ...). En 1997, une deuxième version de la méthode de BW, non pas basée sur les relations brillance de surface - couleur, mais sur l'interférométrie a été tentée sur δ Cep dans le visible avec l'instrument GI2T [8] (Mourard et al. 1997). Puis, quelques années plus tard, les premiers résultats concluants ont été obtenus dans l'infrarouge (Kervella et al. 1999; Lane et al. 2000; Kervella et al. 2001). Depuis lors, la méthode a été appliquée à 12 Céphéides au total, essentiellement dans l'infrarouge (voir Table 3.7). Parmi ces 12 Céphéides, 4 ont été observées dans le visible, mais la variation du diamètre angulaire n'a été mesurée de manière significative que pour une seule Céphéide, ℓ Car (Davis et al. 2009). Une version plus récente de la méthode de BW (SPIPS) utilise l'ensemble des données disponibles, c'est-à-dire interférométriques, photométriques (dans de nombreuses bandes) et les courbes de vitesses radiales (Breitfelder et al. 2015; Merand et al. 2015; Breitfelder et al. 2016).

La méthode de BW est un outil précieux. En effet, *Gaia* ne pourra pas déterminer la distance d'étoiles individuelles dans le LMC. En revanche, avec les futurs instruments E-ELT, JWST, HIRES,... il sera possible de déduire la distance et la métallicité de Céphéides individuelles dans le groupe local, et ceci de manière totalement indépendante de la relation *PL*. Il est intéressant de remarquer que, jusqu'à présent, les distances de BW n'ont pas été utilisées pour déterminer H_0. La raison invoquée, à juste titre probablement par Riess et al. (2009) est la suivante : *"We have not made use of additionnal distance measures to Galactic Cepheids based on the BW method (...) due to uncertainties in their projection factors"*. Ainsi, un des objectifs prioritaires, à la fois dans le cadre du projet Araucaria et de l'ANR *UnlockCepheids*, est d'étalonner les facteurs de projection (à l'aide de *Gaia*) et rendre ainsi la méthode de BW robuste pour l'étalonnage des échelles de distance dans le groupe local. Mes contributions sont multiples au sein de ces projets, mais la plus évidente concerne probablement le facteur de projection et c'est ce que nous allons aborder maintenant.

7. Publication écrite en Allemand
8. Grand Interféromètre à 2 Télescopes situé sur la Plateau de Calern

TABLE 3.7 – Céphéides pour lesquelles la version interférométrique de la méthode de BW a été appliquée. Pour les premières tentatives (indiquées par un astérisque), la pulsation n'a pas été clairement résolue par l'interféromètre et une valeur moyenne du diamètre angulaire a été considérée. Dans le domaine visible, la méthode n'a été appliquée avec succès que pour une seule Céphéide, ℓ Car (Davis et al. 2009) et une enveloppe a été découverte pour δ Cep (voir Sect. 4.3). Dans l'infrarouge, la pulsation a été détectée pour l'ensemble des Céphéides observées, même X Sgr, une Céphéide atypique présentant des ondes de chocs (Mathias et al. 2006).

Cepheids	reference
visible	
δ Cep*	Mourard et al. (1997)
α UMi*, ζ Gem*, δ Cep*, η Aql*	Nordgren et al. (2000)
δ Cep*, η Aql*	Armstrong et al. (2001)
ℓ Car	Davis et al. (2009)
H band	
ζ Gem	Lane et al. (2000)
ζ Gem, η Aql	Lane et al. (2002)
κ Pav	Breitfelder et al. (2015)
ℓ Car	Anderson et al. (2016b)
X Sgr, W Sgr, ζ Gem, β Dor, ℓ Car	Breitfelder et al. (2016)
K band	
ζ Gem*	Kervella et al. (2001)
X Sgr*, η Aql, W Sgr, ζ Gem*, β Dor, Y Oph*, ℓ Car	Kervella et al. (2004d)
δ Cep	Mérand et al. (2005)
Y Oph	Mérand et al. (2007)
FF Aql, T Vul	Gallenne et al. (2012)
δ Cep, η Aql	Merand et al. (2015)



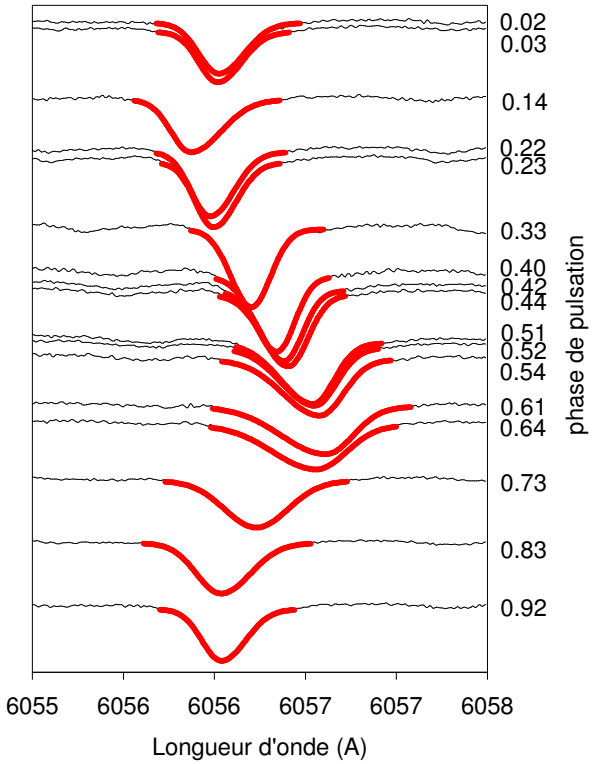


FIGURE 3.8 – A droite : variation du profil spectral d'un raie métallique en fonction de la phase de pulsation (observation HARPS de β Dor). En rouge est indiquée la bi-gaussienne analytique permettant de mesurer l'asymétrie de la raie spectrale. Une fois intégrée dans le temps, la vitesse pulsante (= vitesse radiale x le facteur de projection) permet de déduire la variation du rayon de l'étoile. Ci-dessus, courbe de diamètre angulaire en fonction de la phase de pulsation de l'étoile (ℓ Car). Les points rouge correspondent aux mesures de l'instrument VINCI/VLTI. La forme de la courbe bleue correspond à la variation du rayon de l'étoile déduite de la spectroscopie, tandis que son amplitude est liée à la distance de l'étoile.

Chapitre 4

La méthode de Baade-Wesselink appliquée aux Céphéides : trois problématiques

Comme nous venons de le voir (Section 3.4), la méthode de BW de détermination de distance vise à combiner les dimensions angulaires et réelles, c'est-à-dire en km, de la variation de rayon d'une étoile pulsante. Le principe est le suivant. Il s'agit de faire un ajustement statistique classique dans lequel le χ^2 à minimiser est défini de la manière suivante :

$$\chi^2 = \sum_i \frac{(\theta_{\rm obs}(\phi_i) - \theta_{\rm model}(\phi_i))^2}{\sigma_{\rm obs}(\phi_i)^2}, \tag{4.1}$$

où

— $\theta_{\rm obs}(\phi_i)$ est le diamètre angulaire (prenant en compte l'assombrissement centre-bord de l'étoile) déduit soit des observations interférométriques, soit d'une relation brillance de surface - couleur. ϕ_i est la phase de pulsation correspondant au i-ème point de mesure

— $\sigma_{\rm obs}(\phi_i)$ sont les incertitudes statistiques correspondant aux mesures de diamètre angulaire

— $\theta_{\rm model}(\phi_i)$ est le modèle de diamètre angulaire défini de la manière suivante :

$$\theta_{\rm model}(\phi_i) = \overline{\theta} + 9.3009 \frac{p_{\rm cc-g}}{d} \left(\int RV_{\rm cc-g}(\phi_i) d\phi_i \right) [\rm mas], \tag{4.2}$$

où le facteur de conversion 9.3009 prend en compte la valeur de rayon solaire donné dans Prša et al. (2016). $RV_{\rm cc-g}(\phi_i)$ est la courbe de vitesse radiale (interpolée) correspondant, par exemple, à la méthode très utilisée de la la cross-corrélation (cc) combinée avec un ajustement gaussian (g) du profil moyen, notée (cc-g). Dans l'équation 4.2, on force la moyenne de la courbe de vitesse radiale $RV_{\rm cc-g}$ à zéro de façon à s'affranchir de la vitesse du centre de masse de l'étoile $V_\star$. Les paramètres $\overline{\theta}$ et $p_{\rm cc-g}$ sont le diamètre angulaire moyen (en mas) et le facteur de projection (associé à la méthode cc-g), respectivement. d est la distance de l'étoile. Les quantités $\overline{\theta}$ et d sont ajustées de façon à réduire le χ^2 dans le cas de la méthode de BW classique. On peut aussi ajuster $\overline{\theta}$ et $p_{\rm cc-g}$, et fixer d ; il s'agit alors de la méthode de BW *inverse*.

La méthode de BW a déjà permis de déterminer la distance des Céphéides dans les nuages de Magellan (Storm et al. 2011a,b). D'ici quelques années, il deviendra possible grâce à cette méthode et aux télescopes spatiaux et/ou de nouvelle génération (E-ELT, JWST, ...) de déterminer la distance des Céphéides dans le groupe local (sans passer par la relation *PL*). Mais avant cela, nous devons rendre la méthode plus robuste. Il

est possible de lister tout un ensemble de limitations liées à cette technique, mais les trois principales sont le p-facteur, le k-facteur et l'impact de l'environnement de la Céphéide, que nous allons aborder maintenant.

4.1 Le p-facteur

Le facteur de projection ($p = \frac{V_{\rm puls}}{V_{\rm rad}}$; voir Section 3.4) est une quantité physique complexe qui a fait l'objet de nombreuses études depuis plus de 65 ans. L'approche initiale (van Hoof & Deurinck 1952) consiste à considérer le facteur de projection comme une quantité purement géométrique prenant en compte un seul paramètre physique : l'assombrissement centre-bord de l'étoile. La vitesse radiale $V_{\rm rad}$ mesurée sur la ligne de visée est alors une intégration sur le disque de l'étoile D, de rayon R, du champ de vitesse pulsante $V_{\rm puls}$. Cette intégration est pondérée par la distribution d'intensité de l'étoile $I(x,y)$:

$$V_{\rm rad} = \int_{x,y\in D} \left[V_{\rm puls} \sqrt{1 - \frac{(x^2+y^2)}{R^2}} \right] I(x,y)dxdy \tag{4.3}$$

avec

$$\int_{x,y\in D} I(x,y)dxdy = 1 \tag{4.4}$$

La façon la plus simple de modéliser la distribution d'intensité de l'étoile est de considérer un assombrissement centre-bord linéaire avec un paramètre unique u compris entre 0 (disque uniforme) et 1 (disque assombri) :

$$I(x,y) = I_0(1-u+u*\mu) = I_0(1-u+u\sqrt{1-(x^2+y^2)}) \tag{4.5}$$

Ainsi si l'on observe une raie spectrale dans le domaine visible, le facteur de projection géométrique (noté p_0) s'écrit (Getting 1934) :

$$p_0 = \frac{3}{2} - \frac{u_{\rm V}}{6} \tag{4.6}$$

où le coefficient $u_{\rm V}$, c'est-à-dire l'assombrissement centre-bord, dépend de la température effective, de la gravité de surface, de la métallicité et de la vitesse de microturbulence. On peut par exemple utiliser les tables de Claret & Bloemen (2011) basées sur les modèles de Kurucz (1979) pour déduire $u_{\rm V}$. On peut faire alors plusieurs remarques importantes :

1. L'équation 4.6 *n'est valide que si l'on utilise le premier moment de la raie pour déduire la vitesse radiale* [1]. Ceci a été montré dans ma thèse de Doctorat.
2. Le facteur de projection géométrique vaut $p_0 = 1.5$ dans le cas d'un disque uniforme. Une valeur supérieure à 1.5 est *a priori* irréaliste dans le cas d'une Céphéide car équivalente à un éclaircissement centre-bord.

1. Le premier moment de la raie $RV_{\rm c}$ ("c" pour *centroid*) est défini au sens mathématique par $RV_{\rm c} = \frac{\int_{\rm line} \lambda S(\lambda)d\lambda}{\int_{\rm line} S(\lambda)d\lambda}$, où S est le profil de la raie. L'intégration en longueur d'onde associée à la méthode du premier moment est formellement équivalente à l'intégration spatiale considérée dans l'Eq. 4.3 pour déduire le facteur de projection géométrique. Si l'on utilise un ajustement gaussien pour déduire la position de la raie spectrale, ou encore la vitesse associée au minimum de la raie, la vitesse radiale obtenue est alors *de facto* différente (voir Nardetto et al. (2006b)), mais surtout le lien physique qui lie la vitesse radiale au facteur de projection géométrique est rompu et l'Eq. 4.6 ne peut plus être utilisée.

3. Puisque la température et la gravité de surface varient avec la phase de pulsation, le facteur de projection géométrique est également supposé varier avec la phase de pulsation. Ce dernier est cependant considéré comme *constant* sur le cycle de l'étoile. Nous reviendrons sur cette hypothèse par la suite.
4. Les valeurs du facteur de projection géométrique de δ Cep que l'on trouve dans la littérature sont directement liées à la valeur de l'assombrissement centre-bord *moyen* considéré : $p_0 = \frac{24}{17} = 1.415$ ($u_V = 0.60$, Getting (1934)), $p_0 = 1.375$ ($u_V = 0.75$, van Hoof & Deurinck (1952)), $p_0 = 1.360$ ($u_V = 0.80$, Burki et al. (1982)). La valeur $p = 1.36$ (Burki et al. 1982) a été largement utilisée dans la littérature pendant près de 20 ans. Ces valeurs sont résumées dans la table 4.1. Aux références indiquées dans cette table, nous pouvons rajouter d'autres études qui visaient à l'époque à relier le facteur de projection à l'asymétrie ou à la largeur de la raie, de façon à en déduire sa variation avec la phase (Parsons 1972; Karp 1975c; Hindsley & Bell 1986; Albrow & Cottrell 1994).

Récemment, Neilson et al. (2012b) a utilisé un modèle statique avec un transfert de rayonnement en géométrie sphérique pour déduire le facteur de projection géométrique en fonction de la période et dans différentes bandes spectrales. Il obtient ainsi dans le visible et dans le cas de δ Cep une valeur autour de $p_0 = 1.33$. Il faut également noter qu'il est formellement possible de se passer du facteur de projection en ajustant directement un modèle (statique ou même éventuellement hydrodynamique) sur les profils de raies spectrales. Dans ce cas, la vitesse pulsante est alors un *output*. Ainsi dans les études de Gray & Stevenson (2007) et Hadrava (2009); Hadrava et al. (2009), les modèles ajustés sont statiques et il n'est donc pas étonnant que le facteur de projection déduit *a posteriori* (en comparant la vitesse pulsante issue du code et la vitesse radiale observée) ait une valeur très proche des valeurs des facteurs de projection géométriques dont nous avons discuté plus haut. Le point faible de ces études est que l'ajustement n'est effectué que sur une ou quelques raies spectrales. Or, c'est justement en comparant différentes raies spectrales que toute la finesse liée à la dynamique atmosphérique des Céphéides apparaît.

En effet, les Céphéides ne pulsent pas de manière quasi-hydrostatique. L'interaction entre l'enveloppe pulsante et l'atmosphère est extrêmement complexe (Sanford 1956; Bell & Rodgers 1964; Karp 1975a,b,c; Sasselov & Lester 1990; Wallerstein et al. 2015). Ainsi pour affiner la description du facteur de projection, il devient indispensable de décrire la pulsation de l'atmosphère avec un modèle hydrodynamique (voir Tab. E.1)). A ce jour, le facteur de projection a été étudié avec seulement trois modèles de ce type. Le premier considère un *piston* à la base de l'atmosphère (c'est-à-dire que la vitesse radiale est un *input*) (Sabbey et al. 1995) tandis que le second est *self-consistent* (Nardetto et al. 2004). Sabbey et al. (1995) ont ainsi obtenu une valeur moyenne du facteur de projection de $p = 1.34$ (voir également Marengo et al. (2002, 2003)). Cependant cette valeur a été obtenue avec la méthode du bisecteur pour déduire la vitesse radiale (à partir des profils théoriques), ce qui rend la comparaison avec les autres études difficile. La méthode la plus courante utilisée dans la littérature pour déduire la courbe de vitesse radiale est l'ajustement d'une gaussienne sur un profil moyen cross-correlé (RV_{cc-g}). En considérant cette méthode, le facteur de projection, que l'on peut qualifier alors de *dynamique*, est environ 10% plus faible que dans le cas purement géométrique, avec une valeur autour de $p = 1.25 \pm 0.05$ (Nardetto et al. 2009). Très récemment, un grand pas en avant a été réalisé par Vasilyev et al. (2017). Ce groupe a modélisé une Céphéide de période 2.8 jours ($T_{\rm eff} = 5600$ K, $\log g = 2.0$), soit très proche de δ Cep, en utilisant un code *bi-dimensionnel incluant la convection*. Avant cela, d'autres modèles multi-dimensionnels 2D ou 3D incluant une description de la convection ont vu le jour (Mundprecht et al. 2013, 2015; Geroux & Deupree 2011, 2013, 2014, 2015), mais ces derniers n'incluaient pas de transfert de rayonnement et ne permettaient donc pas de calculer un profil de raie, ni le facteur de projection. Ainsi, après plus d'une décennie de développement, il est maintenant possible grâce au modèle de Vasilyev et al. (2017) d'avoir une idée de l'impact de la convection non seulement sur le

p-facteur, mais aussi sur le k-facteur, que nous aborderons dans la Sect. 4.2. Ainsi, selon la force de la raie considérée, ils obtiennent un facteur de projection de $p \simeq 1.23 - 1.27$, ce qui est parfaitement cohérent avec le modèle hydrodynamique 1D et sans convection décrit dans Nardetto et al. (2004). [2].

En utilisant une méthode basée uniquement sur des observations, Mérand et al. (2005) ont appliqué la méthode de BW *inverse* à partir d'observations interférométriques infrarouge. Le facteur de projection est ajusté tandis que la distance est connue avec une précision d'environ 4% à partir d'une mesure de parallaxe du HST ($d = 274 \pm 11$pc ; Benedict et al. (2002)). Ils ont trouvé : $p = 1.273 \pm 0.021 \pm 0.05$ en considérant $RV_{\mathrm{cc-g}}$ pour la vitesse radiale. La première incertitude est liée à l'ajustement, tandis que la seconde est liée à l'incertitude sur la distance. Groenewegen (2007) a trouvé $p = 1.245 \pm 0.030 \pm 0.050$ en utilisant presque la même distance (273 au lieu de 274 pc), un jeu de données différent pour la vitesse radiale et une méthode d'ajustement légèrement différente. Récemment, Merand et al. (2015) ont développé une méthode intégrée (SPIPS), l'ont appliquée à δ Cep (en combinant interférométrie et photométrie) et ont obtenu $p = 1.29 \pm 0.02 \pm 0.05$. Toutes ces valeurs s'accordent remarquablement bien avec les résultats du modèle hydrodynamique (Nardetto et al. 2009). Une méthode légèrement différente consiste à appliquer la méthode de BW *inverse* aux Céphéides lointaines en utilisant la relation brillance de surface - couleur dans l'infrarouge (voir Fouque & Gieren 1997; Kervella et al. 2004a pour le principe [3]) afin d'en déduire une relation Pp. Dans cette méthode, on considère que la distance BW de chaque Céphéide du LMC est la même (la géométrie du LMC n'est pas prise en compte). Cela permet de contraindre la pente de la relation Pp. En revanche, le point zéro de la relation Pp est fixé soit en utilisant les Céphéides dans les amas galactiques (Gieren et al. 2005b), soit en utilisant les parallaxes HST des Céphéides proches obtenues par van Leeuwen et al. (2007b) (Laney & Joner 2009; Storm et al. 2011b), ou une combinaison des deux (Groenewegen 2013). Laney & Joner (2009) ont utilisé également les *High-Amplitude* δ *Scuti Stars* (HADS) pour déduire une relation Pp (nous y reviendrons dans la Sect. 4.4). Les facteurs de projection obtenus par Laney & Joner (2009) et Groenewegen (2013) sont cohérents avec les valeurs interférométriques tandis que les facteurs de projection de Gieren et al. (2005b) et Storm et al. (2011b) sont significativement plus élevés (voir Table 4.1). Une autre approche novatrice et purement observationnelle utilise les Céphéides appartenant à un système binaire à éclipses. Nous reviendrons sur le principe dans le chapitre sur les binaires à éclipses. Le facteur de projection obtenu pour une Céphéide de période $P = 3.80$ jours (c'est-à-dire comparable à δ Cep) est de $p = 1.21 \pm 0.04$ (Pilecki et al. 2013). Enfin, pour être complet, signalons que des approches semi-théoriques [4] font également intervenir le facteur de projection (Molinaro et al. 2011; Marconi et al. 2017).

2. Cependant, la granulation pose probablement un autre problème. Des variations de cycle à cycle ont été observées dans quatre Céphéides, deux Céphéides de courte période et de faible amplitude (pulsant dans le premier harmonique), QZ Normae et V335 Puppis, ainsi que dans deux céphéides de longue période ℓ Carinae et RS Puppis (Anderson 2014). Ces variations dans les vitesses radiales (de l'ordre de quelques pourcents) ne sont pas synchronisées avec les variations de diamètre angulaire que l'on peut mesurer par interférométrie, ce qui peut avoir un impact sur la variation du facteur de projection de l'ordre de 5% (Anderson et al. 2016b). Ces longues séries de données vélocimétriques sur ℓ Car ont également permis d'étudier les variations de cycle à cycle du gradient de vitesse dans l'atmosphère de l'étoile (Anderson 2016; Anderson et al. 2016a).

3. Il s'agit en fait de la méthode de BW version photométrique dans laquelle les bandes V et K sont utilisées. La méthode SPIPS quant à elle utilise l'ensemble des données disponibles : photométriques (dans toutes les bandes ou presque) et interférométriques.

4. Molinaro et al. (2011) ont développé une nouvelle version de la méthode de Baade-Wesselink, s'appuyant sur l'approche CORS (Caccin et al. 1981), dont l'objectif est de déterminer des rayons moyens à partir de relations brillance de surface - couleur théoriques (c'est à dire basées sur des modèles d'atmosphères). Ces rayons sont alors utilisés pour déterminer des relations période - rayon et période - luminosité à partir de deux estimations du facteur de projection $p = 1.36$ et $p = 1.27$. Les auteurs déduisent de cette étude que la valeur $p = 1.27$ est la plus appropriée, la valeur $p = 1.36$ donnant des incohérences de l'ordre de 2σ sur les relations. Dans le même ordre d'idée, Marconi et al. (2017) ont utilisé des modèles d'atmosphère pour reproduire les courbes photométriques des Céphéides du SMC, ainsi que les courbes de vitesses (déduites à partir de la dérivée du rayon théorique) pour en déduire des valeurs du facteur de projection, dont les valeurs vont de 1.16 à 1.40.

TABLE 4.1 – Liste non exhaustive des facteurs de projection de la littérature dans le cas de δ Cep. La méthode utilisée pour déduire la vitesse radiale est indiquée, et *cc-g* correspond à un ajustement gaussien du profil déduit de la cross-corrélation. Certaines valeurs sont déduites à partir d'une relation entre la période et le facteur de projection en considérant une période de $P = 5.366208$ jours (Engle et al. 2014).

method	p	reference
Modèles géométriques		
centroid	1.415	Getting (1934)
centroid	1.375	van Hoof & Deurinck (1952)
centroid	1.360	Burki et al. (1982)
centroid	1.328	Neilson et al. (2012b)
Modèles hydrodynamiques		
bisector	1.34	Sabbey et al. (1995)
Gaussian	1.27 ± 0.01	Nardetto et al. (2004)
cc-g (Pp)	1.25 ± 0.05	Nardetto et al. (2009)
Observations		
cc-g	$1.273 \pm 0.021 \pm 0.050$	Mérand et al. (2005)
cc-g	$1.245 \pm 0.030 \pm 0.050$	Groenewegen (2007)
cc-g	$1.290 \pm 0.020 \pm 0.050$	Merand et al. (2015)
cc-g	$1.239 \pm 0.034 \pm 0.023$	Nardetto et al. (2017)
cc-g (Pp)	1.47 ± 0.05	Gieren et al. (2005b)
cc-g (Pp)	1.29 ± 0.06	Laney & Joner (2009)
cc-g (Pp)	1.41 ± 0.05	Storm et al. (2011b)
cc-g (Pp)	1.325 ± 0.03	Groenewegen (2013)

Cette petite revue sur le facteur de projection de δ Cep illustre les différentes approches actuellement utilisées. De mon côté, avec de nombreux collaborateurs, j'ai progressé par étapes :

1. Comme déjà mentionné, j'ai d'abord étudié le facteur de projection de façon globale et purement théorique avec le modèle hydrodynamique développé par Fokin (1994). J'ai ainsi trouvé pour δ Cep un p-facteur de $p = 1.27 \pm 0.01$ (Nardetto et al. 2004). J'ai également montré durant ma thèse de Doctorat que la variation du facteur de projection (et donc de l'assombrissement centre-bord) avec la phase n'a pas d'impact sur la distance. Cela produit simplement un décalage en phase de la courbe de rayon de 0.02, ce qui n'affecte pas l'amplitude de la courbe et donc la distance (Nardetto et al. 2006a).

2. En 2007, à l'aide d'une approche semi-théorique, et en rupture avec les méthodes académiques, j'ai *décomposé* le concept du facteur de projection avec une approche cohérente et généralisable à l'ensemble des Céphéides du diagramme Hertzsprung-Russell (HR). J'ai ainsi découvert une relation entre la période des Céphéides et le facteur de projection (relation *Pp*). La décomposition du facteur du projection dans le cas de δ Cep est illustrée par la figure 4.1 et le papier correspondant se trouve dans l'annexe J.

3. Dans Nardetto et al. (2007), la relation *Pp* obtenue ne s'applique qu'à une raie spécifique, ou peut éventuellement être déduite pour différentes raies à l'aide d'une "recette". C'est la raison pour laquelle en 2009, j'ai calculé la correction à appliquer lorsqu'on utilise la méthode de la cross-corrélation ("cc-g") qui est largement utilisée par la communauté (Nardetto et al. 2009) (voir l'annexe K) . L'avantage de la méthode est sa sensibilité (elle permet notamment d'accéder aux Céphéides des nuages de Magellan). Cependant l'inconvénient majeur est qu'elle mélange l'information liée à de nombreuses raies, ce qui induit des hypothèses particulières sur le facteur de projection. De plus, le fait d'utiliser un ajustement gaussien génère également un biais sur le facteur de projection. Ainsi, le facteur de projection est réduit de l'ordre de 5% quelle que soit la période de la Céphéide par rapport à un facteur de projection qui serait déduit à partir d'une raie individuelle et la méthode du premier moment.

4. En 2011, j'ai montré de manière purement théorique que le facteur de projection ne dépend pas de la métallicité de l'étoile (Nardetto et al. 2011a) (voir l'annexe L), ce qui est un point important à prendre en compte lorsqu'on étudie les Céphéides des nuages de Magellan (Storm et al. 2011a,b).

5. Enfin, en 2017, j'ai comparé pour la première fois le modèle hydrodynamique de δ Cep avec des observations HARPS-N d'une qualité exceptionnelle (Nardetto et al. 2017) (voir l'annexe M). Ainsi le modèle re-normalisé [5] reproduit de façon remarquable : (1) le gradient de vitesse atmosphérique déduit des données HARPS-N, (2) la variation de diamètre angulaire établie avec l'instrument FLUOR sur l'interféromètre CHARA, et (3) les facteurs de projection purement observationnels déduits de la méthode de BW inverse (prenant la distance du HST comme référence). Ces résultats semblent indiquer que la décomposition du facteur de projection telle que présentée dans l'article de 2007 est adéquate (voir Fig. 4.2).

5. Dans Nardetto et al. (2017), il a été nécessaire de mettre à l'échelle le modèle hydrodynamique présenté dans Nardetto et al. (2004). En effet, le modèle prédisait des amplitudes de courbes de vitesses radiales inférieures de l'ordre de 7% à celles obtenues à partir des observations HARPS-N. Ainsi, l'idée est de simplement multiplier la courbe de la vitesse pulsante par un facteur de 7%, ce qui augmente alors l'amplitude de la courbe de vitesse radiale de 7% ainsi que la variation de rayon de 7%, tandis que la facteur de projection lui-même reste inchangé par définition. Le fait que le modèle hydrodynamique ne reproduise pas l'amplitude ne manière convenable est attribué au fait qu'il ne prend pas en compte la convection.

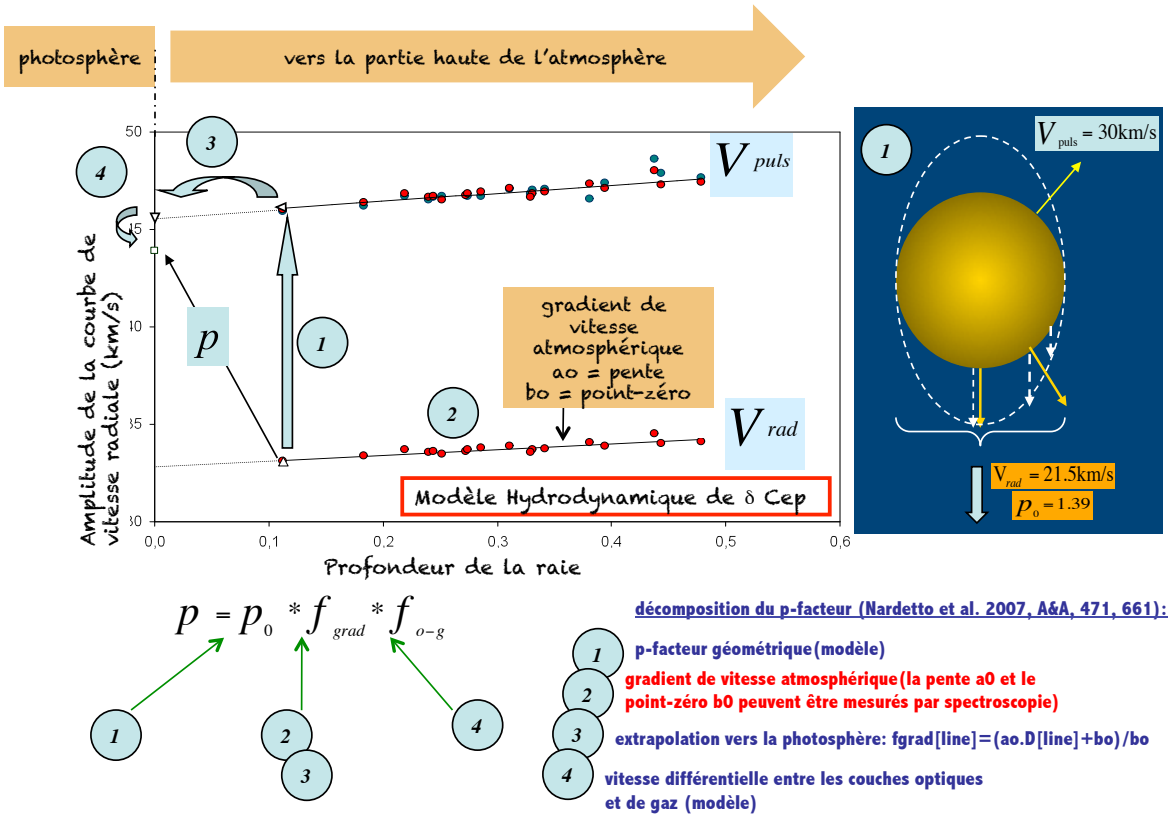


FIGURE 4.1 – Décomposition du facteur de projection illustrée dans le cas de δ Cep et à partir du modèle hydrodynamique *uniquement*. On procède de la manière suivante. Il faut d'abord déterminer le facteur de projection géométrique p_0. Une Céphéide qui pulserait avec un disque ayant une distribution d'intensité uniforme aurait invariablement un facteur de projection de 1.5. Du fait de l'assombrissement centre bord, la vitesse radiale résultante sur la ligne de visée est inférieure à la vitesse pulsante (par exemple 21.5 km s^{-1}au lieu de 30 km s^{-1} ; voir encart) ce qui donne un facteur de projection géométrique *moyen* (on néglige la variation de l'assombrissement centre-bord et du p-facteur avec la phase) pour δ Cep entre 1.36 et 1.39, selon la longueur d'onde considérée dans le domaine visible (car l'assombrissement centre-bord dépend de la longueur d'onde). Ce facteur de projection géométrique permet de passer (étape 1 sur la figure) de l'amplitude de la courbe de vitesse radiale pour une raie donnée (quantité par définition indépendante de la phase et tirée des profils théoriques du modèle ; points rouge en bas sur la figure) à l'amplitude de la courbe de vitesse pulsante correspondante (points rouges en haut), dont la valeur s'accorde effectivement bien avec les valeurs de référence issues directement des couches dans l'atmosphère du modèle hydrodynamique (points verts en haut sur la figure). Cet accord confirme la cohérence de la décomposition du facteur de projection. Il faut ensuite prendre en compte le gradient de vitesse dans les couches de l'atmosphère de l'étoile. Celui-ci est illustré par la relation entre l'amplitude des courbes de vitesses radiales (ΔRV_c, obtenues par la méthode du premier moment ; ceci est indispensable sinon cela ne fonctionne pas du fait des biais associés aux autres méthodes) et la profondeur de la raie (D, prise au rayon minimum, sinon la décomposition n'est plus cohérente). La relation s'écrit ainsi : $\Delta RV_c = a_0 D + b_0$ et peut être directement déduite des observations spectroscopiques (étape 2 sur la figure). La correction sur le facteur de projection géométrique dépendra ainsi de la raie spectrale considérée et s'écrit : $f_{\rm grad} = \frac{a_0 D[line]+b_0}{b_0}$. Ce qu'il faut comprendre ici, c'est que l'on compare l'amplitude de la courbe de vitesse radiale associée à la raie ($a_0 D[line] + b_0$) à l'amplitude de la courbe de vitesse radiale associée à la photosphère b_0. Car justement, il ne faut pas perdre de vue l'objectif final de déduire l'amplitude de la courbe de vitesse pulsante associée à la photosphère de façon à obtenir (après intégration temporelle) la variation de rayon photosphérique, celle-là même qui peut être comparée de manière *cohérente* à la variation de diamètre angulaire de l'étoile déduite de l'interférométrie ou de la photométrie (à partir du *continuum*, c'est-à-dire l'émission du corps noir). Ainsi, une extrapolation vers la photosphère (étape 3 sur la figure) est nécessaire, et plus la raie se forme haut dans l'atmosphère (D élevé), plus la correction $f_{\rm grad}$ est importante et plus le facteur de projection est réduit (jusqu'à 3%). Il reste une dernière subtilité : le rayonnement issu du *continuum* de l'étoile est absorbé par les éléments chimiques présents dans le gaz qui constitue l'atmosphère. La vitesse radiale peut donc être associée à la vitesse du gaz atmosphérique. Ce n'est pas le cas des observations interférométriques ou photométriques, qui elles sont sensibles à la couche optique que constitue la photosphère de l'étoile. En effet, le gaz peut très bien traverser cette couche optique, et la vitesse différentielle entre les deux doit être prise en compte et l'impact sur le facteur de projection corrigé. Cette correction est notée $f_{\rm o-g}$ et peut valoir quelques pourcents selon la Céphéide considérée (étape 4 sur la figure). Finalement, le facteur du projection qui relie très exactement l'amplitude de la courbe de vitesse radiale pour une raie donnée, à la vitesse pulsante de la couche optique constituant la photosphère de l'étoile s'écrit : $p = p_0 f_{\rm grad} f_{\rm o-g}$. Cette décomposition du facteur de projection, dont la cohérence interne a été validée par le code hydrodynamique (Nardetto et al. 2007) a été confirmée dix ans plus tard par une mesure directe du gradient de vitesse dans l'atmosphère de δ Cep (Nardetto et al. 2017).

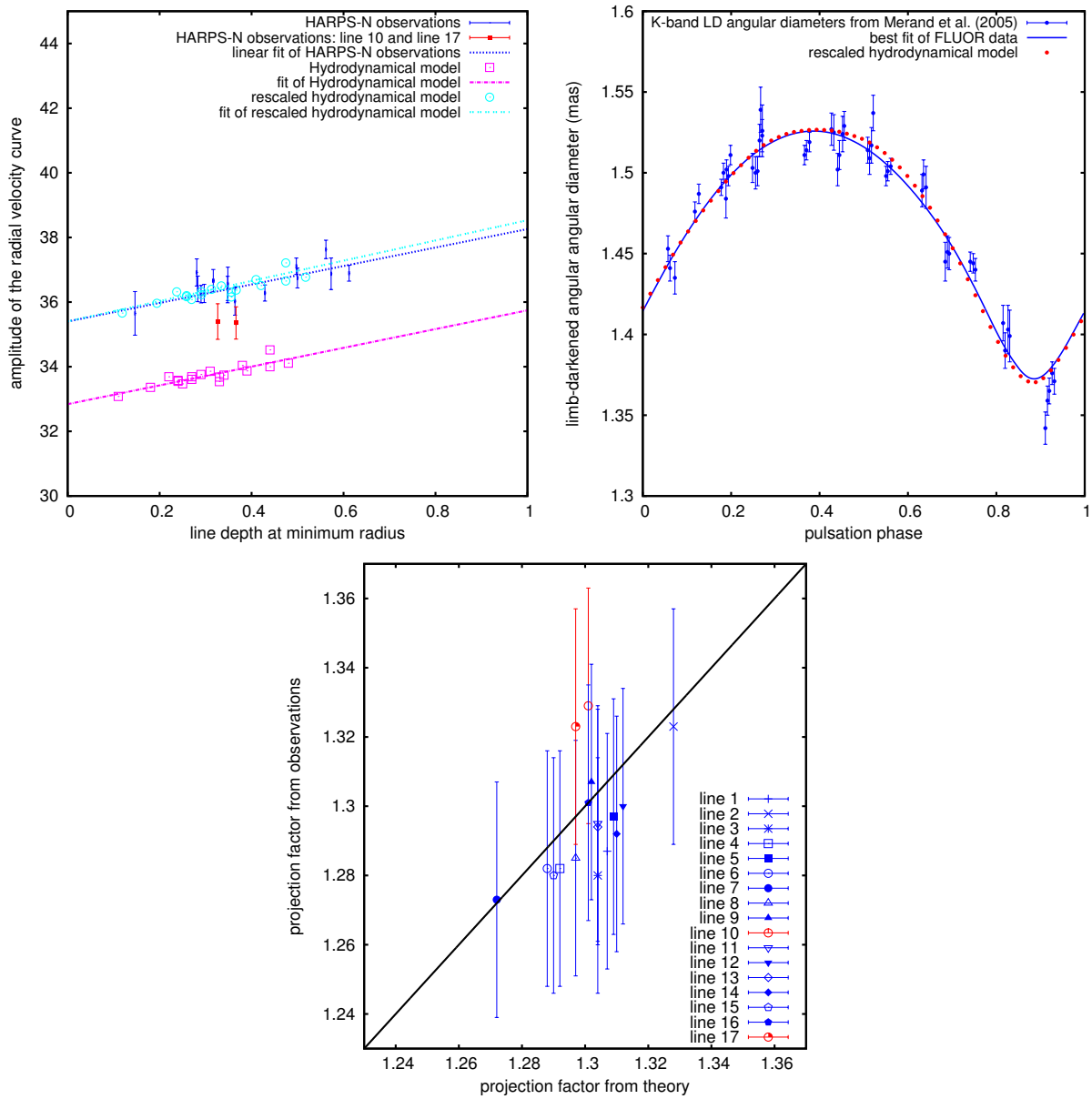


FIGURE 4.2 – Figure en haut à gauche : Comparaison du gradient de vitesse dans l'atmosphère de δ Cep déduit des observations HARPS-N (bleu foncé), du modèle hydrodynamique (magenta) et du modèle hydrodynamique redimensionné (bleu clair). Figure en haut à droite : comparaison de la variation du diamètre angulaire déduite des données FLUOR/CHARA (en bleu) et du modèle hydrodynamique redimensionné (en rouge). Figure du bas : comparaison des facteurs de projection déduits de la méthode de BW inverse (observation) et du modèle hydrodynamique (théorie). Sur ces trois figures, l'accord entre les observations et le modèle est remarquable, ce qui confirme la décomposition du facteur de projection décrite dans Nardetto et al. (2017).

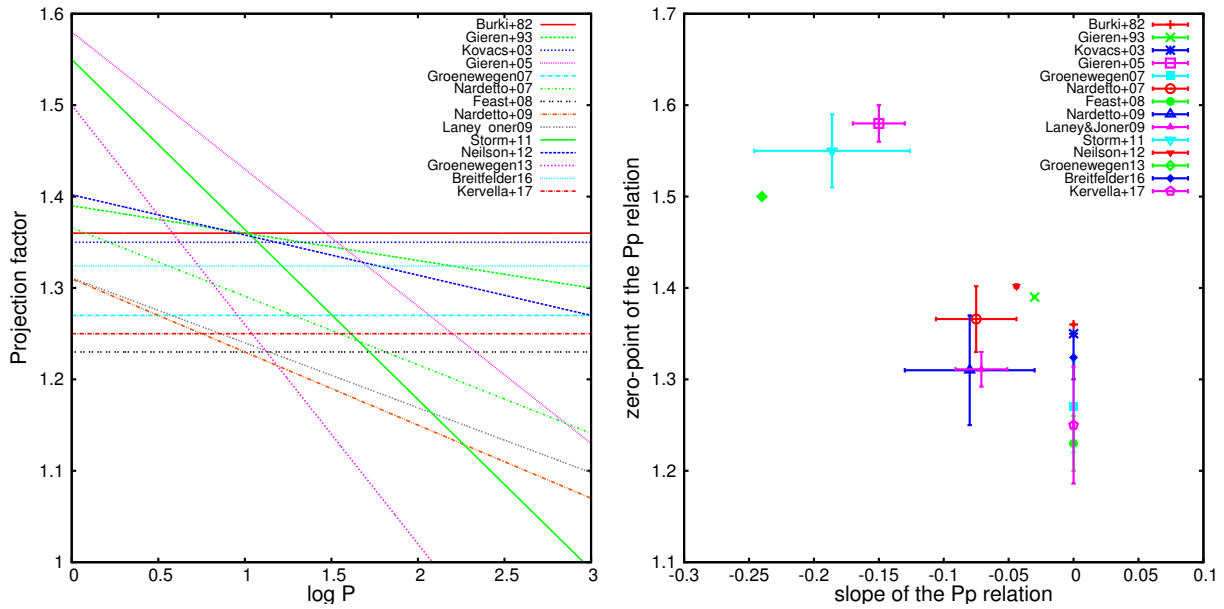


FIGURE 4.3 – A gauche, les relations Pp disponibles à ce jour. A droite, le point-zéro de ces relations est représenté en fonction de leur pente.

Ainsi le facteur de projection *dynamique* de δ Cep semble bien établi et compris physiquement avec une valeur (pour la méthode *cc-g*) autour de 1.25. Cependant, plusieurs points restent à résoudre :

1. Pourquoi les valeurs basées sur la relation brillance de surface - couleur *inverse* dans l'infrarouge sont significativement supérieures (Gieren et al. 2005b; Storm et al. 2011b; Groenewegen 2013) à 1.25. Il est à noter tout de même que la valeur de Merand et al. (2015) qui est hybride (basée sur l'interférométrie et la photométrie) donne une valeur intermédiaire. Est-ce que la relation brillance de surface - couleur est sensible à l'environnement des Céphéides ? Par exemple, il est intéressant de noter que les deux versions de la méthode de Baade-Wesselink basées respectivement sur l'interférométrie et les relations brillance de surface - couleur donnent des résultats cohérents pour la Céphéide longue période ℓ Car (Kervella et al. 2004c), mais pas pour δ Cep (Ngeow et al. 2012). Par ailleurs, toutes ces valeurs relativement plus élevées du facteur de projection sont déduites de relations Pp basées sur les Céphéides du LMC. Est-ce donc un problème lié à la métallicité ou à la géométrie du LMC ?
2. Mais le problème est ensuite plus complexe, comme on le voit sur les figures 4.3ab qui illustrent les différentes relations Pp disponibles à ce jour. Des désaccords importants sont toujours présents et débattus. Or ces relations ont un impact significatif sur les distances. En effet, si l'on utilise un facteur de projection constant (traditionnellement $p = 1.36$ pour toutes les étoiles), au lieu de la relation donnée par (Nardetto et al. 2009) par exemple, alors on peut introduire une différence de l'ordre de 0.10 et 0.03 mag respectivement sur la pente et le point-zéro de la relation PL, ce qui correspond à une différence de l'ordre de 10% en terme de distance.

L'apport de *Gaia* sera considérable pour répondre à ces questions. En effet, en appliquant la méthode de BW inverse aux parallaxes *Gaia* (DR2, Avril 2018), nous aurons très prochainement accès au facteur de projection de 300 Céphéides avec une précision de 3%. Par ailleurs, la distance du LMC et du SMC

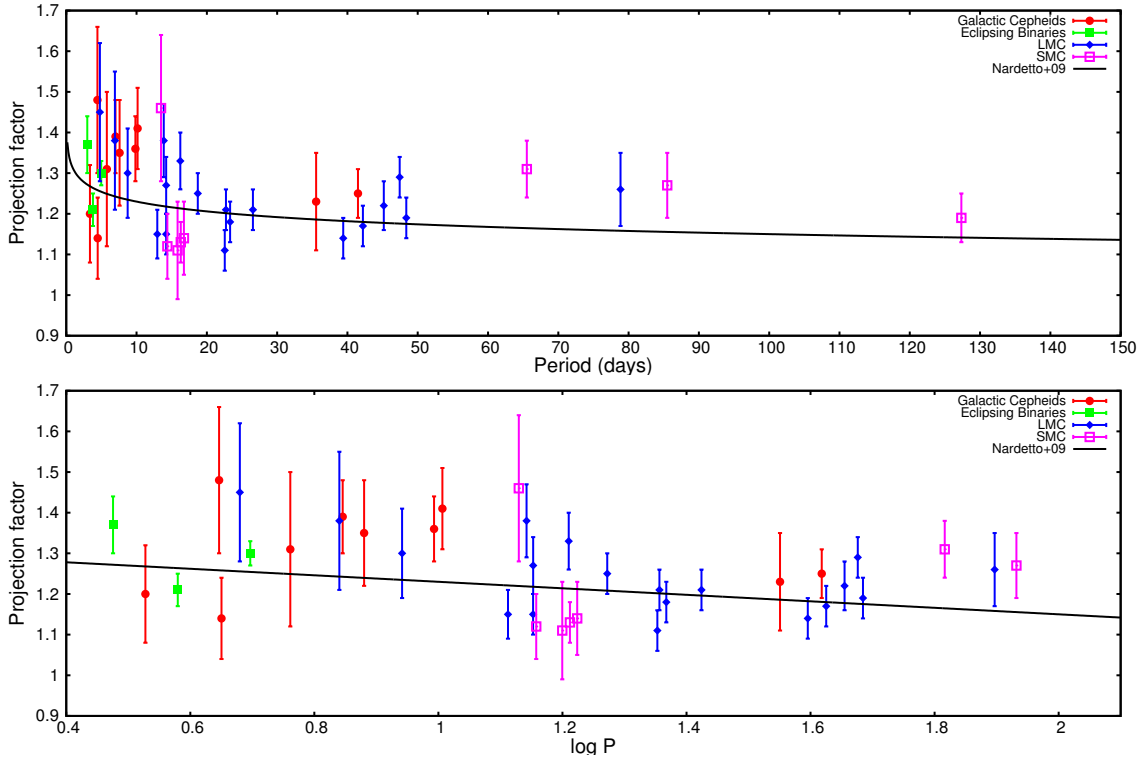


FIGURE 4.4 – Le facteur de projection est représenté en fonction du logarithme de la période. Ces valeurs de p sont purement observationnelles, i.e. soit déduites des méthodes de BW inverses appliquées aux Céphéides galactiques (Breitfelder et al. 2016), du SMC, et du LMC (Gallenne et al. 2017), soit des binaires à éclipses dont l'une des composantes est une Céphéide (voir Sect. 5.4). Avec Gaia, nous serons en mesure de déduire environ 300 p-facteurs de ce type avec une précision de l'ordre de 3%. Notre connaissance du facteur de projection, en particulier sa décomposition, sera alors très utile pour interpréter ces résultats.

deviennent maintenant suffisamment précises pour appliquer les méthodes de BW inverse aux Céphéides de ces galaxies. Le travail a commencé, représenté par la figure 4.9ab. Dans ce contexte, et à terme, la décomposition du facteur de projection sera un outil précieux pour comprendre et analyser l'ensemble de ces facteurs de projection.

4.2 Le k-facteur

Si l'on considère un mouvement axi-symétrique de rotation de la Voie Lactée, les Céphéides présentent un mouvement résiduel d'approche vers le Soleil d'environ 2 km s^{-1}(Fig. 4.5). Ce mouvement résiduel, appelé le k-facteur, a été pour la première fois observé par Joy (1939). Depuis 1939, la question est de savoir si le k-facteur est effectivement lié à un mouvement réel des Céphéides au sein de la Voie Lactée (Camm 1938, 1944; Parenago 1945; Stibbs 1956; Caldwell & Coulson 1987; Moffett & Barnes 1987; Wilson et al. 1991; Pont et al. 1994) ou s'il s'agit d'un phénomène intrinsèque lié à la dynamique atmosphérique de ces étoiles (Wielen 1974; Butler et al. 1996). La réponse est naturellement venue en étudiant les détails de la méthode de BW.

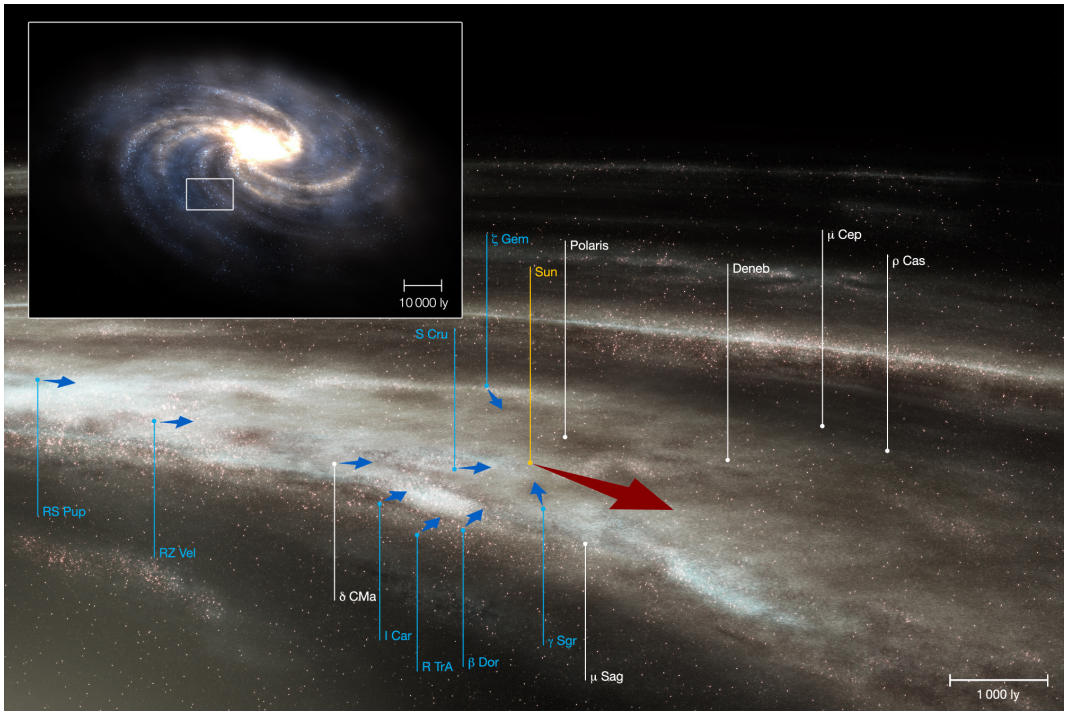


FIGURE 4.5 – Depuis 1939 et jusqu'à récemment, on s'interrogeait sur le fait que les Céphéides de notre voisinage semblaient tomber vers le Soleil avec une vitesse résiduelle de l'ordre de 1 ou 2 km s^{-1}. Etait-ce le résultat d'un mouvement réel des Céphéides au sein de notre Voie Lactée ou une propriété intrinsèque liée à leur dynamique atmosphérique ? Grâce à l'étude de l'asymétrie des raies spectrales, nous avons montré qu'il s'agissait un phénomène intrinsèque aux Céphéides (Nardetto et al. 2008b) [Crédit - ESO Press Release : Pinning down the Milky Way's spin (19 September 2008)]. Très récemment, Vasilyev et al. (2017) ont montré en utilisant un modèle bidimensionnel d'une Céphéide courte période qu'il s'agit d'un phénomène lié à la granulation.

En effet, lorsqu'on applique la méthode de BW, il faut corriger la courbe de vitesse radiale $RV_{\mathrm{cc-g}}$ de la vitesse du centre de masse de l'étoile $V_\star$ (Eq. 4.2) et donc forcer sa moyenne à zéro de façon à ce que l'intégration temporelle donne bien la variation de rayon. Or, si l'on compare les vitesses radiales associées aux premiers moments de trois raies spectrales comme illustré sur la Fig 4.6a dans le cas de β Dor, on s'aperçoit que ces moyennes (notées γ-vitesses) sont différentes d'une raie à l'autre, de l'ordre de quelques pourcents. Ceci est surprenant. En effet, les amplitudes des trois courbes peuvent éventuellement être différentes du fait du gradient de vitesse atmosphérique comme nous l'avons déjà vu dans la section précédente. En revanche, un élément chimique donné à l'origine d'une raie spectrale en absorption dans

l'atmosphère de la Céphéide devrait en principe retrouver sa position initiale après un cycle de pulsation, et les trois courbes devraient avoir une moyenne identique (correspondant à la vitesse du centre de masse de l'étoile), et par extension, cela devrait être aussi le cas pour RV_{cc} qui repose sur des centaines de raies spectrales. Mais ce n'est manifestement pas le cas. Un problème se pose alors : comment véritablement séparer la pulsation de l'étoile de la vitesse de son centre de masse ? Et à quoi correspondent physiquement ces différences de vitesses moyennes ? Ceci a bien sûr son importance dans le cadre de la méthode de BW.

Nous avons alors proposé une approche qui permet de calculer la vitesse du centre de masse de l'étoile, basée sur l'asymétrie des raies (Nardetto et al. 2008b) (voir le papier correspondant dans l'annexe N) . L'asymétrie [6] des trois raies est représentée sur la Fig 4.6b. Il est intéressant de remarquer que les valeurs moyennes de ces trois courbes d'asymétrie (notées γ-asymétries) sont anti-corrélées aux valeurs moyennes des courbes de vitesses radiales. La Fig 4.6c représente la vitesse radiale en fonction de l'asymétrie de la raie spectrale sur le cycle de l'étoile. On observe des boucles (dont la forme est complexe et reliée à la dynamique de l'atmosphère de la Céphéide) et dont les barycentres (les trois croix de couleurs) sont alignés. On peut effectivement généraliser ce résultat en prenant une vingtaine de raies parfaitement "propres", c'est-à-dire non contaminées par d'autres raies stellaires ou telluriques (Fig 4.6d). Dans la mesure où un modèle quasi-statique de Céphéide ne présente pas de résidus de vitesses radiales ni d'asymétrie (point à l'origine du graphique), on fait alors l'hypothèse suivante : *une raie spectrale dont la γ-asymétrie est nulle doit nécessairement avoir une γ-vitesse nulle*. En conséquence, le point zéro de la relation entre la γ-vitesse et la γ-asymétrie correspond à la vitesse du centre de masse de l'étoile. Cette valeur vaut $V_\star = 9.8 \pm 0.1$ km s^{-1}dans le cas de β Dor (Nardetto et al. 2008b). Or, si l'on considère la valeur correspondante issue de la base de données de Fernie et al. (1995), on obtient $<RV_{cc-g}>$ = 7.4 km s^{-1}. La différence entre les deux vaut donc (toujours dans le cas de β Dor) 2.4 ± 0.1 km s^{-1}. On trouve le même comportement pour les huit Céphéides étudiées (Nardetto et al. 2008b) avec une moyenne de 1.8 ± 0.2 km s^{-1}(en prenant comme point référence les courbes cross-corrélées de la littérature). Cette valeur a ensuite été révisée à 1.0 ± 0.2 km s^{-1}en considérant les courbes de vitesses radiales cross-corrélées déduites des données HARPS, i.e. de manière cohérente en utilisant le même jeu de données (Nardetto et al. 2009).

Ainsi, si l'on prend en compte la dynamique atmosphérique des Céphéides, c'est-à-dire si l'on détermine la vitesse du centre de masse des Céphéides avec la méthode proposée ci-dessus, alors les Céphéides ne semblent plus s'approcher du soleil avec une vitesse radiale résiduelle de l'ordre de 1-2km s^{-1}. Il faut alors chercher l'explication du k-facteur non pas dans le mouvement des Céphéides au sein de la Voie Lactée avec un mouvement non axi-symétrique par exemple (Pont et al. 1994) mais en étudiant la physique des Céphéides. Plusieurs pistes ont alors été évoquées pour expliquer le k-facteur : 1) la position des zones de formation des raies dans l'atmosphère des Céphéides n'est pas strictement cyclique ou alors, 2) le décalage vers le bleu observé est dû à des mouvements de convection, de la granulation. Récemment, une réponse a une nouvelle fois été apportée par Vasilyev et al. (2017) à partir de leur modèle bi-dimensionnel incluant la convection. Il semblerait que le k-facteur soit principalement dû à la granulation [7]. Ils trouvent effectivement une valeur du k-facteur moyen (i.e. calculé à partir de nombreuses raies spectrales de forces différentes) entre -0.5 et -1.0 km s^{-1}, ce qui semble compatible avec la valeur obtenue par Nardetto et al. (2009) à partir de la méthode de la cross-corrélation. La question importante à laquelle il faudra répondre dans les années à venir est de quantifier l'impact de ce k-facteur sur la distance de BW des Céphéides.

6. Il existe plusieurs façons de déterminer l'asymétrie d'une raie spectrale. La méthode que nous avons développée dans Nardetto et al. (2006b) (voir Eq. 1) consiste à ajuster deux demi gaussiennes sur la raie spectrale et de comparer leur largeur à mi-hauteur.

7. Il est intéressant d'avoir en tête que le k-facteur, qui est donc mesuré à partir des raies spectrales, est lui aussi affecté par le facteur de projection.

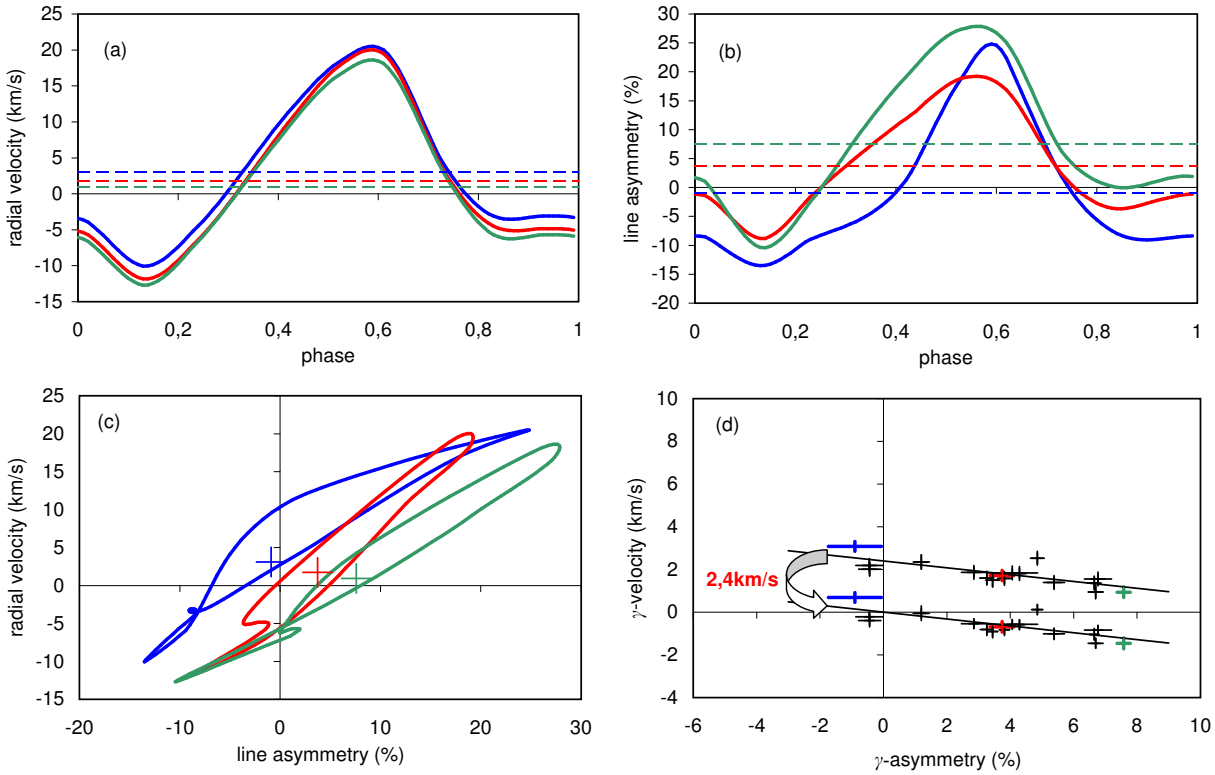


FIGURE 4.6 – Figure explicative du k-facteur des Céphéides (voir le texte).

4.3 L'environnement des Céphéides

Il semblerait que la plupart des Céphéides disposent d'une enveloppe circumstellaire dont la contribution en flux est corrélée à leur période de pulsation (voir Fig. 3.7). Ces enveloppes ont un double impact : (1) elles ont un effet sur la relation *PL* des Céphéides (voir Sect. 3.3) et (2) elles affectent également, dans le cadre de la méthode de BW, l'estimation du diamètre angulaire (interférométrique ou photométrique). Or, la taille, la forme et la nature chimique (gaz et/ou poussière) de ces enveloppes sont très mal connues. Un des *work-packages* de l'ANR *UnlockCepheids* dont je suis responsable vise précisément à caractériser les enveloppes des Céphéides de façon à les intégrer de façon cohérente dans l'approche SPIPS. L'idée *in fine* est de relier les caractéristiques des enveloppes à la position des étoiles dans la bande d'instabilité de façon à fournir des facteurs correctifs dans différentes bandes photométriques, avec l'objectif, par exemple, de débiaiser la future relation *PL* qui sera établie à partir des observations du JWST.

Ces enveloppes ont été découvertes dans l'infrarouge, par interférométrie, imagerie ou par un calcul de SED (voir le Tableau récapitulatif 3.6). Dans le visible, des indices d'enveloppe ont été rapportées par deux études. La première porte sur des séries de profils Hα de huit Céphéides (Nardetto et al. 2008a) (voir le papier correspondant dans l'annexe O). Plus la période d'une Céphéide donnée est élevée, plus ses profils présentent une asymétrie résiduelle vers le bleu importante, avec des vitesses correspondantes (moyennées sur l'ensemble du cycle) de quelques km s^{-1}pour les plus courtes période à -20 km s^{-1}pour les longues périodes. Ces vitesses pourraient être le résultat d'une perte de masse de l'étoile. Pour ℓ Car, non seulement le profil Hα est asymétrique, mais il présente également une composante en absorption statique correspondant une vitesse nulle, que l'on attribue à une enveloppe visible statique (voir Fig. 4.7). Cependant, ℓ Car a également été observée par interférométrie visible avec SUSI (Davis et al. 2009) (voir Tableau 3.7) et bien que la pulsation ait été mesurée pour cette étoile, aucune enveloppe n'a été détectée (seulement une variation d'assombrissement centre-bord avec la phase). Entre 2008 et 2014, mes collaborateurs et moi-même avons décidé d'observer les Céphéides avec VEGA/CHARA. Or, 15860 cycles après sa découverte par J. Goodrick en 1783, δ Cep, l'étoile prototype qui donne son nom aux étoiles de type Céphéides, avait encore quelques secrets à nous livrer. Nous avons ainsi mis en évidence la présence d'un environnement visible autour de cette étoile (Nardetto et al. 2016) (voir l'annexe P). Du fait de l'inadéquation entre le diamètre angulaire de δ Cep (environ 1.4 mas) et la configuration de bases de l'interféromètre CHARA (les plus courtes bases sont de 30 mètres environ), il n'a pas été possible de caractériser véritablement l'environnement. Il peut s'agir d'une enveloppe avec un diamètre de l'ordre de 8.9 ± 3.0 mas avec une contribution en flux de l'ordre de $7 \pm 1\%$. Ou alors, il s'agit un rayonnement d'arrière-plan remplissant le champ de vue de l'interféromètre, mais contribuant toujours à hauteur de 7% en terme de flux (voir Fig. 4.8). Notons que le compagnon de δ Cep récemment découvert (Anderson et al. 2015) n'est pas détectable par l'instrument VEGA. Un deuxième aspect ressort de cette étude : il semblerait que δ Cep s'éloigne d'un modèle de pulsation quasi-statique autour du rayon minimum. La variation de l'assombrissement centre-bord de l'étoile ne peut pas expliquer les données, car l'effet serait d'un ordre de grandeur plus faible d'après les modèles. Notre meilleure hypothèse serait l'existence d'un phénomène de réverbération : au rayon minimum, l'étoile est chaude, brillante, et son flux pourrait se refléter sur l'environnement, ce qui modifierait sa contribution en flux. Il est difficile de conclure pour le moment.

Cette découverte de l'environnement visible des Céphéides n'aura pas d'impact *direct* sur l'étalonnage des distances dans l'univers dans la mesure où la relation *PL*, dans le *visible*, est très dispersée, au contraire de sa contrepartie infrarouge qui, elle, est utilisée pour les distances. En revanche, ces données visibles apporteront très probablement des contraintes très fortes sur les modèles d'enveloppes, et c'est justement à partir de ces modèles que les contributions infrarouges pourront être estimées de manière exacte.

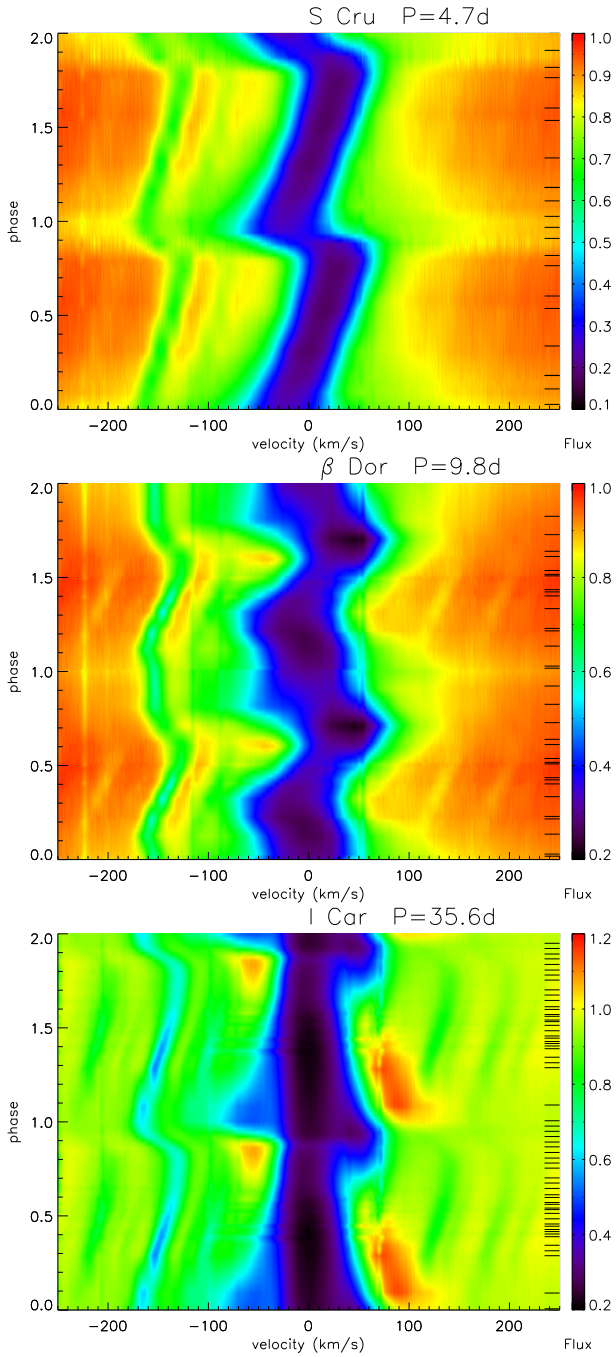


FIGURE 4.7 – Profils Hα des Céphéides en fonction de la période de pulsation. Plus la période de la Céphéide est importante, plus le profil moyen est asymétrique vers le bleu, signature probable d'une perte de masse (Nardetto et al. 2008a)

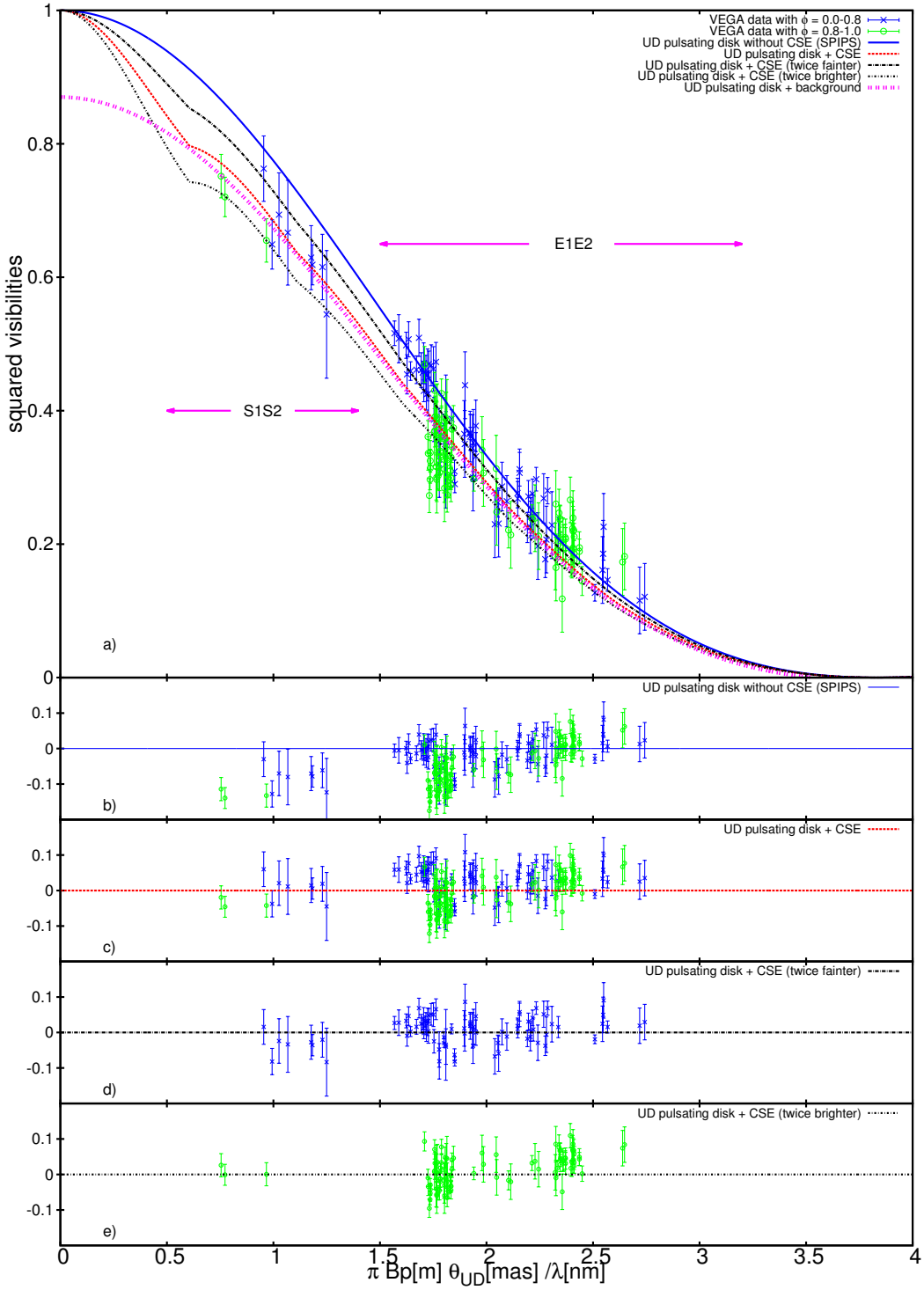


FIGURE 4.8 – a) Les visibilités carrées obtenues avec l'instrument VEGA/CHARA sur δ Cep sont représentées en fonction de $x = \frac{\pi B_p[\mathrm{m}]\theta_{\mathrm{UD}}[\mathrm{mas}]}{\lambda[\mathrm{nm}]}$ de façon à permettre la comparaison entre des données provenant de différentes phases de pulsation (i.e. avec des θ_{UD} et des longueurs d'onde effectives différentes). Cinq modèles sont représentés : (1) un disque pulsant uniforme (UD) de référence issu de l'analyse SPIPS combinant plusieurs bandes photométriques (ligne bleue), (2) le disque pulsant UD SPIPS + une CSE (ligne en pointillés rouge), (3) le disque pulsant UD SPIPS + une CSE 2 fois plus brillante (ligne en pointillés), (4) le disque pulsant UD SPIPS + une CSE 2 fois moins brillante (ligne en tirés), (5) le disque pulsant UD SPIPS + une contribution en flux d'un fond couvrant l'ensemble du champ de vue de l'interféromètre (ligne en magenta). Les résidus entre les observations et les modèles 1 à 4 sont indiqués dans les panels b), c), d) et e), respectivement. Dans les panels d) et e), seules les données correspondant aux intervalles de phase $\phi = 0.0 - 0.8$ et $\phi = 0.8 - 1.0$ sont représentées, respectivement. On peut conclure de l'analyse de ces données que δ Cep est effectivement entourée d'une enveloppe ou d'une contribution en flux d'arrière-plan, et qu'il existe deux régimes $\phi = 0.0 - 0.8$ et $\phi = 0.8 - 1.0$, respectivement, qui pourraient être l'indice d'une réverbération au moment du rayon minimum de l'étoile.

4.4 Une piste de recherche : la comparaison avec les autres types d'étoiles pulsantes

Le p-facteur, le k-facteur et la caractérisation de l'environnement des Céphéides sont des problèmes complexes. Procéder par comparaison avec d'autres types d'étoiles pulsantes, dont le mode radial est dominant, est une approche intéressante. Il s'agit de mettre en évidence certaines tendances dans le diagramme HR : existe-il une relation entre la position de l'étoile pulsante et les gradients de vitesse ? Les effets d'asymétrie des raies sont-ils communs à toutes les étoiles pulsantes ? La relation Pp existe-t-elle pour d'autres types d'étoiles pulsantes que les Céphéides ? Une telle étude comparative permet de placer les Céphéides dans un contexte plus vaste et de mieux comprendre les mécanismes de la pulsation, et de la perte de masse, en lien également avec l'environnement de ces étoiles.

D'abord quelques remarques sur les δ Scuti et les RR Lyrae (Fig. 4.9). Les δ Scuti ont une période comprise entre 0.5 et 5 heures et peuvent pulser dans différents modes : fondamental, multipériodique radial, ou non radial. Dziembowski (1977) a d'abord montré que la méthode de BW permettait de distinguer les modes radiaux et non-radiaux. Puis la méthode de BW a été modifiée de façon à prendre en compte les modes non radiaux en incluant un facteur de projection dépendant de l (Balona & Stobie 1979b,c,a; Stamford & Watson 1981; Hatzes 1996). Les spécialistes du domaine se sont ensuite intéressés aux δ Scuti à forte amplitude qui pulsent dans un mode radial fondamental, les "High Amplitude δ Scuti Stars" (ou HADS). L'application de la méthode de BW pour ces étoiles permet de déterminer leur rayon et donc, en principe, leur relation période-luminosité (Wilson et al. 1993; Milone et al. 1994; Wilson et al. 1998). Mais la méthode la plus utilisée pour étalonner la relation PL reste les mesures de parallaxes d'Hipparcos (Petersen & Hog 1998). Fernie (1992) montre ainsi que les relations PL des δ Scuti et des Céphéides sont compatibles. McNamara et al. (2007) ont déterminé la pente de la relation PL des δ Scuti des nuages de Magellan grâce aux observations photométriques OGLE (voir également McNamara (1997); Petersen & Christensen-Dalsgaard (1999) et Poleski et al. (2010) pour les résultats d'OGLE III). Les δ Scuti, trop faibles, ne peuvent pas véritablement être utilisées pour déterminer des distances dans le groupe local, en revanche, elles s'avèrent très intéressantes car elles sont beaucoup plus nombreuses et proches du Soleil que les Céphéides et il y a donc moins de problème lié au rougissement. Les RR Lyrae, quant à elles, présentent une relation période - métallicité - luminosité (Sollima et al. 2006; Marengo et al. 2017; Muraveva et al. 2015; Benedict et al. 2011). La méthode de BW a été appliquée à ce type d'étoiles à plusieurs reprises (Cacciari et al. 1992; Carney et al. 1992; Liu & Janes 1990; Carrillo et al. 1995). Récemment, Jurcsik et al. (2017) ont déterminé la distance de l'amas globulaire M3 en appliquant la méthode de BW à 26 RR Lyrae ne présentant pas l'effet Blazhko [8] et en utilisant une valeur du facteur de projection de $p = 1.35$ [9]. La distance obtenue, autour de 10.5kpc, est tout à fait compatible avec d'autres méthodes. Appliquer la méthode BW aux RR Lyrae avec (ou même sans) effet Blazhko devrait apporter dans les années à venir des contraintes sur la dynamique atmosphérique de ces étoiles.

8. L'effet Blazhko a été pour la première fois mis en évidence par Sergei Blazhko en 1907 sur l'étoile RW Dra. Il s'agit d'un phénomène propre aux RR Lyrae et caractérisé par une modulation de la courbe de luminosité en amplitude et en période.

9. Cette valeur tirée de Nardetto et al. (2004) n'est pas appropriée car elle a été calculée pour la détermination de la vitesse radiale qui correspond au pixel minimum de la raie. Mais par un heureux hasard, la période des RR Lyrae étant autour de 0.5 jours, la relation Pp de Nardetto et al. (2009) fournit une valeur de $p = 1.33$ (compatible avec la méthode de cross-correlation), ce qui explique probablement les résultats cohérents en terme de distance de M3. Mais des études sur le facteur de projection des RR Lyrae sont nécessaires.

Ainsi, ce projet de comparaison de la dynamique atmosphérique des étoiles pulsantes entre elles a débouché sur une première étude concernant les β-Céphéides [10] α Lup et τ^1 Lup (Nardetto et al. 2013) (voir le papier correspondant dans l'annexe Q). L'objectif de ce travail combinant observations spectroscopiques HARPS et modélisation hydrodynamique est de comparer la dynamique atmosphérique des β Céphéides avec celle des Céphéides, et ce à trois niveaux : valeur du facteur de projection, valeur du gradient de vitesse dans l'atmosphère et, enfin, le k-facteur (et les effets d'asymétrie de raies). Pour α Lup, les modes non-radiaux étant négligeables, j'ai ainsi calculé un facteur de projection théorique de l'ordre de $p = 1.43 \pm 0.01$. Par ailleurs, α Lup présente des raies spectrales dont l'asymétrie moyenne sur l'ensemble du cycle de pulsation est négative et de l'ordre de -7%, ce qui se traduit par une vitesse radiale résiduelle d'éloignement (décalage vers le rouge) de $k = +2.2 \pm 0.8$ km s^{-1}(alors qu'elle est comprise entre 0 et -2 km s^{-1}pour les Céphéides ; voir Sect. 4.2). Pour τ^1 Lup, les modes non-radiaux étant non négligeables, la modélisation hydrodynamique de l'étoile à l'aide du code de Fokin (1994) n'est pas possible. En revanche, τ^1 Lup semble présenter un gradient de vitesse atmosphérique négatif : la vitesse associée aux couches les plus profondes est supérieure à la vitesse des couches de la partie haute de l'atmosphère. Quelle en est la signification ? Est-ce le résultat des modes non-radiaux ? Je me suis également intéressé aux étoiles pulsantes de type δ Scuti. Ainsi dans Guiglion et al. (2013) [11], nous avons tout d'abord estimé l'impact de la rotation (non négligeable pour certaines de ces étoiles) et de l'assombrissement gravitationnel sur le facteur de projection de β Cas en utilisant le code de Domiciano de Souza et al. (2002, 2012) (voir Fig. 4.11). Nous avons également rédigé une section sur le problème complexe de l'impact des modes non-radiaux sur le facteur de projection. Nous avons ensuite continué ce travail pour deux autres δ Scuti, ρ Pup et DX Ceti (Nardetto et al. 2014) (voir l'annexe S). Nous avons ainsi mesuré à partir d'observations HARPS des gradients de vitesse atmosphérique autour de zéro pour ces deux étoiles à partir desquels il a été possible de déduire des valeurs du facteur de projection, en faisant l'hypothèse que la décomposition du facteur de projection développé dans Nardetto et al. (2007) est correcte. Les k-facteurs obtenus sont quant à eux de -0.5 ± 0.1 km s^{-1}pour ρ Pup et 0.0 ± 0.1 km s^{-1}pour AI Vel. Ainsi ces différentes études sur les étoiles pulsantes ont mené à plusieurs conclusions :

1. Il semble exister une relation *Pp* unique s'appliquant aux Céphéides et aux étoiles pulsantes de type δ Scuti (Fig. 4.9), mais ceci devra être confirmé par *Gaia*. Pour les δ Scuti, il faut prendre en compte l'assombrissement gravitationnel si l'étoile tourne plus vite qu'une centaine de km s^{-1}. Le facteur de projection de α Lup (la β-céphéide) est quant à lui plus proche des étoiles de type δ Scuti que des Céphéides.
2. L'intérêt autour du k-facteur est relancé depuis que Vasilyev et al. (2017) ont montré qu'il trouvait son origine dans la granulation des Céphéides. Plus une raie se forme haut dans l'atmosphère, plus le décalage vers le bleu est réduit (k proche de zéro). A l'inverse, une raie se formant proche de la photosphère est très décalée vers le bleu (k très négatif). Or, il est très intéressant de noter que l'on obtient une valeur du k-facteur autour de -1 km s^{-1}pour les Céphéides, +2 km s^{-1}pour la β Céphéide, et entre -0.5 et 0.0 km s^{-1}pour les deux δ Scuti étudiées. Cela semble indiquer que les δ Scuti ont un comportement proche de celui des Céphéides en terme de convection (même si elle semble un peu moins marquée), ce qui n'est pas vraiment étonnant, alors que la β Céphéide aurait un régime très différent, probablement sans convection.

10. Les β-Céphéides sont des étoiles pulsantes de type spectral B qui ne sont pas utilisées pour les distances mais dont la dynamique atmosphérique est tout à fait intéressante à titre de comparaison (voir par exemple le travail effectué pendant mon stage de L3 Fokin et al. (2004)).

11. Guillaume Guiglion a fait sont stage de M2 en 2012 avec moi sur ce sujet. Le papier correspondant se trouve dans l'annexe R.

3. Il existe une relation entre la période des étoiles et les gradients de vitesse dans l'atmosphère (Fig. 4.10). Plus précisément, le gradient de vitesse atmosphérique, ou du moins, le gradient de vitesse dans la zone de l'atmosphère sondée par les raies spectrales, est nul pour des amplitudes de vitesses inférieures à environ 20 km s^{-1}puis augmente de façon proportionnelle avec l'amplitude de vitesse (voir Fig. 4.10). Etant donné que le gradient de vitesse atmosphérique est un facteur correctif contribuant pour quelques pourcents au facteur de projection, cette tendance peut s'avérer très intéressante pour prédire le facteur de projection des étoiles pulsantes en général.
4. Enfin, en étudiant l'environnement de l'étoile prototype des β Céphéides, nous avons découvert à l'aide de l'instrument visible VEGA/CHARA un environnement visible contribuant pour $23 \pm 2\%$ du flux. Mais la situation semble *a priori* différente de celle de δ Cep dans la mesure où un champ magnétique pourrait être responsable du confinement d'un disque en co-rotation autour de l'étoile (Nardetto et al. 2011b) (voir l'annexe T).

Ainsi, comparer les étoiles pulsantes entre elles est certainement une bonne façon de comprendre la physique de la pulsation, de la perte de masse et de l'environnement. Rappelons que "The Optical Gravitational Lensing Experiment" (OGLE [12]) a découvert depuis 1992 plus d'un million d'étoiles variables (céphéides, céphéides de type 2, céphéides anormales, RR Lyrae, δ Scuti, Miras, binaires à éclipses, étoiles de type R CrB) dans notre Galaxie et dans les nuages. Parmi ces étoiles, on trouve des Céphéides double modes (F/1O, 1O/2O, 1O/3O, 2O/3O), triple modes (F/1O/2O, 1O/2O/3O) et même des Céphéides pulsant dans des modes non-radiaux ou encore une Céphéide en fin de pulsation sortant de la bande d'instabilité. Cette diversité d'étoiles est un fabuleux laboratoire pour comprendre la dynamique atmosphérique des étoiles pulsantes.

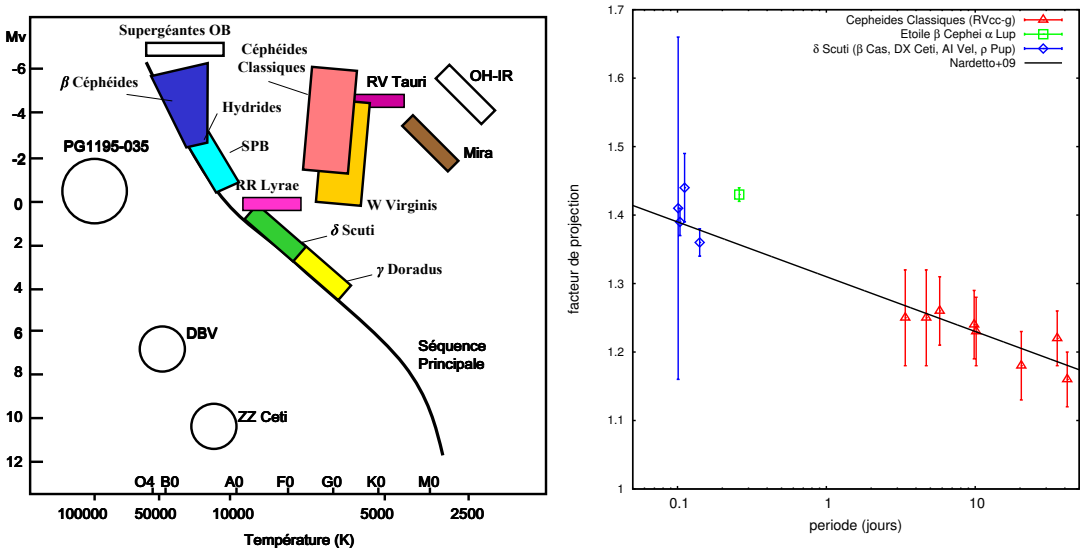


FIGURE 4.9 – La relation *Pp* obtenue pour différents types d'étoiles pulsantes. La dispersion obtenue pour les étoiles de type δ Scuti est liée à l'impact de la rotation, qui du fait de l'assombrissement gravitationnel qu'elle génère, affecte le facteur de projection.

12. http ://ogledb.astrouw.edu.pl/ ogle/OCVS/

Pour conclure ce chapitre, nous pouvons ainsi résumer les limitations de la méthode de Baade-Wesselink :

1. Le facteur de projection est la principale limitation de la méthode : s'il existe un biais de 5% sur le facteur de projection, alors la distance de BW sera également biaisée à hauteur de 5%. Celui-ci dépend (par ordre d'importance) : de l'assombrissement centre-bord de l'étoile (et donc de la phase de pulsation de l'étoile), de la dynamique atmosphérique (i.e. de la profondeur de la raie spectrale considérée et du gradient de vitesse associé), de la méthode utilisée pour déduire la vitesse radiale, et des longueurs d'ondes considérées pour la raie spectrale (spectroscopie) et le continuum (interférométrie ou photométrie) et enfin de la granulation de l'étoile (variations possible de cycle à cycle pour certaines Céphéides proches du bord rouge de la bande d'instabilité).
2. La courbe de vitesse radiale (peu importe la méthode considérée) est corrigée de sa valeur moyenne (le k-facteur) en faisant l'hypothèse que la zone de formation de la raie se retrouve à la même position dans l'atmosphère de l'étoile d'un cycle à l'autre. Ce n'est pourtant pas le cas. L'impact de cette hypothèse sur la distance n'est pas clair, probablement faible, mais nécessite des investigations.
3. L'environnement de l'étoile a un impact sur les mesures interférométriques et photométriques. Corriger la méthode de BW de l'enveloppe est un objectif de l'ANR.

L'objectif à terme est de rendre la méthode de BW robuste de façon à en faire un outil précieux (si ce n'est pas déjà le cas) pour les déterminations de distance dans le groupe local.

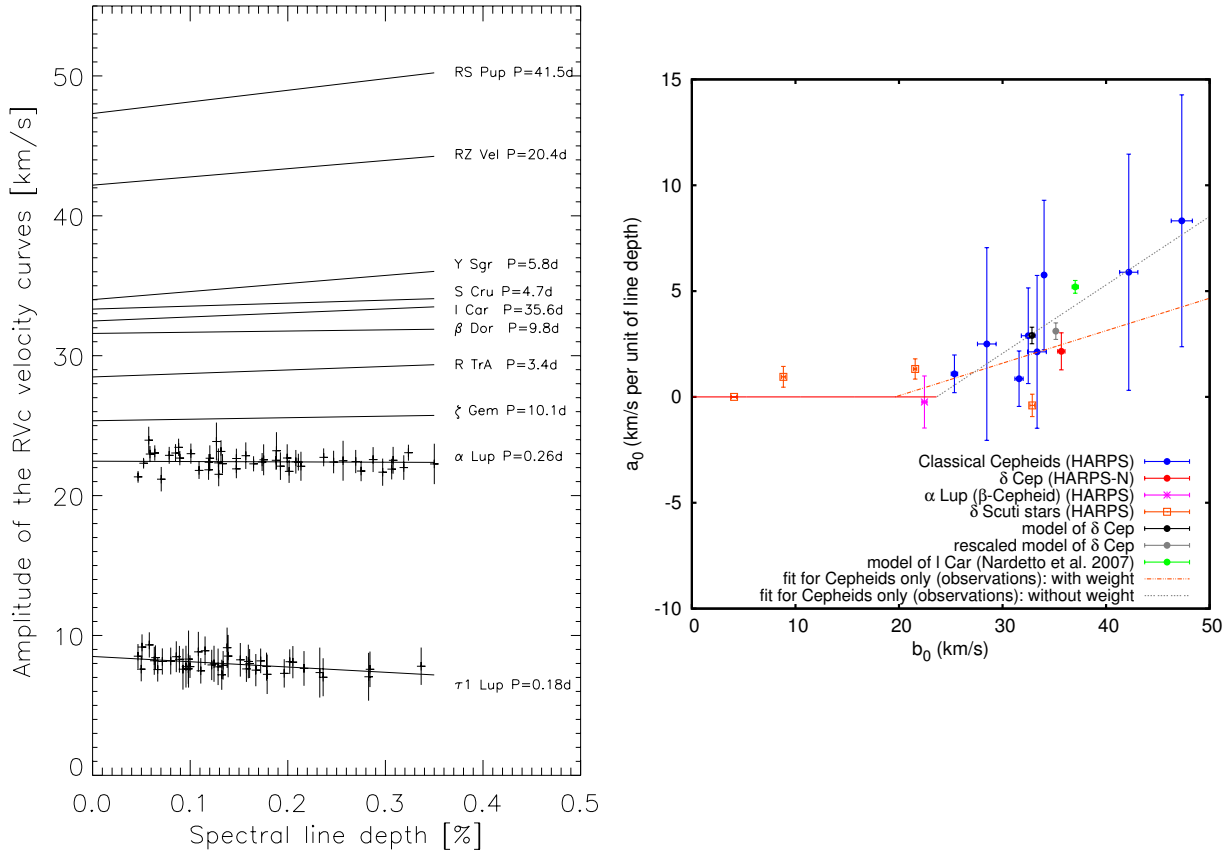


FIGURE 4.10 – A gauche : l'amplitude des courbes de vitesse radiale associées à différentes raies se formant à différents niveaux dans l'atmosphère donne une bonne indication du gradient de vitesse dans l'atmosphère (ou une partie de l'atmosphère). La profondeur de raie *zéro* correspond à la photosphère de l'étoile. Les droites $(a_0 \Delta RV_c + b_0)$ sont tirées de Nardetto et al. (2007) pour les Céphéides, et de Nardetto et al. (2013) pour les deux β Céphéides α Lup et τ^1 Lup. Les données HARPS sont indiquées par des croix pour les β Céphéides. A droite : la pente du gradient de vitesse (a_0) en fonction de l'amplitude de la courbe de vitesse au niveau de la photosphère (b_0). Ces données correspondent aux références suivantes : Céphéides en bleu (Nardetto et al. 2007), δ Cep en rouge (Nardetto et al. 2017), α Lup (Nardetto et al. 2013), étoiles de type δ Scuti (Guiglion et al. 2013; Nardetto et al. 2014) tandis que les valeurs théoriques sont tirées des modèles de δ Cep (Nardetto et al. 2004, 2017) et de ℓ Car (Nardetto et al. 2007). Cette relation est intéressante pour estimer le facteur de projection des étoiles pulsantes dont le mode radial est dominant.

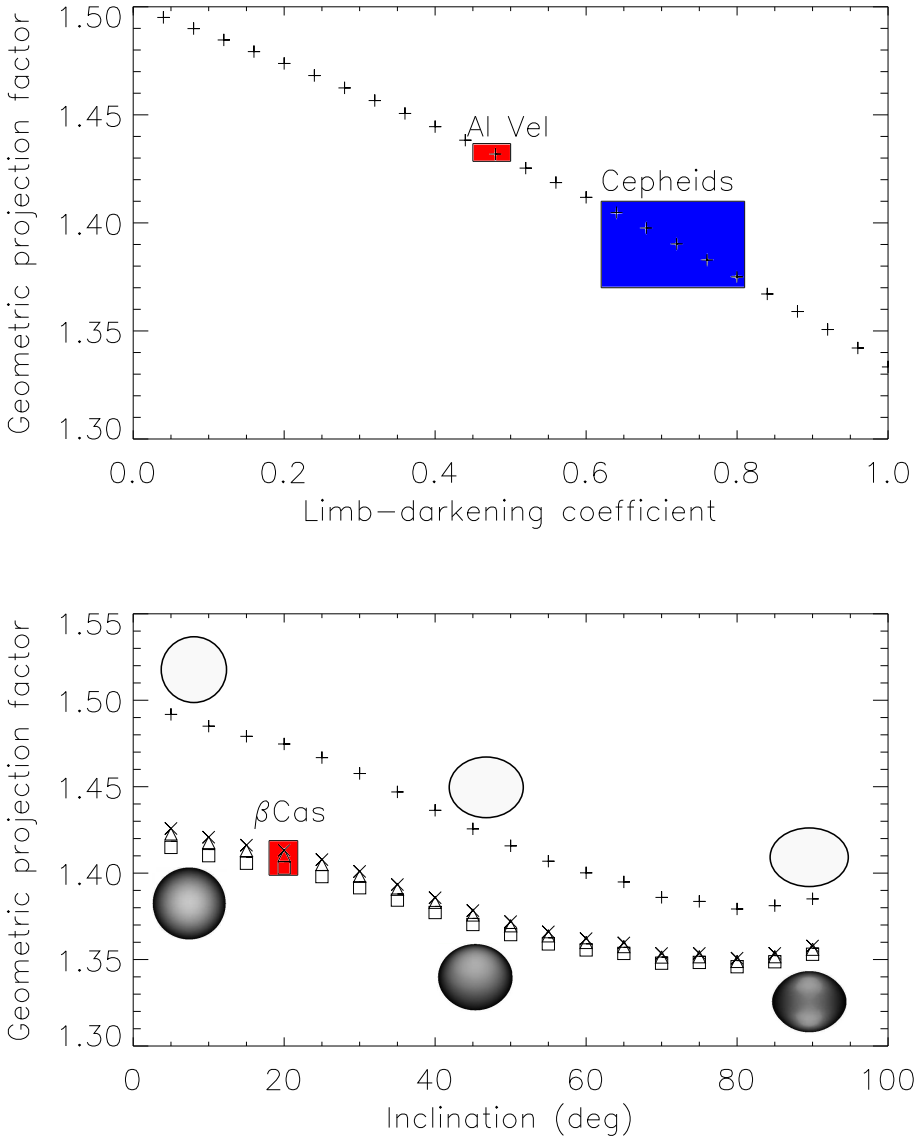


FIGURE 4.11 – Le facteur de projection géométrique est sensible à l'assombrissement centre bord des étoiles. Pour les δ Scuti dont la rotation est négligeable (comme Al Vel), on obtient un facteur de projection géométrique p_0 autour de 1.43, un peu plus élevé que celui des Céphéides autour de 1.37-1.41 du fait d'un assombrissement centre-bord moins prononcé (en haut). Si la rotation est importante comme dans le cas de β Cas (autour de 220 km s^{-1}), il faut alors prendre en compte l'assombrissement gravitationnel Domiciano de Souza et al. (2002, 2012) et le facteur de projection géométrique diminue alors avec l'inclinaison de l'étoile, autour de $i = 20$ deg pour β Cas et ne change pas véritablement d'une longueur d'onde à l'autre : $\lambda = 6000$ Å (carrés), $\lambda = 6500$ Å (triangles), $\lambda = 700$ Å (croix).

Chapitre 5

Les binaires à éclipses et l'interférométrie

Les binaires à éclipses permettent de déterminer la distance des galaxies proches (LMC, SMC, M31 et M33) avec une bonne précision (voir Tableau E.1). Le principe est relativement simple (voir Sect. 3.2). Les paramètres de la binaire, et en particulier les rayons des deux composantes, sont déduits des données spectroscopiques et photométriques. Parallèlement, le diamètre angulaire des deux composantes est une fonction de la magnitude et de la couleur des étoiles (relation brillance de surface - couleur). La combinaison des rayons linéaire et angulaire donne la distance du système (voir Eq. 3.4). La principale source d'erreur de cette méthode provient quasi-totalement de notre méconnaissance de la relation brillance de surface - couleur. De nombreuses études ont d'abord utilisé les binaires à éclipses de type précoce, plus brillantes et faciles à détecter, pour déterminer la distance du LMC et du SMC. Mais dans ce cas, la précision sur la relation brillance de surface - couleur, 6 à 8% actuellement (voir Sect. 5.2), limite la précision que l'on peut espérer obtenir sur la distance des nuages. Les binaires à éclipses de type spectral tardif sont quant à elles extrêmement difficiles à détecter. Dans l'étude de Pietrzyński et al. (2013) par exemple, 16 ans d'observations de OGLE ont été nécessaires pour détecter une douzaine de binaires à éclipses. Ainsi, la précision de 2.2% obtenue sur la distance du LMC est directement liée ou presque à la précision que l'on a actuellement sur la relation brillance de surface - couleur des étoiles de type K (classe III), c'est-à-dire 0.04 magnitude (Di Benedetto 2005). A retenir : un rms de 0.022 magnitude sur la relation brillance de surface - couleur (S_V) correspond à une précision sur le diamètre angulaire de 1%. Pour les mêmes raisons, la précision sur la distance du SMC est aujourd'hui autour de 3% (Graczyk et al. 2014). Outre le LMC et le SMC, quelques binaires à éclipses de type précoce ont été détectées dans M31 et M33. Du fait de l'imprécision sur la relation brillance de surface - couleur (autour de 10% à l'époque), les auteurs ont préféré s'en tenir à des modèles stellaires pour déduire la magnitude absolue des étoiles et ainsi leur distance. Les précisions sur les distances obtenues sont ainsi de 4.4% pour M31 (Vilardell et al. 2010) et de 5.5% pour M33 (Ribas et al. 2005). Ces valeurs ont été utilisées par Riess et al. (2016) pour déterminer la constante de Hubble (voir Sect. 2.1).

La relation brillance de surface - couleur est donc un outil extrêmement utile pour la détermination de distance des binaires à éclipses, mais pas seulement. Nous avons déjà vu qu'elle est utilisée pour l'application de la méthode de BW afin de déterminer la variation de diamètre angulaire de la Céphéide (voir Sect. 3.4). Mais de manière plus générale encore, les diamètres angulaires issus de la relation brillance de surface - couleur, combinés aux mesures de parallaxes Gaia permettront dans les années à venir de déduire le rayon de milliers, voire centaines de milliers d'étoiles. Parmi celles-ci, se trouvent des étoiles hôtes d'exoplanètes dont les mesures de transit photométriques par la mission spatiale PLATO permettront de déduire

le rapport $\frac{R_p}{R_\star}$ avec une précision de l'ordre de 1% et donc par suite, le rayon de la planète R_p ainsi que sa densité. De la même manière, une mesure de rayon stellaire indépendante pose des contraintes importantes dans le cadre de l'étude des étoiles astérosismiques.

Ainsi, contraindre les relations brillance de surface - couleur est aujourd'hui une priorité. L'objectif est d'atteindre 1% de précision pour les étoiles tardives (afin d'accéder à une précision également de 1% sur la distance du LMC et du SMC) et de quelques pourcents (3-5%) pour les étoiles précoces de façon à accéder aux galaxies du groupe local. Pour atteindre ces deux objectifs, il faut déterminer le diamètre angulaire des étoiles proches et dans ce domaine, l'interférométrie est la méthode principalement utilisée.

5.1 Les mesures de diamètre angulaire par interférométrie et l'instrument VEGA/CHARA

Les fentes de Young (ou interférences de Young) désignent en physique une expérience qui consiste à faire interférer deux faisceaux de lumière issus d'une même source, en les faisant passer par deux petits trous percés dans un écran opaque. Cette expérience fut réalisée pour la première fois par Thomas Young en 1801 et permit de comprendre la nature ondulatoire de la lumière. En termes simples, une source ponctuelle monochromatique produit un réseau de franges très contrasté. Imaginons un second point source situé à côté du précédent : deux réseaux de franges légèrement décalés vont se superposer et diminuer ainsi le contraste des franges. On comprend alors intuitivement le lien entre la distribution spatiale d'un objet et le contraste des franges d'interférence (théorème de Van-Cittert-Zernike). Un interféromètre mesure le contraste et la position (ou phase) des franges d'interférence et permet ainsi de remonter au diamètre angulaire de l'étoile observée.

L'histoire de l'interférométrie commence avec l'expérience de Michelson (1881), puis de Michelson & Morley en 1887 qui démontre que la vitesse de la lumière est constante quelque soit le référentiel considéré et que l'éther n'existe pas (Prix Nobel de Physique de 1907). En 1921, au Mont Wilson, situé en Californie sur les hauteurs de Los Angeles, Michelson applique le principe optique de l'interférométrie à l'astrophysique en plaçant deux miroirs de 10 cm à l'extrémité d'une poutre de 6 mètres. Ce dispositif (le premier interféromètre) lui permet de mesurer, et ceci pour la première fois, le diamètre angulaire d'une étoile, Bételgeuse. Il obtient un diamètre de l'ordre de 50 millisecondes d'arc ou *mas* (Michelson & Pease 1921). Il y a alors curieusement une longue période de calme (environ 50 ans) puis Hanbury Brown et al. (1967a,b) développent un concept d'interféromètre à intensité et mesurent le diamètre angulaire de 15 étoiles (de 0.7 mas à 6.5 mas). A la même époque, Gezari et al. (1972) mesurent le diamètre angulaire de 9 étoiles (autour de 10-40 mas) avec le télescope de 5 mètres du Mont Palomar (A Labeyrie est alors deuxième auteur de cette étude). Toujours avec le télescope du Mont Palomar, Labeyrie et al. (1974) découvrent des compagnons autour de 12 étoiles. Puis, seulement 1 an plus tard, mais de l'autre côté de l'Atlantique, au Plateau de Calern, Labeyrie (1975) mesure le diamètre angulaire de l'étoile Vega avec l'Interféromètre à 2 Télescopes (I2T) [1]. Quelques années plus tard, Blazit et al. (1977) mesurent avec l'I2T les diamètres de Capella A et B (respectivement 5.2 ± 1.0 mas et 4.0 ± 2.0 mas). La même année, les premières mesures de diamètre angulaires par occultation lunaire voient le jour (Africano et al. 1977). Dix-sept ans plus tard, le "Grand Interféromètre à 2 Télescopes" (GI2T) est mis en service (Mourard et al. 1994) avec les premières publications (Mourard et al. 1989). Cette histoire est forcément incomplète et insiste sur l'aventure niçoise. En 2016, soit 95 ans après la première mesure de diamètre angulaire par Michelson & Pease (1921), mais seulement 50 ans après les mesures de Hanbury Brown et al. (1967b), Duvert (2016) ont répertorié 1150 mesures

1. Le diamètre angulaire est indiqué comme étant inférieur à 5 mas dans ce papier.

de diamètre angulaires. Ces mesures concernent 627 étoiles, ce qui correspond en moyenne à la mesure du diamètre angulaire de 12 étoiles par an depuis 1967. Les diamètres (uniformes) s'échelonnent entre 0.215 mas (HD209458 ; Boyajian et al. (2015)) et 41 mas (Bételgeuse ; Montargès et al. (2014)) et ont été mesurés par interférométrie optique, interférométrie d'intensité et par occultation lunaire. Il est intéressant de noter que l'étoile la plus faible observée dans le visible et pour laquelle un diamètre angulaire a été déterminée a une magnitude de V=7.7, alors que l'étoile la plus faible observée en infrarouge a une magnitude K=6.3. De même, dans cet échantillon de 627 étoiles, l'étoile la plus éloignée est à 4750 parsecs environ (HD 184283) et la plus proche est proxima du Centaure.

La figure 5.1-haut représente la précision obtenue sur les 1150 diamètres mesurés (en pourcentage) en fonction de leur distance Hipparcos avec un code de couleur différent pour l'interférométrie optique, l'interférométrie d'intensité et la méthode des occultations lunaires. Pour l'interférométrie optique, la taille des disques noirs est proportionnelle au diamètre angulaire de l'étoile observée (à titre indicatif). La précision moyenne obtenue pour l'interférométrie optique (sur 491 objets) est de 2.9% (c'est à dire en prenant en compte toutes les mesures depuis 1981), mais on constate que de nombreuses mesures ont une précision autour de 0.2% de précision (les quelques points en dessous de 0.1% de précision posent tout de même des questionnements). Les moyennes obtenues pour l'interférométrie d'intensité et la méthode des occultations lunaires sont de 10.8% et 6.0%, respectivement, soit significativement au dessus. Aujourd'hui, une précision en dessous de 1% sur le diamètre angulaire est standard en interférométrie optique quelles que soient la distance ou la magnitude de l'étoile, dans les limites actuelles mentionnées plus haut.

La figure 5.1-milieu montre le rayon associé aux 1150 mesures de diamètre angulaire (en combinant ces diamètres avec la distance Hipparcos) en fonction de la distance de l'étoile pour les différents types spectraux. Des lignes correspondant à différentes résolutions spatiales en mas sont également indiquées. Pour les types spectraux O à M, on distingue deux groupes dans le nuage de points, les séquences principales ($R < 10R_{\odot}$ et $d < 300pc$) et les étoiles évoluées ($R > 10R_{\odot}$ et $d > 300pc$). On peut tirer deux conclusions intéressantes de ce diagramme. D'abord, les étoiles de type O, B, A, F ont été beaucoup moins observées (environ 20% des observations) et ce pour la raison qu'il faut une résolution spatiale inférieure à 0.3 mas (ou une magnitude limite plus importante) pour étudier ces étoiles, plus particulièrement pour les étoiles O et B de la séquence principale. On voit ici l'importance d'aller vers de plus basses résolutions spatiales (plus grandes bases combinées à des longueurs d'ondes plus faibles) pour espérer contraindre la relation brillance de surface - couleur des étoiles de type précoce efficacement. L'interférométrie visible est effectivement la méthode la plus appropriée pour mesurer le diamètre angulaire des étoiles avec un rayon inférieur à quelques rayons stellaires et à plus de 100 pc comme l'illustre la Figure 5.1-bas. Il ne faut pas oublier que ceci n'est possible qu'en augmentant la magnitude limite ainsi que la sensibilité des instruments actuels.

Ainsi l'instrument VEGA situé au foyer de l'interféromètre CHARA joue un rôle pionnier dans ce domaine. En effet, le 'Center for High Angular Resolution Astronomy' (CHARA, USA) est un réseau interférométrique situé à l'observatoire du Mount Wilson, en Californie, qui comprend 6 télescopes de 1 mètre sur des bases allant de 30 à 330 mètres. L'instrument VEGA [2], placé au foyer de CHARA, a été développé au sein du Laboratoire Lagrange. De juin 2012 à septembre 2016, en remplacement de Denis Mourard mais avec son aide, je me suis occupé de l'organisation autour de l'instrument, de son exploitation astrophysique et de sa maintenance. Du fait de ses résolutions spatiales et spectrales, VEGA/CHARA offre une large gamme de possibilités en terme d'objets d'étude : étoiles jeunes (AB Aur), étoiles astérosismologiques (HD 49933, γ Equ), étoiles à exoplanètes (13 Cyg, ...), étoiles Be (γ Cas, 48 Per, ψ Per,...), étoiles à vent (Deneb,

2. http://www-n.oca.eu/vega/en/news/index.htm

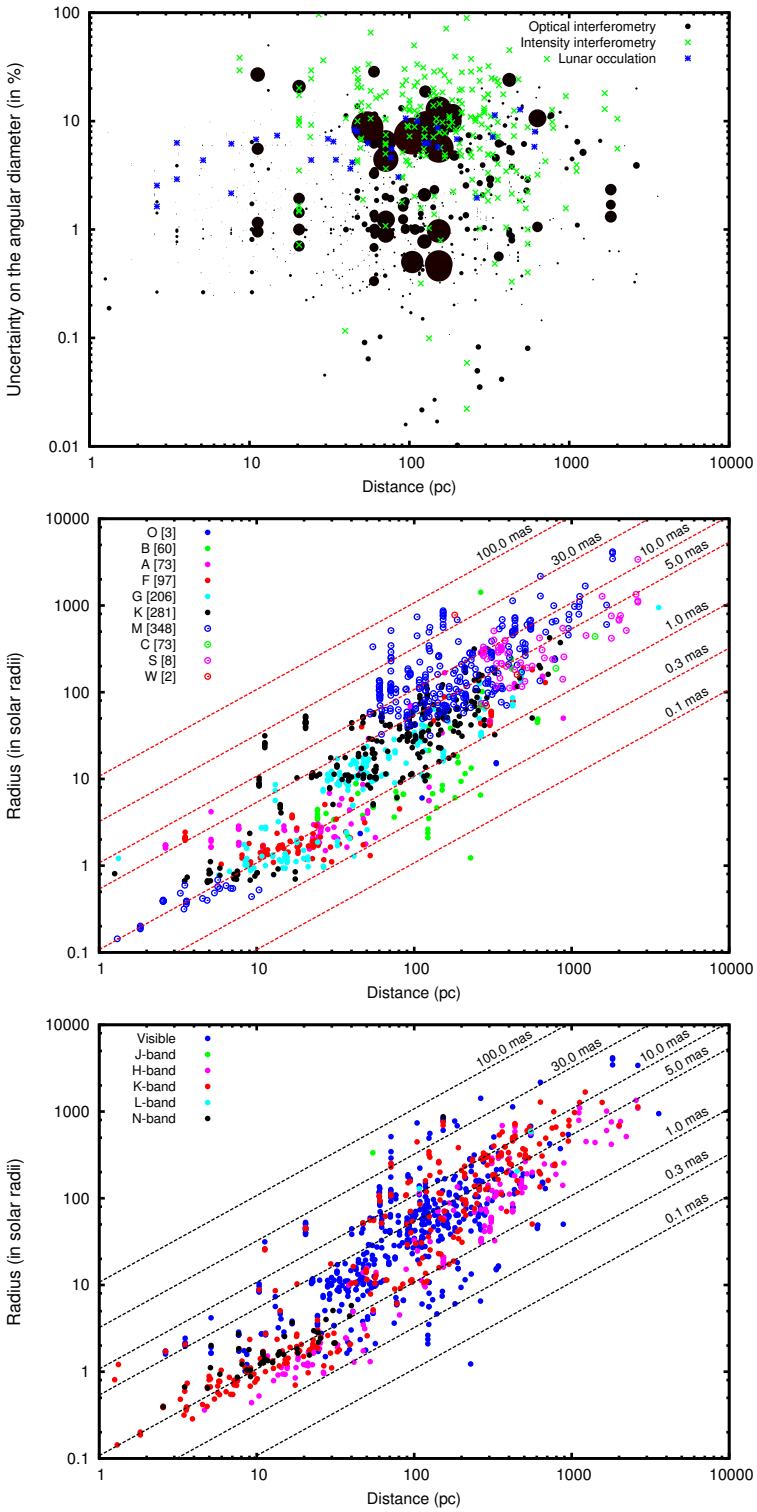


FIGURE 5.1 – Etoiles observées par haute résolution angulaire d'après la base de données du JMDC Duvert (2016).

Rigel)... et comme nous l'avons vu Céphéides (δ Cep). Trente-cinq publications sont repertoriées [3] depuis le lancement de VEGA [4]. Ainsi, avec l'instrument VEGA/CHARA, nous avons fourni le diamètre angulaire de 8 étoiles de type précoces afin d'étalonner la relation brillance de surface - couleur.

3. https://www-n.oca.eu/vega/en/publications/index.htm

4. Depuis 2010, VEGA observe à distance (en mode télécommande depuis Nice) pour environ 70% des nuits affectées et nous disposons d'environ 50 nuits par an. De nombreuses données sont ainsi recueillies chaque année pour satisfaire environ une trentaine de programmes scientifiques. L'instrument est labellisé depuis le début de 2013 comme service d'observation SNO2 de l'INSU et est étroitement lié au SNO5-JMMC, pôle national pour l'exploitation des données interférométriques optiques.

5.2 La relation brillance de surface - couleur des étoiles

Etalonner la relation brillance de surface - couleur n'est pas une chose aisée. Si l'on prend par exemple les 1150 mesures de diamètres angulaires répertoriées dans la base de données du JMDC (Duvert 2016) et que l'on retire les étoiles potentiellement contaminées par un compagnon et les étoiles variables, on obtient les figures 5.2 et 5.3. Le graphique a été divisé en deux pour améliorer la lisibilité. Il contient 558 mesures de diamètre. Les magnitudes K sont tirées du catalogue 2MASS et les magnitudes V de SIMBAD. Pour rappel, la brillance de surface - couleur est donnée par l'équation $S_V = V - 5\log\theta_{LD}$ [5]. Dans ce graphique, l'extinction n'est pas prise en compte, mais il s'avère que la prendre en compte, en utilisant une formule du type $A_V = \frac{0.8}{\pi}$ où π est la parallaxe en secondes d'arc (di Benedetto 1998; Di Benedetto 2005) ne réduit pas la dispersion globale des points. Ceci reste valable si l'on utilise des approches plus élaborées à l'aide des cartes de poussières de Schlegel et al. (1998) par exemple. Ainsi faire un tri selon la méthode employée (interférométrie optique, d'intensité ou occultation lunaire), E(B-V), [Fe/H], le type spectral ou la classe de l'étoile, sur la distance, la précision sur le diamètre, ou le diamètre lui-même, ou encore la précision sur la magnitude K n'améliore pas significativement la dispersion des points.

Un moyen de s'en sortir, est d'utiliser des sous-échantillons (comme le font la plupart des auteurs) et d'appliquer une méthode minutieuse au niveau du calcul de l'extinction. Un exemple est illustré par le papier de Challouf et al. (2014) (voir l'annexe U). Ce travail effectué dans le cadre de la Thèse de Mounir Challouf visait à observer des étoiles de type précoce avec l'instrument VEGA/CHARA afin précisément de contraindre la relation brillance de surface - couleur pour ce type d'étoiles. Chemin faisant, nous avons décidé de reprendre également l'étalonnage pour les étoiles de type tardif. Ainsi 8 étoiles O, B, A ont été observées avec VEGA avec une précision sur le diamètre angulaire de 1.5%. Ensuite, un très gros travail de Mounir a consisté à 1) calculer l'extinction des étoiles (à partir de 7 méthodes différentes ; voir Section 4.1 du papier), 2) effectuer une sélection rigoureuse étoile par étoile (pas de binaires, pas de variabilité, pas d'environnement, pas de vent). Seules les étoiles dont la rotation est rapide et dont on sait qu'elles peuvent avoir un effet sur la relation brillance de surface - couleur ont été conservées pour augmenter la statistique des étoiles précoces. L'effet de cette rotation a été estimé ultérieurement dans un second papier (voir l'annexe V et la Section 5.3). Ce travail a permis d'étalonner la relation brillance de surface couleur pour différentes classes d'étoiles avec une précision de l'ordre de 0.16 mag (ou 7% en terme de diamètre) pour les étoiles précoces, et 0.04 magnitude comme précédemment pour les étoiles tardives. Ce résultat est illustré par la Figure 5.4.

Comment se place ce résultat par rapport à la littérature ? Dans l'annexe F, j'actualise le Tableau I.1 de la Thèse de Mounir Challouf et l'agrémente de notes. Le premier constat est qu'il est extrêmement difficile de comparer les résultats dans la mesure ou les auteurs utilisent des définitions différentes de la relation brillance de surface - couleur. Ainsi j'ai relevé, selon les publications, les définitions suivantes :

1. $S_V = V - 5\log\theta_{LD} = \sum a_k (V-K)^k$
2. $F_V = 4.2207 - 0.1 S_V = \alpha + \beta(V-K)$
3. $\log\theta_{LD} = d_1 + c_1 1(V-K) - 0.2V$
4. $\theta_{LD}(V=0) = 10^{A+B(V-K)}$
5. $\Phi_V = \frac{\theta}{9.305 * 10^{\frac{-V}{5}}} = \sum z_k (V-K)^k$

5. Les diamètres assombris sont donnés dans la base JMDC et leur détermination n'est pas homogène du point de vue de la méthode.

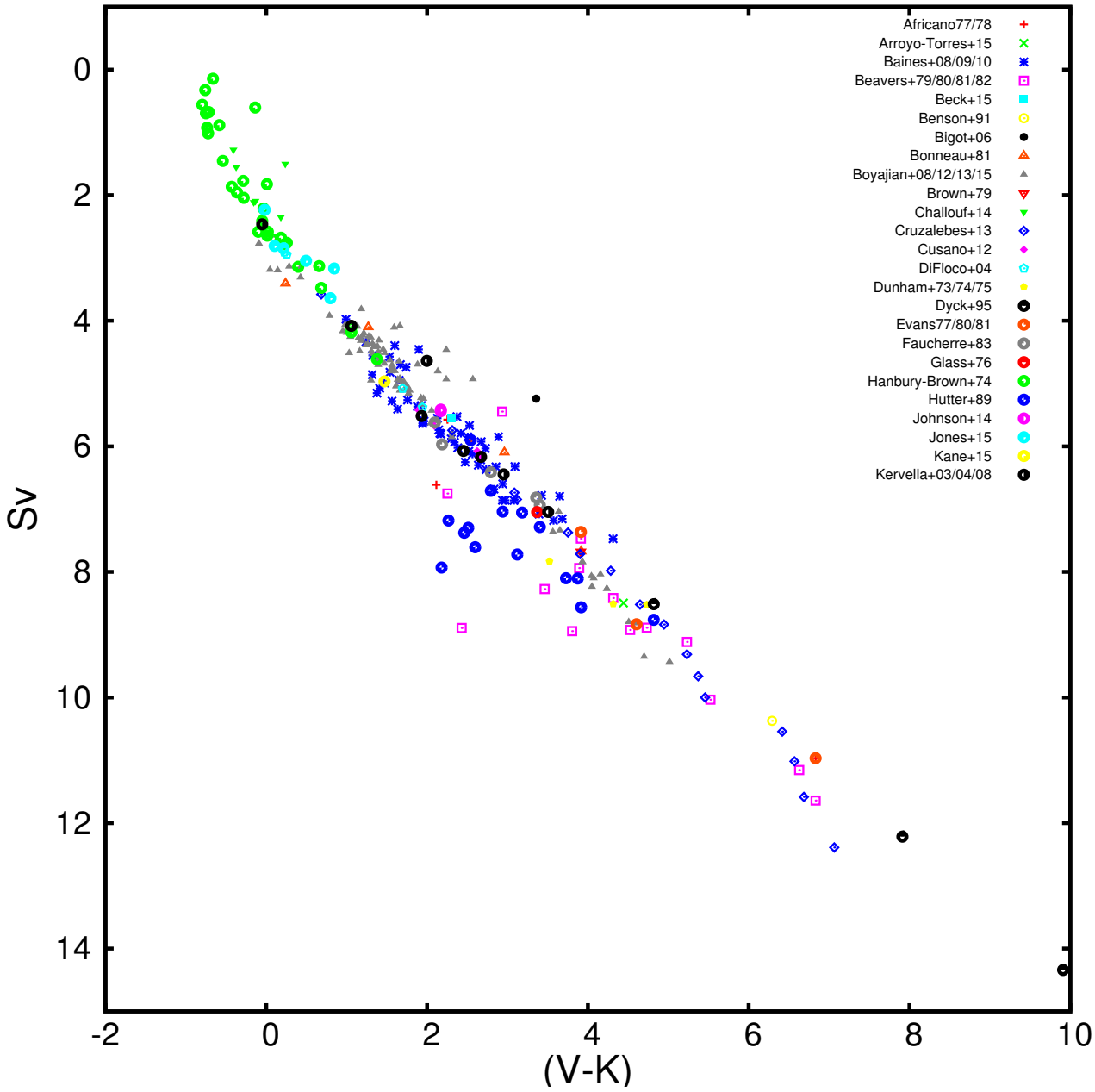


FIGURE 5.2 – Relation brillance de surface - couleur réalisée à partir des 558 mesures de diamètres angulaires (hors binarité et variabilité) listées dans la base de données JMDC de Duvert (2016). Les magnitudes V et K sont tirées respectivement de SIMBAD et du catalogue 2MASS.

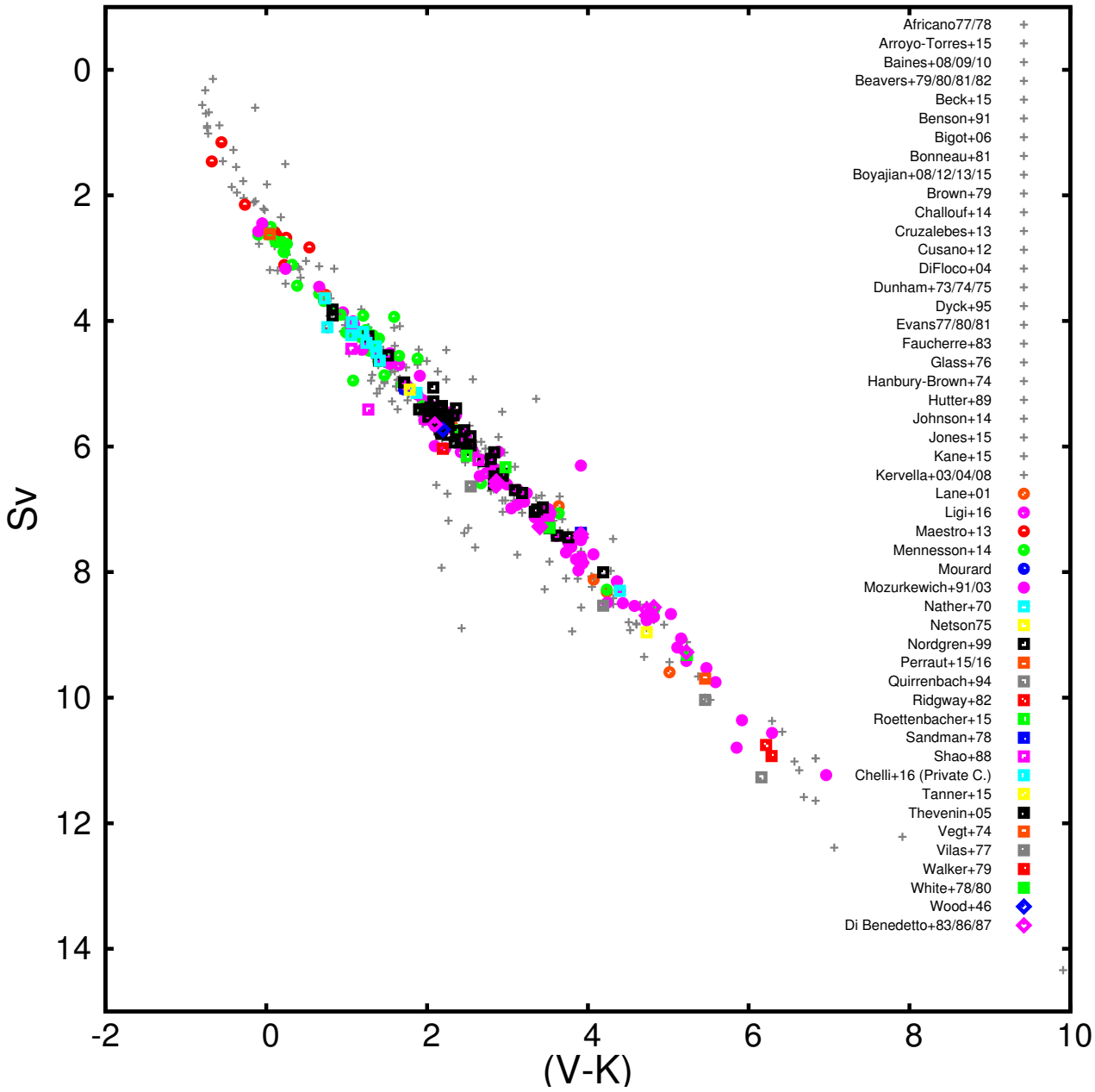


FIGURE 5.3 – Suite de la Figure 5.2.

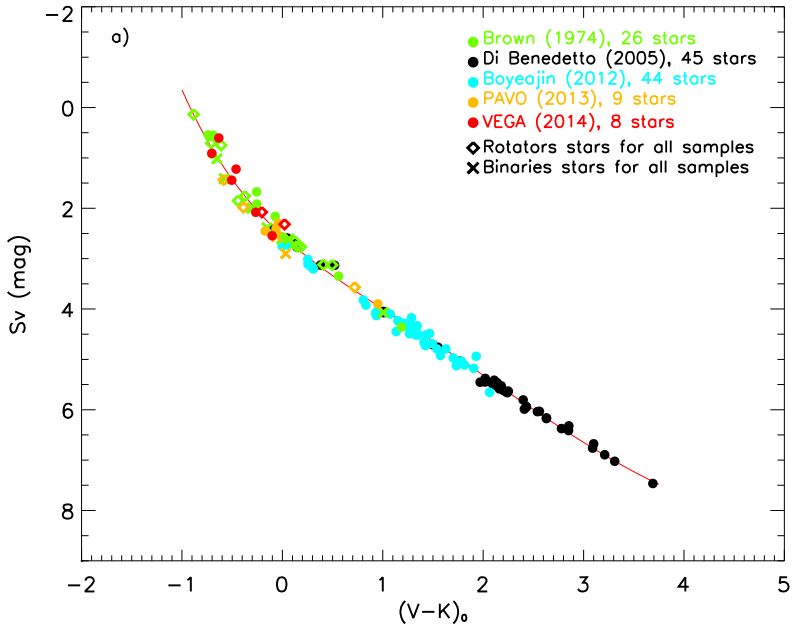


FIGURE 5.4 – Relation brillance de surface - couleur issue du travail de thèse de Mounir Challouf (Challouf et al. 2014).

Dans ces formules, l'indice '0' signifiant habituellement que les magnitudes V ou (V-K) sont corrigées de l'extinction n'est pas indiqué par commodité. Par ailleurs, selon les publications l'indice k vaut 0, 1, 2, ou même 5. En utilisant des formules de passage, on peut comparer les relations brillance de surface - couleur linéaires (les relations non-linéaires sont exclues à ce niveau, car les transformations sont complexes, mais on y reviendra plus loin) en prenant en compte leur intervalle de validité. Ceci est illustré par la Fig. 5.5. On remarque immédiatement que l'ensemble des relations sont assez proches sur l'intervalle $2 < V-K < 4$. En revanche, en dehors de cette intervalle $V-K < 2$ et $V-K > 4$, on note des divergences. Mais ces différences peuvent être en partie [6] expliquées par le fait qu'il faut faire également une distinction selon la classe des étoiles (indiquées entre parenthèses dans la légende de la figure). Ainsi, on peut représenter ces données différemment. Dans les figures 5.6-ab je représente la pente β de la relation $F_V = \alpha + \beta(V-K)$ en fonction de son point zéro α pour les différents auteurs (Fig. 5.6-a) et selon la classe des étoiles pour laquelle la relation est censée être utilisée (Fig. 5.6-b). On peut faire plusieurs remarques :

1. Il semble exister des relations brillance de surface couleur associées à chaque classe d'objet, en particulier (I, II), (III) et (IV, V). Si ce résultat est confirmé, cela pourrait indiquer que les étoiles de classes (IV, V) sont plutôt compatibles avec les propriétés d'un corps noir, tandis que classes III et (I, II) s'en éloigneraient du fait très probablement d'une activité.
2. Les relations pour les classes I, II sont comparativement peu précises [7].

6. Et non "en parti expliquées" comme me l'a très justement fait remarquer mon collègue Frédéric Morand lors de sa Hautement Dense Relecture (HDR) du manuscrit à l'occasion d'observations VEGA nuageuses : "les étoiles ne font pas de politique". Je le remercie ici en catimini pour son aide plus que précieuse ! Cela évitera au lecteur de subir par exemple des "occupations lunaires", car bien sûr, comme le précise Frédéric : "la Lune n'est pas occupée ... ou alors seulement à tourner autour de la Terre !".

7. Curieusement, la relation de di Benedetto (1993) valable pour les classes I, II et donnée sans précision (petite croix rouge sur la figure 5.6-b) est plutôt compatible avec les autres relations associées à la classe V.

3. Les relations pour les classes III sont à l'inverse précises, compatibles entre elles, ce qui est encourageant pour l'établissement d'une relation à 1% de précision pour la détermination de distance des binaires à éclipses de type tardif, qui sont effectivement, dans la plupart des cas, de classe III.
4. La relation brillance de surface - couleur des Céphéides (typiquement de classe III) est plutôt compatible avec les relations établies pour les classes V. Le point de van Belle (1999) (variables) concerne quant à lui les étoiles de type S, Mira, ...
5. Les relations pour les classes V présentent des incohérences. Parmi ces relations, la plus précise est celle de Boyajian et al. (2014) comprenant 124 étoiles (l'incertitude est comprise dans le point). La relation établie par Kervella et al. (2004e), qui inclut peu d'étoiles, mais proches ($d < 15pc$), vient juste après en terme de précision sur les coefficients de la relation. Les relations de Kervella et al. (2004e) et Boyajian et al. (2014) sont incompatibles. Cependant, il faut voir deux choses. Il ne faut pas confondre la précision sur α et β et la dispersion de la relation (ou rms). Ainsi, la relation de Boyajian et al. (2014) contenant de nombreuses étoiles est précise mais présente une dispersion non négligeable qui induit une erreur sur le diamètre de 4.6%. A l'inverse, la relation de Kervella et al. (2004e) est établie sur beaucoup moins d'étoiles, présente une dispersion faible, ce qui correspond finalement à une précision sur le diamètre angulaire de 1%. Par ailleurs, comparer les pentes et les points zéros des relations est intéressant, mais pas forcément la meilleure façon de procéder, surtout si l'on veut inclure les relations non-linéaires dans la comparaison.

Ainsi, une autre façon de comparer les relations (linéaires et non linéaires) des différents auteurs est de comparer directement les diamètres prédits en considérant une étoile typique donnée, par exemple $V-K=2$, $V=6$ et $K=4$ et en prenant bien sûr en compte l'intervalle de validité de la relation en V-K donné par l'auteur. J'obtiens alors les figures Fig. 5.6-cd selon la même distinction (classe d'objet et auteurs) que précédemment. Le point important est qu'ici les incertitudes sur les diamètres sont déduits non pas des incertitudes sur les relations brillance de surface - couleur (quelque soit la définition) mais sur la dispersion de la relation (rms). Les valeurs de diamètre angulaire sont compatibles et ceci est également vrai pour les diamètres estimés avec les relations de Kervella et al. (2004e) et Boyajian et al. (2014). Cependant, avec $V-K$ autour de 2, nous nous sommes placés dans un régime favorable (voir Fig. 5.5). Ainsi, la figure 5.7 représente la même figure mais pour différentes valeurs de V-K allant de 0 à 5 sur la figure de gauche, et pour plus de clarté, seulement de 0 à 3 sur la figure de droite. Pour mieux apprécier ces résultats, on peut considérer trois estimateurs statistiques, représentés en fonction de V-K sur les figures Fig. 5.8abc :

1. Le rapport de l'erreur moyenne sur le diamètre sur le diamètre moyen (telle que déduite des différentes sources bibliographiques) pour un V-K donné. Cette quantité correspond finalement à l'erreur sur le diamètre annoncée par la littérature. On peut ainsi espérer obtenir une précision sur le diamètre d'une étoile précoce ($V-K=0$) de 9% alors que cette valeur descend progressivement jusqu'à moins de 1% pour une étoile tardive ($V-K=6$) (voir Fig. 5.8a).
2. Le rapport de la dispersion des mesures de diamètre sur l'erreur moyenne correspondante, toujours pour un V-K donné. Cela correspond en quelque sorte à un χ^2 réduit. Une valeur de 1 (comme pour les étoiles avec $V-K=0$) veut dire qu'il y a une cohérence entre la précision et la dispersion des mesures. En revanche, les étoiles avec $V-K=3$ ont une précision sur le diamètre probablement sous-estimée, tandis que c'est inverse pour les étoiles tardives avec $V-K=5$, où les précisions annoncées dans la littérature sont probablement deux fois trop grandes (voir Fig. 5.8b).
3. Enfin, le rapport de la dispersion des mesures de diamètres sur la valeur moyenne donne la précision réelle que l'on peut espérer obtenir actuellement à partir des relations brillance de surface couleur

(sans considération de classe). Elle est autour de 8% pour les étoiles précoces ($V-K=0$), 2% pour les étoiles avec $V-K=3$ et 10% pour les étoiles tardives ($V-K=5$) (voir Fig. 5.8c). Il est important de noter que cette valeur de 10% reflète le fait qu'il n'existe pas de relation brillance de surface couleur universelle et qu'il faut prendre en compte la classe et donc très probablement l'activité de l'étoile pour gagner en précision.

On peut alors tirer quelques conclusions d'ordre général :

1. Comme déjà indiqué, il semble clair qu'il existe des relations brillance de surface - couleur spécifiques à trois grands groupes de classes : (I, II), III et (IV, V). Ces relations sont actuellement très peu précises pour les classes (I, II), relativement précises pour les classes III, et incohérentes pour les classes (IV, V). Du point de vue du type spectral, il semble important d'augmenter la précision sur les relations brillance de surface - couleur des étoiles de type précoce (O, B, A, F), actuellement autour de 8%, afin d'accéder à une précision de l'ordre de 3-5%. Ceci est nécessaire pour déduire la distance des galaxies M31 et M33 par la méthode des binaires à éclipses. Pour avancer sur cette thématique, l'interférométrie visible semble la meilleure piste. Cependant, pour cela, il faut prendre en compte l'impact de la rotation et des vents. D'un autre côté, il semble que l'activité des étoiles tardives, par exemple la granulation en lien avec un effet de classe, génère des incohérences (à 2.5σ) dans les estimations de diamètre des étoiles tardives. Il faut également noter que les étoiles évoluées tardives (classe I, II, III) sont généralement trop résolues par interférométrie, ce qui peut aussi poser des difficultés dans l'estimation du diamètre, car les mesures sont alors très sensibles à de nombreux effets physiques. L'imagerie devrait apporter des clefs importantes dans ce domaine.
2. On note que les échantillons de diamètres d'étoiles considérés sont plutôt faibles : 42 pour Kervella et al. (2004e), 124 pour Boyajian et al. (2014) et au maximum 239 pour van Belle (1999) par exemple (voir Tab. F.1), par rapport à un échantillon de diamètres potentiel de 558 (voir Fig. 5.2) qui, comme déjà expliqué, ne prend pas en compte les binaires et les variables. Cela veut dire que beaucoup d'étoiles sont exclues sur la base de critères différents selon les auteurs. Ainsi, les relations obtenues pour un domaine de validité en V-K et pour une classe donnée sont-elles comparables pour autant ? N'y a-t-il pas des effets de sélection. Comment alors obtenir des relations robustes utilisables pour les milliers et centaines de milliers d'étoiles observées avec *Gaia* et PLATO ? Aussi, pour augmenter la précision et l'exactitude de ces relations, il semble important de doubler au minimum l'échantillon d'étoiles pour lesquelles on a une mesure de diamètre angulaire, et l'idéal, serait de le faire en utilisant un seul et même instrument de façon à réduire autant que possible les erreurs systématiques. Cette approche devrait aussi permettre de comprendre les incohérences à 2.5σ observées pour les étoiles tardives.
3. Il faut avoir aussi à l'esprit que l'activité des étoiles (granulation, taches, rotation, vent et environnement) jouent un rôle majeur et contribuent à rompre l'hypothèse de base sur laquelle repose l'établissement des relations brillance - couleur de surface, à savoir qu'une étoile est un corps noir. C'est probablement une des raisons qui explique la forte dispersion obtenue lorsque l'on considère tout l'échantillon. Si l'on veut établir une relation brillance de surface - couleur, il faut donc choisir des étoiles qui sont de bons corps noirs. A l'inverse, si l'on veut utiliser une relation brillance de surface - couleur (dans le contexte *Gaia* ou PLATO) pour estimer le diamètre angulaire d'une étoile quelconque, il faut avoir à l'esprit que le diamètre estimé correspondra à celui d'un corps noir sans activité. Pour améliorer la relation brillance de surface - couleur dans le cadre de la détermination de distance des binaires à éclipses de type tardif, une solution intéressante est de considérer uniquement des étoiles de type K et de classe III de façon à réduire au maximum les divergences entre

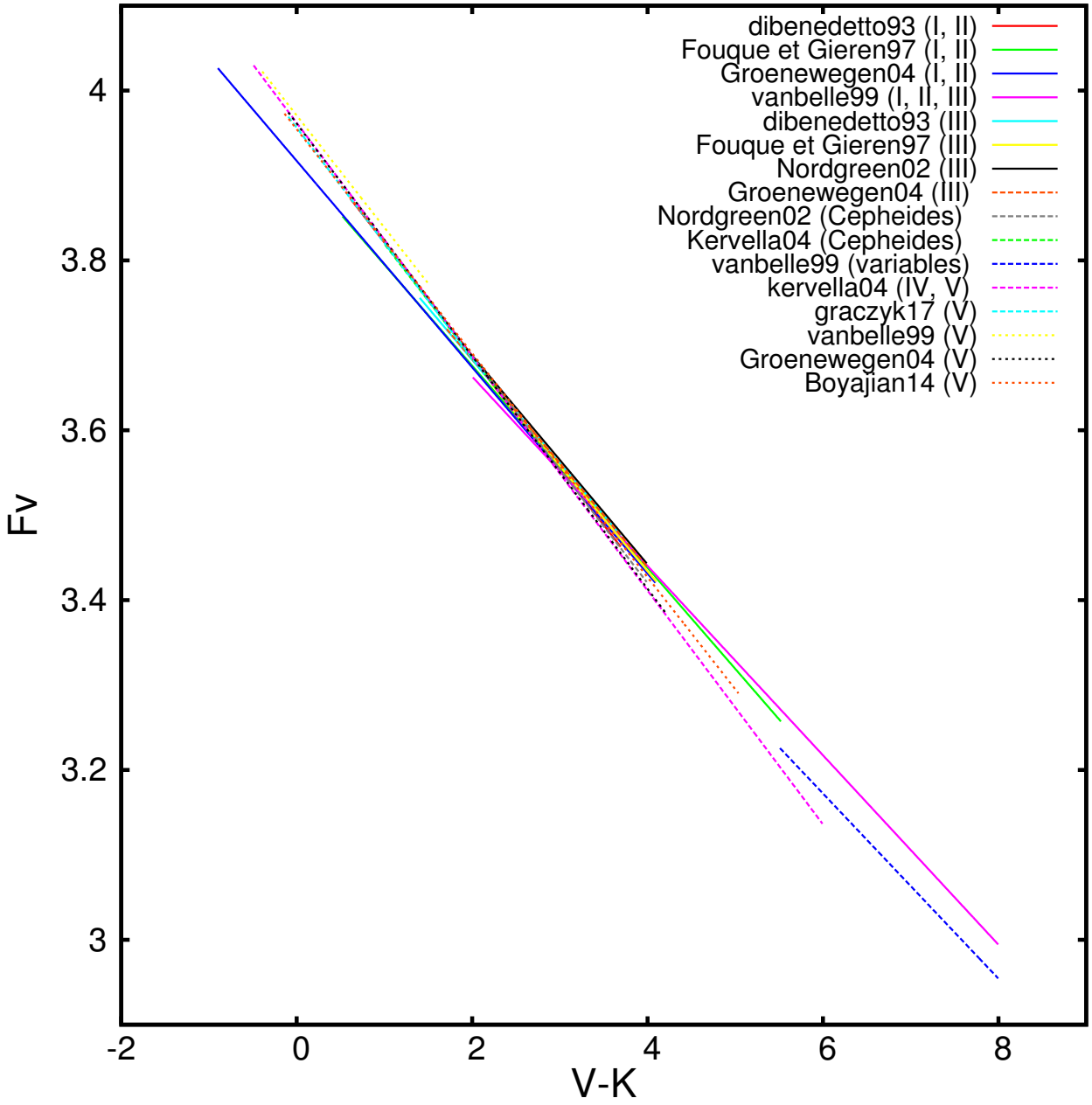


FIGURE 5.5 – Relations brillance de surface - couleur linéaires réalisées à partir des observations à haute résolution angulaire. Les segments de droite correspondent aux domaines de validité des relations.

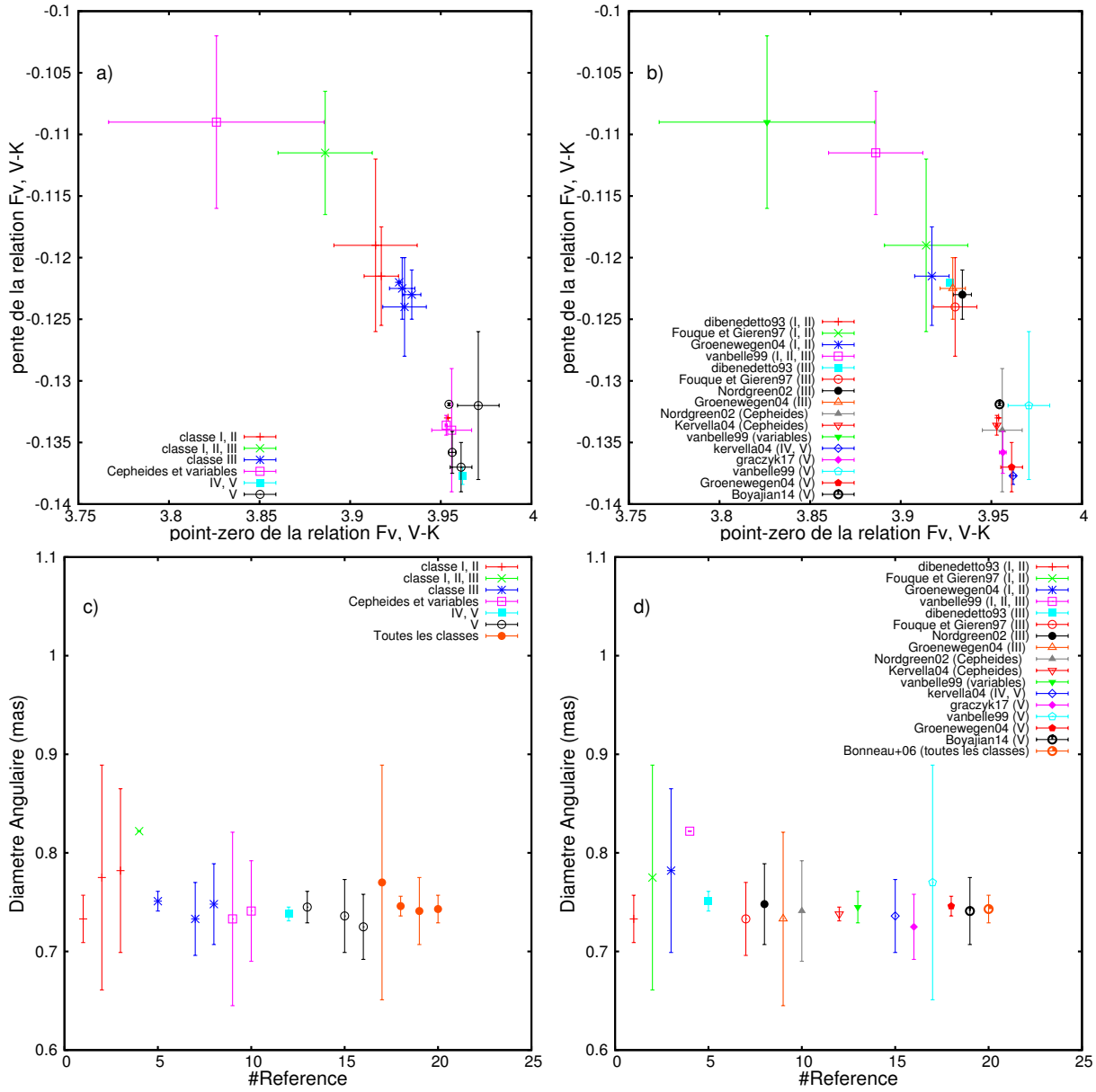


FIGURE 5.6 – En haut, comparaison des pentes et point-zéros des relations brillance de surface - couleur linéaire : code de couleur par classe a), code de couleur par référence b). En bas : les relations brillance de surface couleur linéaires et non-linéaires sont utilisées pour estimer le diamètre angulaire d'une étoile théorique qui aurait une magnitude V de 6 et une couleur $V-K$ de 2 et sont présentées par classe c) et par référence d). Dans ces figures, les références suivantes sont exclues car non valides sur le domaine de couleur V-K=2 : Fouque & Gieren (1997) (classe III, ref 6), van Belle (1999) (variables, ref 11) et van Belle (1999) (classe V, ref 14). La ref 4, bien qu'incompatible avec les autres estimations de diamètre angulaire est valide sur le domaine de couleur considéré dans cette figure.

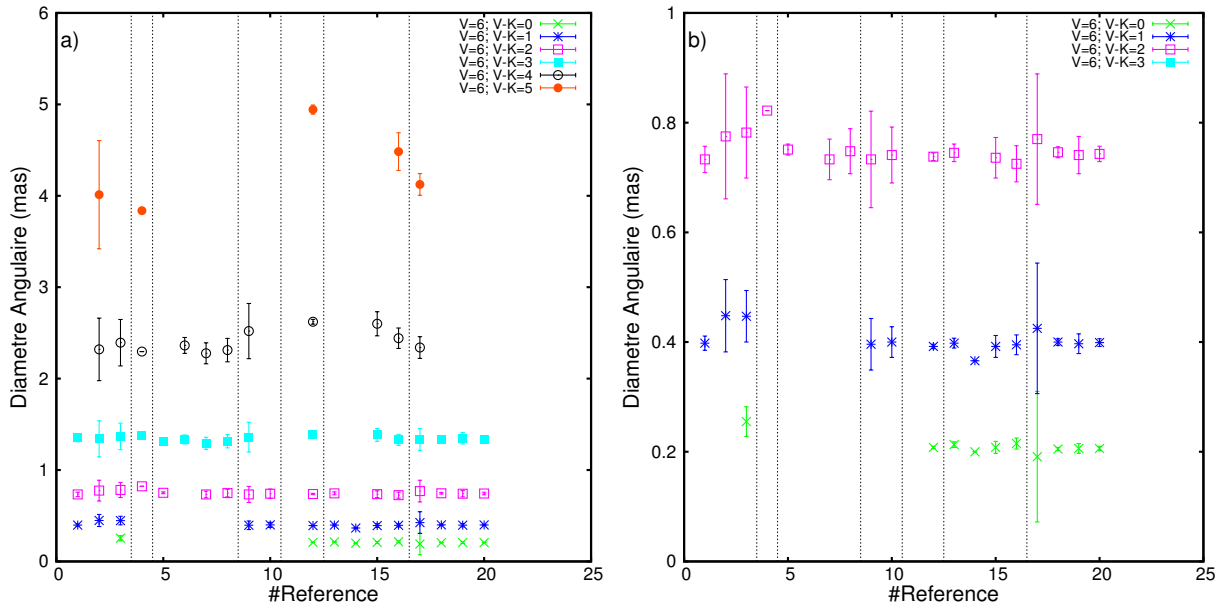


FIGURE 5.7 – Même chose que la figure 5.6cd mais pour différentes valeurs de V-K : de 0 à 5 à gauche et seulement de 0 à 3 à droite (zoom). Pour chaque $V-K$ ne figurent que les estimations de diamètres compatibles avec le domaine de validité de la relation brillance surface couleur utilisée. Les lignes verticales en pointillés séparent les valeurs associées aux différentes classes selon la légende de la Fig. 5.6c.

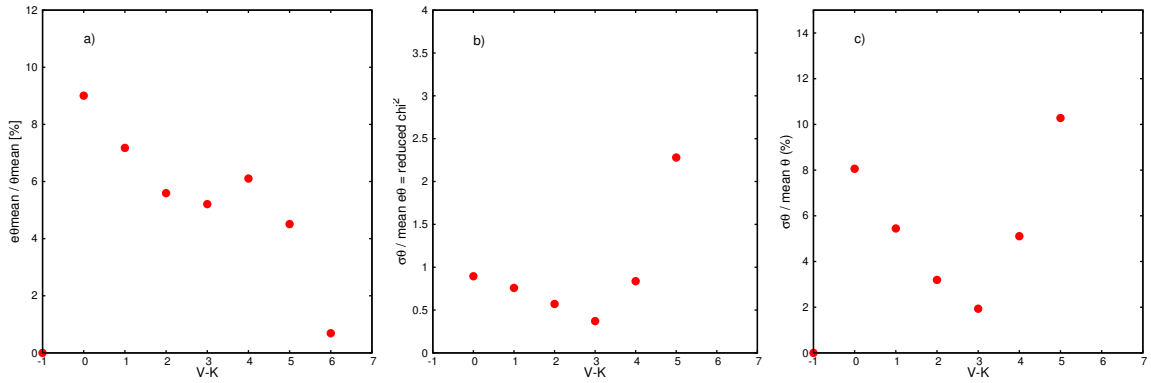


FIGURE 5.8 – Analyse statistique à partir de la figure 5.7. A gauche, il s'agit de l'erreur moyenne sur le diamètre, comparée au diamètre moyen pour différents $V-K$. Cela correspond donc à l'erreur relative en pourcentage telle qu'elle est estimée dans les publications. On prend ici en compte les domaines de validité en $V-K$ des relations. En revanche, toutes les classes sont considérées. Le diagramme du milieu teste la validité des estimations d'erreurs dans la littérature en comparant les estimations entre elles, et notamment leur dispersion, par rapport à l'erreur correspondante qui est annoncée. On obtient en quelque sorte une estimation du χ^2 réduit basé sur l'ensemble de la littérature. Des incohérences importantes sont ainsi observées à V-K=5. Le dernier diagramme à droite donne l'estimation la plus réaliste des erreurs sur les diamètres que l'on peut espérer avoir actuellement, puisqu'on compare la dispersion sur les diamètres issus de la littérature avec le diamètre moyen correspondant.

l'objet utilisé pour étalonner la relation brillance de surface - couleur et l'objet auquel on applique la relation. Ce travail est en cours avec l'instrument Pionier/VLTI.

4. Afin d'étalonner efficacement une relation brillance de surface couleur, disposer d'une photométrie V et K (ou autre) homogène et précise semble enfin un point clef.

Ainsi, pour augmenter la précision et l'exactitude sur les relations brillance de surface - couleur, il faut augmenter/doubler l'échantillon d'étoiles observées par interférométrie, avec un seul et même instrument, en prenant bien garde de considérer un échantillon d'étoiles homogène en terme de classe et de type spectral. Il faudra en particulier augmenter l'échantillon des étoiles de type spectral O, B, A, F et de classe I, II. L'impact de l'activité stellaire est également un point clef car elle est probablement à la source des différences observées entre les relations.

Dans les années à venir, l'instrument SPICA [8] devrait permettre d'avancer sur de nombreux points. Il s'agit d'un instrument à 6 télescopes, fibré, muni d'une caméra de nouvelle génération dans le visible et tirant parti des nouvelles optiques adaptatives du réseau interférométrique CHARA. L'objectif scientifique est de déterminer les paramètres fondamentaux (dont le rayon) de 200 étoiles à exoplanètes, 200 étoiles astérosismiques, ainsi que 600 étoiles "standards" afin d'améliorer la précision et l'exactitude des relations brillance de surface - couleur. Parmi cet échantillon de 1000 étoiles, 200 étoiles seront imagées afin d'étudier l'activité stellaire plus en détail. Les relations brillance de surface - couleur qui découleront de ce travail seront un outil précieux dans le contexte *Gaia* Gaia et PLATO, car elles permettront de déduire le rayon d'étoiles non résolues et trop faibles pour l'interférométrie. Ce projet aura également des répercutions importantes pour l'étalonnage des échelles de distances dans l'univers.

Avant de clore cette section, il est intéressant de souligner que nous avons adopté une méthode un peu différente récemment dans le cadre du projet Araucaria pour étalonner la relation brillance de surface - couleur. La méthode consiste à inverser la méthode des binaires à éclipses à partir des parallaxes *Gaia*. Effectivement, si la distance des binaires à éclipses galactiques est connue, et que d'autre part on dispose des rayons individuels des composantes par photométrie et spectroscopie, alors il est possible d'en déduire le diamètre angulaire des étoiles et ainsi contraindre la relation brillance de surface - couleur. Ce travail original, qui a fait l'objet d'une publication (Graczyk et al. 2017) (voir l'annexe W), donne des résultats compatibles avec les relations déduites par interférométrie. D'autres études suivront avec les futures données *Gaia* avec l'objectif d'atteindre 1% de précision sur la relation.

8. Une ERC déposée par D. Mourard.

5.3 L'impact de la rotation sur la relation brillance de surface - couleur

Nous avons vu que l'activité d'une étoile peut avoir un impact sur sa brillance de surface - couleur. Dans l'étude menée par M. Challouf en 2015, nous avons utilisé le code CHARRON (Domiciano de Souza et al. 2002) pour quantifier l'impact de la rotation rapide sur la relation brillance de surface - couleur des étoiles précoces. Ainsi nous avons calculé 6 modèles statiques de départ (M1 à M6) ayant des couleurs V-K s'échelonnant entre -1 et 0.5. A partir des 6 modèles statiques, nous avons considéré plusieurs valeurs de vitesse de rotation (0, 25, 50, 75 et 95% de la vitesse de rotation critique) et plusieurs valeurs de l'inclinaison de l'axe de rotation par rapport à la ligne de visée (0, 25, 50, 75 et 90 degrés). Tous ces modèles (6x5x5=150 au total) ont leur axe équatorial selon l'axe Est-Ouest sur le plan du ciel. Nous avons alors simulé des observations CHARA (avec trois configurations différentes) et l'analyse a été menée *comme si* les étoiles étaient des étoiles statiques, c'est à dire sphériques, sans aplatissement dû à la rotation et sans assombrissement gravitationnel, afin d'en déduire finalement la relation brillance de surface - couleur. Ainsi, les valeurs de couleurs (V-K) et la brillance de surface - couleur (telle que définie précédemment) sont biaisées par la rotation et l'inclinaison. La figure 5.9-haut illustre ces biais pour le modèle statique de départ M3 ayant une valeur de $V-K=-0.3$ et pour une configuration de CHARA donnée (W2S2-W1W2S2). On a ainsi sur ce graphique 25 modèles correspondant à différentes valeurs de la rotation (exprimées en pourcentage de la vitesse critique V_c) et différentes valeurs d'inclinaison. Les lignes en pointillés correspondent à des valeurs de $V_{\rm rot}\sin i$ identiques. La ligne en pointillé qui traverse la figure correspond à la relation empirique obtenue par Challouf et al. (2014) (Sect. précédente) avec sa dispersion ("dot-dashed lines"). La ligne orange illustre la relation brillance de surface - couleur ajustée sur l'ensemble des 6 modèles statiques qui sont représentés sur la figure 5.9-bas. Sur cette figure, les points bleus correspondent à des inclinaisons différentes (0, 25, 50, 75 et 90 degrés) pour une vitesse de rotation à 95% de la vitesse critique, alors que les points verts correspondent à différentes vitesses de rotations pour une inclinaison donnée et à 90 degrés ("edge-on").

Les conclusions de ce travail sont les suivantes :

1. La vitesse de rotation des étoiles a un impact sur le point-zéro (Δa_0) de la relation brillance de surface - couleur et sur sa dispersion (σ), mais pas sur sa pente (par rapport à la relation brillance de surface - couleur calculée sur les modèles statiques). Ainsi, si on considère des étoiles qui tournent à moins de 50% de la vitesse critique, l'effet est relativement faible avec un impact de 0.01 magnitude sur Δa_0 et σ. Si les étoiles tournent très vite, à plus de 75% de la vitesse critique, alors l'effet peut monter à 0.08 magnitude sur Δa_0 et 0.04 magnitude sur σ.
2. Par ailleurs, l'inclinaison a un impact essentiellement sur la couleur V-K de l'étoile. Ainsi $i<50^\circ$ (resp. $i>50^\circ$) fait que l'étoile apparait plus rouge (resp. plus bleue).
3. Si on considère les 150 modèles, on obtient $\Delta a_0=0.03$ mag et $\sigma=0.04$ mag. Ces valeurs sont peu sensibles aux configurationx de CHARA considérées.
4. La dispersion de ces 150 modèles est compatible avec la relation empirique Challouf et al. (2014) qui présente une dispersion de 0.16 magnitude.
5. Enfin, et c'est la conclusion la plus importante, si l'on désire étalonner la relation brillance de surface - couleur pour les étoiles précoces avec une précision de 0.02 magnitude (ou 1% en terme diamètre), il faut considérer des étoiles dont la vitesse de rotation est inférieure à 50% de la vitesse critique, ou à défaut (si la rotation n'est pas connue), des étoiles dont le $V_{\rm rot}\sin i$ est inférieur à 100km s^{-1}. Si l'on cherche une précision et exactitude meilleure que 0.05 magnitude (ou 4-5 %), ce qui serait déjà un énorme progrès, il faut rejeter les étoiles qui tournent à plus de 75% de la vitesse critique.

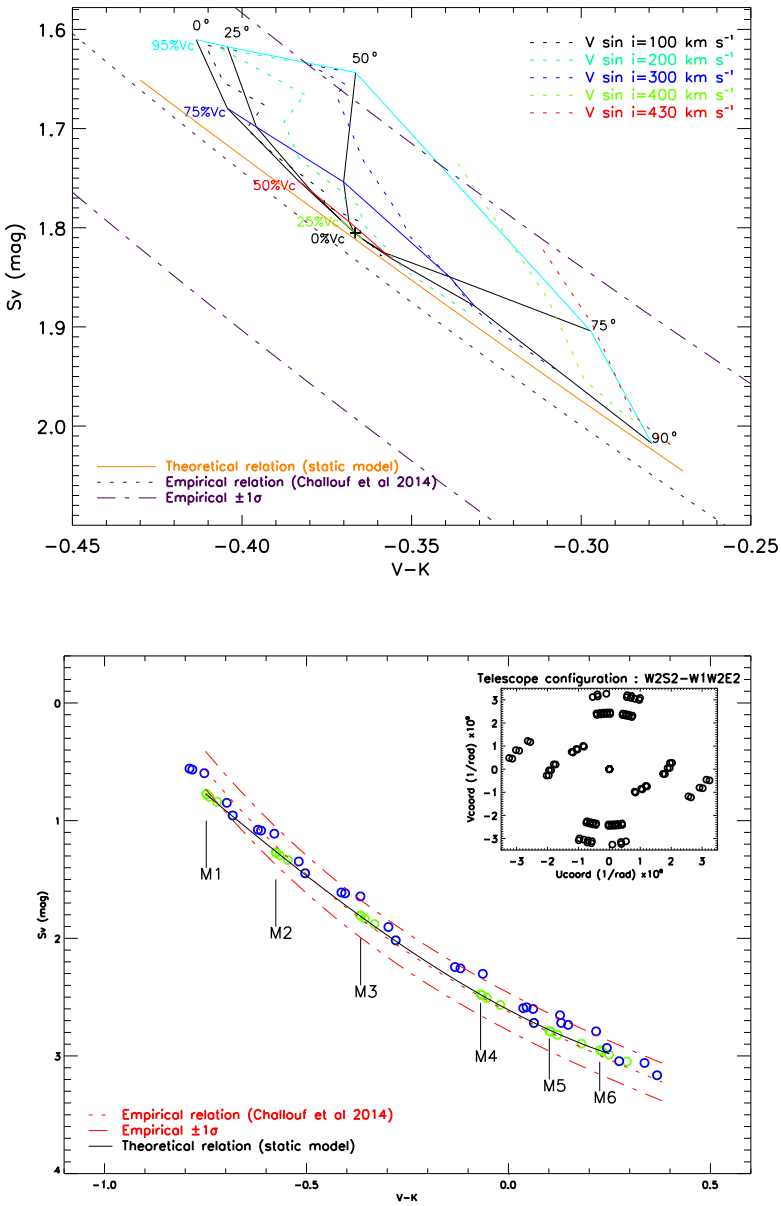


FIGURE 5.9 – Illustration de l'impact de la rotation rapide sur l'étalonnage de la relation brillance de surface - couleur des étoiles de type précoce (voir le texte pour les explications).

5.4 Contraindre le p-facteur et le k-facteur des Céphéides à l'aide des binaires à éclipses

Les binaires à éclipses sont des objets astrophysiques fascinants car non seulement ce sont de bons indicateurs de distance comme nous venons de le voir (à condition de disposer d'une bonne relation brillance de surface - couleur), mais ils permettent également de déterminer la masse des deux composantes du système avec une excellente précision. Ainsi, si par chance on détecte une binaire à éclipses dont l'une des composantes est une étoile pulsante, on peut en déduire sa masse (et de nombreux autres paramètres), ce qui est particulièrement intéressant pour ce type d'objet, en particulier pour tenter de réconcilier les modèles de pulsation et d'évolution dont on sait qu'ils présentent des désaccords à hauteur de 10%. Cependant, très peu d'étoiles pulsantes sont connues pour appartenir à des systèmes avec des éclipses. L'une des plus étudiées est AB Cas, un système binaire de type Algol contenant une δ Scuti (Rodriguez et al. 1998). Rodríguez & Breger (2001) listent également 9 δ Scuti appartenant à des binaires à éclipses. Pendant un temps BM Cas était supposée être une Céphéide galactique dans une binaire à éclipses (Thiessen 1956), mais il est apparu que ce n'était pas le cas (Fernie & Evans 1997). Il faut attendre 2002 pour que trois Céphéides du LMC soient confirmées comme appartenant à des systèmes binaires à éclipses dans le cadre du projet MACHO (Alcock et al. 2002). Cependant, ces détections sont purement photométriques et les masses des Céphéides n'ont pas pu être déterminées. Les auteurs donnent néanmoins des valeurs d'assombrissement centre-bord (intéressantes pour la détermination du facteur de projection) mais assez imprécises.

Ainsi, dans le cadre du projet Araucaria, une binaire à éclipses détachée à deux raies (SB2) comprenant une Céphéide OGLE-LMC-CEP0227 ($P_{\rm puls} = 3.80$ d, $P_{\rm orb} = 309$ d) a été détectée dans le LMC par OGLE (Soszyński et al. 2008). La masse de la Céphéide a ainsi été déterminée pour la première fois avec une précision de 1% (Pietrzyński et al. 2010b) et la valeur obtenue est en accord avec la masse issue des modèles de pulsation, tandis que la masse tirée des modèles d'évolution est significativement plus élevée. Le même exercice fut ensuite réalisé sur OGLE-LMC-CEP-1812, un objet similaire avec une précision sur la masse de la Céphéide de 1.5% (Pietrzyński et al. 2011). Un an plus tard, de la même manière, une binaire à éclipses comprenant une RR Lyrae a été découverte dans le LMC avec une période orbitale de 15.24 jours. Nous avons déterminé sa masse (0.26 masses solaires) avec une précision de 6% (Pietrzyński et al. 2012) (voir l'annexe X). A partir de modèles, nous avons montré que le système devait à l'origine être un système binaire proche composé de deux étoiles de 1.4 et 0.8 masses solaires, respectivement, et une période orbitale de 2.9 jours. Ainsi, un transfert de masse pendant environ 5.5 millions d'année a probablement généré le système actuel, plaçant l'une des deux étoiles dans la bande d'instabilité des RR Lyrae. Seulement 0.2% des RR Lyrae devraient être contaminées par un système comme celui-ci, ce qui implique que les distances déduites des RR Lyrae ne devraient pas être affectées de manière significative par ces systèmes atypiques.

Mais l'histoire ne s'arrête pas là, dans la mesure où, de façon assez inattendue, les binaires à éclipses incluant une étoile pulsante permettent également de déduire deux quantités physiques dont nous avons déjà parlé, à savoir le p-facteur et le k-facteur. Ce résultat remarquable a été obtenu par notre équipe du projet Araucaria menée par B. Pilecki. L'objet OGLE-LMC-CEP-0227 a été observé de manière intense au sol afin de récolter 1045 mesures en bande I, 317 en bande V (Télescope géré par le groupe OGLE à Varsovie) ainsi qu'en bande K (instrument SOFI à la Silla) et à 3.6 et 4.5μm avec le télescope *Spitzer*. Des observations effectuées avec les spectrographes MIKE, HARPS et UVES (123 spectres en tout) ont permis d'apporter des contraintes importantes supplémentaires dans la mesure où cet objet est de type SB2. Un modèle spécifique pour ce type d'objet a été développé. Ainsi, sur la figure 5.10, on voit clairement dans les observations photométriques en bandes I et V (points noirs) la pulsation de la Céphéide ainsi

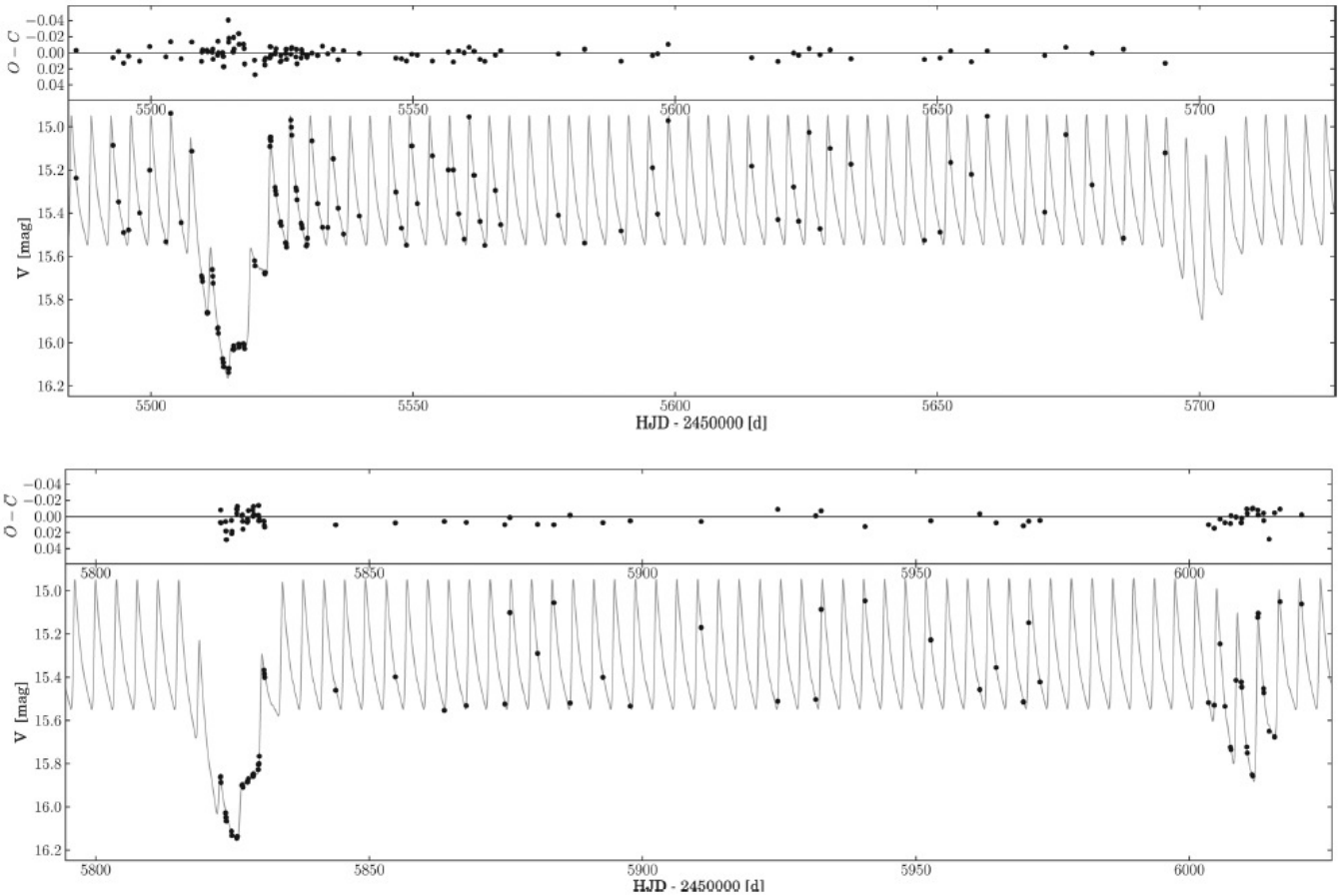


FIGURE 5.10 – Binaire à éclipses composée d'une étoile standard et d'une Céphéide. Les points sont les observations en bande V (en haut) et en bande V (en bas), tandis que le trait noir représente le modèle.

que les éclipses primaires et secondaires. Le trait noir représente le modèle. Ce qui est intéressant, c'est que le passage de la Céphéide devant son compagnon permet, grâce aux observations photométriques, de déterminer directement la variation de son rayon (Fig. 5.11). La dérivée temporelle de cette variation de rayon permet d'en déduire la courbe de vitesse pulsante. Comme l'étoile est SB2, on peut en déduire la courbe de vitesse radiale associée à la Céphéide et donc le facteur de projection qui, rappelons-le, est le rapport de la vitesse pulsante à la vitesse radiale. La valeur ainsi obtenue pour le facteur de projection est de $p = 1.21 \pm 0.03(stat.) \pm 0.04(syst.)$ pour une période de pulsation de 3.8 jours (Pilecki et al. 2013) (voir l'annexe Y). Ce résultat est absolument compatible avec la relation Pp discutée dans le chapitre précédent (Nardetto et al. 2009) qui donne un facteur de projection, pour cette période, de $p = 1.21$. A ce résultat remarquable s'ajoute la question du k-facteur des Céphéides. Grâce à la nature SB2 du système, il est possible de comparer la valeur moyenne de la courbe de vitesse radiale de la Céphéide à la vitesse du centre-de-masse du système binaire. La différence entre ces deux vitesses donne le k-facteur et l'on obtient $k = 0.59$ km s^{-1}, une valeur cohérente avec les valeurs décrites dans Nardetto et al. (2008b).

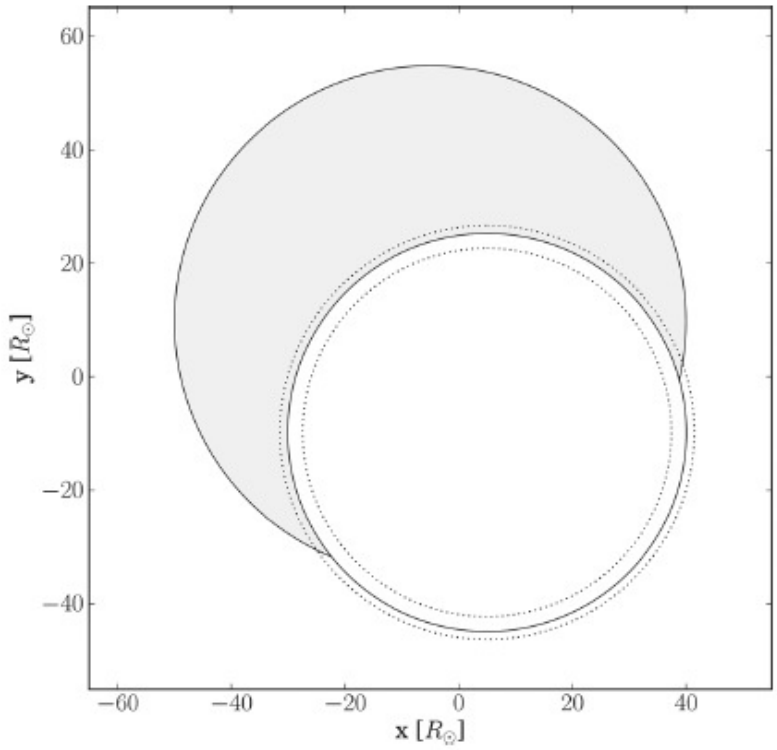


FIGURE 5.11 – Représentation de la binaire à éclipses. La pulsation de la Céphéide, au premier plan, est représentée par les pointillés.

Le même type d'approche a été effectuée sur un autre système OGLE LMC562.05.9009 ($P_{\rm puls} = 2.988$ d, $P_{\rm orb} = 1550$ d) et le facteur de projection est cette fois beaucoup plus élevé, $p = 1.37 \pm 0.07$, ce qui apporte un peu de confusion (Gieren et al. 2015). Suite à la détermination de masse de l'objet OGLE-LMC-CEP-1812, l'objet a été réétudié pour le calcul du facteur de projection, et nous avons obtenu $p = 1.26 \pm 0.09$ [B. Pilecki, private communication]. Enfin, récemment, le même travail a été effectué sur un système comprenant une céphéide de type I et SB1 (OGLE-LMC-T2CEP-098 ; $P_{\rm puls} = 4.974$ d, $P_{\rm orb} = 397.2$ d). Dans ce cas, il y a

une corrélation entre la masse de la Céphéide et le p-facteur. Le résultat est donc moins robuste et nécessite des hypothèses, mais nous avons conclu sur un p-facteur de 1.30 ± 0.03 (Pilecki et al. 2017). Ainsi, avec cette méthode des binaires à éclipses Céphéides, nous avons quatre valeurs du facteur de projection pour des Céphéides courtes périodes s'échelonnant entre 1.21 et 1.37. Pour finir, mentionnons un dernier résultat du groupe Araucaria avec la découverte de la toute première binaire à éclipses composée de deux Céphéides (Gieren et al. 2014). Mais pour ce système, l'analyse est trop délicate pour le calcul du facteur de projection.

Chapitre 6

Synthèse et perspectives

Résumons. Pour comprendre la nature de l'énergie noire, il faut mesurer le taux d'expansion de l'univers, c'est-à-dire la constante de Hubble (H_0), avec une bonne précision, soit 2%, voire 1%. La mesure de H_0 qui utilise le rayonnement de fond cosmologique, c'est à dire à $z = 1100$, est déterminée conjointement avec une vingtaine de paramètres ce qui pose le problème délicat des dégénérescences. D'un autre côté, la méthode qui utilise l'étalonnage des échelles des distances mesure le H_0 localement ($z < 0.15$) et est probablement très sensible à la physique des objets considérés (Céphéides, SNIa, ...). La tension actuellement de 3.4σ entre ces deux estimations est soit liée à une erreur systématique non prise en compte dans l'une ou l'autre méthode, soit elle correspond à un résultat physique à interpréter. Plusieurs pistes d'analyses sont possibles mais l'objectif qui vise à renforcer l'échafaudage des distances dans l'univers est de nos jours extrêmement pertinent. Pour cela, le chemin le plus court actuellement utilisé par la communauté est d'abord d'étalonner la relation période-luminosité des Céphéides, puis de l'utiliser afin de déterminer la distance d'une vingtaine de SNIa situées à environ 5-40 Mpc dans des galaxies qui ont une métallicité proche de celle de la Voie Lactée. Une fois la relation des SNIa étalonnée, on peut finalement mesurer H_0. Les points clefs qui ont été identifiés et qui permettraient d'améliorer la précision et/ou d'extraire une erreur systématique sont les suivants et au nombre de trois.

D'abord, la relation période-luminosité est sensible à la métallicité des Céphéides considérées, que ce soit sa pente ou son point-zéro, et ceci peut avoir un effet de 1%, voire plus sur H_0. Il est communément admis que la pente est toutefois peu sensible à cette métallicité lorsqu'on observe dans l'infrarouge. En revanche, l'impact sur le point-zéro n'est pas clair du tout. Un façon de s'affranchir de cela est d'étalonner la relation période-luminosité en ne considérant que les Céphéides de la Voie Lactée, dont la métallicité est effectivement proche de la métallicité des galaxies hôtes de SNIa. Mais ce n'est pas totalement satisfaisant dans la mesure où la métallicité des galaxies lointaines est déduite des nuages moléculaires et non à partir des Céphéides elles-mêmes. Ainsi, pour quantifier l'impact de la métallicité sur le point-zéro de la relation période-luminosité, il faut déterminer la distance de plusieurs galaxies du groupe local dont la métallicité est effectivement significativement différente. Ce travail permettrait également d'étendre le nombre de galaxies de référence pour l'étalonnage de la relation. C'est bien l'objectif du projet Araucaria : déterminer la distance de galaxies à métallicité élevée (M31, M33, M82, et M83) de façon à en faire de nouvelles références, mais aussi de galaxies à métallicité faible (LMC, SMC, ...) de façon à évaluer l'impact de la métallicité sur la relation. A ce niveau, le problème revient à déterminer la distance des galaxies du groupe local de façon précise, en utilisant une autre méthode que la relation période-luminosité de façon à pouvoir l'étalonner justement. Une méthode récente et prometteuse est de découvrir •t d'utiliser des binaires à éclipses dans ces

galaxies. La distance du LMC a pu ainsi être déterminée avec une précision de 2.2% et celle du SMC avec une précision de 3%. Pour augmenter, la précision sur ces deux distances, il va falloir augmenter la précision sur la relation brillance de surface - couleur des étoiles tardives. Pour aller plus loin en terme de distance, il va falloir très probablement découvrir de nouvelles binaires à éclipses brillantes (donc précoces) dans des galaxies du groupe local. Il faudra ensuite augmenter la précision et l'exactitude de la relation brillance de surface - couleur pour les étoiles précoces. Le meilleur moyen de faire cela est d'utiliser l'interférométrie. Le projet SPICA sur CHARA vise précisément à déterminer la diamètre angulaire d'environ 1000 étoiles pour étalonner cette relation, non seulement pour les distances des binaires à éclipses, mais aussi pour estimer le rayon des étoiles et des planètes en lien avec PLATO et *Gaia*. Prendre en compte l'activité des étoiles (taches, bulles convectives, vent, environnement, rotation) semble maintenant incontournable pour estimer les relations brillance de surface - couleur (qui font l'hypothèse que les étoiles sont des corps noirs), mais aussi pour détecter et déterminer les paramètres des étoiles et des planètes.

Ensuite, outre l'impact de la métallicité sur la relation période-luminosité, sa dispersion est suffisamment importante pour avoir un impact d'environ 1-2% (et même probablement plus) sur H_0. Cette dispersion est en partie intrinsèque, liée à la largeur de la bande d'instabilité, mais elle est aussi due au rougissement, à la binarité ou à l'environnement. Evaluer l'impact de la binarité et de l'environnement, respectivement, sont des objectifs de l'ANR UnlockCepheids. Ainsi, avec toute une gamme d'instruments photométriques, spectroscopiques (VISIR) et interférométriques (MATISSE, Gravity, VEGA, SPICA, ...), nous allons établir des SEDs pour toutes les Céphéides galactiques proches (environ 50) en dissociant bien la contribution de l'étoile et celle de l'environnement. L'objectif est de fabriquer un outil qui permette d'estimer l'impact de l'environnement d'une Céphéide sur la relation période-luminosité, et ce quelle que soit sa position dans la bande d'instabilité. On cherchera donc prioritairement une relation entre la période et l'environnement, mais pas seulement. Par ailleurs, il faut noter que la nature des enveloppes des Céphéides est peu comprise (gaz, type de poussières) et que pour cela, l'interférométrie à haute résolution spectrale et dans les bandes L, M, N sera particulièrement utile pour faire de la minéralogie (MATISSE, code DUSTY). Pour ce qui est de la spectro-interférométrie, les modèles hydrodynamiques sont prêts depuis 2005 (voir Fig. 6.1)... même s'il faudra prévoir quelques développements pour prendre en compte l'environnement. De même, la découverte récente que les enveloppes des Céphéides rayonnent également significativement dans le visible ouvre une voie de recherche intéressante.

Enfin, de manière générale, toutes les méthodes précises et exactes qui permettent de déterminer la distance des galaxies du groupe local sont à regarder avec intérêt. A ce titre, un objectif est de rendre la méthode de Baade-Wesselink suffisamment robuste pour déduire la distance des Céphéides *individuelles* dans les galaxies du groupe local. Pour cela, le point clef est de caractériser et de comprendre la dynamique atmosphérique des Céphéides. Le lien entre le facteur de projection, la distance des Céphéides et H_0 est étroit et c'est bien la raison pour laquelle les distances de BW ne sont généralement par utilisées par la communauté pour contraindre H_0. Cependant, des progrès conceptuels significatifs ont été effectués sur le facteur de projection. La décomposition du facteur de projection semble correcte. Cependant, un ingrédient doit manquer. Bientôt nous pourrons inverser la méthode de BW pour l'ensemble des Céphéides galactiques pour lesquelles on aura une parallaxe *Gaia*. Il y a fort à parier que la relation entre la période et le facteur de projection sera hautement dispersée. Il faudra alors se baser sur la décomposition du facteur de projection pour d'abord comprendre la physique cachée derrière ces valeurs, puis pour construire un outil ou des concepts qui permettent d'estimer le p-facteur d'une façon précise et exacte quel que soit la période de la Céphéide ou sa position dans la bande d'instabilité (ce travail est en cours). Comprendre la dynamique atmosphérique est un ensemble : cela passe aussi par l'étude du k-facteur, grâce à la spectroscopie optique et infrarouge. Une autre piste intéressante pour comprendre la physique de l'atmosphère des Céphéides est

de procéder par comparaison en étudiant d'autres types d'étoiles pulsantes dont le mode radial est dominant (HADS, RR Lyrae, β-Céphéides, ...).

Ces travaux permettront une exploitation des instruments futurs, tels que le JWST et l'ELT. Aujourd'hui, on peut atteindre des magnitudes limites d'environ 28 pour le HST (2.4 mètres dans l'espace) ou pour des télescopes de 8m au sol. Cela correspond pour des magnitude absolues d'environ -5 pour les Céphéides à des distances entre 30 et 40 Mpc. Avec le JWST et l'ELT, nous pourrons pousser ces limites à 100 Mpc et fort probablement augmenter le nombre de SN1a utilisées en tant que calibrateurs.

Ainsi les perspectives de ces recherches sont claires ; elles s'insèrent à l'interface de trois grands projets : le projet Araucaria (les distances dans le groupe local), l'ANR UnlockCepheids (dispersion de la relation période-luminosité des Céphéides) et le projet SPICA (contraindre la relation brillance de surface - couleur pour les binaires à éclipses). A côté de cela, je continuerai à sonder l'atmosphère des Céphéides de façon à améliorer notre connaissance du facteur de projection. Une bien belle aventure en perspective ...

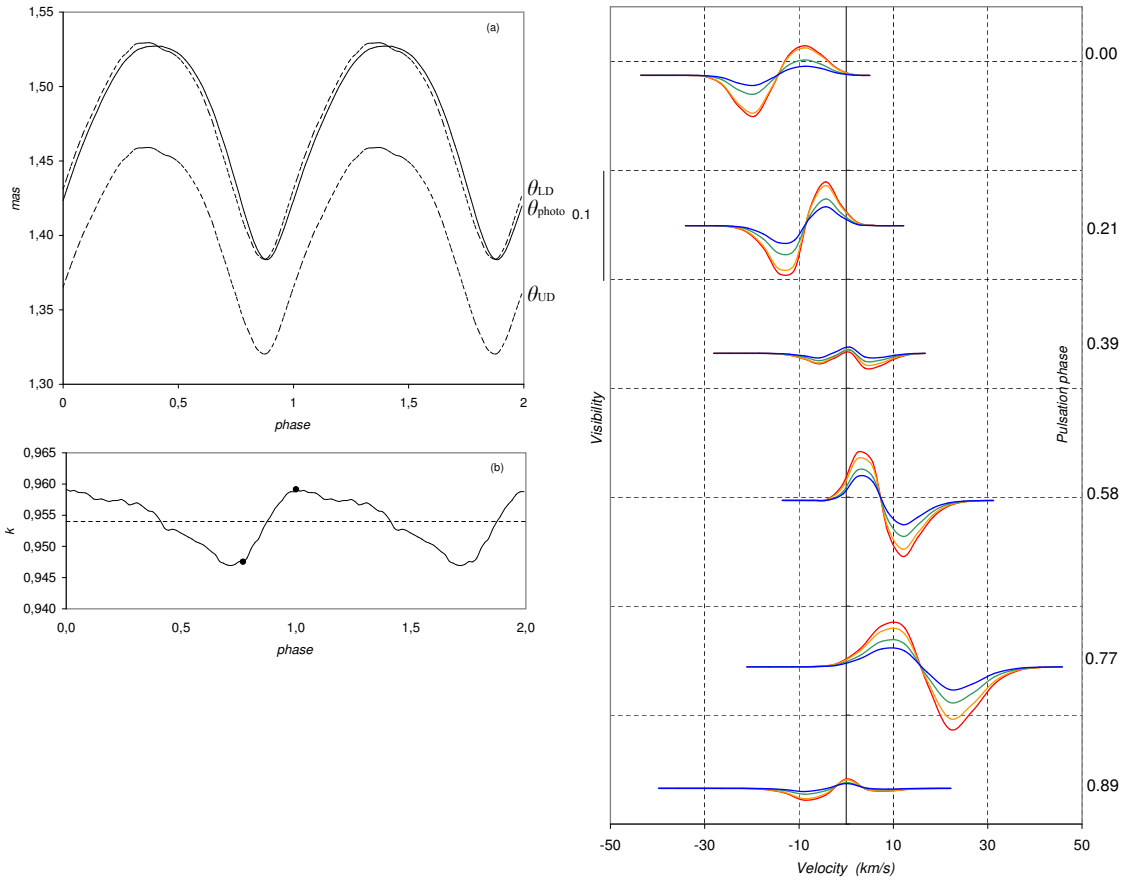


FIGURE 6.1 – Les points clefs des observations interférométriques futures : la mesure directe de l'assombrissement centre-bord (à gauche) et la spectro-interférométrie (à droite). Sur le diagramme de gauche, $\theta_{\rm LD}$ ne prend pas en compte la variation d'assombrissement de δ Cep, tandis que $\theta_{\rm photo}$, déduit du modèle hydrodynamique, prend en compte cette variation. On s'aperçoit que l'amplitude de la courbe de diamètre angulaire reste inchangée, et donc on peut conclure que la variation de l'assombrissement centre-bord n'a pas d'impact sur la distance de BW. mais cela reste à prouver avec des mesures directes de variation d'assombrissement centre bord par interférométrie visible, d'autant qu'une telle mesure permet de déduire directement le facteur de projection géométrique de la Céphéide. A droite, on représente les courbes de visibilité dans différentes raies de profondeurs différentes (différentes couleurs) au cours de la pulsation. Ces résultats théoriques ont été publié à l'époque de ma thèse Nardetto et al. (2006a) et attendent toujours des contraintes observationnelles.

Bibliographie

Abbott, B. P., Abbott, R., Abbott, T. D., et al. 2017, ArXiv e-prints

Adén, D., Feltzing, S., Koch, A., et al. 2009, A&A, 506, 1147

Africano, J. L., Evans, D. S., Fekel, F. C., & Montemayor, T. 1977, AJ, 82, 631

Albrow, M. D. & Cottrell, P. L. 1994, MNRAS, 267, 548

Alcock, C., Allsman, R. A., Alves, D. R., et al. 1997, ApJ, 474, 217

Alcock, C., Allsman, R. A., Alves, D. R., et al. 2002, ApJ, 573, 338

Alibert, Y., Baraffe, I., Hauschildt, P., & Allard, F. 1999, A&A, 344, 551

Andersen, J., Clausen, J. V., Nordstrom, B., Tomkin, J., & Mayor, M. 1991, A&A, 246, 99

Anderson, R. I. 2014, A&A, 566, L10

Anderson, R. I. 2016, MNRAS

Anderson, R. I., Casertano, S., Riess, A. G., et al. 2016a, ApJS, 226, 18

Anderson, R. I., Mérand, A., Kervella, P., et al. 2016b, MNRAS, 455, 4231

Anderson, R. I., Sahlmann, J., Holl, B., et al. 2015, ApJ, 804, 144

Ardeberg, A. & de Groot, M. 1973, A&A, 28, 295

Argon, A. L., Greenhill, L. J., Reid, M. J., Moran, J. M., & Humphreys, E. M. L. 2007, ApJ, 659, 1040

Armstrong, J. T., Mozurkewich, D., Rickard, L. J., et al. 1998, ApJ, 496, 550

Armstrong, J. T., Nordgren, T. E., Germain, M. E., et al. 2001, AJ, 121, 476

Ayres, T. R. 2017, ApJ, 837, 14

Baade, W. 1926, Astronomische Nachrichten, 228, 359

Baade, W. 1956, PASP, 68, 5

Balona, L. A. & Stobie, R. S. 1979a, MNRAS, 187, 217

Balona, L. A. & Stobie, R. S. 1979b, MNRAS, 189, 649

Balona, L. A. & Stobie, R. S. 1979c, MNRAS, 189, 659

Baraffe, I., Alibert, Y., Méra, D., Chabrier, G., & Beaulieu, J.-P. 1998, ApJ, 499, L205

Barbon, R., Ciatti, F., & Rosino, L. 1973, A&A, 29, 57

Barmby, P., Marengo, M., Evans, N. R., et al. 2011, AJ, 141, 42

Barnes, T. G. & Evans, D. S. 1976, MNRAS, 174, 489

Barnes, T. G., Evans, D. S., & Moffett, T. J. 1978, MNRAS, 183, 285

Barnes, T. G., Evans, D. S., & Parsons, S. B. 1976, MNRAS, 174, 503

Behr, A. 1951, Astronomische Nachrichten, 279, 97

Bell, E. F., Slater, C. T., & Martin, N. F. 2011, ApJ, 742, L15

Bell, R. A. & Rodgers, A. W. 1964, MNRAS, 128, 365

Bell, S. A., Hilditch, R. W., Reynolds, A. P., Hill, G., & Clausen, J. V. 1991, MNRAS, 250, 119

Bell, S. A., Hill, G., Hilditch, R. W., Clausen, J. V., & Reynolds, A. P. 1993, MNRAS, 265, 1047

Bellazzini, M., Gennari, N., & Ferraro, F. R. 2005, MNRAS, 360, 185

Bellazzini, M., Gennari, N., Ferraro, F. R., & Sollima, A. 2004, MNRAS, 354, 708

Bellazzini, M., Ibata, R., Martin, N., et al. 2006, MNRAS, 366, 865

Belokurov, V., Walker, M. G., Evans, N. W., et al. 2008, ApJ, 686, L83

Belokurov, V., Walker, M. G., Evans, N. W., et al. 2010, ApJ, 712, L103

Belokurov, V., Walker, M. G., Evans, N. W., et al. 2009, MNRAS, 397, 1748

Belokurov, V., Zucker, D. B., Evans, N. W., et al. 2007, ApJ, 654, 897

Benedict, G. F., McArthur, B. E., Feast, M. W., et al. 2011, AJ, 142, 187

Benedict, G. F., McArthur, B. E., Feast, M. W., et al. 2007, AJ, 133, 1810

Benedict, G. F., McArthur, B. E., Fredrick, L. W., et al. 2002, AJ, 124, 1695

Bennett, C. L., Larson, D., Weiland, J. L., & Hinshaw, G. 2014, ApJ, 794, 135

Bernard, E. J., Monelli, M., Gallart, C., et al. 2009, ApJ, 699, 1742

Bessel, F. W. 1838, MNRAS, 4, 152

Beutler, F., Blake, C., Colless, M., et al. 2011, MNRAS, 416, 3017

Birkinshaw, M. 1999, Phys. Rep., 310, 97

Blazit, A., Bonneau, D., Josse, M., et al. 1977, ApJ, 217, L55

Bonamente, M., Joy, M. K., LaRoque, S. J., et al. 2006, ApJ, 647, 25

Bonanos, A. Z., Castro, N., Macri, L. M., & Kudritzki, R.-P. 2011, ApJ, 729, L9

Bonanos, A. Z., Stanek, K. Z., Kudritzki, R. P., et al. 2006, ApJ, 652, 313

Bonanos, A. Z., Stanek, K. Z., Szentgyorgyi, A. H., Sasselov, D. D., & Bakos, G. Á. 2004, AJ, 127, 861

Bonneau, D., Clausse, J.-M., Delfosse, X., et al. 2006, A&A, 456, 789

Bono, G., Caputo, F., Fiorentino, G., Marconi, M., & Musella, I. 2008, ApJ, 684, 102

Bono, G., Marconi, M., & Stellingwerf, R. F. 1999, ApJS, 122, 167

Boyajian, T., von Braun, K., Feiden, G. A., et al. 2015, MNRAS, 447, 846

Boyajian, T. S., van Belle, G., & von Braun, K. 2014, AJ, 147, 47

Breitfelder, J., Kervella, P., Mérand, A., et al. 2015, A&A, 576, A64

Breitfelder, J., Mérand, A., Kervella, P., et al. 2016, A&A, 587, A117

Bresolin, F., Gieren, W., Kudritzki, R.-P., et al. 2009, ApJ, 700, 309

Bresolin, F., Kudritzki, R.-P., Urbaneja, M. A., et al. 2016, ApJ, 830, 64

Bruntt, H., Evans, N. R., Stello, D., et al. 2008, ApJ, 683, 433

Buchler, J. R. & Goupil, M.-J. 1984, ApJ, 279, 394

Burki, G., Mayor, M., & Benz, W. 1982, A&A, 109, 258

Butler, R. P., Bell, R. A., & Hindsley, R. B. 1996, ApJ, 461, 362

Cacciari, C., Clementini, G., & Fernley, J. A. 1992, ApJ, 396, 219

Caccin, R., Onnembo, A., Russo, G., & Sollazzo, C. 1981, A&A, 97, 104

Caldwell, J. A. R. & Coulson, I. M. 1987, AJ, 93, 1090

Calzetti, D., Conselice, C. J., Gallagher, III, J. S., & Kinney, A. L. 1999, AJ, 118, 797

Camm, G. L. 1938, MNRAS, 99, 71

Camm, G. L. 1944, MNRAS, 104, 163

Cantiello, M., Grado, A., Blakeslee, J. P., et al. 2013, A&A, 552, A106

Caputo, F. 2008, Mem. Soc. Astron. Italiana, 79, 453

Cardelli, J. A., Clayton, G. C., & Mathis, J. S. 1989, ApJ, 345, 245

Carlstrom, J. E., Holder, G. P., & Reese, E. D. 2002, ARA&A, 40, 643

Carney, B. W., Storm, J., & Jones, R. V. 1992, ApJ, 386, 663

Carrera, R., Aparicio, A., Martínez-Delgado, D., & Alonso-García, J. 2002, AJ, 123, 3199

Carrillo, D., Burki, G., Mayor, M., et al. 1995, A&AS, 113, 483

Casertano, S., Riess, A. G., Anderson, J., et al. 2016, ApJ, 825, 11

Challouf, M., Nardetto, N., Mourard, D., et al. 2014, A&A, 570, A104

Chávez, R., Terlevich, E., Terlevich, R., et al. 2012, MNRAS, 425, L56

Chelli, A., Duvert, G., Bourgès, L., et al. 2016, A&A, 589, A112

Ciardullo, R., Feldmeier, J. J., Jacoby, G. H., et al. 2002, ApJ, 577, 31

Ciechanowska, A., Pietrzyński, G., Szewczyk, O., Gieren, W., & Soszyński, I. 2010, Acta Astron., 60, 233

Claret, A. 2000, A&A, 363, 1081

Claret, A. & Bloemen, S. 2011, A&A, 529, A75

Claussen, M. J., Heiligman, G. M., & Lo, K. Y. 1984, Nature, 310, 298

Colavita, M. M., Wallace, J. K., Hines, B. E., et al. 1999, ApJ, 510, 505

Collins, M. L. M., Chapman, S. C., Irwin, M. J., et al. 2010, MNRAS, 407, 2411

Courbin, F., Tewes, M., Djorgovski, S. G., et al. 2010, A&A, 516, L12

Cunha, J. V., Marassi, L., & Lima, J. A. S. 2007, MNRAS, 379, L1

Curtis, H. D. 1920, JRASC, 14, 317

Dalcanton, J. J., Williams, B. F., Seth, A. C., et al. 2009, ApJS, 183, 67

Dall'Ora, M., Clementini, G., Kinemuchi, K., et al. 2006, ApJ, 653, L109

Davies, B., Kudritzki, R.-P., Lardo, C., et al. 2017, ApJ, 847, 112

Davis, J., Jacob, A. P., Robertson, J. G., et al. 2009, MNRAS, 394, 1620

de Grijs, R. 2013, in IAU Symposium, Vol. 289, IAU Symposium, ed. R. de Grijs, 351–360

Delubac, T., Bautista, J. E., Busca, N. G., et al. 2014, ArXiv e-prints

di Benedetto, G. P. 1993, A&A, 270, 315

di Benedetto, G. P. 1998, A&A, 339, 858

Di Benedetto, G. P. 2005, MNRAS, 357, 174

di Benedetto, G. P. & Ferluga, S. 1990, A&A, 236, 449

di Benedetto, G. P. & Rabbia, Y. 1987, A&A, 188, 114

Dinshaw, N., Matthews, J. M., Walker, G. A. H., & Hill, G. M. 1989, AJ, 98, 2249

Djorgovski, S. & Davis, M. 1987, ApJ, 313, 59

Dolphin, A. E., Saha, A., Claver, J., et al. 2002, AJ, 123, 3154

Domiciano de Souza, A., Hadjara, M., Vakili, F., et al. 2012, A&A, 545, A130

Domiciano de Souza, A., Vakili, F., Jankov, S., Janot-Pacheco, E., & Abe, L. 2002, A&A, 393, 345

Dorfi, E. A. & Feuchtinger, M. U. 1991, A&A, 249, 417

Dressler, A., Lynden-Bell, D., Burstein, D., et al. 1987, ApJ, 313, 42

Dunn, L. P. & Jerjen, H. 2006, AJ, 132, 1384

Durrell, P. R., Sarajedini, A., & Chandar, R. 2010, ApJ, 718, 1118

Duvert, G. 2016, VizieR Online Data Catalog, 2345

Dziembowski, W. 1977, Acta Astron., 27, 203

Efstathiou, G. 2014, MNRAS, 440, 1138

Einstein, A. 1905, Annalen der Physik, 322, 549

Einstein, A. 1916, Annalen der Physik, 354, 769

Elgueta, S. S., Graczyk, D., Gieren, W., et al. 2016, AJ, 152, 29

Engle, S. G., Guinan, E. F., Harper, G. M., Neilson, H. R., & Remage Evans, N. 2014, ApJ, 794, 80

Evans, N. R., Buzasi, D., Sasselov, D., & Preston, H. 2004, in Bulletin of the American Astronomical Society, Vol. 36, American Astronomical Society Meeting Abstracts, 1429

Evans, N. R., Guinan, E., Engle, S., et al. 2010, AJ, 139, 1968

Evans, N. R., Sasselov, D. D., & Short, C. I. 2002, ApJ, 567, 1121

Evans, N. R., Schaefer, G. H., Bond, H. E., et al. 2008, AJ, 136, 1137

Faber, S. M. & Jackson, R. E. 1976, ApJ, 204, 668

Fadeyev, Y. A. 2015, MNRAS, 449, 1011

Faucherre, M., Bonneau, D., Koechlin, L., & Vakili, F. 1983, A&A, 120, 263

Fernie, J. D. 1992, AJ, 103, 1647

Fernie, J. D. & Evans, N. R. 1997, PASP, 109, 541

Fernie, J. D., Evans, N. R., Beattie, B., & Seager, S. 1995, Information Bulletin on Variable Stars, 4148, 1

Fernie, J. D., Kamper, K. W., & Seager, S. 1993, ApJ, 416, 820

Ferrarese, L., Mould, J. R., Stetson, P. B., et al. 2007, ApJ, 654, 186

Filippenko, A. V., Riess, A. G., & High-Z Supernova Search Team. 2000, in American Institute of Physics Conference Series, Vol. 540, Particle Physics and Cosmology, ed. J. F. Nieves, 227–246

Fiorentino, G., Monachesi, A., Trager, S. C., et al. 2010, ApJ, 708, 817

Fitzpatrick, E. L. 1999, PASP, 111, 63

Fitzpatrick, E. L. & Massa, D. 2007, ApJ, 663, 320

Fitzpatrick, E. L., Ribas, I., Guinan, E. F., et al. 2002, ApJ, 564, 260

Fitzpatrick, E. L., Ribas, I., Guinan, E. F., Maloney, F. P., & Claret, A. 2003, ApJ, 587, 685

Fokin, A., Mathias, P., Chapellier, E., Gillet, D., & Nardetto, N. 2004, A&A, 426, 687

Fokin, A. B. 1994, A&A, 292, 133

Fokin, A. B., Gillet, D., & Breitfellner, M. G. 1996, A&A, 307, 503

Font-Ribera, A., Kirkby, D., Busca, N., et al. 2013, ArXiv e-prints

Fouqué, P., Arriagada, P., Storm, J., et al. 2007, A&A, 476, 73

Fouque, P. & Gieren, W. P. 1997, A&A, 320, 799

Freedman, W. L. & Madore, B. F. 1990, ApJ, 365, 186

Freedman, W. L. & Madore, B. F. 2010a, ApJ, 719, 335

Freedman, W. L. & Madore, B. F. 2010b, ARA&A, 48, 673

Freedman, W. L. & Madore, B. F. 2011, ApJ, 734, 46

Freedman, W. L., Madore, B. F., Gibson, B. K., et al. 2001, ApJ, 553, 47

Freedman, W. L., Madore, B. F., Scowcroft, V., et al. 2012, ApJ, 758, 24

Gallenne, A., Kervella, P., & Mérand, A. 2012, A&A, 538, A24

Gallenne, A., Kervella, P., Mérand, A., et al. 2017, ArXiv e-prints

Gallenne, A., Mérand, A., Kervella, P., et al. 2014, A&A, 561, L3

Gallenne, A., Mérand, A., Kervella, P., et al. 2013a, A&A, 558, A140

Gallenne, A., Mérand, A., Kervella, P., & Girard, J. H. V. 2011, A&A, 527, A51

Gallenne, A., Merand, A., Kervella, P., et al. 2016, ArXiv e-prints

Gallenne, A., Monnier, J. D., Mérand, A., et al. 2013b, A&A, 552, A21

García-Varela, A., Pietrzyński, G., Gieren, W., et al. 2008, AJ, 136, 1770

Gazak, J. Z., Davies, B., Bastian, N., et al. 2014, ApJ, 787, 142

Geroux, C. M. & Deupree, R. G. 2011, ApJ, 731, 18

Geroux, C. M. & Deupree, R. G. 2013, ApJ, 771, 113

Geroux, C. M. & Deupree, R. G. 2014, ApJ, 783, 107

Geroux, C. M. & Deupree, R. G. 2015, ApJ, 800, 35

Getting, I. A. 1934, MNRAS, 95, 139

Gezari, D. Y., Labeyrie, A., & Stachnik, R. V. 1972, ApJ, 173, L1

Gibson, B. K., Stetson, P. B., Freedman, W. L., et al. 2000, ApJ, 529, 723

Gieren, W., Górski, M., Pietrzyński, G., et al. 2013, ApJ, 773, 69

Gieren, W., Pietrzyński, G., Nalewajko, K., et al. 2006, ApJ, 647, 1056

Gieren, W., Pietrzyński, G., Soszyński, I., et al. 2005a, ApJ, 628, 695

Gieren, W., Pietrzyński, G., Soszyński, I., et al. 2008a, ApJ, 672, 266

Gieren, W., Pietrzyński, G., Soszyński, I., et al. 2009, ApJ, 700, 1141

Gieren, W., Pietrzyński, G., Szewczyk, O., et al. 2008b, ApJ, 683, 611

Gieren, W., Pietrzyński, G., Walker, A., et al. 2004, AJ, 128, 1167

Gieren, W., Pilecki, B., Pietrzyński, G., et al. 2014, ApJ, 786, 80

Gieren, W., Pilecki, B., Pietrzyński, G., et al. 2015, ApJ, 815, 28

Gieren, W., Storm, J., Barnes, III, T. G., et al. 2005b, ApJ, 627, 224

Gil-Merino, R., Wisotzki, L., & Wambsganss, J. 2002, A&A, 381, 428

Giovi, F. & Amendola, L. 2001, MNRAS, 325, 1097

Górski, M., Pietrzyński, G., & Gieren, W. 2011, AJ, 141, 194

Gould, A. 1994, ApJ, 426, 542

Gould, A. 2014, Journal of Korean Astronomical Society, 47, 153

Graczyk, D., Konorski, P., Pietrzyński, G., et al. 2017, ApJ, 837, 7

Graczyk, D., Pietrzyński, G., Thompson, I. B., et al. 2014, ApJ, 780, 59

Graczyk, D., Pietrzyński, G., Thompson, I. B., et al. 2012, ApJ, 750, 144

Gray, D. F. & Stevenson, K. B. 2007, PASP, 119, 398

Greco, C., Dall'Ora, M., Clementini, G., et al. 2008, ApJ, 675, L73

Greenhill, L. J., Jiang, D. R., Moran, J. M., et al. 1995, ApJ, 440, 619

Grillmair, C. J. 2009, ApJ, 693, 1118

Groenewegen, M. A. T. 2004, MNRAS, 353, 903

Groenewegen, M. A. T. 2007, A&A, 474, 975

Groenewegen, M. A. T. 2013, A&A, 550, A70

Groenewegen, M. A. T., Romaniello, M., Primas, F., & Mottini, M. 2004a, A&A, 420, 655

Groenewegen, M. A. T., Romaniello, M., Primas, F., & Mottini, M. 2004b, A&A, 420, 655

Guidorzi, C., Margutti, R., Brout, D., et al. 2017, ArXiv e-prints

Guiglion, G., Nardetto, N., Mathias, P., et al. 2013, A&A, 550, L10

Guinan, E. F., Fitzpatrick, E. L., DeWarf, L. E., et al. 1998, ApJ, 509, L21

Hadrava, P. 2009, A&A, 494, 399

Hadrava, P., Šlechta, M., & Škoda, P. 2009, A&A, 507, 397

Hamuy, M., Phillips, M. M., Suntzeff, N. B., et al. 1996, AJ, 112, 2438

Hanbury Brown, R., Davis, J., & Allen, L. R. 1967a, MNRAS, 137, 375

Hanbury Brown, R., Davis, J., & Allen, L. R. 1974, MNRAS, 167, 121

Hanbury Brown, R., Davis, J., Allen, L. R., & Rome, J. M. 1967b, MNRAS, 137, 393

Harries, T. J., Hilditch, R. W., & Howarth, I. D. 2003, MNRAS, 339, 157

Hatzes, A. P. 1996, PASP, 108, 839

Hatzes, A. P. & Cochran, W. D. 2000, AJ, 120, 979

Hendry, M. A., Rauzy, S., Goodwin, S. P., & Gribbin, J. 2001, MNRAS, 324, 717

Herrnstein, J. R., Moran, J. M., Greenhill, L. J., et al. 1999, Nature, 400, 539

Hertzsprung, E. 1913, Astronomische Nachrichten, 196, 201

Hidalgo, S. L., Aparicio, A., Martínez-Delgado, D., & Gallart, C. 2009, ApJ, 705, 704

Hilditch, R. W., Howarth, I. D., & Harries, T. J. 2005, MNRAS, 357, 304

Hindsley, R. & Bell, R. A. 1986, PASP, 98, 881

Hinshaw, G., Weiland, J. L., Hill, R. S., et al. 2009, ApJS, 180, 225

Hosek, Jr., M. W., Kudritzki, R.-P., Bresolin, F., et al. 2014, ApJ, 785, 151

Hubble, E. 1929a, Proceedings of the National Academy of Science, 15, 168

Hubble, E. P. 1925, ApJ, 62

Hubble, E. P. 1926, ApJ, 63

Hubble, E. P. 1929b, ApJ, 69

Humason, M. L., Mayall, N. U., & Sandage, A. R. 1956, AJ, 61, 97

Humphreys, E. M. L., Argon, A. L., Greenhill, L. J., Moran, J. M., & Reid, M. J. 2005, in Astronomical Society of the Pacific Conference Series, Vol. 340, Future Directions in High Resolution Astronomy, ed. J. Romney & M. Reid, 466

Humphreys, E. M. L., Reid, M. J., Moran, J. M., Greenhill, L. J., & Argon, A. L. 2013, ApJ, 775, 13

Ibata, R., Martin, N. F., Irwin, M., et al. 2007, ApJ, 671, 1591

Irwin, M. J., Belokurov, V., Evans, N. W., et al. 2007, ApJ, 656, L13

Irwin, M. J., Ferguson, A. M. N., Huxor, A. P., et al. 2008, ApJ, 676, L17

Jackson, N. 2015, Living Reviews in Relativity, 18, 2

Jacyszyn-Dobrzeniecka, A. M., Skowron, D. M., Mróz, P., et al. 2016, Acta Astron., 66, 149

Jacyszyn-Dobrzeniecka, A. M., Skowron, D. M., Mróz, P., et al. 2017, Acta Astron., 67, 1

Jang, I. S., Hatt, D., Beaton, R. L., et al. 2017, ArXiv e-prints

Jang, I. S. & Lee, M. G. 2015, ApJ, 807, 133

Jang, I. S. & Lee, M. G. 2017, ApJ, 836, 74

Jarosik, N., Bennett, C. L., Dunkley, J., et al. 2011, ApJS, 192, 14

Jensen, J. B., Tonry, J. L., Thompson, R. I., et al. 2001, ApJ, 550, 503

Jerjen, H., Freeman, K. C., & Binggeli, B. 1998, AJ, 116, 2873

Joy, A. H. 1939, ApJ, 89, 356

Jurcsik, J., Smitola, P., Hajdu, G., et al. 2017, MNRAS, 468, 1317

Kamper, K. W. & Fernie, J. D. 1998, AJ, 116, 936

Karachentsev, I. D., Dolphin, A., Tully, R. B., et al. 2006, AJ, 131, 1361

Karachentsev, I. D., Grebel, E. K., Sharina, M. E., et al. 2003, A&A, 404, 93

Karachentsev, I. D., Sharina, M. E., Grebel, E. K., et al. 2000, ApJ, 542, 128

Karachentsev, I. D., Sharina, M. E., Makarov, D. I., et al. 2002, A&A, 389, 812

Karp, A. H. 1975a, ApJ, 199, 448

Karp, A. H. 1975b, ApJ, 200, 354

Karp, A. H. 1975c, ApJ, 201, 641

Kennicutt, Jr., R. C., Stetson, P. B., Saha, A., et al. 1998, ApJ, 498, 181

Kervella, P., Bersier, D., Mourard, D., Nardetto, N., & Coudé du Foresto, V. 2004a, A&A, 423, 327

Kervella, P., Bersier, D., Mourard, D., et al. 2004b, A&A, 428, 587

Kervella, P., Coudé du Foresto, V., Perrin, G., et al. 2001, A&A, 367, 876

Kervella, P., Coudé du Foresto, V., Traub, W. A., & Lacasse, M. G. 1999, in Astronomical Society of the Pacific Conference Series, Vol. 194, Working on the Fringe : Optical and IR Interferometry from Ground and Space, ed. S. Unwin & R. Stachnik, 22

Kervella, P. & Fouqué, P. 2008, A&A, 491, 855

Kervella, P., Fouqué, P., Storm, J., et al. 2004c, ApJ, 604, L113

Kervella, P., Mérand, A., Perrin, G., & Coudé du Foresto, V. 2006, A&A, 448, 623

Kervella, P., Nardetto, N., Bersier, D., Mourard, D., & Coudé du Foresto, V. 2004d, A&A, 416, 941

Kervella, P., Thévenin, F., Di Folco, E., & Ségransan, D. 2004e, A&A, 426, 297

Kewley, L. J. & Ellison, S. L. 2008, ApJ, 681, 1183

Kochanek, C. S. 1997, ApJ, 491, 13

Kochanek, C. S. 2002, ApJ, 578, 25

Kochanek, C. S. & Schechter, P. L. 2004, Measuring and Modeling the Universe, 117

Koopmans, L. V. E., Treu, T., Fassnacht, C. D., Blandford, R. D., & Surpi, G. 2003, ApJ, 599, 70

Kopylov, A. I., Tikhonov, N. A., Fabrika, S., Drozdovsky, I., & Valeev, A. F. 2008, MNRAS, 387, L45

Krockenberger, M., Noyes, R. W., & Sasselov, D. D. 1994, in Bulletin of the American Astronomical Society, Vol. 26, American Astronomical Society Meeting Abstracts, 36.03

Kudritzki, R. P., Bresolin, F., & Przybilla, N. 2003, ApJ, 582, L83

Kudritzki, R. P., Castro, N., Urbaneja, M. A., et al. 2016, ApJ, 829, 70

Kudritzki, R.-P., Urbaneja, M. A., Bresolin, F., Hosek, Jr., M. W., & Przybilla, N. 2014, ApJ, 788, 56

Kudritzki, R.-P., Urbaneja, M. A., Bresolin, F., et al. 2008, ApJ, 681, 269

Kudritzki, R.-P., Urbaneja, M. A., Gazak, Z., et al. 2012, ApJ, 747, 15

Kurucz, R. L. 1979, ApJS, 40, 1

Labeyrie, A. 1975, ApJ, 196, L71

Labeyrie, A., Bonneau, D., Stachnik, R. V., & Gezari, D. Y. 1974, ApJ, 194, L147

Lacy, C. H. 1977, ApJ, 213, 458

Lane, B. F., Creech-Eakman, M. J., & Nordgren, T. E. 2002, ApJ, 573, 330

Lane, B. F., Kuchner, M. J., Boden, A. F., Creech-Eakman, M., & Kulkarni, S. R. 2000, Nature, 407, 485

Laney, C. D. & Joner, M. D. 2009, in American Institute of Physics Conference Series, Vol. 1170, American Institute of Physics Conference Series, ed. J. A. Guzik & P. A. Bradley, 93–95

Laney, C. D., Joner, M. D., & Pietrzyński, G. 2012, MNRAS, 419, 1637

Lardo, C., Davies, B., Kudritzki, R.-P., et al. 2015, ApJ, 812, 160

Leavitt, H. S. 1908, Annals of Harvard College Observatory, 60, 87

Leavitt, H. S. & Pickering, E. C. 1912, Harvard College Observatory Circular, 173, 1

Lee, B.-C., Mkrtichian, D. E., Han, I., Park, M.-G., & Kim, K.-M. 2008, AJ, 135, 2240

Lee, M. G. & Jang, I. S. 2013, ApJ, 773, 13

Lee, M. G., Yuk, I.-S., Park, H. S., Harris, J., & Zaritsky, D. 2009, ApJ, 703, 692

Lee, T. A. 1970, ApJ, 162, 217

Lemaître, G. 1927, Annales de la Société Scientifique de Bruxelles, 47, 49

Lequeux, J., Peimbert, M., Rayo, J. F., Serrano, A., & Torres-Peimbert, S. 1979, A&A, 80, 155

Lindemann, F. A. 1918, MNRAS, 78, 639

Liu, T. & Janes, K. A. 1990, ApJ, 360, 561

Luck, R. E., Moffett, T. J., Barnes, III, T. G., & Gieren, W. P. 1998, AJ, 115, 605

Lynden-Bell, D., Burstein, D., Davies, R. L., Dressler, A., & Faber, S. M. 1988, in Astronomical Society of the Pacific Conference Series, Vol. 4, The Extragalactic Distance Scale, ed. S. van den Bergh & C. J. Pritchet, 307–316

Macri, L. M., Stanek, K. Z., Bersier, D., Greenhill, L. J., & Reid, M. J. 2006, ApJ, 652, 1133

Madore, B. F. 1982, ApJ, 253, 575

Madore, B. F. & Freedman, W. L. 2012, ApJ, 744, 132

Mager, V. A., Madore, B. F., & Freedman, W. L. 2013, ApJ, 777, 79

Majaess, D., Turner, D., & Gieren, W. 2011, ApJ, 741, L36

Majewski, S. R., Beaton, R. L., Patterson, R. J., et al. 2007, ApJ, 670, L9

Marconi, M., Molinaro, R., Ripepi, V., et al. 2017, MNRAS, 466, 3206

Marengo, M., Evans, N. R., Barmby, P., et al. 2010a, ApJ, 709, 120

Marengo, M., Evans, N. R., Barmby, P., et al. 2010b, ApJ, 725, 2392

Marengo, M., Karovska, M., Sasselov, D. D., et al. 2003, ApJ, 589, 968

Marengo, M., Neeley, J., Bono, G., et al. 2017, in European Physical Journal Web of Conferences, Vol. 152, European Physical Journal Web of Conferences, 07004

Marengo, M., Sasselov, D. D., Karovska, M., Papaliolios, C., & Armstrong, J. T. 2002, ApJ, 567, 1131

Martin, N. F., Coleman, M. G., De Jong, J. T. A., et al. 2008, ApJ, 672, L13

Martin, N. F., McConnachie, A. W., Irwin, M., et al. 2009, ApJ, 705, 758

Masters, K. L., Springob, C. M., Haynes, M. P., & Giovanelli, R. 2006, ApJ, 653, 861

Mathias, P., Gillet, D., Fokin, A. B., et al. 2006, A&A, 457, 575

Matthews, L. D., Marengo, M., Evans, N. R., & Bono, G. 2012, ApJ, 744, 53

McConnachie, A. W. 2012, AJ, 144, 4

McConnachie, A. W., Huxor, A., Martin, N. F., et al. 2008, ApJ, 688, 1009

McConnachie, A. W., Irwin, M. J., Ferguson, A. M. N., et al. 2005, MNRAS, 356, 979

McDonald, P., Seljak, U., Cen, R., et al. 2005, ApJ, 635, 761

McNamara, D. 1997, PASP, 109, 1221

McNamara, D. H., Clementini, G., & Marconi, M. 2007, AJ, 133, 2752

Mei, S., Scodeggio, M., Silva, D. R., & Quinn, P. J. 2003, A&A, 399, 441

Mérand, A., Aufdenberg, J. P., Kervella, P., et al. 2007, ApJ, 664, 1093

Merand, A., Kervella, P., Breitfelder, J., et al. 2015, ArXiv e-prints

Mérand, A., Kervella, P., Coudé du Foresto, V., et al. 2006, A&A, 453, 155

Mérand, A., Kervella, P., Coudé du Foresto, V., et al. 2005, A&A, 438, L9

Michelson, A. A. 1881, Nature, 24, 460

Michelson, A. A. & Pease, F. G. 1921, Proceedings of the National Academy of Science, 7, 143

Milone, E. F., Wilson, W. J. F., Fry, D. J. I., & Schiller, S. J. 1994, PASP, 106, 1120

Miyoshi, M., Moran, J., Herrnstein, J., et al. 1995, Nature, 373, 127

Moffett, T. J. & Barnes, III, T. G. 1987, PASP, 99, 1206

Molinaro, R., Ripepi, V., Marconi, M., et al. 2011, MNRAS, 413, 942

Momany, Y., Held, E. V., Saviane, I., & Rizzi, L. 2002, A&A, 384, 393

Monaco, L., Bellazzini, M., Ferraro, F. R., & Pancino, E. 2004, MNRAS, 353, 874

Montargès, M., Kervella, P., Perrin, G., et al. 2014, A&A, 572, A17

Moretti, M. I., Dall'Ora, M., Ripepi, V., et al. 2009, ApJ, 699, L125

Mourard, D., Bonneau, D., Koechlin, L., et al. 1997, A&A, 317, 789

Mourard, D., Bosc, I., Labeyrie, A., Koechlin, L., & Saha, S. 1989, Nature, 342, 520

Mourard, D., Tallon-Bosc, I., Blazit, A., et al. 1994, A&A, 283, 705

Mozurkewich, D., Armstrong, J. T., Hindsley, R. B., et al. 2003, AJ, 126, 2502

Mundprecht, E., Muthsam, H. J., & Kupka, F. 2013, MNRAS, 435, 3191

Mundprecht, E., Muthsam, H. J., & Kupka, F. 2015, MNRAS, 449, 2539

Muraveva, T., Palmer, M., Clementini, G., et al. 2015, ApJ, 807, 127

Nardetto, N., Fokin, A., Fouqué, P., et al. 2011a, A&A, 534, L16

Nardetto, N., Fokin, A., Mourard, D., & Mathias, P. 2006a, A&A, 454, 327

Nardetto, N., Fokin, A., Mourard, D., et al. 2004, A&A, 428, 131

Nardetto, N., Gieren, W., Kervella, P., et al. 2009, A&A, 502, 951

Nardetto, N., Groh, J. H., Kraus, S., Millour, F., & Gillet, D. 2008a, A&A, 489, 1263

Nardetto, N., Mathias, P., Fokin, A., et al. 2013, A&A, 553, A112

Nardetto, N., Mérand, A., Mourard, D., et al. 2016, A&A, 593, A45

Nardetto, N., Mourard, D., Kervella, P., et al. 2006b, A&A, 453, 309

Nardetto, N., Mourard, D., Mathias, P., Fokin, A., & Gillet, D. 2007, A&A, 471, 661

Nardetto, N., Mourard, D., Tallon-Bosc, I., et al. 2011b, A&A, 525, A67

Nardetto, N., Poretti, E., Rainer, M., et al. 2017, A&A, 597, A73

Nardetto, N., Poretti, E., Rainer, M., et al. 2014, A&A, 561, A151

Nardetto, N., Stoekl, A., Bersier, D., & Barnes, T. G. 2008b, A&A, 489, 1255

Neilson, H. R. 2014, A&A, 563, A48

Neilson, H. R., Engle, S. G., Guinan, E., et al. 2012a, ApJ, 745, L32

Neilson, H. R., Nardetto, N., Ngeow, C.-C., Fouqué, P., & Storm, J. 2012b, A&A, 541, A134

Neilson, H. R., Schneider, F. R. N., Izzard, R. G., Evans, N. R., & Langer, N. 2015, A&A, 574, A2

Nelson, C. A., Cook, K. H., Popowski, P., & Alves, D. R. 2000, AJ, 119, 1205

Ngeow, C.-C., Neilson, H. R., Nardetto, N., & Marengo, M. 2012, A&A, 543, A55

Nikolaev, S., Drake, A. J., Keller, S. C., et al. 2004, ApJ, 601, 260

Nordgren, T. E., Armstrong, J. T., Germain, M. E., et al. 2000, ApJ, 543, 972

Nordgren, T. E., Lane, B. F., Hindsley, R. B., & Kervella, P. 2002, AJ, 123, 3380

Oguri, M. 2007, ApJ, 660, 1

Okamoto, S., Arimoto, N., Yamada, Y., & Onodera, M. 2008, A&A, 487, 103

Olsen, K. A. G. & Salyk, C. 2002, AJ, 124, 2045

Paraficz, D. & Hjorth, J. 2010, ApJ, 712, 1378

Paraficz, D., Hjorth, J., & Elíasdóttir, Á. 2009, A&A, 499, 395

Parenago, P. P. 1945, Popular Astronomy, 53, 441

Parsons, S. B. 1972, ApJ, 174, 57

Pease, F. G. 1921, PASP, 33, 204

Perryman, M. A. C. & ESA. 1997, The HIPPARCOS and TYCHO catalogues (The Hipparcos and Tycho catalogues. Astrometric and photometric star catalogues derived from the ESA Hipparcos Space Astrometry Mission, Publisher : Noordwijk, Netherlands : ESA Publications Division, 1997, Series : ESA SP Series 1200)

Persson, S. E., Madore, B. F., Krzemiński, W., et al. 2004, AJ, 128, 2239

Petersen, J. O. & Christensen-Dalsgaard, J. 1999, A&A, 352, 547

Petersen, J. O. & Hog, E. 1998, A&A, 331, 989

Phillips, M. M. 1993, ApJ, 413, L105

Pietrzyński, G. & Gieren, W. 2002, AJ, 124, 2633

Pietrzyński, G., Gieren, W., Hamuy, M., et al. 2010a, AJ, 140, 1475

Pietrzyński, G., Gieren, W., Soszyński, I., et al. 2006a, ApJ, 642, 216

Pietrzyński, G., Gieren, W., Soszyński, I., et al. 2006b, AJ, 132, 2556

Pietrzyński, G., Gieren, W., Szewczyk, O., et al. 2008, AJ, 135, 1993

Pietrzyński, G., Gieren, W., & Udalski, A. 2003, AJ, 125, 2494

Pietrzyński, G., Gieren, W., Udalski, A., et al. 2004, AJ, 128, 2815

Pietrzyński, G., Gieren, W., Udalski, A., et al. 2007, AJ, 134, 594

Pietrzyński, G., Gieren, W., Udalski, A., et al. 2006c, ApJ, 648, 366

Pietrzyński, G., Górski, M., Gieren, W., et al. 2009a, AJ, 138, 459

Pietrzyński, G., Graczyk, D., Gieren, W., et al. 2013, Nature, 495, 76

Pietrzyński, G., Thompson, I. B., Gieren, W., et al. 2010b, Nature, 468, 542

Pietrzyński, G., Thompson, I. B., Gieren, W., et al. 2012, Nature, 484, 75

Pietrzyński, G., Thompson, I. B., Graczyk, D., et al. 2011, ApJ, 742, L20

Pietrzyński, G., Thompson, I. B., Graczyk, D., et al. 2009b, ApJ, 697, 862

Pilecki, B., Gieren, W., Smolec, R., et al. 2017, ArXiv e-prints

Pilecki, B., Graczyk, D., Pietrzyński, G., et al. 2013, MNRAS, 436, 953

Planck Collaboration, Ade, P. A. R., Aghanim, N., et al. 2016, A&A, 594, A13

Poleski, R., Soszyński, I., Udalski, A., et al. 2010, Acta Astron., 60, 1

Pont, F., Mayor, M., & Burki, G. 1994, A&A, 285

Prša, A., Harmanec, P., Torres, G., et al. 2016, AJ, 152, 41

Pskovskii, Y. P. 1967, Soviet Ast., 11, 63

Rafelski, M., Neeleman, M., Fumagalli, M., Wolfe, A. M., & Prochaska, J. X. 2014, ApJ, 782, L29

Reese, E. D., Carlstrom, J. E., Joy, M., et al. 2002, ApJ, 581, 53

Refsdal, S. 1964, MNRAS, 128, 307

Reid, B. A., Percival, W. J., Eisenstein, D. J., et al. 2010, MNRAS, 404, 60

Reid, B. A., Samushia, L., White, M., et al. 2012, MNRAS, 426, 2719

Reid, M. J., Braatz, J. A., Condon, J. J., et al. 2013, ApJ, 767, 154

Ribas, I., Fitzpatrick, E. L., Maloney, F. P., Guinan, E. F., & Udalski, A. 2002, ApJ, 574, 771

Ribas, I., Jordi, C., Vilardell, F., et al. 2005, ApJ, 635, L37

Richardson, J. C., Irwin, M. J., McConnachie, A. W., et al. 2011, ApJ, 732, 76

Riess, A. G., Casertano, S., Anderson, J., MacKenty, J., & Filippenko, A. V. 2014, ApJ, 785, 161

Riess, A. G., Li, W., Stetson, P. B., et al. 2005, in Bulletin of the American Astronomical Society, Vol. 37, American Astronomical Society Meeting Abstracts, 1460

Riess, A. G., Macri, L., Casertano, S., et al. 2011, ApJ, 730, 119

Riess, A. G., Macri, L., Casertano, S., et al. 2009, ApJ, 699, 539

Riess, A. G., Macri, L. M., Hoffmann, S. L., et al. 2016, ArXiv e-prints

Rigault, M., Aldering, G., Kowalski, M., et al. 2015, ApJ, 802, 20

Rizzi, L., Bresolin, F., Kudritzki, R.-P., Gieren, W., & Pietrzyński, G. 2006, ApJ, 638, 766

Rodríguez, E. & Breger, M. 2001, A&A, 366, 178

Rodriguez, E., Claret, A., Sedano, J. L., Garcia, J. M., & Garrido, R. 1998, A&A, 340, 196

Romaniello, M., Primas, F., Mottini, M., et al. 2008, A&A, 488, 731

Romaniello, M., Primas, F., Mottini, M., et al. 2009, in American Institute of Physics Conference Series, Vol. 1170, American Institute of Physics Conference Series, ed. J. A. Guzik & P. A. Bradley, 99–101

Sabbey, C. N., Sasselov, D. D., Fieldus, M. S., et al. 1995, ApJ, 446, 250

Saha, A., Sandage, A., Labhardt, L., et al. 1997, ApJ, 486, 1

Saha, A., Thim, F., Tammann, G. A., Reindl, B., & Sandage, A. 2006, ApJS, 165, 108

Sakai, S., Ferrarese, L., Kennicutt, Jr., R. C., & Saha, A. 2004, ApJ, 608, 42

Sandage, A. 1958, ApJ, 127, 513

Sandage, A., Bell, R. A., & Tripicco, M. J. 1999, ApJ, 522, 250

Sandage, A., Saha, A., Tammann, G. A., et al. 1994, ApJ, 423, L13

Sandage, A., Saha, A., Tammann, G. A., Panagia, N., & Macchetto, D. 1992, ApJ, 401, L7

Sandage, A. & Tammann, G. A. 1968, ApJ, 151, 531

Sandage, A. & Tammann, G. A. 2008, ApJ, 686, 779

Sandage, A., Tammann, G. A., Saha, A., et al. 2006, ApJ, 653, 843

Sanford, R. F. 1956, ApJ, 123, 201

Sasselov, D. D., Beaulieu, J. P., Renault, C., et al. 1997, A&A, 324, 471

Sasselov, D. D. & Lester, J. B. 1990, ApJ, 362, 333

Sasselov, D. D. & Raga, A. 1992, in Astronomical Society of the Pacific Conference Series, Vol. 26, Cool Stars, Stellar Systems, and the Sun, ed. M. S. Giampapa & J. A. Bookbinder, 549

Schlegel, D. J., Finkbeiner, D. P., & Davis, M. 1998, ApJ, 500, 525

Schmidt, E. G. 2015, ApJ, 813, 29

Scowcroft, V., Bersier, D., Mould, J. R., & Wood, P. R. 2009, MNRAS, 396, 1287

Scowcroft, V., Freedman, W. L., Madore, B. F., et al. 2011, ApJ, 743, 76

Ségransan, D., Kervella, P., Forveille, T., & Queloz, D. 2003, A&A, 397, L5

Sereno, M. 2003, A&A, 412, 341

Sereno, M. & Paraficz, D. 2014, MNRAS, 437, 600

Sesar, B., Hernitschek, N., Dierickx, M. I. P., Fardal, M. A., & Rix, H.-W. 2017, ApJ, 844, L4

Shao, M., Colavita, M. M., Hines, B. E., et al. 1988, ApJ, 327, 905

Shapley, H. 1918, ApJ, 48

Shapley, H. 1919, JRASC, 13, 438

Shappee, B. J. & Stanek, K. Z. 2011, ApJ, 733, 124

Silbermann, N. A., Harding, P., Ferrarese, L., et al. 1999, ApJ, 515, 1

Silk, J. & White, S. D. M. 1978, ApJ, 226, L103

Silva, D. R., Massey, P., DeGioia-Eastwood, K., & Henning, P. A. 2005, ApJ, 623, 148

Slater, C. T., Bell, E. F., & Martin, N. F. 2011, ApJ, 742, L14

Slipher, V. M. 1914, Popular Astronomy, 22, 19

Slipher, V. M. 1917, The Observatory, 40, 304

Sollima, A., Cacciari, C., & Valenti, E. 2006, MNRAS, 372, 1675

Soszyński, I., Gieren, W., Pietrzyński, G., et al. 2006, ApJ, 648, 375

Soszyński, I., Udalski, A., Szymański, M. K., et al. 2008, Acta Astron., 58, 293

Soszyński, I., Udalski, A., Szymański, M. K., et al. 2015, Acta Astron., 65, 297

Soszyński, I., Udalski, A., Szymański, M. K., et al. 2016, Acta Astron., 66, 131

Spergel, D. N., Bean, R., Doré, O., et al. 2007, ApJS, 170, 377

Spergel, D. N., Verde, L., Peiris, H. V., et al. 2003, ApJS, 148, 175

Stamford, P. A. & Watson, R. D. 1981, Ap&SS, 77, 131

Stetson, P. B. & Gibson, B. K. 2001, MNRAS, 328, L1

Stibbs, D. W. N. 1956, MNRAS, 116, 453

Storm, J., Carney, B. W., Gieren, W. P., et al. 2004, A&A, 415, 531

Storm, J., Gieren, W., Fouqué, P., et al. 2011a, A&A, 534, A94

Storm, J., Gieren, W., Fouqué, P., et al. 2011b, A&A, 534, A95

Stothers, R. B. 2009, ApJ, 696, L37

Suchomska, K., Graczyk, D., Smolec, R., et al. 2015, MNRAS, 451, 651

Sunyaev, R. A. & Zeldovich, Y. B. 1972, Comments on Astrophysics and Space Physics, 4, 173

Suyu, S. H., Marshall, P. J., Auger, M. W., et al. 2010, ApJ, 711, 201

Szabados, L. 2003, Information Bulletin on Variable Stars, 5394

Szewczyk, O., Pietrzyński, G., Gieren, W., et al. 2009, AJ, 138, 1661

Szewczyk, O., Pietrzyński, G., Gieren, W., et al. 2008, AJ, 136, 272

Tammann, G. A. 1982, in NATO Advanced Science Institutes (ASI) Series C, Vol. 90, NATO Advanced Science Institutes (ASI) Series C, ed. M. J. Rees & R. J. Stoneham, 371–403

Tammann, G. A. 2006, in Reviews in Modern Astronomy, Vol. 19, Reviews in Modern Astronomy, ed. S. Roeser, 1

Tammann, G. A., Sandage, A., & Reindl, B. 2008, ApJ, 679, 52

The LIGO Scientific Collaboration, the Virgo Collaboration, Abbott, B. P., et al. 2017, ArXiv e-prints

Thiessen, G. 1956, ZAp, 39, 65

Thompson, I. B., Kaluzny, J., Pych, W., et al. 2001, AJ, 121, 3089

Tonry, J. & Schneider, D. P. 1988, AJ, 96, 807

Tonry, J. L., Dressler, A., Blakeslee, J. P., et al. 2001, ApJ, 546, 681

Tremonti, C. A., Heckman, T. M., Kauffmann, G., et al. 2004, ApJ, 613, 898

Trimble, V. 1996, PASP, 108, 1073

Tully, R. B. & Fisher, J. R. 1977, A&A, 54, 661

Tully, R. B., Rizzi, L., Dolphin, A. E., et al. 2006, AJ, 132, 729

Turner, D. G., Kovtyukh, V. V., Usenko, I. A., & Gorlova, N. I. 2013, ApJ, 762, L8

Turner, D. G., Savoy, J., Derrah, J., Abdel-Sabour Abdel-Latif, M., & Berdnikov, L. N. 2005, PASP, 117, 207

Tytler, D., Kirkman, D., O'Meara, J. M., et al. 2004, ApJ, 617, 1

U, V., Urbaneja, M. A., Kudritzki, R.-P., et al. 2009, ApJ, 704, 1120

Udalski, A., Szymanski, M., Kaluzny, J., Kubiak, M., & Mateo, M. 1992, Acta Astron., 42, 253

Udalski, A., Wyrzykowski, L., Pietrzynski, G., et al. 2001, Acta Astron., 51, 221

Urbaneja, M. A., Kudritzki, R.-P., Bresolin, F., et al. 2008, ApJ, 684, 118

Usenko, I. A. & Klochkova, V. G. 2008, MNRAS, 387, L1

Usenko, I. A., Miroshnichenko, A. S., Klochkova, V. G., & Yushkin, M. V. 2005, MNRAS, 362, 1219

van Belle, G. T. 1999, PASP, 111, 1515

van der Marel, R. P., Alves, D. R., Hardy, E., & Suntzeff, N. B. 2002, AJ, 124, 2639

van Hoof, A. & Deurinck, R. 1952, ApJ, 115, 166

van Leeuwen, F. 2013, A&A, 550, L3

van Leeuwen, F., Feast, M. W., Whitelock, P. A., & Laney, C. D. 2007a, MNRAS, 379, 723

van Leeuwen, F., Feast, M. W., Whitelock, P. A., & Laney, C. D. 2007b, MNRAS, 379, 723

Vasilyev, V., Ludwig, H.-G., Freytag, B., Lemasle, B., & Marconi, M. 2017, ArXiv e-prints

Vilardell, F., Ribas, I., Jordi, C., Fitzpatrick, E. L., & Guinan, E. F. 2010, A&A, 509, A70

Wallerstein, G., Albright, M. B., & Ritchey, A. M. 2015, PASP, 127, 503

Walsh, D., Carswell, R. F., & Weymann, R. J. 1979, Nature, 279, 381

Walsh, S. M., Willman, B., Sand, D., et al. 2008, ApJ, 688, 245

Watanabe, M., Yasuda, N., Itoh, N., Ichikawa, T., & Yanagisawa, K. 2001, ApJ, 555, 215

Welch, D. L. 1994, AJ, 108, 1421

Wesselink, A. J. 1946, Bull. Astron. Inst. Netherlands, 10, 91

Wesselink, A. J. 1969, MNRAS, 144, 297

Wielen, R. 1974, A&AS, 15

Willman, B., Masjedi, M., Hogg, D. W., et al. 2006, ArXiv Astrophysics e-prints

Wilson, T. D., Barnes, III, T. G., Hawley, S. L., & Jefferys, W. H. 1991, ApJ, 378, 708

Wilson, W. J. F., Milone, E. F., & Fry, D. J. I. 1993, PASP, 105, 809

Wilson, W. J. F., Milone, E. F., Fry, D. J. I., & van Leeuwen, J. 1998, PASP, 110, 433

Winkler, P. F., Gupta, G., & Long, K. S. 2003, ApJ, 585, 324

Wucknitz, O. 2002, PhD thesis, Hamburger Sternwarte, Germany, Jodrell Bank Observatory (UK), Universität Potsdam, Germany <EMAIL>olaf@astro.physik.uni-potsdam.de</EMAIL>

Wucknitz, O., Biggs, A. D., & Browne, I. W. A. 2004, MNRAS, 349, 14

Zaritsky, D., Kennicutt, Jr., R. C., & Huchra, J. P. 1994, ApJ, 420, 87

Zhao, F.-Y., Strom, R. G., & Jiang, S.-Y. 2006, Chinese J. Astron. Astrophys., 6, 635

Zucker, D. B., Belokurov, V., Evans, N. W., et al. 2006, ApJ, 650, L41

Zucker, D. B., Kniazev, A. Y., Martínez-Delgado, D., et al. 2007, ApJ, 659, L21

Annexe A

Tableau récapitulatif des valeurs de la constante de Hubble depuis 2000.

TABLE A.1 – Liste des valeurs de la constante de Hubble obtenues par différentes méthodes ou hypothèses depuis 2000. Ces valeurs sont représentées sous forme graphique dans la Figure 2.1.

H_0 km/s/Mpc	année	référence
	Céphéide et SNIa : projet CHP	
68^{5}_{-5}	2000.9	Gibson et al. (2000)
71^{6}_{-6}	2001.4	Freedman et al. (2001)
73^{4}_{-4}	2010.3	Freedman & Madore (2010a)
74^{2}_{-2}	2012.8	Freedman et al. (2012)
	Céphéide et SNIa : projet SHOES	
65^{2}_{-2}	2000.6	Filippenko et al. (2000)
73^{5}_{-5}	2005.6	Riess et al. (2005)
74^{4}_{-4}	2009.4	Riess et al. (2009)
74^{2}_{-2}	2011.3	Riess et al. (2011)
73^{2}_{-2}	2016.6	Riess et al. (2016)
	Céphéide et SNIa : Sandage	
62^{5}_{-5}	2006.2	Sandage et al. (2006)
	Masers	
69^{7}_{-7}	2013.3	Reid et al. (2013)
72^{3}_{-3}	2013.7	Humphreys et al. (2013)
	Galaxies : TF et FJ	
76^{1}_{-1}	2000.9	Jensen et al. (2001)
69^{4}_{-4}	2001.4	Tonry et al. (2001)
71^{6}_{-6}	2002.9	Mei et al. (2003)
73^{4}_{-4}	2001.1	Watanabe et al. (2001)
65^{6}_{-6}	2001.5	Hendry et al. (2001)
74^{6}_{-6}	2006.7	Masters et al. (2006)
63^{5}_{-5}	2006.8	Dunn & Jerjen (2006)
	RTGB	
71^{2}_{-2}	2017.2	Jang & Lee (2017)
	Rayonnement de fond cosmologique	
72^{5}_{-5}	2003.7	Spergel et al. (2003)
70^{5}_{-5}	2003.8	Spergel et al. (2003)
71^{4}_{-3}	2003.8	Spergel et al. (2003)
73^{3}_{-3}	2007.5	Spergel et al. (2007)
72^{3}_{-3}	2009.2	Hinshaw et al. (2009)
71^{1}_{-1}	2009.2	Hinshaw et al. (2009)
71^{2}_{-2}	2011.2	Jarosik et al. (2011)
70^{1}_{-1}	2011.2	Jarosik et al. (2011)
70^{2}_{-2}	2013.0	Bennett et al. (2014)
69^{1}_{-1}	2013.1	Bennett et al. (2014)
$67.4^{1.4}_{-1.4}$	2014.2	Planck Collaboration et al. (2016)
$67.9^{1.5}_{-1.5}$	2014.2	Planck Collaboration et al. (2016)
$67.3^{1.2}_{-1.2}$	2014.2	Planck Collaboration et al. (2016)
$67.3^{1.2}_{-1.2}$	2014.2	Planck Collaboration et al. (2016)
$67.9^{1.0}_{-1.0}$	2014.2	Planck Collaboration et al. (2016)
$67.8^{0.8}_{-0.8}$	2014.2	Planck Collaboration et al. (2016)

TABLE A.2 – Suite du Tableau.

H_0 km/s/Mpc	année	référence
	Lentilles gravitationnelles	
71^{6}_{-6}	2000.8	Giovi & Amendola (2001)
64^{4}_{-4}	2000.8	Giovi & Amendola (2001)
48^{4}_{-4}	2001.8	Gil-Merino et al. (2002)
62^{4}_{-4}	2001.8	Gil-Merino et al. (2002)
71^{5}_{-5}	2001.9	Wucknitz (2002)
73^{8}_{-8}	2002.3	Kochanek (2002)
48^{3}_{-3}	2003.4	Kochanek & Schechter (2004)
71^{3}_{-3}	2003.4	Kochanek & Schechter (2004)
75^{7}_{-6}	2003.4	Koopmans et al. (2003)
78^{6}_{-6}	2003.9	Wucknitz et al. (2004)
68^{8}_{-8}	2006.7	Oguri (2007)
62^{8}_{-4}	2009.2	Paraficz et al. (2009)
70^{5}_{-5}	2010.2	Suyu et al. (2010)
66^{6}_{-4}	2010.3	Paraficz & Hjorth (2010)
62^{6}_{-4}	2010.7	Courbin et al. (2010)
69^{6}_{-6}	2014.1	Sereno & Paraficz (2014)
	Sunyaev-Zeldovich	
58^{4}_{-3}	2003.7	Sereno (2003)
77^{10}_{-8}	2005.9	Bonamente et al. (2006)
76^{10}_{-8}	2006.6	Bonamente et al. (2006)
74^{4}_{-4}	2006.9	Cunha et al. (2007)
	BAO	
67^{3}_{-3}	2011.8	Beutler et al. (2011)
	Lymann α	
74^{3}_{-3}	2012.7	Chávez et al. (2012)

Annexe B

L'étalonnage des échelles de distance dans l'univers.

Figure and legend (in English) extracted from de Grijs (2013) : Updated, present-day distance ladder, based on an original idea by Ciardullo (2006). Light orange : Methods of distance determination associated with active star formation ('Population I', intermediate- and high-mass stars). Light green : Distance tracers associated with 'Population II' objects/low-mass stars. Blue : Geometric methods. Red : Supernovae (SNe) Ia, the planetary nebulae (PNe) luminosity function (PNLF) and surface-brightness fluctuations (SBF) are applicable for use with both Populations I and II. Light brown : Methods of distance or H0 determination which are not immediately linked to a specific stellar population. Dashed boxes : Proposed methods. Solid, dashed arrows : Reasonably robust, poorly established calibrations. B–W : Baade–Wesselink. RRL : RR Lyrae. RSGs/FGLR : Red supergiants/flux-weighted gravity–luminosity relationship. TRGB : Tip of the red-giant branch. GCLF : Globular cluster (GC) luminosity function. SZ : Sunyaev–Zel'dovich. CMB/BAO : Cosmic microwave background/baryon acoustic oscillations. Colour–magnitude relation : Refers to galactic colours and magnitudes.

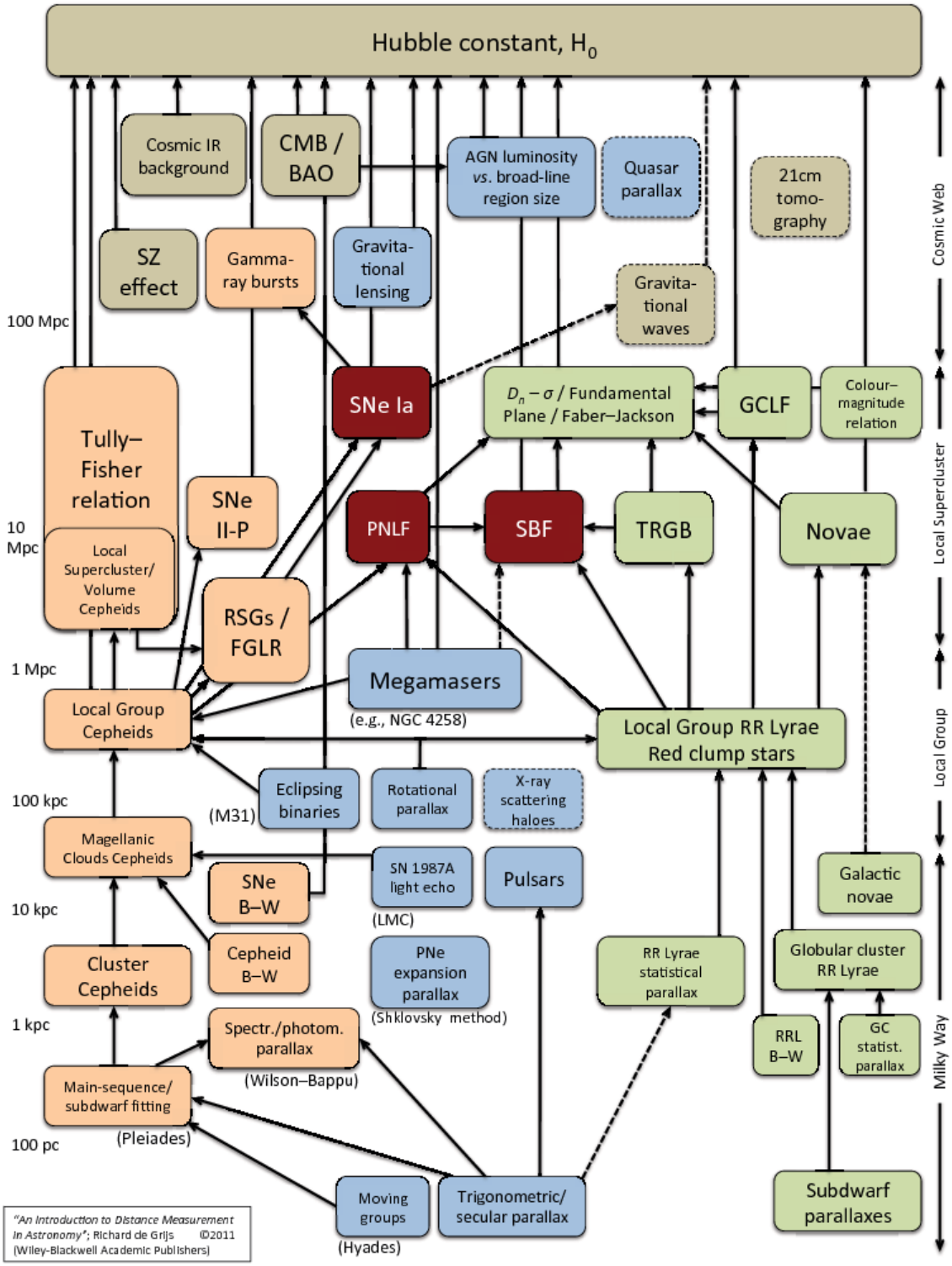


FIGURE B.1 – L'échafaudage des distances dans l'univers

Annexe C

Distance des galaxies déterminées dans le cadre du projet Araucaria

TABLE C.1 – Distances et modules de distance des galaxies obtenus dans le cadre du projet Araucaria à partir de différentes méthodes.

d [kpc]	ed_{stat} [kpc]	ed_{syst} [kpc]	MD [mag]	eMD_{stat} [mag]	eMD_{syst} [mag]	Méthode	Ref
				LMC			
50.0	0.2	1.1	18.49	0.01	0.05	DEBS	Pietrzyński et al. (2013)
49.4	0.5		18.47	0.02		RCS	Laney et al. (2012)
50.1	1.4		18.50	0.06		EBS	Pietrzyński et al. (2009b)
52.0	0.7	2.6	18.58	0.03	0.11	RRL	Szewczyk et al. (2008)
51.5	0.9		18.56	0.04		CEP	Gieren et al. (2005b)
50.1	0.2		18.50	0.01		RCS	Pietrzyński et al. (2003)
49.8	0.2	1.0	18.49	0.01	0.05	RCS	Pietrzyński & Gieren (2002)
				SMC			
62.1	1.9		18.97	0.03	0.04	DEBS	Graczyk et al. (2014)
62.1	0.5		18.97	0.02		RCS	Pietrzyński et al. (2003)
58.3	0.5	1.3	18.83	0.02	0.05	DEBS	Graczyk et al. (2012)
58.9	1.9	1.9	18.85	0.07	0.07	WVIR	Ciechanowska et al. (2010)
62.2	0.9	3.4	18.97	0.03	0.12	RRL	Szewczyk et al. (2009)
				Sculpteur			
87.9	3.2	4.0	19.72	0.08	0.1	RTGB	Górski et al. (2011)
85.9	0.8	4.7	19.67	0.02	0.12	RRL	Pietrzyński et al. (2008)
				Carlina			
104.2	1.4	5.8	20.09	0.03	0.12	RTGB	Pietrzyński et al. (2009a)
107.9	0.7		20.17	0.02		RCS	Pietrzyński et al. (2003)
				Fornax			
147.2	2.0	8.1	20.84	0.03	0.12	RTGB	Pietrzyński et al. (2009a)
148.5	0.9		20.86	0.01		RCS	Pietrzyński et al. (2003)
				NGC 68			
460	10	20	23.31	0.05	0.1	RTGB	Górski et al. (2011)
460	4	0	23.31	0.02		CEP	Gieren et al. (2006)
470	9	11	23.34	0.04	0.05	CEP	Pietrzyński et al. (2004)
				IC 1613			
740	30	30	24.36	0.08	0.09	RTGB	Górski et al. (2011)
720	10	2000	24.291	0.035		CEP	Pietrzyński et al. (2006a)
				M33			
840	30		24.62	0.07		CEP	Gieren et al. (2013)
970	50		24.93	0.11		FGLR	U et al. (2009)
				WLM			
1070	40	60	25.14	0.09	0.12	RTGB	Górski et al. (2011)
995	46		24.99	0.1		FGLR	Urbaneja et al. (2008)
970	19		24.924	0.042		CEP	Gieren et al. (2008b)
1070	10	30	25.144	0.03	0.07	CEP	Pietrzyński et al. (2007)
				NGC 3109			
1300	20		25.571	0.024		CEP	Soszyński et al. (2006)
1290	50		25.55	0.09		FGLR	Hosek et al. (2014)
1250	30	50	25.49	0.05	0.09	TRGB	Górski et al. (2011)
1280	18		25.54	0.03		CEP	Pietrzyński et al. (2006c)
				NGC 300			
1870	17	103	26.36	0.02	0.12	CEP	Rizzi et al. (2006)
1880	40	30	26.37	0.05	0.03	CEP	Gieren et al. (2005a)
1930	40	40	26.43	0.04	0.05	CEP	Gieren et al. (2004)
				NGC 55			
1940	30		26.434	0.037		CEP	Gieren et al. (2008a)
1910	44	79	26.4	0.05	0.09	CEP	Pietrzyński et al. (2006b)
				NGC 7793			
3440	80	130	27.68	0.05	0.08	CEP	Pietrzyński et al. (2010a)
				M81			
3500	200		27.7	0.1		FGLR	Kudritzki et al. (2012)
				NGC 247			
3380	60		27.644	0.036		CEP	Gieren et al. (2009)
3630	150	150	27.8	0.09	0.09	CEP	García-Varela et al. (2008)

Notes : DEBS = Detached Eclipsing Binaries ; RCS = Red Clump Stars ; RRL = RR Lyrae stars ; CEP = Cepheids ; W VIR = W Vir stars (Type 2 Cepheids) ; RTGB = Red Tip of Giant Branch ; FGLR = Flux weighted Gravity–Luminosity Relationship ;

Annexe D

Le cas particulier de Polaris

Polaris est la Céphéide la plus proche de nous à environ $d = 99 \pm 2$ pc (Turner et al. 2013). Sa période de pulsation est d'environ 4 jours. Dinshaw et al. (1989) indiquent que l'amplitude de la courbe de vitesse radiale, à l'origine autour de $2K \simeq 4.5 - 5$ km s^{-1}, a diminué régulièrement depuis 1956, avec une forte décroissance dans les années 80 pour s'établir autour de 1.5 ± 0.08 km s^{-1}en 1989. Cette diminution indiquait pour les auteurs que l'étoile devait sortir de la bande d'instabilité du côté rouge (premier passage) pour finalement s'arrêter de pulser autour de 1995. En 1993, Fernie et al. (1993) publient un papier intitulé *"Goodbye to polaris the Cepheid"* et mesure $2K = 0.59 \pm 0.19$km s^{-1}. Mais l'année suivante, Krockenberger et al. (1994) publient *"Polaris the Cepheid : still pulsating"*. Deux ans plus tard, Kamper & Fernie (1998) trouvent une "erreur sérieuse" dans les mesures spectroscopiques des années précédentes du fait d'une problème lié à la correction des raies telluriques dans la méthode de la cross-corrélation. Ils trouvent que l'amplitude de la vitesse s'est en fait stabilisée autour de 1.6 km s^{-1}, ce qui est ensuite confirmé par une étude importante de Hatzes & Cochran (2000) qui trouvent 1.517 ± 0.047 km s^{-1}, tandis que la période de l'étoile augmente. Les auteurs observent également des vitesses résiduelles dans les données spectroscopiques, qu'ils attribuent à des spots ou des modes non-radiaux. Evans et al. (2002) étudient les raies en émission chromosphérique MgII et montrent par ailleurs que le changement de période de l'étoile (3.2 secondes par an) est assez commun pour les Céphéides pulsant dans le premier harmonique. Evans et al. (2004) montrent alors à partir des données photométriques WIRE que l'étoile pourrait avoir une sorte d'effet Blazhko, typique des étoiles de type RR Lyrae, même si cet effet n'a jamais été observé pour des Céphéides avant cela. Turner et al. (2005) étudient à nouveau le statut évolutionnaire de l'étoile et confirment que l'étoile est dans son premier passage dans la bande d'instabilité, tandis que Usenko et al. (2005) fournissent des paramètres fondamentaux très précis pour cette étoile. Mérand et al. (2006) trouvent alors à l'aide de données FLUOR/CHARA une enveloppe autour de l'étoile contribuant pour $1.5 \pm 0.4\%$ en terme de flux en bande K et située à 2.4 ± 0.1 rayon stellaire, le diamètre angulaire de l'étoile étant mesuré à $\theta = 3.123 \pm 0.008$ mas. Usenko & Klochkova (2008) étudient ensuite le compagnon optique Polaris B et pensent qu'il s'agit d'une F3V. Bruntt et al. (2008) font alors une découverte intéressante : l'amplitude de vitesse radiale a augmenté durant les années 2003 à 2006, indiquant que l'amplitude ne décroît pas continûment mais fait l'objet d'un cycle. Les auteurs mentionnent également la découverte d'un signal dans les données WIRE de l'ordre de 2-6 jours qui pourrait être dû à la granulation. Evans et al. (2008) découvrent pour la première fois le compagnon de Polaris Ab grâce à des images du HST et obtiennent une séparation de 0.17", tandis que le compagnon visuel Polaris B se trouve à 18". La masse de l'étoile est alors établie à 4.5 ± 2.2 masses solaires, et celle du compagnon Polaris Ab à 1.26 ± 0.14 masse solaire. Lee et al. (2008)

confirment la remontée de l'amplitude "2K" de l'étoile à partir de données du spectrographe BOES. Stothers (2009) étudie la variation cyclique de Polaris (mais aussi V473 Lyr) et propose une nouvelle classe de Céphéides Blazhko. Evans et al. (2010) découvrent que Polaris est une source de rayons X avec le satellite CHANDRA. Afin de réconcilier les modèles d'évolution avec le changement de période de l'étoile, Neilson et al. (2012a) soutiennent que l'étoile perd probablement de la masse à hauteur de 10^{-6} Ms/an. Turner et al. (2013) montrent que les paramètres fondamentaux de l'étoile sont cohérents avec une Céphéide pulsant dans le mode fondamental et par ailleurs que la parallaxe Hipparcos de l'étoile est probablement sous-estimée, ce qui est aussitôt démenti par van Leeuwen (2013). Récemment, Neilson (2014) montra à partir de modèle d'évolution que Polaris se trouve probablement au niveau du troisième passage dans la bande d'instabilité et indique que sa distance est forcément supérieure à 118pc. Ceci fut repris et contredit par Fadeyev (2015) qui montra à partir de modèles hydrodynamiques que Polaris doit passer la bande d'instabilité pour la première fois et qu'elle pulse probablement dans le mode fondamental.

Annexe E

La modélisation des Céphéides

TABLE E.1 – Les différents modèles hydrodynamiques dans le monde : (S) correspond à une modélisation de la structure interne de l'étoile basée sur un modèle d'évolution, (E) correspond à la modélisation de l'enveloppe à partir d'un modèle de pulsation, et (A) indique qu'au moins quelques couches dans l'atmosphère sont considérées. Un transfert de rayonnement pour calculer une raie spectrale nécessite un nombre suffisant de couches dans l'atmosphère.

Reference	Parties de l'étoile modélisées	Linéaire ou Non Linéaire	Transfert de Rayonnement	Convection	Nbr. Dimensions
Buchler & Goupil (1984)	E	NL	NON	OUI	1D
Fokin et al. (1996)	E+A	NL	OUI	NON	1D
Sasselov & Raga (1992)	E+A	NL (Piston)	OUI	OUI	1D
Dorfi & Feuchtinger (1991)	E+A	NL	NON	OUI	1D
Bono et al. (1999)	S+E+A	L	NON	OUI	1D
Baraffe et al. (1998)	S+E+A	L	NON	OUI	1D
Mundprecht et al. (2013)	S+E+A	NL	NON	OUI	2D
Geroux & Deupree (2015)	S + E + A	NL	NON	OUI	3D
Vasilyev et al. (2017)	S + E + A	NL	OUI	OUI	2D

Annexe F

La relation brillance de surface - couleur

Les notes ci-dessous se rapportent à la Table F.1 :

1. Wesselink (1969). 18 mesures de diamètres d'étoiles : 14 avec le "Narrabri Intensity Interferometer" (NII) (Hanbury Brown et al. 1967a, 1974), à cela s'ajoutent le Soleil, 1 binaire à éclipses dont on connaît la distance, ainsi que 2 autres étoiles observées avec "The Michelson Interferometer at Mount Wilson Observatory" (Pease 1921; Michelson & Pease 1921; Pease 1921).
2. Barnes & Evans (1976). 27 mesures de diamètres d'étoiles : 16 par occultations lunaires et 11 par interférométrie (voir la Table 1 et les références associées).
3. Barnes et al. (1976, 1978). 25 mesures de diamètres d'étoiles : il s'agit de la liste des 32 diamètres mesurés par le NII (Hanbury Brown et al. 1967a, 1974) à laquelle on a enlevé 7 binaires.
4. di Benedetto & Rabbia (1987). 11 mesures de diamètres effectuées avec l'I2T sur le Plateau de Calern (Blazit et al. 1977; Faucherre et al. 1983). La relation est donnée sur deux intervalle (coupure vers $(V-R)_0 \simeq 1.2$ séparant les types K et M) avec sur les deux portions de droite une très faible dispersion (rms) de 0.002 mag.
5. di Benedetto (1993). 44 mesures de diamètres d'étoiles : 11 mesures effectuées avec l'I2T sur le Plateau de Calern (di Benedetto & Rabbia 1987) + 10 autres obtenues quelques années plus tard (di Benedetto & Ferluga 1990) + 23 par différentes techniques (voir table 3 et 4 de di Benedetto (1993)). Des relations (sans prise en compte de l'extinction) sont données pour les géantes : $F_V = 3.927 - 0.122(V-K)$ (1.4 < V-K < 3.7) (rms = 0.003) et $F_V = 3.833 - 0.101(V-K)$ (rms=0.01) (V-K > 3.7). Pour les supergéantes, on a $F_V = 3.954 - 0.133(V-K)$ (rms = 0.007) ou encore $F_{V_0} = 3.958 - 0.139(V-K)_0$ (si l'extinction est prise en compte). Enfin, des relations différentes de la forme $(0.5 \log \theta = (4.2207 - a) + b * (V-K)_0 - 0.1V_0)$ sont données pour différents types spectraux (voir la table 5) avec une dispersion s'échelonnant entre 0.03 mag (G-K de classe II à V) et 0.08 mag (MIV-V, Mira et C). Pour les supergéantes (généralement plus éloignées et sensibles au rougissement), l'extinction considérée est basée sur les formules classiques $A_V = 3.6E(B-V)$ et $E(V-K) = 3.17E(B-V)$ (Lee 1970).
6. Welch (1994). Premier étalonnage de la relation brillance de surface - couleur sur la base des Céphéides. Une relation est donnée entre F_K et $(V-K)_0$.
7. Fouque & Gieren (1997). 27 mesures de diamètres d'étoiles par interférométrie Michelson, toutes géantes ou supergéantes (voir la table 1 de Fouque & Gieren (1997)). La sélection des étoiles est

TABLE F.1 – Liste des relations brillance de surface - couleur. A ceci il faut rajouter l'idée de Gould (2014) d'utiliser les micro-lentilles gravitationnelles pour déterminer le diamètre angulaire d'une étoile, ainsi que l'approche des pseudo-magnitudes développée par Chelli et al. (2016).

Nb*	Notes	Type Sp.	Couleur	Précision (mag)	Ref
18	1	B-M	B-V	0.12	Wesselink (1969)
27	2	G-M, S, C	V-R, R-I	0.04, 0.08	Barnes & Evans (1976)
25	3	O-G	B-V, V-R, R-I	0.018, 0.025, 0.033	Barnes et al. (1976, 1978)
11	4	K-M	V-R	0.002	di Benedetto & Rabbia (1987)
44	5	F-M, C	V-K	0.03-0.09	di Benedetto (1993)
11	6	Ceps	V-K	0.04	Welch (1994)
27	7	F-M	V-R, V-K, J-K	0.004-0.034	Fouque & Gieren (1997)
22	8	F, G, K	V-K	0.03	di Benedetto (1998)
239	9	B-M	V-K, B-K	0.04-0.05	van Belle (1999)
116	10	Géantes et Ceps	V-R, V-K, J-K	0.01-0.02	Nordgren et al. (2002)
221	11	A-M	V-K, V-R, J-K	0.009-0.05	Groenewegen (2004)
9	12	Ceps	B-V, V-K, B-H	0.0006	Kervella et al. (2004b)
45	13	A, G, K, M	B-UVRIJHKL	0.02	Kervella et al. (2004e)
44	14	A, F, G, K	V-K	0.03	Di Benedetto (2005)
> 100	15	B, A, F, G, K, M	V-K	0.26	Bonneau et al. (2006)
42	16	A-M	BVRI	0.09 - 0.17	Kervella & Fouqué (2008)
124	17	A-M	BUVRIJHKL...	0.08 - 0.15	Boyajian et al. (2014)
132	18	A-M	V-K	0.04-0.16	Challouf et al. (2014)
40	19	EBs	B-K, V-K	0.05-0.11	Graczyk et al. (2017)

faite sur des critères de non-variabilité, d'une bonne précision sur le diamètre (<6%) et une absorption interstellaire inférieure à 0.2 mag pour les géantes (voir la partie 2.1 dans le papier). La plus faible dispersion (rms = 0.004 mag) est obtenue pour les géantes avec l'indice $(V-K)_0$: $F_V = 3.930_{\pm 0.012} - 0.124_{\pm 0.004}(V-K)_0$ (2.22 < V-K < 4.11). Les extinctions utilisées A_V sont déduites de la littérature et discutées dans la table 1, tandis que la loi de rougissement utilisée (voir la discussion détaillée dans le papier) est de : $E(V-K) = 0.88A_V$. La relation obtenue pour les supergéantes est la suivante : $F_V = 3.914_{\pm 0.023} - 0.119_{\pm 0.007}(V-K)_0$ (rms = 0.032 et 0.52 < V-K < 5.53). Les auteurs déduisent également une relation spécifique pour les Céphéides : $F_V = 3.947 - 0.131(V-K)_0$

8. di Benedetto (1998). Amélioration de l'échantillon de di Benedetto (1993) avec l'ajustement d'une relation non-linéaire : $S_V = 2.563 + 1.493(V-K)_0 - 0.046(V-K)_0^2$ pour (rms = 0.030) pour $-0.1 < (V-K)_0 < 3.7$.
9. van Belle (1999). 239 étoiles issues de l'interférométrie essentiellement. van Belle (1999) introduit le concept de diamètre angulaire à la magnitude zéro : $\theta_{V=0} = \theta * 10^{\frac{V}{5}}$. L'idée est que pour comparer le diamètre angulaire d'étoiles à des distances différentes, on peut utiliser le diamètre angulaire des étoiles à la magnitude $V = 0$. Ainsi, il obtient : $\theta_{V=0} = 10^{0.789 \pm 0.119 + 0.218 \pm 0.014 (V-K)}$ pour les variables, $\theta_{V=0} = 10^{0.50 \pm 0.023 + 0.264 \pm 0.012 (V-K)}$ pour les étoiles de la séquence principale et enfin $\theta_{V=0} = 10^{0.669 \pm 0.052 + 0.223 \pm 0.010 (V-K)}$ pour les classes III, II et I.
10. Nordgren et al. (2002). 57 géantes observées avec NPOI et 59 Céphéides. Les relations obtenues sont $F_{Vo} = 3.934_{\pm 0.005} - 0.123_{\pm 0.002}(V-K)_0$ (N=57, rms=0.011) pour les géantes et $F_{Vo} = 3.956_{\pm 0.011} - 0.134_{\pm 0.005}(V-K)_0$ (N=59, rms=0.026).
11. Groenewegen (2004). Liste de 221 étoiles issues de l'interférométrie avec une précision sur le diamètre assombri meilleure que 3%. L'extinction considérée est basée sur la distance des objets ainsi que leurs coordonnées galactiques (référence citée dans le papier mais non référencée Grenon & Gomez (1992)). La formule obtenue est (selon le concept de van Belle (1999)) : $\log \theta_{V=0} = 0.584 \pm 0.014 + 0.245 \pm 0.005(V-K)_0$ (N=74, rms=0.024) pour les géantes (III) et $\log \theta_{V=0} = 0.519 \pm 0.012 + 0.274 \pm 0.004(V-K)_0$ (N=20, rms=0.022) pour les étoiles de la séquence principale et $\log \theta_{V=0} = 0.607 \pm 0.019 + 0.243 \pm 0.008(V-K)_0$ (N=21, rms=0.046) pour les supergéantes.

12. Kervella et al. (2004b). 9 Céphéides observées avec VINCI/VLTI (Kervella et al. 2004d) qui amènent à la relation suivante : $F_V = -0.1336 \pm 0.0008(V-K) + 3.9530 \pm 0.0006$. L'extinction considérée est $A_\lambda = R_\lambda E(B-V)$ tandis que le rougissement s'écrit $R_K = \frac{R_V}{11}$ avec $R_V = 3.07 + 0.28(B-V) + 0.04E(B-V)$.
13. Kervella et al. (2004e). 29 étoiles différentes mais 45 mesures de diamètres angulaires obtenues avec les instruments suivants : NII (Hanbury Brown et al. 1967a, 1974), Mk III (Shao et al. 1988), PTI (Colavita et al. 1999) and NPOI (Armstrong et al. 1998). Plusieurs étoiles ont été exclues de l'échantillon de base : les systèmes doubles (dont des binaires à éclipses), β Pic qui présente un environnement, α Eri un rotateur rapide et deux étoiles de très faible masse (présence de molécules, variabilité, activité chromosphérique). Le passage d'un diamètre uniforme θ_{UD} à θ_{LD} est traité de manière homogène en utilisant les tables de (Claret 2000). Les étoiles de l'échantillon sont à moins de 15 pc et l'extinction est négligée. La relation ainsi obtenue est de la forme : $\log \theta_{LD} = 0.0755 \pm 0.0008(V-K) + 0.5170 \pm 0.0017 - 0.2K$ avec une dispersion inférieure à 1% sur le diamètre (rms = 0.022).
14. Di Benedetto (2005). Amélioration de l'échantillon de di Benedetto (1998) avec l'ajustement d'une relation non-linéaire : $S_V = 2.565 \pm 0.016 + 1.483 \pm 0.015(V-K)_0 - 0.044 \pm 0.005(V-K)_0^2$ pour (rms = 0.040) pour $-0.1 < (V-K)_0 < 3.7$.
15. Bonneau et al. (2006). Le nombre d'étoiles n'est pas donné mais les diamètres sont issus de mesures interférométriques, d'occultation lunaires et de binaires à éclipses (Barnes et al. 1978; Andersen et al. 1991; Ségransan et al. 2003; Mozurkewich et al. 2003). L'extinction est calculée avec les équations suivantes : mag[λ_0] =mag[λ] - A_λ, $R_\lambda = \frac{A_\lambda}{E(B-V)}$ et $A_\lambda = \frac{A_V R_\lambda}{R_V}$ avec $R_V = 3.10$ (Fitzpatrick 1999). Les résultats sont donnés sous la forme de l'équation suivante : $\phi_V = \frac{\theta}{9.306.10^{\frac{-m_V}{5}}} = \sum_k a_k CI^k$ avec avec $C_0 = 0.32561925$, $C_1 = 0.31467316$, $C_2 = 0.09401181$, $C_3 = -0.0187446$, $C_4 = 0.00818989$ (rms = 0.15).
16. Kervella & Fouqué (2008). 42 étoiles naines ou sous-géantes. Ce papier fait suite à Kervella et al. (2004b) et se limite au domaine visible. Des relations non-linéaires sont ajustées avec une dispersion s'échelonnant entre 0.09 et 0.17 magnitude.
17. Boyajian et al. (2014). 124 étoiles de la séquence principale avec des mesures de diamètres meilleures que 5%. L'extinction n'est pas prise en compte. Des relations sont données dans de nombreuses bandes photométriques et en V, (V-K), les auteurs obtiennent : $\log \theta_{V=0} = 0.53246 \pm 0.00057 + 0.26382 \pm 0.00028(V-K)$ (N=97 ; rms = 0.1).
18. Challouf et al. (2014). 132 étoiles dont 8 étoiles de type précoce observées par VEGA/CHARA. L'extinction est traitée de 7 manières différentes et une relation valable sur un intervalle important $-0.931 \leq V-K \leq 3.69$ est donnée sous la forme : $S_v = \sum_{n=0}^{n=5} C_n (V-K)_0^n$ avec $C_0 = 2.568 \pm 0.005$, $C_1 = 1.690 \pm 0.011$, $C_2 = -0.524 \pm 0.016$, $C_3 = 0.351 \pm 0.017$, $C_4 = -0.104 \pm 0.008$, $C_5 = 0.011 \pm 0.001$.
19. Graczyk et al. (2017). 40 binaires à éclipses galactiques dont on a la distance ont permis de déduire une relation brillance de surface - couleur du type : $S_V = 2.625 \pm 0.015 + 0.959 \pm 0.009(V-K)$ (N=28, rms=0.047). Concernant l'extinction, la carte de Schlegel et al. (1998) est utilisée. Concernant le rougissement, les auteurs considèrent : $R_V = 3.1$ d'après (Fitzpatrick & Massa 2007).

Annexe G

Calibrating the Cepheid period-luminosity relation from the infrared surface brightness technique. I. The p-factor, the Milky Way relations, and a universal K-band relation

A&A 534, A94 (2011)
DOI: 10.1051/0004-6361/201117155
© ESO 2011

Astronomy & Astrophysics

Calibrating the Cepheid period-luminosity relation from the infrared surface brightness technique

I. The *p*-factor, the Milky Way relations, and a universal *K*-band relation⋆

J. Storm[1], W. Gieren[2], P. Fouqué[3], T. G. Barnes[4], G. Pietrzyński[2,5], N. Nardetto[2,6], M. Weber[1], T. Granzer[1], and K. G. Strassmeier[1]

[1] Leibniz-Institut für Astrophysik Potsdam (AIP), An der Sternwarte 16, 14482 Potsdam, Germany
e-mail: jstorm@aip.de
[2] Universidad de Concepción, Departamento de Astronomía, Casilla 160-C, Concepción, Chile
[3] IRAP, Université de Toulouse, CNRS, 14 Av. E. Belin, 31400 Toulouse, France
[4] University of Texas at Austin, McDonald Observatory, 82 Mt. Locke Rd, McDonald Observatory, TX 79734, USA
[5] Warsaw University Observatory, Al. Ujazdowskie 4, 00-478 Warsaw, Poland
[6] Laboratoire Fizeau, UNS/OCA/CNRS UMR6525, Parc Valrose, 06108 Nice Cedex 2, France

Received 28 April 2011 / Accepted 23 July 2011

ABSTRACT

Aims. We determine period-luminosity relations for Milky Way Cepheids in the optical and near-IR bands. These relations can be used directly as reference for extra-galactic distance determination to Cepheid populations with solar metallicity, and they form the basis for a direct comparison with relations obtained in exactly the same manner for stars in the Magellanic Clouds, presented in an accompanying paper. In that paper we show that the metallicity effect is very small and consistent with a null effect, particularly in the near-IR bands, and we combine here all 111 Cepheids from the Milky Way, the LMC and SMC to form a best relation.
Methods. We employ the near-IR surface brightness (IRSB) method to determine direct distances to the individual Cepheids after we have recalibrated the projection factor using the recent parallax measurements to ten Galactic Cepheids and the constraint that Cepheid distances to the LMC should be independent of pulsation period.
Results. We confirm our earlier finding that the projection factor for converting radial velocity to pulsational velocity depends quite steeply on pulsation period, $p = 1.550 - 0.186 \log(P)$ in disagreement with recent theoretical predictions. We find PL relations based on 70 Milky Way fundamental mode Cepheids of $M_K = -3.33(\pm0.09)(\log(P) - 1.0) - 5.66(\pm0.03)$, $W_{VI} = -3.26(\pm0.11)(\log(P) - 1.0) - 5.96(\pm0.04)$. Combining the 70 Cepheids presented here with the results for 41 Magellanic Cloud Cepheids which are presented in an accompanying paper, we find $M_K = -3.30(\pm0.06)(\log(P) - 1.0) - 5.65(\pm0.02)$, $W_{VI} = -3.32(\pm0.08)(\log(P) - 1.0) - 5.92(\pm0.03)$.
Conclusions. We delineate the Cepheid PL relation using 111 Cepheids with direct distances from the IRSB analysis. The relations are by construction in agreement with the recent HST parallax distances to Cepheids and slopes are in excellent agreement with the slopes of apparent magnitudes versus period observed in the LMC.

Key words. stars: variables: Cepheids – stars: fundamental parameters – stars: distances – distance scale

1. Introduction

In this series of papers we calibrate the Cepheid period-luminosity (PL-) relation using the infrared surface brightness (IRSB) method. In Paper II we address the effect of metallicity on both the slope and the zero point of the relations in both the optical and near-IR bands finding very small (consistent with zero) effects in the near-IR and small, but possibly significant effects in the optical.

Gieren et al. (2005) made a first determination of the LMC PL relations based on thirteen stars with IRSB based distances. They found that the distances to the individual Cepheids were dependent on the pulsation period which of course is unphysical. They found that the problem could be resolved by changing the adopted projection (*p*-) factor relation, which converts observed radial velocities into pulsation velocities that are needed for Baade-Wesselink type analysis.

In the present paper we use the new and largely expanded data set from Paper II for now 36 LMC Cepheids together with the new direct geometric parallax measurements from Benedict et al. (2007) to empirically determine the appropriate *p*-factor relation to be used in the analyses.

We present new accurate radial velocity data for 14 galactic Cepheids expanding the sample to a total of 77 Cepheids, 70 of which can be used to delineate the Milky Way PL relations. We have reanalyzed the complete sample using exactly the same code and calibrations as for the LMC sample and adopting exactly the same reddening law to allow a direct comparison.

Based on the (near-) universality of the PL relations we combine the Milky Way, LMC and SMC samples to determine PL relations based on 111 Cepheids which at the same time constrain the slopes very well, and which are tied directly to the parallax zero point from Benedict et al. (2007). These relations thus form a very solid basis for the Cepheid distance scale.

⋆ Full Table 3 is only available at the CDS via anonymous ftp to cdsarc.u-strasbg.fr (130.79.128.5) or via http://cdsarc.u-strasbg.fr/viz-bin/qcat?J/A+A/534/A94

The paper is structured as follows: in Sect. 2 we present the data from the literature as well as new radial velocity data for fourteen Milky Way Cepheids. In Sect. 3 we present the IRSB method and use the Benedict et al. (2002, 2007) parallaxes as well as the results from Paper II on 36 LMC Cepheids with IRSB distances to constrain the p-factor relation. We then use the new p-factor relation to determine distances and luminosities for 77 Cepheids and derive new PL relations for the 70 fundamental mode pulsators with good data sets. We proceed to combine the data with the Magellanic Cloud sample to give our best global PL relations which can be used for distance determination to other galaxies. In Sect. 4 we compare the results with other recent investigations and in Sect. 5 we summarize our conclusions.

2. The data

We have searched the literature for optical (V-band) and near-infrared (K-band) light curves as well as radial velocity curves. The starting point for the search was the catalogues of complete phase coverage K-band light curves for Milky Way Cepheids published by Welch et al. (1984), Laney & Stobie (1992) and Barnes et al. (1997). Since the publication of those papers a rich literature of high quality optical and radial velocity data has materialized and for the majority of the stars it is now possible to apply the near-infrared surface brightness method to determine distances and luminosities.

In addition to the literature data we have obtained new, accurate, radial velocity curves for 14 of these Cepheids to improve the phase coverage and/or data quality for these stars.

We have selected the data sets according to quality and completeness, but also to ensure, as far as possible, that the data have been obtained close in time to the near-infrared data to reduce possible errors due to period variations of the stars. Known double mode pulsators have been disregarded a priori as the application of the IRSB method to such stars could only be attempted if all the data were truly simultaneous. Thus the list of references reflects this pre-selection and does not include the data sets that were not used for the analysis. A number of first overtone pulsators has also been included, but they are of course not used for the delineation of the fundamental mode pulsator PL relations.

In Table 1 we present the list of stars and the references to the data sets which we have used in the present analysis. A more complete list of of data sets can be found in Groenewegen (2008).

The BVI_c photometry reported here is all on the Johnson-Kron-Cousins system and the different data sets have been transformed to this system when necessary. Similarly all the near-IR data have been transformed to the SAAO system as necessary using the transformations from Carter (1990).

The radial velocity data have all been obtained using high resolution ($R > 20\,000$) spectrographs. Most of the radial velocities have been derived using cross-correlation techniques or techniques which are equivalent. In this way the radial velocities are assumed to be on a common system and we have not seen indications of significant systematic differences between datasets for any of our stars for which we have had data from different techniques. This is an important point for the application of the IRSB method as the conversion from radial velocities to pulsational velocities, the so called p-factor, depends to some extent on the procedure which was used for deriving the radial velocity from the input data.

2.1. New radial velocity measurements

For fourteen of the stars the radial velocity curves were either missing or they were of limited quality. We have obtained 381 new radial velocity measurements for these stars (see Table 2) using the STELLA Echelle Spectrograph (SES) mounted on the fully robotic 1.2 m STELLA-I telescope (Strassmeier et al. 2004, 2010; and Weber et al. 2008) at the Izaña Observatory on Tenerife, Spain. SES is a fiber-fed echelle spectrograph with a $2k \times 2k$ CCD detector covering the wavelength range from 388 to 882 nm with small inter-order gaps starting at 732 nm and increasing towards the red. The resolving power is $R = 55\,000$ giving a spectral resolution of 0.12 Å at 650 nm.

The spectra were obtained in fully robotic mode in the period from March 2007 until July 2010 and reduced using the automatic data reduction pipeline (Ritter & Wasshüttl 2004; Weber et al. 2008) developed for the instrument.

The radial velocities returned by the pipeline were corrected for instrumental velocity offsets and placed on the CORAVEL system by applying the offset of $+0.503$ km s^{-1} determined by Strassmeier et al. (in prep.) The radial velocities are tabulated in Table 3 and plotted in Fig. 1.

2.2. Pulsation velocities

The p-factor (see Sect. 3.4), which is used to convert the observed radial velocities into pulsational velocities, depends to some extent on the spectrograph and the procedure used for extracting the velocities as different spectral features might carry different weight in deriving the pulsational velocity. To investigate this effect for the STELLA velocities we have observed the star TT Aql for which an excellent CORAVEL based velocity curve is available (Imbert 1999).

We follow the procedure described by Storm et al. (2004) to determine the ratio between the p-factors for STELLA and CORAVEL based velocities, $\eta_{\rm STELLA} = p_{\rm STELLA}/p_{\rm COR}$, for the relevant phase interval, $0 \le \phi \le 0.8$. In Fig. 2 we plot the difference in pulsational velocity,

$$\Delta V_{\rm puls} = p_{\rm COR}({\rm RV}_{\rm COR} - V_\gamma) - \eta p_{\rm COR}({\rm RV}_{\rm STELLA} - V_\gamma) \quad (1)$$

as a function of phase between the linearly interpolated observed radial velocities for the two spectrographs for three different values of η. It appears that in the phase interval from 0.15 to 0.75 where the velocity difference curve is smooth, the formally best value is $\eta = 1.03$. It is however also clear that the uncertainty is rather large and given that the datasets have been obtained at epochs differing by about ten years, we choose not to apply any additional corrections to the STELLA velocities but assume that the STELLA and CORAVEL p-factors agree to within 3%. For the present sample of 14 stars with STELLA velocities a 3% effect on the p-factor translates into a 1% effect on the slopes of the final PL relations which is much smaller than the statistical errors.

For some stars we have used the radial velocity data from Nardetto et al. (2009) using the HARPS data pipeline. This data set also contains data for a star, ζ Gem, for which a good CORAVEL data set is available from Bersier (1994). Unfortunately the period of the star is not perfectly constant over time so it has been necessary to shift the two radial velocity curves with respect to each other to obtain a good match. Proceeding then as for the STELLA dataset we find that the two data sets are in good agreement and that $\eta_{\rm HARPS} = 1.00 \pm 0.03$ as can be seen in Fig. 3.

Table 1. List of data sources.

ID	Optical	K-band	Rad. vel.	ID	Optical	K-band	Rad. vel.
η Aql	4, 17	3, 4	9, 12, 29, 35	U Nor	7, 16, 20	2	8, 21
U Aql	17	3	32	QZ Nor	6, 47	2	28, 41
FF Aql	13, 17	3	53	TW Nor	16, 20	2, 3, 58	23, 41
FM Aql	4, 17	3, 4	35	V340 Nor	42	2	23
FN Aql	17, 20	3	34	Y Oph	7, 17, 20	2	27, 55
SZ Aql	17, 20	2	35, 40	BF Oph	10, 17	2	11, 14, 15
TT Aql	4, 7, 13, 17, 20	3, 4	1	X Pup	17, 20	2	1
V496 Aql	10, 17, 47	3	1, 48	AQ Pup	7, 17	2, 22, 24	1
RT Aur	13, 17	4	12, 34	BN Pup	7, 16, 20	2, 22	1
ℓ Car	20, 38	2	40	LS Pup	7	2, 22	1
U Car	7, 20	2, 3	8, 40	RS Pup	17, 20, 47	2	9
V Car	20	2	15	VZ Pup	7, 20	2, 22	1
CT Car	51	2, 22	21, 41, 47	KQ Sco	7	2, 3	8, 54
VY Car	7	2	8, 15	RY Sco	7, 16, 17, 20	2	8, 14, 15
WZ Car	7, 20	2, 22	8	EV Sct	17, 20	2	9, 19, 23
SU Cas	4, 17	4	9, 23	RU Sct	17, 20	2, 3	19, 41
KN Cen	7	2	8, 21	SS Sct	17, 20	3	54
V Cen	10, 20	2	11, 15	S Sge	4, 13, 17	3, 4	34
VW Cen	7, 20	2	8	GY Sge	43	2	19, 34
XX Cen	39	2	8	U Sgr	10, 17	2	9, 23
δ Cep	4, 17	4	9, 12, 23, 29, 35	W Sgr	17, 20	3, 59, 60	23
SU Cru	20	2	8, 21	X Sgr	17, 20	3, 57	1
X Cyg	13, 17	3, 4	9, 29	Y Sgr	17, 20	3	1, 56
CD Cyg	17	3	26	BB Sgr	10, 17	2	1
DT Cyg	17	3	23	WZ Sgr	17	2, 3	34
SU Cyg	13, 17	3	31	XX Sgr	17	3	1
VZ Cyg	4, 17	3, 4	1	YZ Sgr	17, 47	3	1, 48
β Dor	20, 33	2	37	V350 Sgr	10, 17	3	11, 27, 34
ζ Gem	13	57	1	SZ Tau	4, 17	2, 4	23
X Lac	4, 17	4	23	T Vel	47, 20	2	11, 15
Y Lac	4, 17	4	26	CS Vel	44, 45	2, 22	23, 41
Z Lac	4, 17	4	36	RY Vel	7, 16	2, 3	8, 21
BG Lac	4, 17	4	26	RZ Vel	7, 16, 20	2	8, 56
GH Lup	7, 20	2	8	SW Vel	7, 16, 20	2	21, 27
T Mon	47, 7	2	9, 23	S Vul	43	2, 3	34
CV Mon	17, 20	2	9, 41	T Vul	13, 17	3, 4	23
S Mus	46	2, 3	30	U Vul	4, 13, 17	4	23, 25
UU Mus	16, 39	2	8	SV Vul	13, 17	2, 3	23, 26
S Nor	44, 46	2	23				

References. (1) This paper; (2) Laney & Stobie (1992); (3) Welch, et al. (1984); (4) Barnes et al. (1997); (6) Berdnikov & Turner (1995); (7) Coulson, & Caldwell (1985); (8) Coulson et al. (1985); (9) Storm et al. (2004); (10) Gieren (1981b); (11) Gieren (1981a); (12) Kiss (1998b); (13) Kiss (1998a); (14) Barnes et al. (1988); (15) Lloyd Evans (1980); (16) Madore (1975); (17) Moffett & Barnes (1984); (19) Metzger et al. (1991); (20) Pel (1976); (21) Pont et al. (1994); (22) Schechter et al. (1992); (23) Bersier et al. (1994); (24) Welch (1985); (25) Imbert (1996); (26) Imbert (1999); (27) Petterson et al. (2005); (28) Kienzle et al. (1999); (29) Butler & Bell (1997); (30) Evans (1990); (31) Imbert (1984); (32) Welch et al. (1987); (33) Shobbrook (1992); (34) Gorynya et al. (1998); (35) Barnes et al. (2005); (36) Sugars & Evans (1996); (37) Wallerstein et al. (1992); (38) Bersier (2002); (39) Coulson et al. (1985); (40) Bersier (2002); (41) Metzger et al. (1992); (42) Bersier et al. (1994); (43) Berdnikov (1986, 1987, 1992, 1992, 1992, 1992, 1992); (44) Berdnikov & Turner (1998); (45) Berdnikov & Turner (2000); (46) Walraven et al. (1964); (47) Berdnikov & Caldwell (2001); (48) Caldwell et al. (2001); (51) Pojmanski et al.; (53) Evans (1990); (54) Groenewegen (2008); (55) Nardetto et al. (2006); (56) Nardetto et al. (2009); (57) Feast et al. (2008); (58) McGonegal et al. (1983); (59) Kimeswenger et al. (2004); (60) Wisniewski & Johnson (1968).

Table 2. Cepheids for which we have obtained new radial velocity curves.

Star	N_{obs}	Star	N_{obs}
TT Aql	25	LS Pup	26
V496 Aql	19	VZ Pup	29
ζ Gem	65	X Sgr	19
VZ Cyg	20	Y Sgr	15
X Pup	42	BB Sgr	18
AQ Pup	38	XX Sgr	20
BN Pup	31	YZ Sgr	14

Notes. For each star the number of new data points is listed as well.

For another star, ℓ Car, there is a similar possibility of a direct comparison between CORAVEL and HARPS data. The radial velocity curves from different data sets exhibit some variations though, and the conclusions are less straight forward than for ζ Gem, but they do agree with a value of η which is indistinguishable from unity, which we will adopt in the following.

3. The analysis

3.1. The IRSB method

The infrared surface-brightness (IRSB) method is a variant of the Baade-Wesselink method originally developed by

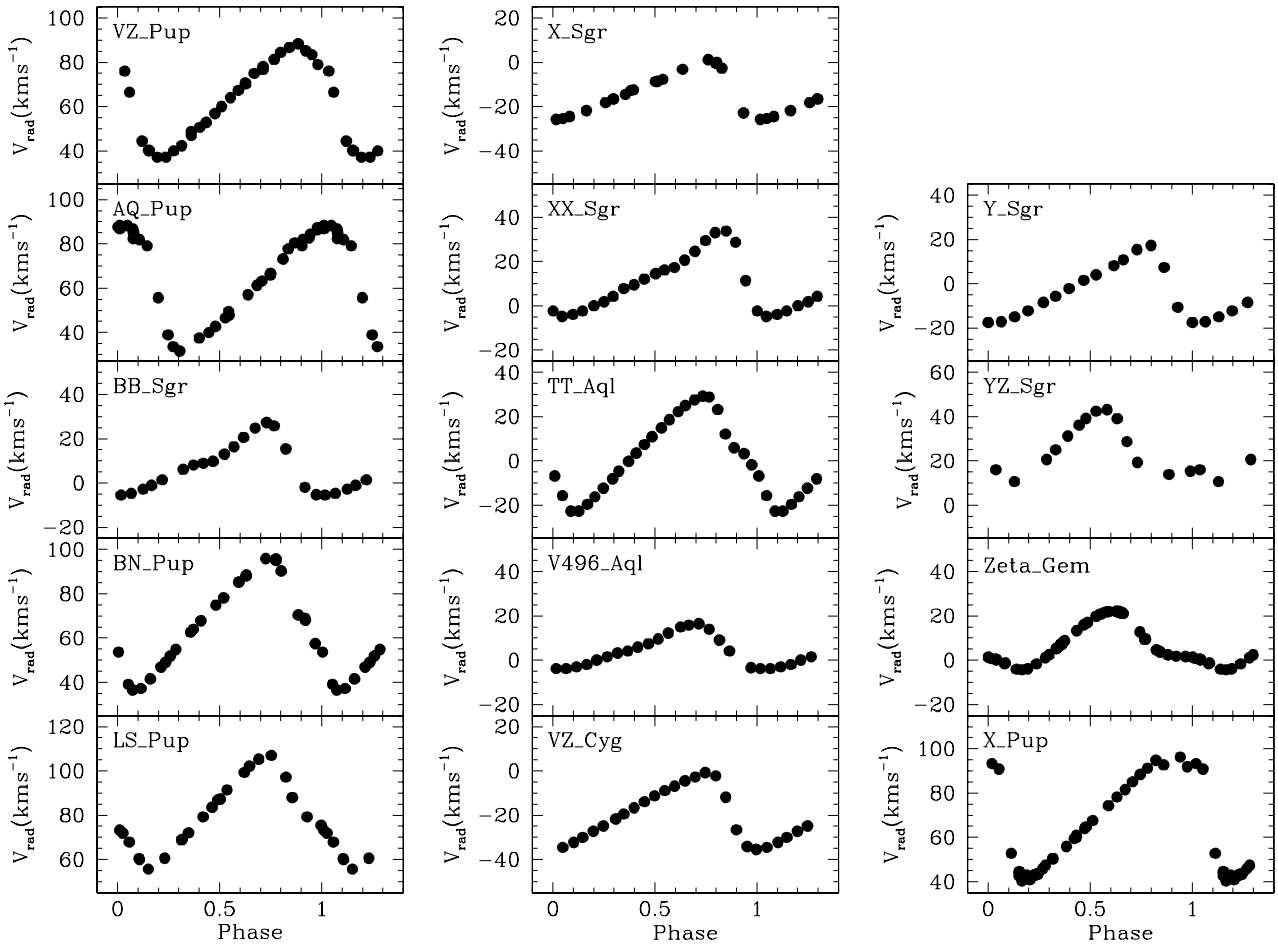


Fig. 1. The new radial velocity curves for fourteen Milky Way Cepheids from the STELLA echelle spectrograph as tabulated in Table 3.

Table 3. Heliocentric radial velocities (RV) measured with the STELLA echelle Spectrograph (SES) as returned by the data reduction pipeline and offset to the CORAVEL velocity zero point.

Star	HJD (Days)	Phase	RV (km s^{-1})	σ(RV) (km s^{-1})
TTAql	2 454 175.76609	0.53	14.79	0.04
TTAql	2 454 213.73669	0.29	−8.15	0.06
TTAql	2 454 218.64326	0.65	24.95	0.07
TTAql	2 454 222.59739	0.94	3.25	0.02
TTAql	2 454 223.59473	0.01	−6.92	0.02
...	...	...	...	...

Notes. The complete table is available in electronic from the CDS.

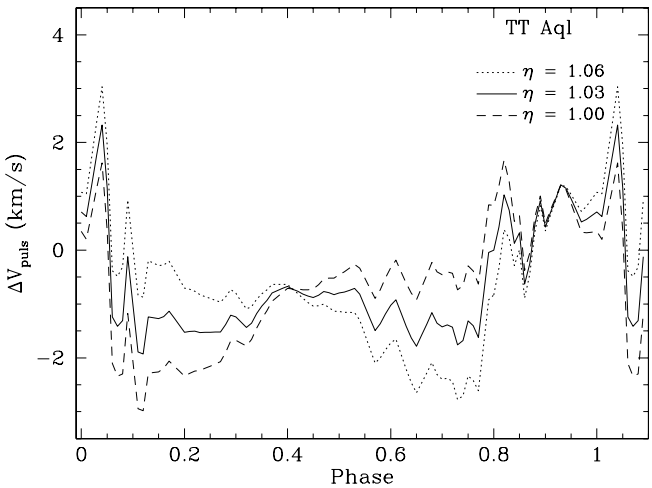


Fig. 2. The difference in pulsational velocity as a function of phase between CORAVEL and STELLA measurements for three different choices of η where $\eta = p_{\rm STELLA}/p_{\rm COR}$.

Barnes & Evans (1976) in the optical wavelengths. It is based on a functional relation between a colour index and the surface brightness parameter in the V-band, F_V. It was originally calibrated by Welch (1994) and a few years later Fouqué & Gieren (1997). They determined a very tight linear relationship between the $(V-K)$ colour index and F_V based on interferometric angular diameters of giant stars found in the literature, thus extending the method to the near-infrared. The scatter in this relation was significantly smaller than was the case for the optical colour indices used previously. A detailed description of the implementation of the method which we use in the present paper can be found in Storm et al. (2004).

Recently direct interferometric angular diameter measurements of Cepheids have become available (Nordgren et al. 2002; Kervella et al. 2004a; Mérand et al. 2005) allowing a direct comparison between the surface-brightness relation for static stars with actual pulsating stars. On this basis Kervella et al. (2004b) find excellent agreement between static and pulsating

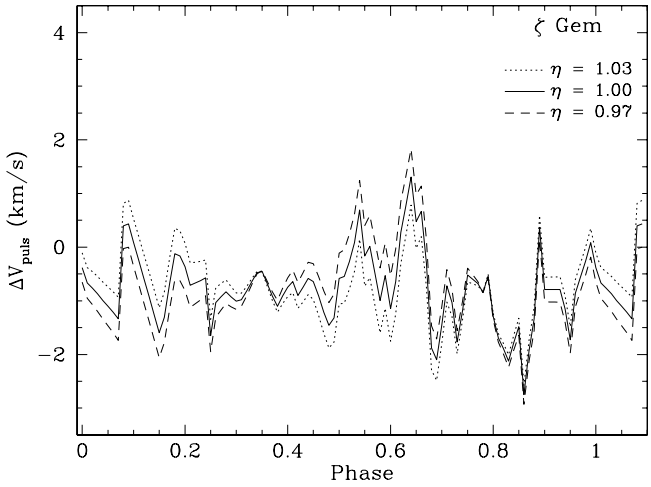


Fig. 3. The difference in pulsational velocity as a function of phase between CORAVEL and HARPS measurements for three different choices of η where $\eta = p_{\rm HARPS}/p_{\rm COR}$.

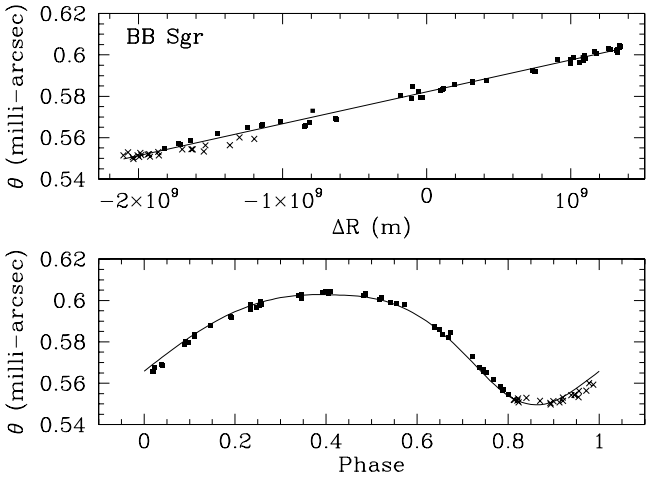


Fig. 4. The IRSB fit to the data for the star BB Sgr. The deviation between photometric and spectroscopic angular diameters in the phase interval $\phi \in [0.8, 1.0]$ is evident and is observed for many of the Cepheids in our sample. This phase interval is therefore disregarded in the fit for all the stars.

stars as well as with the relation determined by Fouqué & Gieren (1997) for static stars. They find a best fit relation of

$$F_V = -0.1336(V-K)_0 + 3.9530 \quad (2)$$

with the coefficients determined to better than 2%. We adopt their relation for the following analysis.

The surface brightness measure F_V is directly related to the stellar angular diameter, θ through the relation

$$F_V(\phi) = 4.2207 - 0.1V_0(\phi) - 0.5\log\theta(\phi) \quad (3)$$

where V_0 is the de-reddened visual magnitude, and ϕ is the phase.

At the same time geometry gives us the stellar angular diameter from the stellar radius, $R(\phi)$, through the relation

$$\theta(\phi) = 2R(\phi)/d = 2(R_0 + \Delta R(\phi))/d \quad (4)$$

where ϕ is the pulsation phase, d is the distance and R is the radius.

Integrating the radial velocity curve then gives the radius variation, $\Delta R(\phi)$ between a reference radius, R_0 and the given phase, ϕ as

$$\Delta R(\phi) = \int -p[V_r(\phi) - V_\gamma]{\rm d}\phi \quad (5)$$

where p is the so called projection factor converting radial velocity into pulsational velocity, $V_r(\phi)$ is the observed radial velocity and V_γ is the systemic velocity.

We can now solve Eq. (4) for the two parameters, mean radius, R_0, and distance, d by linear regression to the observed values of $\theta(\phi)$ from Eq. (3) and $\Delta R(\phi)$ from Eq. (5). As discussed in Storm et al. (2004) we use the OLS bi-sector fit from Isobe et al. (1990) for the regression fit. We fit only the phase interval $\phi \in [0.0, 0.8]$ where the shapes of the two curves usually agrees very well, and we avoid the phase region $\phi \in [0.8, 1.0]$ where the agreement often is quite poor, most likely due to shocks in the stellar atmosphere. We also allow for a small phase shift between the photometric and radial velocity data to optimize the quality of the fit. The effect on the final PL relation of these phase shifts is mainly to decrease the scatter in the relation.

An example of the fit for the star BB Sgr is shown in Fig. 4. In the upper panel the data used for the actual OLS bi-sector fit (see Storm et al. 2004, for more details on this) can be seen and in the lower panel the corresponding photometric angular diameters have been plotted as filled squares for the points used in the fit and red crosses for the points in the phase interval $\phi \in [0.8, 1.0]$ which have been disregarded in the fits. The curve in the lower panel delineates the corresponding spectroscopic angular diameter.

3.2. Absorption

In order to derive dereddened magnitudes for our Cepheids we use the colour excess values as given in Fouqué et al. (2007). These values are on the system defined by Laney & Caldwell (2007) and as discussed by Fouqué et al. (2007), these values are in agreement with the system established by Tammann et al. (2003), who recalibrated the original measurements compiled by Fernie (1995).

For the reddening law we similarly adopt the choice made by Fouqué et al. (2007), namely the law determined by Cardelli et al. (1989) with a total-to-selective absorption in the V band of $R_V = 3.23$ as determined by Sandage et al. (2004). For the other bands we use $A_I = 0.608\times A_V$, $A_K = 0.119\times A_V$, $A_J = 0.292\times A_V$, and $A_H = 0.181 \times A_V$.

3.3. Fourier coefficients and identification of fundamental mode pulsators

Before we attempt to establish the PL relations we have to identify the fundamental mode pulsators in the sample. This is difficult without referring to the period-luminosity diagram. We use the Fourier parameters for the radial velocity data and the diagrams from Kienzle et al. (1999) to reject overtone pulsators. To be conservative we use the A_1 parameter (the radial velocity amplitude) to reject s-type Cepheids from our final sample as well. In this way we might remove some bona fide fundamental pulsators as well, but we ensure that we have a uniform sample.

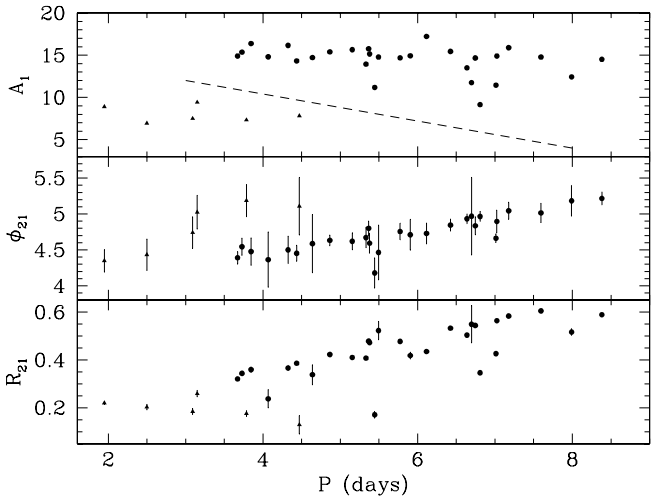


Fig. 5. The Fourier parameters based on the radial velocity data for the Cepheids with periods less than 9 days. The dashed line indicates the adopted division between normal Cepheids and *s*-Cepheids based on Fig. 2 in Kienzle et al. (1999). Filled circles indicate fundamental pulsators and the triangles, first overtone pulsators.

The Fourier parameters for all the Cepheids based on the data sets given in Table 1 are tabulated in Table 4. The error estimates on the parameters have been calculated using the approximative formula given by Petersen (1986).

In Fig. 5 the Fourier parameters for the short period Cepheids have been plotted and the *s*-Cepheids identified as the stars with A_1 below the dashed line. These stars are DT Cyg, EV Sct, FF Aql, SU Cas, SZ Tau, and QZ Nor. SU Cas is the shortest-period Cepheid in our sample and was probably the first Galactic Cepheid for which pulsation in the first overtone mode was firmly established by Gieren (1976, 1982). Two stars lie below the sequence of fundamental mode pulsators in the A_1 vs. P plot but above the dashed line and in the other Fourier parameters they appear unremarkable, so they are not obvious *s*-Cepheids or overtone pulsators. These stars are X Lac, and V496 Aql and we will keep them in the sample of fundamental mode stars.

3.4. Constraining the projection factor

For any Baade-Wesselink type method it is necessary to determine the pulsational velocity of the surface of the star as this is the velocity curve which is matched against the angular diameter curve from the photometry. The same is the case when the angular diameter curve is directly determined from interferometry. The conversion from the observed radial velocity to pulsational velocity is commonly parametrized with the projection factor, p.

The p-factor is largely a geometrical correction taking into account the fact that the radial velocity that we measure is based on light coming from all points of the hemisphere of the star which is visible to the observer and not just from the surface element which move along the line of sight to the star. In fact as discussed by Sabbey et al. (1995) the p-factor depends on the temperature of the star, which changes with pulsation period, as it depends on the limb darkening of the star.

The p-factor used for converting the observed radial velocities into pulsational velocities has direct consequences for the derived distances, as it scales directly with the stellar radius variation, and is probably the largest source of systematic error for the method. In the past we (e.g. Gieren et al. 1993; Storm et al. 2004; Barnes et al. 2005) have used a relation with a weak period dependence, $p = 1.39 - 0.03 \log P$, based on theoretical work by Hindsley & Bell (1986).

Later we (Gieren et al. 2005) found that the use of this p-factor relation with the IRSB method for LMC Cepheids leads to an unphysical dependence of the distance modulus on the pulsation period. We found that a p-factor relation of $p = 1.58 - 0.15 \log P$ removed this period effect, but the conclusion was not very firm due to the limited sample of only 13 LMC Cepheids.

On the theoretical side, Nardetto et al. (2007) have carefully analyzed individual line profiles from pulsating atmosphere models and they also found a relation which was steeper than the Hindsley & Bell (1986) slope. Nardetto et al. (2009) generalized this work to match the cross-correlation technique used in most observational work on radial velocities and found a relation

$$p = 1.31(\pm 0.06) - 0.08(\pm 0.05) \log P. \quad (6)$$

With the sample of 36 LMC Cepheids, presented in Storm et al. (2011, hereinafter Paper II), covering a wide range of periods we are in a much better position to constrain the p-factor relation empirically. Furthermore the recent direct parallax measurements for ten Milky Way Cepheids by Benedict et al. (2002, 2007) using the *Hubble* Space Telescope Fine Guidance Sensor provide a fundamental set of reference data which we can use to calibrate the p-factor relation.

For three of the ten stars with HST parallaxes (Y Sgr, X Sgr, and ζ Gem) we present new radial velocities here, significantly improving the available data quality. For one star, W Sgr, which is a known binary (Szabados 2003) the IRSB fit is clearly very poor and we disregard this star in the further analysis. X Sgr is known to be affected by a double shockwave in its atmosphere (Mathias et al. 2006) but the IRSB fit looks fine and the agreement with the HST parallax is excellent so we keep it in the sample. This leaves us with nine stars in common.

As a first step we use the theoretical relation from Nardetto et al. (2009) in Eq. (6) and apply the IRSB method to these nine stars. We find a disappointing difference of -0.30 ± 0.05 mag in the distance moduli, the IRSB distances being shorter. Applying the Nardetto et al. relation to the LMC Cepheids in Paper II we similarly find an unlikely result, namely an LMC distance modulus of 18.26 ± 0.04, much shorter than the canonical value of 18.50. So if we proceed using first principles, we have a serious conflict with the Benedict et al. (2007) result as well as with most recent works on the LMC distance that have confined the true distance modulus to a value between 18.4 and 18.6 (e.g. Pietrzyński et al. 2009; Szewczyk et al. 2008).

To reconcile these results we have to conclude either that the theoretical p-factor relation is incorrect due to the lack of some physics, or that there is a period dependence in the IRSB method which is not properly accounted for in the current theoretical p-factor relation. We attempt to constrain this effect empirically and parametrize it as a part of the p-factor relation which we retain as having the simple linear form $p = \alpha_p \times \log(P) + \beta_p$.

We need to determine two parameters, namely the slope (α_p) and the zero point (β_p) of the p-factor relation. We have two independent constraints, namely that there should be no systematic dependence of the LMC Cepheid distances with pulsation period, and we should reproduce, on average, the Benedict et al. (2007) distances.

It turns out that these two constraints are largely orthogonal in the (β_p, α_p) plane as can be seen in Fig. 6. To determine these parameters we simply apply the IRSB method to each sample of stars (Milky Way and LMC) for an array of slopes

Table 4. Fourier parameters for the stars based on the radial velocity data.

ID	Period (day)	Systemic velocity (km s^{-1})	A_1 (km s^{-1})	R_{21}	R_{31}	ϕ_{21}	ϕ_{31}	$\sigma(R_{21})$	$\sigma(R_{31})$	$\sigma(\phi_{21})$	$\sigma(\phi_{31})$
SU Cas	1.94932	−7.36	8.90	0.220	0.053	4.348	2.576	0.006	0.006	0.157	0.235
DT Cyg	2.49921	−1.70	6.93	0.203	0.045	4.434	2.067	0.012	0.012	0.218	0.326
EV Sct	3.09099	17.26	7.50	0.185	0.046	4.741	2.748	0.012	0.012	0.221	0.330
SZ Tau	3.14895	−0.65	9.42	0.259	0.075	5.024	3.784	0.013	0.013	0.233	0.346
SS Sct	3.67125	−7.24	14.90	0.298	0.097	4.449	2.616	0.002	0.002	0.096	0.143
RT Aur	3.72832	19.57	15.36	0.319	0.145	4.618	3.057	0.004	0.004	0.131	0.194
QZ Nor	3.78655	−39.50	7.33	0.176	0.043	5.186	4.732	0.012	0.012	0.223	1.855
SU Cyg	3.84549	0.08	16.38	0.334	0.147	4.545	2.836	0.010	0.010	0.209	0.303
BF Oph	4.06751	−28.90	14.81	0.222	0.137	4.420	3.110	0.035	0.035	0.423	0.580
Y Lac	4.32378	−22.20	16.16	0.340	0.192	4.570	2.884	0.010	0.010	0.208	0.303
T Vul	4.43541	−2.90	14.32	0.358	0.162	4.517	2.829	0.004	0.004	0.123	0.185
FF Aql	4.47085	−0.09	7.83	0.129	0.057	5.108	3.615	0.039	0.039	0.400	0.593
T Vel	4.63982	5.75	14.72	0.314	0.103	4.665	3.037	0.038	0.038	0.446	0.615
VZ Cyg	4.86445	−18.30	15.39	0.392	0.155	4.716	3.302	0.002	0.002	0.082	0.123
V350 Sgr	5.15424	7.73	15.65	0.380	0.193	4.701	3.320	0.004	0.004	0.129	0.191
BG Lac	5.33191	−18.10	13.94	0.378	0.194	4.758	3.431	0.006	0.006	0.155	0.230
δ Cep	5.36630	−16.40	15.76	0.443	0.293	4.900	3.381	0.003	0.003	0.110	0.163
CV Mon	5.37879	19.28	15.15	0.437	0.212	4.672	3.219	0.005	0.005	0.152	0.225
X Lac	5.44453	−25.20	11.18	0.161	0.022	4.216	2.001	0.013	0.013	0.233	0.344
V Cen	5.49392	−23.60	14.78	0.483	0.190	4.531	2.691	0.035	0.035	0.418	0.583
Y Sgr	5.77335	−1.57	14.68	0.442	0.237	4.851	3.593	0.004	0.004	0.129	0.192
CS Vel	5.90474	26.85	14.93	0.388	0.171	4.802	3.522	0.013	0.013	0.237	0.346
FM Aql	6.11423	−5.01	17.22	0.403	0.198	4.822	3.821	0.006	0.006	0.159	0.234
XX Sgr	6.42414	12.65	15.44	0.492	0.205	4.949	3.904	0.002	0.002	0.092	0.136
BB Sgr	6.63714	8.40	13.50	0.466	0.152	5.047	4.346	0.001	0.001	0.076	0.113
V Car	6.69668	12.60	11.75	0.508	0.165	5.085	4.615	0.071	0.071	0.595	0.819
U Sgr	6.74523	2.70	14.67	0.503	0.190	4.939	4.005	0.005	0.005	0.139	0.206
V496 Aql	6.80703	5.10	9.15	0.322	0.063	5.082	4.625	0.001	0.001	0.076	0.114
X Sgr	7.01283	−12.70	11.45	0.395	0.148	4.748	3.459	0.001	0.001	0.065	0.098
U Aql	7.02410	−0.11	14.90	0.521	0.183	5.005	4.279	0.007	0.007	0.176	0.261
η Aql	7.17678	−14.80	15.89	0.539	0.246	5.169	4.062	0.004	0.004	0.131	0.194
W Sgr	7.59503	−27.70	14.78	0.559	0.189	5.136	3.921	0.005	0.005	0.146	0.217
U Vul	7.99069	0.24	12.43	0.478	0.104	5.321	3.970	0.013	0.013	0.236	0.349
S Sge	8.38209	−13.40	14.51	0.544	0.115	5.358	4.086	0.002	0.002	0.098	0.146
GH Lup	9.27787	−16.10	4.38	0.146	0.000	5.823	0.000	0.183	0.183	0.870	-1.634
FN Aql	9.48151	12.67	14.60	0.163	0.156	0.566	5.571	0.005	0.005	0.137	0.232
YZ Sgr	9.55369	22.88	13.74	0.444	0.122	0.016	4.347	0.002	0.002	0.083	0.127
S Mus	9.66007	−0.14	12.85	0.479	0.137	5.820	-2.260	0.011	0.011	0.209	0.338
S Nor	9.75424	5.54	14.31	0.332	0.161	0.255	-1.444	0.007	0.007	0.168	0.373
β Dor	9.84308	8.87	14.01	0.313	0.192	0.337	4.914	0.017	0.017	0.263	0.626
ζ Gem	10.15073	7.44	11.81	0.243	0.137	0.459	5.046	0.001	0.001	0.066	0.099
TW Nor	10.78618	−56.60	18.78	0.193	0.218	0.685	5.181	0.013	0.013	0.233	1.316
Z Lac	10.88564	0.09	18.43	0.180	0.172	0.209	5.059	0.008	0.008	0.181	0.269
XX Cen	10.95337	−16.20	14.23	0.340	0.140	0.308	5.238	0.051	0.051	0.474	0.689
V340 Nor	11.28700	−40.30	8.58	0.265	0.053	0.206	4.441	0.016	0.016	0.413	0.391
UU Mus	11.63641	−16.90	20.12	0.200	0.205	0.049	5.724	0.044	0.044	0.462	69.984
U Nor	12.64371	−22.20	16.88	0.135	0.087	0.206	4.921	0.044	0.044	0.448	0.646
SU Cru	12.84760	−30.30	11.06	0.009	0.096	3.232	5.500	0.067	0.067	1.272	0.792
BN Pup	13.67310	67.57	24.86	0.206	0.021	4.495	1.650	0.001	0.001	0.069	0.103
TT Aql	13.75496	3.83	21.93	0.139	0.140	4.517	6.262	0.001	0.001	0.049	0.364
LS Pup	14.14640	81.50	22.64	0.069	0.126	6.180	5.978	0.001	0.001	0.075	0.112
VW Cen	15.03618	−30.60	22.72	0.213	0.049	4.674	0.357	0.038	0.038	0.579	0.603
X Cyg	16.38633	7.85	22.18	0.228	0.058	4.559	0.890	0.004	0.004	0.135	0.209
Y Oph	17.12633	−7.12	7.75	0.114	0.034	5.503	4.257	0.024	0.024	0.313	0.466
SZ Aql	17.14071	6.45	25.38	0.263	0.039	4.563	1.735	0.003	0.003	0.112	0.167
CT Car	18.05765	111.10	23.42	0.307	0.139	4.576	2.444	0.015	0.015	0.275	0.389
VY Car	18.90728	1.86	22.22	0.272	0.112	4.518	2.374	0.029	0.029	0.417	0.514
RU Sct	19.70062	−5.16	21.14	0.244	0.014	4.753	3.027	0.009	0.009	0.236	0.330
RY Sco	20.32014	−18.00	15.85	0.050	0.070	4.077	4.236	0.045	0.045	0.643	0.672
RZ Vel	20.39690	24.81	22.96	0.206	0.172	4.564	1.875	0.023	0.023	0.446	0.940
WZ Sgr	21.84960	−17.40	23.05	0.323	0.138	4.542	2.606	0.003	0.003	0.109	0.160
WZ Car	23.01320	−14.40	22.78	0.341	0.147	4.468	2.546	0.033	0.033	0.598	0.779
VZ Pup	23.17100	63.52	23.00	0.303	0.121	4.446	2.450	0.001	0.001	0.068	0.088
SW Vel	23.44313	23.75	26.88	0.378	0.200	4.645	2.962	0.009	0.009	0.222	0.304
X Pup	25.96100	72.02	24.12	0.363	0.143	4.565	2.891	0.001	0.001	0.081	3.168
T Mon	27.03569	20.67	22.57	0.345	0.202	4.580	2.983	0.005	0.005	0.152	0.220
RY Vel	28.13117	−10.60	16.18	0.267	0.127	4.333	2.464	0.039	0.039	0.600	0.602
KQ Sco	28.69580	−30.30	13.84	0.940	0.611	3.943	4.083	0.038	0.038	0.628	0.616
AQ Pup	30.10400	61.02	23.91	0.276	0.062	4.733	3.298	0.001	0.001	0.066	0.099
KN Cen	34.02964	−37.20	21.71	0.295	0.341	3.861	2.323	0.036	0.036	0.569	0.655
ℓ Car	35.54804	2.28	16.77	0.296	0.150	4.639	2.949	0.005	0.005	0.153	0.225
U Car	38.81233	0.21	21.00	0.347	0.116	4.494	2.531	0.022	0.022	0.374	0.503
RS Pup	41.47446	25.91	19.81	0.444	0.192	4.615	3.103	0.008	0.008	0.185	0.267
SV Vul	44.98561	−1.57	19.54	0.408	0.197	4.495	3.108	0.003	0.003	0.115	0.167
GY Sge	51.56031	15.96	13.15	0.301	0.104	4.766	3.118	0.014	0.014	0.250	0.362
S Vul	68.77426	1.52	13.26	0.335	0.208	4.742	3.323	0.008	0.008	0.181	0.268

and zero points for the p-factor relation and see where the constraints are fulfilled. We have varied the zero-point in the range $\beta_p \in [1.2, 1.75]$ in steps of 0.05 and the slope of the relation in the range $\alpha_p \in [-0.31, 0.01]$ in steps of 0.03.

Table 5. Distances for Cepheids with HST parallax measurements from Benedict et al. (2007).

(1) ID	(2) log(P)	(3) d(HST) (pc)	(4) d(IRSB) (pc)	(5) Δd (pc)	(6) $\sigma(\Delta d)$ (pc)
FF Aql	0.650390	355.9	369.8	14.0	42.3
RT Aur	0.571489	416.7	389.0	−27.6	33.0
ℓ Car	1.550820	497.5	517.6	20.1	47.9
δ Cep	0.729678	273.2	266.7	−6.5	20.3
β Dor	0.993131	318.5	326.6	8.1	22.0
ζ Gem	1.006500	359.7	385.5	25.8	38.3
W Sgr†	0.880529	438.6	216.8	−221.8	71.1
X Sgr	0.845893	333.3	322.1	−11.2	28.1
Y Sgr	0.761428	469.5	436.5	−33.0	75.6
T Vul	0.646934	526.3	542.0	15.7	59.4

Notes. The HST distances are given in Col. 3, the IRSB distances using our preferred p-factor relation from Eq. (7) are given in Col. 4 and the difference in Col. 5. The uncertainty on the difference is given in the last column. † Not considered in the fits. This star is a known spectroscopic binary.

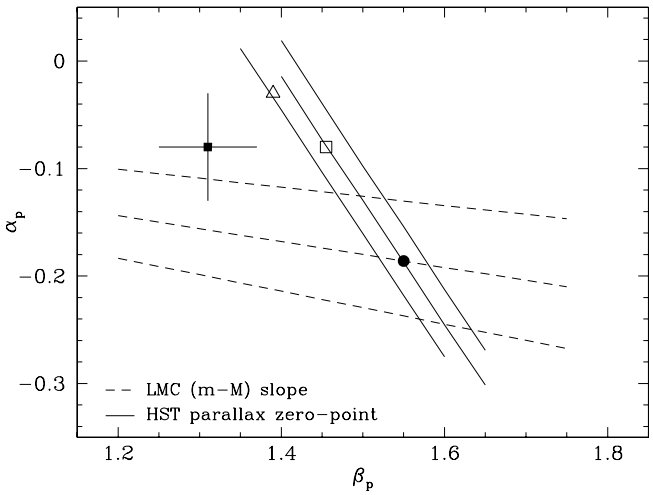


Fig. 6. Constraints on the p-factor relation from the HST parallax of Milky Way Cepheids (full line), and from requiring the LMC distance to be independent of the pulsation period of the stars (dashed line), see Sect. 3.4 for details. The one sigma contours are also shown with thin lines. The filled square with error bars shows the theoretical relation from Nardetto et al. (2009), the open triangle the Hindsley & Bell (1986) relation and the filled circle the best fit. The open square shows the theoretical constraint shifted in β to comply with the HST parallax values.

In Table 5 we have listed the stars with parallax distances from Benedict et al. (2002, 2007). For each pair (α_p, β_p) we have determined the IRSB distance, d(IRSB), to these stars and computed the difference $\Delta(d) = d(\mathrm{HST}) - d(\mathrm{IRSB})$. To weight the points independently of distance, we have normalized the values by dividing by the average distance, $d_{\mathrm{avg}} = (d(\mathrm{HST}) + d(\mathrm{IRSB}))/2.$, before computing the offset $\Delta(d)/d_{\mathrm{avg}}$. We then took the mean value of these offsets and determined the values in the $\beta_p - \alpha_p$ plane where this mean offset is zero. This is a straight line which is shown in Fig. 6 as a full line with the two thin parallel lines showing the estimated 1-σ interval.

We then turn to the LMC data set and proceed as for the Milky Way sample and carry out the IRSB analysis for the same set of (α_p, β_p) values. We then look for the points where the slope of the LMC distance modulus as a function of log(P) is zero. For each individual Cepheid distance we apply the distance modulus correction $\Delta(m - M)$ from van der Marel & Cioni (2001) to correct for the inclination of the LMC disk before determining the slope. In the β_p, α_p plane the resulting constraint is shown as a dashed line and the two thin dashed lines indicate the estimated 1-σ interval.

The best estimate is:

$$p = 1.550(\pm 0.04) - 0.186(\pm 0.06) \log P. \quad (7)$$

This is shown as a filled circle in Fig. 6. The p-factor law is even a bit steeper with period than the relation which we found earlier (Gieren et al. 2005) and it differs even more from the recent theoretical relation from Nardetto et al. (2009) which is shown as a filled square in Fig. 6. For reference the relation from Hindsley & Bell (1986) has been plotted as an open triangle in the figure. It agrees within one σ with the HST parallax constraint but not with the constraints from the period dependence for the LMC sample. Additionally, the open square shows a relation where we have adopted the slope $\alpha_p = -0.08$ from Nardetto et al. (2009) but forced the zero point, β_p, to give agreement with the HST parallaxes.

We can look at the problem in a slightly different way and determine the p-factor for each of the Cepheids with measured HST parallax distances, and plot them as a function of log(P) by forcing the IRSB distance to be equal to the parallax distance. We have done this and show the results in Fig. 7. A linear fit to these values gives $p = -0.28(\pm 0.08) \log(P) + 1.65(\pm 0.07)$. Within the errors this agrees with our relation (Eq. (7)). We prefer, however, to use the relation in Eq. (7) as it is based on many more stars, especially at pulsation periods longer than ten days. The linear fit is shown in the figure as well as our adopted relation (labelled LMC and HST ZP) and the Hindsley & Bell (1986) and Nardetto et al. (2009) relations. The horizontal line at

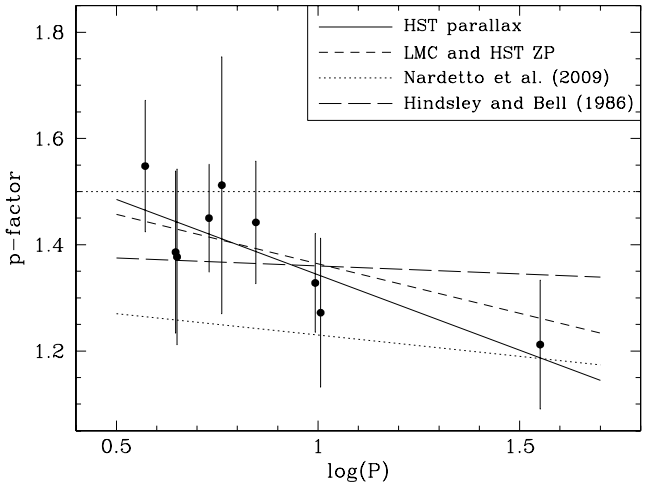


Fig. 7. The p-factor values derived for each of the HST parallax Cepheids with the only constraint being that the IRSB distance should agree with the parallax distance. The full line shows the linear regression fit to the points. The line labelled "LMC and HST ZP" shows our adopted relation based on the constraints from the LMC Cepheids and forcing the distance zero point to agree with the HST parallax values. The stippled line delineates the theoretical relation from Nardetto et al. (2009) and the long dashed line the classical Hindsley & Bell (1986) relation. The horizontal line at $p = 1.5$ shows the physical limit above which the theoretical p-factor would indicate an unphysical limb-brightening.

Table 6. Derived quantities for different adopted p-factor relations, $p = \beta_p + \alpha_p \log P$, for the LMC (LMC), and Milky Way (MW) samples.

α_p	−0.03	−0.08	−0.08	−0.186
β_p	1.39	1.31	1.455	1.550
Parameter				
$(m-M)_0$(LMC)	18.50 ± 0.04	18.26 ± 0.04	18.50 ± 0.04	18.45 ± 0.04
$(m-M)_0$(LMC) slope	0.31 ± 0.10	0.22 ± 0.10	0.24 ± 0.10	0.00 ± 0.10
Δd (pc)	−5 ± 11	−40 ± 9	0 ± 10	0 ± 7
$\Delta d/d_{\rm avg}$	−0.02 ± 0.02	−0.11 ± 0.02	0.00 ± 0.02	0.00 ± 0.02
a_K	−3.58 ± 0.09	−3.49 ± 0.08	−3.50 ± 0.09	−3.33 ± 0.09
b_K	−5.65 ± 0.03	−5.45 ± 0.03	−5.67 ± 0.03	−5.66 ± 0.03
a_V	−2.92 ± 0.10	−2.83 ± 0.10	−2.84 ± 0.10	−2.67 ± 0.10
b_V	−3.95 ± 0.03	−3.73 ± 0.03	−3.97 ± 0.03	−3.96 ± 0.03
a_{Wvi}	−3.51 ± 0.11	−3.42 ± 0.12	−3.43 ± 0.11	−3.26 ± 0.12
b_{Wvi}	−5.95 ± 0.04	−5.74 ± 0.04	−5.97 ± 0.04	−5.96 ± 0.04
a_{Wjk}	−3.69 ± 0.10	−3.60 ± 0.10	−3.61 ± 0.09	−3.44 ± 0.09
b_{Wjk}	−5.95 ± 0.03	−5.74 ± 0.03	−5.98 ± 0.03	−5.96 ± 0.03

Notes. Each column corresponds to a different p-factor relation where the slope and zero point are given in the first two rows. The PL relations are of the form $M_m = a_m \times (\log(P) - 1.0) + b_m$ where the index m refers to the photometric band.

$p = 1.5$ indicates the limit above which the p-factor would imply an unphysical limb-brightening instead of the expected limb-darkening. We note that for the short period stars the p-factor is coming close to this limit.

In Table 6 we have summarized the resulting values of true LMC modulus, the distance offset to the HST parallax data, the slope of the LMC Cepheid moduli as a function of period, for the different assumed p-factor relations. From this Table we can see that the Hindsley & Bell (1986) relation leads to more than 2σ deviation for the slope of the LMC distance modulus and thus seems to be ruled out. The Nardetto et al. (2009) relation disagrees on both the constraints, and seems to be ruled out as well. Changing the value of β_p to $\beta_p = 1.455$ brings the distance zero point into agreement with the HST parallax value, but still the distances to the LMC Cepheids are significantly dependent on the pulsation period. We thus adopt the fitted relation from Eq. (7) in the following.

In Fig. 8 we have plotted the distance difference between the HST parallax distances and our IRSB based distance when using the revised p-factor relation. We note that the scatter is very small and that the data are consistent with no period dependence of the differences.

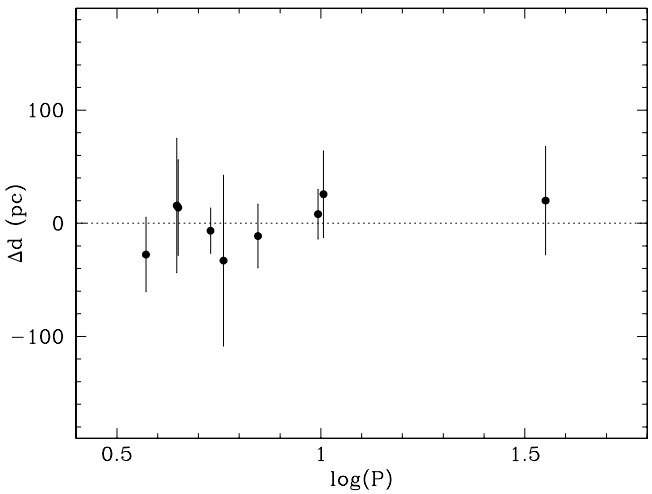


Fig. 8. The difference between the geometrical parallax distance measures for nine Cepheids from Benedict et al. (2007) and the IRSB distances values, plotted as a function of $\log P$. The revised p-factor relation determined in this paper has been used to calculate the IRSB distances to the stars.

3.5. The period-luminosity relations

Using the p-factor relation derived in the previous section together with the reddenings discussed in Sect. 3.2 we obtain the distances and absolute magnitudes for our Milky Way Cepheids as given in Table 7. In that Table we present the adopted pulsation period as well as the distance modulus with the formal uncertainty from our OLS bi-sector fit (see Storm et al. 2004, for details). As discussed by Barnes et al. (2005) these uncertainties are underestimated by on average a factor of 3.4 when compared to the uncertainties returned by the Bayesian fitting technique employed in that paper. In the columns 7 to 12 we give the absolute magnitudes in the $B, V, I, J, H, \& K$ bands and in Cols. 13 and 14 we give the Wesenheit indices (Madore 1982) in the $(V-I)$ band defined as $W_{VI} = M_V - 2.54(M_V - M_I)$ and in the near-IR J and K band, $W_{JK} = M_K - 0.688(M_J - M_K)$. In Col. 15 we give the adopted reddening value and in Col. 16 the adopted phase shift between the radial velocity data and the photometric data (see Storm et al. 2004, for details).

Using the data from Table 7 for the fundamental mode pulsators, and after eliminating the binary Cepheid W Sgr which exhibits a very poor IRSB fit, we are ready to determine the PL relations in the different bands. In Table 8 we list the resulting relations together with the observed dispersions around the fits. These are our best estimates of the Milky Way Cepheid PL relations. In Fig. 9 we plot the PL relations in the K, and V bands as well as in the Wesenheit indices W_{VI} and W_{JK}. We note that the dispersion around the fits range between 0.22 and 0.39 mag, the B-band relation showing a significantly larger dispersion than the others. For the other bands the dispersion is only weakly dependent on the wavelength suggesting that the errors on the absolute magnitudes are dominated by the distance errors rather

Table 7. Distances and intensity-averaged absolute magnitudes for the complete sample of Milky Way Cepheids based on the IRSB method as calibrated in this paper.

(1) ID	(2) $\log P$	(3) d (pc)	(4) $\sigma(d)$ (pc)	(5) $(m-M)_0$ (mag)	(6) $\sigma_{(m-M)}$ (mag)	(7) M_B (mag)	(8) M_V (mag)	(9) M_I (mag)	(10) M_J (mag)	(11) M_H (mag)	(12) M_K (mag)	(13) W_{VI} (mag)	(14) W_{JK} (mag)	(15) $E(B-V)$ (mag)	(16) $\Delta\phi$
SU Cas	0.289884	418	12	8.10	0.06	−2.53	−2.97	−3.52	−3.82	−4.05	−4.08	−4.37	−4.25	0.259	0.000
DT Cyg	0.397804	621	30	8.97	0.11	−2.82	−3.32	−3.87	−4.25	−4.51	−4.54	−4.71	−4.75	0.040	0.030
EV Sct	0.490098	1766	82	11.24	0.10	−2.72	−3.21	−3.90	−4.19	−4.45	−4.46	−4.97	−4.64	0.655	0.045
SZ Tau	0.498166	558	6	8.73	0.02	−2.62	−3.16	−3.80	−4.18	−4.49	−4.53	−4.78	−4.77	0.295	−0.005
SS Sct	0.564814	1000	33	10.00	0.07	−2.21	−2.83	−3.55	−3.92	−4.24	−4.27	−4.65	−4.51	0.325	−0.035
RT Aur	0.571489	389	4	7.95	0.02	−2.16	−2.69	−3.30	−3.75	−4.01	−4.05	−4.23	−4.26	0.059	0.005
QZ Nor	0.578244	1346	38	10.64	0.06	−2.00	−2.62		−3.76	−4.07	−4.12		−4.38	0.263	0.020
SU Cyg	0.584952	909	21	9.79	0.05	−2.77	−3.24	−3.79	−4.17	−4.45	−4.50	−4.64	−4.73	0.098	0.000
BF Oph	0.609329	708	10	9.25	0.03	−2.04	−2.67	−3.35	−3.77	−4.10	−4.16	−4.39	−4.43	0.235	0.030
Y Lac	0.635863	2430	35	11.93	0.03	−2.97	−3.48	−4.08	−4.43	−4.74	−4.79	−4.99	−5.04	0.217	−0.005
T Vul	0.646934	543	5	8.67	0.02	−2.54	−3.12	−3.74	−4.13	−4.44	−4.50	−4.70	−4.75	0.060	0.020
FF Aql	0.650390	369	11	7.84	0.06	−2.54	−3.10	−3.72	−4.10	−4.38	−4.42	−4.68	−4.63	0.196	−0.030
T Vel	0.666501	1002	11	10.00	0.02	−2.28	−2.91		−4.05	−4.40	−4.47		−4.76	0.289	0.000
VZ Cyg	0.687034	1897	35	11.39	0.04	−2.68	−3.29	−3.98	−4.36	−4.68	−4.74	−5.04	−5.01	0.266	0.035
V350 Sgr	0.712165	990	23	9.98	0.05	−2.86	−3.47	−4.15	−4.55	−4.89	−4.93	−5.20	−5.19	0.299	0.000
BG Lac	0.726883	1776	26	11.25	0.03	−2.68	−3.33	−4.05	−4.42	−4.76	−4.82	−5.16	−5.09	0.300	0.005
δ Cep	0.729678	267	5	7.13	0.04	−2.83	−3.41	−4.07	−4.45	−4.78	−4.84	−5.08	−5.11	0.072	0.000
CV Mon	0.730685	1547	24	10.95	0.03	−2.40	−2.97	−3.75	−4.22	−4.58	−4.65	−4.94	−4.94	0.722	0.020
X Lac	0.735997	1852	38	11.34	0.04	−3.45	−4.02	−4.68	−5.05	−5.38	−5.42	−5.70	−5.68	0.336	0.040
V Cen	0.739882	643	20	9.04	0.07	−2.58	−3.16	−3.82	−4.25	−4.58	−4.65	−4.85	−4.93	0.294	0.000
Y Sgr	0.761428	437	15	8.20	0.07	−2.40	−3.07	−3.78	−4.25	−4.61	−4.67	−4.87	−4.95	0.188	−0.030
CS Vel	0.771201	3184	108	12.52	0.07	−2.59	−3.19		−4.37	−4.71	−4.78		−5.07	0.737	0.015
FM Aql	0.786342	1182	28	10.36	0.05	−3.31	−4.00	−4.80	−5.12	−5.47	−5.52	−6.05	−5.79	0.589	−0.010
XX Sgr	0.807815	1042	42	10.09	0.09	−2.33	−2.92	−3.65	−4.11	−4.44	−4.47	−4.77	−4.73	0.521	−0.025
BB Sgr	0.821971	868	13	9.69	0.03	−2.96	−3.66	−4.42	−4.86	−5.22	−5.29	−5.60	−5.59	0.281	0.000
V Car	0.825860	869	16	9.69	0.04	−2.16	−2.86		−4.04	−4.40	−4.47		−4.77	0.166	0.000
U Sgr	0.828997	579	6	8.81	0.02	−2.73	−3.42	−4.18	−4.61	−4.96	−5.02	−5.34	−5.30	0.402	0.000
V496 Aql	0.832958	829	26	9.59	0.07	−2.37	−3.12		−4.32	−4.68	−4.70		−4.96	0.397	−0.055
X Sgr	0.845893	322	5	7.54	0.04	−3.23	−3.74	−4.35	−4.75	−5.06	−5.11	−5.28	−5.36	0.237	0.000
U Aql	0.846591	592	19	8.86	0.07	−2.91	−3.58	−4.31	−4.72	−5.06	−5.11	−5.44	−5.38	0.360	0.015
η Aql	0.855930	255	4	7.03	0.09	−2.89	−3.55	−4.27	−4.70	−5.04	−5.10	−5.38	−5.38	0.129	0.000
W Sgr	0.880529	217	16	6.68	0.16	−1.73	−2.37	−3.03	−3.47	−3.80	−3.88	−4.05	−4.17	0.108	0.040
U Vul	0.902584	658	12	9.09	0.04	−3.22	−3.92	−4.73	−5.03	−5.34	−5.37	−6.00	−5.60	0.603	0.005
S Sge	0.923352	671	16	9.13	0.05	−3.13	−3.84	−4.55	−5.00	−5.34	−5.41	−5.66	−5.70	0.099	0.000
GH Lup	0.967448	1307	23	10.58	0.04	−3.21	−4.07	−4.90	−5.42	−5.82	−5.90	−6.18	−6.23	0.347	−0.040
FN Aql	0.976878	1175	20	10.35	0.04	−2.81	−3.53	−4.36	−4.75	−5.12	−5.17	−5.63	−5.46	0.486	−0.030
YZ Sgr	0.980171	1137	13	10.28	0.03	−3.10	−3.84		−5.07	−5.44	−5.49		−5.77	0.281	−0.010
S Mus	0.984980	858	17	9.67	0.04	−3.30	−3.98		−5.25	−5.62	−5.71		−6.02	0.140	0.010
S Nor	0.989194	950	11	9.89	0.02	−3.27	−4.04	−4.81	−5.33	−5.72	−5.79	−6.01	−6.12	0.179	0.000
β Dor	0.993131	327	5	7.57	0.03	−3.25	−4.00	−4.73	−5.18	−5.57	−5.63	−5.85	−5.94	0.051	0.000
ζ Gem	1.006497	386	9	7.93	0.05	−3.29	−4.13		−5.33	−5.74	−5.81		−6.13	0.014	0.050
TW Nor	1.032868	2190	105	11.70	0.10	−2.96	−3.74		−5.29	−5.68	−5.76		−6.08	1.157	0.015
Z Lac	1.036854	1879	42	11.37	0.05	−3.42	−4.15	−4.95	−5.37	−5.76	−5.82	−6.18	−6.13	0.370	0.000
XX Cen	1.039548	1586	19	11.00	0.03	−3.35	−4.06	−4.80	−5.26	−5.63	−5.70	−5.94	−6.00	0.271	−0.030
V340 Nor	1.052579	1738	80	11.20	0.10		−3.87		−5.23	−5.66	−5.74		−6.08	0.322	−0.035
UU Mus	1.065819	3146	132	12.49	0.09	−3.26	−4.00	−4.79	−5.34	−5.74	−5.82	−6.02	−6.14	0.404	0.005
U Nor	1.101875	1289	39	10.55	0.07	−3.34	−4.08	−4.88	−5.43	−5.82	−5.89	−6.13	−6.21	0.857	0.000
SU Cru	1.108822	1274	87	10.53	0.15	−3.04	−3.80		−5.41	−6.05	−6.15		−6.66	0.952	0.010
BN Pup	1.135867	3817	82	12.91	0.05	−3.60	−4.37	−5.17	−5.67	−6.08	−6.15	−6.41	−6.48	0.416	0.020
TT Aql	1.138459	968	15	9.93	0.03	−3.33	−4.20	−5.11	−5.57	−5.98	−6.04	−6.51	−6.36	0.435	0.005
LS Pup	1.150646	4819	113	13.41	0.05	−3.69	−4.46	−5.25	−5.76	−6.17	−6.23	−6.47	−6.56	0.462	−0.030
VW Cen	1.177138	3417	68	12.67	0.04	−2.94	−3.84	−4.76	−5.43	−5.91	−6.01	−6.19	−6.42	0.439	0.000
X Cyg	1.214482	1127	8	10.26	0.02	−3.69	−4.62	−5.48	−6.00	−6.43	−6.53	−6.82	−6.89	0.228	0.000
CD Cyg	1.232334	2427	45	11.93	0.04	−3.79	−4.57	−5.45	−5.93	−6.33	−6.40	−6.80	−6.72	0.493	0.000
Y Oph	1.233609	548	6	8.70	0.03	−3.90	−4.62	−5.44	−5.87	−6.21	−6.26	−6.71	−6.53	0.647	0.020
SZ Aql	1.234029	2138	28	11.65	0.03	−3.88	−4.74	−5.68	−6.20	−6.62	−6.70	−7.13	−7.05	0.534	0.020
CT Car	1.256661	10422	224	15.09	0.05	−5.32	−4.71	−5.28	−6.16	−6.63	−6.74	−6.17	−7.14	0.570	0.000
VY Car	1.276818	1728	21	11.19	0.03	−3.57	−4.51	−5.38	−5.95	−6.38	−6.47	−6.74	−6.83	0.242	0.005
RU Sct	1.294480	1895	40	11.39	0.04	−4.12	−4.85	−5.81	−6.47	−6.61	−6.66	−7.29	−6.79	0.911	−0.010
RY Sco	1.307927	1128	16	10.26	0.03	−3.84	−4.56	−5.42	−5.94	−6.32	−6.39	−6.74	−6.70	0.718	0.000
RZ Vel	1.309564	1370	14	10.68	0.02	−3.74	−4.57	−5.41	−5.99	−6.40	−6.49	−6.71	−6.83	0.300	0.005
WZ Sgr	1.339443	1774	35	11.24	0.04	−3.66	−4.62	−5.60	−6.25	−6.74	−6.84	−7.12	−7.25	0.435	−0.015
WZ Car	1.361977	3538	108	12.74	0.07	−3.89	−4.68	−5.51	−6.09	−6.50	−6.58	−6.79	−6.92	0.372	0.000
VZ Pup	1.364945	4591	37	13.31	0.02	−4.45	−5.15	−5.91	−6.37	−6.75	−6.80	−7.07	−7.09	0.455	−0.075
SW Vel	1.370016	2554	34	12.04	0.03	−4.21	−5.02	−5.87	−6.43	−6.85	−6.94	−7.18	−7.29	0.344	−0.020
X Pup	1.414321	2720	24	12.17	0.02	−4.26	−5.03	−5.90	−6.39	−6.82	−6.88	−7.24	−7.22	0.421	−0.105
T Mon	1.431915	1309	19	10.59	0.03	−4.04	−5.04		−6.57	−7.04	−7.13		−7.52	0.179	0.000
RY Vel	1.449158	2336	36	11.84	0.03	−4.40	−5.23	−6.08	−6.66	−7.04	−7.12	−7.38	−7.44	0.545	0.000
KQ Sco	1.457818	2796	93	12.23	0.07	−4.16	−5.23	−6.28	−7.03	−7.52	−7.61	−7.91	−8.02	0.869	−0.015
AQ Pup	1.478624	3210	55	12.53	0.04	−4.65	−5.51	−6.42	−6.92	−7.35	−7.44	−7.82	−7.80	0.518	−0.245
KN Cen	1.531857	3586	78	12.77	0.05	−4.65	−5.47	−6.33	−7.00	−7.48	−7.58	−7.66	−7.98	0.791	0.005
ℓ Car	1.550816	518	5	8.57	0.02	−4.18	−5.32	−6.30	−6.94	−7.45	−7.53	−7.83	−7.94	0.146	−0.015
U Car	1.588970	1407	17	10.74	0.03	−4.39	−5.30	−6.20	−6.80	−7.23	−7.32	−7.59	−7.68	0.263	−0.025
RS Pup	1.617420	1810	30	11.29	0.04	−4.78	−5.76	−6.70	−7.28	−7.73	−7.82	−8.15	−8.19	0.457	0.035
SV Vul	1.652569	1895	15	11.39	0.02	−4.64	−5.67	−6.63	−7.16	−7.57	−7.62	−8.11	−7.93	0.462	0.000
GY Sge	1.708102	2869	34	12.29	0.03	−5.39	−6.36		−7.80	−8.17	−8.19		−8.46	1.310	−0.025
S Vul	1.837426	3762	59	12.88	0.03	−5.36	−6.46		−8.08	−8.51	−8.57		−8.91	0.787	0.050

Notes. The σ values are the nominal values returned by the bi-sector fitting algorithm. The Wesenheit indices based on the (V, I) and (J, K) photometry are given as well as the adopted reddening. The last column gives the adopted phase shift, $\Delta\phi$, between spectroscopic and photometric data.

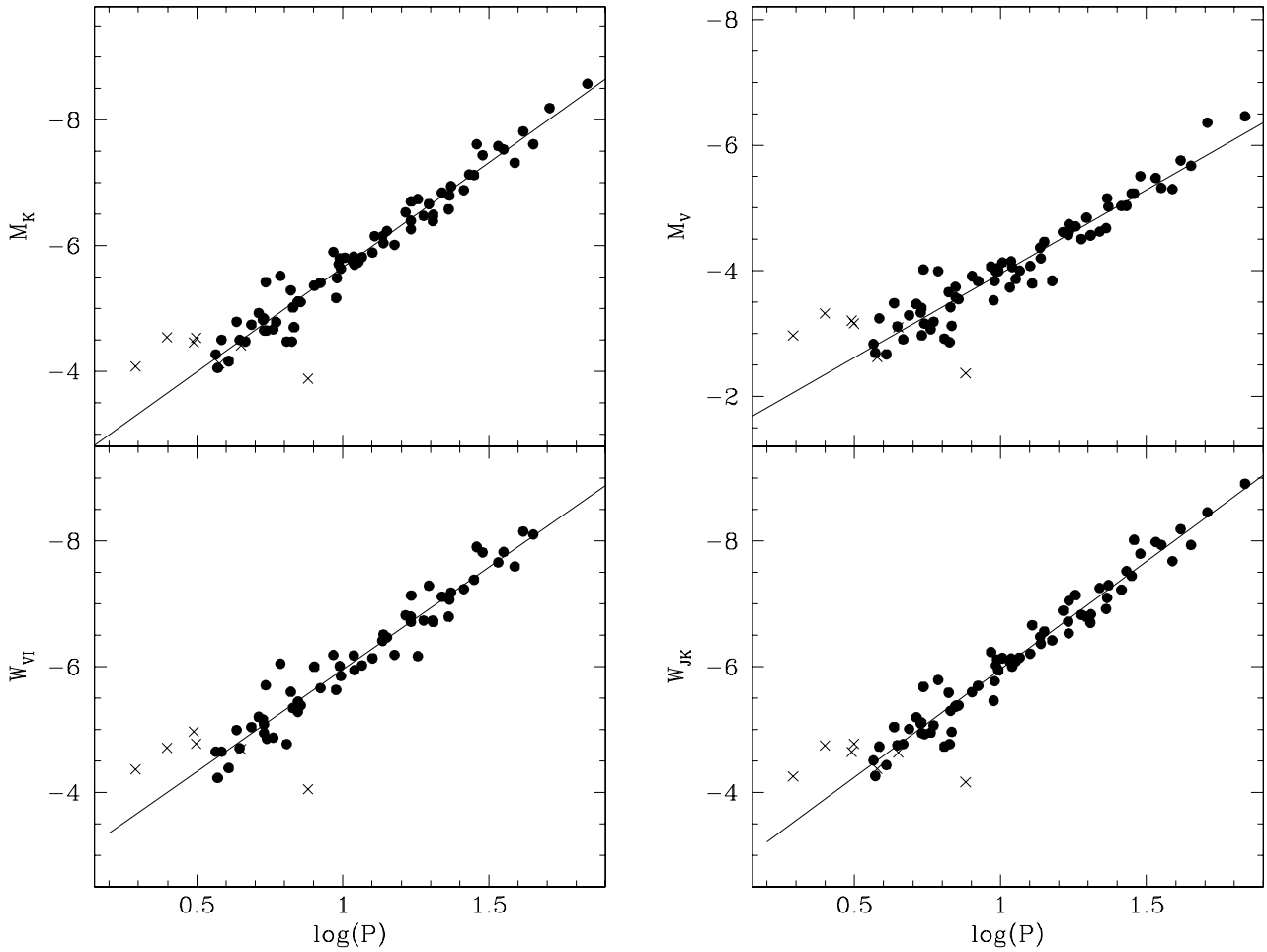


Fig. 9. The period-luminosity relations based on the IRSB luminosities for our sample of Milky Way Cepheids in the K- and V-bands as well as in the Wesenheits indices. The filled circles represent the fundamental mode Cepheids, and the crosses indicate stars which have been disregarded in the linear regression for reasons mentioned in the text.

Table 8. Period-luminosity relations for the Milky Way Cepheids of the form $M = a \times (\log(P) - 1.0) + b$.

Band	a	b	σ
M_B	-2.13 ± 0.13	-3.28 ± 0.05	0.39
M_V	-2.67 ± 0.10	-3.96 ± 0.03	0.26
M_I	-2.81 ± 0.10	-4.76 ± 0.03	0.23
W_{VI}	-3.26 ± 0.11	-5.96 ± 0.04	0.26
M_J	-3.18 ± 0.09	-5.22 ± 0.03	0.22
M_H	-3.30 ± 0.08	-5.59 ± 0.03	0.22
M_K	-3.33 ± 0.09	-5.66 ± 0.03	0.22
W_{JK}	-3.44 ± 0.09	-5.96 ± 0.03	0.23

Notes. The dispersion around the fit is also tabulated as well as the formal uncertainties on the coefficients as returned from the linear regression.

than by the intrinsic width of the PL relation and/or errors in the absorption corrections. We note that Persson et al. (2004) found a dispersion of only 0.11 mag for the K-band relation in the LMC whereas in Paper II we have obtained a value of 0.22 mag, again suggesting that the dispersion in our current work is dominated by distance errors rather than intrinsic luminosity variations between Cepheids of similar periods in the sample due to the finite width of the instability strip, or errors in the reddenings.

3.6. The combined sample

In Paper II we show that the PL relations for the Milky Way and Large Magellanic Cloud samples are identical within the uncertainties, particularly in the near-IR bands. This means that we can combine the data from the two papers to derive a PL relation based on a total of 111 Cepheids. In Fig. 10 we have plotted the K-band absolute magnitudes for the Milky Way, LMC and SMC Cepheids from the two papers together. The agreement is excellent, and a linear regression to the combined sample leads to a best determination for the K-band PL relation of:

$$M_K = -3.30(\pm 0.06)(\log P - 1.0) - 5.65(\pm 0.02) \quad (8)$$

with a dispersion of 0.22 mag. Due to the limited metallicity dependence of this relation found in Paper II, this relation can be directly used for distance determination to galaxies with metallicities between SMC and solar.

We have listed the combined relations in the other bands, including the Wesenheit indices in Table 9, in all cases without applying any metallicity corrections to the absolute magnitudes. The relations have been used in Paper II to determine the PL relation zero-point dependence on metallicity, γ, and for convenience we have tabulated those values here as well.

Table 9. The period-luminosity relations based on the combined samples of Milky Way, LMC and SMC Cepheids in the form $M = a(\log(P) - 1.0) + b$.

Band	a (mag dex^{-1})	b (mag)	Std.dev. (mag)	γ (mag dex^{-1})
M_V	-2.73 ± 0.07	-3.97 ± 0.03	0.26	+0.09
M_I	-2.91 ± 0.07	-4.75 ± 0.02	0.23	−0.06
W_{VI}	-3.32 ± 0.08	-5.92 ± 0.03	0.26	−0.23
M_J	-3.19 ± 0.06	-5.20 ± 0.02	0.22	−0.10
M_K	-3.30 ± 0.06	-5.65 ± 0.02	0.22	−0.11
W_{JK}	-3.38 ± 0.06	-5.96 ± 0.02	0.23	−0.10

Notes. The metallicity effect, γ, on the zero point determined in Paper II is given in the last column. The estimated uncertainty on the γ value is estimated to be 0.10 mag dex^{-1} in Paper II.

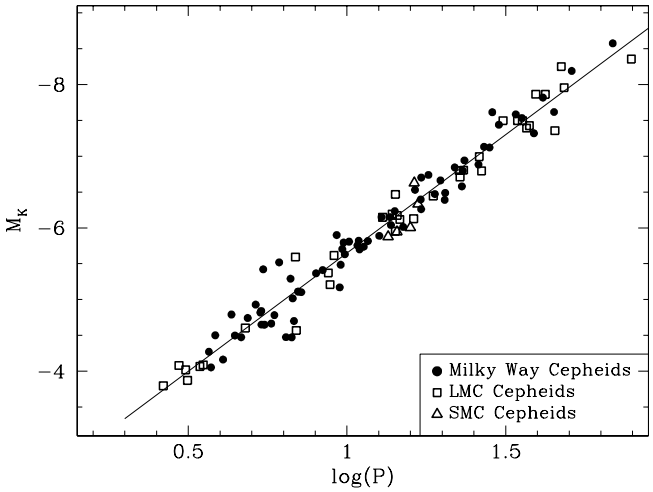


Fig. 10. The period-luminosity relation in the K-band for the complete sample of Milky Way, LMC and SMC Cepheids having IRSB-determined distances in our papers. The overtone pulsators and stars which have been eliminated for other reasons as discussed earlier have been eliminated from the plot for clarity.

4. Discussion

The slopes of the PL relations which we find depend directly on the adopted p-factor relation and as we have shown the revised, empirically-determined relation is necessary to give pulsation period-independent distances to LMC Cepheids. In Paper II we further show that the adopted p-factor relation also reproduces the slopes of the apparent magnitude versus $\log(P)$ relations both in the near-IR and in the optical bands. The revised p-factor relation confirms our earlier findings (Gieren et al. 2005) based on a much smaller sample of LMC Cepheids. Still, it is at odds with the recent careful theoretical study by Nardetto et al. (2009). We do not have a ready explanation for this disagreement but suspect that it is either due to some missing physics in the theoretical approach or some previously undetected period dependence in the IRSB method, which we have eliminated through the parametrization chosen here. If the problem does not originate from the pulsational velocities, i.e. with the p-factor, it would have to originate with the surface-brightness calibration. The calibration is based on mostly short period Cepheids with only a single long period (35 days) Cepheid. However, Kervella et al. (2004b) show a quite convincing comparison of surface-brightness relations for short and long period stars and the fact that the relation agrees well with the relation for static stars is also suggestive that the cause for the steep slope is not buried here. The remaining problem seems to be with the short period stars where the revised p-factor relation leads to values which get close to 1.5, suggesting a uniform disk and no limb-darkening. However, the short period stars are the ones which are most numerous in the sample used by Kervella et al. (2004b) and thus the ones which have the best empirical constraints. Still we intend to make direct comparisons with interferometric studies as done by Kervella et al. (2004c) for ℓ Car in an attempt to understand the reason for the effect which we see. For our main purpose of investigating the effect of metallicity on the Cepheid PL relation by comparing Milky Way and Magellanic Cloud Cepheids we are working in a *purely differential* way so the actual p-factor relation cancels out as long as it is the same for both samples of stars, i.e. metal independent, which from theoretical considerations seems to be a good assumption (Nardetto et al. 2011).

Groenewegen (2007) argues for a constant p-factor relation based on a comparison with a subset of the HST parallax stars but the scatter in his Fig. 2 is very large. With our new high precision radial velocity data for three of the HST parallax stars, we confirm our p-factor relation (see Fig. 7) through excellent agreement with the full set of Benedict et al. (2007) results on a star by star basis. We also base our p-factor relation on a much larger sample of LMC Cepheids. This sample has a large number of stars with pulsation periods significantly longer than ten days, thus forming a much firmer basis for constraining the p-factor relation. In a following paper, Groenewegen (2008) discusses the use of the Nardetto et al. (2007) relation and finds no significant difference to a constant value. At the same time he finds period-luminosity relations for Milky Way Cepheids which are very similar to the relations presented in the previous section. He finds in the K-band a relation with a slope of -3.38 ± 0.08, in good agreement with our value of -3.33 ± 0.09, similarly he finds a slope in the V-band of -2.60 ± 0.09 whereas we find a value of -2.67 ± 0.10. It thus seems as if, in spite of the fact that we apply the same method, there are significant differences in the implementation of the technique which might affect the results.

Recently Molinaro et al. (2011), based on the CORS variant of the Baade-Wesselink method and using Walraven photometry for 26 galactic Cepheids and a constant p-factor of 1.27, found a PL relation of $M_V = -2.78(\pm0.11)\log(P) - 1.42(\pm0.11)$. Again the slope is in good agreement with our relation whereas the zero point at a period of ten days differs by 0.23 mag, our value being fainter.

There are presently very few alternative routes to delineating the Milky Way PL relation apart from the Baade-Wesselink type methods. There is of course the recent direct parallaxes to ten Cepheids with the HST fine guidance sensors by Benedict et al. (2007), but this constitutes a modest sample of stars for a PL relation. The classical approach is the zero-age main sequence (ZAMS) fitting to OB associations and open clusters containing Cepheids (see e.g. Feast & Walker 1987, and references therein). Turner (2010) rederived the Milky Way PL relation based on the ZAMS fitting to OB associations and open clusters containing Cepheids finding $M_V = -2.78(\pm0.12)\log(P) - 1.29(\pm0.10)$. In Fig. 11 we compare the ZAMS fitting based distance moduli with the IRSB based moduli for the stars in common, and we find very good agreement with no significant period dependence. The unweighted mean difference is 0.12 ± 0.06 mag so we do find a slight zero point offset. We have excluded the star SU Cas in the comparison as it is an outlier, even if the IRSB fit appears well defined and does not indicate any obvious problem with the data.

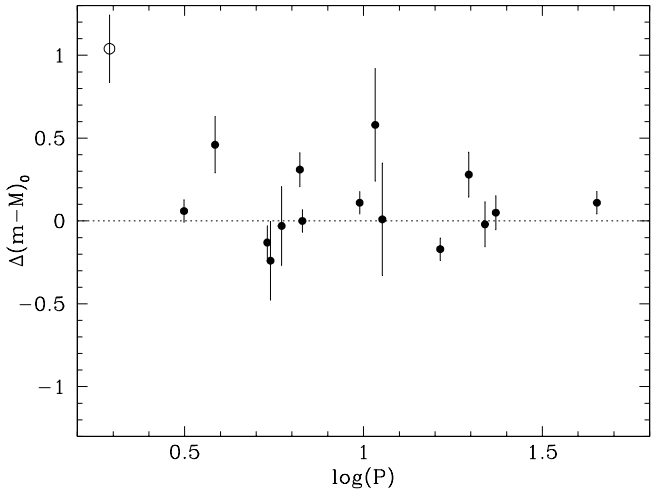


Fig. 11. The difference in derived distance modulus $\Delta(m-M) = (m-M)_{\rm ZAMS} - (m-M)_{\rm IRSB}$. The open symbol shows the star SU Cas which has been disregarded in the comparison.

Benedict et al. (2007) found a slope of -2.43 ± 0.12 in the V band from the HST parallax measurements, a value which is only slightly shallower than our value of -2.67 ± 0.10 and certainly not steeper than our value.

We argue that most recent investigations agree to within the errors with the slope of our relation and they disagree with the earlier findings of Sandage et al. (2004) and Storm et al. (2004), that the Milky Way PL relations are significantly steeper than the LMC relations. In fact, in Paper II we find that if anything the optical Milky Way PL relations might be slightly shallower than the LMC relations.

In Paper II we find that both the slopes and the zero-points of the near-IR PL relations are insensitive to metallicity. In addition the K-band PL relation is very insensitive to reddening making this relation our preferred standard candle. We argue that the best calibration of this relation is the combined K-band PL relation given in Table 9 with the small metallicity effect of $\gamma = -0.10 \pm 0.10$ mag dex^{-1} also given in that table. We note that for most extra-galactic Cepheid samples the metallicity is close to the range from LMC to solar and the failure to correct for the metallicity effect leads to systematic errors of the order of only 0.02 mag in the distance modulus.

In the optical bands, the LMC and Milky Way slopes are less in agreement differing by up to 0.2 mag dex^{-1} as shown in Paper II. However in the compilation by Bono et al. (2010) the slopes in the V and I bands for extra-galactic samples show a large spread of the order 1 mag dex^{-1}, much larger than our observed difference between the LMC and Milky Way samples. The slope variations in that paper do not seem to be strongly correlated with metallicity variations so from that point of view our combined SMC, LMC, MW relation also provides the better reference relation as it is based on more stars.

5. Conclusions and summary

We have obtained new, accurate, radial velocity curves for fourteen Milky Way Cepheids including three Cepheids with direct parallax measures from Benedict et al. (2007), expanding the sample of Milky Way fundamental mode Cepheids to which we can determine precise IRSB distances to a total of 70 stars.

We have empirically redetermined the p-factor relation, which converts the observed radial velocities into pulsation velocities needed for the IRSB method, using two fundamental physical constraints. The first constraint is that the distance to LMC Cepheids should be independent of their pulsation periods, and the second constraint is that on average we should reproduce the distances to the Cepheids with parallaxes from Benedict et al. (2007). We find quite a steep relation, $p = 1.550(\pm0.04) - 0.186(\pm0.06)\log(P)$ which is not easily reconciled with recent theoretical work (e.g. Nardetto et al. 2009). However, this revised relation gives rise to PL relations which are in excellent agreement with other independent determinations both for the Milky Way, as shown in the present paper, and for the LMC, as shown in Paper II.

Using the revised p-factor relation we have determined precise PL relations in the $V, I, J,$ & K bands, as well as the Wesenheit indices W_{VI} , & W_{JK} for these Milky Way stars. These relations can be used for distance determination to other galaxies with solar abundance.

In Paper II we compared these relations to similar relations for a sample of LMC Cepheids and we found that the effect of metallicity on the slopes is negligible in the near-IR and small, possibly consistent with zero, in the optical bands as well. Including also a sample of SMC Cepheids we find that the zero points of the PL relations depend on metallicity to a varying degree, but in most bands the effect is small, of the order -0.10 ± 0.10 mag dex^{-1}, which is consistent with a zero effect. Consequently we argue that it is warranted to combine the three samples of Cepheids giving us a total sample of 111 Cepheids with IRSB distances which can be used to delineate accurate absolute, universal PL relations.

Our best standard candle is the K-band PL relation as it is not only insensitive to reddening and shows a low intrinsic dispersion, but it also exhibits no metallicity dependence on the slope and only a weak dependence on the zero point consistent with a null effect. The K-band relation based on the full sample of Cepheids presented here is $M_K = -3.30(\pm0.06)[\log(P) - 1.0] - 5.65(\pm0.02)$. The combined relation in the optical W_{VI} index is $W_{VI} = -3.32(\pm0.08)[\log(P) - 1.0] - 5.92(\pm0.03)$.

Acknowledgements. This research has made use of the SIMBAD database, operated at CDS, Strasbourg, France. STELLA is funded by AIP through the State of Brandenburg and the Federal Ministry for Education and Science in Germany. It is operated jointly by AIP and the Instituto de Astrofisica de Canarias (IAC) at the Teide Observatory of the IAC. The authors thank the staff of the IAC for their great and continuous support to run STELLA. WG and GP gratefully acknowledge financial support for this work from the Chilean Center for Astrophysics FONDAP 15010003, and from the BASAL Centro de Astrofisica y Tecnologias Afines (CATA) PFB-06/2007.

References

Barnes, T. G., & Evans, D. S. 1976, MNRAS, 174, 489
Barnes, T. G., Moffett, T. J., & Slovak, M. H. 1988, ApJS, 66, 43
Barnes, T. G., Fernley, J. A., Frueh, M. L., et al. 1997, PASP, 109, 645
Barnes, T. G., Jeffery, E. J., Montemayor, T. J., & Skillen, I. 2005a, ApJS, 156, 227
Barnes, T. G., Storm, J., Jefferys, W. H., Gieren, W. P., & Fouqué, P. 2005b, ApJ, 631, 572
Benedict, G. F., McArthur, B. E., Fredrick, L. W., et al. 2002, AJ, 124, 1695
Benedict, G. F., McArthur, B. E., Feast, M. W., et al. 2007, AJ, 133, 1810
Berdnikov, L. N. 1986, Variable Stars, 22, 369
Berdnikov, L. N. 1987, Variable Stars, 22, 530
Berdnikov, L. N. 1992a, A&A Transactions, 2, 1
Berdnikov, L. N. 1992b, A&A Transactions, 2, 31
Berdnikov, L. N. 1992c, A&A Transactions, 2, 43
Berdnikov, L. N. 1992d, Pisma V. Astron. Zhurnal, 18, 325
Berdnikov, L. N. 1992e, Pisma V. Astron. Zhurnal, 19, 210
Berdnikov, L. N., & Caldwell, J. A.R. 2001, J. Astr. Data, 7, 3
Berdnikov, L. N., & Turner, D. G. 1995, Pisma V. Astron. Zhurnal, 21, 803

Berdnikov, L. N., & Turner, D. G. 1998, A&A Transactions, 16, 291
Berdnikov, L. N., & Turner, D. G. 2000, A&A Transactions, 18, 657
Bersier, D. 2002, ApJS, 140, 465
Bersier, D., Burki, G., & Burnet, M. 1994a, A&AS, 108, 9
Bersier, D., Burki, G., Mayor, M., & Duquennoy, A. 1994b, A&AS, 108, 25
Bono, G., Caputo, F., Marconi, M., & Musella, I. 2010, ApJ, 715, 277
Butler R. P., & Bell R. A. 1997, ApJ, 480, 767
Caldwell, J. A. R., Coulson, I. M., Dean, J. F., & Berdnikov, L. N. 2001, J. Astr. Data, 7, 4
Cardelli, J. A., Clayton, G. C., & Mathis, J. S. 1989, ApJ, 345, 245
Carter, B. S. 1990, MNRAS, 242, 1
Coulson, I. M., & Caldwell, J. A. R. 1985, SAAO Circulars, 9, 5
Coulson, I. M., Caldwell, J. A. R., & Gieren, W. P. 1985, ApJS, 57, 595
Evans, N. R. 1990, PASP, 102, 551
Evans, N. R., Welch, D. L., Scarfe, C. D., & Teays, T. J. 1990, AJ, 99, 1598
Feast, M. W., & Walker, A. R. 1987, ARA&A, 25, 345
Feast, M. W., Laney, C. D., Kinman, T. D., van Leeuwen, F., & Whitelock, P. A. 2008, MNRAS, 386, 2115
Fernie, J. D., Beattie, B., Evans, N. R., & Seager, S. 1995, IBVS No. 4148
Fouqué, P., & Gieren, W. P. 1997, A&A, 320, 799
Fouqué, P., Arriagada, P., Storm, J., et al. 2007, A&A, 476, 73
Gieren, W. P. 1976, A&A, 47, 211
Gieren, W. P. 1981a, ApJS, 46, 287
Gieren, W. P. 1981b, ApJS, 47, 315
Gieren, W. 1982, PASP, 94, 960
Gieren, W. P., Barnes, T. G., & Moffett, T. J. 1993, ApJ, 418, 135
Gieren, W., Storm, J. Barnes, T. G., et al. 2005, ApJ, 627, 224
Gorynya, N. A., Samus', N. N., Sachkov, M. E., et al. 1998, AstL, 24, 815
Groenewegen, M. A. T. 2007, A&A, 474, 975
Groenewegen, M. A. T. 2008, A&A, 488, 25
Hindsley, R. B., & Bell, R. A. 1986, PASP, 98, 881
Imbert, M. 1984, A&AS, 58, 529
Imbert, M. 1996, A&AS, 116, 497
Imbert, M. 1999, A&AS, 14079
Isobe, T., Feigelson, E. D., Akritas, M. G., & Babu, G. J. 1990, ApJ, 364, 104
Kervella, P., Nardetto, N., Bersier, D., Mourard, D., & Coudé de Foresto, V. 2004a, A&A, 416, 941
Kervella, P., Bersier, D., Mourard, D., et al. 2004b, A&A, 428, 587
Kervella, P., Fouqué, P., Storm, J., et al. 2004c, ApJ, 604, L113
Kienzle, F., Moskalik, P., Bersier, D., & Pont, F. 1999, A&A, 341, 818
Kimeswenger, S., Lederle, C., Richichi, A., et al. 2004, A&A, 413, 1037
Kiss, L. L. 1998a, J. Astr. Data, 4, 3
Kiss, L. L. 1998b, MNRAS, 297, 825
Laney, C. D., & Caldwell, J. A.R. 2007, MNRAS, 377, 147
Laney, C. D., & Stobie, R.S; 1992, A&AS, 93, 93
Lloyd Evans, T. 1980, SAAO Circulars, 1, 257
Madore, B. F. 1975, ApJS, 29, 219
Madore, B. F. 1982, ApJ, 253, 575
Mathias, P., Gillet, D., Fokin, A. B., et al. 2006, A&A, 457, 575
McGonegal, R., McAlary, C. W., McLaren, R. A., & Madore, B. F. 1983, ApJ, 269, 641
Mérand, A., Kervella, P., Coudé du Foresto, V., et al. 2005, A&A, 438, L9
Metzger, M. R., Caldwell, J. A. R., McCarthy, J. K., & Schecter, P. L. 1991, ApJS, 76, 803
Metzger, M. R., Caldwell, J. A.R., & Schecter, P. L. 1992, AJ, 103, 529
Moffett, T. J., & Barnes, T. G. 1984, ApJS, 55, 389
Molinaro, R., Ripepi, V., Marconi, M., et al. 2011, MNRAS, 413, 942
Nardetto, N., Mourard, D., Kervella, P., et al. 2006, A&A, 453, 309
Nardetto, N., Mourard, D., Mathias, P., Fokin, A., & Gillet, D. 2007, A&A, 471, 661
Nardetto, N., Gieren, W., Kervella, P., et al. 2009, A&A, 502, 951
Nardetto, N., Fokin, A., Fouqué, P., et al. 2011, A&A, in press
Nordgren, T. E., Lane, B. F., Hindsley, R. B., & Kervella, P. 2002, AJ, 123, 3380
Ritter, A., & Wasshüttl, A. 2004, Astron. Nachr., 325, 663
Pel, J. W. 1976, A&AS, 24, 413
Persson, S. E., Madore, B. F., Krzemiński, W., et al. 2004, AJ, 128, 2239
Petersen, J. O. 1986, A&A, 170, 59
Petterson, O. K. L., Cottrell, P. L., Albrow, M. D., & Fokin, A. 2005, MNRAS, 362, 1167
Pietrzyński, G., Thompson, I. B., Graczyk, D., et al. 2009, ApJ, 697, 862
Pont, F., Mayor, M., & Burki, G. 1994, A&A, 285, 415
Sabbey, C. N., Sasselov, D. D., Fieldus, M. S., et al. 1995, ApJ, 446, 250
Sandage, A., Tammann, G. A., & Reindl, B. 2004, A&A, 424, 43
Schechter, P. L., Avruch, I. M., Caldwell, J. A.R., & Keane, M. J. 1992, AJ, 104, 1930
Shobbrook, R. R. 1992, MNRAS, 255, 486
Storm, J., Carney, B. W., Gieren, W. P., et al. 2004, A&A, 415, 531
Storm, J., Gieren, W. P., Fouqué, P., et al. 2011, A&A, 534, A95. (Paper II)
Strassmeier, K. G., Granzer, T., Weber, M., et al. 2004, Astron. Nachr., 325, 527
Strassmeier, K. G., Granzer, T., Weber, M., et al. 2010, Adv. Astr., 19
Sugars, B. J. A., & Evans, N. R. 1996, AJ, 112, 1670
Szabados L. 2003, Inf. Bull. Var. Stars, No. 5394
Szewczyk, O., Pietrzyński, G., Gieren, W., et al. 2008, AJ, 136, 272
Tammann, G. A., Sandage, A., & Reindl, B. 2003, A&A, 404, 423
Turner, D. G. 2010, Astrophys. Space Sci., 326, 219
van der Marel, R. P., & Cioni, M.-R. L. 2001, AJ, 122, 1807
Wallerstein, G., Jacobsen, T. S., Cottrell, P. L., Clark, M., & Albrow, M. 1992, MNRAS, 259, 474
Walraven, J. H., Tinbergen, J., & Walraven, T. 1964, Bull. Astr. Netherlands, 17, 520
Weber, M., Granzer, T., Strassmeier, K., & Woche, M. 2008, Proc. SPIE, 7019, 70190L
Welch, D. L. 1985, Ph.D. Thesis, University of Toronto
Welch, D. L. 1994, AJ, 108, 1421
Welch, D. L., Wieland, F., McAlary, C. W., et al. 1984, ApJS, 54, 547
Welch, D. L., Evans, N. R., Lyons, R. W., et al. 1987, PASP, 99, 610
Wisniewski, W. Z., & Johnson, H. L. 1968, Comm. Lunar Planetary Lab., Tucson, 7, 57

Annexe H

Calibrating the Cepheid period-luminosity relation from the infrared surface brightness technique. II. The effect of metallicity and the distance to the LMC

A&A 534, A95 (2011)
DOI: 10.1051/0004-6361/201117154
© ESO 2011

Astronomy & Astrophysics

Calibrating the Cepheid period-luminosity relation from the infrared surface brightness technique

II. The effect of metallicity and the distance to the LMC⋆,⋆⋆

J. Storm[1], W. Gieren[2], P. Fouqué[3], T. G. Barnes[4], I. Soszyński[5], G. Pietrzyński[2,5], N. Nardetto[2,6], and D. Queloz[7]

[1] Leibniz-Institut für Astrophysik Potsdam (AIP), An der Sternwarte 16, 14482 Potsdam, Germany
e-mail: jstorm@aip.de
[2] Universidad de Concepción, Departamento Astronomía, Casilla 160-C, Concepción, Chile
[3] IRAP, Université de Toulouse, CNRS, 14 Av. E. Belin, 31400 Toulouse, France
[4] University of Texas at Austin, McDonald Observatory, 82 Mt. Locke Rd, McDonald Observatory, TX 79734, USA
[5] Warsaw University Observatory, Al. Ujazdowskie 4, 00-478 Warsaw, Poland
[6] Laboratoire Fizeau, UNS/OCA/CNRS UMR6525, Parc Valrose, 06108 Nice Cedex 2, France
[7] Observatoire Astronomique de l'Université de Genève, Chemin de Maillettes 51, 1290 Sauverny, Switzerland

Received 28 April 2011 / Accepted 23 July 2011

ABSTRACT

Context. The extragalactic distance scale builds directly on the Cepheid period-luminosity (PL) relation as delineated by the sample of Cepheids in the Large Magellanic Cloud (LMC). However, the LMC is a dwarf irregular galaxy, quite different from the massive spiral galaxies used for calibrating the extragalactic distance scale. Recent investigations suggest that not only the zero-point but also the slope of the Milky Way PL relation differ significantly from that of the LMC, casting doubts on the universality of the Cepheid PL relation.

Aims. We want to make a differential comparison of the PL relations in the two galaxies by delineating the PL relations using the same method, the infrared surface brightness method (IRSB), and the same precepts. We furthermore extend the metallicity baseline for investigating the zero-point dependence, by applying the method to five SMC Cepheids as well.

Methods. The IRSB method is a Baade-Wesselink type method to determine individual distances to Cepheids. We apply a newly revised calibration of the method as described in an accompanying paper (Paper I) to 36 LMC and five SMC Cepheids and delineate new PL relations in the $V, I, J, \& K$ bands as well as in the Wesenheit indices in the optical and near-IR.

Results. We present 509 new and accurate radial velocity measurements for a sample of 22 LMC Cepheids, enlarging our earlier sample of 14 stars to include 36 LMC Cepheids. The new calibration of the IRSB method is directly tied to the recent HST parallax measurements to ten Milky Way Cepheids, and we find a LMC barycenter distance modulus of 18.45 ± 0.04 (random error only) from the 36 individual LMC Cepheid distances. In the J, K bands we find identical slopes for the LMC and Milky Way PL relations and only a weak letallicity effect on the zero points (consistent with a zero effect), metal poor stars being fainter. In the optical we find the Milky Way slopes are slightly shallower than the LMC slopes (but again consistent with no difference in the slopes) and small effects on the zero points. However, the important Wesenheit index in V, $(V - I)$ shows a metallicity effect on the slope and on the zero point which is likely to be significant.

Conclusions. We find a significant metallicity effect on the W_{VI} index $\gamma(W_{VI}) = -0.23 \pm 0.10$ mag dex^{-1} as well as an effect on the slope. The K-band PL relation on the other hand is found to be an excellent extragalactic standard candle being metallicity insensitive in both slope and zero-point and at the same time being reddening insensitive and showing the least internal dispersion.

Key words. stars: variables: Cepheids – stars: fundamental parameters – stars: distances – Magellanic Clouds – distance scale

1. Introduction

The Cepheid period-luminosity (PL-) Relation is fundamental to the calibration of the extra-galactic distance scale and thus to the determination of the Hubble constant. Modern reviews on the calibration of the Cepheid distance scale can be found in e.g. Freedman & Madore (1991), Fouqué et al. (2003), Sandage & Tammann (2006), Fouqué et al. (2007), and Barnes (2009) while Freedman & Madore (2010) review the present status of the quest for the Hubble constant. A dissenting view can be found e.g. in Sandage et al. (2009) and references therein.

The value of the PL relation rests with its universality, in particular that the PL relation slope and zero points are independent of metallicity. The zero point has long been suggested to be metallicity dependent and the HST key project on the extragalactic distance scale (Freedman et al. 2001) corrected for this based on the empirical studies available at that time (e.g. Freedman & Madore 1990; Sasselov et al. 1997; Kochanek 1997; Kennicutt et al. 1998) with an estimated effect in the W_{VI} index of -0.2 ± 0.2 mag dex^{-1} in the sense that metal-poor Cepheids are fainter than metal-rich Cepheids. However, the size and even the sign of the effect is still disputed.

⋆ Based on observations collected at the European Organisation for Astronomical Research in the Southern Hemisphere, Chile, Programme-IDs 076-C.0158, 078.D-0299, & 080.D-0318.
⋆⋆ Full Table 2 is only available at the CDS via anonymous ftp to cdsarc.u-strasbg.fr (130.79.128.5) or via http://cdsarc.u-strasbg.fr/viz-bin/qcat?J/A+A/534/A95

Udalski et al. (2001) found no effect on the slope nor on the zero-point when comparing the metal-poor Cepheids of IC 1613 with those in the Magellanic Clouds based on TRGB distances to those galaxies. On the other hand Romaniello et al. (2008) found a significant effect with the opposite sign when comparing Milky Way and Magellanic Cloud Cepheids with individual spectroscopic metallicity determinations. Sakai et al. (2004) and Storm et al. (2004), found an effect of similar size and sign as that adopted by the HST key project, but the latter study also showed a significant difference in the slopes of the Milky Way and LMC relations, as also found by Sandage et al. (2004). Recently Bono et al. (2010) have argued for no significant effect in the W_{VI} and W_{JK} index on the basis of empirical as well as theoretical arguments.

Observationally, we are in the dilemma of either using a large sample of Cepheids, like in the Large Magellanic Cloud (LMC), which constrains very well the slope of the relation for a low metallicity sample of stars and which leaves the zero point to be determined from secondary indicators, or of using direct geometric distances (parallaxes) to a handful of nearby, solar metallicity, Milky Way Cepheids which constrain well the zero point of the PL relation but which do not constrain the slope very well.

Baade-Wesselink type methods which use the pulsational properties of the Cepheids to determine direct distances to individual Cepheids promise to resolve this dilemma by yielding direct individual distances to a large sample of Milky Way and Magellanic Cloud Cepheids spanning a significant range of metallicities. In particular, the near-infrared surface brightness (IRSB) method (Fouqué & Gieren 1997), a near-infrared variant of the Barnes-Evans method (Barnes & Evans 1976) shows great promise in achieving this goal as it is insensitive to reddening errors. The technique has also been shown to be independent of the metallicity of the Cepheids (Storm et al. 2004). A few years ago the IRSB method was re-calibrated using interferometrically measured, phase-resolved angular diameters of Cepheids by Kervella et al. (2004). This was an extremely important achievement as it proved that the pulsating Cepheid variables indeed obey the same surface brightness-colour relation as the stable yellow giant stars which were used to construct the surface brightness-colour relation adopted in the original calibration of the technique (Fouqué & Gieren 1997). The improved version of the IRSB technique was then applied to Milky Way Cepheids by Storm et al. (2004) and Groenewegen (2008), and for the first time to extragalactic Cepheids by Storm et al. (2004) (SMC) and Gieren et al. (2005a) (LMC).

In our earlier application of the method to Milky Way Cepheids (Storm et al. 2004), we found that the slopes of the resulting PL relations in all optical and near-infrared bands were significantly steeper than the those directly observed in the Large Magellanic Cloud by the OGLE Project and by Persson et al. (2004), thus challenging the universality of the PL relation. Gieren et al. (2005a) then analyzed thirteen LMC Cepheids, for which the data required for the IRSB analysis were available at the time, in an identical fashion and found that the PL relation slopes in the LMC were very similar to the one obtained for the Milky Way sample, but different from the observed apparent slope of the LMC sample. We interpreted this as evidence for the existence of an as yet undetected period-dependent systematic error in the IRSB method, but the limited size of the LMC sample prevented firm conclusions.

To put our previous analysis on a firmer basis, we present in the present paper new and very accurate radial velocity curves for 22 additional LMC Cepheids (Sect. 2) thus almost tripling the existing sample for an IRSB analysis to a total of 36 stars.

Table 1. LMC Cepheids for which we have obtained new radial velocity curves with the HARPS and FEROS high-resolution spectrographs at ESO-La Silla.

HV873	HV914	HV2405	HV12452
HV876	HV1005	HV2527	HV12505
HV877	HV1006	HV2538	HV12717
HV878	HV1023	HV2549	U1
HV881	HV2282	HV5655	
HV900	HV2369	HV6093	

To allow a purely differential comparison with solar metallicity Cepheids we present a similar analysis for 77 Milky Way Cepheids in an accompanying paper (Storm et al. 2011, hereinafter Paper I). In that paper we also combine the new empirical constraints on the projection (p-)factor, converting Cepheid radial into pulsational velocities, as obtained from the present LMC study and the recent HST parallax measurements to ten Galactic Cepheids (Benedict et al. 2007), to obtain a new empirical calibration of the p-factor relation to be used in our IRSB distance analysis.

In Sect. 3 We briefly describe the IRSB method in its present form and we discuss the choice of the p-factor relation. We present the resulting LMC period-luminosity relations in optical and near-infrared bands in Sect. 4 where we also compare to the SMC and Milky Way samples to estimate the effect of metallicity on the PL relations. In Sect. 5 we discuss our results and compare them to other recent investigations. Section 6 summarizes our results.

2. The data

2.1. The LMC Cepheid sample

We have selected 22 Cepheids in the LMC (see Table 1) showing a wide range of periods, all having high-quality near-IR lightcurves from Persson et al. (2004) and very accurate optical photometry from OGLE-III (Udalski et al. 2008; Soszyński et al. 2008). From their optical lightcurves, all these Cepheids are clearly fundamental mode pulsators. For these stars we have obtained radial velocity curves as will be described in the next section. A typical data set (HV 2282) is shown in Fig. 1.

Gieren et al. (2005a) performed a first IRSB analysis on a sample of 13 Cepheids in the LMC, six of which belonging to the young blue, massive cluster NGC 1866. These stars will all be used in the following analysis. To this sample we have added the star HV2827. The radial velocity data for this star comes from Imbert et al. (1987), the optical photometry from Moffet et al. (1998) and the near-IR photometry from Persson et al. (2004). For all the stars we have transformed the near-IR photometry to the SAAO system using first the transformations given by Persson et al. (2004) to transform the LCO data to the CTIO system, and then applying the transformations given by Carter (1990) to transform from the CTIO to the SAAO system. In this way we ensure to be on a common system with the Milky Way sample presented in the accompanying Paper I, and to be on the same photometric system which was used by Kervella et al. (2004) for the calibration of the surface-brightness versus colour relation.

2.2. Spectroscopic data

Using the HARPS instrument on the ESO 3.6 m telescope and the FEROS instrument on the ESO/MPG 2.2 m telescope, both

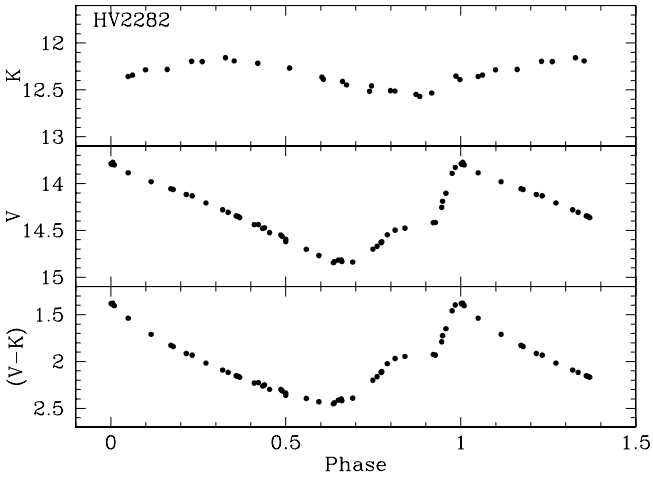


Fig. 1. The photometric V and K light curves, and the $(V - K)$ colour curve as used in our IRSB analysis for the LMC Cepheid variable HV2282. This is a typical set of photometric light and colour curves in the present study based on the optical photometry from OGLE-III (Udalski et al. 2008; Soszyński et al. 2008), and the near-IR photometry from Persson et al. (2004).

at ESO La Silla, Chile, we have obtained 509 new radial velocity measurements for the above described sample of 22 LMC Cepheids. HARPS was used for 20 of the stars while FEROS was used for two additional Cepheids, HV914 and HV12717.

HARPS (Mayor et al. 2003) is a fiber-fed cross-dispersed echelle spectrograph mounted inside a vacuum vessel for improved wavelength stability. It has a spectral resolution of $R = 115\,000$ (3.2 pix) and the wavelength range reaches from 380 to 690 nm. HARPS was used to observe 20 LMC Cepheids in the sample. Radial velocity observations were obtained during a single, 16-night, visitor observing run in December 2005 which were later complemented with service mode observations in the following two seasons to cover phase gaps in the velocity curves.

We used the standard reduction pipeline using cross-correlation with a G2-type spectral mask (Baranne et al. 1996; Pepe et al. 2002) to extract radial velocities from the spectral data.

FEROS (Kaufer et al. 1999) is also a fiber-fed crossed-dispersed spectrograph. It has a resolution of $R = 48\,000$ (2.2 pix) covering the wavelength range from 360 to 920 nm. The Cepheid radial velocities were extracted using the cross-correlation method with the FEROS pipeline.

Both instruments are known to be very stable with wavelength drifts well below 100 m/s. As our main objective was to obtain well covered, accurate radial velocity curves we made relatively short exposures with resulting low signal to noise ratios of 5 to 10. This was found sufficient to keep the errors of the individual radial velocity measurements below 100 m/s, which meets the precision we desired.

The Heliocentric Julian dates and the individual radial velocities are tabulated in Table 2 and the radial velocity curves are plotted in Fig. 2. A few data points appear to be misidentifications as they are close to the systemic velocity of the star but do not fall on the velocity curve (see HV873, HV878, and U1). They have been marked with crosses in the figure and are not considered in the further analysis. In the case of HV1005 we found two points with similar offsets from the radial velocity curve. These two data points were obtained two years later than the majority of the data, obtained during the sixteen consecutive nights (see above), thus suggesting the possibility of orbital motion for this star. We have simply disregarded those two points in the following analysis.

Table 2. New radial velocities for the 22 LMC Cepheids.

ID	HJD (days)	RV ($\mathrm{km\,s^{-1}}$)
HV873	2 453 701.7205	247.46
HV873	2 453 702.7489	250.14
HV873	2 453 703.7567	252.64
HV873	2 453 704.7536	255.15
HV873	2 453 705.7469	257.52
HV873	2 453 706.7521	259.96
...	...	...

Notes. The complete table is available in the electronic form from the CDS.

3. The IRSB method

3.1. The surface brightness-colour relation

The infrared surface brightness (IRSB) method is a variant of the Baade-Wesselink method originally developed by Barnes & Evans (1976) in the optical spectral range. It matches the angular diameter variation of a Cepheid as determined from photometry, with the radius variation of the pulsating star as determined from an integration of its pulsational velocity curve.

In Paper I we present a more detailed discussion of the method, which relates the surface brightness parameter, F_V, to a colour index $(V - K)_0$ to determine the angular diameter variation of the star.

Here we use the relation

$$F_V = 4.2207 - 0.1V_0 - 0.5 \log \theta \quad (1)$$

$$= -0.1336(V - K)_0 + 3.9530 \quad (2)$$

as determined by Kervella et al. (2004).

3.2. The projection factor

Knowledge of the projection (p-) factor which converts an observed radial velocity of a Cepheid into the pulsational velocity at its surface is crucial for any kind of Baade-Wesselink analysis. The p-factor has to take into account not only the geometrical projection effects across the observed stellar disk but also fold this with the effect of limb darkening and possibly take into consideration non-LTE effects due to the dynamic behaviour of the pulsating atmosphere.

Recent empirical (Gieren et al. 2005a) and theoretical (Nardetto et al. 2007, 2009) work has shown that the p-factor relation from Hindsley & Bell (1989), which shows a slight period dependence of the p-factor and was used in our early work (Gieren et al. 1993), is not appropriate. In fact the new data presented here (see Sect. 4.3) largely supports the empirical findings of Gieren et al. (2005a) that the p-factor depends quite strongly on pulsational period or the derived distances to the LMC Cepheids become period dependent, which is clearly unphysical. We have discussed this issue in more detail in Paper I. In that paper, we find the best fitting relation to be:

$$p = 1.550(\pm 0.04) - 0.186(\pm 0.06) \log P \quad (3)$$

which we will adopt here.

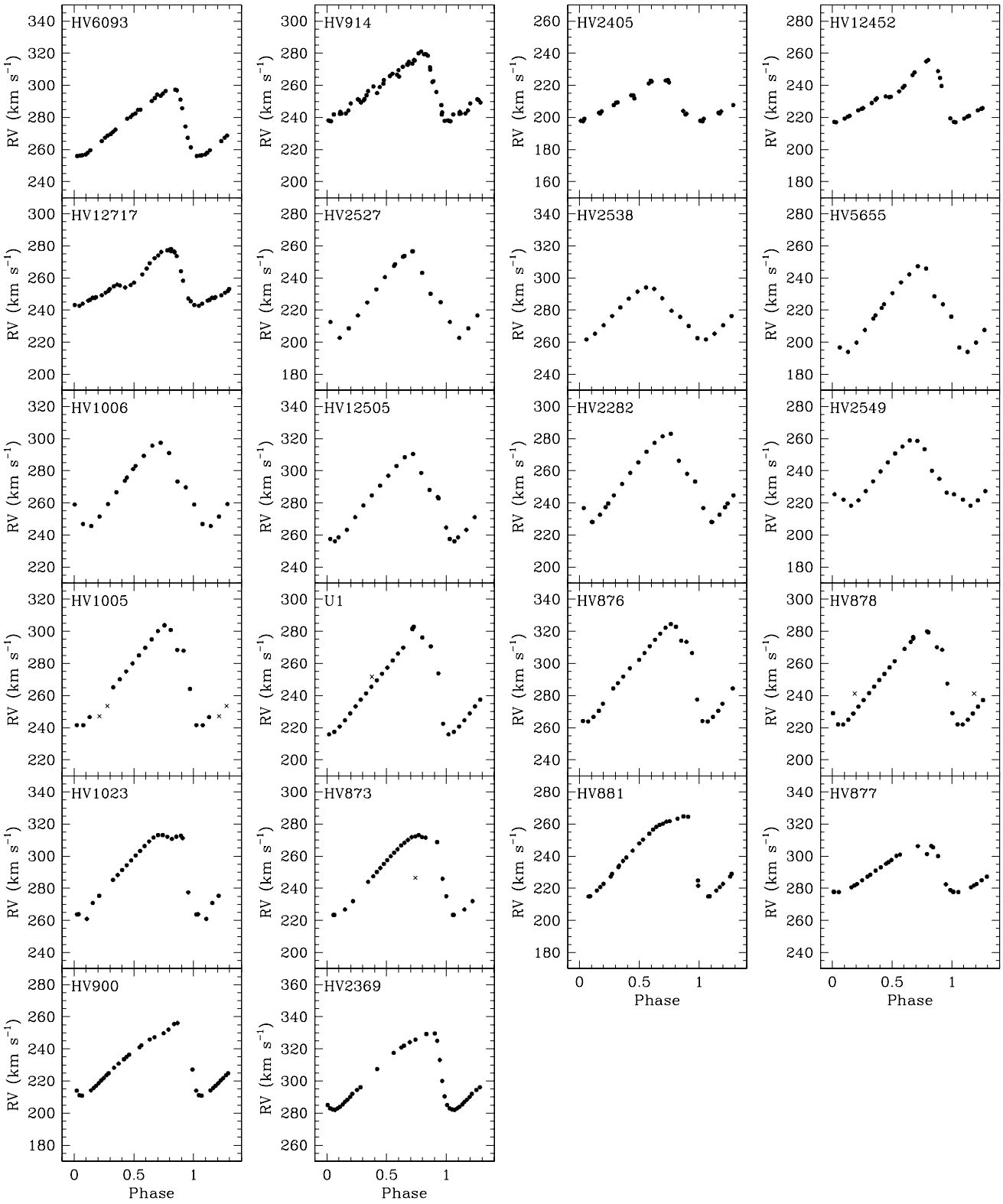


Fig. 2. The new radial velocity curves for 22 LMC Cepheids from HARPS and FEROS (HV 914 and HV 12717) data. The crosses indicate points that have not been used in the analysis. The radial velocity range in each panel is 120 km s^{-1} so the amplitudes in the panels are directly comparable. The panels are arranged according to increasing pulsational period.

It is important to note that the exact choice of the *p*-factor relation has no bearing on the conclusions regarding the effect of metallicity on the PL relations in the present paper, as long as the *p*-factor relation used in the analysis is the same for both samples, the Milky Way and the LMC. Any change in the relation would affect both Milky Way and LMC Cepheids in the same way but the differentials would remain the same. This of course is based on the implicit assumption that the *p*-factor is independent of metallicity. Work is currently underway to further investigate this point.

3.3. The reddening

The reddenings for the LMC stars were taken from the catalogue of Persson et al. (2004) whenever possible. For the NGC 1866 stars we adopted values of $E(B-V) = 0.06$ following the discussion in Storm et al. (2005). The reddening is very low for all the stars and the star-to-star variation is very low as well, so reddening errors can only marginally affect the resulting period-luminosity relations, even in the optical bands. We have adopted the reddening law from Cardelli et al. (1989) with a total-to-selective absorption of $R_V = 3.23$ following the discussion in Fouqué et al. (2007). In this way we are proceeding exactly in the same way as for the Milky Way Cepheids in Paper I.

3.4. Adopted metallicity

We adopt the mean metallicity estimates for the Milky Way, LMC and SMC Cepheids from the discussion by Luck et al. (1998) based on new and literature measures for Cepheids and supergiants. They find for the Milky Way [Fe/H] = +0.03 based on 69 stars with $\sigma = 0.14$, for the LMC [Fe/H] = −0.34 based on 32 stars with $\sigma = 0.15$ and for the SMC [Fe/H] = −0.68 based on 25 stars with $\sigma = 0.13$. These values are largely supported by Romaniello et al. (2008) who found values of −0.30 dex and −0.75 dex respectively. We note that the Cepheids in NGC 1866 might be slightly more metal-poor, [Fe/H] = −0.5, based on the spectroscopic study of three cluster giants by Hill et al. (2000) and the photometric measurement for NGC 1866 of -0.48 ± 0.18 by Hilker et al. (1995) from Strömgren photometry, but we do not make this distinction in the following.

4. Results

4.1. Distances and absolute magnitudes

We have applied the IRSB method as described in the previous section to find the distances and absolute magnitudes for the LMC Cepheids reported in Table 3 and for the SMC sample of Storm et al. (2004) in Table 4. The absolute magnitudes are intensity-averaged magnitudes.

4.2. The distances to the LMC and the SMC

On the basis of the individual distances to the Cepheids in the LMC we can now determine the distance to the LMC barycenter. First we correct the measured distance of each Cepheid by the distance offset from the LMC disk model of van der Marel & Cioni (2001) as tabulated in the last column of Table 3 and then compute the mean of the resulting values. We find $(m-M)_0(LMC) = 18.45 \pm 0.04$ (random error only) with a standard deviation of 0.22 mag. As the Cepheids are well distributed across the face of the LMC the uncorrected mean modulus is identical to within 0.01 mag to the adopted barycentric distance modulus value.

For the SMC we only have five stars so the random error is significantly larger than is the case for the LMC. Additionally, the SMC is well known to exhibit more pronounced depth effects than the LMC, so some additional scatter is to be expected. We find from the five Cepheids an unweighted mean value of $(m-M)_0$(SMC) = 18.92 ± 0.14 with a standard deviation of 0.32 mag. The offset in modulus with respect to the LMC of 0.47 mag is in excellent agreement with the very accurate value of 0.44 ± 0.05 mag found by Cioni et al. (2000) from an investigation of a large sample of tip of the red-giant branch (TRGB) stars in the reddening insensitive near-infrared, thus giving us confidence that our five stars are indeed representative of the SMC as a whole.

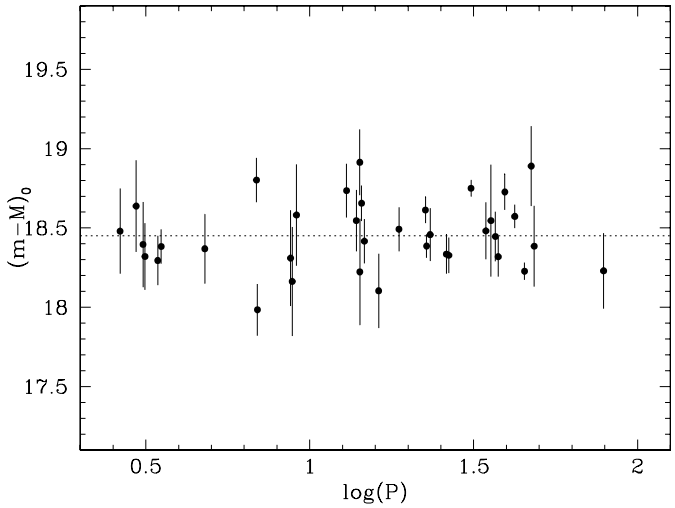


Fig. 3. The IRSB-based distance moduli of 36 Cepheids in the LMC using the new p-factor relation derived in Paper I, plotted as a function of their pulsation period. The moduli have been referred to the LMC barycenter using the LMC disk model of van der Marel & Cioni (2001).

4.3. Constraints on the p-factor relation

As discussed in Sect. 3.2 we can use the IRSB distances to the 36 LMC Cepheids to place constraints on the p-factor relation. We have rederived the distances to the individual LMC Cepheids using different p-factor relations, as discussed in more detail in Paper I, and we computed the individual LMC barycentric distances as before. In Table 5 we list the resulting mean LMC distance moduli as well as the slope of the distance modulus as a function of pulsation period, for each of the p-factor relations we tested in this process. The function distance modulus versus pulsation period must of course have a zero slope, and with the present large sample of 36 stars we are able to place strong constrains on the slope. In the table it can be seen that the original Hindsley & Bell (1989) relation gives a very plausible LMC distance but a strong and unphysical period dependence of the distance moduli. Similarly the Nardetto et al. (2009) relation gives a slope which deviates at the level of 2σ from the uncorrelated relation and the LMC distance becomes uncomfortably short at 18.26 mag. The third relation uses the slope of the p-factor relation from Nardetto et al. (2009) but with a zero point which yields IRSB distances to Milky Way Cepheids in agreement with the recent parallaxes from Benedict et al. (2007). The last column corresponds to the relation derived in Paper I which we have adopted here, which yields LMC Cepheid distance moduli which are totally independent of their pulsation period. This is borne out in Fig. 3 where we show the LMC center distance moduli based on the individual LMC Cepheid moduli corrected for the disk model of van der Marel and Cioni (2001) as a function of log P. It is evident that with the adopted p-factor relation there is no significant correlation between pulsational period and derived distance to the LMC Cepheids.

Table 3. Distances and absolute magnitudes for the LMC Cepheids calculated using the precepts given in Paper I, using the new p-factor relation.

(1) ID	(2) log(P)	(3) d (kpc)	(4) $\sigma(d)$ (kpc)	(5) $(m-M)_0$ (mag)	(6) $\sigma_{(m-M)}$ (mag)	(7) M_V (mag)	(8) M_I (mag)	(9) M_J (mag)	(10) M_H (mag)	(11) M_K (mag)	(12) W_{VI} (mag)	(13) W_{JK} (mag)	(14) $E(B-V)$ (mag)	(15) $\Delta\phi$	(16) $\Delta(m-M)$ (mag)
HV 12199	0.421469	49.7	1.8	18.48	0.08	−2.41	−3.01	−3.13		−3.80	−3.94	−4.26	0.060	0.035	−0.058
HV 12203	0.470427	53.4	2.1	18.64	0.09	−2.71	−3.31	−3.66		−4.08	−4.24	−4.37	0.060	0.050	−0.058
HV 12202	0.491519	47.8	1.7	18.40	0.08	−2.53	−3.14	−3.60		−4.02	−4.09	−4.30	0.060	0.030	−0.058
HV 12197	0.497456	46.1	1.3	18.32	0.06	−2.42	−3.07	−3.44		−3.87	−4.07	−4.17	0.060	−0.015	−0.057
HV 12204	0.536402	45.6	1.0	18.30	0.05	−2.79	−3.33	−3.67		−4.07	−4.17	−4.34	0.060	0.015	−0.059
HV 12198	0.546887	47.5	0.7	18.38	0.03	−2.63	−3.27	−3.69		−4.09	−4.26	−4.36	0.060	0.020	−0.059
HV 6093	0.679885	47.2	1.4	18.37	0.06	−3.25	−3.86	−4.21		−4.60	−4.79	−4.87	0.058	−0.015	−0.048
HV 914	0.837489	57.6	1.1	18.80	0.04	−4.10	−4.79	−5.18	−5.54	−5.59	−5.84	−5.88	0.070	−0.035	0.013
HV 2405	0.840331	39.5	0.9	17.98	0.05	−3.06	−3.77	−4.14	−4.52	−4.57	−4.86	−4.86	0.070	−0.015	0.046
HV 12452	0.941457	45.9	1.9	18.31	0.09	−3.74	−4.48	−4.94	−5.32	−5.37	−5.62	−5.67	0.058	0.030	0.058
HV 12717	0.946628	42.9	2.0	18.16	0.10	−3.62	−4.33	−4.77	−5.14	−5.21	−5.42	−5.51	0.058	−0.005	0.065
HV 12816	0.959466	52.0	2.3	18.58	0.09	−4.29	−4.88	−5.24	−5.56	−5.62	−5.79	−5.88	0.070	0.015	−0.075
HV 2527	1.112251	55.8	1.3	18.73	0.05	−4.36	−5.21	−5.66	−6.09	−6.15	−6.51	−6.49	0.070	0.005	0.041
HV 2538	1.142118	51.2	1.3	18.55	0.06	−4.39	−5.28	−5.70	−6.14	−6.19	−6.64	−6.53	0.100	−0.040	−0.019
HV 5655	1.152657	60.7	1.7	18.91	0.06	−4.69	−5.53	−5.96	−6.41	−6.47	−6.84	−6.81	0.100	−0.015	0.046
HV 1006	1.152786	44.1	2.0	18.22	0.10	−4.17	−4.95	−5.48	−5.90	−5.95	−6.15	−6.28	0.100	0.005	−0.010
HV 12505	1.158115	53.9	0.8	18.66	0.03	−4.14	−5.04	−5.63	−6.11	−6.17	−6.43	−6.55	0.100	−0.005	0.031
HV 2282	1.166636	48.2	0.9	18.42	0.04	−4.41	−5.19	−5.66	−6.07	−6.12	−6.38	−6.44	0.100	0.015	0.051
HV 2549	1.210289	41.8	1.3	18.10	0.07	−4.50	−5.31	−5.69	−6.06	−6.13	−6.56	−6.43	0.058	0.020	0.052
HV 1005	1.272209	49.9	0.9	18.49	0.04	−4.72	−5.47	−5.98	−6.41	−6.45	−6.62	−6.77	0.100	0.015	−0.023
U1	1.353098	52.8	0.6	18.61	0.02	−4.82	−5.70	−6.28	−6.74	−6.80	−7.07	−7.16	0.100	0.010	0.060
HV 876	1.356342	47.6	0.5	18.39	0.02	−5.06	−5.86	−6.27	−6.67	−6.71	−7.10	−7.02	0.100	0.005	0.005
HV 878	1.367445	49.2	1.1	18.46	0.05	−5.11	−5.66	−6.35	−6.75	−6.80	−6.52	−7.12	0.058	−0.010	0.055
HV 12815	1.416910	46.5	0.8	18.34	0.04	−5.08	−5.96	−6.48	−6.94	−6.99	−7.32	−7.35	0.070	−0.030	−0.075
HV 1023	1.424235	46.3	0.7	18.33	0.03	−4.77		−6.28	−6.75	−6.79		−7.15	0.070	0.025	−0.049
HV 899	1.492039	56.2	0.4	18.75	0.01	−5.71	−6.52	−7.02	−7.45	−7.50	−7.78	−7.82	0.110	0.025	0.018
HV 873	1.537311	49.7	1.2	18.48	0.05	−5.87		−7.08	−7.46	−7.50		−7.79	0.130	−0.010	0.080
HV 881	1.552820	51.2	2.5	18.55	0.10	−5.55		−6.97	−7.41	−7.50		−7.85	0.030	−0.065	0.062
HV 879	1.566167	48.9	1.0	18.45	0.05	−5.27	−6.25	−6.84	−7.32	−7.39	−7.75	−7.78	0.060	0.015	0.044
HV 909	1.574986	46.1	0.8	18.32	0.04	−5.75	−6.52	−6.97	−7.36	−7.43	−7.70	−7.74	0.058	−0.065	0.048
HV 2257	1.595153	55.6	0.8	18.73	0.03	−5.90	−6.80	−7.35	−7.81	−7.87	−8.19	−8.22	0.060	−0.005	0.054
HV 2338	1.625350	51.8	0.5	18.57	0.02	−5.95	−6.83	−7.36	−7.80	−7.86	−8.19	−8.21	0.040	−0.015	0.070
HV 877	1.655215	44.2	0.3	18.23	0.02	−5.21		−6.80	−7.31	−7.36		−7.74	0.100	0.070	0.017
HV 900	1.675637	60.0	2.0	18.89	0.07	−6.32		−7.72	−8.17	−8.25		−8.62	0.058	−0.060	0.042
HV 2369	1.684646	47.5	1.6	18.39	0.07	−6.02		−7.46	−7.90	−7.96		−8.29	0.095	0.005	−0.029
HV 2827	1.896354	44.3	1.4	18.23	0.07	−6.18	−7.20	−7.81	−8.29	−8.36	−8.75	−8.73	0.080	0.035	−0.079

Notes. In Cols. 3 and 4 we give the IRSB distance and the associated error estimate. In Cols. 5 and 6 follows the distance modulus, and in Cols. 7 through 13, we give the absolute magnitudes in the different bands as well as the Wesenheits indices. Finally in Col. 14 we give the adopted reddening and in Col. 15 the adopted phase shift between spectroscopic and photometric angular diameters. Column 16 gives the magnitude correction to refer the distance moduli to the LMC barycenter.

Table 4. Distances and absolute magnitudes for the SMC Cepheids calculated by using the same precepts as in Table 3.

ID	log P	d (kpc)	$\sigma(d)$ (kpc)	$(m-M)_0$ (mag)	$\sigma_{(m-M)}$ (mag)	M_V (mag)	M_I (mag)	M_J (mag)	M_K (mag)	W_{VI} (mag)	W_{JK} (mag)	$E(B-V)$ (mag)	$\Delta\phi$
HV 1345	1.129638	55.5	1.8	18.72	0.07	−4.06	−4.80	−5.41	−5.88	−5.96	−6.20	0.030	0.025
HV 1335	1.157807	59.9	1.6	18.89	0.06	−4.37	−5.06	−5.56	−5.95	−6.12	−6.21	0.090	−0.055
HV 1328	1.199645	52.2	2.1	18.59	0.09	−4.47	−5.15	−5.60	−6.00	−6.20	−6.28	0.000	0.020
HV 1333	1.212014	76.5	1.4	19.42	0.04	−4.94	−5.69	−6.20	−6.63	−6.84	−6.92	0.070	−0.005
HV 822	1.223810	62.1	2.2	18.96	0.08	−4.54	−5.38	−5.89	−6.33	−6.67	−6.64	0.030	−0.010

Notes. Column headings are the same as in the previous table.

4.4. The LMC period-luminosity relations

In Table 6 the period-luminosity relations we obtain for the LMC in the different photometric bands are given in the form:

$$M = a(\pm\sigma(a))[\log(P) - 1.0] + b(\pm\sigma(b)). \quad (4)$$

The relations have been determined from a linear regression to the absolute magnitudes and log(P) values given in Table 3. In the table the corresponding relations for the Milky Way sample determined in Paper I are given for comparison. These relations are based on Cepheid distances calculated with exactly the same precepts as in this paper, using the same p-factor relation and IRSB calibration so we can perform a direct comparison of the relations. The relations in the K- and V-bands as well as in the $V, (V-I)$ Wesenheit index are shown in Figs. 4–6 with the Milky Way relations overplotted.

The dispersions of the Milky Way and LMC samples around the ridge line PL relations given in Table 6 are very similar for all the bands, and we note that there is not a big difference in the dispersion as a function of photometric band. The J and K-band values are only marginally smaller than those for the optical bands and the W_{VI} index performs only slightly better than the V-band. If however we consider the LMC Cepheids to be at the same distance we can determine apparent PL relations without involving the individual distances from the IRSB method. In this case the dispersion reduces in W_{VI} from 0.24 to 0.15 mag, in V from 0.26 to 0.19 mag and in the K-band the value even decreases from 0.21 to 0.09 mag. Removing only two stars from the W_{VI} relation further reduces that disperion to 0.09 mag illustrating that the uncertainty on these numbers are quite large due to the small sample size. The fact that the dispersion can be reduced so much by adopting a common distance to all the

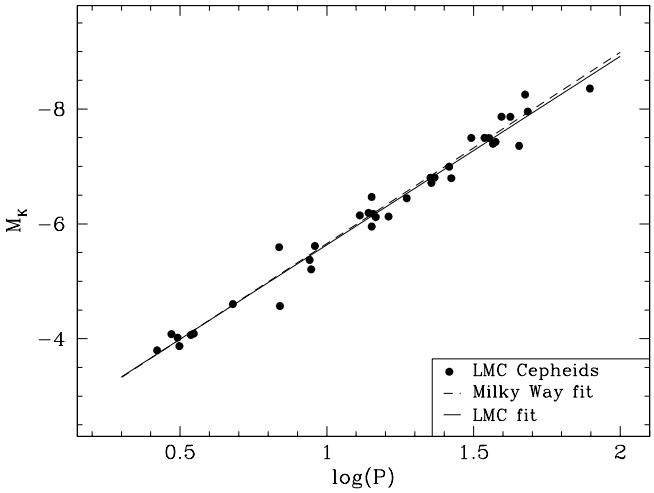


Fig. 4. The K-band period-luminosity relation for our sample of LMC Cepheids based on the absolute magnitudes determined with the IRSB method as calibrated in Paper I. The best fitting line from the data is overplotted in black, and the best fitting line to the Milky Way sample of Paper I is overplotted with a dashed line in red. It is appreciated that the LMC and Milky Way PL relations agree extremely well both in slope and zero point.

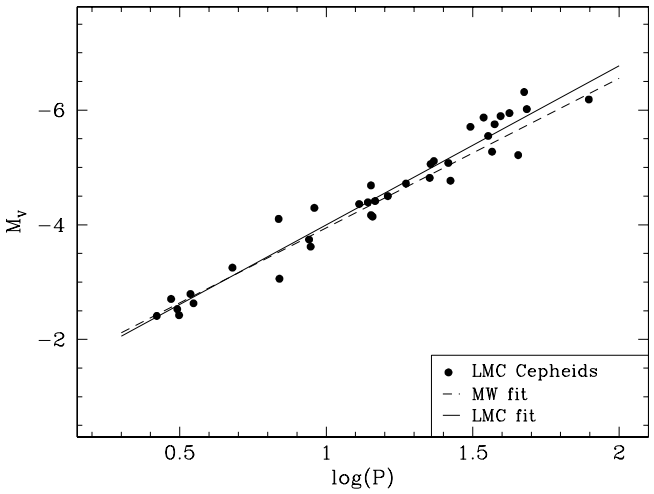


Fig. 5. The V-band PL relation for our sample of LMC Cepheids based on the absolute magnitudes determined by the IRSB method. Overplotted is the linear regression fit (solid line) as well as the corresponding Milky Way relation (dashed line).

stars suggests that the observed dispersion in the PL relations is dominated by errors in the distance moduli rather than intrinsic dispersion in the luminosities or reddening errors and the standard error on the individual distance moduli is about 0.2 mag.

The dispersion of the LMC and MW samples are also very similar suggesting that the LMC data quality is equal to that for the Milky Way sample. Barnes et al. (2005) performed a careful Bayesian analysis of the data presented in Storm et al. (2004) and found that the formal error estimates from the regression fitting, which are also the errors tabulated here in Table 3, were systematically underestimated. On average these errors should be multiplied by a factor of 3.4 to be in agreemeent with the Bayesian error estimates. In fact the error estimates for the distance moduli presented in Table 3 have a mean value of 0.051 mag, which results in a revised mean error estimate of 0.17 mag, very similar to

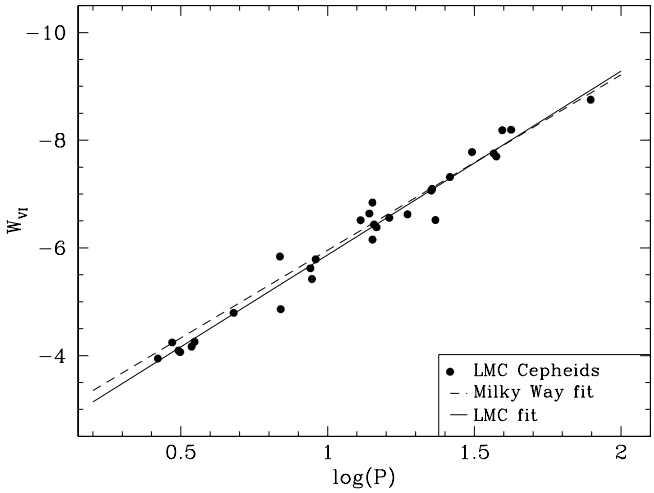


Fig. 6. The optical $(V - I)$ Wesenheit index PL relation for our sample of LMC Cepheids, based on the absolute magnitudes determined by the IRSB method as calibrated in Paper I. Overplotted is the linear regression fit (solid line) as well as the corresponding Milky Way relation (dashed line).

the standard error of 0.2 mag estimated above from the K-band PL relation.

4.5. The effect of metallicity

The LMC Cepheid PL relations in Table 6 can be compared directly to the relations derived in Paper I for the Milky Way sample which have been tabulated for convenience in Table 6. The slopes of the relations are in excellent agreement in the case of the near-infrared J and K bands. In the V band and in the Wesenheit indices, the agreement is slightly worse but well within one σ, whereas the I band slopes differ at the level of about one σ. Since the slopes of the PL relations for both LMC and Milky Way Cepheids are very well constrained from our samples, we conclude that our results present strong evidence that the slope of the Cepheid PL relation, particularly in the near-infrared J and K bands, is identical for the solar metallicity Milky Way and more metal-poor LMC samples. These PL relations are thus independent of metallicity in the range from solar to LMC metallicity. The universality of the PL relation slopes appears to be confirmed in this metallicity range.

We can further extend the metallicity baseline by including the 5 SMC Cepheids in the sample. Given the low number of Cepheids and the narrow range of periods for these stars, we cannot constrain the slope of the PL relation at this metallicty, but we can constrain the zero point offset. In Fig. 7 we have overplotted the SMC Cepheids on the LMC Cepheids for the K-band and obviously there is good agreement. Considering the excellent agreement between the LMC and the Milky Way from Table 6 this further supports the universality of the zero point of the K-band relation.

We can quantify any offsets in the PL relation magnitude zero points as a function of metallicity by comparing the zero point offset for each of the three samples with the reference PL relations determined in Paper I on the basis of all available Cepheids. For each band and sample we computed the mean magnitude offsets, tabulated them in Table 7 and plotted them as a function of metallicity in Fig. 8. For each band we have fit the weighted least square regression line to the magnitude offset as a function of metallicity. The resulting metallicity effect

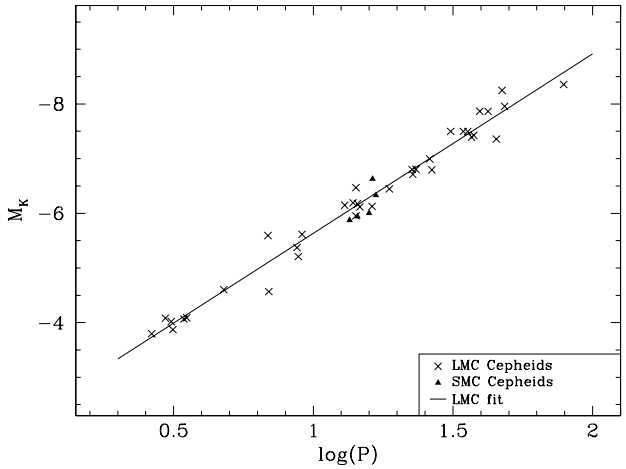


Fig. 7. The K-band absolute magnitudes for our sample of SMC Cepheids (filled triangles) overplotted on the LMC Cepheid PL relation (Fig. 4), crosses are the individual LMC Cepheids.

Table 5. Derived LMC true distance modulus and the slope of the individual Cepheid distance moduli as a function of their pulsation period, for different p-factor relations (see text) $p = \beta_p + \alpha_p \log P$.

α_p	β_p	$(m-M)_0$	$(m-M)_0$ slope
−0.03	1.39	18.50 ± 0.04	0.31 ± 0.10
−0.08	1.31	18.26 ± 0.04	0.22 ± 0.10
−0.08	1.455	18.50 ± 0.04	0.24 ± 0.10
−0.186	1.550	18.45 ± 0.04	0.00 ± 0.10

Table 6. Period-luminosity relations for the LMC in the various optical and near-infrared bands as determined from a linear regression to the absolute magnitudes from the IRSB analysis.

Band	a (mag dex^{-1})	b (mag)	Dispersion (mag)
M_V (LMC)	−2.78 ± 0.11	−4.00 ± 0.05	0.26
M_V (MW)	−2.67 ± 0.10	−3.96 ± 0.03	0.26
M_I (LMC)	−3.02 ± 0.10	−4.74 ± 0.04	0.21
M_I (MW)	−2.81 ± 0.10	−4.76 ± 0.03	0.23
W_{VI} (LMC)	−3.41 ± 0.11	−5.87 ± 0.05	0.24
W_{VI} (MW)	−3.26 ± 0.11	−5.96 ± 0.04	0.26
M_J (LMC)	−3.22 ± 0.09	−5.17 ± 0.04	0.21
M_J (MW)	−3.18 ± 0.09	−5.22 ± 0.03	0.22
M_K (LMC)	−3.28 ± 0.09	−5.64 ± 0.04	0.21
M_K (MW)	−3.33 ± 0.09	−5.66 ± 0.03	0.22
W_{JK} (LMC)	−3.31 ± 0.09	−5.95 ± 0.04	0.21
W_{JK} (MW)	−3.44 ± 0.09	−5.96 ± 0.03	0.23

Notes. The relations have been fitted in the form $M = a[\log(P) - 1] + b$. The fourth column gives the dispersion around the fit. Our results for the Milky Way Cepheids are included for comparison.

slopes have been tabulated in Table 7. We estimate the error on the slopes to be of the order 0.10 mag dex^{-1} based on the error bars on the individual points and the fact that the baseline is smaller than one dex. From Fig. 8 and Table 7 it can be seen that a zero metallicity effect *cannot* be ruled out by the data in most cases but that the effect is significant and the strongest for the W_{VI} index. For extra-galactic distance determination most Cepheid samples will have metallicities in the range from LMC

Table 7. Offsets of each metallicity sample (Milky Way, LMC, and SMC) with respect to the reference PL relations from Paper I, i.e. assuming a fixed PL relation slope irrespective of metallicity.

Band	Δb(MW) (mag)	Δb(LMC) (mag)	Δb(SMC) (mag)	γ (mag dex^{-1})
M_V	+0.02	−0.03	−0.00	+0.09
M_I	−0.00	+0.01	+0.08	−0.06
W_{VI}	−0.03	+0.04	+0.18	−0.23
M_J	−0.01	+0.03	+0.06	−0.10
M_K	−0.01	+0.02	+0.10	−0.11
W_{JK}	−0.00	+0.01	+0.13	−0.10
σ	±0.03	±0.04	±0.11	±0.10

Notes. The last column gives the slope, γ, of the weighted linear regression fit to the data.

to solar and the zero-point offsets in this range is clearly very small in all the bands.

The only bands for which we have excellent agreement between the PL relation slopes are the J and K bands, and the zero-point offsets in both of these bands are small so they each form an excellent basis for a standard candle. In the V band and the W_{JK} index the PL relation slopes are marginally in agreement and also for these two bands the zero-point offsets are small. The I band and the W_{VI} index have significant differences in the PL slopes. The W_{VI} index zero-point is also significantly more metallicity dependent than is the case for the other bands making this index inferior to the J and K-bands as a standard candle.

We note that we have assumed a simple linear metallicity dependence, but it is of course entirely possible that the dependence, if present, has a more complex functional form.

We emphasize that the metallicity effect on both the slopes and zero points discussed here is *entirely independent of the choice of the p-factor relation*, whereas the absolute values of the slopes and zero points as well as the resulting LMC and SMC distances do depend on the adopted p-factor relation.

5. Discussion

We can now compare the slopes of our LMC PL relations with independent measures from apparant magnitudes versus log(P). In the near-infrared we use the relations from Persson et al. (2004) which is based on 92 LMC Cepheids with excellent J and K light curves. They found slopes of −3.261 ± 0.042 and −3.153 ± 0.051 in K and J respectively, in excellent agreement with our values of −3.28 ± 0.09 and −3.22 ± 0.09. In the optical we can compare to the relations from the OGLE project (Udalski 2000) and we similarly find very good agreement. They find in the V and I-bands slopes of −2.775 ± 0.031 and −2.977 ± 0.021, to be compared with our values of −2.78 ± 0.11 and −3.02 ± 0.10 respectively. The fact that we reproduce the slopes of the PL relations in the LMC so well strongly supports our empirical calibration of the p-factor used with the IRSB method and confirms our earlier results (Gieren et al. 2005a) based on a much smaller sample of LMC Cepheids.

The LMC distance modulus of 18.45 ± 0.04 is only slightly shorter than the "canonical" value of 18.50 ± 0.10 as adopted by Freedman et al. (2001) and by the ARAUCARIA project (Gieren et al. 2005b; Pietrzyński et al. 2010a), and slightly longer than the value of 18.39 ± 0.01(random) ± 0.07(systematic) suggested by Freedman & Madore (2010) in their recent review. It is thus in good agreement with most recent results, as would be expected considering that we (see Paper I) have

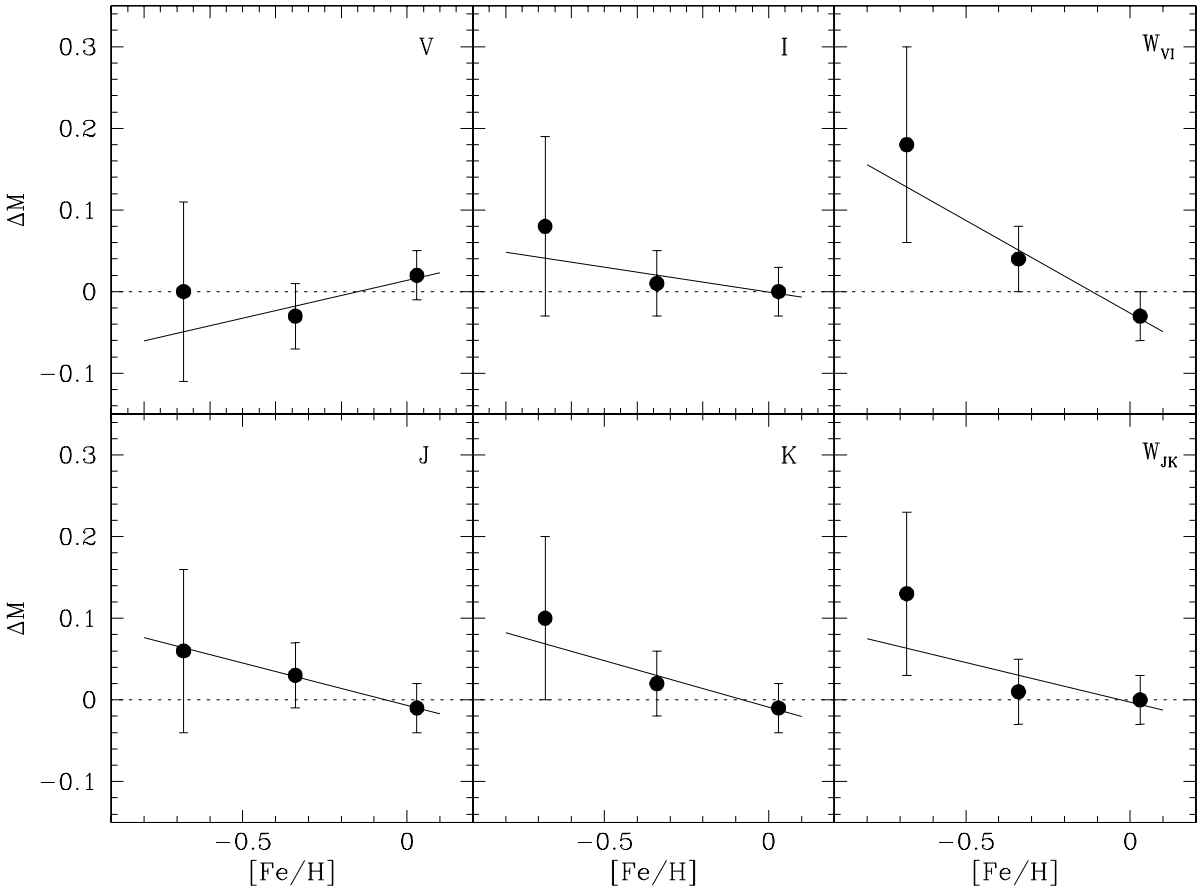


Fig. 8. The zero point offsets, $\Delta M = M - M_{\rm comb}$, for each band with respect to the reference PL relations from Paper I as a function of sample metallicity. The full lines show the weighted linear regression fit to the data. It can be seen that especially in the limited but for extragalactic distance determination most important metallicity range from LMC to solar abundance, the zero point offsets are in general indistinguishable from zero.

calibrated the IRSB method to match the distances to nine Milky Way Cepheids with direct parallaxes from Benedict et al. (2007). These distances are accurate to 4–10%, which seems the largest single remaining systematic uncertainty in the IRSB method assuming that the p-factor relation has been accurately established from our new and improved constraints (which is supported by the arguments given above). The total systematic uncertainty of our present determination of the LMC distance is difficult to quantify, but expected to be about ±5%, which is better than most other techniques which have been used to measure the LMC distance over the years. An exciting possibility to constrain the IRSB method even further, in a very direct way, will be the comparison of the IRSB-determined distance to the LMC Cepheid OGLE-LMC-CEP0227 which is a member in a double-lined eclipsing binary system (Pietrzynski et al. 2010b). Work is underway to determine the distance to this binary from orbital analysis.

In Sect. 4.5 we compared the slopes of the PL relations from the Milky Way and LMC samples finding insignificant differences in the near-IR bands and small (but possibly also non-significant) differences in the optical bands. This result is in good agreement with the findings by Gieren et al. (2005a) but at odds with earlier findings by us (Fouqué et al. 2003; Storm et al. 2004) where we found that the slope of the galactic relations were significantly steeper than those in the LMC and SMC. The reason for this difference was the inappropriate p-factor relation used in the earlier work for determining the Milky Way PL relations. Note that in the present work the choice of the p-factor relation has no bearing on the difference in slope between the Milky Way and LMC PL relations as we are now applying the method to both samples of Cepheids, this was not possible previously as the necessary data for the LMC stars was not yet available. Sandage (2004) also argued that there is a significant difference in slope between the Milky Way and LMC PL relations in the optical bands, the Milky Way relation being steeper. This conclusion was largely based on these older IRSB results, as well as on Cepheids in OB associations from Feast (1999). As we show in Paper I the revised IRSB distances are, apart from a small zero point offset, in very good agreement with the latest results on open cluster Cepheids from Turner (2010) and does not exhibit a period dependence.

We do not support the conclusion of a strong effect of metallicity on the slope of optical (V, I) Cepheid PL relations as reached, for example, by Tammann et al. (2011) or Storm et al. (2004), in fact we find that for these bands the Milky Way PL relations are slightly shallower than the LMC relations, only for the W_{JK} index we find that the Milky Way relation is steeper than the LMC relation.

In Table 7 we summarized the PL relation zero point variation as a function of metallicity. We have made the simplest assumption of a linear relation and found the slopes of the zero point offset versus metallicity relations, γ. Clearly the effects in the near-IR are small and even in the V band the effect appears to be small, albeit with the opposite sign as for the other bands.

The largest effect we find is in the W_{VI} index and our value of $\gamma(W_{VI}) = -0.23 \pm 0.10$ mag dex^{-1} is in excellent agreement with the value of -0.24 ± 0.05 mag dex^{-1}found by Sakai et al. (2004) and other measurements which have been adopted in the recent review paper by Freedman & Madore (2010). This result is slightly at odds with the findings of Bono et al. (2010) who on the basis of data on 48 external galaxies finds no significant metallicity effect on neither slope nor zero point for the Wesenheits indices W_{VI} and W_{JK}. At the same time we do agree with them that the PL relation slopes are less affected in the J and K-bands and more affected in the optical V and I bands and we also agree on the most likely sign of the effect namely that metal-rich PL relations are shallower than metal-poor ones.

It is interesting to note that the most significant metallicity effect is found for the W_{VI} index and that this effect can largely be attributed to the colour difference between Milky Way and LMC Cepheids as found by Sandage et al. (2004). They compared period-colour relations for both Milky Way and LMC Cepheids and found that the LMC Cepheids for a given period are bluer by about 0.05 mag. Feeding this into the Wesenheits index ($W_{VI} = V - 2.54(V - I)$), we find an offset of $0.00 - 2.54 \times -0.05 = 0.13$ mag in the case where the offset is fully in the I-band and $-0.05 - 2.54 \times -0.05 = 0.08$ mag in the case where the effect is fully in the V-band. Disregarding the subtle effects of differences in the slopes of the period-colour relations, these results are comparable to the offset of 0.09 mag, metal-poor Cepheids being fainter, which we find between the Milky Way and LMC W_{VI} relations in Table 6 at a period of 10 days.

The emerging conclusion based on our data and analysis is that for accurate distance measurements to galaxies the K-band Cepheid PL relation is the best suited tool: it is metallicity-independent both regarding the slope and the zero point, it is very insensitive to reddening, and it has a smaller intrinsic dispersion than any optical PL relation. It is likely, as indicated in recent work from Spitzer data, that mid-infrared Cepheid PL relations are even superior to their near-infrared relations because of their even lower sensitivity to reddening, and lower intrinsic dispersions (Madore et al. 2009). Yet, their dependence on metallicity has still to be investigated and they cannot be exploited from the ground making them exceedingly expensive to use.

6. Conclusions and summary

We have obtained new and very accurate radial velocity curves for 22 LMC Cepheids thus expanding the sample of LMC Cepheids to 36 for which we can apply the IRSB distance analysis. We have applied the newly calibrated IRSB technique of Paper I to these 36 LMC Cepheids as well as to 5 SMC Cepheids. The IRSB analysis yields individual distances from which we calculate absolute magnitudes in optical and near-infrared bands. These magnitudes define tight period-luminosity relations in the V, I, J, K bands and in the Wesenheit indices.

We show that the PL relations are in excellent agreement with the observed apparent magnitude versus $\log(P)$ relations in both the optical and near-IR bands lending strong support to the empirical calibration of the p-factor relation in Paper I.

By comparing the LMC Cepheid PL relations to their Milky Way counterparts reported in Paper I that were established with exactly the same precepts, we find practically identical Milky Way and LMC PL relation slopes in the near-infrared bands, arguing for the universality of the Cepheid PL relation in this spectral range. The zero points exhibit a slight metallicity effect, $\gamma(M_K) = -0.10 \pm 0.10$ mag dex^{-1} in the sense that metal-poor Cepheids are fainter than metal-rich Cepheids. If we restrict ourselves only to the metallicity range between solar and LMC, our results are consistent with universal PL relations (in both slope and zero point) in the near-infrared J and K bands.

In the optical bands, we find that the slopes depend weakly on metallicity, the Milky Way slopes being slightly shallower than the LMC slopes, but this difference might not be significant.

The optical PL relation zero points exhibit a metallicity effect of similar size as in the near-IR albeit the sign is opposite in the V-band. The W_{VI} index shows the strongest zero point effect on metallicity where we find $\gamma(W_{VI}) = -0.23 \pm 0.10$ mag dex^{-1}. We stress that the zero-point offsets are based on a rather long metallicity baseline ranging from SMC to solar metallicity.

Our direct distances to the LMC Cepheids leads to a true LMC distance modulus of 18.45 ± 0.04 mag, with an estimated systematic uncertainty of 5% which mainly comes from the uncertainty on the HST parallaxes of nine Milky Way Cepheids that have been used to define the absolute zero point of the IRSB technique. Our distances to the SMC Cepheids leads to an SMC distance of 18.92 ± 0.14.

Both the W_{VI} metallicity effect and the LMC distance which we find are in agreement with the latest values adopted by Freedman & Madore (2010) in their recent review on the Hubble constant.

Considering the significant metallicity effect on the W_{VI} index, not only on the zero-point but most likely also on the slope, we argue that the best standard candle is presently provided by the PL relation in the K-band as it is metallicity insensitive, reddening insensitive and exhibits the lowest intrinsic scatter.

Acknowledgements. We thank Roeland van der Marel for providing his code for computing the LMC distance correction for the stars. A great thanks is due to the La Silla support staff and in particular to the service mode team which managed so well to cover the phase gaps left after the first visitor mode run. We gratefully acknowledge financial support for this work from the Chilean Center for Astrophysics FONDAP 15010003, and from the BASAL Centro de Astrofisica y Tecnologias Afines (CATA) PFB-06/2007.

References

Baranne, A., Queloz, D., Mayor, M., et al. 1996, A&AS, 119, 373
Barnes, T. G. 2009, AIP Conf. Proc., 1170, 3
Barnes, T. G., & Evans, D. S. 1976, MNRAS, 174, 489
Barnes, T. G., Storm, J., Jefferys, W. H., Gieren, W. P., & Fouqué, P. 2005, ApJ, 631, 572
Benedict, G. F., McArthur, B. E., Feast, M. W., et al. 2007, AJ, 133, 1810
Bono, G., Caputo, F., Marconi, M., & Musella, I. 2010, ApJ, 715, 277
Cardelli, J. A., Clayton, G. C., & Mathis, J. S. 1989, ApJ, 345, 245
Carter, B. S. 1990, MNRAS, 242, 1
Cioni, M.-R. L., van der Marel, R. P., Loup, C., & Habing, H. J. 2000, A&A, 359, 601
Feast, M. 1999, PASP, 111, 775
Fouqué, P., & Gieren, W. 1997, A&A, 320, 799
Fouqué, P., Storm, J., & Gieren, W. P. 2003, Lect. Notes Phys., 635, 21
Fouqué, P., Arriagada, P., Storm, J., et al. 2007, A&A, 476, 73
Freedman, W. L., & Madore, B. F. 1990, ApJ, 365, 186
Freedman, W. L., & Madore, B. F. 1991, PASP, 103, 933
Freedman, W. L., & Madore, B. F. 2010, ARA&A, 48, 673
Freedman, W. L., Madore, B. F., Gibson, B. K., et al. 2001, ApJ, 553, 47
Gieren, W., Storm, J., Barnes, T., et al. 2005a, ApJ, 627, 224
Gieren, W., Pietrzyński, G., Soszyński, I., et al. 2005b, ApJ, 628, 695
Groenewegen, M. A. T. 2008, A&A, 488, 25
Hilker, M., Richtler, T., & Gieren, W. 1995, A&A, 294, 648
Hill, V., François, P., Spite, M., Primas, F., & Spite, F. 2000, A&A, 364, 19
Hindsley, R. B., & Bell, R. A. 1989, ApJ, 341, 1004
Imbert, M. 1987, A&A, 175, 30
Kaufer, A., Stahl, O., Tubbesing, S., et al. 1999, The Messenger, 95, 8
Kennicutt, R. C., Jr., Stetson, P. B., Saha, A., et al. 1998, ApJ, 498, 181

Kervella, P., Bersier, D., Mourard, D., et al. 2004, A&A, 428, 587
Kochanek, C. S. 1997, ApJ, 491, 13
Luck, R. E., Moffett, T. J., Barnes, T. G., & Gieren, W. P. 1998, AJ, 115, 605
Madore, B. F., Freedman, W. L., Rigby, J., et al. 2009, ApJ, 695, 988
Mayor, M., Pepe, F., Queloz, D., et al. 2003, The Messenger, 114, 20
Moffett, T. J., Gieren, W., Barnes, T. G., & Gomez, M. 1998, ApJS, 117, 135
Nardetto, N., Mourard, D., Mathias, P., Fokin, A., & Gillet, D. 2007, A&A, 471, 661
Nardetto, N., Gieren, W., Kervella, P., et al. 2009, A&A, 502, 951
Pepe, F., Mayor, M., Galland, F., et al. 2002, A&A, 388, 632
Persson, S. E., Madore, B. F., Krzemiński, W., et al. 2004, AJ, 128, 2239
Pietrzyński, G., Gieren, W., Hamuy, M., et al. 2010a, AJ, 140, 1475
Pietrzyński, G., Thompson, I. B., Gieren, W., et al. 2010b, Nature, 468, 542
Romaniello, M., Primas, F., Mottini, M., et al. 2008, A&A, 488, 731
Sakai, S., Ferrarese, L., Kennicutt, R. C., Jr., & Saha, A. 2004, ApJ, 608, 42
Sandage, A., & Tammann, G. A. 2006, ARA&A, 44, 93
Sandage, A., Tammann, G. A., & Reindl, B. 2004, A&A, 424, 43
Sandage, A., Tammann, G. A., & Reindl, B. 2009, A&A, 493, 471
Sasselov, D. D., Beaulieu, J. P., Renault, C., et al. 1997, A&A, 324, 471
Soszyński, I., Poleski, R., Udalski, A., et al. 2008, Acta Astron., 58, 163
Storm, J., Carney, B. W., Gieren, W. P., et al. 2004, A&A, 415, 531
Storm, J., Gieren, W. P., Fouqué, P., Barnes, T. G., & Gómez, M. 2005, A&A, 440, 487
Storm, J., W. Gieren, & P. Fouqué, et al. 2011, A&A, 534, A94 (Paper I)
Tammann, G. A., Reindl, B., & Sandage, A 2011, A&A, 531, A134
Turner, D. G. 2010, Astrophys. Space Sci., 326, 219
Udalski, A. 2000, Acta Astron., 50, 279
Udalski, A., Wyrzykowski, L., Pietrzyński, G., et al. 2001, Acta Astron., 51, 221
Udalski, A., Szymański, M. K., Soszyński, I, & Poleski, R. 2008, Acta Astron., 58, 69
van der Marel, R., & Cioni, M.-R. 2001, AJ, 122, 1807

Annexe I

An eclipsing-binary distance to the Large Magellanic Cloud accurate to two per cent

LETTER

doi:10.1038/nature11878

An eclipsing-binary distance to the Large Magellanic Cloud accurate to two per cent

G. Pietrzyński[1,2], D. Graczyk[1], W. Gieren[1], I. B. Thompson[3], B. Pilecki[1,2], A. Udalski[2], I. Soszyński[2], S. Kozłowski[2], P. Konorski[2], K. Suchomska[2], G. Bono[4,5], P. G. Prada Moroni[6,7], S. Villanova[1], N. Nardetto[8], F. Bresolin[9], R. P. Kudritzki[9], J. Storm[10], A. Gallenne[1], R. Smolec[11], D. Minniti[12,13], M. Kubiak[2], M. K. Szymański[2], R. Poleski[2,14], Ł. Wyrzykowski[2], K. Ulaczyk[2], P. Pietrukowicz[2], M. Górski[2] & P. Karczmarek[2]

In the era of precision cosmology, it is essential to determine the Hubble constant to an accuracy of three per cent or better[1,2]. At present, its uncertainty is dominated by the uncertainty in the distance to the Large Magellanic Cloud (LMC), which, being our second-closest galaxy, serves as the best anchor point for the cosmic distance scale[2,3]. Observations of eclipsing binaries offer a unique opportunity to measure stellar parameters and distances precisely and accurately[4,5]. The eclipsing-binary method was previously applied to the LMC[6,7], but the accuracy of the distance results was lessened by the need to model the bright, early-type systems used in those studies. Here we report determinations of the distances to eight long-period, late-type eclipsing systems in the LMC, composed of cool, giant stars. For these systems, we can accurately measure both the linear and the angular sizes of their components and avoid the most important problems related to the hot, early-type systems. The LMC distance that we derive from these systems (49.97 ± 0.19 (statistical) ± 1.11 (systematic) kiloparsecs) is accurate to 2.2 per cent and provides a firm base for a 3-per-cent determination of the Hubble constant, with prospects for improvement to 2 per cent in the future.

The modelling of early-type eclipsing binary systems consisting of hot stars is made difficult by the problem of obtaining accurate flux calibrations for early-type stars and by the degeneracy between the stellar effective temperatures and reddening[8,9]. As a result, the distances determined from such systems are of limited (~5–10%) accuracy. More-accurate distances can be obtained using binary systems composed of cool stars; however, among the frequent dwarf stars in the LMC such systems are too faint to be accurately analysed with present-day telescopes.

The Optical Gravitational Lensing Experiment (OGLE) has been monitoring around 35 million stars in the field of the LMC for more than 16 years[10]. Using this unique data set, we have detected a dozen extremely scarce, very long-period (60–772-d) eclipsing binary systems composed of intermediate-mass, late-type giants located in a quiet evolutionary phase on the helium-burning loop[11] (Supplementary Table 1). These well-detached systems provide an opportunity to use the full potential of eclipsing binaries as precise and accurate distance indicators, and to calibrate the zero point of the cosmic distance scale with an accuracy of about 2% (refs 5, 12, 13).

To do so, we observed eight of these systems (Fig. 1 shows one example) over the past 8 yr, collecting high-resolution spectra with the MIKE spectrograph at the 6.5-m Magellan Clay telescope at the Las Campanas Observatory and with the HARPS spectrograph attached to the 3.6-m telescope of the European Southern Observatory on La Silla, together with near-infrared photometry obtained with the 3.5-m New Technology Telescope located on La Silla.

The spectroscopic and OGLE V- and I-band photometric observations of the binary systems were then analysed using the 2007 version of the standard Wilson–Devinney code[14,15], in the same way as in our recent work on a similar system in the Small Magellanic Cloud[9]. Realistic errors in the derived parameters of our systems were obtained from extensive Monte Carlo simulations (Fig. 2). The astrophysical parameters of all the observed eclipsing binaries were determined with an accuracy of a few per cent (Supplementary Tables 2–9).

For late-type stars, we can use the very accurately calibrated (2%) relation between their surface brightness and $V-K$ colour to determine their angular sizes from optical (V) and near-infrared (K) photometry[16]. From this surface-brightness/colour relation (SBCR), we can derive angular sizes of the components of our binary systems directly from the definition of the surface brightness. Therefore, the distance can be measured by combining the angular diameters of the binary components derived in this way with their corresponding linear dimensions obtained from the analysis of the spectroscopic and photometric data. The distances measured with this very simple but accurate one-step method are presented in Supplementary Table 12. The statistical errors in the distance determinations were calculated by adding quadratically the uncertainties in absolute dimensions, $V-K$ colours, reddening and the adopted reddening law. The reddening uncertainty contributes very little (0.4%) to the total error[11,17]. A significant change in the reddening law (from $R_v = 3.1$ to 2.7, where R_v is the ratio of total to selective absorption) causes an almost negligible contribution, at the level of 0.3%. The accuracy of the $V-K$ colour for all components of our eight binary systems is better than 0.014 mag (0.7%). The resulting statistical errors in the distances are very close to 1.5%, and are dominated by the uncertainty in the absolute dimensions. By calculating a weighted mean from the individual distances to the eight target eclipsing binary systems, we obtain a mean LMC distance of 49.88 ± 0.13 kpc.

Our distance measurement might be affected by the geometry and depth of the LMC. Fortunately, the geometry of the LMC is simple and well studied[18]. Because nearly all the eclipsing systems are located very close to the centre of the LMC and to the line of nodes (Fig. 3), we fitted the distance to the centre of the LMC disk plane, assuming its spatial orientation[18]. We obtained an LMC barycentre distance of 49.97 ± 0.19 kpc (Fig. 4), which is nearly identical to the simple weighted mean value. This shows that the geometrical structure of the LMC has no significant influence on our present distance determination.

[1]Universidad de Concepción, Departamento de Astronomía, Casilla 160-C, Concepción, Chile. [2]Warsaw University Observatory, Aleje Ujazdowskie 4, 00-478 Warszawa, Poland. [3]Carnegie Observatories, 813 Santa Barbara Street, Pasadena, California 91101-1292, USA. [4]Dipartimento di Fisica Università di Roma Tor Vergata, Via della Ricerca Scientifica 1, 00133 Rome, Italy. [5]INAF-Osservatorio Astronomico di Roma, Via Frascati 33, 00040 Monte Porzio Catone, Italy. [6]Dipartimento di Fisica Università di Pisa, Largo B. Pontecorvo 2, 56127 Pisa, Italy. [7]INFN, Sezione di Pisa, Via E. Fermi 2, 56127 Pisa, Italy. [8]Laboratoire Lagrange, UMR7293, UNS/CNRS/OCA, 06300 Nice, France. [9]Institute for Astronomy, 2680 Woodlawn Drive, Honolulu, Hawaii 96822, USA. [10]Leibniz Institute for Astrophysics, An der Sternwarte 16, 14482 Postdam, Germany. [11]Nicolaus Copernicus Astronomical Centre, Bartycka 18, 00-716 Warszawa, Poland. [12]Departamento de Astronomía y Astrofísica, Pontificia Universidad Católica de Chile, Vicuña Mackenna 4860, Casilla 306, Santiago 22, Chile. [13]Vatican Observatory, V00120 Vatican City, Italy. [14]Ohio State University, 140 West 18th Avenue, Columbus, Ohio 43210, USA.

©2013 Macmillan Publishers Limited. All rights reserved

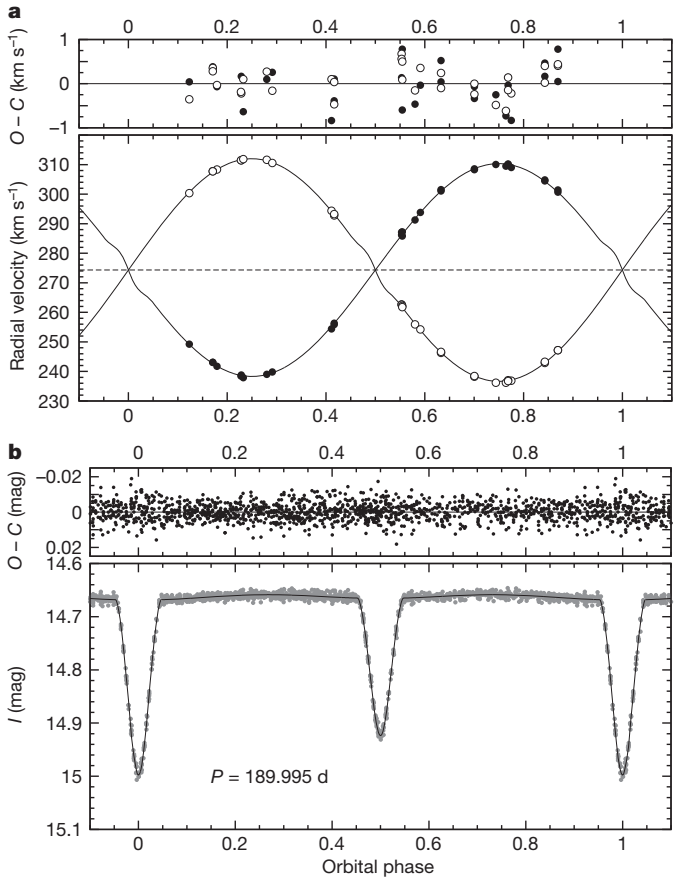


Figure 1 | Change of the brightness of the binary system OGLE-LMC-ECL-06575 and the orbital motion of its components. **a**, The main panel shows the orbital motion of the two binary components in the system OGLE-LMC-ECL-06575. Filled circles, primary component; open circles, secondary component. The top panel shows the residuals of the fit (see below): observed radial velocities (O) minus the computed radial velocities (C). **b**, The main panel shows the I-band light curve (1,200 epochs collected over 16 yr) of OGLE-LMC-ECL-06575 together with the solution obtained using the Wilson–Devinney code. P, orbital period. The top panel shows the residuals of the observed magnitudes from the computed orbital light curve. All individual radial velocities were determined by the cross-correlation method using appropriate template spectra and spectra from the Magellan Inamori Kyocera Echelle (MIKE) and High Accuracy Radial Velocity Planet Searcher (HARPS) spectrographs, yielding in all cases velocity accuracies better than 200 m s^{-1} (error bars smaller than the plotted symbols). The orbit (mass ratio, systemic velocity, velocity amplitudes, eccentricity and periastron passage) was fitted with a least-squares method to the measured velocities. The resulting parameters are presented in Supplementary Tables 2–9. The spectroscopic orbits, light curves and solutions for the remaining systems are of similar quality.

The systematic uncertainty in our distance measurement comes from the calibration of the SBCR and the accuracy of the zero points in our photometry. The root mean squared scatter in the current SBCR is 0.03 mag (ref. 13), which translates to an accuracy of 2% in the respective angular diameters of the component stars. Because the surface brightness depends only very weakly on metallicity[16,17], this effect contributes to the total error budget at the level of only 0.3% (ref. 9). Both optical (V) and near-infrared (K) photometric zero points are accurate to 0.01 mag (0.5%). Combining these contributions quadratically, we determine a total systematic error of 2.1% in our present LMC distance determination.

The LMC contains significant numbers of different stellar distance indicators, and, being the second-closest galaxy to our own, offers us a unique opportunity to study these indicators with the utmost precision. For this reason, this galaxy has an impressive record of several hundred distance measurements[2,3,19]. Unfortunately, almost all LMC

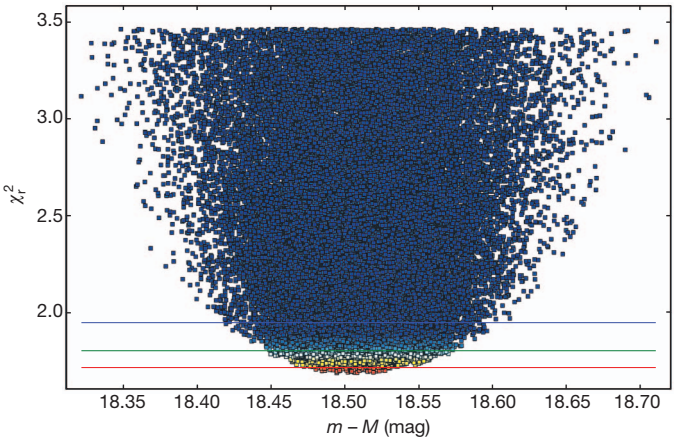


Figure 2 | Error estimation of the distance for one of our target binary systems. The reduced χ^2 map (goodness of fit) for the system OGLE-LMC-ECL-15260 showing the dependence of the goodness of fit to the V-band and I-band light curves on the distance modulus of the primary component. This map was obtained from 110,000 models computed with the Wilson–Devinney code[14,15] within a broad range of the primary and secondary radii, R_1 and R_2, the orbital inclination, i, the phase shift, ϕ, the secondary's temperature, T_2, and albedo, A_2. In each case the distance, d, was calculated from the V-band surface-brightness/colour ($V-K$) relation[16] and translated into distance modulus using $m-M=5\log(d)-5$, where m and M are the observed and absolute brightnesses, respectively. The horizontal lines correspond to the standard-deviation limits of the derived distance modulus, of 18.509 mag (50.33 kpc): 1σ, 2σ and 3σ, from bottom to top.

distance determinations are dominated by systematic errors, with each method having its own sources of uncertainties. This prevents a calculation of the true LMC distance by simply taking the mean of the

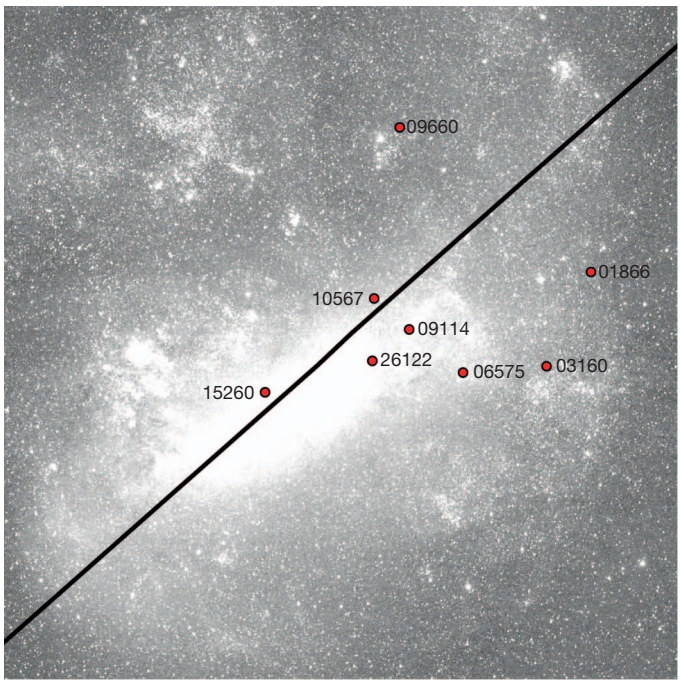


Figure 3 | Location of the observed eclipsing systems in the LMC. Most of our eight systems (circles) are located quite close to the geometrical centre of the LMC and to the line of nodes (line), resulting in very small corrections to the individual distances for the geometrical extension of this galaxy (in all cases smaller than the corresponding statistical error in the distance determination). The effect of the geometrical structure of the LMC on the mean LMC distance reported here is therefore negligible. The background image has a field of view of $8^\circ \times 8^\circ$ and is taken from the All Sky Automated Survey wide-field sky survey[28].

©2013 Macmillan Publishers Limited. All rights reserved

RESEARCH LETTER

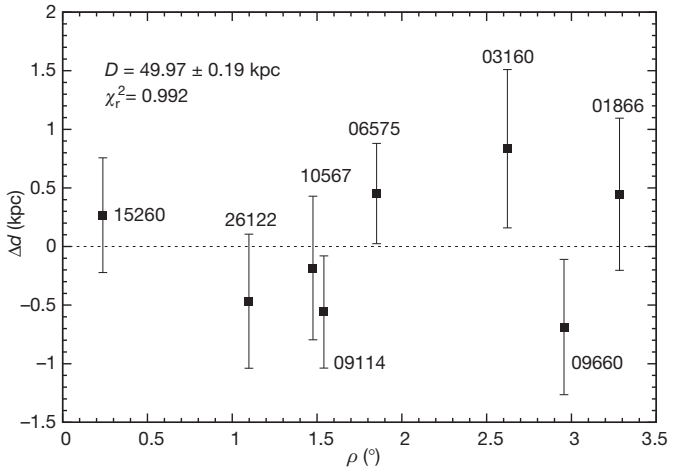


Figure 4 | Consistency among the distance determinations for the target binary systems. Distance offsets, Δd, between our particular eclipsing binary systems and the best-fitted LMC disk plane, plotted against the angular distance of the systems from the LMC centre, ρ. The identification of the systems is the same as in Fig. 3. The error bars correspond to 1σ errors. We assumed the model of the LMC from ref. 18. We fitted one parameter, the distance to the centre of the LMC (RA = 5 h 25 min 06 s; dec. = -69° 47′ 00″), using a fixed spatial orientation of the LMC disk (inclination, $i = 28^\circ$; position angle of the nodes, $\theta = 128^\circ$). The resulting distance to the LMC barycentre is 49.97 ± 0.19 kpc, with a reduced χ^2 value very close to unity.

reported distances resulting from different techniques. Our present LMC distance measurement, of 49.97 ± 0.19 (statistical) $\pm$ 1.11 (systematic) kpc (that is, a true distance modulus of 18.493 ± 0.008 (statistical) $\pm$ 0.047 (systematic) mag), agrees well, within the combined errors, with the most recent determinations of the distance to the LMC[19,20,21]. Our purely empirical method allows us to estimate both statistical and systematic errors in a very reliable way, which is normally not the case, particularly in distance determinations relying in part on theoretical predictions of stellar properties and their dependences on environment. In particular, our result provides a significant improvement over previous LMC distance determinations made using observations of eclipsing binaries[7,22]. Those studies were based on early-type systems for which no empirical SBCR is available, and so had to rely on theoretical models to determine the effective temperature. Our present determination is based on many (eight) binary systems and does not resort to model predictions.

The classical approach to deriving the Hubble constant (H_0) consists of deriving an absolute calibration of the Cepheid period–luminosity relation (CPLR), which is then used to determine the distances to nearby galaxies containing type Ia supernovae[23]. These supernovae are excellent standard candles that extend out to the region of unperturbed Hubble flow once their peak brightnesses are calibrated this way, and provide the most accurate determination of H_0 (ref. 24). An alternative approach to calibrate the CPLR with Cepheids in the LMC is to calibrate it in our own Milky Way galaxy using Hubble Space Telescope (HST) parallax measurements of the Cepheids nearest to the Sun[25]. However, the CPLR that results from that approach is less accurate for two reasons. First, the Cepheid sample with HST parallaxes is very small (ten stars) relative to the Cepheid sample in the LMC (2,000 stars), which can be used to establish the CPLR once the LMC distance is known. Second, the average accuracy of the HST Cepheid parallaxes is 8% (ref. 25) and suffers from systematic uncertainties that are not completely understood, including Lutz–Kelker bias[26,27]. Therefore, at present the preferred route to determining the Hubble constant is that which uses the highly abundant LMC Cepheid population whose mean distance is now known, with the result of this work, to 2.2%. This result reduces the uncertainty in H_0 to a very firmly established 3%.

We have good reason to believe that there is significant room to improve on the high-accuracy LMC distance determination reported here, by improving the calibration of the SBCR for late-type stars[12,16], which is the dominant source of systematic error in our present determination. This work is in progress, and a determination of the distance to the LMC accurate to 1% should be possible once the SBCR calibration is refined. This will have a corresponding effect on further improving the accuracy of H_0. This is similar to the accuracy of the geometrical distance to the LMC, which is to be delivered by Gaia mission in around 12 years from now. The eclipsing-binary technique will then probably provide the best opportunity to check on the future Gaia measurements for possible systematic errors.

Received 19 August; accepted 20 December 2012.

1. Komatsu, E. *et al.* Seven-year Microwave Anisotropy Probe (WMAP) observations: cosmological interpretation. *Astrophys. J. Suppl. Ser.* **192,** 18–65 (2011).
2. Freedman, W. L. & Madore, B. F. The Hubble constant. *Annu. Rev. Astron. Astrophys.* **48,** 673–710 (2010).
3. Schaefer, B. E. A problem with the clustering of recent measures of the distance to the Large Magellanic Cloud. *Astron. J.* **135,** 112–119 (2008).
4. Lacy, C. H. Distances to eclipsing binaries: an application of the Barnes-Evans relation. *Astrophys. J.* **213,** 458–463 (1977).
5. Paczyński, B. in *The Extragalactic Distance Scale* (eds Livio, M., Donahue, M. & Panagia, N.) 273–280 (Space Telescope Sci. Inst. Ser., Cambridge Univ. Press, 1997).
6. Guinan, E. F. The distance to the Large Magellanic Cloud from the eclipsing binary HV 2274. *Astrophys. J.* **509,** L21–L24 (1998).
7. Fitzpatrick, E. L., Ribas, I., Guinan, E. F., Maloney, F. P. & Claret, A. Fundamental properties and distances of Large Magellanic Cloud eclipsing binaries. IV. HV 5936. *Astrophys. J.* **587,** 685–700 (2003).
8. Groenewegen, M. A. T. & Salaris, M. The LMC eclipsing binary HV 2274 revisited. *Astrophys. J.* **366,** 752–764 (2001).
9. Graczyk, D. *et al.* The Araucaria project: an accurate distance to the late-type double-lined eclipsing binary OGLE SMC113.3 4007 in the Small Magellanic Cloud. *Astrophys. J.* **750,** 144–156 (2012).
10. Udalski, A. *et al.* The Optical Gravitational Lensing Experiment: OGLE-III photometric maps of the Large Magellanic Cloud. *Acta Astron.* **58,** 89–102 (2008).
11. Graczyk, D. *et al.* The Optical Gravitational Lensing Experiment: the OGLE-III catalog of variable stars. XII. Eclipsing binary stars in the Large Magellanic Cloud. *Acta Astron.* **61,** 103–122 (2011).
12. Kruszewski, A. & Semeniuk, I. Nearby Hipparcos eclipsing binaries for color-surface brightness calibration. *Acta Astron.* **49,** 561–575 (1999).
13. Pietrzyński, G. *et al.* The Araucaria project: determination of the Large Magellanic Cloud distance from late-type eclipsing binary systems. I. OGLE051019.64–685812.3. *Astrophys. J.* **697,** 862–866 (2009).
14. Wilson, R. E. & Devinney, E. J. Realization of accurate close-binary light curves: application to MR Cygni. *Astrophys. J.* **166,** 605–620 (1971).
15. Van Hamme, W. & Wilson, R. E. Third-body parameters from whole light and velocity curves. *Astrophys. J.* **661,** 1129–1151 (2007).
16. Di Benedetto, G. P. Predicting accurate stellar angular diameters by the near-infrared surface brightness technique. *Mon. Not. R. Astron. Soc.* **357,** 174–190 (2005).
17. Thompson, I. B. *et al.* Cluster AgeS Experiment. The age and distance of the globular cluster ω Centauri determined from observations of the eclipsing binary OGLEGC 17. *Astron. J.* **121,** 3089–3099 (2001).
18. van der Marel, R. P., Alves, D. R., Hardy, E. & Suntzeff, N. B. New understanding of Large Magellanic Cloud structure, dynamics, and orbit from carbon star kinematics. *Astron. J.* **124,** 2639–2663 (2002).
19. Mazzarella, J. M. NED for a new era. *Astron. Soc. Pacif. Conf.* **376,** 153–162 (2007).
20. Walker, A. R. The Large Magellanic Cloud and the distance scale. *Astrophys. Space Sci.* **341,** 43–49 (2012).
21. Monson, A. J. *et al.* The Carnegie Hubble Program: The Leavitt Law at 3.6 and 4.5 μm in the Milky Way. *Astrophys. J.* **759,** 146–165 (2012).
22. Bonanos, A. Z., Castro, N., Macri, L. M. & Kudritzki, R. P. The distance to the massive eclipsing binary LMC-SC1–105 in the Large Magellanic Cloud. *Astrophys. J.* **729,** L9–L15 (2011).
23. Freedman, W. L. *et al.* Final results from the Hubble Space Telescope key project to measure the Hubble constant. *Astrophys. J.* **553,** 47–72 (2001).
24. Riess, A. G. *et al.* A 3% solution: determination of the Hubble constant with the Hubble Space Telescope and Wide Field Camera 3. *Astrophys. J.* **730,** 119–137 (2011).
25. Benedict, G. F. *et al.* Hubble Space Telescope fine guidance sensor parallaxes of galactic Cepheid variable stars: period-luminosity relations. *Astron. J.* **133,** 1810–1827 (2007).
26. Lutz, T. E. & Kelker, D. H. On the use of trigonometric parallaxes for the calibration of luminosity systems: theory. *Publ. Astron. Soc. Pacif.* **85,** 573–578 (1973).
27. van Leeuwen, F., Feast, M. W., Whitelock, P. A. & Laney, C. D. Cepheid parallaxes and the Hubble constant. *Mon. Not. R. Astron. Soc.* **379,** 723–737 (2007).
28. Pojmański, G. The All Sky Automated Survey. *Acta Astron.* **47,** 467–481 (1997).

Supplementary Information is available in the online version of the paper.

Acknowledgements We acknowledge financial support for this work from the BASAL Centro de Astrofísica y Tecnologias Afines (CATA), the Polish Ministry of Science, the

©2013 Macmillan Publishers Limited. All rights reserved

Foundation for Polish Science (FOCUS, TEAM), the Polish National Science Centre and the GEMINI-CONICYT fund. The OGLE project has received funding from the European Research Council 'Advanced Grant' Program. We thank the staff astronomers at Las Campanas and ESO La Silla, who provided expert support in data acquisition. We thank J. F. Gonzalez for making the IRAF scripts rvbina and spbina available to us. We also thank O. Szewczyk and Z. Kołaczkowski for their help with some of the observations.

Author Contributions G.P.: photometric and spectroscopic observations and reductions. D.G.: spectroscopic observations, modelling and data analysis. W.G.: observations and data analysis. I.B.T.: observations, RV determination, data analysis. B.P.: spectroscopic observations and reductions, RV measurements. A.U., I.S. and S. K.: optical observations and data reductions. P.K., K.S., M.K., M.K.S., R.P., Ł.W., K.U., P.P., M.G. and P.K.: observations. G.B., P.G.P.M., N.N., F.B., R.P.K., J.S., A.G. and R.S.: data analysis. S.V.: analysis of the spectra. G.P. and W.G. worked jointly to draft the manuscript with all authors reviewing and contributing to its final form

Author Information Reprints and permissions information is available at www.nature.com/reprints. The authors declare no competing financial interests. Readers are welcome to comment on the online version of the paper. Correspondence and requests for materials should be addressed to G.P. (pietrzyn@astrouw.edu.pl).

©2013 Macmillan Publishers Limited. All rights reserved

SUPPLEMENTARY INFORMATION

doi:10.1038/nature11878

1) Observations and target binary systems

All eclipsing systems studied in this letter, and listed in Supplementary Table 1, were discovered based on the OGLE-II and OGLE-III data[11]. Additional *V* and *I* band observations were collected with the Warsaw 1.3 m telescope at Las Campanas Observatory in the course of the OGLE IV project, and with the 1.3 m telescope at Cerro Tololo Observatory. Once the preliminary periods were calculated the new observations were secured mostly during eclipses, which resulted in a very good phase coverage of all targets. All photometric data were reduced with the image subtraction technique[29] and were calibrated based on the OGLE-III data[10]. The finding chart for all systems can be found on the OGLE Project webpage (ftp://ftp.astrouw.edu.pl/ogle/ogle3/OIII-CVS/lmc/ecl/fcharts)[11]. The raw OGLE V-band and I-band light curves are available at ftp://ftp.astrouw.edu.pl/ogle/ogle3/OIII-CVS/lmc/ecl/phot.

The near infrared photometry was performed with the ESO-La Silla 3.5 m NTT telescope equipped with the SOFI imager. Each system was observed outside of the eclipses during at least 5 different nights through *J* and *K* filters under photometric conditions together with a large number (12-16) of photometric standards from the UKIRT system[30]. The accuracy of the zero points obtained for every night was about 0.02 mag in both *J* and *K* bands. For more details regarding the observations, reduction and calibrations of the near-infrared data the reader is referred to (29).

High resolution echelle spectra were collected with the Las Campanas Observatory Magellan Clay 6.5 m telescope and the MIKE echelle spectrograph[32], and with the ESO 3.6 m telescope and the HARPS fiber-fed echelle spectrograph[33]. In the case of the MIKE observations, a 0.7 arcsec slit was used giving a resolution of about 40,000. The spectra were reduced with the dedicated pipeline software[34]. Exposure times ranged from 1200 sec to 3600 sec depending on observing conditions, and a typical resulting S/N ratio was between 7 and 30 at a wavelength of 450 nm. The HARPS observations were obtained at a resolution of 80,000 and a S/N of about 4-10 at 500 nm for integrations in the range from one minute to half an hour, and were reduced with the data reduction software developed by the Geneva observatory. Radial velocities were calculated with the Broadening Function (BF) formalism[35] and TODCOR[36]. We used templates from a library[37]. Templates were matched to the estimated mean effective temperature and gravity of the components. Both determinations agree with each other within 100 m/s.

Id	R.A. (2000)	Dec. (2000)	P [days]
OGLE-LMC-ECL-09660	$05^h\ 11^m\ 49^s.45$	−67°05'45.2	167.6350 ± 0.0016
OGLE-LMC-ECL-10567	$05^h\ 14^m\ 01^s.89$	−68°41'18.2	117.8708 ± 0.0012
OGLE-LMC-ECL-26122	$05^h14^m06^s.04$	−69°15'56.9	771.7806 ± 0.0048
OGLE-LMC-ECL-09114	$05^h10^m19^s.64$	−68°58'12.2	214.1707 ± 0.0009
OGLE-LMC-ECL-06575	$05^h04^m32^s.87$	−69°20'51.0	189.8215 ± 0.0010
OGLE-LMC-ECL-01866	$04^h52^m15^s.28$	−68°19'10.3	251.0068 ± 0.0043
OGLE-LMC-ECL-03160	$04^h55^m51^s.48$	−68°13'48.0	150.0198 ± 0.0018
OGLE-LMC-ECL-15260	$05^h25^m25^s.66$	−69°33'04.5	157.3243 ± 0.0008

Supplementary Table 1. Selected eclipsing binary systems.

The periods reported in this table and in all Supplementary Information are true orbital periods linked with the observed periods through the following formula:

$P = P_{OBS} \times \left(1 + \frac{\gamma}{c}\right)^{-1}$ where γ is the systemic velocity and c velocity of light, respectively.

2) The essentials of the modelling

The V and I-band light curves were cleaned from obvious outliers. No sigma clipping was applied. Both light curves and the two radial velocity curves – one per each component of a system – were analysed simultaneously for each system with the Wilson-Devinney code version 2007. We will denote by a subscript "1" the primary component and by a subscript "2" the secondary component of the system. We fitted the following set of adjustable parameters: the semi-major axis a, the mass ratio of the components q, the systemic velocity of the system γ, the apparent orbital period P_{obs}, the modified surface potentials Ω_1 and Ω_2, the secondary's mean surface temperature T_2, the internal luminosity of the primary component in the two bands $L1_V$, $L1_I$ and the orbital inclination i. In case of circular systems we fitted the epoch of the primary eclipse HJD0 and in some cases the albedo of the secondary A_2, while in the cases of eccentric systems we fitted the phase shift φ and additionally the orbital eccentricity e and the argument of periastron ω. The initial values of adjustable parameters for the Wilson-Devinney code were found by a trial-and-error procedure.

The temperature of the primary T_1 (which is important because it scales the temperature of the secondary component and influences the limb darkening coefficients) was set as follows. The initial value was set to 5000 K, as this value is a reasonable assumption for late type giant stars. Then we run the WD code to obtain a preliminary model from which we obtained the components' light ratios in the *V*- and *I*-band. Additionally we extrapolated the model to calculate the *K*-band light ratio using theoretical limb darkening coefficients in this band. Combining these light ratios with the observed magnitudes in the *V*-, *I*- and *K*-bands, and using the reddenings derived from red clump stars in the fields containing our eclipsing binaries, we calculated the intrinsic colors $(V–I)_0$, $(V–K)_0$ of both stars. Using several calibrations between color indices and effective temperature[38,39,40,41] we estimated the temperatures of both components, especially the primary's temperature T_1. Then we run the WD code again with the new temperatures. Once updated reddening estimates were obtained we repeated the procedure. We iterated the temperature determination several times until full consistency of the model parameters was obtained, especially an agreement between the distance obtained from the surface brightness calibration and the distance resulting from bolometric flux scaling.

For most of our systems a correlation between the relative radii of both components can be observed. This is usual in the case of eclipsing binaries with partial eclipses. Two of our systems, LMC-ECL-09114 and LMC-ECL-09660, show total eclipses thus this correlation is unimportant in their case. However for the rest of the sample the influence of this correlation on the stellar radii and the resulting distance determination had to be investigated. To this end we first calculated approximate spectroscopic light ratios from the intensity of absorption lines and compared them to our light curve model predictions. A disagreement was found only for system LMC-ECL-10567. Subsequently we performed Monte Carlo simulations to investigate multi-dimensional parameter space and possible correlations between parameters. Some details of these simulations are given at the end of this section.

Initially we used a logarithmic limb darkening law in all cases utilizing pre-computed tables of theoretical limb darkening coefficients (setting LD= -2 in the WD2007 code). Additionally, we computed models with linear limb darkening (setting LD= -1) and also models where coefficients of the linear limb darkening law were treated as adjustable parameters (setting LD = +1). Usually models computed with linear and logarithmic law limb darkenings result in similar reduced χ^2 values. However models with adjusted coefficients of linear limb darkening usually lead to considerably better fits to the light curves. Exceptions are the systems LMC-ECL-26122, LMC-ECL-01866 and LMC-ECL-10567. In the first one no improvement in the reduced χ^2 can be seen. In the second case this procedure leads to a solution with very low coefficients (below zero) indicating limb brightening. In the last system the fitted coefficients are peculiar: unacceptably high and larger in the infrared than in optical. In those three cases we adopted the solution obtained with fixed coefficients of the logarithmic limb darkening law.

We tested the possible presence of a third light in our light curves and spectra. We could not detect any additional source of absorption lines in our spectra. We tested our spectra using the CCF, TODCOR and BF methods with different templates corresponding to a

temperature range from 3500 to 7000 K but we failed to detect any third light source stronger that 1% of the combined signal of the two components of the systems. We also computed models setting the third light parameter *l*3 (being a fraction of the total observed flux) as an adjustable parameter of a solution for all our systems. Only in the case of LMC-ECL-10567 we found a small contribution of a third light in the optical *V*-band light curve, however in the *I*-band the third light contribution is insignificant. The third light in this system, if real, might be a faint blue companion or an optical blend (*V*~20 mag; *I*~21.5 mag) e.g. a white dwarf or even a QSO.

After inspection of the absorption lines broadening, which mostly comes from rotational broadening, we concluded that the rotation velocities of the components are consistent with both components being synchronized. Thus in all our computations the rotation parameter *F* was fixed at 1.0 for both stars of a given eclipsing binary system, corresponding to the rotation being synchronous with the orbital period.

We estimated statistical errors on the parameters by performing Monte-Carlo simulations. We calculated a large number of models (usually over one hundred thousand per system) with input parameters randomly selected from a broad range of possible values and compared them to the *V*-band and *I*-band light curves to compute the residuals of the model and the resulting reduced χ^2. In the Monte-Carlo simulations we allowed to vary the following parameters : the modified surface potentials Ω_1 and Ω_2, the secondary's mean surface temperature T_2, the orbital inclination i, the epoch of the primary eclipse HJD0 and in some cases, the albedo of the secondary A_2. The spectroscopic parameters during the simulations were kept fixed. The resulting χ^2 maps and parameter correlation maps were used to derive realistic errors on the model parameters. For example, the radii correlation in the case of eclipsing binaries with partial eclipses is only marginally affecting our distances because the prime source of statistical error is the uncertainty of the sum of the radii R_1+R_2. Although for our systems, on average, radii are known with an accuracy of 3%, the sum of the radii is always known with an accuracy better than 2.0%. The largest source of uncertainty in the radii sum determination turns out to be the correlation between the orbital inclination and the radii.

Parameter	Primary	Secondary
(m-M) = distance modulus	18.489	18.489
$M/M_{\odot}$ = mass	2.969 ± 0.020	2.988 ± 0.018
$R/R_{\odot}$ = *radius*	23.75 ± 0.66	43.87 ± 1.14
T =effective temperature	5352 ± 70 K	4677 ± 75 K

K = velocity amplitude	35.13 ± 0.06 km/s	34.91 ± 0.08 km/s
e = eccentricity	0.0517 ± 0.0013	
ω = periastron passage	212.1 ± 1.5 deg	
γ = systemic velocity	286.24 ± 0.04 km/s	
P =orbital period	167.6350 ± 0.0016 days	
i =inclination	87.81 ± 0.31 deg	
$a/R_{\odot}$ = orbit size	232.00 ± 0.32	
q = mass ratio	1.0065 ± 0.0027	
A = albedo	0.5 (fixed)	
x_V =linear limb darkening coeff.	0.697 ± 0.098	0.726 ± 0.036
x_I= linear limb darkening coeff.	0.450 ± 0.077	0.391 ± 0.039
V (observed magnitude)	17.303	16.799
V−I (observed color)	0.959	1.234
V−K (observed color)	2.190	2.830
E(B-V) reddening	0.127 ± 0.020	
[Fe/H] = metallicity	−0.44 ± 0.10	

Supplementary Table 2. Astrophysical parameters of the OGLE-LMC-ECL-09660 system

Parameter	Primary	Secondary
(m-M) = distance modulus	18.489	18.491

$M/M_{\odot}$ =mass	3.345 ± 0.040	3.183 ± 0.038
$R/R_{\odot}$ = *radius*	25.6 ± 1.6	36.0 ± 2.0
T =effective temperature	5067 ± 73 K	4704 ± 80 K
K = velocity amplitude	39.31 ± 0.13 km/s	41.32 ± 0.14 km/s
e = eccentricity	0.0 (fixed)	
ω = periastron passage	90 (fixed)	
γ = systemic velocity	265.10 ± 0.08 km/s	
P =orbital period	117.8708 ± 0.0012 days	
i = inclination	83.47 ± 0.33 deg	
$a/R_{\odot}$ = orbit size	189.13 ± 0.45	
q = mass ratio	0.9515 ± 0.0043	
A = albedo	0.5 (fixed)	0.100 ± 0.053
x_V =linear limb darkening coeff.	not adjusted	not adjusted
x_I = linear limb darkening coeff.	not adjusted	not adjusted
$l3_V$ = third light	0.0482 ± 0.0305	
$l3_I$ = third light	0.0036 ± 0.0315	
$l3_K$ = third light	0.0 (fixed)	
V (observed magnitude)	17.374	17.114
V−I (observed color)	1.019	1.158
V−K (observed color)	2.355	2.730
E(B-V) reddening	0.102 ± 0.020	

[Fe/H] = metallicity	−0.81 ± 0.20

Supplementary Table 3. Astrophysical parameters of the OGLE-LMC-ECL-10567 system

Parameter	Primary	Secondary
(m-M) = distance modulus	18.470	18.468
$M/M_{\odot}$ = mass	3.593 ± 0.055	3.411 ± 0.047
$R/R_{\odot}$ = *radius*	32.71 ± 0.51	22.99 ± 0.48
T =*effective temperature*	4989 ± 80 K	4995 ± 81 K
K = *velocity amplitude*	23.80 ± 0.10 km/s	25.08 ± 0.14 km/s
e = eccentricity	0.4186 ± 0.0019	
ω = periastron passage	302.3 ± 0.2 deg	
γ = systemic velocity	266.38 ± 0.07 km/s	
P =orbital period	771.7806 ± 0.0048 days	
i = inclination	88.45 ± 0.04 deg	
$a/R_{\odot}$ = orbit size	677.64 ± 2.36	
q = *mass ratio*	0.9491 ± 0.0067	
A = albedo	0.5 (fixed)	
x_V =linear limb darkening coeff.	not adjusted	not adjusted
x_I= linear limb darkening coeff.	not adjusted	not adjusted
V (observed magnitude)	17.067	17.827

V−I (observed color)	1.093	1.088
V−K (observed color)	2.561	2.558
E(B-V) reddening	0.140 ± 0.020	
[Fe/H] = metallicity	−0.15 ± 0.10	

Supplementary Table 4. Astrophysical parameters of the OGLE-LMC-ECL-26122 system

Parameter	Primary	Secondary
(m-M) = distance modulus	18.465	18.465
$M/M_{\odot}$ = mass	3.303 ± 0.028	3.208 ± 0.026
$R/R_{\odot}$ = *radius*	26.18 ± 0.31	18.64 ± 0.30
T =*effective temperature*	5288 ± 81 K	5470 ± 96 K
K = *velocity amplitude*	32.76 ± 0.08 km/s	33.37 ± 0.10 km/s
e = eccentricity	0.0393 ± 0.0018	
ω = periastron passage	97.1 ± 0.3 deg	
γ = systemic velocity	272.04 ± 0.05 km/s	
P =orbital period	214.1707 ± 0.0009 days	
i =inclination	88.77 ± 0.17 deg	
$a/R_{\odot}$ = orbit size	281.38 ± 0.54	
q = *mass ratio*	0.9711 ± 0.0037	
A = albedo	0.5 (fixed)	

x_V =linear limb darkening coeff.	0.632 ± 0.068	0.555 ± 0.106
x_I = linear limb darkening coeff.	0.323 ± 0.067	0.319 ± 0.082
V (observed magnitude)	17.217	17.783
$V-I$ (observed color)	1.059	0.984
$V-K$ (observed color)	2.319	2.188
$E(B-V)$ reddening	0.160 ± 0.020	
[Fe/H] = metallicity	−0.23 ± 0.10	

Supplementary Table 5. Astrophysical parameters of the OGLE-LMC-ECL-09114 system.

Parameter	Primary	Secondary
$(m-M)$ = distance modulus	18.497	18.497
$M/M_{\odot}$ = mass	4.152 ± 0.030	3.966 ± 0.032
$R/R_{\odot}$ = *radius*	39.79 ± 1.35	49.35 ± 1.45
T =*effective temperature*	4903 ± 72 K	4681 ± 77 K
K = *velocity amplitude*	36.03 ± 0.09 km/s	37.72 ± 0.07 km/s
e = eccentricity	0.0 (fixed)	
ω = periastron passage	90 (fixed)	
γ = systemic velocity	274.32 ± 0.05 km/s	
P =orbital period	189.8215 ± 0.0010 days	

i = inclination	82.06 ± 0.13 deg	
$a/R_{\odot}$ = orbit size	279.44 ± 0.44	
q = mass ratio	0.9552 ± 0.0034	
A = albedo	0.5 (fixed)	0.648 ± 0.043
x_V =linear limb darkening coeff.	0.789 ± 0.076	0.791 ± 0.068
x_I= linear limb darkening coeff.	0.336 ± 0.071	0.337 ± 0.065
V (observed magnitude)	16.642	16.490
V−I (observed color)	1.099	1.190
V−K (observed color)	2.529	2.775
E(B-V) reddening	0.107 ± 0.020	
[Fe/H] = metallicity	−0.45 ± 0.10	

Supplementary Table 6. Astrophysical parameters of the OGLE-LMC-ECL-06575 system

Parameter	Primary	Secondary
(m-M) = distance modulus	18.496	18.496
$M/M_{\odot}$ = mass	3.575 ± 0.028	3.574 ± 0.038
$R/R_{\odot}$ = *radius*	28.20 ± 1.06	46.96 ± 0.61
T =effective temperature	5327 ± 72 K	4541 ± 85 K
K = velocity amplitude	33.27 ± 0.14 km/s	33.28 ± 0.05 km/s
e = eccentricity	0.2412 ± 0.0008	
ω = periastron passage	15.5 ± 0.3	

γ = systemic velocity	293.44 ± 0.04 km/s	
P =orbital period	251.0068 ± 0.0043 days	
i =inclination	83.34 ± 0.10 deg	
$a/R_{\odot}$ = orbit size	322.68 ± 0.73	
q = *mass ratio*	0.9997 ± 0.0045	
A = albedo	0.5 (fixed)	
x_V =linear limb darkening coeff.	not adjusted	not adjusted
x_I= linear limb darkening coeff.	not adjusted	not adjusted
V (observed magnitude)	16.916	16.842
$V-I$ (observed color)	0.952	1.250
$V-K$ (observed color)	2.170	2.973
E(B-V) reddening	0.115 ± 0.020	
[Fe/H] = metallicity	−0.70 ± 0.10	

Supplementary Table 7. Astrophysical parameters of the OGLE-LMC-ECL-01866 system.

Parameter	Primary	Secondary
(m-M) = distance modulus	18.505	18.505
$M/M_{\odot}$ = mass	1.792 ± 0.027	1.799 ± 0.028
$R/R_{\odot}$ = *radius*	16.36 ± 1.06	37.42 ± 0.52
T =*effective temperature*	4954 ± 83 K	4490 ± 82 K

K = *velocity amplitude*	30.47 ± 0.14 km/s	30.35 ± 0.11 km/s
e = eccentricity	0.0 (fixed)	
ω = periastron passage	90 (fixed)	
γ = systemic velocity	267.68 ± 0.08 km/s	
P =orbital period	150.0198 ± 0.0018 days	
i = inclination	83.36 ± 0.57 deg	
$a/R_{\odot}$ = orbit size	182.01 ± 0.52	
q = *mass ratio*	1.0039 ± 0.0058	
A = albedo	0.5 (fixed)	
x_V =linear limb darkening coeff.	0.763 ± 0.174	0.796 ± 0.139
x_I= linear limb darkening coeff.	0.623 ± 0.112	0.567 ± 0.069
V (observed magnitude)	18.589	17.453
V−*I* (observed color)	1.076	1.308
V−*K* (observed color)	2.542	3.062
E(B-V) reddening	0.123 ± 0.020	
[Fe/H] = metallicity	−0.48 ± 0.20	

Supplementary Table 8. Astrophysical parameters of the OGLE-LMC-ECL-03160 system.

Parameter	Primary	Secondary
(m-M) = distance modulus	18.509	18.509

$M/M_{\odot}$ = mass	1.440 ± 0.024	1.426 ± 0.022
$R/R_{\odot}$ = *radius*	23.51 ± 0.69	42.17 ± 0.33
T =*effective temperature*	4706 ± 87 K	4320 ± 81 K
K = *velocity amplitude*	27.67 ± 0.11 km/s	27.93 ± 0.14 km/s
e = eccentricity	0.0 (fixed)	
ω = periastron passage	90 (fixed)	
γ = systemic velocity	276.66 ± 0.06 km/s	
P =orbital period	157.3243 ± 0.0008 days	
i =inclination	82.99 ± 0.39 deg	
$a/R_{\odot}$ = orbit size	174.25 ± 0.56	
q = *mass ratio*	0.9905 ± 0.0059	
A = albedo	0.5 (fixed)	0.530 ± 0.031
x_V =linear limb darkening coeff.	0.676 ± 0.092	0.936 ± 0.049
x_I= linear limb darkening coeff.	0.598 ± 0.060	0.660 ± 0.031
V (observed magnitude)	18.066	17.390
$V-I$ (observed color)	1.149	1.392
$V-K$ (observed color)	2.737	3.213
$E(B-V)$ reddening	0.100 ± 0.020	
[Fe/H] = metallicity	−0.47 ± 0.15	

Supplementary Table 9. Astrophysical parameters of the OGLE-LMC-ECL-15260 system.

3) Reddening determination and its influence on the distance determination

We used two different techniques to derive the reddening. For all our systems but one (LMC-ECL-15260) we managed to co-add and disentangle their spectra using the RaVeSpAn software developed by our group, implementing the method proposed in (42). The disentangled spectra were renormalized with the luminosity ratio of the secondary to the primary L2/L1(λ) from our best model. Based on the analysis of the spectra of individual components we calculated a standard set of atmospheric parameters (the effective temperature T_{eff}, gravity log g, microturbulance velocity v_t and metallicity [Fe/H]). Synthetic *V–I* colors were calculated utilizing two calibrations between atmospheric parameters and the intrinsic color $(V–I)_o$ [40,41]. Comparing the colors obtained in this way to the corresponding observed colors, we calculated reddenings with a typical accuracy of 0.02 mag. In addition we used OGLE-III photometry[10] in order to calculate the mean red clump brightness in the *V* and *I* bands in 7x7 arcmin regions centered on our binary systems. In all cases, we were able to calculate the mean red clump magnitudes with an accuracy better than 0.01 mag. Following other studies of red clump stars[43] we assumed a *V-I* color of 0.72 (e.g. median color of RC stars in the LMC) as the color corresponding to the foreground reddening E(B-V) = 0.075 mag[44]. Then the reddening was determined from the observed color of red clump stars using the reddening law[45], which is appropriate for the LMC and was used in all calculations presented in our letter. In order to check our determinations we also calculated the reddening for three other fields where accurate reddenings were obtained based on Strömgren photometry[46], UBV photometry[8] and spectral analysis[22]. As can bee seen in Table 1, our determinations agree very well with the corresponding values of the reddenings reported in the literature. Finally, we estimated reddenings from the LMC reddening maps[47] based on OGLE-III photometry of RR Lyrae stars. All the determinations are in good agreement (see Table 2). As the final reddening we adopted the mean from the available determinations.

Field	R.A. (2000)	Dec. (2000)	E(B-V) $_{RC}$	E(B-V) $_{Lit}$	Reference
P168.6	$5^h29^m53^s$	-69°09’23’’	0.151	0.140	Larsen et al. 2000
P169.3	$5^h34^m48^s$	-69°42’36’’	0.119	0.110	Bonanos et al. 2011
P126.4	$5^h02^m40^s$	-68°24’21’’	0.119	0.103	Groenewegen & Salaris (2001)

Supplementary Table 10. Comparison of the reddenings obtained with red clump stars to the corresponding values reported in the literature, for three fields in the LMC.

System	$E(B-V)_{RC}$	$E(B-V)_{RR\ Lyr}$	$E(B-V)_{spec}$	$E(B-V)_{adopted}$
OGLE-LMC-ECL-09660	0.126	0.13	0.126	0.127
OGLE-LMC-ECL-10567	0.126	0.106	0.075	0.102
OGLE-LMC-ECL-26122	0.138	0.127	0.155	0.140
OGLE-LMC-ECL-09114	0.139	0.131	0.21	0.160
OGLE-LMC-ECL-06575	0.107	0.101	0.113	0.107
OGLE-LMC-ECL-01866	0.119	0.15	0.075	0.115
OGLE-LMC-ECL-03160	0.126	0.124	0.12	0.123
OGLE-LMC-ECL-15260	0.11	0.091	----	0.100

Supplementary Table 11. Reddening determinations for our target eclipsing systems based on an analysis of their disentangled spectra, red clump stars, and RR Lyrae stars.

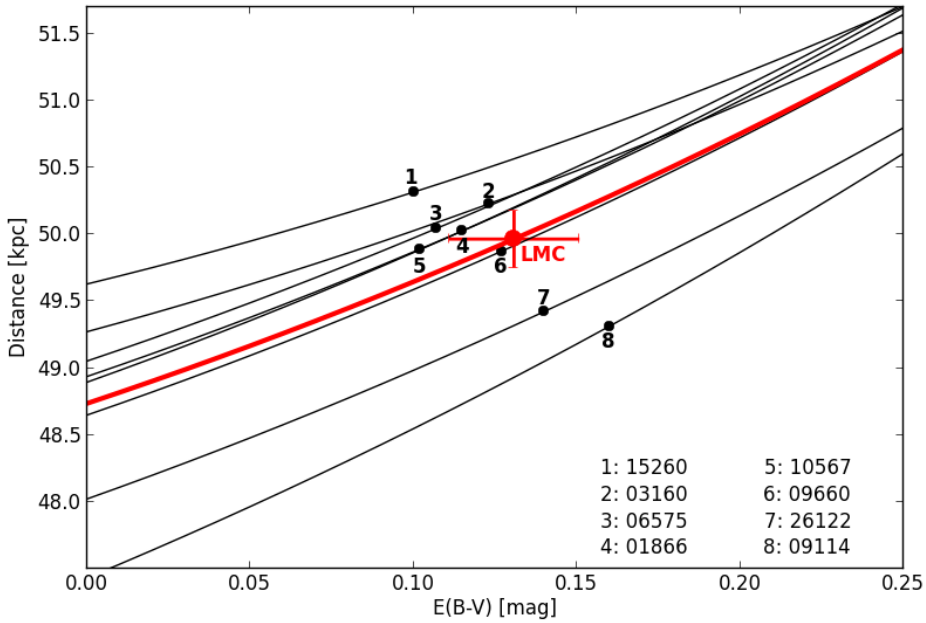


Figure S1. The final distances of the studied eclipsing systems calculated as a function of the adopted reddening. The thick red line is an average relation obtained from all systems. Points correspond to distances of individual systems identified in the plot legend. The larger red point denotes our distance determination to LMC. As can be appreciated from the error bars, a change of the reddening by 0.02 mag (1 σ) causes a change in the distance by 0.4% only (215 pc). This confirms the previous conclusions[9,17] that our method of distance determination is only very slightly dependent on the adopted reddening.

4) Distance determination

The surface brightnesses of the components of the studied systems were derived based on their disentangled (*V*-*K*) colors using the calibration $S_v = 2.656 + 1.483 \times (V-K)_0 - 0.044 \times (V-K)_0^2$ [16]. The angular diameters were obtained directly from the definition of the surface brightness ($\phi[mas] = 10^{0.2 \times (S_v - V_0)}$). Finally distances to individual stars were derived combining their angular diameters obtained this way, and their linear diameters determined from the analysis of the spectroscopic and photometric data ($d[pc] = 9.2984 \times \frac{R[R_{sun}]}{\phi[mas]}$).

In case of models with fixed theoretical limb darkening coefficients the disentangling of colors was performed in the way described in the Section 2. As a final distance we adopted the mean distance of both components of a system. The difference in the distance moduli of the components of the same system is not larger than 0.002 mag in

all cases. Such small differences serve as an independent check of consistency and reliability of our results.

For models with adjusted limb darkening coefficients we employed another strategy to obtain the individual colors because we cannot extrapolate model predictions for the K-band in this case (there is no possibility to obtain appropriate limb darkening coefficients by their adjustment because of the lack of the K-band light curve). We assumed that both components of a system are at the same distance from us and we made iterations until we found a K-band components' light ratio fulfilling our assumption. Then we computed the disentangled (V–K) colors of the components.

In Supplementary Table 12 we list the individual and mean distances measured for all studied systems. As can be seen, the obtained distances are in excellent agreement.

System	$(m-M)_1$	$(m-M)_2$	$(m-M)_{mean}$	σ_{m-M}	$\Delta(m-M)$
OGLE-LMC-ECL-09660	18.489	18.489	18.489	0.025	0.035
OGLE-LMC-ECL-10567	18.489	18.491	18.490	0.027	0.007
OGLE-LMC-ECL-26122	18.470	18.468	18.469	0.025	-0.005
OGLE-LMC-ECL-09114	18.465	18.465	18.465	0.021	-0.004
OGLE-LMC-ECL-06595	18.497	18.497	18.497	0.019	-0.021
OGLE-LMC-ECL-01866	18.496	18.496	18.496	0.028	-0.021
OGLE-LMC-ECL-03160	18.505	18.505	18.505	0.029	-0.012
OGLE-LMC-ECL-15260	18.509	18.509	18.509	0.021	0.004

Supplementary Table 12. Individual distance moduli of the studied eclipsing binary systems. The symbols 1,2 and mean refer to the individual primary (1) and secondary (2) components of our eclipsing systems. The fifth column gives the total statistical uncertainty for the mean distance modulus. The geometrical corrections calculated from the model[18] are given in the last column.

System	$(m-M)_{fix}$	$(m-M)_{fit}$	$\Delta(m-M)$
OGLE-LMC-ECL-09660	18.490	18.489	-0.001
OGLE-LMC-ECL-10567	18.490	18.506	0.016
OGLE-LMC-ECL-26122	18.469	18.482	0.013
OGLE-LMC-ECL-09114	18.481	18.465	-0.016
OGLE-LMC-ECL-06575	18.52	18.497	-0.023
OGLE-LMC-ECL-01866	18.496	18.496	0.000
OGLE-LMC-ECL-03160	18.511	18.505	-0.006
OGLE-LMC-ECL-15260	18.500	18.509	0.009

Supplementary Table 13. Comparison of the distance moduli of our systems as determined by fitting limb darkening coefficients (fit), and by using theoretical values of the limb darkening coefficients (fix). The average of the differences listed in the third column is -0.00075, which clearly shows that the way the limb darkening is chosen for our systems has a negligible effect on the final distance determination presented in our letter.

References

29. Udalski, A. 2003, Acta Astron., 53, 291

30. Hawarden, T. G., Leggett, S. K., Letawsky, M. B., Ballantyne, D. R., & Casali, M. M. 2001, MNRAS, 325, 563

31. Pietrzynski, G., et al. 2006, ApJ, 642, 216

32. Bernstein, R., Shectman, S. A., Gunnels, S. M., Mochnacki, S. & Athey, A. 2003, SPIE, 4841, 1694

33. Mayor, M. et al. 2003, The Messenger, 114, 20

34. Kelson, D. D. 2003, PASP, 115, 688

35. Rucinski, S.M. 1992, AJ, 104, 1968

36. Mazeh, T., Zucker, S. 1994, ApJ, 420, 806

37. Coelho, P., Barbuy, Melendez, J., Sciavon, R.P., & Castilho, B.V. 2005, A&A, 443, 735

38. di Benedetto, G. P. 1998, A&A, 339, 858

39. Ramirez, I., & Melendez, J. 2005, ApJ, 626, 465

40. Casagrande, L., Ramırez, I., Melendez, J., Bessell, M., & Asplund, M. 2010, A&A, 512, 54

41. Worthey, G. & Lee, H. 2011, ApJS, 193, 1

42. Gonzales, J.F., Levato, H., 2005, A&A, 448, 283

43. Subramanian, A., Subramanian, S., ApJL, 703, L37

44. Schlegel, D. J., Finkbeiner, D. P., & Davis, M. 1998, ApJ, 500, 525

45. Cardelli, J. A., Clayton, G. C., & Mathis, J. S. 1989, ApJ, 345, 245

46. Larsen, S.S., Clausen, J.V., Storm, J., 2000, A&A, 364, 455

47. Pejcha, Ondřej; Stanek, K. Z., ApJ, 704, 1730

Annexe J

High-resolution spectroscopy for Cepheids distance determination. II. A period-projection factor relation

A&A 471, 661–669 (2007)
DOI: 10.1051/0004-6361:20066853
© ESO 2007

Astronomy & Astrophysics

High-resolution spectroscopy for Cepheids distance determination

II. A period-projection factor relation⋆

N. Nardetto[1], D. Mourard[2], Ph. Mathias[2], A. Fokin[2,3], and D. Gillet[4]

[1] Max-Planck-Institut für Radioastronomie, Auf dem Hügel 69, 53121 Bonn, Germany
e-mail: nardetto@mpifr-bonn.mpg.de
[2] Observatoire de la Côte d'Azur, Dpt. Gemini, UMR 6203, 06130 Grasse, France
[3] Institute of Astronomy of the Russian Academy of Sciences, 48 Pjatnitskaya Str., Moscow 109017, Russia
[4] Observatoire de Haute Provence, 04870 Saint-Michel l'Observatoire, France

Received 1 December 2006 / Accepted 5 May 2007

ABSTRACT

Context. The projection factor is a key quantity for the interferometric Baade-Wesselink (hereafter IBW) and surface-brightness (hereafter SB) methods of determining the distance of Cepheids. Indeed, it allows a consistent combination of angular and linear diameters of the star.
Aims. We aim to determine consistent projection factors that include the dynamical structure of the Cepheids' atmosphere.
Methods. Hydrodynamical models of δ Cep and ℓ Car have been used to validate a spectroscopic method of determining the projection factor. This method, based on the amplitude of the radial velocity curve, is applied to eight stars observed with the HARPS spectrometer. The projection factor is divided into three sub-concepts : (1) a geometrical effect, (2) the velocity gradient within the atmosphere, and (3) the relative motion of the "optical" pulsating photosphere compared to the corresponding mass elements (hereafter $f_{\rm o-g}$). Both, (1) and (3) are deduced from geometrical and hydrodynamical models, respectively, while (2) is derived directly from observations.
Results. The Fe I 4896.439 Å line is found to be the best one to use in the context of IBW and SB methods. A coherent and consistent period-projection factor relation (hereafter *Pp* relation) is derived for this specific spectral line: $p = [-0.064 \pm 0.020] \log P + [1.376 \pm 0.023]$. This procedure is then extended to derive dynamic projection factors for any spectral line of any Cepheid.
Conclusions. This *Pp* relation is an important tool for removing bias in the calibration of the period-luminosity relation of Cepheids. Moreover, it reveals a new physical quantity $f_{\rm o-g}$ to investigate in the near future.

Key words. techniques: spectroscopic – stars: atmospheres – stars: oscillations (including pulsations) – stars: variables: Cepheids – stars: distances

1. Introduction

The period-luminosity relation (hereafter *PL* relation) of the Cepheids is the basis of the extragalactic distance scale, but its calibration is still uncertain at a $\Delta M = \pm 0.10$ mag level. Long-baseline interferometers currently provide a new, quasi-geometric way to calibrate the Cepheids *PL* relation. Indeed, it is now possible to determine the distance of galactic Cepheids up to 1 kpc with the interferometric Baade-Wesselink method, hereafter IBW method; see for e.g. Sasselov & Karovska (1994) and Kervella et al. (2004). Interferometric measurements lead to angular diameter estimations over the whole pulsation period, while the stellar radius variations can be deduced from the integration of the pulsation velocity. The latter is linked to the observational velocity deduced from spectral line profiles by the projection factor p. In this method, angular and linear diameters have to correspond to the same physical layer in the star to correctly estimate the distance. The projection factor is currently the most important limiting quantity of the IBW method. Indeed, in addition to limb-darkening effects, it is related to the velocity gradient and, more generally, to the dynamical structure of the Cepheid atmosphere.

In 1993, Butler studied the velocity gradient in the atmosphere of four Cepheids using the excitation potential of spectral lines, together with their asymmetry. Then, Butler et al. (1996) introduced the velocity gradient in hydrostatic stellar atmosphere models and found a 20% reduction on the amplitude of the pulsation velocity curve in the case of η Aql. In addition, the γ-velocity was reduced by 2 km s^{-1}.

Fokin et al. (1996) studied the velocity gradient in the atmosphere of δ Cep, based on hydrodynamical modelling. It was found to be an important source of broadening for metallic spectral lines, being similar to rotation or geometrical projection effects.

Using an improved version of the hydrodynamical model of δ Cep, Nardetto et al. (2004, hereafter Paper I) proposed an interferometric definition of the projection factor. A difference of a few km s^{-1}was found between the amplitude of the photospheric and line-forming region's velocity curves, leading to a bias of 5% on the derived distance. This theoretical result has been observationally confirmed using trigonometric parallax measurements of the HST and optical long baseline interferometry by Mérand et al. (2005). Nardetto et al. (2006a) show that spectro-interferometry provides a new geometric view of the Cepheids' atmosphere. However, the combination of different techniques (high-resolution spectroscopy, spectro- and

⋆ Table 1 is only available in electronic form at
http://www.aanda.org

Article published by EDP Sciences and available at http://www.aanda.org or http://dx.doi.org/10.1051/0004-6361:20066853

differential- interferometry) is needed to efficiently constrain the physical parameters of the Cepheid atmosphere and, in particular, the projection factor.

Recently, while comparing radial velocity curves of different species, Petterson et al. (2005) found some evidence of a relation between the velocity gradient in the Cepheids' atmosphere and their period. Using a selected sample of absorption metallic lines, we propose to probe the velocity gradient in the Cepheids' atmosphere in order to determine *dynamic* projection factors. First, by using δ Cep and ℓ Car hydrodynamic models, we present a new spectroscopic method for determining the velocity gradient. Then, the method is applied to the eight Cepheids observed with the HARPS instrument. We discuss the choice of the spectral line and then derive a specific period-projection factor relation (hereafter *Pp* relation). Results are discussed within the framework of the *PL* relation. Finally, we propose a general method (for all lines and all stars) of determining the projection factor.

2. Cepheids observed and selected spectral lines.

Ten stars have been observed with the HARPS spectrometer ($R = 120\,000$) : R Tra, S Cru, Y Sgr, β Dor, ζ Gem, Y Oph, RZ Vel, ℓ Car, RS Pup, and X Sgr. In the first paper of this series, Nardetto et al. (2006b, hereafter Paper II) showed that the radial velocity associated with the centroid of the spectral line, together with the line asymmetry, are very important tracers of the dynamical structure of the Cepheids' atmosphere. X Sgr was studied separately by Mathias et al. (2006) because of its very atypical behavior showing several components in the spectral lines profiles. Y Oph is not considered here due to its insufficient phase coverage (see Paper II, Fig. 3).

Using Kurucz's models 1992, we identified about 150 unblended spectral lines. In Paper II, we considered only the unblended metallic line Fe I 6056.005 Å. In this second paper, we have carefully selected 17 spectral lines following two criteria: (1) in order to avoid bias in the determination of the line depth, the continuum must be perfectly defined for all pulsation phases and for all stars. An example of the quality required is given in paper II for the Fe I 6056.005 Å spectral line (see Fig. 1); (2) the selected sample of lines has to cover a wide range of depth. The selected spectral lines are presented in Table 1. Depending on the star and the spectral line considered, the line depth can range from 2% to 55%.

3. Hydrodynamical models

The hydrodynamical model of δ Cep is presented in Paper I. In addition, we have derived a new, consistent model of ℓ Car. Since the main stellar quantities of l Car (HD 84810) are still uncertain, we tried several sets of luminosity L, effective temperature $T_{\rm eff}$, and mass M in order to get suitable observational quantities, such as the pulsation period P, the average radius of the star $\overline{R}$, bolometric and radial velocity curves, and the line profiles. The *ML* relation was taken from Chiosi et al. (1993), and the OPAL opacity tables (Rogers & Iglesias 1992) were used.

This leads to the following set of parameters for a 154-zone model: $M = 11.5\,M_\odot$, $L = 21000\,L_\odot$, $T_{\rm eff} = 5225$ K, $Y = 0.28$, and $Z = 0.02$, which corresponds to a typical Pop. I chemical composition. The inner boundary has been fixed at about $T = 3.5 \times 10^6$ K, corresponding to 4% of the photospheric radius, so the model envelope with the atmosphere contains about 53% of the stellar mass. The atmosphere itself contains about 10^{-4} of the total stellar mass.

We started the hydrodynamical calculations with a linear, non-adiabatic fundamental-mode velocity profile having a value of 10 km s^{-1} at the surface. At the limit cycle, the pulsation period is 34.4 days, very close (3%) to the observational ($P = 35.6$ days) value deduced by Szabados et al. (1989). Bolometric and pulsation velocity amplitudes are 1.3 mag and 50 km s^{-1}, respectively. The relative radius amplitude at the surface is $\Delta R/R = 17\,\%$. The mean photospheric radius is about $\overline{R} = 180\,R_\odot$.

For the hydrodynamical models of δ Cep and ℓ Car used in this paper (see Sect. 4), a careful analysis of the dynamical structure of their atmospheres was performed based on radiative transfer computations (under local thermal equilibrium) of all spectral lines in Table 1.

We only derived the photospheric pulsation velocity for other Cepheids (see Sect. 4.4). Thus, the physical parameters are only roughly estimated since the dynamical structure of the Cepheids' atmosphere is not considered. The period and the radius of the Cepheids are consistent with observations at the 2% and 3% levels respectively, while the mass follows the period-mass relation of Choisi et al. (1993) within 13%. The effective temperature and luminosity were mostly constrained by the period and the radius. R TrA was not modeled because of its extremely short period. A specific and in-depth study would be necessary to model this star.

The hydrodynamical models are presented in Table 2.

4. New insights into understanding the projection factor

In this section, we propose a division of the projection factor into sub-concepts in order to allow a direct constraint from HARPS spectroscopic observations. To test this method, we consider the hydrodynamic models of δ Cep and ℓ Car.

4.1. The projection factor definition

First of all, we have to provide a definition for the projection factor that should be applied in the IBW and SB methods. This has already be done in Paper I, but it must now be refined and adapted to the method proposed here.

We define the interferometric projection factor as

$$p = \frac{\Delta V_{\rm p}^{\rm o}}{\Delta R V_{\rm c}} \qquad (1)$$

where $\Delta V_{\rm p}^{\rm o}$ is the amplitude of the pulsation velocity curve associated to the photosphere (subscript p) of the star. It corresponds exactly to the *optical* (subscript o) barycenter of the photosphere defined by $\tau_{\rm c} = 2/3$, where $\tau_{\rm c}$ is the optical depth in the continuum. $\Delta R V_{\rm c}$ is the amplitude of the radial velocity curve obtained with the centroid method, i.e. the first moment of the spectral line. This definition is justified for the following reasons:

First, we consider the pulsation velocity instead of the radius, as already proposed in Paper I, in order to allow a direct application to spectroscopic observations.

Second, we consider velocity amplitudes to avoid difficulties related to the γ-velocity. The γ-velocity is the averaged value of the radial velocity curve over one pulsation period. This quantity depends on the line considered. Moreover, as shown in Paper I, the projection factor is mainly constrained by velocity amplitudes, which also justifies this choice.

Third, we consider the RV_c velocity instead of the radial velocity associated to the Gaussian fit method, as in Paper I. This is required for obtaining a projection factor independent of the rotation of the star and the natural width of the spectral lines (see Fig. 8, Paper II). We insist on this definition of the radial velocity since it is absolutely required to allow important comparisons between the projection factors of Cepheids.

In the next section, we consider the Fe I 4896.439 Å spectral line as a reference. But the results, in terms of consistency, can be generalized to any other spectral line. We find $p = 1.33$ for δ Cep and $p = 1.27$ for ℓ Car. These values are our references in the following. If we apply a minimization process between $V_p^o(\phi)$ and $pRV_c(\phi)$, with p the only free parameter, we find differences of 0.01, which provides a good estimate of the uncertainty on the projection factor.

4.2. Decomposition of the projection factor

We now divide the projection factor:

$$p = p_o\, f_{grad}\, f_{o-g} \quad (2)$$

into different quantities where,

- $f_{o-g} = \frac{\Delta V_p^o}{\Delta V_p^g}$, where ΔV_p^g is the gas (subscript g) velocity associated to the *optical* barycenter ($\tau_c = 2/3$) of the photosphere. Thus, f_{o-g} is linked to the distinction between the *optical* and *gas* photospheric layers. The *optical* layer is the location where the continuum and line photons are generated (e.g. the location of the photosphere). The *gas* layer is the location of some mass element in the hydrodynamic model mesh where, at some moment in time, the photosphere is located. Given that the location of the photosphere moves through different mass elements as the star pulsates, the two "layers" have different velocities, hence the necessity of the f_{o-g} definition. Indeed, the interferometer in the continuum is only sensitive to the *optical* layer.
- $f_{grad} = \frac{\Delta V_p^g}{\Delta V_l^g}$, where ΔV_l^g is the *gas* velocity associated to the optical barycenter ($\tau_l = 2/3$) of the line-forming (subscript l) region. Thus, f_{grad} is linked to the velocity gradient in the atmosphere of the star. This quantity depends on the line considered.
- $p_o = \frac{\Delta V_l^g}{\Delta RV_c}$ is the geometrical projection factor. It corresponds to an integration of the pulsation velocity field (associated with the line-forming region) projected on the line of sight and weighted by the surface brightness of the star (including limb-darkening in the spectral line). To derive p_o, we use intensity distributions in the continuum provided by the model. As described in Nardetto et al. (2006a), there is a relation between the pulsation velocity and the limb-darkening (and thus p_o): the intensity profile corresponding to the highest velocity *at contraction* is the most limb-darkened, while the profile corresponding to the highest velocity *at expansion* is the least limb-darkened. Given that our definition of p_o is related to the amplitude of radial and pulsation velocity curves, we consider the median value (peak-to-peak) of the $p_o(\phi)$ curve to derive the p_o-factor. However, considering intensity distribution *in the continuum* is an approximation. Indeed, hydrodynamic effects can result in much limb-darkening, especially at the wavelengths corresponding to spectral lines (see e.g. Marengo et al. 2003). Nevertheless, this seems to be negligible since we obtain a good decomposition of the projection factor.

To test this decomposition, we deduced these three quantities directly from the hydrodynamical model, considering the Fe I 4896.439 Å metallic line. For δ Cep, we find $f_{o-g} = 0.963$, $f_{grad} = 0.993$, and $p_o = 1.390$; and for ℓ Car $f_{o-g} = 0.944$, $f_{grad} = 0.982$, and $p_o = 1.366$. The corresponding projection factors are $p[\delta\,\text{Cep}] = 0.963 * 0.993 * 1.390 = 1.33$ and $p[\ell\,\text{Car}] = 0.944 * 0.982 * 1.366 = 1.27$, which correspond to our reference values. The physical decomposition of the projection factor is thus consistent.

One can notice that the p-factors presented in this paper are independent of the pulsation phase. Indeed, they correspond to a specific definition based on velocity amplitudes (Eq. (1)). Figure 1 represents the projection factor decomposition in the case of the Fe I 4896.439 Å line for δ Cep and ℓ Car: ΔRV_c ($\triangle$), ΔV_l^g ($\triangleleft$), ΔV_p^g ($\triangledown$), and ΔV_p^o ($\square$).

4.3. Is there a consistent way to derive f_{grad} directly from observations?

Let assume a linear relation between the line depth and the position of the line-forming region in the atmosphere of the star. Then, considering different spectral lines spread all over the atmosphere, it should be possible to determine the velocity gradient within the atmosphere. Moreover, by extrapolation to the zero line depth, it should be possible to reach the photospheric pulsation velocity.

To test these ideas, we consider the spectral line depth corresponding to the minimum extension of the star (D in the following). We discuss this choice below. Then, we derive ΔRV_c for all spectral lines in Table 1. From this quantity, one should be able to probe the velocity gradient in the atmosphere and *directly* derive f_{grad}. For that, we plot ΔRV_c as a function of the line depth for all spectral lines (Fig. 1). We find a linear correlation ($\Delta RV_c = a_0 D + b_0$) given by the following relations: $\Delta RV_c[\delta\,\text{Cep}] = 2.90D + 32.84$ and $\Delta RV_c[\ell\,\text{Car}] = 5.20D + 37.02$. Interestingly, these relations are spectroscopic observables.

Then, following our decomposition, we translate (D, ΔRV_c) points into (D, $p_o \Delta RV_c$) with $p_o[\delta\,\text{Cep}] = 1.390$ and $p_o[\ell\,\text{Car}] = 1.366$ (Fig. 1). The new relations are then: $p_o\Delta RV_c[\delta\,\text{Cep}] = 4.03D + 45.64$ and $p_o\Delta RV_c[\ell\,\text{Car}] = 7.10D + 50.53$. Another possible way to derive p_o, instead of using hydrodynamical modeling, is to consider a linear law for the continuum-intensity distribution of the star defined by $I(\cos(\theta)) = 1 - u_V + u_V \cos(\theta)$, where u_V is the limb-darkening of the star in the V band (Claret et al. 2000), and u_V is related to the effective temperature T_{eff}, the surface gravity $\log g$, the star metallicity, and the turbulent velocity. Using this method to derive p_o, we find that a slight correction must be applied to allow a comparison between geometric and hydrodynamic modeling. We find $p_o[\text{hydro}] = p_o[\text{geo}] - 0.010$ for δ Cep and $p_o[\text{hydro}] = p_o[\text{geo}] - 0.025$ for ℓ Car. As already mentioned, the limb-darkening in the continuum used to derive $p_o[\text{hydro}]$ is linked to the pulsation velocity and, more generally, to the whole dynamical structure of the Cepheid atmosphere. Such a dynamical effect could explain the difference that we find between $p_o[\text{hydro}]$ and $p_o[\text{geo}]$. From this, we estimate a 0.01 uncertainty on p_o. The limb-darkening (and thus p_o) will be studied in detail by interferometry in the near future.

We then overplot the amplitude of the modeled pulsation velocity curves corresponding to the different line-forming regions ΔV_l^g. Two important points have to be mentioned here.

1. The superimposition of $p_o\Delta RV_c$ and ΔV_l^g values is very satisfactory for both stars. Thus, even if the ΔRV_c quantity includes all the dynamical structure of the line-forming region

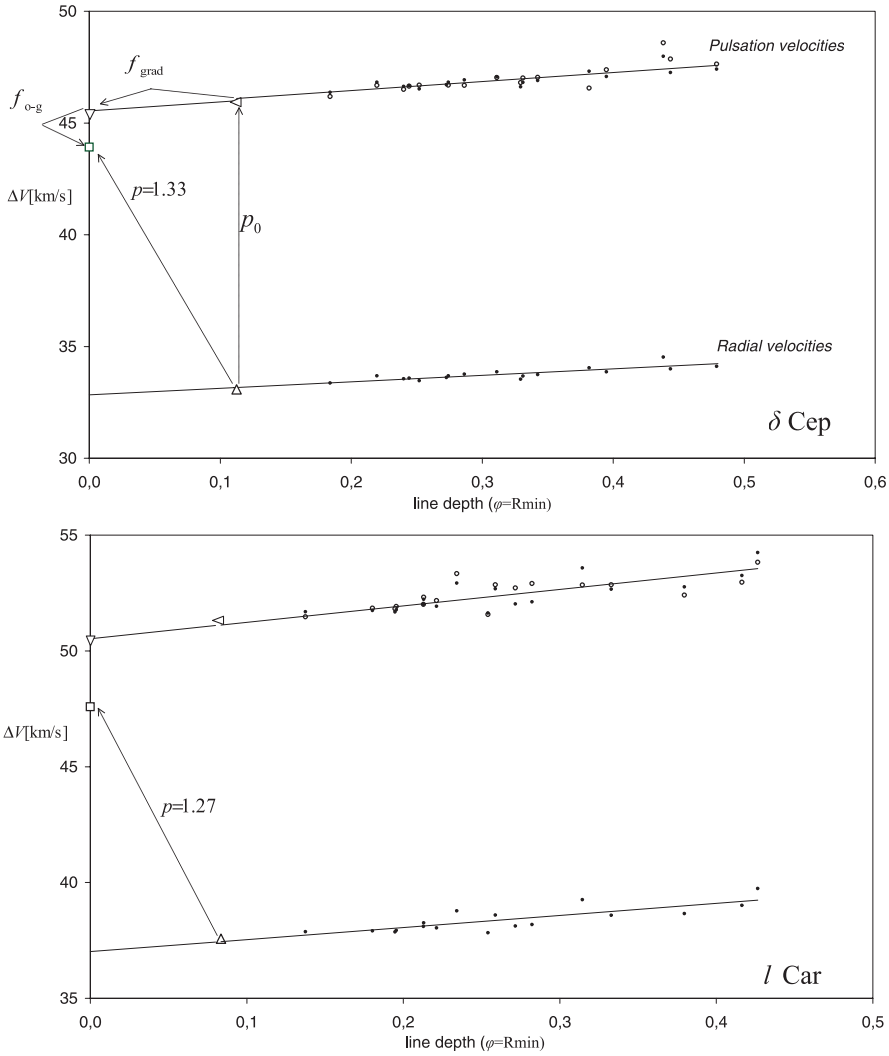


Fig. 1. The projection factor decomposition ($p = p_o f_{grad} f_{o-g}$) in the case of the Fe I 4896.439 Å spectral line: ΔRV_c (△), ΔV_l^g (◁), ΔV_p^g (▽) and ΔV_p^o (□). Reference values $p = 1.33$ and $p = 1.27$ are indicated for δ Cep and ℓ Car, respectively. The proposed method of the f_{grad} determination is to first derive ΔRV_c as a function of the line depth for all spectral lines (lower part, black points). Then, when translating (D, ΔRV_c) points into (D, $p_o \Delta RV_c$), a new linear relation is found (upper part of the figure, black points). This new relation is (1) coherent with the pulsation velocity gradient in the atmosphere (open circles) and (2) its zero-point is consistent with the pulsation velocity corresponding to the *gaseous* layer of the photosphere: ΔV_p^g (▽).

(including the limb darkening), it seems, on average, to give direct access to the *gas* velocity corresponding to $\tau_l = 2/3$, i.e. ΔV_l^g. In particular, the limb darkening (and thus the p_o-factor) seems to be independent of the spectral line considered. For any line depth D, we still have $\Delta V_l^g = p_o \Delta RV_c$.

2. We find that the zero-points of the (D, $p_o \Delta RV_c$) relations, 45.64 [δ Cep] and 50.53 [ℓ Car], are close to the reference values derived directly from the pulsation velocities of the model, $\Delta V_p^g = 45.60$[δ Cep] and 50.40[ℓ Car]. This means that, in both cases, the extrapolation to the photosphere is verified. We thus have $\Delta V_p^g = p_o b_o$. This is the key point that shows that the method proposed here is consistent and can be applied to any Cepheid. To allow this very important condition, one has to use the spectral line depth corresponding to the minimum extension of the star ($D \equiv D(\phi = R_{min})$). If another estimator is used, for example $D \equiv D(\phi = R_{max})$, or the line depth averaged over the entire pulsation cycle $D \equiv \langle D \rangle$, then the condition $\Delta V_p^g = p_o b_o$ disappears. Indeed, by extrapolating the three $p_o \Delta RV_c$ linear relations corresponding to the three estimators ($D(\phi = R_{max})$, $\langle D \rangle$, and $D(\phi = R_{min})$, respectively) towards the zero line depth, we find different agreements compared to the reference values derived directly from the variation in the photospheric pulsation velocity of the model: −1.13%, −0.70%, and 0.09% for δ Cep and −4.53%, −3.29%, and 0.25% for ℓ Car (see Fig. 2). The best extrapolation is thus obtained for the "minimum" estimator. We emphasize that this result is verified for both models (δ Cep and ℓ Car) that have very different physical properties : in period (5.4d, 35.5d), radius (43.4 $R_\odot$, 180 $R_\odot$), mass (4.8 $M_\odot$, 11.5 $M_\odot$), and effective temperature (5877 K, 5225 K). The "minimum" estimator of the line depth (D) is used for all Cepheids in the whole paper. Considering this estimator (link to the minimum extension of the star) does not mean that our projection factors are related to any specific pulsation phase. It only means that we have to use this estimator to get the right extrapolation of the amplitude (peak-to-peak) of the pulsation velocity toward the photosphere.

Thus, taking the linear correlation $\Delta RV_c = a_0 D + b_0$ into account, we propose the following relation to observationally derive f_{grad}:

$$f_{grad} = \frac{b_0}{a_0 D + b_0}. \quad (3)$$

This quantity can be derived directly from observations. In the case of our models and using the line depth corresponding to Fe I 4896.439 Å , we find $f_{grad} = 0.990$ [δ Cep] and $f_{grad} = 0.988$ [ℓ Car]. These results are very consistent with the same quantities derived directly from our projection factor decomposition. Consequently, translating these quantities into the projection factor $p = p_o f_{grad} f_{o-g}$, we find the reference values. We have thus found a new way to determine f_{grad} directly from observations.

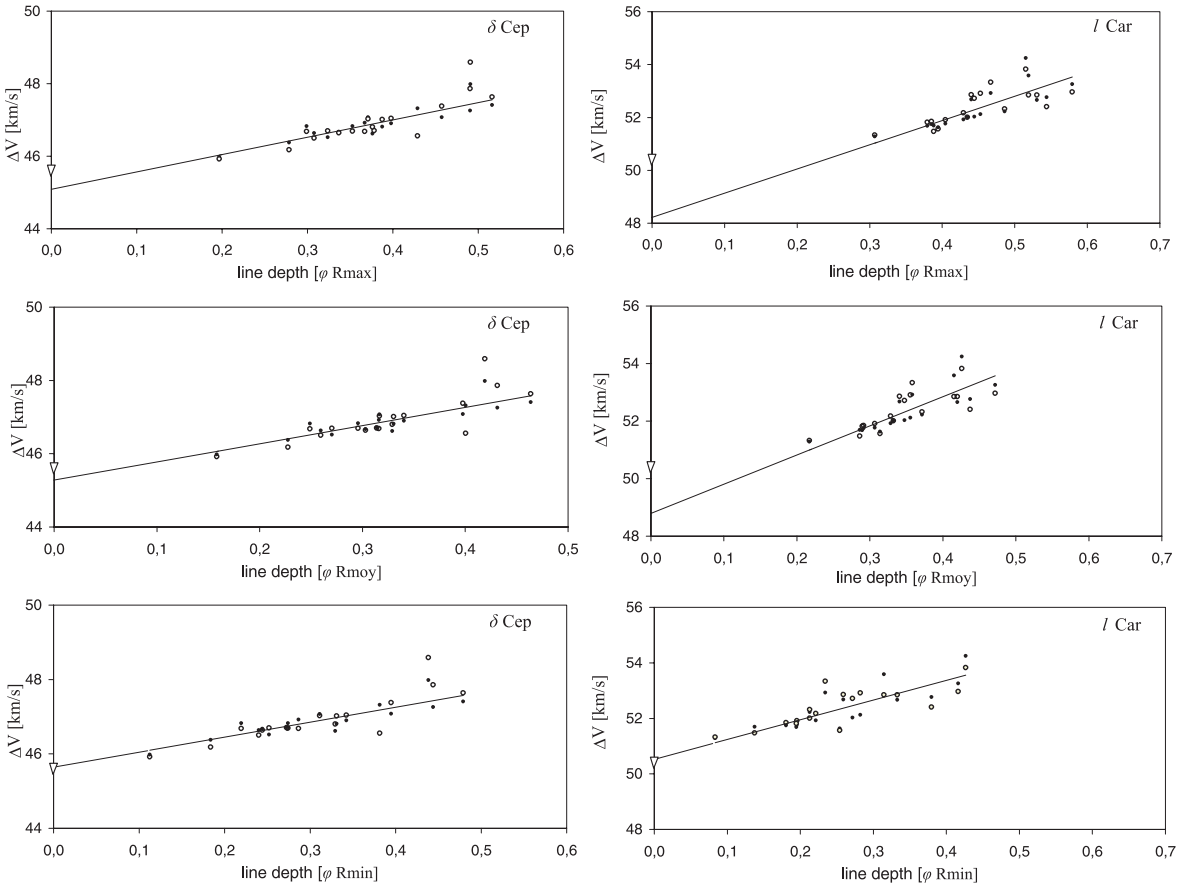


Fig. 2. $\Delta V_{\rm l}^{\rm g}$ (open circles) as a function of the line depth estimators $D(\phi = R_{\rm max})$, $\langle D \rangle$, and $D(\phi = R_{\rm min})$. Black points correspond to the $p_{\rm o}\Delta RV_{\rm c}$ quantity. The symbol $\triangledown$ indicates $\Delta V_{\rm p}^{\rm g}$; i.e., the amplitude of the photospheric pulsation velocity associated to the *gas*. We find good agreement between $\Delta V_{\rm l}^{\rm g}$ and $p_{\rm o}\Delta RV_{\rm c}$, which both present an interesting linear relation. Through extrapolation (dashed line), we find that the best estimator of the line-forming region is the line depth associated with the minimum radius, a result confirmed for δ Cep and ℓ Car hydrodynamic models.

Table 2. Hydrodynamical models of Cepheids.

Name	P [days]	$T_{\rm eff}$ [K]	$\frac{L}{L_\odot}$	$\frac{M}{M_\odot}$	$\frac{\overline{R}}{R_\odot}$
S Cru	4.7	5900	1900	5.6	42
δ Cep	5.4	5877	1995	4.8	43
Y Sgr	5.7	5850	2200	5.0	45
β Dor	9.9	5500	3500	5.5	65
ζ Gem	10.4	5500	3600	5.0	64
RZ Vel	21.6	5400	7450	7.0	109
ℓ Car	34.4	5225	21000	11.5	180
RS Pup	42.9	5100	22700	9.7	186

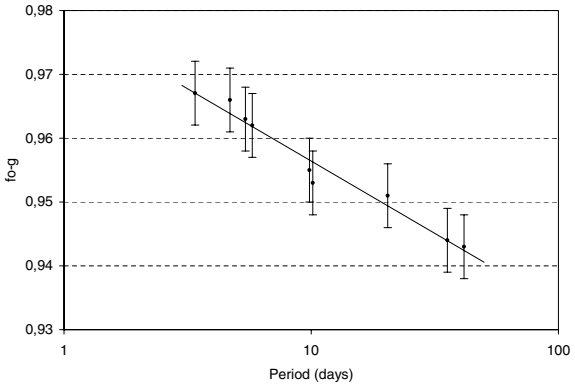


Fig. 3. $f_{\rm o-g}$ as a function of the period.

4.4. Hydrodynamic modeling of $f_{\rm o-g}$

The third quantity $f_{\rm o-g}$ is difficult to determine directly from observations. It requires a precise knowledge of the dynamical structure of the Cepheid atmosphere and line-forming regions. In the cases of δ Cep and ℓ Car, the model gives $f_{\rm o-g} = 0.963$ and 0.944, respectively.

In order to test the $Pf_{\rm o-g}$ relation, we modeled the other Cepheids of our sample (see Table 2). We only consider the velocity curves corresponding to the *optical* and *gas* photospheric layers. Consequently, no radiative transfer is calculated, and the resulting physical parameters of these models should be considered with caution. Nevertheless, these uncertainties are not critical for deriving $f_{\rm o-g}$. The results are 0.966[S Cru], 0.962[Y Sgr], 0.955[β Dor], 0.953[ζ Gem], 0.951[RZ Vel], and 0.943[RS Pup]. We consider a 0.05 uncertainty on $f_{\rm o-g}$.

Using these results (based on eight models), we obtain the following linear relation:

$$f_{\rm o-g} = [-0.023 \pm 0.005] \log P + [0.979 \pm 0.005]. \quad (4)$$

Using this relation we find $f_{\rm o-g} = 0.967$ for R TrA. $f_{\rm o-g}$ is plotted as a function of the period in Fig. 3.

This linearity can be understood with the following picture. Let us assume two atmospheres of short- and long-period Cepheids (noted S and L) at expansion. The *gas* velocity is

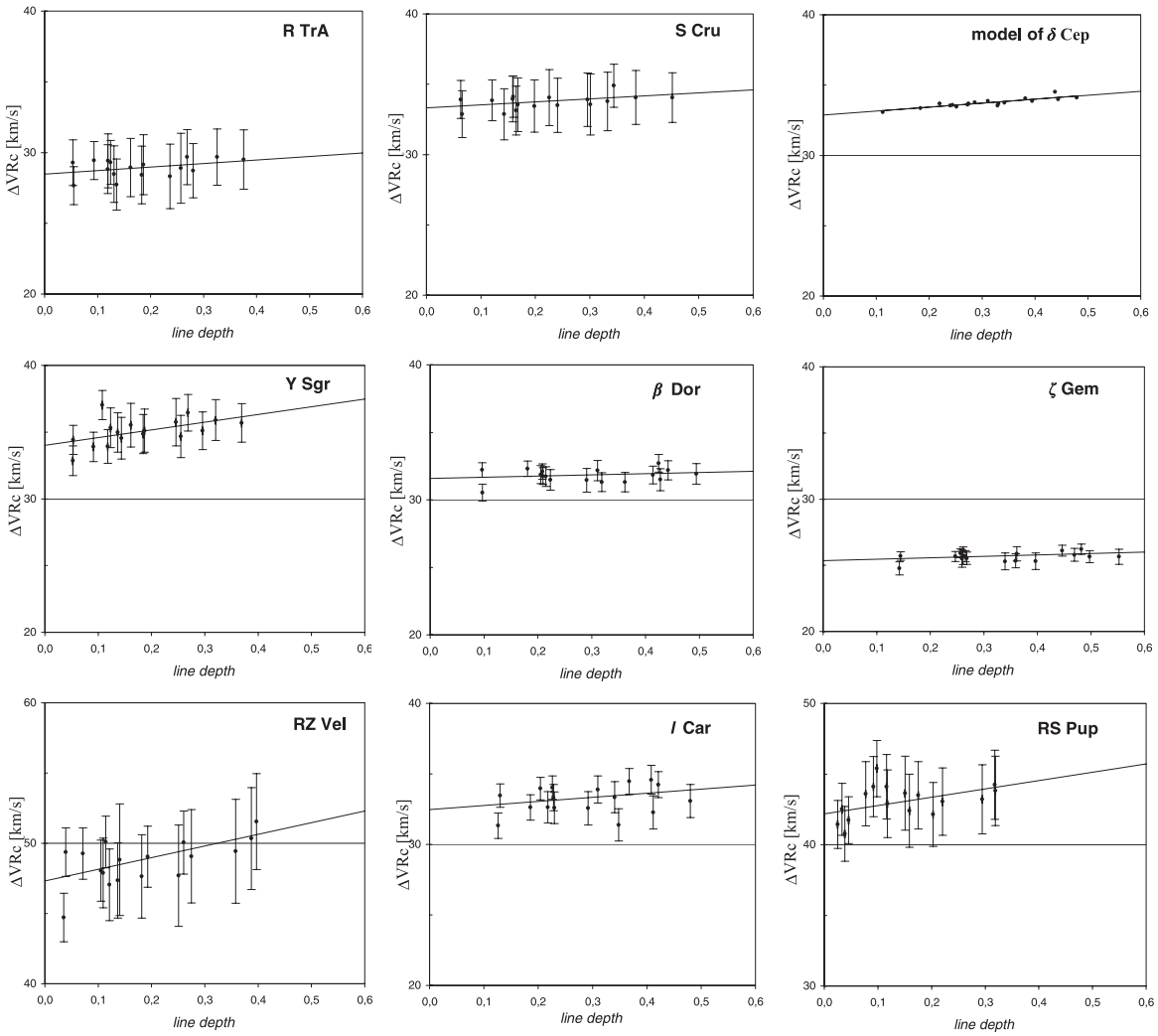


Fig. 4. ΔRV_c as a function of the depth D of the spectral line considered. Uncertainties are indicated. Stars are presented with increasing period. The δ Cep model is also indicated for comparison. Linear correlations are derived for all stars (see Table 3). The $f_{\rm grad}$ quantity is derived from these relations.

assumed to be the same for both atmospheres. Then, due to a geometrical effect (the radius of L is larger than the radius of S), the volume of L increases faster than S. Consequently, the density and temperature (in the adiabatic limit) also decrease faster in L. The lower atomic level of this line depopulates faster for L than for S, the opacity in the line also falls faster, the spectral line forms lower in the atmosphere (closer to the photosphere), and finally, the *optical* radius increases less. As a consequence, the velocity of the *optical* layer decreases for a long-period Cepheid, while the *gas* velocity is supposed to be the same. This picture can be generalized at contraction and for the photospheric layer. Thus, $f_{\rm o-g} = \frac{\Delta V_{\rm p}^{\rm o}}{\Delta V_{\rm p}^{\rm g}}$ decreases with the period of the Cepheid. Even if the $Pf_{\rm o-g}$ relation seems secured, we keep in mind that it must be studied in detail going further in our understanding of the dynamical structure of Cepheid's atmosphere. Important links between $f_{\rm o-g}$, the γ-velocity, line asymmetry, and velocity gradients should be found.

5. Direct measurement of velocity gradients from HARPS observations

This section only deals with observations. For the eight stars observed, we derive RV_c and the line depth as a function of the pulsation phase for all spectral lines of Table 1. Corresponding uncertainties are estimated based on the signal-to-noise ratio.

From interpolated curves (through periodic cubic spline functions), we derive ΔRV_c = MAX(RV_c) – MIN(RV_c) for all stars and lines. We also determine the pulsation phase corresponding to the minimum extension of the stars in order to derive D. ΔRV_c is represented as a function of line depth D for all stars in Fig. 4. Significant linear relations (see Table 3) are found between these two quantities. The amplitude of the velocity curves increases with the line depth (or with the position of the line-forming region in the atmosphere). This validates a posteriori the use of the line depth as an estimator of the line-forming region. From the coefficients provided in Table 3, we are now able to derive the $f_{\rm grad}$ quantity for each star using Eq. (3).

However, if one wants to compare the velocity gradient within the atmosphere of different Cepheids, the question of methodology arises. Two strategies are possible. One can consider (1) the same line depth for all stars or (2) the same spectral line. Because a given spectral line does not have the same depth for all stars, the choice is important. We first use strategy (1) to determine which spectral lines are most fitting for the IBW method, and then consider a specific spectral line to compare the velocity gradient in the Cepheids' atmosphere.

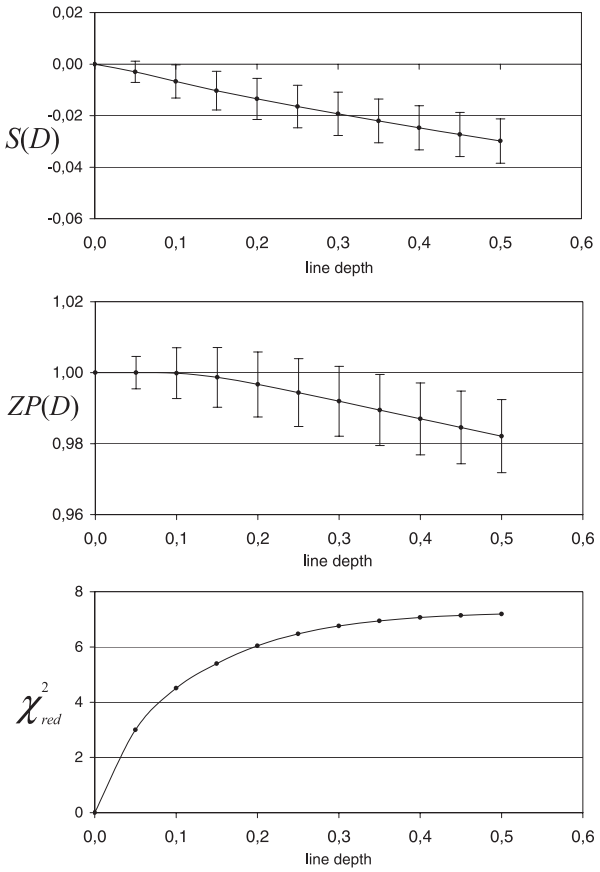


Fig. 5. Slope and zero-point of the Period-$f_{\rm grad}$ relation ($f_{\rm grad} = S(D)\log P + ZP(D)$) as a function of the line depth. The reduced χ^2 is also indicated.

First, we test the existence of a linear relation between $f_{\rm grad} = \frac{b_0}{a_0 D + b_0}$ and the logarithm of the period ($\log P$) for eleven different line depths from 0 to 0.5 in increments of 0.05. By a minimization process, we obtain the relations: $f_{\rm grad} = S(D)\log P + ZP(D)$, where the slope ($S$) and the zero-point ($ZP$) are related to the line depth considered. The variables S, ZP, and the reduced χ^2 are represented as a function of the line depth in Fig. 5. The physical interpretation of these curves is as follows.

First, for a line depth of zero, the velocity gradient is also zero for all stars (or $f_{\rm grad} = 1$). Thus, $S = 0$, $ZP = 1$, and there is no uncertainty on $f_{\rm grad}$. The reduced χ^2 is 0 since the linear relation is perfect.

Then, for low depths, the $f_{\rm grad}$ estimator is quite different for each star, but the effect is low and the $f_{\rm grad} = S(D)\log P + ZP(D)$ relation is still not very sensitive to the velocity gradient. Moreover, the uncertainty on $f_{\rm grad}$ is low, and the same is true for S and ZP. The reduced χ^2 is good, as the linearity is well-conserved.

However, for large depths, the $f_{\rm grad}$ estimator becomes more and more sensitive (but also more uncertain) to the velocity gradient. The dispersion between the different stars is amplified. As a consequence, the linearity is verified at a lower level: the reduced χ^2 gets larger.

From this picture, our objective is to find the best spectral lines to use in determining $f_{\rm grad}$ (and then the projection factor) in the context of the IBW method. Spectral lines with depths lower than 0.1 seem to be the best choice. Such spectral lines are indeed less sensitive to the velocity gradient. It is obvious that a spectral line that forms close to the photosphere implies small differences (in velocity) between the line-forming region and the photosphere. In this case, $f_{\rm grad}$ is close to 1 and the corresponding uncertainty is low. Indeed, from Fig. 5, we clearly see that the uncertainties on S and ZP are decreasing for low depths. From Table 1, we find that the Fe I 4896.439 Å spectral line is the best. It has the lowest depth, averaged over all pulsation phases for all stars ($D = 0.08$).

Table 3. Linear relations between the amplitude of the velocity curves and the line depth (at minimum extension of the star), $\Delta RV_c = a_0 D + b_0$ are given for all stars, together with the 1σ uncertainty. The *reduced* χ^2, defined as $\chi^2_{\rm red} = \frac{\chi^2}{N-\nu}$ with N the number of spectral lines and ν the number of degrees of freedom is also indicated.

Star	a_0	b_0	$\chi^2_{\rm red}$
R TrA	2.50 ± 4.55	28.48 ± 0.90	2
S Cru	2.13 ± 3.61	33.33 ± 0.90	2
Y Sgr	5.76 ± 3.53	34.01 ± 0.12	20
β Dor	0.86 ± 1.31	31.59 ± 0.40	9
ζ Gem	1.09 ± 0.89	25.35 ± 0.31	7
RZ Vel	8.32 ± 5.95	47.31 ± 1.02	6
ℓ Car	2.89 ± 2.26	32.48 ± 0.67	15
RS Pup	5.89 ± 5.58	42.19 ± 0.88	4

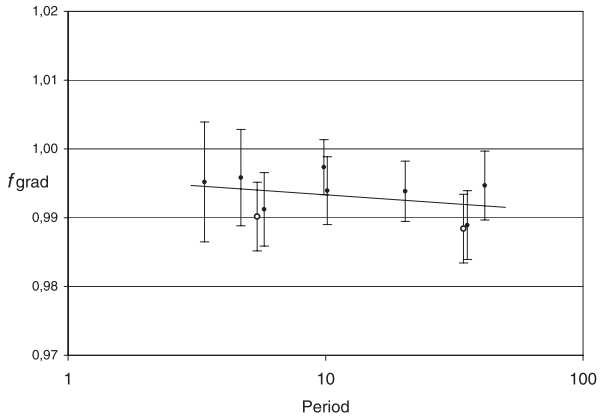


Fig. 6. $f_{\rm grad}$ in the case of the Fe I 4896.439 spectral line is represented as a function of the period. Open circles corresponds to the hydrodynamic models. The slope and the zero-point of the relation depend on the line depth (see Fig. 5).

In Fig. 6 we present $f_{\rm grad}$ as a function of the logarithm of the period for the Fe I 4896.439 Å spectral line. We obtain a linear relation between the velocity gradient and the logarithm of the period. Results are given in Table 4 for observations only (O), and for observations + the δ Cep and ℓ Car hydrodynamical models (O+C). Consequently, we can conclude that the velocity gradient is larger in long-period Cepheids than in short-period Cepheids. Moreover, if we compare this observational result to the hydrodynamical models of δ Cep and ℓ Car, we find very good agreement (see Fig. 6). The two models presented are thus extremely good.

6. A period-projection factor relation

We now determine the projection factors of Cepheids considering the Fe I 4896.439 Å spectral line. The $p_{\rm o}$-factors are not determined directly using the continuum intensity distribution of the hydrodynamical models. As explained in Sect. 4.4, these models (except for δ Cep and ℓ Car) are only used to derive $f_{\rm o-g}$; no radiative transfer in the atmosphere is

Table 4. Linear relation between $f_{\rm grad}$ and the logarithm of the period: $f_{\rm grad} = S \log P + ZP$ for the Fe I 4896.439 Å spectral line.

	S	ZP	$\chi^2_{\rm red}$
O	-0.003 ± 0.005	0.997 ± 0.006	2
O + C	-0.003 ± 0.004	0.996 ± 0.005	3

computed, and the observed spectral lines profiles (and radial velocity curves) are not used to constrain the models. Consequently, we are not certain about the dynamical structure of the modeled Cepheids' atmosphere and, in particular, about $f_{\rm grad}$. And if $f_{\rm grad}$ is wrong, the limb darkening within the line (and thus the $p_{\rm o}$-factor) could be affected. Consequently, we consider a conservative approach when deriving $p_{\rm o}$[geo] from the hydrodynamic parameters of Table 2. We then apply a slight correction: $p_{\rm o}$[hydro]= $p_{\rm o}$[geo]$-(0.0174 \log P - 0.0022)$ using the results based on δ Cep and ℓ Car hydrodynamic models, which were studied in detail (Sect. 3). The resulting linear relation is

$$p_{\rm o} = [-0.031 \pm 0.008] \log P + [1.413 \pm 0.009]. \quad (5)$$

The $f_{\rm o-g}$ quantities have been deduced directly from the hydrodynamical models (see Sect. 4.4), and $f_{\rm grad}$ was determined from observations in the previous section. From $p_{\rm o}$, $f_{\rm o-g}$, and $f_{\rm grad}$, we can now determine consistent projection factors for all stars. A summary of the results is given in Table 5 and illustrated in Fig. 7.

By combining all quantities ($p_{\rm o}$, $f_{\rm grad}$ and $f_{\rm o-g}$), we are able to derive a Pp relation for the first time (see Fig. 7b). This result is a combination of observed and theoretical considerations. The resulting linear law (including observed and modeled stars) is:

$$p = [-0.064 \pm 0.020] \log P + [1.376 \pm 0.023]. \quad (6)$$

This relation holds for the Fe I 4896.439 Å spectral line, which presents the lowest line depth in our sample.

From this relation, two facts must be pointed out. First, the $Pp_{\rm o}$ relation is based on the general physical properties of Cepheids (effective temperature, surface gravity), while $Pf_{\rm grad}$ is derived directly from observations and states that the velocity gradient within the atmosphere is larger in long-period Cepheids. The linearity of the $Pf_{\rm o-g}$ relation is qualitatively understood (Sect. 4.3) and has been quantitatively verified based on eight models. Second, results concerning the δ Cep and ℓ Car hydrodynamic models are highly secured: (1) the projection factor of δ Cep was confirmed observationally by Mérand et al. (2005); (2) the velocity gradient in the atmosphere of these stars is confirmed by HARPS observations (see Sect. 5); (3) the $p_{\rm o}$ estimations are coherent at a 0.025 level with the geometrical models; and (4) from points 1, 2, and 3, we can reasonably feel secure in the estimations of $f_{\rm o-g}$ for δ Cep, ℓ Car, and for all stars.

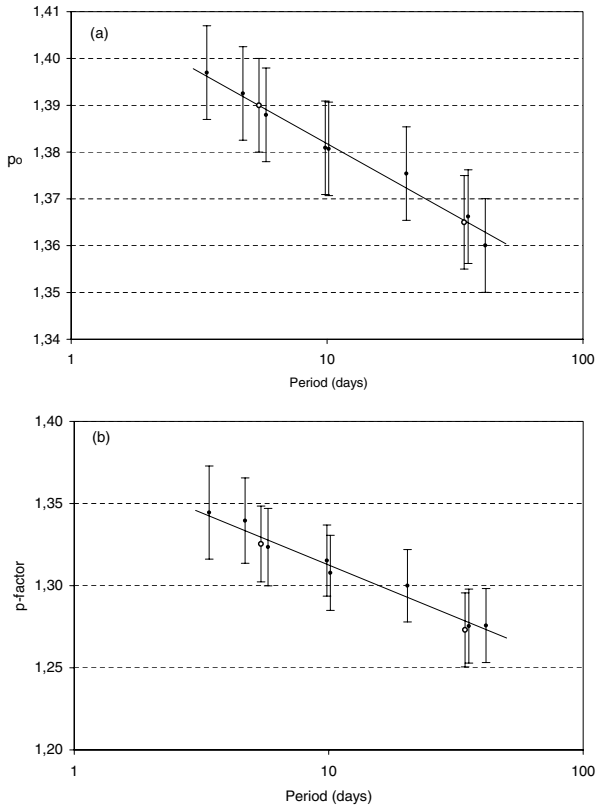


Fig. 7. The projection factor ($p = p_{\rm o} f_{\rm grad} f_{\rm o-g}$) as a function of the logarithm of the period (diag. b), together with $p_{\rm o}$ (diag. a). Black points and open circles correspond to observations and models.

7. Discussion

The derived Pp relation will be useful in the context of the IBW and SB methods. For example, if we compare Eq. (6) with the usual value widely used in the community $p = 1.36$ (Burki et al. 1982), we obtain a correction for the projection factor depending on the period. It is then possible to translate it into a bias on distances and absolute magnitudes. By this process, we obtain the relation:

$$\Delta M_V = 0.10 \log P - 0.03 \quad (7)$$

where ΔM_V is the correction to consider on the PL relation. We thus conclude that one can make an errors of 0.10 and 0.03 on the slope and zero-point of the PL relation, respectively, if $p = 1.36$ is used for all stars instead of the Pp relation. This correction is, however, only indicative because it is indeed restricted to our definition of the projection factor (Eq. (1)) and to the Fe I 4896.439 Å spectral line.

It is now possible to refine the IBW and SB methods. First, we suggest using the $RV_{\rm c}$ radial velocity to avoid bias related to the rotation velocity of the star (even if Cepheids are supposed to be slow rotators) and the width of the spectral line. One then has to determine the $RV_{\rm c}$ curve and force the average to be zero in order to avoid γ-velocity effects. Due to our careful definition of p (Eq. (1)), the projection factors proposed in this paper are indeed independent of the γ-velocity. The spectral line considered must have a depth lower than 0.1 and should be the same for all considered Cepheids. The low depth of the spectral line is required to diminish the impact of the velocity gradient. If the Fe I 4896.439 Å is used, one can use Eq. (6) directly to determine the dynamic projection factors of Cepheids. If not, we propose the following method. Given the line depth of the spectral line considered for each Cepheid, it is possible to determine the $f_{\rm grad}$ from Table 3 and Eq. (3). If the Cepheid being studied is not in our sample, Fig. 5 can be used. Then $p_{\rm o}$ can be determined using a geometrical model. However, the consistency (at a level lower than 0.025 on p) between interferometric observations, geometrical, and hydrodynamical models should be studied in detail in the future. For $f_{\rm o-g}$, one can use Eq. (4), even if this relation has to be confirmed observationally in the future. For this purpose, the development of theory and hydrodynamical models is required. Finally, the projection factor of Cepheids, following

Table 5. Derived projections factors for all stars computed from the decomposition presented in Eq. (2).

Name	HD	P^b [days]	p_o^c	f_{grad}^d	f_{o-g}^e	p^f
R TrA	135592	3.38925	$1.396_{\pm 0.010}$	$0.995_{\pm 0.009}$	$0.967_{\pm 0.005}$	$1.34_{\pm 0.03}$
S Cru	112044	4.68976	$1.392_{\pm 0.010}$	$0.996_{\pm 0.007}$	$0.966_{\pm 0.005}$	$1.34_{\pm 0.03}$
Y Sgr	168608	5.77338	$1.387_{\pm 0.010}$	$0.991_{\pm 0.005}$	$0.962_{\pm 0.005}$	$1.32_{\pm 0.02}$
β Dor	37350	9.84262	$1.380_{\pm 0.010}$	$0.997_{\pm 0.004}$	$0.955_{\pm 0.005}$	$1.31_{\pm 0.02}$
ζ Gem	52973	10.14960	$1.380_{\pm 0.010}$	$0.994_{\pm 0.005}$	$0.953_{\pm 0.005}$	$1.31_{\pm 0.02}$
RZ Vel	73502	20.40020	$1.375_{\pm 0.010}$	$0.994_{\pm 0.004}$	$0.951_{\pm 0.005}$	$1.30_{\pm 0.02}$
ℓ Car	84810	35.55134	$1.366_{\pm 0.010}$	$0.989_{\pm 0.005}$	$0.944_{\pm 0.005}$	$1.27_{\pm 0.02}$
RS Pup	68860	41.51500	$1.360_{\pm 0.010}$	$0.995_{\pm 0.005}$	$0.943_{\pm 0.005}$	$1.28_{\pm 0.02}$
δ *Cep*[a]	213306	5.419	$1.390_{\pm 0.010}$	$0.990_{\pm 0.005}$	$0.963_{\pm 0.005}$	$1.33_{\pm 0.02}$
ℓ *Car*[a]	84810	35.60	$1.366_{\pm 0.010}$	$0.988_{\pm 0.005}$	$0.944_{\pm 0.005}$	$1.27_{\pm 0.02}$

[a] δ Cep and ℓ Car are hydrodynamical models.
[b] The corresponding Julian dates (T_o) can be found in Paper II.
[c] p_o is derived from the linear limb-darkening laws of Claret et al. (2000) based on the static models of Kurucz (1992). We then apply a slight correction based on the δ Cep and ℓ Car hydrodynamical models: $p_o[\text{hydro}] = p_o[\text{geo}] - (0.0174 \log P - 0.0022)$ to take the dynamical structure of the Cepheid's atmosphere into account.
[d] f_{grad} is derived directly from observations using Eq (3). It is important to notice that the results indicated here correspond to the Fe I 4896.439 Å line. In the case of a modeled star, it is derived directly from the hydrodynamical model (see Sect. 4.3).
[e] f_{o-g} is derived directly from the hydrodynamical models (see Sect. 4.4).
[f] p-factors defined by $p = p_o f_{grad} f_{o-g}$. p_o and f_{o-g} are derived from geometrical and hydrodynamical models respectively. f_{grad} is derived from observations.

our decomposition, is $p = p_o\, f_{grad}\, f_{o-g}$. This procedure should be applied to avoid bias in the calibration of the *PL* relation.

However, we know that the masking cross-correlation method is widely used to increase the signal-to-noise ratio on radial velocity measurements. In that case however, one cannot exclude the impact of the rotation, the spectral lines' width, and γ-velocities effects. Nevertheless, we can still provide a *Pp* relation that is more appropriate considering an average line depth of $D = 0.25$. We find $p = [-0.075 \pm 0.031] \log P + [1.366 \pm 0.036]$.

Another important point is that we provide visible projection factors that should be used with visible spectroscopic observations. If one used infrared spectroscopic observations to derive the pulsation velocity, one should use specific infrared projection factors. Indeed, in the infrared, the limb darkening is supposed to be lower and the corresponding p_o-factors higher (certainly about 4%). But, spectral lines also form higher in the atmosphere (i.e. in the upper part of the atmosphere), which supposes a lower f_{grad}. More studies have to be carried out to derive an infrared *Pp* relation.

8. Conclusion

In the application of the IBW method, the projection factor is a key quantity. Up to now, the period-dependency of the projection factor has never been studied in detail. Here, we have presented a new spectroscopic method for directly measuring the velocity gradient in the Cepheids' atmosphere. This method has been successfully validated by the hydrodynamical models of δ Cep and ℓ Car. We find a physical relation between the period of the star and its dynamical atmospheric structure.

The models also show that the *optical* layers (observed by continuum interferometer) and the *gas* layers have to be distinguished in the interferometric definition of the projection factor. However, this quantity is still very difficult to determine directly from observations.

Combining the results obtained directly from observations and our knowledge of the dynamical structure of the δ Cep and ℓ Car atmosphere, we have been able to derive a very consistent *Pp* relation for the Fe I 4896.439 Å spectral line:

$$p = [-0.064 \pm 0.020] \log P + [1.376 \pm 0.023]. \quad (8)$$

We emphasize that, if a constant projection factor is used to constrain the *PL* relation, an error of 0.10 and 0.03 magnitudes can be done, respectively, on the slope and zero-point of the *PL* relation. This can even be much more if the wrong definition of the radial velocity is used or if one does not consider γ-velocity effects. We have thus presented (see discussion) a careful methodology to be applied in the context of the IBW and SB methods.

Acknowledgements. Based on observations collected at La Silla observatory, Chile, in the framework of European Southern Observatory's programs 072.D-0419 and 073.D-0136. This research made use of the SIMBAD and VIZIER databases at the CDS, Strasbourg (France). We thank C. Catala for useful discussions of the line-forming region estimator, P. Kervella for having provided the HARPS data and M. Fekety as well as Joli Adams for their careful English correction of the paper. N. Nardetto acknowledges the Max Planck Institut for Radioastronomy for financial support.

References

Burki, G., Mayor, M., & Benz, W. 1982, A&A, 109, 258
Butler, R. P. 1993, ApJ, 415, 323
Butler, R. P., Bell, R. A. & Hindsley, R. B. 1996, ApJ, 461, 362
Chiosi, C., Wood, P. R. & Capitanio, N. ApJ, 86, 541
Claret, A. 2000, A&A, 363, 1081
Fokin A. B., Gillet D. & Breitfellner M. G. 1996, A&A, 307, 503
Kervella P., Nardetto N., Bersier D., et al. 2004, A&A, 416, 941
Kurucz, R. L. 1992, The Stellar Populations of Galaxies, IAU Symp, 149, 225
Marengo, M., Karovska, M., Sasselov, D. D., et al. 2003, ApJ, 589, 975
Mathias, P., Gillet, D., Fokin, A., et al. 2006, A&A, 457, 575M
Mérand, A., Kervella, P., Coudé du Foresto, V. et al. 2005, A&A, 438, L9
Nardetto, N., Fokin, A., Mourard, D., et al. 2004, A&A, 428, 131 (Paper I)
Nardetto, N., Fokin, A., Mourard, D., et al. 2006a, A&A, 454, 327
Nardetto, N., Mourard, D., Kervella, P., et al. 2006b, A&A 453, 309 (Paper II)
Petterson, O. K.L., Cottrell, P. L., Albrow, M. D., & Fokin, A. 2005, MNRAS, 362, 1167
Rogers, F. J., & Iglesias, C. A., 1992, ApJS, 69, 495
Sasselov, D. D., & Karovska, M., 1994, ApJ, 432, 367
Szabados, L. 1989, Communications of the Konkoly Observatory Hungary, 94, 1

Online Material

Table 1. Spectral lines used in this study.

Name	Wavelength (Å)
Fe I	4683.560
Fe I	4896.439
Fe I	5054.643
Ni I	5082.339
Fe I	5367.467
Fe I	5373.709
Fe I	5383.369
Ti II	5418.751
Fe I	5576.089
Fe I	5862.353
Fe I	6024.058
Fe I	6027.051
Fe I	6056.005
Si I	6155.134
Fe I	6252.555
Fe I	6265.134
Fe I	6336.824

Annexe K

High-resolution spectroscopy for Cepheids distance determination. V. Impact of the cross-correlation method on the p-factor and the γ-velocities

A&A 502, 951–956 (2009)
DOI: 10.1051/0004-6361/200912333
© ESO 2009

Astronomy & Astrophysics

High-resolution spectroscopy for Cepheids distance determination

V. Impact of the cross-correlation method on the p-factor and the γ-velocities[⋆, ⋆⋆]

N. Nardetto[1], W. Gieren[1], P. Kervella[2], P. Fouqué[3], J. Storm[4], G. Pietrzynski[1,5], D. Mourard[6], and D. Queloz[7]

[1] Departamento de Astronomía, Universidad de Concepción, Casilla 160-C, Concepción, Chile
e-mail: nnardetto@astro-udec.cl
[2] Observatoire de Paris-Meudon, LESIA, UMR 8109, 5 Place Jules Janssen, 92195 Meudon Cedex, France
[3] Observatoire Midi-Pyrénées, Laboratoire d'Astrophysique, UMR 5572, Université Paul Sabatier, Toulouse 3, 14 avenue Edouart Belin, 31400 Toulouse, France
[4] Astrophysikalisches Institut Postdam, An der Sternwarte 16, 14482 Postdam, Germany
[5] Warsaw University Observatory, AL. Ujazdowskie 4, 00-478 Warsaw, Poland
[6] OCA/CNRS/UNS, Dpt. Fizeau, UMR6525, Avenue Copernic, 06130 Grasse, France
[7] Observatoire de Genève, Université de Genève, 51 Ch. des Maillettes, 1290 Sauverny, Switzerland

Received 15 April 2009 / Accepted 14 May 2009

ABSTRACT

Context. The cross correlation method (hereafter *CC*) is widely used to derive the radial velocity curve of Cepheids when the signal to noise ratio of the spectra is low. However, if it is used with an inaccurate projection factor, it might introduce some biases in the Baade-Wesselink (BW) methods of determining the distance of Cepheids. In addition, it might affect the average value of the radial velocity curve (or γ-velocity) important for Galactic structure studies.
Aims. We aim to derive a period-projection factor relation (hereafter *Pp*) appropriate to be used together with the CC method. Moreover, we investigate whether the CC method can explain the previous estimates of the "K-term" of Cepheids.
Methods. We observed eight galactic Cepheids with the HARPS⋆⋆⋆ spectrograph. For each star, we derive an interpolated CC radial velocity curve using the HARPS pipeline. The amplitudes of these curves are used to determine the correction to be applied to the semi-theoretical projection factor. Their average value (or γ-velocity) are also compared to the center-of-mass velocities derived in previous works.
Results. The correction in amplitudes allows us to derive a new *Pp* relation: $p = [-0.08 \pm 0.05] \log P + [1.31 \pm 0.06]$. We also find a negligible wavelength dependence (over the optical range) of the *Pp* relation. We finally show that the γ-velocity derived from the CC method is systematically blue-shifted by about 1.0 ± 0.2 km s^{-1} compared to the center-of-mass velocity of the star. An additional blue-shift of 1.0 km s^{-1} is thus needed to totally explain the previous calculation of the "K-term" of Cepheids (around 2 km s^{-1}).
Conclusions. The new *Pp* relation we derived is a reliable tool for distance scale calibration, and especially to derive the distance of LMC Cepheids with the infrared surface brightness technique. Further studies should be devoted to determining the impact of the signal to noise ratio, the spectral resolution, and the metallicity on the *Pp* relation.

Key words. techniques: spectroscopic – stars: atmospheres – stars: oscillations – stars: variables: Cepheids – stars: distances

1. Introduction

The Baade-Wesselink (hereafter *BW*) method of determining the distance of Cepheids was recently used to calibrate the period-luminosity (*PL*) of Galactic Cepheids (Fouqué et al. 2007). The basic principle of this method is to compare the linear and angular size variation of a pulsating star in order to derive its distance through a simple division. The angular diameter is either derived by interferometry (for e.g. Kervella et al. 2004; Davis et al. 2008) or using the infrared surface brightness (hereafter IRSB) relation (Gieren et al. 1998, 2005a). However, when determining the linear radius variation of the Cepheid by spectroscopy, one has to use a conversion projection factor from radial to pulsation velocity. This quantity has been studied using hydrodynamic calculations by Sabbey et al. (1996), and more recently Nardetto et al. (2004, 2007).

Following the work of Burki et al. (1982), we showed in Nardetto et al. (2006, hereafter Paper I) that the first moment of the spectral line is the only method which is independent of the spectral line width (average value and variation) and the rotation velocity of the star. The centroid radial velocity (RV_c), or the first moment of the spectral line profile, is defined as

$$RV_c = \frac{\int_{\rm line} \lambda S(\lambda) {\rm d}\lambda}{\int_{\rm line} S(\lambda) {\rm d}\lambda} \cdot \quad (1)$$

We thus used this definition of the radial velocity in paper two of this series (Nardetto et al. 2007, hereafter Paper II), to derive a semi-theoretical period-projection factor (hereafter *Pp*) relation

⋆ Based on observations made with ESO telescopes at the Silla Paranal Observatory under programme IDs 072.D-0419 and 073.D-0136.
⋆⋆ Tables 4 and 5 are only available in electronic form at the CDS via anonymous ftp to cdsarc.u-strasbg.fr (130.79.128.5) or via http://cdsweb.u-strasbg.fr/cgi-bin/qcat?J/A+A/502/951
⋆⋆⋆ High Accuracy Radial velocity Planetary Search project developed by the European Southern Observatory.

based on spectroscopic measurements with the HARPS high resolution spectrograph. This relation was derived from the specific Fe I 4896.439 Å spectral line which has a relatively low depth for all stars at all pulsation phase (around 8% of the continuum). It was shown that such a low depth value is suitable to reduce the uncertainty on the projection factor due to the velocity gradient between the photosphere (corresponding to angular diameter measurements) and the line-forming region (corresponding to the radius estimation from spectroscopic measurements).

In the cross-correlation method (hereafter CC method), a mask (composed of hundreds or thousands) of spectral lines is convolved to the observed spectrum. The resulting average profile is then fitted by a Gaussian. In such a method, there is first a mix of different spectral lines forming at different levels (more or less sensitive to a velocity gradient). Second, the resulting velocity can be dependent on the abundances or effective temperature (through the line width), or the rotation of the stars. Third, in Paper III of this series (Nardetto et al. 2008), we derived calibrated center-of-mass velocities of the stars of our HARPS sample. By comparing these so-called γ-velocities with the ones found in the literature (generally based on the CC method) and in particular in the Galactic Cepheid Database (Fernie et al. 1995), we obtained an average correction of 1.8 ± 0.2 km s^{-1}. This result shows that the "K-term" of Cepheids stems from an intrinsic property of Cepheids. But, it shows also that the cross-correlation might introduce a bias (up to a few kilometers per second) on the average value of the radial velocity curve.

After a careful definition of the projection factor (Sect. 2), we apply the cross-correlation method to the Cepheids of our HARPS sample (Sect. 3), in order to derive a period-projection factor relation appropriate for the CC method (Sect. 4). As the HARPS pipeline also provides cross-correlated radial velocities for each spectral order, we take the opportunity to study the wavelength dependence of the projection factor law (Sect. 5). Finally, we quantify the impact of the CC method on the γ-velocities (Sect. 6).

2. Definition of the "CC projection factor"

In this section, we recall some results obtained in Paper II and we define the projection factor suitable for the cross-correlation method. In Paper II, we defined the projection factor as:

$$p = \frac{\Delta V_{\rm p}^{\rm o}}{\Delta RV_{\rm c}} \tag{2}$$

where $\Delta V_{\rm p}^{\rm o}$ is the amplitude of the pulsation velocity curve associated with the photosphere of the star. $\Delta RV_{\rm c}$ is the amplitude of the radial velocity curve obtained from the first moment of the spectral line. Because of the atmospheric velocity gradient, $\Delta RV_{\rm c}$ depends on the spectral line considered. Using a selection of 17 spectral lines, we thus derived an interpolated relation between $\Delta RV_{\rm c}$ and D, where D is the line depth corresponding to the minimum radius of the star:

$$\Delta RV_{\rm c} = a_0 D + b_0. \tag{3}$$

This relation was then used to quantify the correction ($f_{\rm grad}$) to be applied to the projection factor due to the velocity gradient (see Eq. (3) of Paper II). The Fe I 4896.439 Å spectral line (which forms close to the photosphere) was found to provide the lowest correction. The amplitude of the radial velocity curve corresponding to the Fe I 4896.439 Å spectral line was finally used (see $f_{\rm grad}$ in Table 5 of Paper II) to derive the semi-theoretical Pp relation. It is defined (Eq. (3)) as $\Delta RV_{\rm c}[4896] = a_0 D_{4896} + b_0$, where a_0 and b_0 are indicated in Table 3 of Paper II. D_{4896} is derived from the interpolation of the line depth curve at the particular phase corresponding to the minimum radius of the star (i.e. when $RV_{\rm c}$ corrected from the γ-velocity $\simeq$0). D_{4896} and $\Delta RV_{\rm c}[4896]$ are given in Table 1 of this paper.

Table 1. The Cepheids studied listed with increasing period.

Cepheid	$P^{(a)}$ [days]	D_{4896} [%]	$\Delta RV_{\rm c}[4896]$ [km s^{-1}]
R TrA	3.38925	6	$28.6_{\pm 0.5}$
S Cru	4.68976	6	$33.5_{\pm 0.5}$
Y Sgr	5.77338	5	$34.3_{\pm 0.5}$
β Dor	9.84262	10	$31.7_{\pm 0.5}$
ζ Gem	10.14960	14	$25.5_{\pm 0.5}$
RZ Vel	20.40020	4	$47.6_{\pm 0.5}$
ℓ Car	35.55134	13	$32.8_{\pm 0.5}$
RS Pup	41.51500	4	$42.4_{\pm 0.5}$

[a] The corresponding Julian dates ($T_{\rm o}$) can be found in Paper II.

The projection factor suitable to the cross-correlation method (hereafter $p_{\rm cc}$) is then simply:

$$p_{\rm cc} = p\frac{\Delta RV_{\rm c}[4896]}{\Delta RV_{\rm cc}} = p f_{\rm cc} \tag{4}$$

where $\Delta RV_{\rm cc}$ is the amplitude of the radial velocity curve obtained with the cross-correlation method, and $f_{\rm cc}$ the correction factor to be applied. Our definition of $p_{\rm cc}$ is independent of the γ-velocities.

3. The CC method applied to HARPS observations

We consider eight Cepheids which have been observed with the HARPS spectrometer (R = 120 000): R Tra, S Cru, Y Sgr, β Dor, ζ Gem, RZ Vel, ℓ Car, RS Pup. Information about observations (number of measurements, pulsation phases) can be found in Paper I.

We apply the HARPS pipeline to our data in order to calculate the cross-correlated radial velocities (Baranne et al. 1996; Pepe et al. 2002). The basic principle of the CC method is to build a mask, made of zero and non-zero value-zones, where the non-zero zones correspond to the theoretical positions and widths of thousands of metallic spectral lines at zero velocity, carefully selected from a synthetic spectrum of a G2 star. A relative weight is considered for each spectral line according to its depth (derived directly from observations of a G2 type star). An average spectral line profile is finally constructed by shifting the mask as a function of the Doppler velocity. The corresponding radial velocity is derived applying a classical χ^2 minimization algorithm between the observed line profile and a Gaussian function. The whole profile is considered in the fitting procedure, not only the line core. The average value of the fitted Gaussian corresponds to the cross-correlated radial velocity (hereafter $RV_{\rm cc}$). The HARPS instrument has 72 spectral orders. The pipeline provides $RV_{\rm cc}$ averaged over the 72 spectral orders, or independently for each order. We first use the averaged values and the corresponding uncertainties.

The $RV_{\rm cc}$ curves are then carefully interpolated using a periodic cubic spline function. This function is calculated either directly on the observational points or using arbitrary pivot points. In the latter case, a classical minimization process between observations and the interpolated curve is used to optimize the position of the pivot points (Mérand et al. 2005). For Y Sgr and

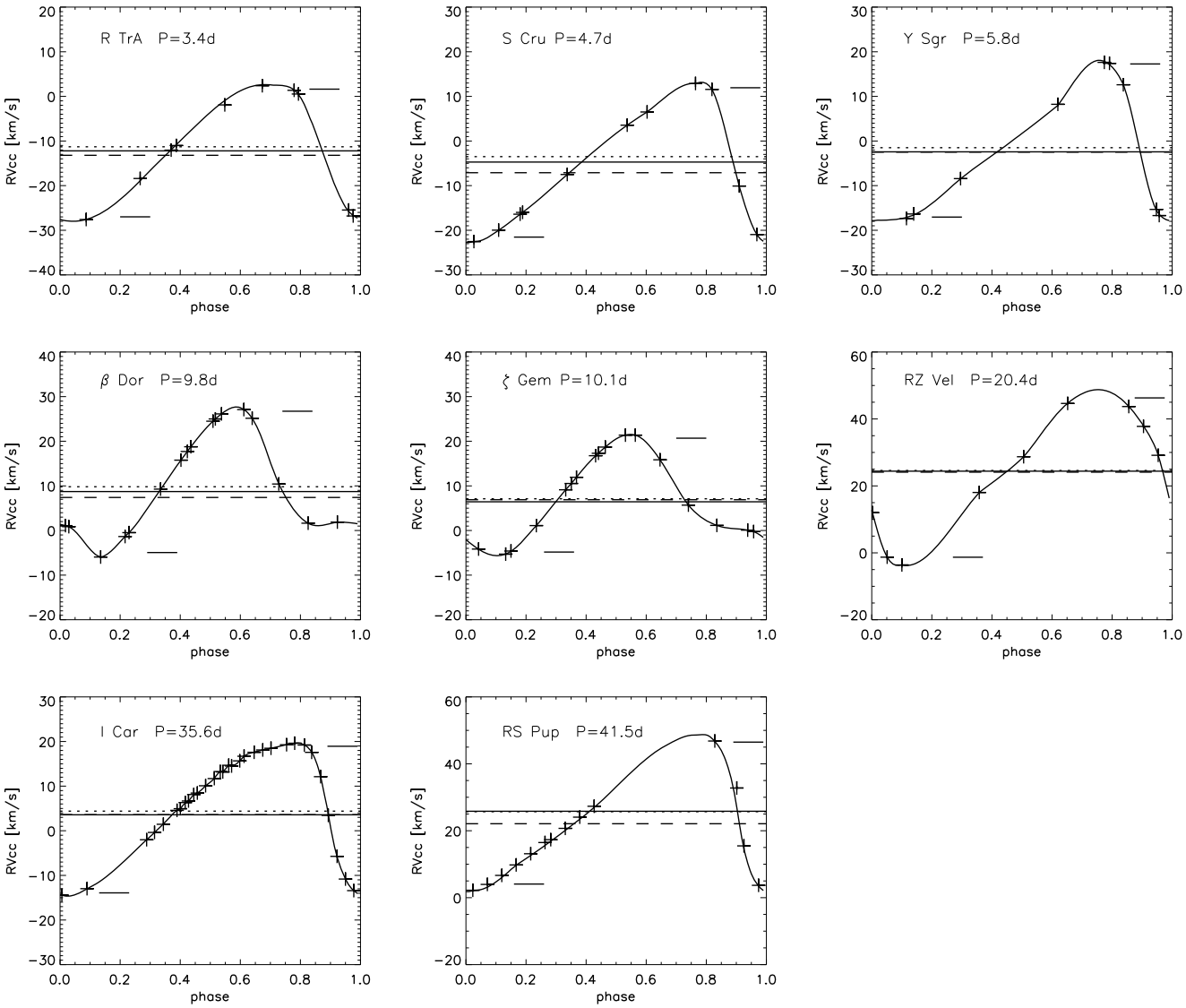


Fig. 1. Interpolated radial velocity curves based on the cross-correlation method are presented for each Cepheid in our sample. Uncertainties are too small to be seen (around 0.5 km s^{-1}). The horizontal lines near *extrema* give an indication of $\Delta RV_c[4896]$. The short horizontal lines are the γ-velocities (see Sect. 6) corresponding to the CC method (solid line), the center-of-mass velocity of Paper III (dotted line) and from Fernie et al. (1995, dashed line).

RS Pup, pivot points are used due to an inadequate phase coverage. When the phase coverage is good (which is the case for all other stars), the two methods are equivalent (Fig. 1). From these curves we are finally able to calculate ΔRV_{cc} (Table 2). The statistical uncertainty on ΔRV_{cc} is set as the average value of the uncertainty obtained for all measurements over a pulsation cycle of the star.

4. A *Pp* relation dedicated to the CC method

From $\Delta RV_c[4896]$ and ΔRV_{cc} obtained for all stars we derive the correction factor f_{cc} using Eq. (2). The result is plotted as a function of the period in Fig. 2a. No particular trend is found. However, the f_{cc} correction factors are clearly statistically dispersed around a mean value of 0.93 ± 0.02.

Following our definition ($p_{cc} = p f_{cc}$), the corrected projection factors suitable for the CC method are given in Table 2. The relation between the period and p_{cc} remains clear according to the statistical uncertainties:

$$p_{cc} = p f_{cc} = [-0.08 \pm 0.05] \log P + [1.31 \pm 0.06]. \quad (5)$$

The corresponding reduced χ^2 is 1.2. We refer to this relation in the following using Pp_{cc}. We recall that the *Pp* relation we found in Paper II dedicated to the FeI *4896* spectral line was: $p = [-0.064 \pm 0.020] \log P + [1.376 \pm 0.023]$. These two relations are shown in Fig. 2b. The impact of the cross-correlation method on the zero-point of the *Pp* is thus significant, while the slope increases only slightly (in absolute value) from −0.064 to −0.08.

We have several possible explanations for these results. The cross-correlation induces two biases:

1. The cross-correlated radial velocities are derived using a Gaussian fit, making the result sensitive both to the spectral line width (i.e. the effective temperature and abundances) and the rotation velocity projected on the line of sight. These two quantities, independently, and even more the combination of both, are not expected to vary linearly with the logarithm of the period. This might explain why no clear linear relation is found between f_{cc} and the period of the star. However, the mean values of the correction factors (around 0.93 ± 0.02) have a non negligible impact on the zero-point of the *Pp* relation, which decreases from 1.376 to 1.31 (5%).

Table 2. The projection factor (p_{cc}) and the γ-velocities (V_γ[CC]) derived from the CC radial velocity curves.

Name	$p(a)$	ΔRV_{cc} [km s^{-1}]	f_{cc}	p_{cc}	V_γ[GCD](b) [km s^{-1}]	V_γ[N08](c) [km s^{-1}]	V_γ [CC] [km s^{-1}]
R TrA	$1.35_{\pm0.03}$	$30.6_{\pm0.6}$	$0.93_{\pm0.03}$	$1.25_{\pm0.07}$	$-13.2_{\pm2.0}$	$-11.3_{\pm0.3}$	$-12.2_{\pm0.6}$
S Cru	$1.34_{\pm0.03}$	$35.9_{\pm0.6}$	$0.93_{\pm0.03}$	$1.25_{\pm0.07}$	$-7.1_{\pm2.0}$	$-3.5_{\pm0.4}$	$-4.7_{\pm0.6}$
Y Sgr	$1.33_{\pm0.03}$	$36.0_{\pm0.5}$	$0.95_{\pm0.03}$	$1.26_{\pm0.05}$	$-2.5_{\pm2.0}$	$-1.5_{\pm0.2}$	$-2.4_{\pm0.5}$
β Dor	$1.32_{\pm0.02}$	$33.5_{\pm0.2}$	$0.94_{\pm0.02}$	$1.24_{\pm0.05}$	$7.4_{\pm2.0}$	$9.8_{\pm0.1}$	$8.7_{\pm0.2}$
ζ Gem	$1.31_{\pm0.02}$	$27.2_{\pm0.2}$	$0.94_{\pm0.03}$	$1.23_{\pm0.05}$	$6.9_{\pm2.0}$	$7.1_{\pm0.1}$	$6.4_{\pm0.2}$
RZ Vel	$1.30_{\pm0.02}$	$52.5_{\pm0.7}$	$0.91_{\pm0.02}$	$1.18_{\pm0.05}$	$24.1_{\pm2.0}$	$24.6_{\pm0.4}$	$24.4_{\pm0.7}$
ℓ Car	$1.28_{\pm0.02}$	$34.3_{\pm0.2}$	$0.96_{\pm0.02}$	$1.22_{\pm0.04}$	$3.6_{\pm2.0}$	$4.4_{\pm0.1}$	$3.6_{\pm0.2}$
RS Pup	$1.27_{\pm0.02}$	$46.9_{\pm0.5}$	$0.90_{\pm0.02}$	$1.16_{\pm0.04}$	$22.1_{\pm2.0}$	$25.7_{\pm0.2}$	$25.8_{\pm0.5}$

[a] The projection factor as derived in Paper II. [b] The γ-velocities derived from the Galactic Cepheid Database (Fernie et al. 1995). [c] The γ-velocities or calibrated center-of-mass velocities of the stars from Paper III.

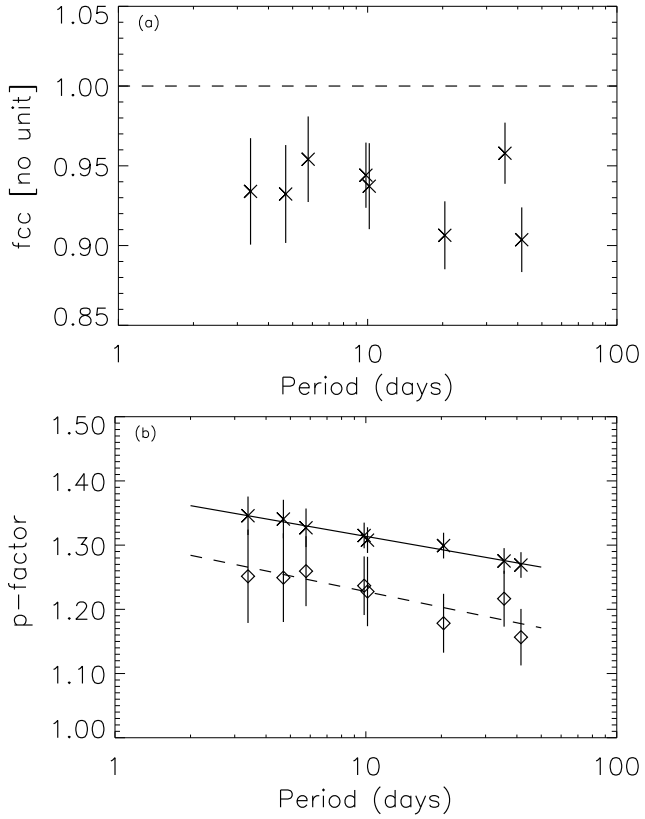


Fig. 2. a) The correction factor f_{cc} induced on the projection factor by the cross-correlation method is shown as a function of the logarithm of the period of the star. **b)** The period-projection factor (p) relation from Paper II (crosses and solid line) and the corrected relation suitable for the cross-correlation method $p_{cc} = pf_{cc}$ (diamonds and dashed line).

2. The cross-correlation method implies a mix of different spectral lines forming at different levels. In the Pp relation, the only quantity sensitive to the line depth is f_{grad} (as defined in Paper II) which compares the amplitude of the pulsation velocity corresponding to the line-forming region, and the photosphere. It is thus an estimate of the velocity gradient within the pulsating atmosphere of the star. The Pp relation was derived in Paper II for the *4896* spectral line which forms very close to the photosphere ($D = 8\%$), while the cross-correlated radial velocity is a mix of thousands of spectral lines forming at different levels, with an average depth of around $D \simeq 25\%$. The cross-correlation method is thus more sensitive to the velocity gradient (because the average line depth is large), which may explain the increase (in absolute value) of the slope from −0.064 to −0.08. Moreover, in Paper II we provided a very rough estimate of the Pp relation associated with the cross-correlation method, considering *only* the impact of the velocity gradient (which means discarding the bias related to the Gaussian fit). We found $p = [-0.075 \pm 0.031] \log P + [1.366 \pm 0.036]$ (see Sect. 7 of Paper II). The slope we find here (−0.08) is consistent with this previous rough estimate of −0.075.

These results are important to take into account when deriving the distance of Galactic or LMC/SMC Cepheids using the cross-correlation method. We emphasize that our Pp_{cc} is consistent with the result by Mérand et al. (2005), who found $p = 1.27$ for δ Cep ($P = 5.36$).

5. Wavelength dependence of the projection factor

With the data at hand, we check for a possible dependence of the projection factor on the wavelength range used for the cross-correlation radial velocity measurement. For each order, we derive the cross-correlated interpolated radial velocity curves, and then the corresponding amplitudes $\Delta RV_{cc}(\lambda)$. Orders 59, 68 and 72 are not considered due to instrumental characteristics and/or unrealistic results. For all stars, $\Delta RV_{cc}(\lambda)$ is plotted as a function of the wavelength, defined as the orders' average values (Fig. 3a). We find linear relations between these two quantities:

$$\Delta RV_{cc}(\lambda) = a_\lambda \lambda + b_\lambda, \quad (6)$$

where a_λ and b_λ are listed in Table 3. For consistency with the previous section the $\Delta RV_{cc}(\lambda)$ quantities have been slightly shifted in velocity in such a way that:

$$\Delta RV_{cc} = a_\lambda 502.2 \text{ nm} + b_\lambda, \quad (7)$$

where ΔRV_{cc} is derived from Table 2 and 502.2 nm is the wavelength averaged over all orders.

We also find a relation between a_λ and the logarithm of the period of the star:

$$a_\lambda = [-0.005 \pm 0.001] \log P - [0.002 \pm 0.001]. \quad (8)$$

From these results we can make two comments. First, the amplitude of the cross-correlated radial velocity curves decreases with wavelength. From hydrodynamical modelling, we know that the spectral lines form over a larger part of the atmosphere in the infrared compared to optical (Sasselov et al. 1990). This effect might help us to understand our result: the more extended the line forming regions are, the lower the amplitude of the radial velocity curves. Second, this effect is greater for long-period

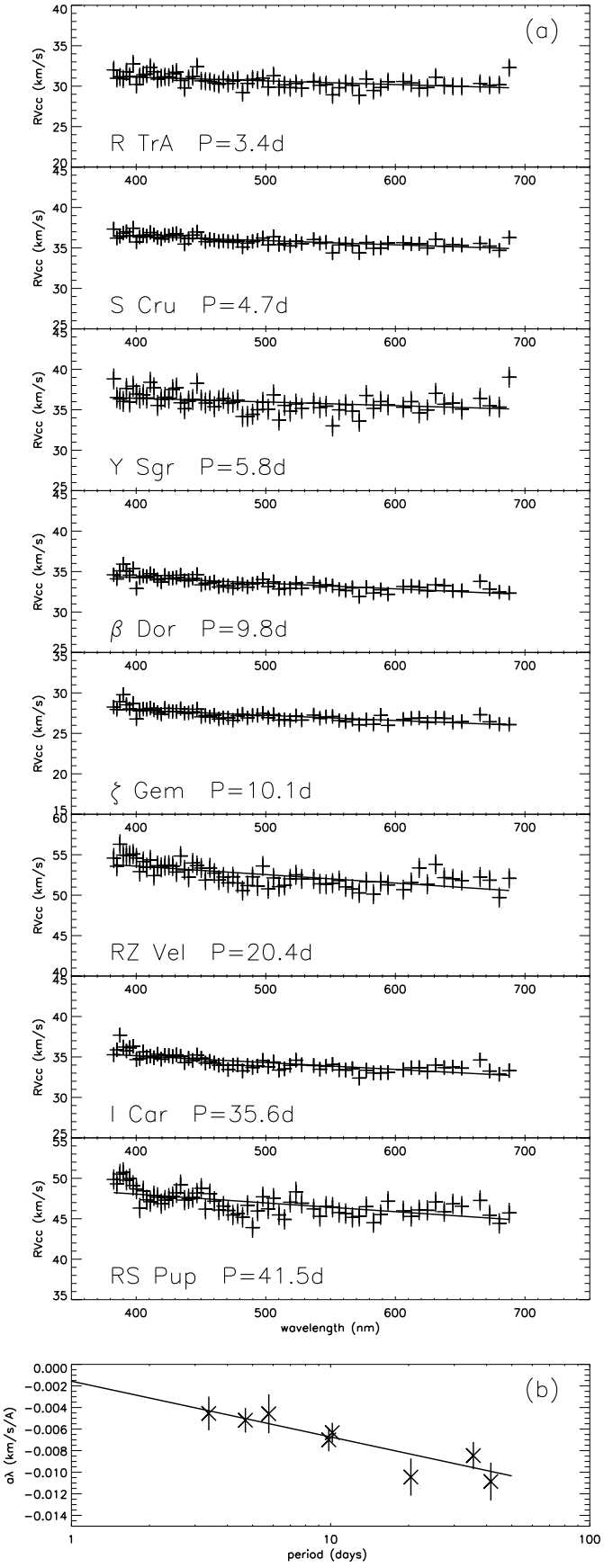


Fig. 3. **a)** Wavelength dependency of the amplitude of the cross-correlated radial velocity curves for each star in our sample. The corresponding linear relation are defined as: $\Delta RV_{cc} = a_\lambda \lambda + b_\lambda$. **b)** The corresponding slopes (a_λ) as a function of the period.

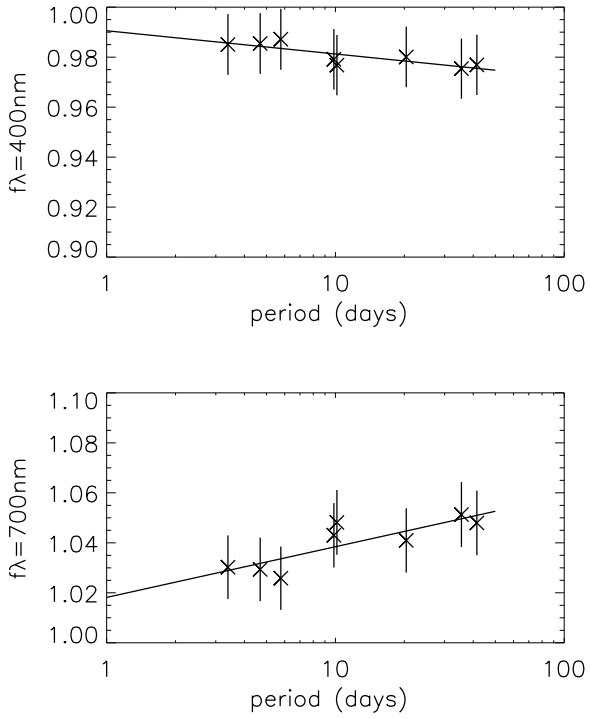


Fig. 4. Corrections to apply to the Pp_{cc} relation (Eq. (5)) in the blue (λ = 400 nm) and in the red (λ = 700 nm).

Table 3. Coefficients of the linear relations between the amplitude of the radial velocity curve and the wavelength.

Name	a_λ	b_λ
R TrA	$-0.005_{\pm 0.002}$	$32.93_{\pm 0.80}$
S Cru	$-0.005_{\pm 0.001}$	$38.50_{\pm 0.58}$
Y Sgr	$-0.005_{\pm 0.002}$	$38.26_{\pm 0.92}$
β Dor	$-0.007_{\pm 0.001}$	$37.06_{\pm 0.54}$
ζ Gem	$-0.006_{\pm 0.001}$	$30.39_{\pm 0.46}$
RZ Vel	$-0.010_{\pm 0.002}$	$57.76_{\pm 0.88}$
ℓ Car	$-0.008_{\pm 0.001}$	$38.54_{\pm 0.64}$
RS Pup	$-0.011_{\pm 0.002}$	$52.39_{\pm 0.89}$

Cepheids than short-period Cepheids. A reason might be that the mean radius, the size of the line-forming regions and the velocity gradient increase with the logarithm of the period.

In order to quantify the wavelength dependency of the Pp_{cc} relation, we define two correction factors ($f_{\lambda=400\text{ nm}} = \frac{\Delta RV_{cc}(\lambda=400\text{ nm})}{\Delta RV_{cc}}$ and $f_{\lambda=700\text{ nm}} = \frac{\Delta RV_{cc}(\lambda=700\text{ nm})}{\Delta RV_{cc}}$). We find the following correcting relation as a function of the logarithm of the period:

$$f_{\lambda=400\text{ nm}} = [-0.01 \pm 0.01] \log P + [0.99 \pm 0.01], \quad (9)$$

and

$$f_{\lambda=700\text{ nm}} = [0.02 \pm 0.01] \log P + [1.02 \pm 0.01]. \quad (10)$$

The reduced χ^2 values are respectively 0.3 and 1.3. These relations are shown in Fig. 4. We find that such corrections are currently irrelevant given our statistical uncertainties on the Pp_{cc} relation (Eq. (5)).

6. The CC γ-velocity and the K-term of Cepheids

Interestingly, for each Cepheid in our sample, we found in Paper III a linear relation between the γ-velocities (derived using the first moment method) of the various spectral lines and

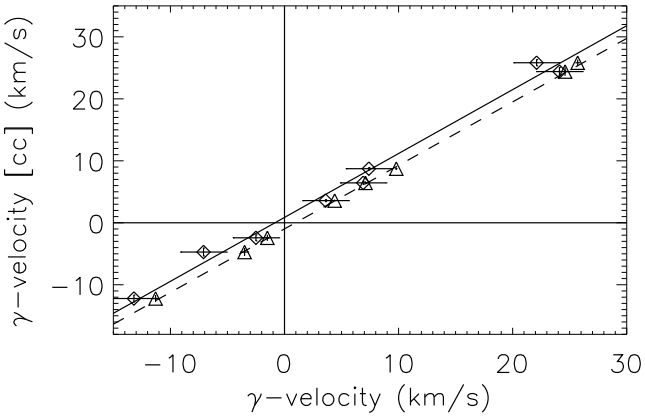


Fig. 5. V_γ [CC] as a function of V_γ[GCD] (diamond) and V_γ[N08] (triangles). The solid and dashed line are the corresponding linear interpolation.

their corresponding γ-asymmetries. Using these linear relations, we provided a physical reference to derive the center-of-mass γ-velocity of the stars (V_γ[N08]): it should be zero when the γ-asymmetry is zero. These values are consistent with an axisymmetric rotation model of the Galaxy. Conversely, previous measurements of the γ-velocities found in the literature (for e.g. Fernie et al. 1995: the Galactic Cepheid Database, hereafter V_γ[GCD]) were based on the cross-correlation method, and by using generally only a few measurements over the pulsation cycle. These results led to an apparent "fall" of Galactic Cepheids towards the Sun (compared to an axisymmetric rotation model of the Milky Way) with a mean velocity of about 2 km s^{-1}. This residual velocity shift has been dubbed the "K-term", and was first estimated by Joy (1939) to be −3.8 km s^{-1}.

We aim to understand why such a 2 km s^{-1} error was obtained before. An hypothesis is that the cross-correlation method is biased by the dynamical structure of the atmosphere of Cepheids. To verify this hypothesis, we have the unique opportunity to compare quantitatively and in a consistent way V_γ[N08], V_γ[GCD] and the γ-velocities derived from our HARPS cross-correlated radial velocity curves (hereafter V_γ[CC]). The comparison is done by plotting V_γ[CC] as a function of V_γ[GCD] and V_γ[N08] respectively (Fig. 5). The data are presented in Table 2 and the resulting linear relations are respectively:

$$V_\gamma[\mathrm{CC}] = [1.03 \pm 0.06]V_\gamma[\mathrm{GCD}] + [0.86 \pm 0.78], \quad (11)$$

and

$$V_\gamma[\mathrm{CC}] = [1.02 \pm 0.02]V_\gamma[\mathrm{N08}] - [0.99 \pm 0.17]. \quad (12)$$

The reduce χ^2 values are respectively 3.0 and 3.8.

Several conclusions can be drawn. The slope of these relations are similar and close to one, which means that there is no particular trend of the γ-velocity with the period of the star, or at least, it remains negligible here. As in Paper III, we find a systematic difference of 0.86 + 0.99 $\simeq$ 1.8 km s^{-1} between V_γ[N08] and V_γ[GCD], which is consistent with the K-term of Cepheids. However, the γ-velocities we derive in this Paper using the cross-correlation method are systematically lower by (0.9±0.8) km s^{-1} than the ones found in the literature (V_γ[GCD]), and they are systematically larger by 1.0 ± 0.2 km s^{-1} than the calibrated center-of-mass velocities (V_γ[N08]). As a consequence, the cross-correlation method alone cannot explain alone the K-term. The CC method is sensitive to the dynamical structure of the Cepheids' atmosphere in such a way that it is responsible for ≃50% of the K-term. An additional term is required to explain the presence of such offsets in previous determinations of the gamma-velocity. It could be related, for instance, to the quality of observations in the past (Joy et al. 1939) or to the different methods used to derive the γ-velocity (Pont et al. 1994).

7. Conclusions

By comparing the amplitude of our cross-correlated radial velocity curves with previous results based on the first moment method (Paper II), we derived a new *Pp* relation applicable to radial velocities measured by the cross-correlation method. This relation is crucial for the distance scale calibration, and in particular to derive the distances of LMC and SMC Cepheids (Gieren et al. 2005a; Gieren et al. 2009, in preparation). We also find a slight dependence of the *Pp* relation on the wavelength. Considering our current uncertainties this effect is negligible, but it might become significant in the near future. The next steps are to test the impact of the signal to noise ratio, the spectral resolution and the metallicity on the projection factor. The latter point will require a large sample of Cepheids with well-measured metallicities. These studies (including this work) are part of the international "Araucaria Project" whose purpose is to provide an improved local calibration of the extragalactic distance scale out to distances of a few Megaparsecs (Gieren et al. 2005b). Moreover, the fact that the cross-correlation method over-estimates the amplitude of the radial velocity curve and under-estimates the γ-velocity (compared to the calibrated values presented in Paper III) might have some implications for other kinds of pulsating stars, for e.g. in asteroseismology.

Moreover, we show in Paper III that the K-term of Cepheids vanishes if one considers carefully the dynamical structure of Cepheid atmosphere. From the results presented in this paper, we can state that the cross-correlation method might not be totally responsible for the K-term found in the previous studies (only 50% seems to be a consequence of the cross-correlation method). There seems to be another contribution whose nature should be investigated.

Acknowledgements. Based on observations collected at La Silla observatory, Chile, in the framework of European Southern Observatory's programs 072.D-0419 and 073.D-0136. This research has made use of the SIMBAD and VIZIER databases at CDS, Strasbourg (France). N.N. and W.G. acknowledge financial support from the FONDAP Center of Astrophysics 15010003, and the BASAL Center of Astrophysics CATA. N.N. acknowledges the Geneva team for support in using the HARPS pipeline.

References

Baranne, A., Queloz, D., Mayor, M., et al. 1996, A&AS, 119, 373
Burki, G., Mayor, M., & Benz, W. 1982, A&A, 109, 258
Davis, J., Jacob, A. P., Robertson, J. G., et al. 2009, MNRAS, tmp, 244
Fernie, J. D., Beattie, B., Evans, N.R., & Seager, S. 1995, IBVS No. 4148
Fouqué, P., Arriagada, P., Storm, J., et al. 2007, A&A, 476, 73
Gieren, W. P., Fouqué, P., & Gómez, M. 1998, ApJ, 496, 17
Gieren, W. P., Storm, J., Barnes, T. G., et al. 2005a, ApJ, 627, 224
Gieren, W., Pietrzynski, G., Bresolin, F., et al. 2005b, Msngr, 121, 23
Joy, A. H. 1939, ApJ, 89, 356
Kervella, P., Nardetto, N., Bersier, D., et al. 2004, A&A, 416, 941
Mérand, A., Kervella, P., Coude du Foresto, V., et al. 2005, A&A, 438, L9
Nardetto, N., Fokin, A., Mourard, D., et al. 2004, A&A, 428, 131
Nardetto, N., Mourard, D., Kervella, P., et al. 2006, A&A, 453, 309 (Paper I)
Nardetto, N., Mourard, D., Mathias, Ph., et al. 2007, A&A, 471, 661N (Paper II)
Nardetto, N., Stoekl, A., Bersier, D., et al. 2008, A&A, 489, 1255 (Paper III)
Pepe, F., Mayor, M., Galland, F., et al. 2002, A&A, 388, 632
Pont, F., Mayor, M., & Burki, G. 1994, A&A, 285, 415
Sabbey, C. N., Sasselov, D. D., Fieldus, M. S., et al. 1995, ApJ, 446, 250
Sasselov, D. D., Lester, J. B., & Fieldus, M. S. 1990, ApJ, 362, 333

Annexe L

The Baade-Wesselink p-factor applicable to LMC Cepheids

A&A 534, L16 (2011)
DOI: 10.1051/0004-6361/201117459
© ESO 2011

Astronomy & Astrophysics

L E

The Baade-Wesselink *p*-factor applicable to LMC Cepheids⋆

N. Nardetto[1], A. Fokin[1,2], P. Fouqué[3], J. Storm[4], W. Gieren[5], G. Pietrzynski[5,6], D. Mourard[1], and P. Kervella[7]

[1] Laboratoire Fizeau, UNS/OCA/CNRS UMR6525, Parc Valrose, 06108 Nice Cedex 2, France
e-mail: Nicolas.Nardetto@oca.eu
[2] Institute of Astronomy of the Russian Academy of Sciences, 48 Pjatnitskaya Str., Moscow 109017, Russia
[3] Observatoire Midi-Pyrénées, Laboratoire d'Astrophysique, UMR 5572, Université Paul Sabatier – Toulouse 3, 14 avenue Edouard Belin, 31400 Toulouse, France
[4] Leibniz-Institut für Astrophysik Potsdam (AIP), An der Sternwarte 16, 14482 Potsdam, Germany
[5] Departamento de Astronomía, Universidad de Concepción, Casilla 160-C, Concepción, Chile
[6] Warsaw University Observatory, Al. Ujazdowskie 4, 00-478 Warsaw, Poland
[7] LESIA, Observatoire de Paris, CNRS UMR 8109, UPMC, Université Paris Diderot, 5 place Jules Janssen, 92195 Meudon, France

Received 10 June 2011 / Accepted 26 September 2011

ABSTRACT

Context. Recent observations of LMC Cepheids bring new constraints on the slope of the period-projection factor relation (hereafter *Pp* relation) that is currently used in the Baade-Wesselink (hereafter BW) method of distance determination. The discrepancy between observations and theoretical analysis is particularly significant for short period Cepheids
Aims. We investigate three physical effects that might possibly explain this discrepancy: (1) the spectroscopic S/N that is systematically lower for LMC Cepheids (around 10) compared to Galactic ones (up to 300), (2) the impact of the metallicity on the dynamical structure of LMC Cepheids, and (3) the combination of infrared photometry/interferometry with optical spectroscopy.
Methods. To study the S/N we use a very simple toy model of Cepheids. The impact of metallicity on the projection factor is based on the hydrodynamical model of δ Cep already described in previous studies. This model is also used to derive the position of the optical versus infrared photospheric layers.
Results. We find no significant effect of S/N, metallicity, and optical-versus-infrared observations on the *Pp* relation.
Conclusions. The *Pp* relation of Cepheids in the LMC does not differ from the Galactic relation. This allows its universal application to determine distances to extragalactic Cepheids via BW analysis.

Key words. stars: oscillations – stars: abundances – stars: distances

1. Introduction

For decades the Cepheid stars have been used to calibrate the distance scale and the Hubble constant through their well-known period-luminosity (*PL*) relation (Riess et al. 2009a,b, 2011; and Freedman et al. 2010, for a review). Recently, using the Baade-Wesselink (*BW*) method to determine distances of Cepheids, Storm et al. (2011b, second paper of the series) has found that the *K*-band *PL* relation is nearly universal and can be applied to any host galaxy regardless of its metallicity.

The projection factor is a key quantity of the BW methods: it is used to convert the radial velocity into the pulsation velocity of the star. In their first paper Storm et al. (2011a) *directly* constrained the period-projection factor (*Pp*) relation from observations. The zero point is based on the HST trigonometric parallaxes of Galactic Cepheids (Benedict et al. 2007; Groenewegen 2007; Fouqué et al. 2007; Mérand et al. 2004), and the slope is derived from BW distances of LMC Cepheids (all Cepheids in the LMC used by Storm et al. can be assumed to be at the same distance, leading to an extra constraint on the projection factor relation). Their relation is at 2 sigmas of the semi-theoretical relation of Nardetto et al. (2007, 2009). For instance for δ Cep, they find $p = 1.41 \pm 0.05$, while the theoretical value is $p = 1.25 \pm 0.05$ (Nardetto et al. 2009). An effect of the physical nature of LMC Cepheids on the slope of the *Pp* relation is not excluded and should be investigated. This question of the universality of the *Pp* relation is critical because it is a common assumption in the BW analysis of extragalactic Cepheids.

The spectroscopic S/N is systematically lower for LMC Cepheids (around 10) than Galactic ones (up to 300). In Sect. 1, we investigate the impact of S/N on the radial velocity, hence on the projection factor. In Sect. 2, we determine whether the projection factor should be corrected when observing LMC Cepheids of lower metallicity. Then, when combining an *optical* spectroscopic determination of the projection factor with an angular diameter derived from *infrared* observations, a mismatch of the position of the photosphere is not excluded. We investigate this possibility in Sect. 3. using new CRIRES spectroscopic observations and hydrodynamical modelling.

2. S/N and *p*-factor

The amplitude of the radial velocity curve depends on the method used to derive the position of the spectral line profile. Two main methods are currently used: the Gaussian fit and the first moment (or centroid). Only the first moment method is insensitive to the width of the spectral line (turbulence and/or stellar rotation) and is thus appropriate for comparing the dynamical structure of Cepheid's atmosphere (Burki et al. 1982; Nardetto

⋆ Based on observations made with ESO telescopes at the Silla Paranal Observatory under programme ID 280.A-5018(A).

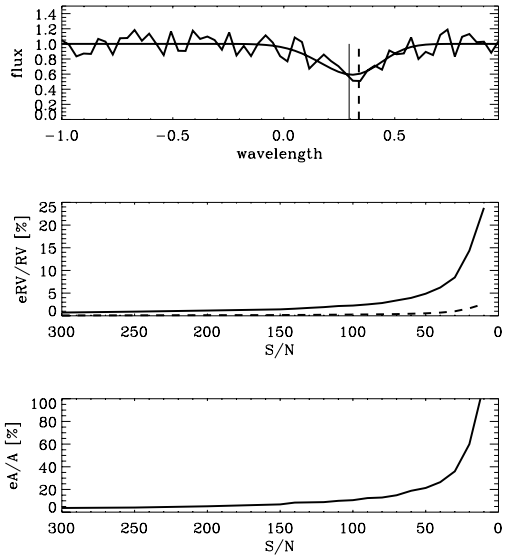


Fig. 1. a) The modelled random spectral line profile derived from our toy model (with $V_{\rm rad} = 20$ km s^{-1}) together with the degraded profile (S/N of 10). The vertical lines correspond to the centroid (solid) and Gaussian (dashed) radial velocities. One hundred random spectral lines are calculated. **b)** The relative uncertainties of the radial velocities as a function of the S/N (same legend). **c)** The relative uncertainty on the bi-Gaussian line asymmetry as a function of the S/N.

et al. 2006). However, these two methods are not suitable for LMC Cepheids with spectra of very low S/N (around 10). The method currently used for distant (and thus faint) Cepheids is to cross-correlate thousands of spectral lines, derive a residual spectral line and apply the Gaussian fit method to determine the radial velocity (Baranne et al. 1986). Compared to a single line measurement of the radial velocity (using the first moment method), the projection factor is actually reduced (regardless of the period of the Cepheid) by about 5% when using the cross-correlation method (Nardetto et al. 2009). The S/N might affect these different methods of radial velocity determination.

We want to verify this assumption using a toy model already described in Nardetto et al. (2006). The modelled spectral line profile (Fig. 1a) is randomly degraded from an S/N of 300 to 10, by steps of 10. This is done one hundred times. For each S/N, we derive the mean radial velocity corresponding to the Gaussian and centroid methods (averaged over the 100 profiles), together with their respective mean uncertainties. A first result is that the mean radial velocity derived from both methods (Gaussian fit and first moment) is insensitive to the S/N. This is a good indication that the cross-correlation method is probably not biased by the S/N.

Additional results have to be mentioned. The first moment method can lead to statistical uncertainties as large as 20% when the S/N is lower around 10 (Fig. 1b). The Gaussian fit method is more robust with a few percent precision for an S/N of 10. One should, however, consider that these results depend mainly on the radial velocity considered (i.e. the pulsation phase considered) and the spectral line depth. When using the cross-correlation method, the relative uncertainty on the radial velocity can drop to less than 1%. We also take the opportunity to show that line asymmetry (derived using the bi-Gaussian method described in Nardetto et al. 2006) is highly sensitive to the S/N (Fig. 1c). While the mean value of the spectral asymmetry is stable with the S/N (as found for the radial velocities), an S/N of 100 is required to derive a line asymmetry at a 10% relative precision level. Studying the dynamical structure of pulsating stars atmospheres thus requires a minimum S/N of 100. The conclusion of this section is that the S/N should not affect the period-projection factor relation of Galactic versus LMC Cepheids.

Table 1. Hydrodynamical models and corresponding p-factors.

Parameters	MW	LMC
L [$L_\odot$]	1995	2290
M [$M_\odot$]	4.8	4.8
$T_{\rm eff}$ [K]	5877	6100
X	0.700	0.730
Y	0.280	0.262
Z	0.020	0.008
P [days]	5.41	5.38
p_0	1.390	1.390
$f_{\rm grad}$	0.990	0.975
line for $f_{\rm grad}$ [Å]	FeI 4896	FeI 5373
$f_{\rm og}$	0.963	0.963
$p = p_0 f_{\rm grad} f_{\rm og}$	1.325	1.305

3. Metallicity and *p*-factor

The metallicity of Cepheids has an impact on their κ-mechanism that drives the pulsation through an opacity process. As a consequence, the amplitude of the pulsation velocity of the star is affected by the metallicity: the lower the metallicity, the larger the amplitude of the pulsation velocity (Klagyivik & Szabados 2007; Klagyivik & Szabados 2009). But in principle, if the amplitude of the *pulsation* velocity is higher, the *radial* velocity should also be larger in the same proportion, and the projection factor $p = \frac{V_{\rm puls}}{V_{\rm rad}}$ should *not* change. The key-point is then to know whether the velocity gradient in the atmosphere of the star changes with the metallicity in such a way that the projection factor for a given spectral line will change. To answer this question, we consider the hydrodynamical model of δ Cep in the Milky Way (Nardetto et al. 2004), based on the code by Fokin et al. (2004), and compare it to a consistent LMC model of the same star. The fundamental parameters of the LMC model of δ Cep are determined as follows. Following Luck et al. (1998) and Romaniello et al. (2008), we first assume $Z = 0.008$ (very close to their respective values of 0.01 and 0.009). We then consider a helium-to-metal enrichment ratio $\frac{\Delta Y}{\Delta Z}$ of 1.5 (consistent with the value of 2.1 ± 0.9 derived by Casagrande et al. 2007), which leads to $X = 0.730$ and $Y = 0.262$. Then, we assume the same mass for δ Cep in the Milky Way and the LMC (i.e. $M = 4.8\ M_\odot$) and we simply use the mass-luminosity relation of Chiosi et al. (1993, Eq. (25)) to derive the luminosity of δ Cep in the LMC. We obtain $L = 2290\ L_\odot$. Finally, using the Milky Way and LMC analytical relations of the red edge instability strip by Bono et al. (2000, Table 5), we find an expected effective temperature of about $T_{\rm eff} = 6100$ K. All parameters used in the code are presented in Table 1 for the Galactic and LMC models of δ Cep. We find a pulsation period of $P = 5.38$ d (in LMC), which is consistent with theoretical results by Bono et al. (2000, Table 6).

For both models (with Galactic and LMC metallicities), we calculated the spectral line profiles for the 17 metallic lines presented in Nardetto et al. (2007, hereafter Paper I) using radiative transfer equations in a moving atmosphere. The calculation is made at 40 equidistant pulsation phases. We finally plotted the amplitude of the *radial* (using the first moment method) and *pulsation* velocity curves as a function of the line depth at minimum radius (see Fig. 2) in order to measure the velocity gradient and

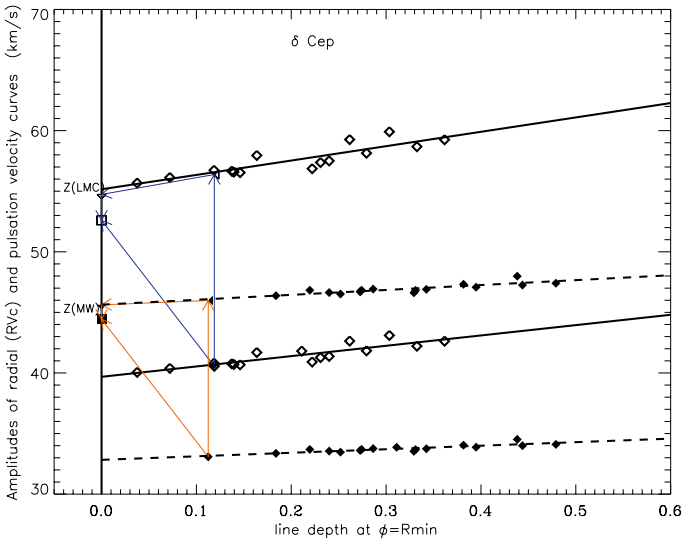


Fig. 2. The decomposition of the projection factor. The filled and open diamonds correspond to the Milky Way and LMC models of δ Cep. For a given model, the lower (resp. higher) values are the amplitudes of the radial (resp. pulsation) velocity curves for each spectral line considered. The red and blue arrows indicate the decomposition of the projection factor for the MW and LMC respectively: $\uparrow$ (p_0), $\leftarrow$ ($f_{\rm grad}$), $\downarrow$ ($f_{\rm og}$) and $\nwarrow$ ($p = p_0 f_{\rm grad} f_{\rm og}$). For detailed explanations, refer to Nardetto et al. (2007).

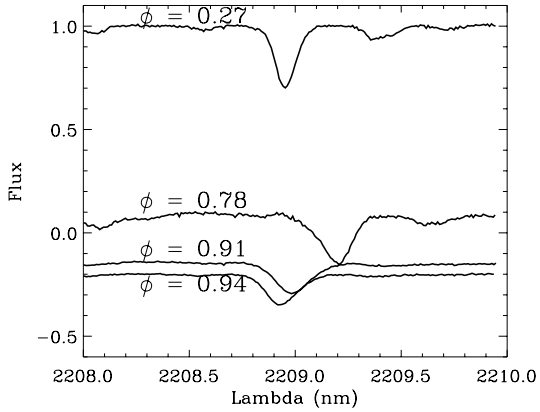


Fig. 3. The CRIRES spectral line profiles (CaI 22090.0 Å) of ℓ Car as a function of the pulsation phase.

perform the decomposition of the projection factor as explained in Paper I. There are three subconcepts involved in the decomposition of the projection factor: 1/ the geometric projection factor mainly related to the limb-darkening of the star (p_0), 2/ the correction due to the velocity gradient within the atmosphere ($f_{\rm grad}$) and 3/ the correction due to the relative motion between the *optical* and *gas* layers corresponding to the photosphere ($f_{\rm og}$); for a detailed definition of these two layers, refer to Eqs. (1) and (3) of Nardetto et al. (2004). This decomposition of the projection factor for the Milky Way and the LMC models of δ Cep are indicated in Fig. 2, and the corresponding values can be found in Table 1. To compare the MW and LMC projection factors properly, we have to consider two spectral lines of similar depth (around 0.1): FeI 4896.439 Å for the MW and FeI 5373.709 Å for the LMC. These choices only have an impact on $f_{\rm grad}$.

We find that the projection factor is about the same for the Galactic and LMC models (at a 1.5% level). This basically means that even if the amplitude of the radial and pulsation velocity curves are larger for the LMC metallicity model, the structure of the atmosphere is relatively unchanged: the velocity gradient is larger (in absolute terms), but it is the same relative to the amplitude of the velocities. As a conclusion, the p-factor value appropriate for a Cepheid of a given period should not depend on its metallicity, and the large discrepancy obtained for the *Ppñ* relations (observation versus theory), especially for short-period Cepheids (for δ Cep, $p = 1.41$[observations] versus $p = 1.25$[theory]), is not explained by a difference of metallicity.

4. Optical *p*-factor versus infrared diameters

When applying the BW method, infrared photometry/interferometry is often combined with optical spectroscopy to derive the distance of the star. In principle, the radial velocity curve derived from *optical* spectroscopy has to be combined with an *optical* projection factor to obtain the pulsation velocity associated to the *optical* photospheric layer. As a consequence, to get an accurate determination of the distance, the limb-darkened angular diameter derived from the infrared surface brightness method or from infrared long-baseline interferometry must correspond to the same *optical* photospheric layer. In other words, an implicit assumption in the BW method is to consider that the photospheric layer in the *optical* and in the *infrared* are associated with the same material in the star. However, the larger the wavelength, the lower the position of the photosphere in the star (see theoretical results by Sasselov et al. 1990, Figs. 21 and 22). This effect seems to be stronger for long-period Cepheids (their Fig. 21), than for short-period Cepheids (their Fig. 22). Verifying these theoretical results with observations is extremely difficult. The best is probably to use interferometry. From the spectrocopic point of view, one can compare the optical and infrared radial velocity curves of two spectral lines of similar depths (using the first moment method). However, the velocity ratio obtained has to be corrected from the velocity gradient and from optical-versus-gas layer effect ($f_{\rm grad}$ and $f_{\rm og}$, respectively). For instance, it is probably not possible to perform this analysis for atypical Cepheids, like X Sgr presenting a double shock wave in the atmosphere (Mathias et al. 2006), as done by Sasselov et al. (1990).

We present infrared CRIRES observations of ℓ Car obtained in 2008–2009 at four different pulsation phases (S/N of about 300 in the continuum). We find three unblended spectral lines, Brγ 21661.2 Å and two metallic lines: FeII 21266.1 Å and CaI 22090.0 Å. In Fig. 3, we present the CaI spectral line flux as a function of time. The first moment radial velocity and depth (as a percentage of continuum) are indicated in Fig. 4, together with HARPS observations of a spectral line of similar depth. The dashed line in Fig. 4 (lower panel) is the optical HARPS radial velocity curve multiplied by 1.30, showing that the infrared radial velocity curve has an amplitude that is about 30% larger than in the optical. The conclusion is that, even if these two metallic lines in the optical and in the infrared have a similar depth (which means in principle that their line-forming regions have a similar optical depths, and that they form approximatively at the same position in the atmosphere compared to the photosphere), the infrared amplitude of the radial velocity curve is significantly larger than the optical one. This suggests (as explained above) that the photospheric layer is probably forming higher in the infrared than in the optical (which seems to be in contradiction with Sasselov et al. 1990). More data are required to confirm this result.

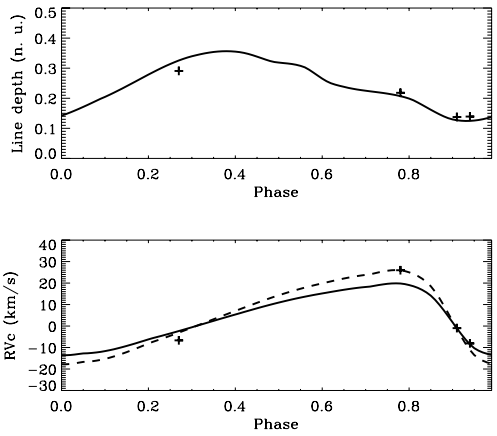


Fig. 4. The line depth (*up*) and the first moment radial velocity (*down*) corresponding to the infrared CRIRES spectral line of ℓ Car (crosses) is compared to the optical 4896A HARPS spectral line of similar depth (solid line). The meaning of the dashed line is explained in the text.

We address this question theoretically using our hydrodynamical models of δ Cep and ℓ Car. The model of ℓ Car is described in Paper I. We consider the solar metallicity. Concerning δ Cep, the optical and infrared photospheric layers ($\tau_c = 1$) form at the same layer in the atmosphere, whereas for ℓ Car the infrared photosphere forms 2% higher than the optical one. This implies a 2% increase only in the projection factor, which seems to be in contradiction with Sasselov et al. (1990) and also CRIRES data. This delicate question will be studied in more detail later, using a larger sample of infrared (resp. optical) spectroscopic (resp. interferometric) data. In either case, this effect (optical versus infrared) should affect the Milky Way and LMC Cepheids in the same way.

5. Conclusions

We find that the S/N, metallicity, and optical-versus-infrared observations (but this last point has to be confirmed) cannot explain the discrepancy between the theoretical and empirical period-projection factor relation based on LMC observations. Other possibilities can be considered, such as limb darkening for instance. Indeed, following the relation by Storm et al. (2011a), the very short-period Cepheids should have a projection factor close to 1.45–1.5. This means a limb-darkening close to zero (uniform disk). By constraining this limb darkening using interferometry (for instance VEGA/CHARA in optical, Mourard et al. 2009), one can derive a geometric projection factor that should help in resolving the discrepancy. However, our results seem to indicate that the *Pp* relation is universal. This is extremely precious when applying the BW method to extragalactic Cepheids.

Acknowledgements. W.G. and G.P. gratefully acknowledge financial support for this work from the Chilean Center for Astrophysics FONDAP 15010003, and from the BASAL Centro de Astrofisica y Tecnologias Afines (CATA) PFB-06/2007. Support from the Polish grant N203 387337 and TEAM subsidy of the Fundation for Polish Science (FNP) is also acknowledged. This research received the support of PHASE, the high angular resolution partnership between ONERA, Observatoire de Paris, CNRS and University Denis Diderot Paris 7. N.N. acknowledges F. Millour, J. Groh, and S. Kraus, who helped prepare the CRIRES DDT proposal, and L. Szabados for a careful reading of the paper. We finally thank the referee for his extremely useful comments.

References

Baranne, A., Queloz, D., Mayor, M., et al. 1996, A&AS, 119, 373
Benedict, G. F., Mc Arthur, B. E., Feast, M. W., et al. 2007, ApJ, 133, 1810
Bono, G., Castellani, V., & Marconi, M. 2000, ApJ, 529, 293
Burki, G., Mayor, M., & Benz, W. 1982, A&A, 109, 258
Casagrande, L., Flynn, C., Portinari, L., et al. 2007, MNRAS, 382, 1516
Chiosi, C., Wood, P. R., & Capitano, N. 1993, ApJS, 86, 541
Fokin, A., Mathias, Ph., Chapellier, E., et al. 2004, A&A, 426, 687
Freedman, W. L., & Madore, B. F. 2010, ARA&A, 48, 673
Fouqué, P., Arriagada, P., & Storm, J. 2007, A&A, 518, A51
Groenewegen, M. A. T. 2007, A&A, 474, 975
Klagyivik, P., & Szabados, L. 2007, AN, 328, 825
Klagyivik, P., & Szabados, L. 2009, AN, 504, 959
Luck, R. E., Moffett, T. J., Barnes, T. G., III, & Gieren, W. P. 1998, AJ, 115, 605
Marquette, J. B., Beaulieu, J. P., & Buchler, J. R. 2009, A&A, 495, 249
Mathias, P., Gillet, D., Fokin, A., et al. 2006, A&A, 457, 575
Mérand, A., Kervella, P., & Coudé du Foresto, V. 2005, A&A, 447, 783
Mourard, D., Clausse, J. M., & Marcotto, A. 2009, A&A, 508, 1073
Nardetto, N., Fokin, A., Mourard, D., et al. 2004, A&AP, 428, 131
Nardetto, N., Mourard, D., Kervella, P., et al. 2006, A&A, 453, 309
Nardetto, N., Mourard, D., Mathias, Ph., Fokin, A., & Gillet, D. 2007, A&A, 471, 661
Nardetto, N., Gieren, W., Kervella, P., et al. 2009, A&A, 502, 951
Riess, A. G., Lucas, M., Weidong, L., et al. 2009a, ApJ, 699, 539
Riess, A. G., Lucas, M., Casertano, S., et al. 2009b, ApJ, 183, 109
Riess, A. G., Lucas, M., Casertano, S., et al. 2010, ApJ, 730, 119
Romaniello, M., Primas, F., Mottini, M., et al. 2008, A&A, 488, 731
Sasselov, D. D., & Lester, J. B. 1990, ApJ, 362, 333
Storm, J., Gieren, W., & Fouqué, P. 2011a, A&A, 534, A94
Storm, J., Gieren, W., & Fouqué, P. 2011b, A&A, 534, A95

Annexe M

HARPS-N high spectral resolution observations of Cepheids I. The Baade-Wesselink projection factor of δ Cep revisited

A&A 597, A73 (2017)
DOI: 10.1051/0004-6361/201629400
© ESO 2017

Astronomy & Astrophysics

HARPS-N high spectral resolution observations of Cepheids I. The Baade-Wesselink projection factor of δ Cep revisited⋆

N. Nardetto[1], E. Poretti[2], M. Rainer[2], A. Fokin[3], P. Mathias[4,5], R. I. Anderson[6], A. Gallenne[7,8], W. Gieren[8,9], D. Graczyk[8,9,10], P. Kervella[11,12], A. Mérand[7], D. Mourard[1], H. Neilson[13], G. Pietrzynski[10], B. Pilecki[10], and J. Storm[14]

[1] Université Côte d'Azur, OCA, CNRS, Lagrange, France
e-mail: Nicolas.Nardetto@oca.eu
[2] INAF–Osservatorio Astronomico di Brera, via E. Bianchi 46, 23807 Merate (LC), Italy
[3] Institute of Astronomy of the Russian Academy of Sciences, 48 Pjatnitskaya Str., 109017 Moscow, Russia
[4] Université de Toulouse, UPS-OMP, Institut de Recherche en Astrophysique et Planétologie, 31400 Toulouse, France
[5] CNRS, UMR 5277, Institut de Recherche en Astrophysique et Planétologie, 14 avenue Édouard Belin, 31400 Toulouse, France
[6] Department of Physics and Astronomy, The Johns Hopkins University, 3400 N. Charles St, Baltimore, MD 21218, USA
[7] European Southern Observatory, Alonso de Córdova 3107, Casilla 19001, Santiago 19, Chile
[8] Departamento de Astronomía, Universidad de Concepción, Casilla 160-C, Concepción, Chile
[9] Millenium Institute of Astrophysics, Santiago, Chile
[10] Nicolaus Copernicus Astronomical Center, Polish Academy of Sciences, ul. Bartycka 18, 00-716 Warszawa, Poland
[11] LESIA (UMR 8109), Observatoire de Paris, PSL, CNRS, UPMC, Univ. Paris-Diderot, 5 place Jules Janssen, 92195 Meudon, France
[12] Unidad Mixta Internacional Franco-Chilena de Astronomía, CNRS/INSU, France (UMI 3386) and Departamento de Astronomía, Universidad de Chile, Camino El Observatorio 1515, Las Condes, Santiago, Chile
[13] Department of Astronomy & Astrophysics, University of Toronto, 50 St. George Street, Toronto, ON, M5S 3H4, Canada
[14] Leibniz Institute for Astrophysics, An der Sternwarte 16, 14482 Potsdam, Germany

Received 26 July 2016 / Accepted 21 October 2016

ABSTRACT

Context. The projection factor p is the key quantity used in the Baade-Wesselink (BW) method for distance determination; it converts radial velocities into pulsation velocities. Several methods are used to determine p, such as geometrical and hydrodynamical models or the inverse BW approach when the distance is known.
Aims. We analyze new HARPS-N spectra of δ Cep to measure its cycle-averaged atmospheric velocity gradient in order to better constrain the projection factor.
Methods. We first apply the inverse BW method to derive p directly from observations. The projection factor can be divided into three subconcepts: (1) a geometrical effect (p_0); (2) the velocity gradient within the atmosphere ($f_{\rm grad}$); and (3) the relative motion of the optical pulsating photosphere with respect to the corresponding mass elements ($f_{\rm o-g}$). We then measure the $f_{\rm grad}$ value of δ Cep for the first time.
Results. When the HARPS-N mean cross-correlated line-profiles are fitted with a Gaussian profile, the projection factor is $p_{\rm cc-g} = 1.239 \pm 0.034({\rm stat.}) \pm 0.023({\rm syst.})$. When we consider the different amplitudes of the radial velocity curves that are associated with 17 selected spectral lines, we measure projection factors ranging from 1.273 to 1.329. We find a relation between $f_{\rm grad}$ and the line depth measured when the Cepheid is at minimum radius. This relation is consistent with that obtained from our best hydrodynamical model of δ Cep and with our projection factor decomposition. Using the observational values of p and $f_{\rm grad}$ found for the 17 spectral lines, we derive a semi-theoretical value of $f_{\rm o-g}$. We alternatively obtain $f_{\rm o-g} = 0.975 \pm 0.002$ or 1.006 ± 0.002 assuming models using radiative transfer in plane-parallel or spherically symmetric geometries, respectively.
Conclusions. The new HARPS-N observations of δ Cep are consistent with our decomposition of the projection factor. The next step will be to measure p_0 directly from the next generation of visible interferometers. With these values in hand, it will be possible to derive $f_{\rm o-g}$ directly from observations.

Key words. stars: oscillations – techniques: spectroscopic – stars: individual: delta Cep – stars: distances – stars: atmospheres – stars: variables: Cepheids

1. Introduction

Since their period-luminosity (PL) relation was established (Leavitt & Pickering 1912), Cepheid variable stars have been used to calibrate the distance scale (Hertzsprung 1913) and then the Hubble constant (Riess et al. 2011; Freedman et al. 2012; Riess et al. 2016). The discovery that the K-band PL relation is nearly universal and can be applied to any host galaxy whatever its metallicity (Storm et al. 2011a) is a considerable step forward in the use of Cepheids as distance indicators. Determining the distances to Cepheids relies on the Baade-Wesselink (BW) method, which in turn relies on a correct evaluation of the projection factor p. This is necessary to convert the radial

⋆ Table A.1 is also available at the CDS via anonymous ftp to cdsarc.u-strasbg.fr (130.79.128.5) or via http://cdsarc.u-strasbg.fr/viz-bin/qcat?J/A+A/597/A73

A&A 597, A73 (2017)

Table 1. Non-exhaustive history of the determination of the Baade-Wesselink projection factor in the case of δ Cep.

Method	p	Reference
Geometrical models		
Centroid	1.415	Getting (1934)
Centroid	1.375	van Hoof & Deurinck (1952)
Centroid	1.360	Burki et al. (1982)
Centroid	1.328	Neilson et al. (2012)
Hydrodynamical models		
Bisector	1.34	Sabbey et al. (1995)
Gaussian	1.27 ± 0.01	Nardetto et al. (2004)
cc-g (Pp)	1.25 ± 0.05	Nardetto et al. (2009)
Observations		
cc-g	1.273 ± 0.021 ± 0.050	Mérand et al. (2005)
cc-g	1.245 ± 0.030 ± 0.050	Groenewegen (2007)
cc-g	1.290 ± 0.020 ± 0.050	Merand et al. (2015)
cc-g (Pp)	1.47 ± 0.05	Gieren et al. (2005b)
cc-g (Pp)	1.29 ± 0.06	Laney & Joner (2009)
cc-g (Pp)	1.41 ± 0.05	Storm et al. (2011b)
cc-g (Pp)	1.325 ± 0.03	Groenewegen (2013)

Notes. The method used to derive the radial velocity is indicated, and cc-g corresponds to a Gaussian fit of the cross-correlated line profile. For the values of the projection factor derived from a published period projection factor relation, we consistently use a period of $P = 5.366208$ days (Engle et al. 2014).

velocity variations derived from the spectral line profiles into photospheric pulsation velocities (Nardetto et al. 2004).

The projection factor of δ Cep, the eponym of the Cepheid variables, has been determined by means of different techniques, which we summarize here (see Table 1 and the previous review by Nardetto et al. 2014b):

- Purely geometric considerations lead to the identification of two contributing effects only in the projection factor, i.e., the limb darkening of the star and the motion (expansion or contraction) of the atmosphere. Nardetto et al. (2014b) described this classical approach and its recent variations (e.g., Gray & Stevenson 2007; Hadrava et al. 2009).
- To improve the previous method we should consider that Cepheids do not pulsate in a quasi-hydrostatic way and the dynamical structure of their atmosphere is extremely complex (Sanford 1956; Bell & Rodgers 1964; Karp 1975; Sasselov & Lester 1990; Wallerstein et al. 2015). Therefore, improving the determination of the BW projection factor requires a hydrodynamical model that is able to describe the atmosphere. To date, the projection factor has been studied with two such models: the first is based on a *piston* in which the radial velocity curve is used as an input (Sabbey et al. 1995) and the second is a *self-consistent* model (Nardetto et al. 2004). Sabbey et al. (1995) found a mean value of the projection factor $p = 1.34$ (see also Marengo et al. 2002, 2003). However, this value was derived using the bisector method of the radial velocity determination (applied to the theoretical line profiles). This makes it difficult to compare this value with other studies. As commonly done in the literature, if a Gaussian fit of the cross-correlated line-profile is used to derive the radial velocity RV_{cc-g} ("cc" for cross-correlated and "g" for Gaussian), then the measured projection factor tends to be about 11% smaller than the initial geometrical projection factor is found, i.e., $p = 1.25 \pm 0.05$ (Nardetto et al. 2009).
- As an approach entirely based on observations, Mérand et al. (2005) applied the inverse BW method to infrared interferometric data of δ Cep. The projection factor is then fit, where the distance of δ Cep is known with 4% uncertainty from the HST parallax ($d = 274 \pm 11$ pc; Benedict et al. 2002). They found $p = 1.273 \pm 0.021 \pm 0.050$ using RV_{cc-g} for the radial velocity. The first error is the internal one due to the fitting method. The second is due to the uncertainty of the distance. Groenewegen (2007) found $p = 1.245 \pm 0.030 \pm 0.050$ when using almost the same distance (273 instead of 274 pc), a different radial velocity dataset and a different fitting method of the radial velocity curve. Recently, Merand et al. (2015) applied an integrated inverse method (SPIPS) to δ Cep (by combining interferometry and photometry) and found $p = 1.29 \pm 0.02 \pm 0.05$. These values agree closely with the self-consistent hydrodynamical model. Another slightly different approach is to apply the infrared surface brightness inverse method to distant Cepheids (see Fouque & Gieren 1997; Kervella et al. 2004a, for the principles) in order to derive a period projection factor relation (Pp). In this approach the distance to each LMC Cepheid is assumed to be the same by taking into account the geometry of LMC. This constrains the slope of the Pp relation. However, its zero-point is alternatively fixed using distances to Cepheids in Galactic clusters (Gieren et al. 2005b), HST parallaxes of nearby Cepheids derived by van Leeuwen et al. (2007; Laney & Joner 2009; Storm et al. 2011b), or a combination of both (Groenewegen 2013). Laney & Joner (2009) also used high-amplitude δ Scuti stars to derive their Pp relation (see also Fig. 10 in Nardetto et al. 2014a). The projection factors derived by Laney & Joner (2009) and Groenewegen (2013) are consistent with the interferometric values, while the projection factors from Gieren et al. (2005b) and Storm et al. (2011b) are significantly greater (see Table 1).

– Pilecki et al. (2013) constrained the projection factor using a short-period Cepheid (P = 3.80 d, similar to the period of δ Cep) in a eclipsing binary system. They found $p = 1.21 \pm 0.04$.

This non-exhaustive review shows just how complex the situation regarding the value of the BW projection factor of δ Cep is. This paper is part of the international "Araucaria Project", whose purpose is to provide an improved local calibration of the extragalactic distance scale out to distances of a few megaparsecs (Gieren et al. 2005a). In Sect. 2 we present new High Accuracy Radial velocity Planet Searcher for the Northern hemisphere (HARPS-N) observations. Using these spectra together with the Mérand et al. (2005) data obtained with the Fiber Linked Unit for Optical Recombination (FLUOR, Coudé du Foresto et al. 1997) operating at the focus of the Center for High Angular Resolution Astronomy (CHARA) array (ten Brummelaar et al. 2005) located at the Mount Wilson Observatory (California, USA), we apply the inverse BW method to derive the projection factor associated with the RV_{cc-g} radial velocity and for 17 individual spectral lines (Sect. 3). In Sect. 4, we briefly describe the hydrodynamical model used in Nardetto et al. (2004) and review the projection factor decomposition into three sub-concepts ($p = p_0 f_{grad} f_{o-g}$, Nardetto et al. 2007). In Sect. 4.1, we compare the observational and theoretical projection factors. We then compare the hydrodynamical model with the observed atmospheric velocity gradient (Sect. 4.2) and the angular diameter curve of FLUOR/CHARA (Sect. 4.3). In Sect. 5 we derive the f_{o-g} quantity from the previous sections. We conclude in Sect. 6.

2. HARPS-N spectroscopic observations

HARPS-N is a high-precision radial-velocity spectrograph installed at the Italian Telescopio Nazionale Galileo (TNG), a 3.58-m telescope located at the Roque de los Muchachos Observatory on the island of La Palma, Canary Islands, Spain (Cosentino et al. 2012). HARPS-N is the northern hemisphere counterpart of the similar HARPS instrument installed at the ESO 3.6 m telescope at La Silla Observatory in Chile. The instrument covers the wavelength range from 3800 to 6900 Å with a resolving power of $R \simeq 115\,000$. A total of 103 spectra were secured between 27 March and 6 September 2015 in the framework of the OPTICON proposal 2015B/015 (Table A.1). In order to calculate the pulsation phase of each spectrum, we used P = 5.366208 d (Engle et al. 2014) and T_0 = 2 457 105.930 d, the time corresponding to the maximum approaching velocity determined from the HARPS-N radial velocities. The data are spread over 14 of the 30 pulsation cycles elapsed between the first and last epoch. The final products of the HARPS-N data reduction software (DRS) installed at TNG (on-line mode) are background-subtracted, cosmic-corrected, flat-fielded, and wavelength-calibrated spectra (with and without merging of the spectral orders). We used these spectra to compute the mean-line profiles by means of the least-squares deconvolution (LSD) technique (Donati et al. 1997). As can be seen in Fig. 1, the mean profiles reflect the large-amplitude radial pulsation by distorting the shape in a continuous way.

The DRS also computes the star's radial velocity by fitting a Gaussian function to the cross-correlation functions (CCFs). To do this, the DRS uses a mask including thousands of lines covering the whole HARPS-N spectral ranges. The observer can select the mask among those available online and the G2 mask was the closest to the δ Cep spectral type. As a further step, we re-computed the RV values by using the HARPS-N DRS in the offline mode on the Yabi platform, as in the case of τ Boo (Borsa et al. 2015). We applied both library and custom masks, ranging spectral types from F5 to G2. We obtained RV curves fitted with very similar sets of least-squares parameters showing only some small changes in the mean values. Table A.1 lists the RV_{cc-g} values obtained from the custom F5I mask, also plotted in panel a) of Fig. 2 with different symbols for each pulsation cycle. The RV curve shows a full amplitude of 38.4 km s^{-1} and an average value (i.e., the A_0 value of the fit) of $V_\gamma = -16.95$ km s^{-1}. As a comparison, we calculate the centroid of the mean line profiles RV_{cc-c} ("cc" for cross-correlated and "c" for centroid) and plot the residuals in panel b) of Fig. 2. The RV_{cc-c} curve has an amplitude 1.2 km s^{-1} lower than that of the RV_{cc-g} value. This result is similar to that reported in the case of β Dor (Fig. 2 in Nardetto et al. 2006). The implications of this difference on the projection factor is discussed in Sect. 3.1.

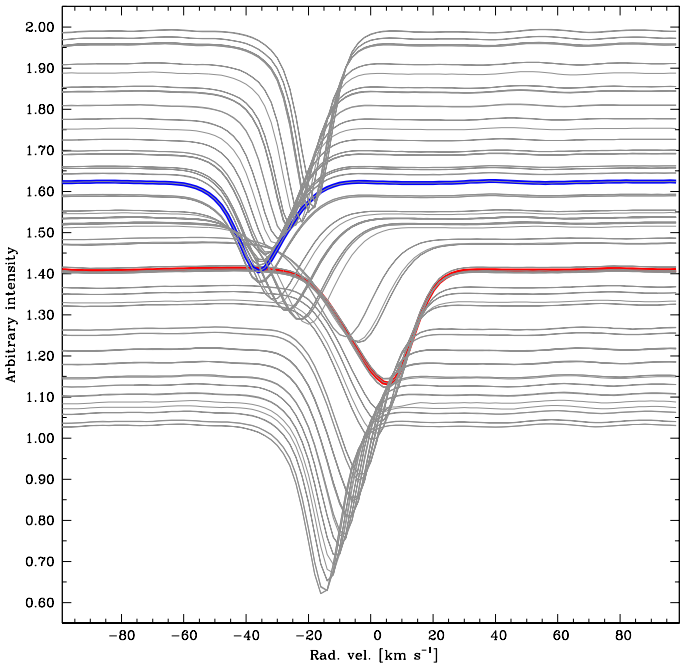


Fig. 1. Mean line profile changes during the pulsation cycle of δ Cep. The line profile with the highest receding motion is highlighted in red, the one with the highest approaching motion in blue.

Consistent with Anderson et al. (2015), we find no evidence for cycle-to-cycle differences in the RV amplitude as exhibited by long-period Cepheids (Anderson 2014; Anderson et al. 2016). We also investigated the possible effect of the binary motion due to the companion (Anderson et al. 2015). Unfortunately, the HARPS-N observations are placed on the slow decline of the RV curve and they only span 160 days. We were able to detect a slow drift of -0.5 ± 0.1 m s^{-1} d^{-1}. The least-squares solution with 14 harmonics leaves a r.m.s. residual of 49 m s^{-1}. Including a linear trend did not significantly reduce the residual since the major source of error probably lies in the fits of the very different shapes of the mean-line profiles along the pulsation cycle (Fig. 1). We also note that surface effects induced by convection and granulation (Neilson & Ignace 2014) could contribute to increasing the residual r.m.s. These effects are also observed in the light curves of Cepheids (Derekas et al. 2012, 2017; Evans et al. 2015; Poretti et al. 2015).

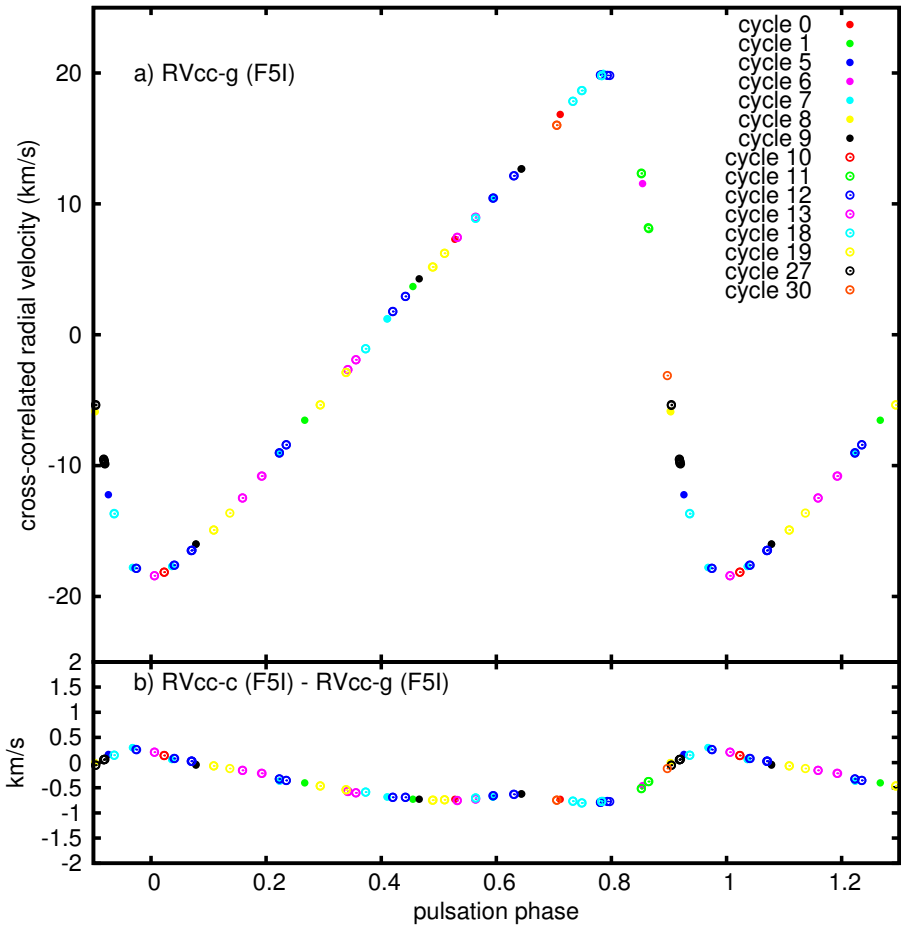


Fig. 2. Panel **a)**: HARPS-N radial velocities associated with the Gaussian fit of the cross-correlated line profile (RV_{cc-g} using F5I template) plotted as a function of the pulsation phase of the star after correction of the γ-velocity (i.e., $V_\gamma = -16.95$ km s^{-1}). The cycle of observations are shown in different colors. The data are reproduced from one cycle to the other. The precision on the measurements is between 0.5 and 1.5 m s^{-1} (error bars are lower than symbols). Panel **b)** residuals between RV_{cc-c} (F5I) and RV_{cc-g} (F5I) after correction of their respective γ-velocities.

3. Inverse Baade-Wesselink projection factors derived from observations

3.1. Using the cross-correlated radial velocity curve

We describe the interferometric version of the BW method as follows. We apply a classical χ^2 minimization

$$\chi^2 = \sum_i \frac{(\theta_{\rm obs}(\phi_i) - \theta_{\rm model}(\phi_i))^2}{\sigma_{\rm obs}(\phi_i)^2}, \quad (1)$$

where

- $\theta_{\rm obs}(\phi_i)$ are the interferometric limb-darkened angular diameters obtained from FLUOR/CHARA observations (Mérand et al. 2005), with ϕ_i the pulsation phase corresponding to the ith measurement (Fig. 3);
- $\sigma_{\rm obs}(\phi_i)$ are the statistical uncertainties corresponding to FLUOR/CHARA measurements;
- $\theta_{\rm model}(\phi_i)$ are the modeled limb-darkened angular diameters, defined as

$$\theta_{\rm model}(\phi_i) = \overline{\theta} + 9.3009\,\frac{p_{\rm cc-g}}{d}\left(\int RV_{\rm cc-g}(\phi_i){\rm d}\phi_i\right)[\rm mas], \quad (2)$$

where the conversion factor 9.3009 is defined using the solar radius given in Prša et al. (2016).

The $RV_{\rm cc-g}(\phi_i)$ is the interpolated HARPS-N cross-correlated radial velocity curve shown in panel a) of Fig. 2. It is obtained using the Gaussian fit, i.e., the most common approach in the literature. The parameters $\overline{\theta}$ and $p_{\rm cc-g}$ are the mean angular diameter of the star (in mas) and the projection factor (associated with the Gaussian fit of the CCFs), respectively, while d is the distance to the star. The quantities $\overline{\theta}$ and $p_{\rm cc-g}$ are fit in order to minimize χ^2, while d is fixed to $d = 272 \pm 3$(stat.) $\pm$ 5(syst.) pc (Majaess et al. 2012).

We find $\overline{\theta} = 1.466 \pm 0.007$ mas and $p_{\rm cc-g} = 1.239 \pm 0.031$, where the uncertainty on the projection factor (hereafter $\sigma_{\rm stat-fluor}$) is about 2.5% and stems from FLUOR/CHARA angular diameter measurements. If we apply this procedure 10 000 times using a Gaussian distribution for the assumed distance that is centered at 272 pc and has a half width at half maximum (HWHM) of 3 pc (corresponding to the statistical precision on the distance of Majaess et al. 2012), then we obtain a symmetric distribution for the 10 000 values of $p_{\rm cc-g}$ with a HWHM $\sigma_{\rm stat-d} = 0.014$. If the distance is set to 277 pc and 267 pc (corresponding to the systematical uncertainty of ±5 pc of Majaess et al. 2012), we find $p = 1.262$ and $p = 1.216$, respectively. We have a systematical uncertainty $\sigma_{\rm syst-d} = 0.023$ for the projection factor. We thus find $p_{\rm cc-g} = 1.239 \pm 0.031$ ($\sigma_{\rm stat-fluor}$) ± 0.014 ($\sigma_{\rm stat-d}$) ± 0.023 ($\sigma_{\rm syst-d}$). These results are illustrated in Fig. 4. Interestingly, if we use the $RV_{\rm cc-c}$ curve in Eq. (2) (still keeping $d = 272$ pc), we obtain $p_{\rm cc-c} = 1.272$ while the uncertainties remain unchanged.

The distance of δ Cep obtained by Majaess et al. (2012) is an average of Hipparcos (van Leeuwen 2007) and HST (Benedict et al. 2002) trigonometric parallaxes, together with the cluster main sequence fitting distance. If we rely on the direct distance to δ Cep obtained only by HST (Benedict et al. 2002), i.e., 273 ± 11 pc, then $\sigma_{\rm stat-d}$ is larger with a value of 0.050 (compared to 0.014 when relying on Majaess et al. 2012). A distance $d = 244 \pm 10$ pc was obtained by Anderson et al. (2015) from

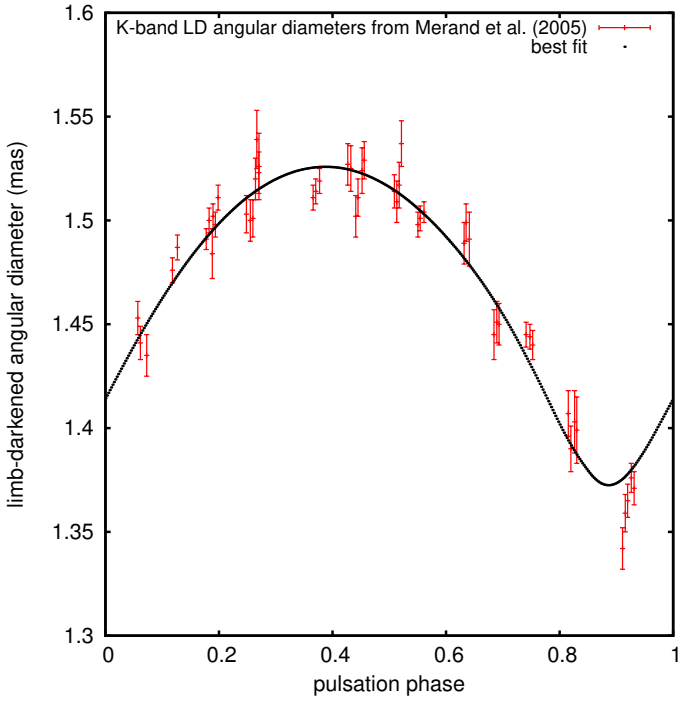


Fig. 3. Inverse BW method applied to FLUOR/CHARA data (Mérand et al. 2005) considering a distance for δ Cep of $d = 272 \pm 3 \pm 5$ pc (Majaess et al. 2012) and the HARPS-N cross-correlated radial velocity curve. The black dotted line corresponds to the best fit.

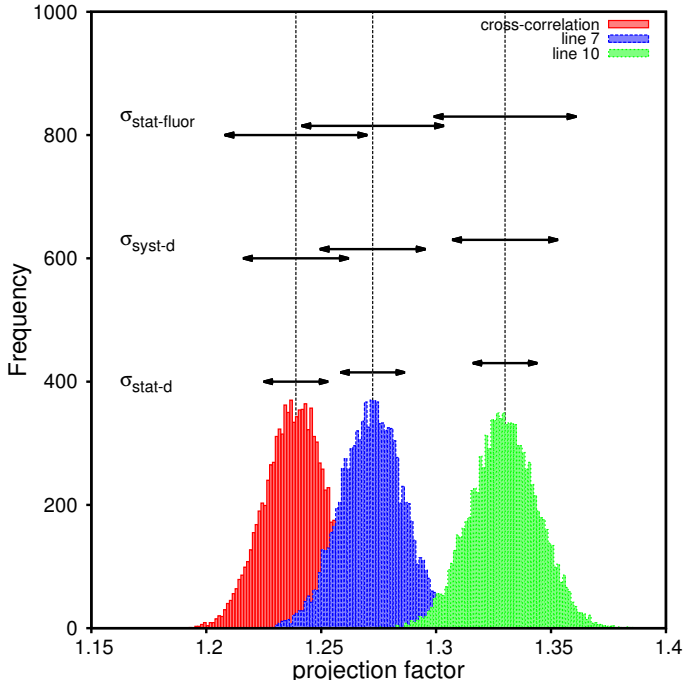


Fig. 4. Inverse BW method described in Sect. 3 applied considering a Gaussian distribution for the distance. The resulting projection factor distributions are shown in three particular cases: when using the cross-correlated radial velocity curve RV_{cc-g} (red), the RV_c radial velocity curve of line 7 (blue), and the RV_c radial velocity curve of line 10 (green). The quantities σ_{stat-d} and σ_{syst-d} are the uncertainties on the projection factor due to the statistical and systematical uncertainties on the distance, respectively. The quantity $\sigma_{stat-fluor}$ stems from the statistical uncertainties on the FLUOR/CHARA interferometric measurements.

Table 2. Spectral lines used this study.

No.	El.	Wavelength (Å)	Ep (eV)	$\log(gf)$
1	Fe I	4683.560	2.831	–2.319
2	Fe I	4896.439	3.883	–2.050
3	Ni I	5082.339	3.658	–0.540
4	Fe I	5367.467	4.415	0.443
5	Fe I	5373.709	4.473	–0.860
6	Fe I	5383.369	4.312	0.645
7	Ti II	5418.751	1.582	–2.110
8	Fe I	5576.089	3.430	–1.000
9	Fe I	5862.353	4.549	–0.058
10	Fe I	6003.012	3.881	–1.120
11	Fe I	6024.058	4.548	–0.120
12	Fe I	6027.051	4.076	–1.089
13	Fe I	6056.005	4.733	–0.460
14	Si I	6155.134	5.619	–0.400
15	Fe I	6252.555	2.404	–1.687
16	Fe I	6265.134	2.176	–2.550
17	Fe I	6336.824	3.686	–0.856

the reanalysis of the HIPPARCOS astrometry of δ Cep. It leads to a very small projection factor $p_{cc-g} = 1.14 \pm 0.031 \pm 0.047$ compared to other values listed in Table 1.

3.2. Using the first moment radial velocity curves corresponding to individual spectral lines

We use the 17 unblended spectral lines (Table 2) that were previously selected for an analysis of eight Cepheids with periods ranging from 4.7 to 42.9 d (Nardetto et al. 2007). These lines remain unblended for every pulsation phase of the Cepheids considered. Moreover, they were carefully selected in order to represent a wide range of depths, hence to measure the atmospheric velocity gradient (Sect. 4.2). For each of these lines, we derive the centroid velocity (RV_c), i.e., the first moment of the spectral line profile, estimated as

$$RV_c = \frac{\int_{line} \lambda S(\lambda) d\lambda}{\int_{line} S(\lambda) d\lambda}, \quad (3)$$

where $S(\lambda)$ is the observed line profile. The radial velocity measurements associated with the spectral lines are presented in Fig. 5a together with the interpolated RV_{cc-g} curve. The RV_c curves plotted have been corrected for the γ-velocity value corresponding to the RV_{cc-g} curve, i.e., $V_\gamma = -16.95$ km s^{-1}. The residuals, i.e., the γ-velocity offsets, between the curves of Fig. 5a are related to the line asymmetry and the k-term value (see Nardetto et al. 2008, for Cepheids; and Nardetto et al. 2013, 2014a, for other types of pulsating stars). This will be analyzed in a forthcoming paper. The final RV_c curves used in the inverse BW approach are corrected from their own residual γ-velocity in such a way that the interpolated curve has an average of zero. The residual of these curves compared to the RV_{cc-g} and RV_{cc-c} curves are shown in panel b and c, respectively. We then apply the same method as in Sect. 3.1. The measured projection factor values $p_{obs}(k)$ associated with each spectral line k are listed in Table 3. The statistical and systematical uncertainties in the

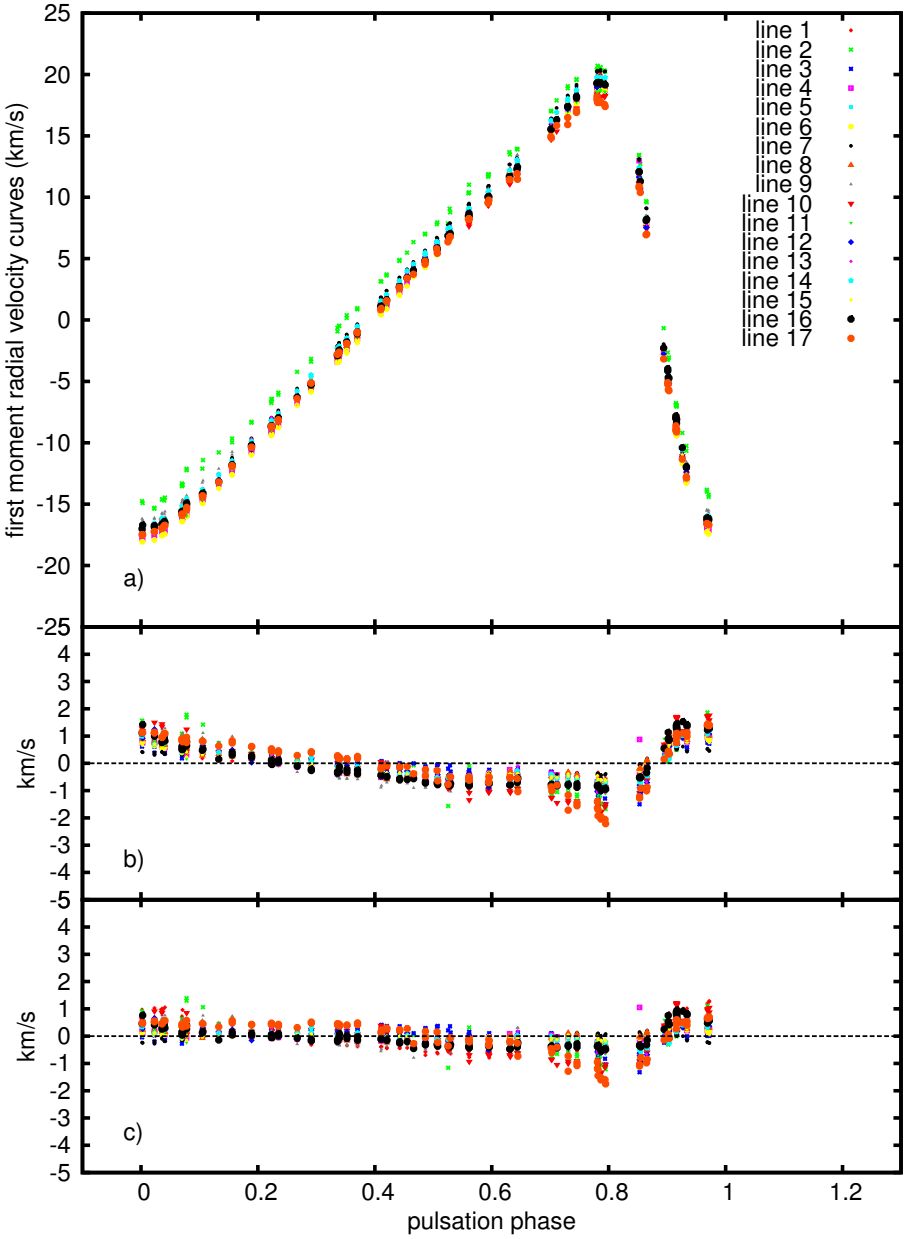


Fig. 5. **a)** First moment radial velocity curves (RV_c) associated with the 17 lines of Table 2. The γ-velocity associated with the cross-correlated radial velocity curve, RV_{cc-g} in Fig. 2a, has been removed from these curves, i.e., $V_\gamma = -16.95$ km s^{-1}. The γ offset residuals are known to be related to the k-term (Nardetto et al. 2008). The residuals between the RV_c curves and the RV_{cc-g} in Fig. 2a (resp. RV_{cc-c}) are plotted in panel **b)** (resp. **c)**) after correcting each RV_c curve from its V_γ value.

case of individual lines are the same as those found when using the RV_{cc-g} curve. The projection factor values range from 1.273 (line 7) to 1.329 (line 10), whereas the value corresponding to the cross-correlation method is 1.239 (see Fig. 4). This shows that the projection factor depends significantly on the method used to derive the radial velocity and the spectral line considered. To analyze these values it is possible to use hydrodynamical simulations and the projection factor decomposition into three terms introduced by Nardetto et al. (2007).

4. Comparing the hydrodynamical model of δ Cep with observations

Our best model of δ Cep was presented in Nardetto et al. (2004) and is computed using the code by Fokin (1991). The hydrodynamical model requires only five input fundamental parameters: $M = 4.8\,M_\odot$, $L = 1995\,L_\odot$, $T_{\rm eff} = 5877$ K, $Y = 0.28$, and $Z = 0.02$. At the limit cycle the pulsation period is 5.419 d, very close (1%) to the observed value.

4.1. Baade-Wesselink projection factors derived from the hydrodynamical model

The projection factors are derived directly from the hydrodynamical code for each spectral line of Table 2 following the definition and procedure described in Nardetto et al. (2007). The computed projection factors range from 1.272 (line 7) to 1.328 (line 2). In Fig. 6 we plot the theoretical projection factors ($p_{\rm hydro}$) as a function of the observational values (listed in Table 3). In this figure the statistical uncertainties on the observational projection factors, i.e., $\sigma_{\rm stat-fluor}$ and $\sigma_{\rm stat-d}$, have been summed quadratically (i.e., $\sigma = 0.034$). The agreement is excellent since the most discrepant lines (10 and 17, in red in the figure) show observational projection factor values only about 1σ larger than the theoretical values.

4.2. Atmospheric velocity gradient of δ Cep

In Nardetto et al. (2007), we split the projection factor into three quantities: $p = p_{\rm o}\, f_{\rm grad}\, f_{\rm o-g}$, where p_0 is the geometrical

Table 3. The observational quantities, D, $p_{\rm obs}$, and $f_{\rm grad}$, are listed for each line of Table 2.

	HARPS-N observations			Hydrodynamical model	
Line	D^a	$p_{\rm obs}\pm\sigma_{\rm fluor-stat}\pm\sigma_{\rm d-stat}\pm\sigma_{\rm d-syst}{}^b$	$f_{\rm grad}{}^c$	$p_{\rm hydro}{}^d$	$p_0{}^e$
Line 1	0.281 ±0.001	1.287 ±0.031±0.014±0.023	0.983 ±0.007	1.307	1.360
Line 2	0.147 ±0.001	1.323 ±0.031±0.014±0.023	0.991 ±0.004	1.328	1.365
Line 3	0.348 ±0.001	1.280 ±0.031±0.014±0.023	0.979 ±0.009	1.304	1.369
Line 4	0.573 ±0.001	1.282 ±0.031±0.014±0.023	0.967 ±0.014	1.292	1.375
Line 5	0.297 ±0.001	1.297 ±0.031±0.014±0.023	0.982 ±0.008	1.309	1.375
Line 6	0.612 ±0.001	1.282 ±0.031±0.014±0.023	0.964 ±0.015	1.288	1.375
Line 7	0.562 ±0.001	1.273 ±0.031±0.014±0.023	0.967 ±0.014	1.272	1.376
Line 8	0.500 ±0.001	1.285 ±0.031±0.014±0.023	0.971 ±0.012	1.297	1.378
Line 9	0.364 ±0.001	1.307 ±0.031±0.014±0.023	0.979 ±0.009	1.302	1.383
Line 10	0.326 ±0.001	1.329 ±0.031±0.014±0.023	0.981 ±0.008	1.301	1.387
Line 11	0.429 ±0.001	1.295 ±0.031±0.014±0.023	0.975 ±0.011	1.304	1.385
Line 12	0.283 ±0.001	1.300 ±0.031±0.014±0.023	0.983 ±0.007	1.312	1.385
Line 13	0.290 ±0.002	1.294 ±0.031±0.014±0.023	0.983 ±0.008	1.304	1.386
Line 14	0.317 ±0.002	1.292 ±0.031±0.014±0.023	0.981 ±0.008	1.310	1.387
Line 15	0.497 ±0.001	1.280 ±0.031±0.014±0.023	0.971 ±0.012	1.290	1.389
Line 16	0.348 ±0.001	1.301 ±0.031±0.014±0.023	0.979 ±0.009	1.301	1.389
Line 17	0.366 ±0.001	1.323 ±0.031±0.014±0.023	0.978 ±0.009	1.297	1.390

Notes. The quantities $p_{\rm hydro}$, p_0 and $f_{\rm o-g}$ are derived from hydrodynamical model. $^{(a)}$ The line depth D is calculated at minimum radius of the star. $^{(b)}$ The observational projection factors $p_{\rm obs}$ is derived from HARPS-N and FLUOR/CHARA interferometric data using the inverse BW approach (Sect. 3.2). $^{(c)}$ The $f_{\rm grad}$ coefficient involved in the projection factor decomposition ($p = p_0 f_{\rm grad} f_{\rm o-g}$, Nardetto et al. 2007) is derived from Eqs. 5 and 6 (Sect. 4.2). $^{(d)}$ The inverse projection factors $p_{\rm hydro}$ is calculated with the hydrodynamical model (Sect. 4.1). $^{(e)}$ The modeled geometric projection factor p_0 is derived in the continuum next to each spectral line. The $f_{\rm o-g}$ quantity, which is obtained using the projection factor decomposition ($f_{\rm o-g} = \frac{p_{\rm obs}}{p_0\, f_{\rm grad}}$), is derived in Sect. 5.

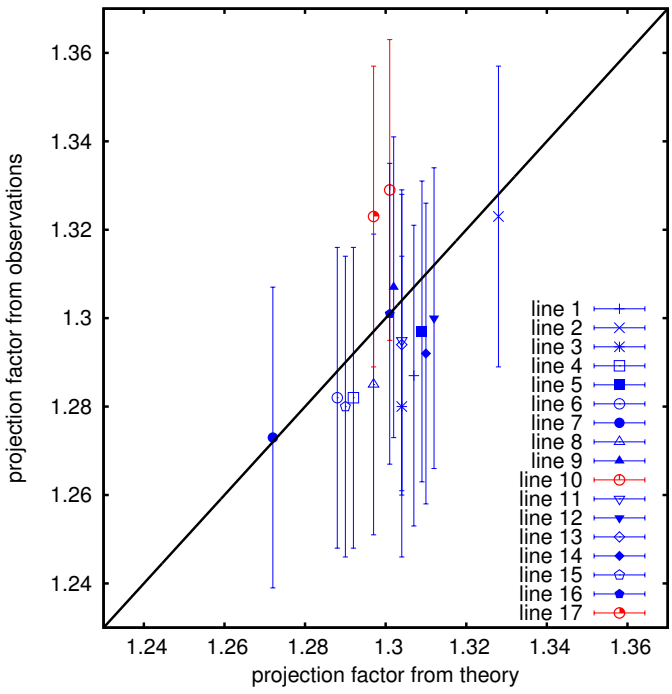


Fig. 6. Observational projection factors derived using the inverse BW approach described in Sect. 3 compared to the theoretical values obtained from the hydrodynamical model (Sect. 4.1).

projection factor (linked to the limb darkening of the star); $f_{\rm grad}$, which is a cycle-integrated quantity linked to the velocity gradient in the atmosphere of the star (i.e., between the considered line-forming region and the photosphere); and $f_{\rm o-g}$, which is the relative motion of the optical pulsating photosphere with respect to the corresponding mass elements.

We derive $f_{\rm grad}$ directly from HARPS-N observations. In Nardetto et al. (2007), we showed that the line depth taken at the minimum radius phase (hereafter D) traces the height of the line-forming regions in such a way that the projection factor decomposition is possible. By comparing $\Delta RV_{\rm c}$ with the depth, D, of the 17 selected spectral lines listed in Table 2, we directly measure $f_{\rm grad}$. If we define a_0 and b_0 as the slope and zero-point of the linear correlation (the photosphere being the zero line depth),

$$\Delta RV_{\rm c} = a_0 D + b_0, \tag{4}$$

then the velocity gradient correction on the projection factor is

$$f_{\rm grad} = \frac{b_0}{a_0 D + b_0}. \tag{5}$$

In Anderson (2016) the atmospheric velocity gradient is defined as the difference between velocities determined using weak and strong lines at each pulsation phase. In our description of the projection factor, $f_{\rm grad}$ is calculated with Eqs. (4) and (5), i.e., considering the amplitude of the radial velocity curves from individual lines. In the following we thus refer to $f_{\rm grad}$ as a cycle integrated quantity.

In Fig. 7 we plot the HARPS-N measurements with blue dots, except for lines 10 and 17 for which we use red squares. These two values are about 2σ below the other measurements, as already noted in Fig. 6. After fitting all measured $\Delta RV_{\rm c}$[obs] with a linear relation we find

$$\Delta RV_{\rm c}[{\rm obs}] = [2.86 \pm 0.84] D + [35.40 \pm 0.36]. \tag{6}$$

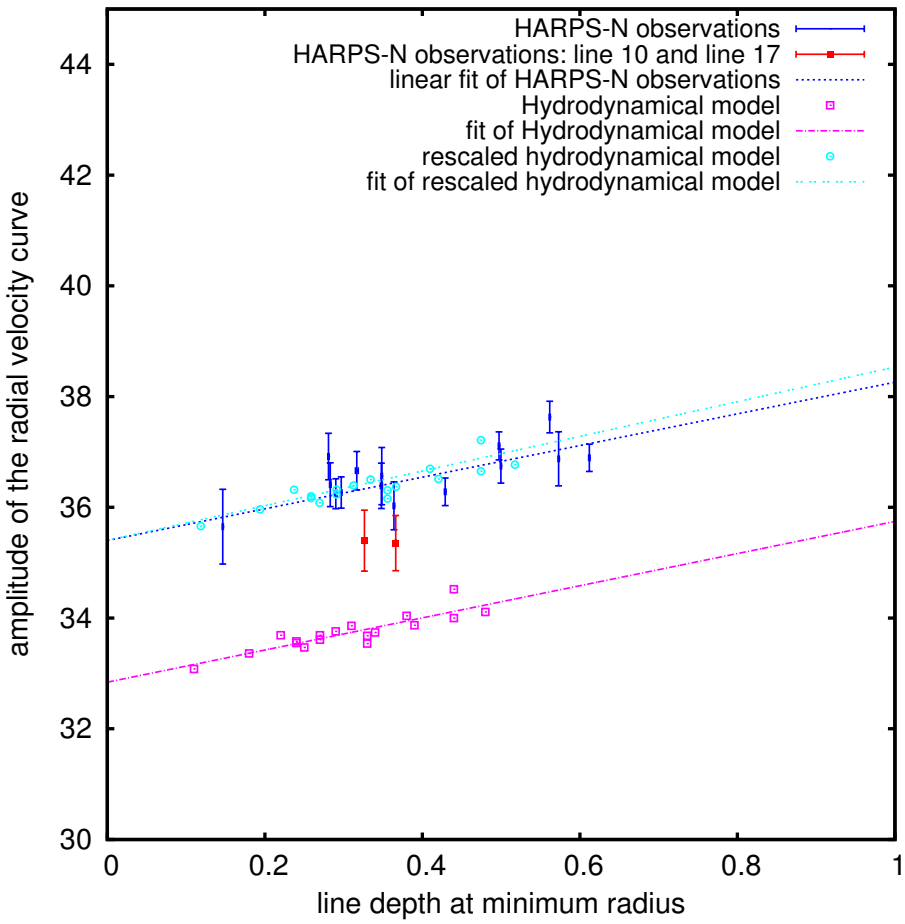


Fig. 7. Amplitude of the radial velocity curves for the 17 spectral lines listed in Table 2 plotted versus the line depth for the hydrodynamical model (magenta squares), and for the HARPS-N spectroscopic observations (blue dots, except lines 10 and 17 plotted with filled red squares). A rescale of the model with a multiplying factor (i.e., f_c) is necessary to fit the data (light blue circles).

The reduced χ^2 is 1.4 and decreases to 1.1 if lines 10 and 17 are not considered (but with approximately the same values of a_0 and b_0). For comparison, the reduced χ^2 is 2.5 if a horizontal line is fitted. The same quantities derived from the hydrodynamical model are shown in Fig. 7 (ΔRV_c[mod], magenta squares). The corresponding relation is

$$\Delta RV_c[\mathrm{mod}] = [2.90 \pm 0.39]D + [32.84 \pm 0.13]. \quad (7)$$

The slopes of Eqs. (6) and (7) are consistent, while the theoretical zero-point is about 2.6 km s^{-1} below the corresponding observational value, which means that the amplitudes of the theoretical radial velocity curves are 2.6 km s^{-1} (or 7.8%) smaller on average. Such disagreement occurs because our code is self-consistent, i.e., the radial velocity curve is not used as an input like in a *piston* code, and because the treatment of convection in the code is missing which can slightly bias (by a few percent) the input fundamental parameters. The two- or three-dimensional models that properly describe the coupling between the pulsation and the convection (Geroux & Deupree 2015; Houdek & Dupret 2015) are currently not providing synthetic profiles, hence preventing the calculation of the projection factor. Therefore, we rely on our purely radiative hydrodynamical code (as previously done in Nardetto et al. 2004, 2007) to study the atmosphere of Cepheids. Its consistency with the spectroscopic and interferometric observables is satisfactory as soon as we consider a multiplying correcting factor of $f_c = 1.078$. Consequently, Eq. (7) becomes

$$\Delta RV_c[\mathrm{mod}] = [2.90D + 32.84] * f_c. \quad (8)$$

The corresponding values are shown in Fig. 7 with light blue squares, and the agreement with observations is now excellent. If the theoretical amplitudes of the radial velocity curves are underestimated, why do we obtain the correct values of the projection factors in Sect. 4.1? The answer is that the projection factor depends only on the ratio of pulsation to radial velocities. If the pulsation velocity curve has an amplitude that is 7.8% larger, then the radial velocity curve (whatever the line considered) and the radius variation (see Sect. 4.3), also have amplitudes that are 7.8% larger and the derived projection factor remains the same.

Small differences in the velocity amplitudes between the RV_{cc-c} and RV_c curves (Fig. 5c) are due to the use of different methods and line samples (a full mask and 17 selected lines, respectively).

4.3. Angular diameter curve

In Fig. 8, we compare our best-fit infrared angular diameters from FLUOR/CHARA (same curve as Fig. 3) with the photospheric angular diameters derived directly from the model assuming a distance of $d = 272$ pc (Majaess et al. 2012). Following the projection factor decomposition, this photospheric angular diameter is calculated by integrating the pulsation velocity associated with the photosphere of the star. We consider this to be the layer of the star for which the optical depth in the continuum (in the vicinity of the Fe I 6003.012 Å spectral line) is $\tau_c = \frac{2}{3}$. However, to superimpose the computed photospheric angular diameter curve on the interferometric one, we again need a correction factor f_c. We find that the rescaled model (magenta open squares) is consistent with the solid line, which corresponds to the integration of the HARPS-N RV_{cc-g} curve (multiplied consistently by p_{cc-g}).

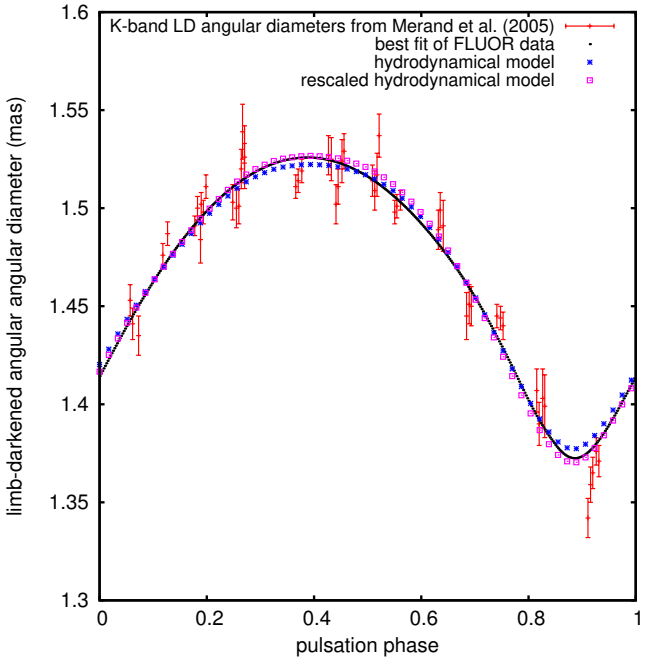


Fig. 8. FLUOR/CHARA limb-darkened angular diameter curve compared to the hydrodynamical model (see the text).

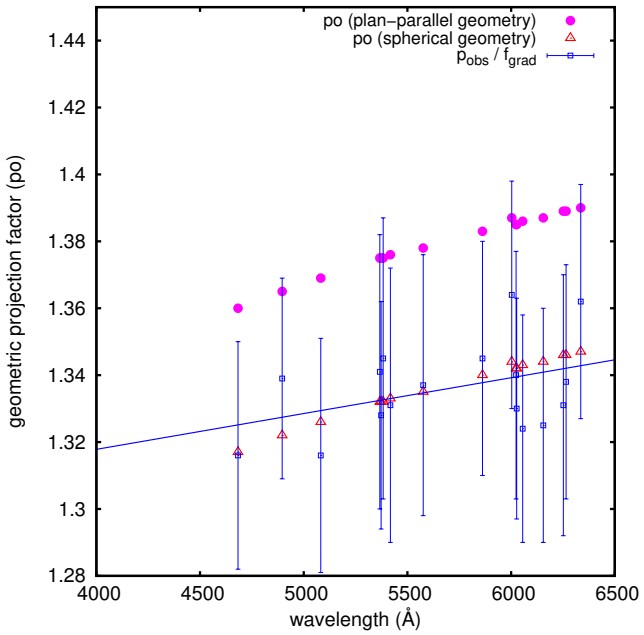


Fig. 9. Geometric projection factors calculated using radiative transfer in plane-parallel and in spherical geometry used together with the observational quantity $\frac{p_{\rm obs}}{f_{\rm grad}}$ in order to derive $f_{\rm o-g}$ (see Sect. 5).

We rescaled the outputs of the hydrodynamical code, i.e., the atmospheric velocity gradient (Sect. 4.2), the radial velocity, and the angular diameter curves, by the same quantity $f_{\rm c}$ in order to reproduce the observations satisfactorily. This scaling leaves the hydrodynamical projection factors unchanged and in agreement with the observational values (Table 2). This can be seen using Eq. (2): if we multiply each part of this equation by $f_{\rm c}$, the result in terms of the projection factor is unchanged.

5. Determining $f_{\rm o\text{-}g}$

The variable $f_{\rm o-g}$ is linked to the distinction between the *optical* and *gas* photospheric layers. The *optical* layer is the location where the continuum is generated ($\tau_{\rm c} = \frac{2}{3}$). The *gas* layer is the location of some mass element in the hydrodynamic model mesh where, at some moment in time, the photosphere is located. Given that the location of the photosphere moves through different mass elements as the star pulsates, the two layers have different velocities, hence it is necessary to define $f_{\rm o-g}$ in the projection factor decomposition. The $f_{\rm o-g}$ quantity is independent of the spectral line considered and is given by

$$f_{\rm o-g} = \frac{p_{\rm obs}(k)}{p_{\rm o}(k)\, f_{\rm grad}(k)}, \qquad (9)$$

where k indicates the spectral line considered. From the previous sections, we now have the ability to derive $f_{\rm o-g}$. In Sect. 3, we derived the projection factors $p_{\rm obs}(k)$ for 17 individual lines. In Sect. 4.2, we determined $f_{\rm grad}(k) = \frac{b_0}{a_0 D_k + b_0}$ using Eq. (5) (see Table 3). The last quantity required to derive $f_{\rm o-g}$ is the geometric projection factor $p_{\rm o}$ (see Eq. (9)). There is currently no direct estimation of $p_{\rm o}$ for δ Cep. If we rely on the hydrodynamical model, $p_{\rm o}$ can be inferred from the intensity distribution next to the continuum of each spectral line. The list of geometric projection factors are listed in Table 3 and plotted in Fig. 9 with magenta dots. These calculations are done in the plane-parallel radiative transfer approximation. On the other hand, Neilson et al. (2012) showed that the p-factor differs significantly as a function of geometry where those from plane-parallel model atmospheres are 3−7% greater then those derived from spherically symmetric models. Using their Table 1, we find for δ Cep a spherically symmetric geometrical projection factor of 1.342 in the R-band (i.e., with an effective wavelength of 6000 Å). In Fig. 9, if we shift our results (magenta dots) by 0.043 in order to get 1.342 at 6000 Å (a decrease of 3.2%), we roughly estimate the geometrical projection factors in spherical geometry as a function of the wavelength (red open triangles). In Fig. 9, we now plot the $\frac{p_{\rm obs}(k)}{f_{\rm grad}(k)}$ quantity for each individual spectral line with their corresponding uncertainties (blue open squares). If we divide the $\frac{p_{\rm obs}(k)}{f_{\rm grad}(k)}$ quantities obtained for each individual spectral line by the corresponding value of $p_{\rm o}(k)$ calculated in plane-parallel geometry, we obtain $f_{\rm o-g} = 0.975 \pm 0.002$, with a reduced χ^2 of 0.13. This indicates that our uncertainties (the quadratic sum of $\sigma_{\rm stat-fluor}$, $\sigma_{\rm stat-d}$ and the statistical uncertainty on $f_{\rm grad}$) are probably overestimated. This value is several σ greater than that found directly with the hydrodynamical model of δ Cep: $f_{\rm o-g} = 0.963 \pm 0.005$ (Nardetto et al. 2007, their Table 5). Using the values of $p_{\rm o}$ from Neilson et al. (2012) (blue open triangles), we obtain $f_{\rm o-g} = 1.006 \pm 0.002$. Thus, $f_{\rm o-g}$ depends significantly on the model used to calculate $p_{\rm o}$.

6. Conclusion

Our rescaled hydrodynamical model of δ Cep is consistent with both spectroscopic and interferometric data modulo a rescaling factor that depends on the input parameters of the model $(M, L, T_{\rm eff}, Z)$. In particular, it reproduces the observed amplitudes of the radial velocity curves associated with a selection of 17 unblended spectral lines as a function of the line depth in a very satisfactory way. This is a critical step for deriving the correct value of the projection factor. This strongly suggests that our decomposition of the projection factor into three physical terms is adequate. The next difficult step will be to measure p_0

directly from the next generation of visible-wavelength interferometers. With such values in hand, it will be possible to derive f_{o-g} directly from observations.

The projection factor is a complex quantity that is particularly sensitive to the definition of the radial velocity measurement. More details should be given and perhaps a standard procedure applied in future analyses. For instance, the CCFs are generally fitted with a Gaussian. This produces a velocity value sensitive to stellar rotation and to both the line width and depth (Nardetto et al. 2006). Thus, additional biases in the distance determination are introduced, in particular when comparing the projection factors of different Cepheids. Conversely, investigating the projection factor of individual lines is useful for learning how to mitigate the impact of the radial velocity modulation (Anderson 2014) and the possible angular-diameter modulation (Anderson et al. 2016) on the BW distances.

In this study, we found $p_{cc-g} = 1.24 \pm 0.04$ a value that is consistent with the *Pp* relation of Nardetto et al. (2009), i.e., $p_{cc-g} = 1.25 \pm 0.05$. However, a disagreement is still found between the interferometric and the infrared surface-brightness approaches (and their respective projection factors) in the case of δ Cep (Ngeow et al. 2012), while an agreement is found for the long-period Cepheid ℓ Car (Kervella et al. 2004b). This suggests that the *p*-factors adopted in these approaches might be affected by something not directly related to the projection factor itself but rather to other effects in the atmosphere or close to it, such as a static circumstellar environment (Nardetto et al. 2016). However, it is worth mentioning that the two methods currently provide *absolutely the same results in terms of distances*. After a long history (since Getting 1934), the BW projection factor remains a key quantity in the calibration of the cosmic distance scale, and one century after the discovery of the Period-Luminosity relation (Leavitt 1908), Cepheid pulsation is still a distinct challenge. With Gaia and other high-quality spectroscopic data, it will soon be possible to better constrain the *Pp* relation.

Acknowledgements. The observations leading to these results have received funding from the European Commission's Seventh Framework Programme (FP7/2013−2016) under grant agreement No. 312430 (OPTICON). The authors thank the GAPS observers F. Borsa, L. Di Fabrizio, R. Fares, A. Fiorenzano, P. Giacobbe, J. Maldonado, and G. Scandariato. The authors thank the CHARA Array, which is funded by the National Science Foundation through NSF grants AST-0606958 and AST-0908253 and by Georgia State University through the College of Arts and Sciences, as well as the W. M. Keck Foundation. This research has made use of the SIMBAD and VIZIER Available at `http://cdsweb.u-strasbg.fr/` databases at CDS, Strasbourg (France), and of the electronic bibliography maintained by the NASA/ADS system. W.G. gratefully acknowledges financial support for this work from the BASAL Centro de Astrofisica y Tecnologias Afines (CATA) PFB-06/2007, and from the Millenium Institute of Astrophysics (MAS) of the Iniciativa Cientifica Milenio del Ministerio de Economia, Fomento y Turismo de Chile, project IC120009. We acknowledge financial support for this work from ECOS-CONICYT grant C13U01. Support from the Polish National Science Center grant MAESTRO 2012/06/A/ST9/00269 is also acknowledged. E.P. and M.R. acknowledge financial support from PRIN INAF-2014. N.N., P.K., A.G., and W.G. acknowledge the support of the French-Chilean exchange program ECOS- Sud/CONICYT (C13U01). The authors acknowledge the support of the French Agence Nationale de la Recherche (ANR), under grant ANR-15-CE31-0012- 01 (project UnlockCepheids) and the financial support from "Programme National de Physique Stellaire" (PNPS) of CNRS/INSU, France.

References

Anderson, R. I. 2014, A&A, 566, L10
Anderson, R. I. 2016, MNRAS, 463, 1707
Anderson, R. I., Sahlmann, J., Holl, B., et al. 2015, ApJ, 804, 144
Anderson, R. I., Mérand, A., Kervella, P., et al. 2016, MNRAS, 455, 4231
Bell, R. A., & Rodgers, A. W. 1964, MNRAS, 128, 365
Benedict, G. F., McArthur, B. E., Fredrick, L. W., et al. 2002, AJ, 124, 1695
Borsa, F., Scandariato, G., Rainer, M., et al. 2015, A&A, 578, A64
Burki, G., Mayor, M., & Benz, W. 1982, A&A, 109, 258
Cosentino, R., Lovis, C., Pepe, F., et al. 2012, in SPIE Conf. Ser., 8446, 1
Coudé du Foresto, V., Ridgway, S., & Mariotti, J.-M. 1997, A&AS, 121, 379
Derekas, A., Szabó, G. M., Berdnikov, L., et al. 2012, MNRAS, 425, 1312
Derekas, A., Plachy, E., Molnar, L., et al. 2017, MNRAS, 464, 1553
Donati, J.-F., Semel, M., Carter, B. D., Rees, D. E., & Collier Cameron, A. 1997, MNRAS, 291, 658
Engle, S. G., Guinan, E. F., Harper, G. M., Neilson, H. R., & Remage Evans, N. 2014, ApJ, 794, 80
Evans, N. R., Szabó, R., Derekas, A., et al. 2015, MNRAS, 446, 4008
Fokin, A. B. 1991, MNRAS, 250, 258
Fouque, P., & Gieren, W. P. 1997, A&A, 320, 799
Freedman, W. L., Madore, B. F., Scowcroft, V., et al. 2012, ApJ, 758, 24
Geroux, C. M., & Deupree, R. G. 2015, ApJ, 800, 35
Getting, I. A. 1934, MNRAS, 95, 139
Gieren, W., Pietrzynski, G., Bresolin, F., et al. 2005a, The Messenger, 121, 23
Gieren, W., Storm, J., Barnes, III, T. G., et al. 2005b, ApJ, 627, 224
Gray, D. F., & Stevenson, K. B. 2007, PASP, 119, 398
Groenewegen, M. A. T. 2007, A&A, 474, 975
Groenewegen, M. A. T. 2013, A&A, 550, A70
Hadrava, P., Šlechta, M., & Škoda, P. 2009, A&A, 507, 397
Hertzsprung, E. 1913, Astron. Nachr., 196, 201
Houdek, G., & Dupret, M.-A. 2015, Liv. Rev. Sol. Phys., 12, 8
Karp, A. H. 1975, ApJ, 201, 641
Kervella, P., Bersier, D., Mourard, D., Nardetto, N., & Coudé du Foresto, V. 2004a, A&A, 423, 327
Kervella, P., Fouqué, P., Storm, J., et al. 2004b, ApJ, 604, L113
Laney, C. D., & Joner, M. D. 2009, in AIP Conf. Ser. 1170, eds. J. A. Guzik, & P. A. Bradley, 93
Leavitt, H. S. 1908, Annals of Harvard College Observatory, 60, 87
Leavitt, H. S., & Pickering, E. C. 1912, Harvard College Observatory Circular, 173, 1
Majaess, D., Turner, D., & Gieren, W. 2012, ApJ, 747, 145
Marengo, M., Sasselov, D. D., Karovska, M., Papaliolios, C., & Armstrong, J. T. 2002, ApJ, 567, 1131
Marengo, M., Karovska, M., Sasselov, D. D., et al. 2003, ApJ, 589, 968
Merand, A., Kervella, P., Breitfelder, J., et al. 2015, A&A, 584, A80
Mérand, A., Kervella, P., Coudé du Foresto, V., et al. 2005, A&A, 438, L9
Nardetto, N., Fokin, A., Mourard, D., et al. 2004, A&A, 428, 131
Nardetto, N., Mourard, D., Kervella, P., et al. 2006, A&A, 453, 309
Nardetto, N., Mourard, D., Mathias, P., Fokin, A., & Gillet, D. 2007, A&A, 471, 661
Nardetto, N., Stoekl, A., Bersier, D., & Barnes, T. G. 2008, A&A, 489, 1255
Nardetto, N., Gieren, W., Kervella, P., et al. 2009, A&A, 502, 951
Nardetto, N., Mathias, P., Fokin, A., et al. 2013, A&A, 553, A112
Nardetto, N., Poretti, E., Rainer, M., et al. 2014a, A&A, 561, A151
Nardetto, N., Storm, J., Gieren, W., Pietrzyński, G., & Poretti, E. 2014b, in Precision Asteroseismology, eds. J. A. Guzik, W. J. Chaplin, G. Handler, & A. Pigulski, IAU Symp., 301, 145
Nardetto, N., Mérand, A., Mourard, D., et al. 2016, A&A, 593, A45
Neilson, H. R., & Ignace, R. 2014, A&A, 563, L4
Neilson, H. R., Nardetto, N., Ngeow, C.-C., Fouqué, P., & Storm, J. 2012, A&A, 541, A134
Ngeow, C.-C., Neilson, H. R., Nardetto, N., & Marengo, M. 2012, A&A, 543, A55
Pilecki, B., Graczyk, D., Pietrzyński, G., et al. 2013, MNRAS, 436, 953
Poretti, E., Le Borgne, J. F., Rainer, M., et al. 2015, MNRAS, 454, 849
Prša, A., Harmanec, P., Torres, G., et al. 2016, AJ, 152, 41
Riess, A. G., Macri, L., Casertano, S., et al. 2011, ApJ, 730, 119
Riess, A. G., Macri, L. M., Hoffmann, S. L., et al. 2016, ApJ, 826, 56
Sabbey, C. N., Sasselov, D. D., Fieldus, M. S., et al. 1995, ApJ, 446, 250
Sanford, R. F. 1956, ApJ, 123, 201
Sasselov, D. D., & Lester, J. B. 1990, ApJ, 362, 333
Storm, J., Gieren, W., Fouqué, P., et al. 2011a, A&A, 534, A94
Storm, J., Gieren, W., Fouqué, P., et al. 2011b, A&A, 534, A95
ten Brummelaar, T. A., McAlister, H. A., Ridgway, S. T., et al. 2005, ApJ, 628, 453
van Hoof, A., & Deurinck, R. 1952, ApJ, 115, 166
van Leeuwen, F. 2007, Astrophys. Space Sci. Libr., 350
van Leeuwen, F., Feast, M. W., Whitelock, P. A., & Laney, C. D. 2007, MNRAS, 379, 723
Wallerstein, G., Albright, M. B., & Ritchey, A. M. 2015, PASP, 127, 503

Appendix A: Additional table

Table A.1. HARPS-N spectroscopic data of δ Cep.

BJD	ϕ	RV_{cc-g}	$\sigma_{RV_{cc-g}}$	BJD	ϕ	RV_{cc-g}	$\sigma_{RV_{cc-g}}$
2 457 108.765	0.53	–9.6505	0.0004	2 457 174.601	0.80	2.8618	0.0009
2 457 109.760	0.71	–0.1170	0.0005	2 457 175.553	0.97	–34.7911	0.0010
2 457 112.747	0.27	–23.4763	0.0003	2 457 175.554	0.97	–34.8038	0.0009
2 457 113.753	0.46	–13.2657	0.0003	2 457 175.721	0.01	–35.3598	0.0008
2 457 137.747	0.93	–29.1695	0.0016	2 457 175.722	0.01	–35.3590	0.0008
2 457 142.728	0.85	–5.3965	0.0012	2 457 176.545	0.16	–29.4283	0.0008
2 457 143.703	0.04	–34.6591	0.0008	2 457 176.546	0.16	–29.4176	0.0008
2 457 143.704	0.04	–34.6507	0.0007	2 457 176.723	0.19	–27.7502	0.0006
2 457 144.709	0.22	–25.9233	0.0006	2 457 176.724	0.19	–27.7408	0.0006
2 457 144.710	0.22	–25.9144	0.0006	2 457 177.526	0.34	–19.6200	0.0007
2 457 145.712	0.41	–15.7395	0.0003	2 457 177.527	0.34	–19.6091	0.0007
2 457 145.714	0.41	–15.7263	0.0003	2 457 177.598	0.36	–18.8642	0.0005
2 457 146.695	0.59	–6.5524	0.0007	2 457 177.599	0.36	–18.8540	0.0006
2 457 146.696	0.59	–6.5400	0.0007	2 457 178.543	0.53	–9.5137	0.0007
2 457 147.726	0.79	3.0172	0.0012	2 457 178.544	0.53	–9.5015	0.0008
2 457 147.727	0.79	3.0182	0.0012	2 457 178.718	0.56	–7.9788	0.0011
2 457 148.704	0.97	–34.7264	0.0007	2 457 178.720	0.56	–7.9717	0.0020
2 457 148.705	0.97	–34.7357	0.0008	2 457 204.523	0.37	–18.0216	0.0005
2 457 153.719	0.90	–22.7805	0.0016	2 457 204.524	0.37	–18.0121	0.0005
2 457 153.720	0.90	–22.8391	0.0017	2 457 205.547	0.56	–8.0510	0.0007
2 457 154.659	0.08	–32.9507	0.0028	2 457 205.548	0.56	–8.0441	0.0007
2 457 154.661	0.08	–32.9407	0.0027	2 457 206.455	0.73	0.8814	0.0008
2 457 156.745	0.47	–12.6738	0.0016	2 457 206.457	0.73	0.8987	0.0007
2 457 157.695	0.64	–4.2804	0.0025	2 457 206.538	0.75	1.7037	0.0009
2 457 157.697	0.64	–4.2640	0.0023	2 457 206.539	0.75	1.7139	0.0009
2 457 159.734	0.02	–35.0911	0.0010	2 457 206.723	0.78	2.8518	0.0013
2 457 159.735	0.02	–35.0878	0.0010	2 457 206.724	0.78	2.8540	0.0015
2 457 169.546	0.85	–4.5949	0.0012	2 457 207.546	0.94	–30.6013	0.0009
2 457 169.547	0.85	–4.6461	0.0013	2 457 207.547	0.94	–30.6337	0.0009
2 457 169.614	0.86	–8.7664	0.0012	2 457 208.471	0.11	–31.8710	0.0010
2 457 169.615	0.87	–8.8388	0.0014	2 457 208.472	0.11	–31.8670	0.0010
2 457 170.558	0.04	–34.5581	0.0010	2 457 208.621	0.14	–30.5734	0.0011
2 457 170.559	0.04	–34.5525	0.0009	2 457 209.466	0.29	–22.3141	0.0008
2 457 170.718	0.07	–33.4392	0.0011	2 457 209.467	0.29	–22.3028	0.0010
2 457 170.719	0.07	–33.4328	0.0011	2 457 209.708	0.34	–19.8308	0.0006
2 457 170.721	0.07	–33.4184	0.0009	2 457 209.709	0.34	–19.8196	0.0006
2 457 170.721	0.07	–33.4142	0.0008	2 457 210.515	0.49	–11.7732	0.0009
2 457 171.536	0.22	–25.9946	0.0010	2 457 210.515	0.49	–11.7647	0.0009
2 457 171.540	0.22	–25.9575	0.0009	2 457 210.623	0.51	–10.7254	0.0008
2 457 171.600	0.24	–25.3673	0.0006	2 457 210.624	0.51	–10.7162	0.0008
2 457 171.602	0.24	–25.3431	0.0006	2 457 255.670	0.90	–22.2876	0.0014
2 457 172.596	0.42	–15.1771	0.0005	2 457 255.671	0.90	–22.3447	0.0013
2 457 172.598	0.42	–15.1607	0.0005	2 457 255.745	0.92	–26.4495	0.0010
2 457 172.712	0.44	–14.0256	0.0005	2 457 255.746	0.92	–26.5002	0.0009
2 457 172.713	0.44	–14.0132	0.0005	2 457 255.748	0.92	–26.6127	0.0010
2 457 173.530	0.59	–6.5085	0.0010	2 457 255.749	0.92	–26.6636	0.0010
2 457 173.532	0.60	–6.4944	0.0010	2 457 255.751	0.92	–26.7676	0.0010
2 457 173.725	0.63	–4.8069	0.0007	2 457 255.752	0.92	–26.8161	0.0010
2 457 173.726	0.63	–4.7941	0.0007	2 457 270.699	0.70	–0.9438	0.0008
2 457 174.531	0.78	2.8942	0.0013	2 457 270.700	0.71	–0.9308	0.0008
2 457 174.535	0.78	2.8976	0.0014	2 457 271.731	0.90	–20.0635	0.0007
2 457 174.597	0.79	2.8737	0.0008				
Days		$km\,s^{-1}$	$km\,s^{-1}$	days		$km\,s^{-1}$	$km\,s^{-1}$

Annexe N

High-resolution spectroscopy for Cepheids distance determination. III. A relation between γ-velocities and γ-asymmetries

A&A 489, 1255–1262 (2008)
DOI: 10.1051/0004-6361:200809587
© ESO 2008

Astronomy & Astrophysics

High-resolution spectroscopy for Cepheids distance determination⋆,⋆⋆

III. A relation between γ-velocities and γ-asymmetries

N. Nardetto[1], A. Stoekl[2], D. Bersier[3], and T. G. Barnes[4,5]

[1] Max-Planck-Institut für Radioastronomie, Auf dem Hügel 69, 53121 Bonn, Germany
e-mail: nardetto@mpifr-bonn.mpg.de
[2] CRAL, Université de Lyon, CNRS (UMR5574), École Normale Supérieure de Lyon, 69007 Lyon, France
[3] Astrophysics Research Institute, Liverpool John Moores University, Twelve Quays House, Egerton Wharf, Birkenhead, CH41 1LD, UK
[4] University of Texas at Austin, McDonald Observatory, 1 University Station, C1402, Austin, TX 78712-0259, USA
[5] currently on assignment to the National Science Foundation, 4201 Wilson Boulevard, Arlington, VA 22230, USA

Received 15 February 2008 / Accepted 1 April 2008

ABSTRACT

Context. Galactic Cepheids in the vicinity of the Sun have a residual line-of-sight velocity, or γ-velocity, which shows a systematic blueshift of about 2 km s^{-1} compared to an axisymmetric rotation model of the Milky Way. This term is either related to the space motion of the star and, consequently, to the kinematic structure of our Galaxy, or it is the result of the dynamical structure of the Cepheids' atmosphere.
Aims. We aim to show that these residual γ-velocities are an intrinsic property of Cepheids.
Methods. We observed eight galactic Cepheids with the HARPS⋆⋆⋆ spectroscope, focusing specifically on 17 spectral lines. For each spectral line of each star, we computed the γ-velocity (resp. γ-asymmetry) as an average value of the interpolated radial velocity (resp. line asymmetry) curve.
Results. For each Cepheid in our sample, a linear relation is found between the γ-velocities of the various spectral lines and their corresponding γ-asymmetries, showing that residual γ-velocities stem from the intrinsic properties of Cepheids. We also provide a physical reference to the stellar γ-velocity: it should be zero when the γ-asymmetry is zero. Following this definition, we provide very precise and physically calibrated estimates of the γ-velocities for all stars of our sample [in km s^{-1}]: -11.3 ± 0.3 [R TrA], -3.5 ± 0.4 [S Cru], -1.5 ± 0.2 [Y Sgr], 9.8 ± 0.1 [β Dor], 7.1 ± 0.1 [ζ Gem], 24.6 ± 0.4 [RZ Vel], 4.4 ± 0.1 [ℓ Car], 25.7 ± 0.2 [RS Pup]. Finally, we investigated several physical explanations for these γ-asymmetries like velocity gradients or the relative motion of the line-forming region compared to the corresponding mass elements. However, none of these hypotheses seems to be entirely satisfactory to explain the observations.
Conclusions. To understand this very subtle γ-asymmetry effect, further numerical studies are needed. Cepheids' atmosphere are strongly affected by pulsational dynamics, convective flows, nonlinear physics, and complex radiative transport. Hence, all of these effects have to be incorporated simultaneously and consistently into the numerical models to reproduce the observed line profiles in detail.

Key words. techniques: spectroscopic – stars: atmospheres – stars: oscillations – stars: variables: Cepheids – stars: distances

1. Introduction

Cepheids are very important astrophysical objects due to their well-known period-luminosity (*PL*) relation. Based on this relation, a multi-decade work allowed us to determine the kinematic structure of the Milky Way (in particular its rotation) and to reach cosmologically significant extragalactic distances (see Hubble Space Telescope Key Project, Freedman et al. 2001). In the second paper of this series, Nardetto et al. (2007) (hereafter Paper II) established a clear link between the distance scale and the dynamical structure of Cepheids' atmosphere through a period-projection factor (*Pp*) relation. Similarly, studies concerning the kinematics of the Milky Way might be closely related to the dynamical structure of Cepheids' atmosphere.

Concerning the distance scale, near-infrared interferometry currently provides a new, quasi-geometrical way to determine the distance of galactic Cepheids up to 1 kpc (see e.g. Sasselov & Karovska 1994; and Kervella et al. 2004). The basic principle of the Interferometric Baade-Wesselink method (IBW) is to compare the linear and angular size *variation* of a pulsating star in order to derive its distance through a simple division. The key point is that interferometric measurements *in the continuum* lead to angular diameters corresponding to the *photospheric* layer, while the linear stellar radius variation is deduced by spectroscopy, i.e., based on line-forming regions which form higher in the atmosphere. Thus, radial velocities $V_{\rm rad}$, which are derived from line profiles, include the integration in two directions: over the stellar surface through limb-darkening and over

⋆ Based on observations made with ESO telescopes at the Silla Paranal Observatory under programme IDs 072.D-0419 and 073.D-0136.
⋆⋆ Table 2 is only available in electronic form at http://www.aanda.org
⋆⋆⋆ High Accuracy Radial velocity Planetary Search project developed by the European Southern Observatory.

the atmospheric layers through velocity gradients. All these phenomena are currently merged in one specific quantity, generally considered constant with time: the projection factor p, defined as $V_{\rm puls} = pV_{\rm rad}$, where $V_{\rm puls}$ is defined as the *photospheric* pulsation velocity (Nardetto et al. 2004). $V_{\rm puls}$ is then integrated with time to derive the photospheric radius variation. The precision in the distance currently obtained with the IBW method is a few percent. However, it remains strongly dependent on the projection factor. If a constant projection factor is used (generally $p = 1.36$ for all stars) to derive the *PL* relation, errors of 0.10 and 0.03 on the slope and zero-point of the *PL* relation can be introduced. This means that distances can be overestimated by 10% for long-period Cepheids (Paper II).

In Paper II, we divide the projection factor into three subtopics: (1) a geometrical effect related to the limb-darkening; (2) the velocity gradient within the atmosphere; and (3) the differential motion of the "optical" pulsating photosphere compared to the corresponding mass elements, called $f_{\rm o-g}$. Even if the *Pp* relation was recently confirmed by HST observations (Fouqué et al. 2007), the $f_{\rm o-g}$ is relatively uncertain and currently entirely based on hydrodynamical calculations. Nevertheless, a key point is that this quantity should be, in principle, related to the so-called γ-velocity term. As Sabbey et al. (1995) noted, the changing depth of the spectral line-forming region over a Cepheid pulsation cycle leads to unequal *extrema* in the line asymmetry curve. Such phenomenon was also observed in the first paper of this series (Nardetto et al. 2006, hereafter Paper I). Spectral lines are thus not associated with the same gas particles during the pulsation cycle. Formally, they do not comply with path conservation, stated as

$$\int V_{\rm rad} {\rm d}\phi = 0$$

where the integral is over a whole cycle. Path conservation is, however, a fundamental assumption in the BW method (Gautschy 1987).

The state of the art of the BW methods, concerning the γ-velocity is the following: the γ-velocity is generally removed, i.e. the average value of the radial velocity curve is forced to zero before integrating. However, the differential motion between the line-forming region and the gas also modifies the velocity amplitude. The $f_{\rm o-g}$ was introduced, based on hydrodynamical models in Paper II, in order to correct this velocity amplitude effect. The next step is to find a correlation between $f_{\rm o-g}$ and the γ-velocity. In this paper, we will provide some indications, but the problem remains unsolved.

The γ-velocities are also of great importance for the determination of the kinematic structure of the Milky Way. Galactic Cepheids in the solar vicinity show a residual line-of-sight velocity (a "K-term") in their radial velocities which is systematically blueshifted of about 2 km s^{-1} compared to an axisymmetric rotation model of the Milky Way (Camm 1938, 1944; Parenago 1945; Stibbs 1956; Wielen 1974; Caldwell & Coulson 1987; Moffett & Barnes 1987; Wilson et al. 1991; Pont et al. 1994). Wielen (1974) found no correlation of the K-term with any obvious parameter such as period, amplitude or distance, and concluded that the K-term is an intrinsic property of Cepheid atmospheres. On the other hand, Pont et al. (1994) tried to revive Camm (1944) and Parenago's (1945) suggestion that the K-term is due to a real effect in the dynamics of the Galaxy. In addition, Butler et al. (1996) found a γ-velocity reduced by 2 km s^{-1} by introducing velocity gradients in hydrostatic stellar atmospheres models. The K-term problem is still a matter of debate today.

Based on very high quality HARPS observations and careful methodology (Sect. 2), we will show that γ-velocities are due to intrinsic properties of Cepheids (Sect. 3). Finally, we discuss our results in Sect. 4.

2. HARPS observations

Ten stars have been observed with the HARPS spectrometer ($R = 120\,000$): R Tra, S Cru, Y Sgr, β Dor, ζ Gem, Y Oph, RZ Vel, ℓ Car, RS Pup and X Sgr. X Sgr is an atypical Cepheid presenting several components in the spectral line profiles. It was studied separately by Mathias et al. (2006). Y Oph is not studied here in detail due to its insufficient phase coverage (see Paper II, Fig. 3). We thus consider 8 Cepheids in this paper.

Using Kurucz models 1992 we have identified about 150 unblended spectral lines. In Paper II, we carefully selected 17 spectral lines following two criteria: (1) the continuum must to be perfectly defined for all pulsation phases of all stars, in order to avoid bias in the determination of the line depth; (2) the selected sample of lines has to cover a large range of depth. The spectral lines selected are presented in Table 1 of Paper II.

As in Paper I, we use bi-Gaussian fits to derive line asymmetries. We repeat here the main equations in order to show that there is no a priori link between the line asymmetry and our *centroid* method of the radial velocity determination. The centroid radial velocity ($RV_{\rm c}$), or the first moment of the spectral line profile, has been estimated as

$$RV_{\rm c} = \frac{\int_{\rm line} \lambda S(\lambda) {\rm d}\lambda}{\int_{\rm line} S(\lambda) {\rm d}\lambda} \quad (1)$$

where $S(\lambda)$ is the *observed* line profile. Then, the radial velocity corresponding to the minimum pixel, full width at half-maximum (*FWHM*), and asymmetry are derived simultaneously by applying a classical χ^2 minimization algorithm between the observed line profile ($S(\lambda)$) and a modeled spectral line profile ($f(\lambda)$). The corresponding reduced χ^2 is

$${\chi_{\rm red}}^2 = \frac{1}{N-\nu} \sum_{i=0}^{N} \frac{(S(\lambda_i) - f(\lambda_i))^2}{\sigma(\lambda_i)^2} \quad (2)$$

with N being the number of pixels in the spectral line, ν the number of degrees of freedom and $\sigma(\lambda_i) = SNR * f(\lambda_i)$ the statistical uncertainty associated to each pixel. *SNR* is the estimate of the signal-to-noise Ratio in the continuum.

The analytic line profile is defined by

$$f(\lambda) = 1 - D \exp\left(\frac{4 \ln 2 (\lambda - \lambda_{\rm m})^2}{(FWHM(1+A))^2} \right) \text{ if } \lambda > \lambda_{\rm m} \quad (3)$$

and

$$f(\lambda) = 1 - D \exp\left(\frac{4 \ln 2 (\lambda - \lambda_{\rm m})^2}{(FWHM(1-A))^2} \right) \text{ if } \lambda < \lambda_{\rm m} \quad (4)$$

with four free parameters: D, the depth of the line (dimensionless); $\lambda_{\rm m}$, the wavelength associated to the minimum of the line (in Å); *FWHM*, the Full-Width at Half-Maximum in the line (in Å); and A, the line asymmetry relative to the *FWHM* (in %). Online tables (Nardetto et al. 2007) present the resulting values of $RV_{\rm m}$, $RV_{\rm c}$, *FWHM*, D, A, *SNR*, and $\chi^2_{\rm red}$ together with the corresponding uncertainties computed from the fitting method. In the following, we will only use $RV_{\rm c}$ and A, which are clearly *independent* given the manner of their determinations.

Table 1. Linear relations between the γ-velocities and the γ-asymmetries $V_\gamma = a_0 A_\gamma + b_0$ for all stars. The last column corresponds to the final physically calibrated γ-velocities for each star (see Sect. 3.1 for details). The subscripts give the 1σ uncertainty.

Name	HD	P^a [days]	a_0 [km s^{-1}/%]	$\chi^2_{\rm red}$	$V_{\gamma \rm GCD}$ [km s^{-1}]	Correction b_0 [km s^{-1}]	$V_{\gamma\star}$ [km s^{-1}]
R TrA	135592	3.38925	$-0.13_{\pm 0.05}$	3	−13.2	$1.9_{\pm 0.3}$	$-11.3_{\pm 0.3}$
S Cru	112044	4.68976	$-0.16_{\pm 0.07}$	2	−7.1	$3.6_{\pm 0.4}$	$-3.5_{\pm 0.4}$
Y Sgr	168608	5.77338	$-0.19_{\pm 0.04}$	14	−2.5	$1.0_{\pm 0.2}$	$-1.5_{\pm 0.2}$
β Dor	37350	9.84262	$-0.16_{\pm 0.02}$	30	7.4	$2.4_{\pm 0.1}$	$9.8_{\pm 0.1}$
ζ Gem	52973	10.14960	$-0.11_{\pm 0.02}$	22	6.9	$0.2_{\pm 0.1}$	$7.1_{\pm 0.1}$
RZ Vel	73502	20.40020	$-0.14_{\pm 0.09}$	1	24.1	$0.5_{\pm 0.4}$	$24.6_{\pm 0.4}$
ℓ Car	84810	35.55134	$-0.15_{\pm 0.03}$	15	3.6	$0.8_{\pm 0.1}$	$4.4_{\pm 0.1}$
RS Pup	68860	41.51500	$-0.13_{\pm 0.05}$	4	22.1	$3.6_{\pm 0.2}$	$25.7_{\pm 0.2}$

[a] The corresponding Julian dates (T_o) can be found in Paper II.

We insist on the RV_c definition of the radial velocity since it is absolutely required to allow direct comparisons between γ-velocities of different spectral lines from different Cepheids. Indeed, it is the *only* method which provides a radial velocity independent of the rotation (projected on the line of sight) and the natural width of the spectral line (Burki et al. 1982, and Paper I).

The RV_c and A quantities for 17 selected spectral lines for each of the 8 stars have been interpolated over the pulsation phase using a periodic cubic spline function. The interpolation is performed either directly on the observational points (e.g. β Dor) or using arbitrary pivot points (e.g. RZ Vel). In the latter case, a classical minimization process between the observations and the interpolated curve is used to optimize the position of the pivot points. All interpolated curves presented in this study were derived using one of these two methods. Finally, A_γ and V_γ are calculated by *averaging* the $A(\phi)$ and $RV_c(\phi)$ interpolated curves, where ϕ is the pulsation phase. The corresponding uncertainties are defined as the average values of individual uncertainties on the observational points.

3. A relation between γ-velocities and γ-asymmetries

The aim of this section is to study the γ-velocities and to show that they consist of two components: one related to the space motion of the star itself, and one (the K-term) related to the dynamical structure of Cepheids' atmosphere.

3.1. Methodology presented in the case of β Dor

To introduce our methodology we discuss the exemplary case of β Dor in detail.

First, interpolated radial velocity curves derived from all spectral lines were corrected by the γ-velocity found in the Galactic Cepheid Database of the David Dunlap Observatory[1] (Fernie et al. 1995, hereafter $V_{\gamma \rm GCD}$, see Table 1).

Figure 1 shows the spectral line profile of two metallic lines Fe 4896.4 ($D \simeq 8\%$ of the continuum) and Fe 6024.1 ($D \simeq 30\%$) as a function of the pulsation phase. We translated wavelengths into velocities for comparison. We used spectral lines with different line depths for clarity, but the results are actually *independent* of the line depth. Two qualitative key-points concerning Fig. 1 should be mentioned: (1) the Fe 4896.4 spectral line (smaller line depth) seems to be systematically redshifted compared to the Fe 6024.1 spectral line (look, for instance, at the pixel minimum of each profile) and (2) its asymmetry is also systematically larger (in absolute value) from phase $\phi = 0.82$ to $\phi = 0.23$, while it is systematically lower (in absolute value) from phase $\phi = 0.33$ to $\phi = 0.61$. This leads us to the idea of a correlation between the γ-velocity and the γ-asymmetry. In Figs. 2a,b we present the corresponding interpolated radial velocity and asymmetry curves for these two spectral lines. Another line of intermediate depth is also presented (Fe 5373, solid line). From the interpolated curves, we now calculate the γ-velocities and -asymmetries corresponding to each spectral line (horizontal lines). An anti-correlation is clearly seen.

In Fig. 2c, $RV_c - A$ plots and the corresponding (A_γ, V_γ) average values (crosses) for the three different lines are presented. Although the $RV_c - A$ plots have different shapes (and this is confirmed for all spectral lines), which is the result of the dynamical structure of the Cepheid atmosphere, the average values (big crosses) are aligned, confirming the correlation found in Figs. 2a,b.

Figure 2d is a generalization of diagram (c) for all spectral lines. The $RV_c - A$ curves are not included for clarity. Upper values correspond to residual γ-velocities $V_\gamma(i)$ of the 17 selected spectral lines i after the GCD γ-velocity correction. A linear fit is performed, and we find the relation

$$V_\gamma(i) - V_{\gamma \rm GCD} = a_0 A_\gamma(i) + b_0,$$

with $a_0 = -0.16 \pm 0.02$ [km s^{-1} per %] and $b_0 = 2.4 \pm 0.1$ [km s^{-1}]. The origin of the plot is taken as a reference: the γ-velocity is assumed to be zero when the γ-asymmetry is zero. This means that all points

$$(A_\gamma(i), V_\gamma(i) - V_{\gamma \rm GCD})$$

are translated into

$$(A_\gamma(i), V_\gamma(i) - (V_{\gamma \rm GCD} + b_0))$$

which allows the definition of a physically calibrated γ-velocity for β Dor

$$V_{\gamma\star} = V_{\gamma \rm GCD} + b_0 = 7.4 + 2.4 = 9.8_{\pm 0.1} \text{ km s}^{-1}.$$

This quantity is very precise due to the very high S/N and spectral resolution of HARPS data.

In principle, the line asymmetry and the γ-asymmetry are supposed to be the result of the dynamical structure of the Cepheid atmosphere *only*. The $V_\gamma(i)A_\gamma(i)$ (hereafter $V_\gamma A_\gamma$) correlation found is then a strong indication that residual γ-velocities (after correction by the GCD γ-velocities) are related to intrinsic physical properties of Cepheids' atmosphere and not to a real effect in dynamics of the Galaxy (see discussion).

[1] http://www.astro.utoronto.ca/DDO/research/cepheids/

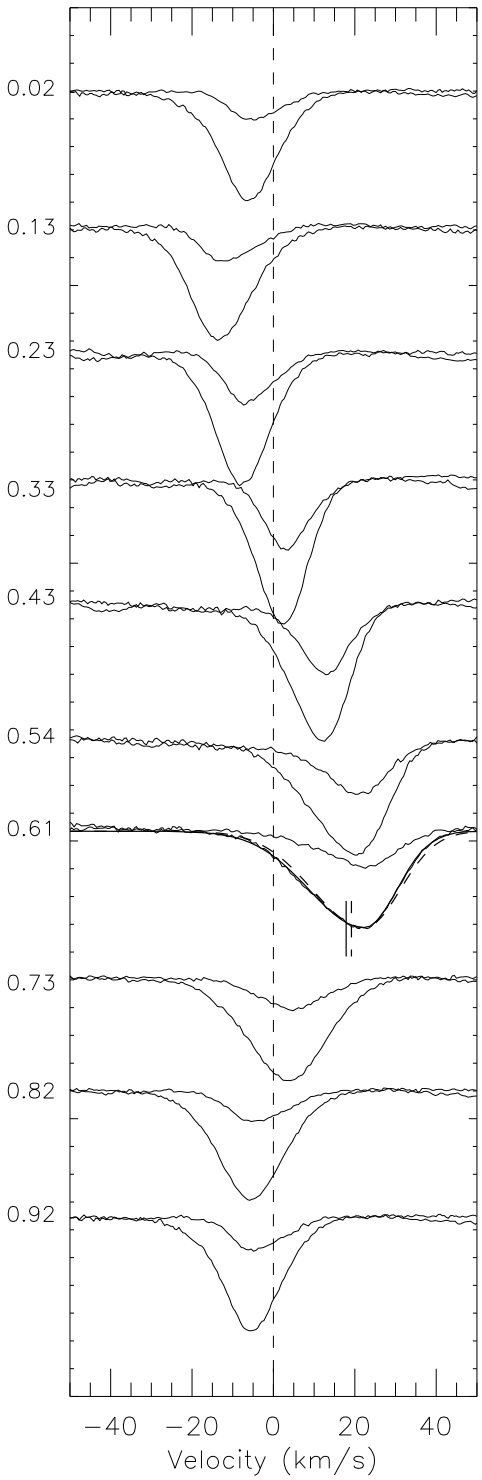


Fig. 1. Fe 4896.4 ($D \simeq 8\%$) and Fe 6024.1 ($D \simeq 30\%$) spectral lines evolution of β Dor. Pulsation phases are given on the left of each profile. Wavelengths have been translated into velocities for comparison (positive velocities correspond to a redshift, motion toward us). The systematic difference in lines asymmetries and velocities is clear. The solid and dashed lines at $\phi = 0.61$ show that modifying artificially the line asymmetry induces a change in the resulting centroid velocity (see Sect. 4).

3.2. $V_\gamma A_\gamma$ linear curves of all stars of our sample

V_γ and A_γ were derived for all spectral lines and for all stars of our sample using the same method as presented in the case of β Dor.

Table 1 gives $V_{\gamma\mathrm{GCD}}$, the slope a_0 of the interpolated $V_\gamma A_\gamma$ curves, the correction b_0 applied, and our final γ-velocities $V_{\gamma\star}$ for each star. The *reduced* χ^2, defined as $\chi^2_{\mathrm{red}} = \frac{\chi^2}{N-\nu}$ with N being the number of spectral lines and ν the number of degrees of freedom, is also indicated. The $V_\gamma A_\gamma$ plots are shown in Fig. 3. Linear correlation curves between V_γ and A_γ are found for all stars of our sample, and our b_0 corrections range from 0.2 to 3.6 km s^{-1}. The average value is 1.8 ± 0.2 km s^{-1}, which is consistent with the 2 km s^{-1} "K-term" found in the literature. We discuss these important observational results in the next section.

4. Discussion

4.1. γ-velocities

The linear relation between A_γ and V_γ can be easily understood. The basic principle is demonstrated in Fig. 1 for the pulsation phase $\phi = 0.61$. For clarity, we only present the argument for one pulsation phase.

The solid line is the bi-Gaussian fit of the Fe 6024.1 spectral line. Artificially decreasing the bi-Gaussian asymmetry of this spectral line by the *average* asymmetry of the Fe 6024.1 line, $A_\gamma = 7.58\%$, as shown in Fig. 1 with a dashed-line, we find that the centroid-velocity increases (i.e. is redshifted) by an amount of +1.45 km s^{-1}. To illustrate this, we included in Fig. 1 the computed line positions RV_c by vertical lines before (solid line) and after (dot-dashed line) modification of the bi-Gaussian asymmetry. Generally, we find that forcing the average line asymmetry A_γ to zero by uniformly changing the line asymmetry *by the same amount* at all phases alters the derived centroid velocities RV_c in such a way that the resulting γ-velocity becomes zero. For instance, the point ($A_\gamma = 7.58\%$, $V_\gamma = 1.45$ km s^{-1}) of the $V_\gamma A_\gamma$ linear curve of β Dor (Fig. 3) translates into ($A_\gamma = 0\%$, $V_\gamma = 0$ km s^{-1}).

This result is obtained universally, regardless which spectral line or star is considered. Basically, we can conclude that the γ-velocities are a side-effect of the line asymmetries and related to the problem of determining line positions of asymmetric lines. This view is also supported by the high conformity of the slopes a_0 of the $V_\gamma A_\gamma$ relation for all sample stars (see Table 1) which (almost) agree within 1σ uncertainties.

Although this method of arbitrarily modifying the line asymmetry is a rather ad hoc method, it still allowed us to gain some insight into the origin of the γ-velocities. In particular, it shows (1) that the residual γ-velocities are related to the shapes of the spectral lines and, consequently, to an intrinsic property of Cepheids; and (2) that the main physical question is not to understand the γ-velocities, but to understand the γ-asymmetries.

Another important point is that this interpretation provides a physical meaning to the γ-velocities and, hence, a physical *reference*. The relation between γ-asymmetry and γ-velocity allows us to compute the contribution of the dynamical Cepheid's atmosphere to the γ-velocity. We can thus really provide a γ-velocity corresponding to the space motion of the star itself ($V_{\gamma\star}$), independently of the dynamical structure of its atmosphere. From Table 1, we find an *average* systematic red-shift correction of $b_0 = 1.8 \pm 0.2$ km s^{-1} (averaged over 8 stars) between our physically calibrated γ-velocities and the ones found in the GCD, commonly used by the community. Consequently, the K-term (blueshifted) found in the literature is not due to the kinematic structure of the Galaxy, but to a bias in the previous methods of deriving the γ-velocities (cross-correlation, Gaussian fit of the spectral line), most likely due to these $A_\gamma V_\gamma$ linear relations. By using only one metallic line to derive the γ-velocity, one can

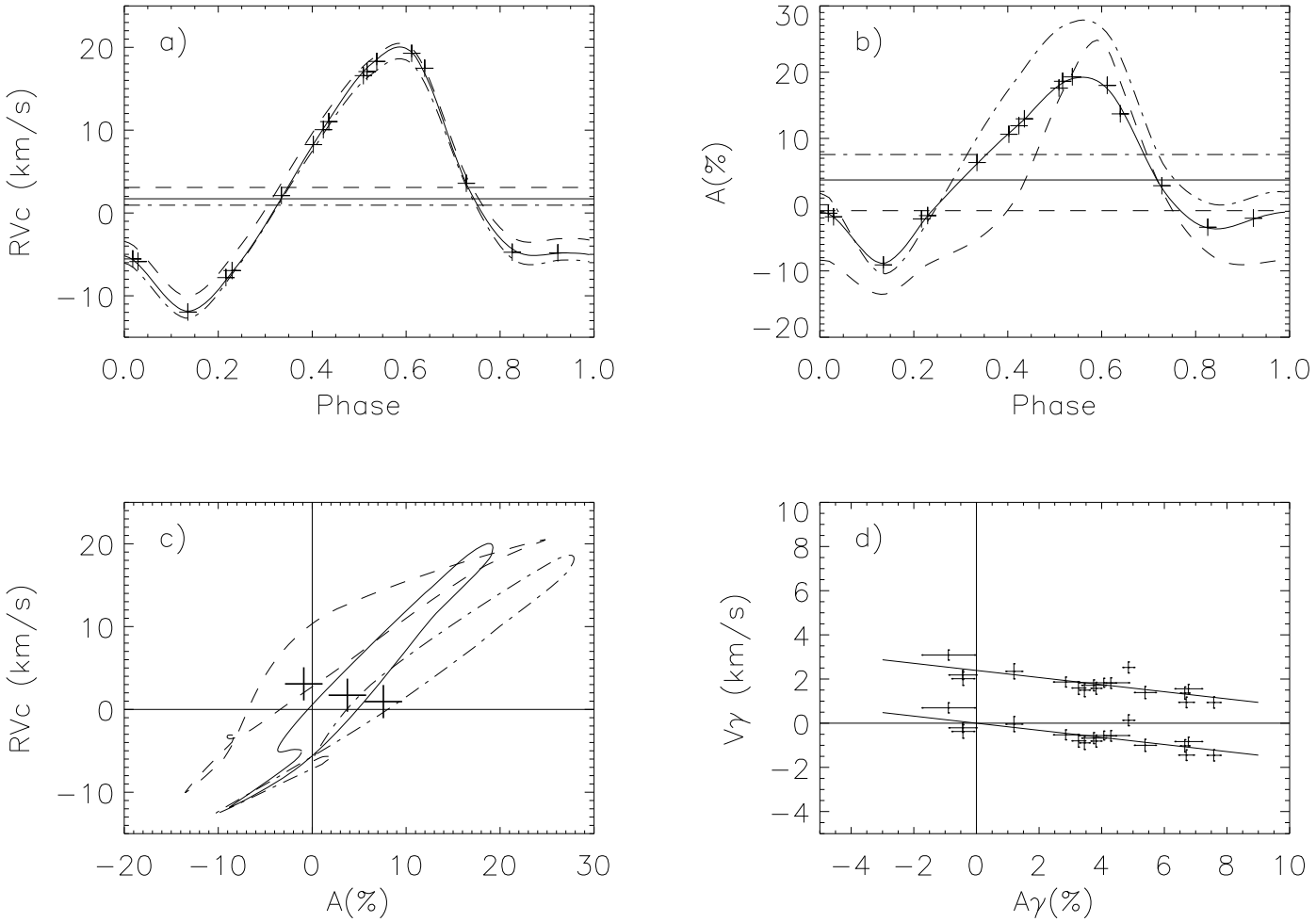


Fig. 2. RV_c **a)** and A **b)** are represented as a function of the pulsation phase for three spectral lines in the case of β Dor: Fe 4896.4 (dashed line), Fe 5373.7 (solid line), and Fe 6024.1 (dot-dashed line). The RV_c curves include only the GCD γ-velocity correction. The actual measurements (crosses) are only indicated in the case of the Fe 5373.7 line. The corresponding uncertainties are too small to be visible in the plot. Horizontal lines correspond to the average values V_γ and A_γ of the interpolated curves, respectively. **c)** $RV_c - A$ plots and the corresponding (A_γ, V_γ) average values (crosses) for the three different lines. Although the $RV_c - A$ plots have different shapes, the average values are aligned. (d) Generalization of diagram **c)** for all spectral lines. The $RV_c - A$ plots are not included for clarity. The upper values are without any correction except the GCD γ-velocity. The origin of the plot is then used as a physical reference for all spectral line γ-velocities of the star (lower values). The $V_\gamma A_\gamma$ correlation found is a strong indication that γ-velocities are related to intrinsic physical properties of Cepheids' atmospheres.

make, for instance, an error (or find inconsistencies) ranging from –2 to +1 km s^{-1}. Finally, our results are thus consistent with an axisymmetric rotation model of the Milky Way.

4.2. γ-asymmetries

Different aspects of the γ-asymmetries must be pointed out.

- The γ-asymmetries are different from one spectral line to the other. This was the motivation for our $A_\gamma V_\gamma$ relations. Moreover, A_γ can be positive or negative;
- given the precision of our data, we find no particular link between the line depth (i.e. where the line forms within the atmosphere, see Paper II) and the γ-asymmetries. Moreover, no relation was found between the γ-asymmetries and the wavelength;
- in order to investigate phase shifts, which might be related to the γ-asymmetries, we integrate radial velocities over time (after correcting by the corresponding $V_\gamma(i)$) and obtain the radius as a function of the pulsation phase for different spectral lines. Such phase shifts are observed clearly *only* for R TrA and RS Pup (see Fig. 4);
- one can see in Fig. 2b that the difference in asymmetry between the Fe 6024.8 Å (dot-dashed line) and Fe 4896.4 Å (dashed line) asymmetry curves is surprisingly almost *constant* with the pulsation phase. Even it is not a general rule (see solid line of Fig. 2b), this effect is frequent in our data, and seems to be important to understand the meaning of the γ-asymmetries;
- although the $A(\phi)$ and $RV_c(\phi)$ curves vary in phase, there is no *strict* correlation between the line asymmetry $A(\phi)$ and the radial velocity $RV_c(\phi)$ as a function of the pulsation phase ϕ (see Fig. 2c). The slope and shape of the $RV_c - A$ curves depend on the limb-darkening, the spectral line width, and the rotation velocity. However, the loop and the shift in asymmetry (γ-asymmetry) are mainly due to the dynamical structure of the Cepheid atmosphere. They cannot be explained by *static* geometrical models of pulsating stars (see Paper I for details);
- in the stellar rest frame (defined by $V_{\gamma\star}$), one has for a given spectral line and at a specific pulsation phase ϕ, $RV_c(\phi) = 0$

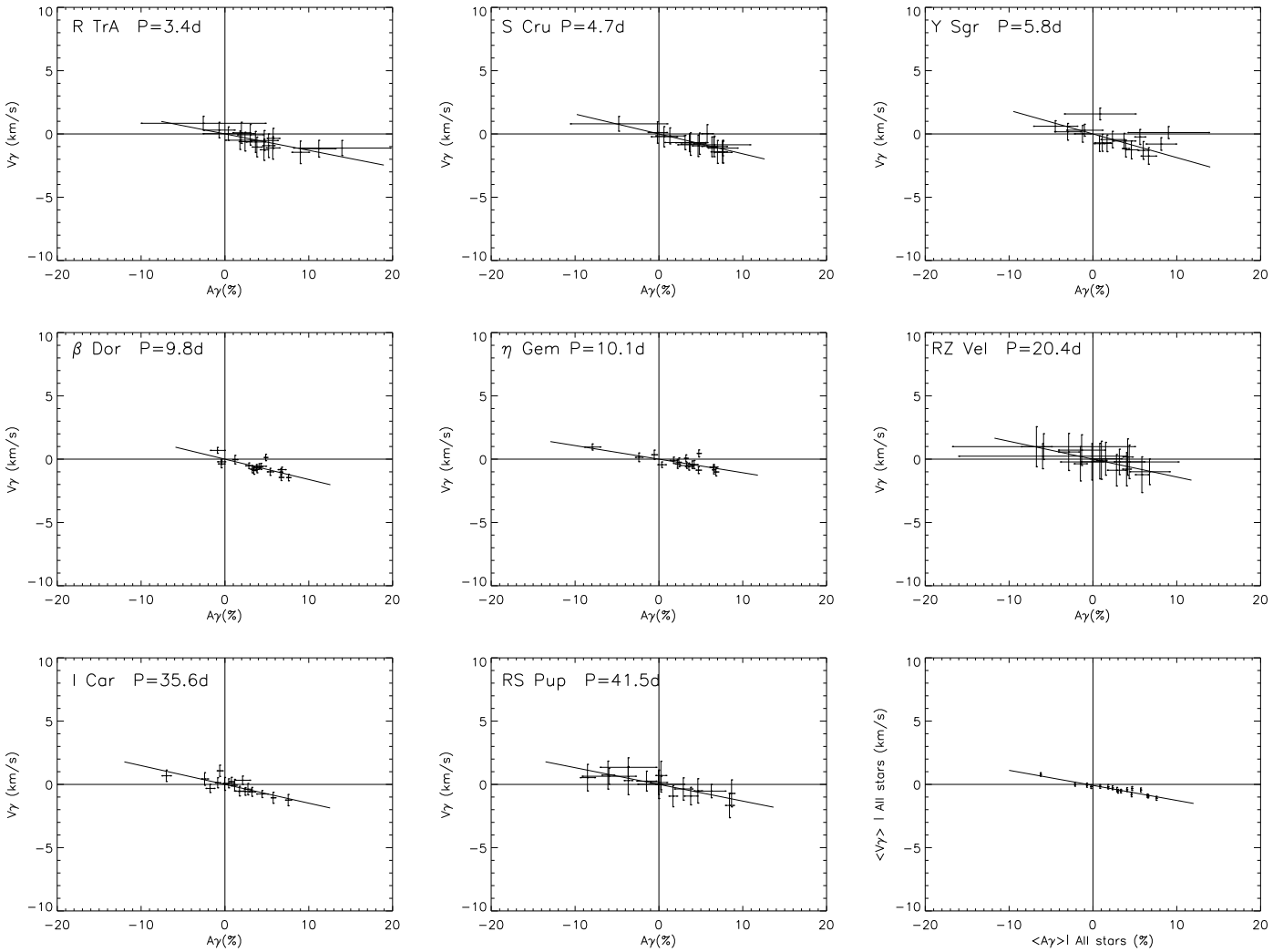


Fig. 3. Same as Fig. 2d for all Cepheids of our sample. The origin of the $V_\gamma A_\gamma$ plots are used as physical references. The correction applied ($V_{\gamma\star} = V_\gamma \mathrm{GCD} + b_0$), together with the slope values (a_0), are indicated in Table 1. In the last panel an weighted average is done over all stars. The resulting $V_\gamma A_\gamma$ linear curve is very precise ($a_0 = 0.15 \pm 0.01$).

while $A(\phi) \neq 0$ or, on the contrary, $A(\phi) = 0$ but $RV_c(\phi) \neq 0$; i.e. $RV_c(\phi) = 0$ does not imply $A(\phi) = 0$;

– interestingly, we find a relation between the γ-asymmetries and the pulsation period of Cepheids. In particular, if we define $\langle A_\gamma \rangle$ as the average of the A_γ quantity over all spectral lines for a given star, then we find the following linear relation

$$\langle A_\gamma \rangle = [-1.6 \pm 0.3] \log P + [6.7 \pm 0.9],$$

where P is the period in days of the Cepheid. The reduced χ^2 we obtain is 6. This relation (hereafter $\langle A_\gamma \rangle$) is represented by Fig. 5. We already presented such a relation in Paper I for the Fe 6056.005 Å spectral line. This new relation can be considered as a generalization over all spectral lines of our sample;

What could explain the observed γ-asymmetries? To answer this question, we investigate three different hypotheses: (1) the limb-darkening variation with time and within the spectral line; (2) velocity gradients; and (3) the relative motion of the line-forming region compared to the corresponding mass elements.

(1) The time- and wavelength dependence of the limb-darkening within the spectral lines does not explain why the line asymmetry is *not zero* when the radial velocity is zero. When for instance the star is at minimum or maximum expansion (i.e. radial velocity is zero), whatever the limb-darkening distribution might be, if there are no dynamical effects within the atmosphere, then the spectral line should be symmetric. This is clearly not what we observe. Consequently, the time- and wavelength dependence of the limb-darkening may have some effects on the variation of line asymmetry over the pulsation phase, but it can not be responsible for all properties mentioned above.

(2) Velocity gradients in the atmosphere can indeed cause an asymmetric spectral line. Line asymmetry $A(\phi)$ and radial velocity $RV_c(\phi)$ basically vary in phase, even if there is not a strict correlation. This is thus a strong indication that radial velocity gradients are, to some degree, responsible for the line asymmetries in these stars. However, they cannot explain, for instance, the *systematic* shift in asymmetry (almost constant with the pulsation phase) observed between the 6024.8 Å and Fe 4896.4 Å spectral line (Fig. 2). Butler et al. (1996) introduced a number of velocity gradients in their model. They found that "the effect of this velocity gradient is to reduce the amplitude of the pulsational velocity curve at optical depth of $\tau = \frac{2}{3}$ by 20% and to decrease the

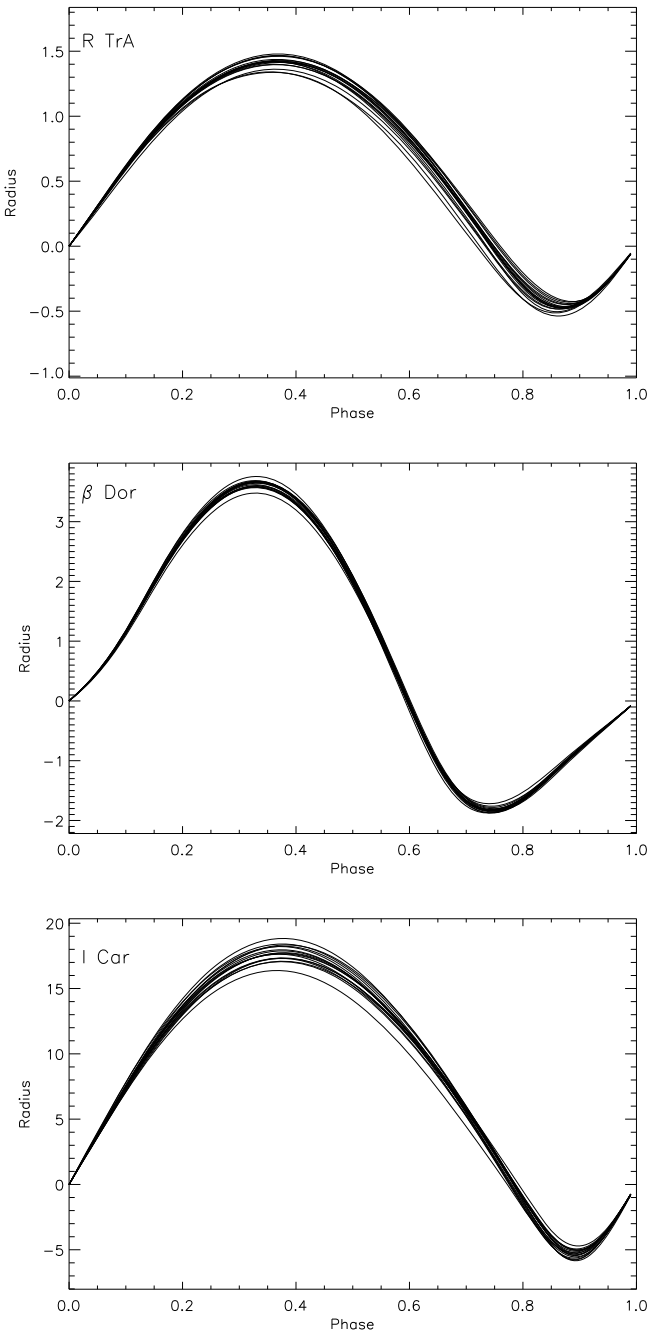


Fig. 4. Radius (in solar radii) as a function of the pulsation phase for spectral lines of our sample. The radial velocity curves have been corrected from their γ-velocities in order to investigate phase shifts. Important differences are found from one line to the other, which are mainly due to the velocity gradient within the atmosphere. Actually, there is a linear relation between the amplitude of the radius variation and the line depth (see for instance Fig. 4 of Paper II). This indicates why it is essential to use *dynamic* projection factors. A phase shift is observed only for R TrA and RS Pup.

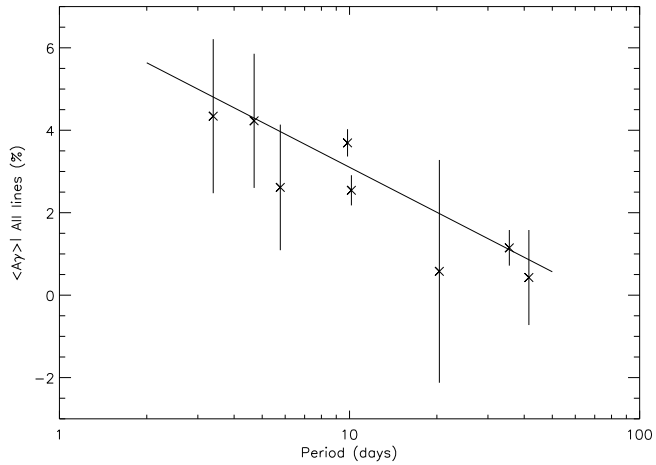


Fig. 5. A_γ averaged (without weighting) over all lines is given as a function of the pulsation period of the star. The plot is a generalization of Fig. 14a of Paper I.

γ-velocity by 2 km s^{-1} relative to the standard assumption of a comoving atmosphere". However, the main differences they obtain in their velocity curves are near *extrema*. For instance, in their Fig. 11, all curves (with and without velocity gradient) vanish at the same pulsation phase. This is not what we observe in our Fig. 2a, where *systematic* shifts are obtained. In their study, Butler et al. (1996) applied a "closure" constraint: "It is assumed that each layer of the stellar atmosphere returns to its starting position after a pulsation cycle". Thus, let us now discuss the last hypothesis:

(3) The relative motion of the line-forming region with respect to the corresponding mass elements. When the line-forming region moves relative to the background atmospherical structure, it will also move with respect to the background velocity field. Thus, the line experiences an apparent change in velocity, which has a comparable effect as a velocity gradient, but with a lower intensity. This explains why line-forming regions do not comply with the *path* conservation, as discussed in the introduction. However, this cannot explain, for instance, the *systematic* shift in asymmetry (or in velocity) observed between the 6024.8 Å and Fe 4896.4 Å spectral lines. Indeed, it would mean that the line-forming regions corresponding to these two spectral lines have a *systematic relative* motion (V_γ) compared to the background, whatever the pulsation cycle considered. Either there are cycle-to-cycle differences in the *path* of the line-forming regions (which we cannot confirm with our data) or one should invoke another physical explanation.

5. Conclusions

We found γ-asymmetries varying from one spectral line to another, as well as a global dependency on the period of the star or, correspondingly, on the spatial extension of the Cepheids' atmosphere. Right now, we have no clear physical explanations for this effect. Most likely, it results from a combination of several effects in the dynamical structure of the Cepheids' atmosphere, such as phase- and wavelength-dependence of the intensity distribution within the different spectral lines, velocity gradients, non-linear pulsational effects, shock fronts, and relative motions between line-forming regions (specific to each spectral line considered) and the material.

In order to further investigate the line asymmetries, improved numerical models are required. Since Cepheids' atmospheres are not in a hydrostatic state but characterized by pulsational dynamics, one has to perform non-linear, time-dependent simulations of the underlying pulsation. Snapshots from this temporal evolution (including the velocity field) can then be used to compute a detailed frequency-dependent radiative transport. In order to resolve narrow features such as shock fronts or sharp ionization regions, high spatial resolution, especially in the

line-forming regions, is needed. Although convective transport plays only a minor role in the stellar structure of Cepheids in that temperature range (≃5500 K, see Table 2 in Paper II), there can still be considerable convective velocities (some km s^{-1}). As a consequence, the consistent inclusion of the convective velocity field – and of the interaction of convection with pulsation – in the numerical models might be crucial for the computation of line asymmetries. Dynamics in the circumstellar envelope (Kervella et al. 2006; Mérand et al. 2006, 2007; Nardetto et al. 2008) is also important. Confronting such models with observations (spectral line profiles, spatial- and spectral- visibility curves from interferometry) may finally lead the way to a complete picture of the relevant effects in Cepheids' atmospheres.

However, even now, we already have a clear evidence from our observed linear $A_\gamma V_\gamma$ relation that the residual γ-velocities (or K-term) seen in Cepheids are the result of the dynamical structure of their atmosphere. This provides a physical meaning to the γ-velocities and a physical reference: *the γ-velocity should be zero when the γ-asymmetry is zero*. This definition of the γ-velocities could be used for kinematical studies of the Galaxy, even though this method requires high signal-to-noise and high-resolution spectroscopic observations. Using only one metallic line to derive the γ-velocity can inflict errors (or inconsistencies) ranging from –2 to 1 km s^{-1}.

Acknowledgements. Based on observations collected at La Silla observatory, Chile, in the framework of European Southern Observatory's programs 072.D-0419 and 073.D-0136. We thanks Kervella for having provided the HARPS data and Fekety for her careful English correction of the paper. This research has made use of the SIMBAD and VIZIER databases at CDS, Strasbourg (France). This material is based in part upon work by TGB while serving at the National Science Foundation. Any opinions, findings, and conclusions or recommendations expressed in this material are those of the authors and do not necessarily reflect the views of the National Science Foundation. N.N. acknowledges the Max Planck Institut for Radioastronomy for financial support.

References

Burki, G., Mayor, M., & Benz, W. 1982, A&A, 109, 258
Butler, R. P., Bell, R. A., & Hindsley, R. B. 1996, ApJ, 461, 362
Caldwell, J. A. R., & Coulson, I. M. 1987, AJ, 93, 1090
Camm, G. L. 1938, MNRAS, 99, 71
Camm, G. L. 1944, MNRAS, 104,163
Fernie, J. D., Beattie, B., Evans, N. R., & Seager, S. 1995, IBVS, 4148
Freedman, W., Madore, B. F., Gibson, B. K., et al. 2001, ApJ, 553, 47
Fouqué, P., Arriagada, P., Storm, J., et al. 2007, A&A, 476, 73
Gautschy, A. 1987, Vistas Astron., 30, 197
Kervella, P., Nardetto, N., Bersier, D., et al. 2004, A&A, 416, 941
Kervella, P., Mérand, A., Perrin, G., & Coudé Du Foresto, V. 2006, A&A, 448, 623
Kurucz, R. L. 1992, The Stellar Populations of Galaxies, IAU Symp., 149, 225
Mathias, P., Gillet, D., Fokin, A., et al. 2006, A&A, 457, 575
Mérand, A., Kervella, P., Coudé du Foresto, V., et al. 2006, A&A, 453, 155
Mérand, A., Aufdenberg, J. P., Kervella, et al. 2007, ApJ, 664, 1093
Moffett, T. J., & Barnes, T. G. III 1987, PASP, 99, 1206
Nardetto, N., Fokin, A., Mourard, D., et al. 2004, A&A, 428, 131
Nardetto, N., Mourard, D., Kervella, P., et al. 2006, A&A, 453, 309 (Paper I)
Nardetto, N., Mourard, D., Mathias, Ph., et al. 2007, A&A, 471, 661 (Paper II)
Nardetto, N., Mourard, D., Kervella, P., et al. 2007, yCat, 34530309N
Nardetto, N., Groh, J. H., Kraus, S., et al. 2008, A&A, 489, 1263
Parenago, P. P. 1945, PA, 53, 441
Pont, F., Mayor, M., & Burki, G. 1994, A&A, 285, 415
Sabbey, C. N., Sasselov, D. D., Fieldus, M. S., et al. 1995, ApJ, 446, 250
Sasselov, D. D., & Karovska, M. 1994, ApJ, 432, 367
Stibbs, D. W. N. 1956, MNRAS, 116, 453
Wielen, R. 1974, A&AS, 15, 1
Wilson, T. D., Barnes, T. G., Hawley, S. L., & Jefferys, W. H. 1991, ApJ, 378, 708

N. Nardetto et al.: High-resolution spectroscopy for Cepheids distance determination. III., *Online Material p 1*

Table 2. A_γ and V_γ for all spectral lines of all stars.

Line (Å)	R TrA		S Cru		Y Sgr		β Dor	
	A_γ[%]	V_γ[km s^{-1}]	A_γ[%]	V_γ[km s^{-1}]	A_γ[%]	V_γ[km s^{-1}]	A_γ[%]	V_γ[km s^{-1}]
Fe 4683.560	$0.40_{\pm3.01}$	$0.02_{\pm0.53}$	$3.12_{\pm2.41}$	$-0.68_{\pm0.56}$	$-4.49_{\pm2.58}$	$0.61_{\pm0.43}$	$-0.44_{\pm0.43}$	$-0.21_{\pm0.21}$
Fe 4896.439	$-2.58_{\pm7.39}$	$0.84_{\pm0.55}$	$-4.80_{\pm5.76}$	$0.80_{\pm0.58}$	$0.82_{\pm4.23}$	$1.58_{\pm0.46}$	$-0.90_{\pm0.84}$	$0.70_{\pm0.23}$
Fe 5054.643	$13.95_{\pm5.75}$	$-1.11_{\pm0.60}$	$6.55_{\pm4.30}$	$-0.86_{\pm0.61}$	$8.99_{\pm4.81}$	$0.11_{\pm0.47}$	$4.07_{\pm0.80}$	$-0.56_{\pm0.20}$
Ni 5082.339	$11.19_{\pm1.95}$	$-1.17_{\pm0.66}$	$7.60_{\pm1.74}$	$-1.12_{\pm0.61}$	$8.12_{\pm1.77}$	$-0.80_{\pm0.49}$	$6.77_{\pm0.43}$	$-0.83_{\pm0.19}$
Fe 5367.467	$3.81_{\pm0.55}$	$-1.04_{\pm0.78}$	$6.31_{\pm0.58}$	$-1.02_{\pm0.78}$	$1.68_{\pm0.49}$	$-0.74_{\pm0.65}$	$3.82_{\pm0.16}$	$-0.81_{\pm0.27}$
Fe 5373.709	$1.78_{\pm1.73}$	$-0.50_{\pm0.73}$	$3.63_{\pm1.64}$	$-0.69_{\pm0.70}$	$-3.02_{\pm1.54}$	$0.17_{\pm0.66}$	$3.74_{\pm0.38}$	$-0.68_{\pm0.25}$
Fe 5383.369	$4.66_{\pm0.44}$	$-1.25_{\pm0.84}$	$7.61_{\pm0.46}$	$-1.42_{\pm0.88}$	$3.90_{\pm0.39}$	$-1.16_{\pm0.66}$	$6.65_{\pm0.14}$	$-1.03_{\pm0.28}$
Ti 5418.751	$5.75_{\pm0.72}$	$-0.35_{\pm0.79}$	$5.75_{\pm0.65}$	$0.02_{\pm0.71}$	$5.59_{\pm0.61}$	$-0.24_{\pm0.59}$	$4.85_{\pm0.18}$	$0.13_{\pm0.25}$
Fe 5576.089	$2.39_{\pm0.70}$	$-0.61_{\pm0.74}$	$4.67_{\pm0.68}$	$-0.94_{\pm0.84}$	$0.77_{\pm0.61}$	$-0.77_{\pm0.61}$	$3.45_{\pm0.16}$	$-0.89_{\pm0.30}$
Fe 5862.353	$1.96_{\pm1.02}$	$0.09_{\pm0.84}$	$-0.18_{\pm1.11}$	$0.12_{\pm0.85}$	$-1.25_{\pm0.96}$	$0.01_{\pm0.66}$	$1.20_{\pm0.25}$	$-0.04_{\pm0.34}$
Fe 6024.058	$5.70_{\pm0.77}$	$-1.11_{\pm0.89}$	$6.98_{\pm0.77}$	$-1.42_{\pm0.90}$	$4.58_{\pm0.67}$	$-1.26_{\pm0.71}$	$7.58_{\pm0.21}$	$-1.45_{\pm0.25}$
Fe 6027.051	$4.68_{\pm1.59}$	$-0.52_{\pm0.78}$	$6.59_{\pm1.49}$	$-0.99_{\pm0.81}$	$3.71_{\pm1.31}$	$-0.56_{\pm0.61}$	$5.38_{\pm0.33}$	$-1.00_{\pm0.27}$
Fe 6056.005	$3.02_{\pm1.53}$	$-0.07_{\pm0.82}$	$0.60_{\pm1.53}$	$-0.22_{\pm0.80}$	$2.33_{\pm1.40}$	$-0.44_{\pm0.65}$	$-0.43_{\pm0.35}$	$-0.38_{\pm0.30}$
Si 6155.134	$-0.70_{\pm1.82}$	$0.31_{\pm0.61}$	$1.30_{\pm1.67}$	$-0.16_{\pm0.63}$	$-1.01_{\pm2.12}$	$0.29_{\pm0.47}$	$2.85_{\pm0.38}$	$-0.53_{\pm0.22}$
Fe 6252.555	$5.19_{\pm0.68}$	$-0.93_{\pm0.93}$	$4.83_{\pm0.70}$	$-0.77_{\pm0.84}$	$5.99_{\pm0.61}$	$-1.30_{\pm0.70}$	$4.29_{\pm0.16}$	$-0.58_{\pm0.24}$
Fe 6265.134	$3.63_{\pm1.10}$	$-0.63_{\pm0.83}$	$3.75_{\pm1.12}$	$-0.80_{\pm0.89}$	$1.11_{\pm0.92}$	$-0.70_{\pm0.67}$	$3.26_{\pm0.21}$	$-0.80_{\pm0.28}$
Fe 6336.824	$8.99_{\pm1.01}$	$-1.45_{\pm0.89}$	$7.59_{\pm1.03}$	$-1.46_{\pm0.84}$	$6.62_{\pm0.88}$	$-1.75_{\pm0.65}$	$6.70_{\pm0.23}$	$-1.44_{\pm0.24}$
average	$4.34_{\pm1.87}$		$4.23_{\pm1.63}$		$2.61_{\pm1.52}$		$3.69_{\pm0.33}$	
Line (Å)	ζ Gem		RZ Vel		ℓ Car		RS Pup	
	A_γ[%]	V_γ[km s^{-1}]	A_γ[%]	V_γ[km s^{-1}]	A_γ[%]	V_γ[km s^{-1}]	A_γ[%]	V_γ[km s^{-1}]
Fe 4683.560	$0.33_{\pm0.46}$	$-0.44_{\pm0.22}$	$-6.01_{\pm10.00}$	$0.24_{\pm0.99}$	$-1.78_{\pm0.49}$	$-0.32_{\pm0.32}$	$-5.97_{\pm3.18}$	$0.64_{\pm0.63}$
Fe 4896.439	$-7.95_{\pm0.92}$	$0.96_{\pm0.24}$	$-5.89_{\pm10.86}$	$0.99_{\pm1.02}$	$2.10_{\pm0.86}$	$0.33_{\pm0.33}$	$-3.67_{\pm3.32}$	$1.35_{\pm0.75}$
Fe 5054.643	$3.30_{\pm0.80}$	$-0.50_{\pm0.22}$	$3.15_{\pm7.02}$	$-0.22_{\pm1.01}$	$2.41_{\pm0.78}$	$-0.56_{\pm0.30}$	$0.22_{\pm2.75}$	$0.01_{\pm0.61}$
Ni 5082.339	$6.51_{\pm0.44}$	$-0.62_{\pm0.20}$	$6.75_{\pm2.37}$	$-1.00_{\pm1.01}$	$4.42_{\pm0.64}$	$-0.76_{\pm0.27}$	$6.24_{\pm1.65}$	$-0.53_{\pm0.52}$
Fe 5367.467	$3.95_{\pm0.19}$	$-0.43_{\pm0.30}$	$1.00_{\pm0.58}$	$-0.09_{\pm1.51}$	$-0.87_{\pm0.27}$	$0.13_{\pm0.40}$	$-0.03_{\pm0.39}$	$0.01_{\pm1.13}$
Fe 5373.709	$3.56_{\pm0.41}$	$-0.59_{\pm0.28}$	$1.51_{\pm1.87}$	$0.03_{\pm1.30}$	$1.73_{\pm0.49}$	$-0.53_{\pm0.38}$	$-0.04_{\pm0.99}$	$0.15_{\pm0.94}$
Fe 5383.369	$6.53_{\pm0.16}$	$-0.84_{\pm0.33}$	$4.01_{\pm0.47}$	$-0.79_{\pm1.32}$	$5.75_{\pm0.23}$	$-1.06_{\pm0.43}$	$8.66_{\pm0.31}$	$-0.71_{\pm1.07}$
Ti 5418.751	$4.75_{\pm0.20}$	$0.45_{\pm0.28}$	$4.14_{\pm0.57}$	$0.17_{\pm1.43}$	$-0.62_{\pm0.31}$	$1.07_{\pm0.44}$	$4.65_{\pm0.45}$	$-0.52_{\pm0.96}$
Fe 5576.089	$2.39_{\pm0.19}$	$-0.25_{\pm0.35}$	$-1.49_{\pm0.74}$	$-0.37_{\pm1.36}$	$-0.03_{\pm0.21}$	$0.04_{\pm0.50}$	$-3.67_{\pm0.47}$	$0.30_{\pm1.11}$
Fe 5862.353	$-0.56_{\pm0.30}$	$0.35_{\pm0.37}$	$-2.89_{\pm1.21}$	$0.57_{\pm1.46}$	$-2.42_{\pm0.36}$	$0.43_{\pm0.49}$	$-6.09_{\pm0.72}$	$0.73_{\pm1.11}$
Fe 6024.058	$6.80_{\pm0.24}$	$-1.01_{\pm0.32}$	$5.83_{\pm0.78}$	$-1.23_{\pm1.41}$	$7.54_{\pm0.31}$	$-1.24_{\pm0.44}$	$8.42_{\pm0.48}$	$-1.66_{\pm0.97}$
Fe 6027.051	$4.19_{\pm0.37}$	$-0.43_{\pm0.32}$	$4.32_{\pm1.78}$	$-0.21_{\pm1.32}$	$2.73_{\pm0.42}$	$-0.38_{\pm0.45}$	$2.90_{\pm1.05}$	$-0.37_{\pm0.88}$
Fe 6056.005	$-2.40_{\pm0.41}$	$0.15_{\pm0.34}$	$-6.75_{\pm1.79}$	$0.98_{\pm1.58}$	$-7.00_{\pm0.51}$	$0.68_{\pm0.45}$	$-8.53_{\pm0.85}$	$0.53_{\pm1.05}$
Si 6155.134	$1.74_{\pm0.43}$	$-0.09_{\pm0.25}$	$-1.35_{\pm2.76}$	$0.71_{\pm1.21}$	$0.44_{\pm0.64}$	$0.08_{\pm0.36}$	$-1.49_{\pm1.14}$	$0.26_{\pm0.78}$
Fe 6252.555	$3.22_{\pm0.19}$	$0.07_{\pm0.27}$	$0.81_{\pm0.75}$	$-0.16_{\pm1.40}$	$0.77_{\pm0.27}$	$0.22_{\pm0.34}$	$1.66_{\pm0.47}$	$-0.93_{\pm0.84}$
Fe 6265.134	$2.20_{\pm0.24}$	$-0.38_{\pm0.35}$	$-0.13_{\pm1.30}$	$-0.21_{\pm1.44}$	$1.14_{\pm0.23}$	$-0.07_{\pm0.46}$	$0.23_{\pm0.60}$	$0.70_{\pm1.13}$
Fe 6336.824	$4.70_{\pm0.27}$	$-0.87_{\pm0.26}$	$2.81_{\pm1.09}$	$-0.88_{\pm1.24}$	$3.22_{\pm0.35}$	$-0.59_{\pm0.35}$	$3.78_{\pm0.77}$	$-0.92_{\pm0.69}$
average	$2.54_{\pm0.37}$		$0.58_{\pm2.70}$		$1.15_{\pm0.43}$		$0.43_{\pm1.15}$	

Annexe O

High-resolution spectroscopy for Cepheids distance determination. IV. Time series of Hα line profiles

A&A 489, 1263–1269 (2008)
DOI: 10.1051/0004-6361:200809589
© ESO 2008

Astronomy & Astrophysics

High-resolution spectroscopy for Cepheids distance determination⋆

IV. Time series of Hα line profiles

N. Nardetto[1], J. H. Groh[1], S. Kraus[1], F. Millour[1], and D. Gillet[2]

[1] Max-Planck-Institut für Radioastronomie, Auf dem Hügel 69, 53121 Bonn, Germany
e-mail: nardetto@mpifr-bonn.mpg.de
[2] Observatoire de Haute-Provence, 04870 Saint-Michel l'Observatoire, France

Received 15 February 2008 / Accepted 1 April 2008

ABSTRACT

Context. In recent years, infrared interferometry has revealed the presence of faint dusty circumstellar envelopes (CSE) around Cepheids. However the size, shape, chemical nature, and the interaction of the CSE with the star itself are still under investigation. The presence of a CSE might have an effect on the angular diameter estimates used in the interferometric Baade-Wesselink and surface-brightness methods of determining the distance of Cepheids.
Aims. By studying Hα profiles as a function of the period, we investigate the permanent mass loss and the CSE around Cepheids. Our high spectral- and time-resolution data, combined with a very good S/N, will be useful in constraining future hydrodynamical models of Cepheids atmosphere and their close environment.
Methods. We present HARPS⋆⋆ high-resolution spectroscopy (R = 120 000) of eight galactic Cepheids: R Tra, S Cru, Y Sgr, β Dor, ζ Gem, RZ Vel, ℓ Car, and RS Pup, providing a good period sampling (P = 3.39 d to P = 41.52 d). The Hα line profiles are described for all stars using a 2D (wavelength versus pulsation phase) representation. For each star, an average spectral line profile is derived, together with its first moment (γ-velocity) and its asymmetry (γ-asymmetry).
Results. Short-period Cepheids show Hα line profiles following the pulsating envelope of the star, while long-period Cepheids show very complex line profiles and, in particular, large asymmetries. We find a new relationship between the period of Cepheids and their γ-velocities and -asymmetries. These results may be related to the dynamical structure of the atmosphere and to a permanent mass loss of Cepheids. In particular, we confirm for ℓ Car a dominant absorption component whose velocity is constant and nearly of zero km s^{-1} in the stellar rest frame. This component is attributed to the presence of circumstellar envelope.
Conclusions. To understand these very subtle γ effects, fully consistent hydrodynamical models are required, including pulsating and evolutionary theories, convective energy transport, adaptive numerical meshes, and a refined calculation of the radiative transfer.

Key words. techniques: spectroscopic – stars: atmospheres – stars: oscillations – stars: variables: Cepheids – stars: distances

1. Introduction

Cepheids are key astrophysical objects due to their well-known period-luminosity (*PL*) relationship. Based on this relationship, a multi-decade work has reached cosmologically significant extragalactic distances (see Hubble Space Telescope Key Project, Freedman et al. 2001). In particular, two methods have recently been used to calibrate the *PL* relationship, namely the infrared surface brightness (IRSB) and the interferometric Baade-Wesselink (IBW) methods of determining the distance of Cepheids (Fouqué et al. 2007).

The basic principle behind these methods is to compare the linear and angular size *variation* of a pulsating star to derive its distance through a simple division. The caveat is that interferometric (IBW) or photometric (IRSB) measurements *in the continuum* lead to angular diameters corresponding to the *photospheric* layer, while the linear stellar radius variation is deduced from spectroscopy, i.e., based on line-forming regions that form in higher layers of the atmosphere. Thus, radial velocities $V_{\rm rad}$, which are derived from line profiles, include the integration in two directions: over the stellar surface through limb darkening, and over the atmospheric layers through velocity gradients. All these phenomena are currently merged into one specific quantity, generally considered as constant with time: the projection factor p, defined as $V_{\rm puls} = pV_{\rm rad}$, where $V_{\rm puls}$ is defined as the *photospheric* pulsation velocity (Nardetto et al. 2004). Then, $V_{\rm puls}$ is integrated with time to derive the photospheric radius variation. The precision in the distance currently obtained with the IBW and IRSB methods is a few percent; however, they remain strongly dependent on the projection factor. If a constant projection factor is used (generally p = 1.36 for all stars, Burki et al. 1982) to derive the *PL* relationship, errors of 0.10 and 0.03 on the slope and zero-point of the *PL* relationship can be introduced. It means that distances can be overestimated by 10% for long-period Cepheids (Nardetto et al. 2007a, hereafter Paper II).

⋆ Based on observations made with ESO telescopes at the Silla Paranal Observatory under program IDs 072.D-0419 and 073.D-0136.
⋆⋆ High Accuracy Radial velocity Planetary Search project developed by the European Southern Observatory.

Article published by EDP Sciences

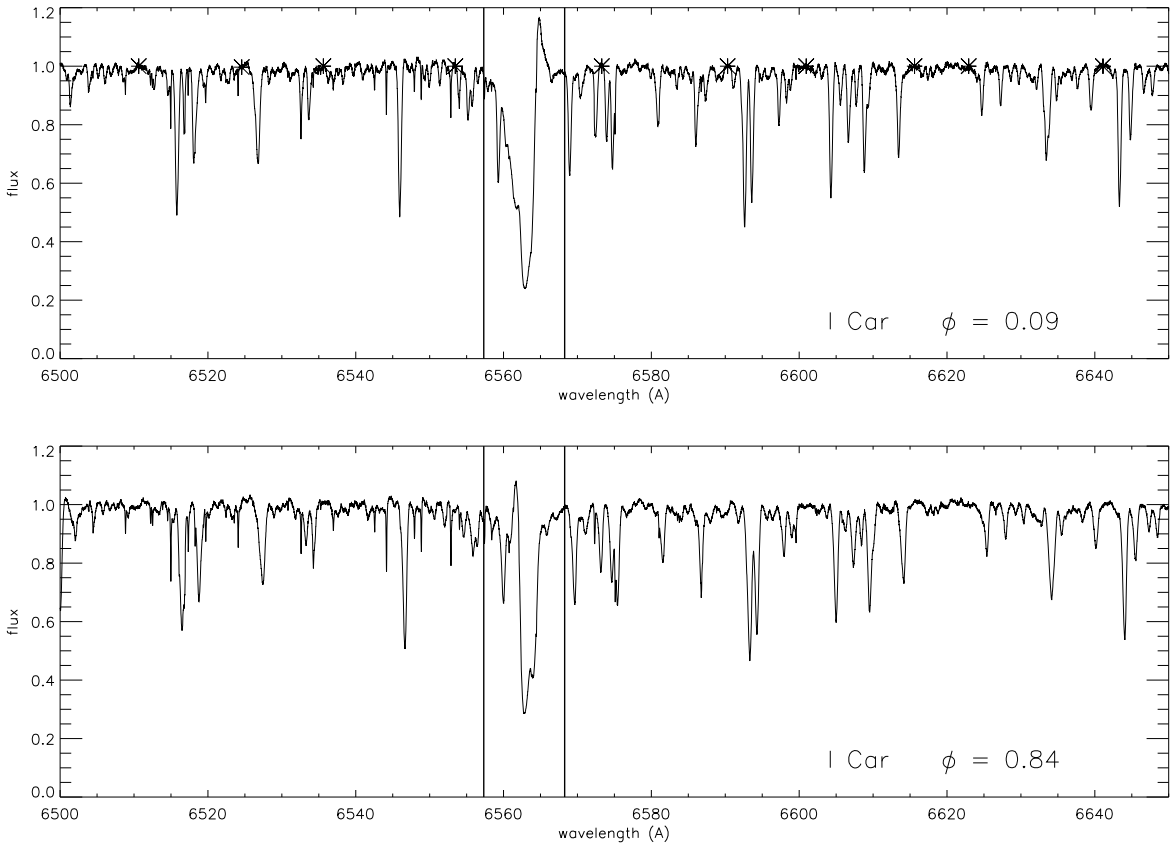


Fig. 1. Typical HARPS spectrum (ℓ Car, $\phi = 0.09$ and $\phi = 0.84$) around Hα. In this study, we focus on the [−250, 250] km s^{-1} velocity range represented in the figure by the two vertical lines, while the whole wavelength range 6500−6650 Å was used in the normalization process. Ten points (crosses on *the upper panel*) are used in the interpolation of the continuum. Within the [−250, 250] km s^{-1} velocity range, we clearly see that the blue wing of the Hα line is blended by a metallic line identified as either Fe 6559.763 Å or possibly Ti 6559.588 Å.

In recent years, infrared interferometry has revealed the presence of faint (few percent of near-infrared continuum flux), dusty circumstellar envelopes (CSE) around Cepheids (Kervella et al. 2006; Mérand et al. 2006, 2007). However, the size (the CSE is 3−4 times larger than the star), shape, chemical nature, and the interaction of the CSE with the star itself are still under investigation. Such envelopes have a non-negligible effect on the angular diameter estimates used in the IBW and IRSB methods of determining the distance of Cepheids. If the CSE is not considered, the distance can be underestimated by a few percent. In addition, Mérand et al. (2007) show a relationship between the period of the Cepheid and the brightness of the CSE compared to the stellar near-infrared continuum flux. From these results, one cannot exclude a link between the period, the mass loss, and the presence of a circumstellar shell around Cepheids. The knowledge of these CSE is particularly important in the case of the bright, long period cepheids, which can be used to improve the primary distance scale to Virgo and beyond. Recently, Kervella et al. (2008) determine the distance of the long period Cepheid RS Pup from its light echoes, while Nardetto et al. (2006, hereafter Paper I) found a broadening of the metallic spectral lines at certain phases that could indicate the presence of a strong velocity gradient (compression or shock wave). In this context, studying and understanding the Hα profile variations of Cepheids as a function of the period is a key. This spectral line is indeed sensitive both to pulsation and the putative hydrogen circumstellar medium.

We present the time series of Hα profiles for eight Cepheids, with a very high spectral resolution and a good time coverage. Our aim is not to provide a full picture of the mechanisms involved in the formation of Hα line profiles, but mainly to characterize them and to investigate a relationship with the period of the star. With such high S/N, high-resolution data will be useful for supporting future hydrodynamical models of Cepheids' atmosphere and their close environment. In Sect. 2, we present our data and the Hα profile of the studied Cepheids. Section 3 presents an analysis in terms of γ-velocities and -asymmetries and Sect. 4 is devoted to the particular case of ℓ Car.

2. The high-resolution Hα line profiles of Cepheids

Ten Cepheids were observed with the HARPS spectrometer: R Tra, S Cru, Y Sgr, X Sgr, β Dor, ζ Gem, Y Oph, RZ Vel, ℓ Car and RS Pup, having a good period sampling from $P = 3.39$ d to $P = 41.52$ d (Paper I). X Sgr is an atypical Cepheid presenting several components in the spectral line profiles, and has been studied separately by Mathias et al. (2006). Y Oph is not studied in detail here due to its insufficient phase coverage. Thus, we consider 8 Cepheids in this paper. The spectral resolution is $R = \frac{\lambda}{\Delta\lambda} = 120\,000$ and the average S/N is 300 per pixel. We used the standard ESO/HARPS pipeline reduction package for bias subtraction, flat-fielding, and order extraction.

We paid special attention to the normalization process. For each spectrum, the continuum was defined by interpolating ten points (using a spline function), chosen carefully over the 6500−6650 Å wavelength range (Fig. 1). We consequently estimate the uncertainty on the continuum level to be about 1% (i.e. around 3 times the average noise).

Our observations generally spread over a few pulsation cycles (2 to 4). Assuming negligible cycle-to-cycle variations, our total dataset provides a very good pulsation phase coverage. Journal of observations and online data are available in Nardetto et al. (2007b). Combining very high spectral resolution and good time coverage, we derive 2D maps using an interpolation method based on the so-called Delaunay triangles (see "triangulate" function in IDL[1] and Renka 1982). The wavelength and pulsation phase sampling of the maps are respectively 0.06 Å and 0.02. To describe Hα line profiles (6562.797 Å), we classified the Cepheids in our sample in three groups: short- (R TrA, S Cru, and Y Sgr), medium- (β Dor and ζ Gem), and long-period Cepheids (RZ Vel, ℓ Car and RS Pup), corresponding to Figs. 2–4, respectively. All diagrams are given in the stellar rest frame with positive velocities corresponding to receding motion. The data were duplicated over 2 cycles for clarity. The γ-velocities (average value of the radial velocity curve derived from a metallic line) were corrected using the Galactic Cepheid Database of the David Dunlap Observatory[2] (Fernie et al. 1995). The plots are presented over the [−250, 250] km s^{-1} velocity range around Hα, to avoid complex line blendings on the extreme parts of the line wings (Fig. 1). The only *strong* remaining metallic line within this velocity range is Fe 6559.763 Å (or possibly Ti 6559.588 Å). The vertical lines that sometimes appear faint (for instance at −220 km s^{-1} for β Dor or +170 km s^{-1} for ℓ Car) are telluric lines, and they have negligible influence on our results.

Following our three groups, several features should be mentioned:

- Short-period Cepheids [3 to 6 days] confirm the observations by Wallerstein (1972) that in stars with periods less than 13 d, the Hα line profiles behaves similar to other absorption lines. In the left part of each panel, one can indeed use the track corresponding to the Fe 6559.763 Å metallic line profile (around −160 km s^{-1}) as a reference. This track is quite faint for short-period stars, but clearly visible for medium- and long-period Cepheids. Otherwise, these short-period Cepheids show very similar profiles from one star to the next.
- Medium-period Cepheids [around 10 days], namely β Dor and ζ Gem, are different from the short-period Cepheids simply by the shape of their radial velocity curve. These stars are indeed very close to the $\frac{P_2}{P_0} = 0.5$ resonance, where P_0 and P_2 are respectively the periods corresponding to the fundamental and the second overtone modes (Kovacs et al. 1990). We even notice that ζ Gem ($P = 9.8$ d) is less affected by the resonance compared to β Dor ($P = 10.1$ d).
- Long-period Cepheids [20 to 42 days] show a clear asymmetry in the Hα line profiles, which is present during most of the pulsation cycle. The line asymmetry is studied in detail for all stars of our sample in the next section. Long-period Cepheids also present a complicated structure consisting of multi-components in absorption or in emission, which might be explained by means of the presence of a turbulent layer (maybe due to a shockwave) in the upper atmosphere of the star, and by the presence of a circumstellar shell (see e.g. Rodgers & Bell 1968; Grenfell & Wallerstein 1969; Schmidt 1970; Wallerstein 1972, 1979, 1983, 1992; Böhm-Vitense & Love 1994). In addition, as shown by detailed models of the fine structure of radiative shocks (Fadeyev & Gillet 2004),

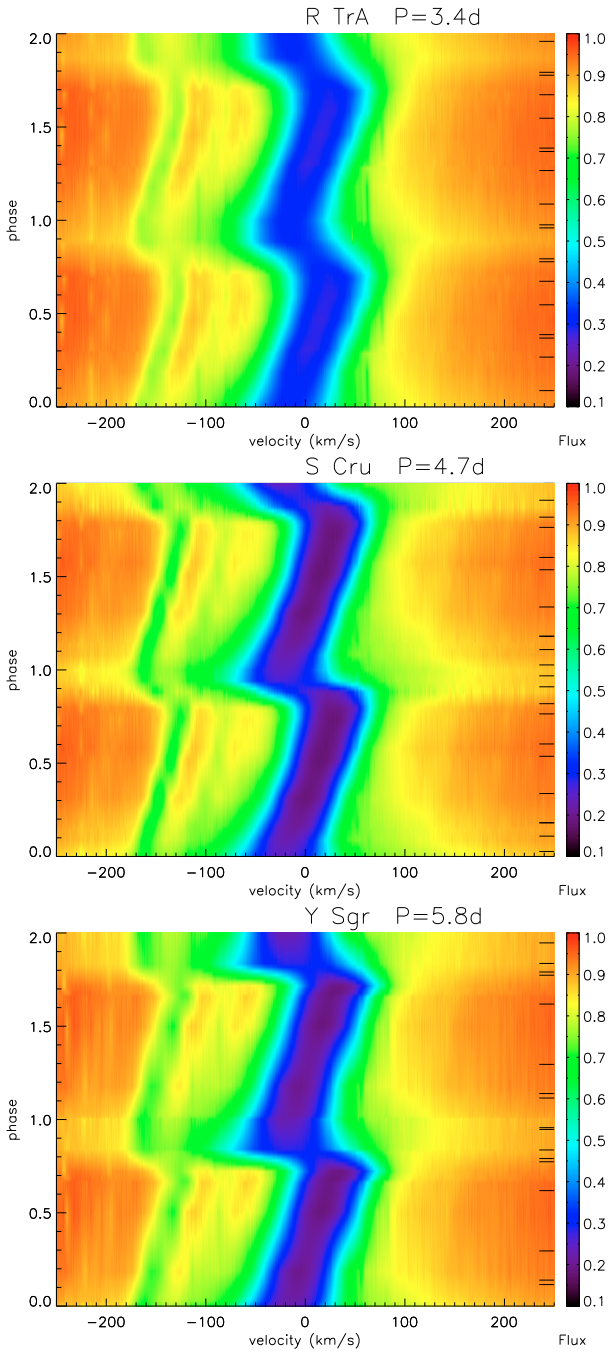


Fig. 2. Hα line profiles of short-period Cepheids R TrA, S Cru and Y Sgr, ordered by increasing period *from top to bottom*. Time series of HARPS spectra are interpolated to provide a 2-dimensional map of the Hα profile in the [−250, 250] km s^{-1} velocity range. Diagrams are given in the stellar rest frame with positive velocities corresponding to receding motion (red-shifted). The pulsation phase is indicated on *the left* edge of each panel and on *the right* we quoted the pulsation phases corresponding to our observations (data are duplicated over two pulsation cycles for clarity). For each star the color bar (indicating the flux) is from 0.1 to 1.0.

[1] Interface Definition Language.

[2] http://www.astro.utoronto.ca/DDO/research/cepheids/

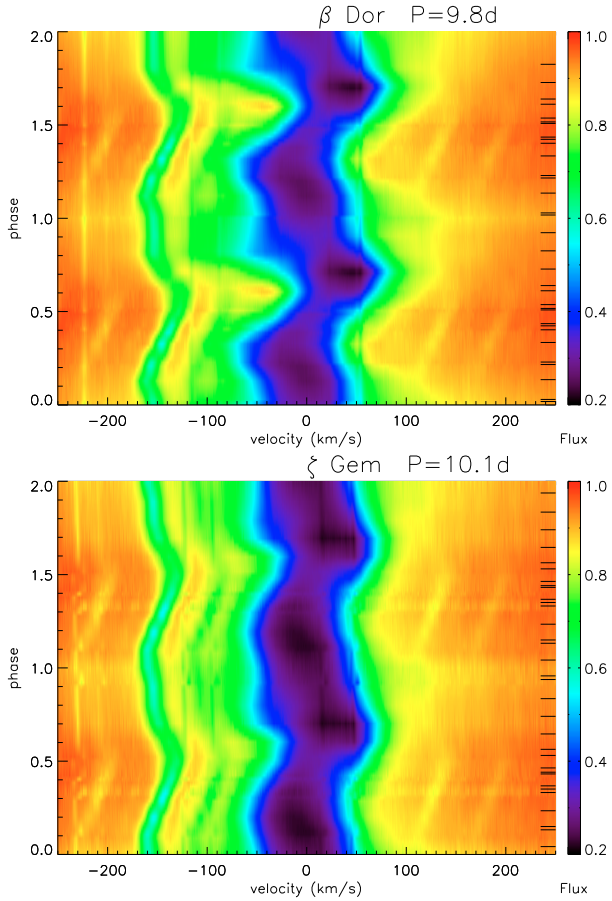


Fig. 3. Same as Fig. 2 but for the medium-period Cepheids β Dor and ζ Gem. For each star the color bar is from 0.2 to 1.0.

hydrogen emission lines might also be formed within the de-excitation region of the shockwave. We discuss the particular case of ℓ Car in Sect. 4.

3. A relationship between the period and the γ-velocities and -asymmetries

The γ-velocity (resp. γ-asymmetry) is usually defined as the average of the radial velocity curve (resp. line asymmetry curve) over a complete pulsation cycle. An interpolation over the pulsation phase is then absolutely required to derive the γ-velocity (resp. γ-asymmetry) properly. This method is referred hereafter as the 1D method. Physically, the γ-velocity is either related to star motion itself, consequently to the kinematical structure of our Galaxy, or to the dynamical structure of the spectral line-forming region. For instance, if the γ-asymmetry is not zero, then the corresponding γ-velocity is at least partially due to an intrinsic physical property of the Cepheid. Such a study has already been done by Nardetto et al. (2008, hereafter Paper III) for metallic lines.

We apply a new method here for deriving the γ-velocities (V_γ) and asymmetries (A_γ). For each star, we first derive an unweighted average spectral line profile over all pulsation phases using the interpolated profiles of the 2D map. Once the average spectral line profiles are derived for all stars (Fig. 5), the metallic line profile between -180 and -110 km s^{-1} is removed using a

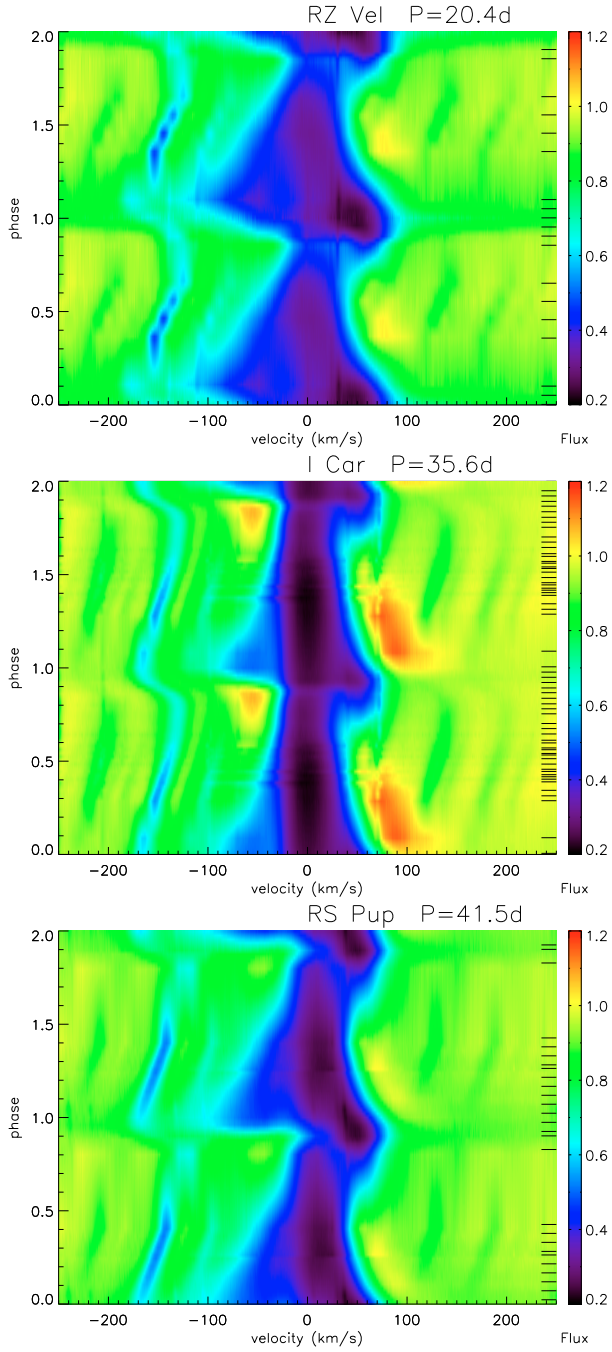


Fig. 4. Same as Fig. 2 but for the long-period Cepheids RZ Vel, ℓ Car and RS Pup. For each star the color bar is from 0.2 to 1.2.

linear interpolation (in the wavelength space). Then, we use the first-moment definition to derive V_γ:

$$V_\gamma = \frac{\int_{\rm line} \lambda S(\lambda) {\rm d}\lambda}{\int_{\rm line} S(\lambda) {\rm d}\lambda}, \quad (1)$$

where $S(\lambda)$ is the observed *average* line profile over the $[-250, 250]$ km s^{-1} velocity interval. We insist on this first-moment definition, since it is absolutely required to allow important comparisons between the γ-velocities of different Cepheids. Indeed, it is the *only* method (compared to the Gaussian fit or pixel minimum methods) that provides a radial velocity independent of the rotation (projected on the line of sight) and the natural width of the spectral line (Burki et al. 1982; Paper I). To

measure the Hα line asymmetry, we use here the method first mentioned by Sabbey et al. (1995), which uses the entire line profile. An asymmetry percentage was determined from the difference and sum of the areas of the red and blue profile halves, $\frac{(A_{\rm red}-A_{\rm blue})}{A_{\rm total}} * 100$, and the spectral channel with minimum flux was used to define the line center. The method used in Paper I, based on two semi-Gaussians, is not applicable here, providing reduced χ^2 higher than 200.

Even if this 2D-method is not *strictly* equivalent to the previous 1D-method, this approach is more robust and also easier to apply in the context of the Hα profiles. A comparison between both methods was possible for the short- and medium-period Cepheids, and we found good consistencies at a level of 2 km s^{-1} for the γ-velocity and 2% for the line asymmetry. However, the 1D-method cannot be applied for long-period Cepheids. Indeed, in this case, the Hα profiles are complex, with multiple components in absorption and/or in emission (Fig. 1), and with a significant variation from one pulsation phase to the other, implying different problems: (1) there is no obvious definition of the line asymmetry, and (2) the resulting radial velocity and asymmetry curves are extremely difficult to interpolate, making V_γ and A_γ uncertain. By deriving our Hα 2D maps, we make a very efficient 2D interpolation based on triangles, which is more robust than the usual 1D interpolation over the pulsation phase.

Statistical uncertainties (given the high S/N and the high spectral resolution) are less than 1 km s^{-1} and 1%, respectively. Uncertainties on V_γ and A_γ are clearly dominated by systematic errors. First, the choice of the velocity window [−250, 250] km s^{-1} can modify the γ-velocity and γ-asymmetry by 5 km s^{-1} and 5%, respectively, while the choice of the continuum (within 3%) also has an impact of about 6 km s^{-1} and 6%, respectively. These systematic errors mainly come from the limits of the spectral line being not clearly determined because of many blends that cannot be corrected satisfactorily (see Fig. 1). In the case of RS Pup, the phase coverage also shows a gap between 0.4 and 0.8, which keeps the 2D-interpolation from being totally secure: a break is observed in the track of the Fe 6559.763 Å metallic line near $\phi = 0.55$. However, in the case of the Hα line, the general tendency remains satisfactory (only a small unavoidable artefact is observed on the red wing at $\phi = 0.6$), which makes the average spectral line quite relevant. We quantify the impact of the phase coverage on V_γ and A_γ by artificially removing the observed spectral lines profiles of ℓ Car found between phases 0.4 and 0.8. We find a decrease in the absolute values of V_γ and A_γ of about 2 km s^{-1} and 2%, respectively. For other stars than RS Pup, the phase coverage seems satisfactory. Global uncertainties on V_γ and A_γ are finally estimated to be 8 km s^{-1} and 8% for all stars.

Following this strategy, our observations suggest a linear relationship between the period of the star and the Hα γ-velocities and γ-asymmetries:

$$V_\gamma[\mathrm{km\,s^{-1}}] = [-9.1 \pm 3.3] \log P + [12.1 \pm 8.4], \quad (2)$$

$$A_\gamma[\%] = [5.1 \pm 3.5] \log P - [0.6 \pm 8.4]. \quad (3)$$

These relationships are presented in Fig. 5. The reduced χ^2 are 1.8 and 0.7. First, the anti-correlation between these two relationships follows the expectation that the more the line is asymmetric, the larger the first moment of the spectral line. Therefore, it clearly shows that the γ-velocities obtained are due to an intrinsic physical property in Cepheids and not to their residual individual motions within the Galaxy.

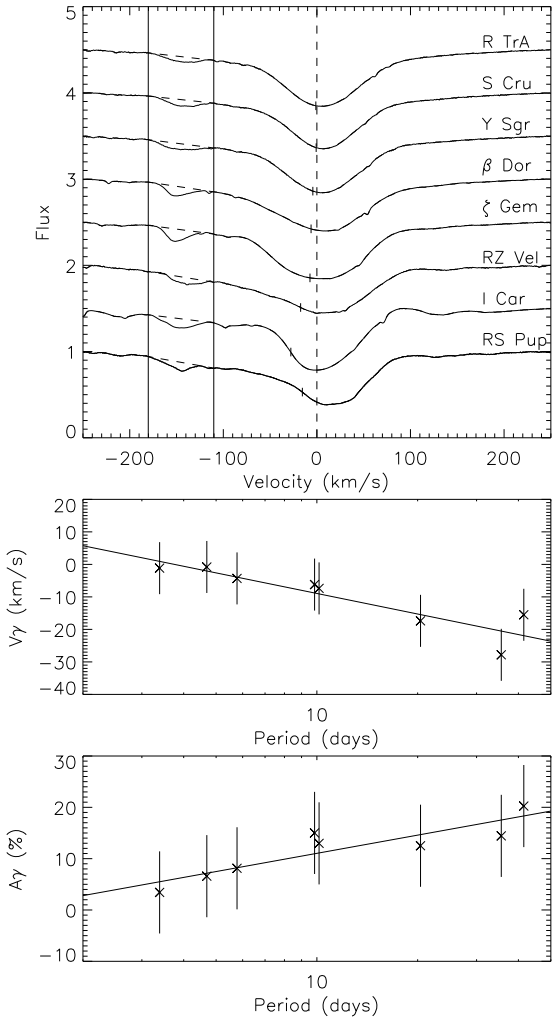


Fig. 5. For each map of Figs. 2–4 an average spectral line profile is calculated. The resulting profiles (arbitrarily shifted by 0.5 in flux) are presented by increasing period on *the upper panel* of this figure. The metallic line profile between −180 and −110 km s^{-1} is removed using a linear interpolation (dashed lines), and for each star we derive the first moment of the average spectral line profile (V_γ, indicated on each profile by a vertical line) and the spectral line asymmetry (A_γ).

Different physical mechanisms can be proposed to explain non-zero γ-asymmetries (or -velocities): (1) the dynamical structure of the Cepheids' atmosphere and in particular a velocity gradient, and (2) the differential velocity of the line-forming region compared to the corresponding mass elements. However, it has been shown that the γ-asymmetries averaged over 17 metallic spectral lines (Table 1, Paper II) are only a few percent, and they show a decrease with the period of the Cepheid (Fig. 5, Paper III). In comparison, γ-asymmetries measured for the Hα line profiles increase with the period and reach 20% for long-period Cepheids. As a consequence, we suggest that γ-asymmetries (or -velocities) corresponding to metallic and Hα lines are the result of different physical mechanisms. Then, even if the γ-velocities of Hα line profiles might be partially due to the dynamical structure of the Cepheids' atmosphere, it seems reasonable to also invoke some possible permanent mass loss from Cepheids with typical velocities *projected on the line-of-sight* up to −20 km s^{-1}. Moreover, it should be mentioned that our results do not exclude a variation in the mass loss rate with the pulsation phase. Historically, Deasy (1988) examined the

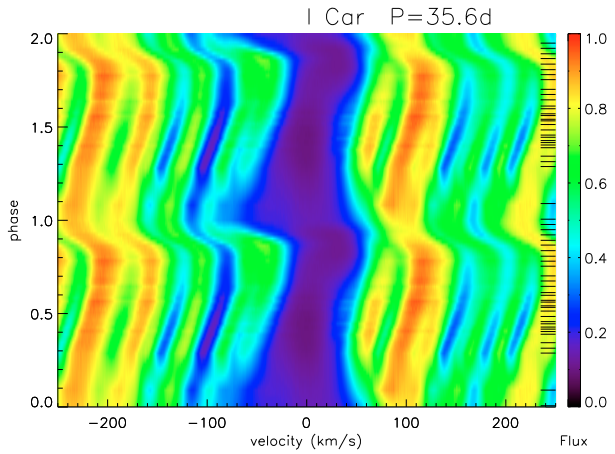


Fig. 6. Time variation of the Hβ profile of ℓ Car in the [−250, 250] km s^{-1} velocity range.

evidence of mass loss from classical Cepheid variables based on infrared and ultraviolet observations. Mass loss rates derived for several stars range between 10^{-10} $M_\odot$ yr^{-1} and 10^{-6} $M_\odot$ yr^{-1}. Moreover, the mass loss seems greater in long-period Cepheids (Willson et al. 1988; Kervella et al. 2008), which is consistent with our results.

Interestingly, from a careful analysis of the period-V_γ relationship, and taking the errors into account, it is also possible that the stars are separated into two groups, with $V_\gamma \simeq 0$ km s^{-1} (for $P < 10$ days) and $V_\gamma \simeq -20$ km s^{-1} (for $P > 20$ days). If this is true, and the high absolute value of V_γ for long-period Cepheids is indeed due to permanent mass loss, there might be a minimum threshold value of the period to initiate the permanent mass loss.

The Hδ, Hγ, and Hβ hydrogen spectral lines, which are expected to form between the metallic and the Hα line-forming regions, are unfortunately extremely blended, which prevents us from applying our 1D or 2D-methods for determining V_γ and A_γ satisfactorily. As an example, the Hβ profile of ℓ Car is presented in Fig. 6.

To interpret these relationships and to tell which part is related to the dynamical structure of the Cepheids' atmosphere and which to a permanent mass loss, fully consistent hydrodynamical models are required, including pulsating and evolutionary theories, convective energy transport, adaptive numerical meshes, and a refined calculation of the radiative transfer within the pulsating atmosphere and also in the expected circumstellar envelope of the Cepheids. Such detailed modeling is beyond the scope of this paper.

4. The particular case of ℓ Car

The long period Cepheid ℓ Car has the largest apparent angular diameter on the sky, allowing high-precision spectro-interferometric measurements. Thus, ℓ Car is an ideal candidate for further observational and theoretical investigations.

Historically, Dawe (1969) showed that the Ca II k line has one blue emission and two absorption components that are not all directly linked to pulsation. In particular, the material seems to be accelerated outwards, which suggests an expansion or an outflow. Schmidt & Parsons (1984) inferred from the variation of Mg II h and k profiles that the central absorption has a circumstellar origin, while the increase in the emission around phase of light maximum is related to a shock wave. This latter is confirmed by Böhm-Vitense & Love (1994), who estimated a shock velocity of 100 km s^{-1}, i.e., on the order of the escape velocity: mass loss is enabled from pulsation, as also pointed out by Deasy (1988). A closer look at the Mg II profiles led the authors to suggest that the quantity of mass ejected at each pulsation period is different. However, Taylor et al. (1997) see no cycle-to-cycle variations in the low photosphere where metallic lines are formed. Hence, interactions between the propagating wave and the atmosphere seem to play a major role. Böhm-Vitense & Love (1994) also pointed out the presence of a circumstellar shell and emission blobs in O I profiles at a distance of about 1000 AU from the star. Baldry et al. (1997) confirmed the presence of mass loss and of a circumstellar shell from the variation in the Hα line.

From our observation (Fig. 4), we find that the Hα profile of ℓ Car is composed of:

- an absorption component more or less following the pulsation of the star;
- a dominant absorption component whose velocity (pixel corresponding to the minimum of the spectral line) is nearly zero km s^{-1} in the stellar rest frame (Rodgers & Bell 1968; Baldry et al. 1997). This means it does not take part in the pulsation, and we attribute this component to a circumstellar shell, which is certainly the result of the on going permanent mass loss of ℓ Car. This component might also be present for other Cepheids, even if it should then be quite weak since it is not observed in the data;
- near $\phi = 0$, a red emission component appears (around 100 km s^{-1}) whose velocity and intensity slowly decreases until $\phi = 0.5$. This red emission has a maximum of 1.17 ± 0.01 (17% of the continuum) near $\phi = 0.08$;
- near $\phi = 0.6$, a blue emission appears (around −55 km s^{-1}) and reaches its peak at $\phi = 0.84$ with a maximum in flux of 1.1 ± 0.01, and decreases again up to phase 0.9;
- the positive asymmetry of the Hα line (especially at phases between 0.0 and 0.3) is certainly related to some permanent mass loss around the star as discussed in Sect. 3.

In contrast to ℓ Car, RZ Vel, and RS Pup show very weak red emission components, respectively 1.02 ± 0.01 and 1.01 ± 0.01. Such Hα spectral line characterization is extremely important to support future hydrodynamical modeling.

5. Conclusion

We presented very high-quality time series of Hα profile variations of Cepheids. For the first time, is was possible to derive 2-dimensional wavelength versus time maps. The short-period Cepheids show typical Hα line profiles that follow the pulsating envelope of the star, while long-period Cepheids exhibit a more complex spectroscopic behavior. Using these maps, we found new relationships between the period of Cepheids and their γ-velocities and asymmetries. These results may be related to the whole dynamical structure of Cepheids and also to some permanent mass loss in Cepheids. This kind of relationship, together with the shape of Hα profiles, remain extremely difficult to explain and require further theoretical investigations, which include the hydrodynamics and radiative transfer in the pulsating atmospheres of Cepheids and their circumstellar envelopes.

Acknowledgements. Based on observations collected at La Silla Observatory, Chile, in the framework of European Southern Observatory's programs 072.D-0419 and 073.D-0136. We thanks D. Bersier, P. Kervella, and P. Mathias

for useful discussions, and in particular P. Kervella for having provided the HARPS data. N.N., J.H.G., and F.M. acknowledge the Max Planck Institut for Radioastronomy for financial support.

References

Baldry, I. K., Taylor, M. M., Bedding, T. R., & Booth, A. J. 1994, MNRAS, 289, 979
Böhm-Vitense, E., & Love, S. G. 1994, ApJ, 420, 401
Burki, G., Mayor, M., & Benz, W. 1982, A&A, 109, 258
Deasy, H. P. 1988, MNRAS, 231, 673
Dawe, J. A. 1969, MNRAS, 145, 377
Fadeyev, Y. A., & Gillet, D. 2004, A&A, 420, 423
Fernie, J. D., Beattie, B., Evans, N. R., & Seager, S. 1995, IBVS, 4148
Freedman, W., Madore, B. F., Gibson, B. K., et al. 2001, ApJ, 553, 47
Fouqué, P., Arriagada, P., Storm, J., et al. 2007, A&A, 476, 73
Kervella, P., Mérand, A., Perrin, G., & Coudé Du Foresto, V. 2006, A&A, 448, 623
Kervella, P., Mérand, A., Szabado, L., et al. 2008, A&A, 480, 167
Kovacs, G., Kisvarsanyi, E. G., & Buchler, J. R. 1990, ApJ, 351, 606
Grenfell, T. C., & Wallerstein, G. 1969, PASP, 81, 732
McAlary, C. W., & Welch, D. L. 1986, AJ, 91, 1209
Mathias, P., Gillet, D., Fokin, A., et al. 2006, A&A, 457, 575
Mérand, A., Kervella, P., Coudé du Foresto, V., et al. 2006, A&A, 453, 155
Mérand, A., Aufdenberg, J. P., Kervella, P., et al. 2007, ApJ, 664, 1093
Nardetto, N., Fokin, A., Mourard, D., et al. 2004, A&A, 428, 131
Nardetto, N., Mourard, D., Kervella, P., et al. 2006, A&A, 453, 309 (Paper I)
Nardetto, N., Mourard, D., Mathias, Ph., et al. 2007a, A&A, 471, 661 (Paper II)
Nardetto, N., Mourard, D., Kervella, P., et al. 2007b, yCat, 34530309
Nardetto, N., Stoekl, A., Bersier, D., & Barnes, T. G. 2008, 489, 1255 (Paper III)
Renka, R. 1982, Interpolation of Data on the Surface of a Sphere, Oak Ridge National Laboratory Report ORNL/CSD-108
Rodgers, A. W., & Bell, R. A. 1968, MNRAS, 138, 23
Sabbey, C. N., Sasselov, D. D., Fieldus, M. S., et al. 1995, ApJ, 446, 250
Sasselov, D. D., & Karovska, M. 1994, ApJ, 432, 367
Schmidt, E. G., & Parsons, S. B. 1984, ApJ, 279, 202
Taylor, M. M., Albrow, M., Booth, A. J., et al. 1997, MNRAS, 292, 662
Wallerstein, G. 1972, PASP, 84, 656
Wallerstein, G. 1979, PASP, 91, 772
Wallerstein, G. 1983, PASP, 95, 422
Wallerstein, G., Jacobsen, T. S., Cottrell, P. L., Clark, M., & Albrow, M. 1992, MNRAS, 259, 474
Willson, L. A., Bowen, G. H., & Struck-Marcell, C. 1988, ComAp, 12, 17

Annexe P

VEGA/CHARA interferometric observations of Cepheids. I. A resolved structure around the prototype classical Cepheid δ Cep in the visible spectral range

A&A 593, A45 (2016)
DOI: 10.1051/0004-6361/201528005
© ESO 2016

Astronomy & Astrophysics

VEGA/CHARA interferometric observations of Cepheids

I. A resolved structure around the prototype classical Cepheid δ Cep in the visible spectral range⋆

N. Nardetto[1], A. Mérand[2], D. Mourard[1], J. Storm[3], W. Gieren[4,5], P. Fouqué[6], A. Gallenne[2,4], D. Graczyk[4,5,7], P. Kervella[8,9], H. Neilson[10], G. Pietrzynski[7], B. Pilecki[7], J. Breitfelder[8], P. Berio[1], M. Challouf[1,11], J.-M. Clausse[1], R. Ligi[1], P. Mathias[12,13], A. Meilland[1], K. Perraut[14,15], E. Poretti[16], M. Rainer[16], A. Spang[1], P. Stee[1], I. Tallon-Bosc[17], and T. ten Brummelaar[18,19]

(Affiliations can be found after the references)

Received 18 December 2015 / Accepted 6 June 2016

ABSTRACT

Context. The B-W method is used to determine the distance of Cepheids and consists in combining the angular size variations of the star, as derived from infrared surface-brightness relations or interferometry, with its linear size variation, as deduced from visible spectroscopy using the projection factor. The underlying assumption is that the photospheres probed in the infrared and in the visible are located at the same layer in the star whatever the pulsation phase. While many Cepheids have been intensively observed by infrared beam combiners, only a few have been observed in the visible.

Aims. This paper is part of a project to observe Cepheids in the visible with interferometry as a counterpart to infrared observations already in hand.

Methods. Observations of δ Cep itself were secured with the VEGA/CHARA instrument over the full pulsation cycle of the star.

Results. These visible interferometric data are consistent in first approximation with a quasi-hydrostatic model of pulsation surrounded by a static circumstellar environment (CSE) with a size of $\theta_{\rm CSE} = 8.9 \pm 3.0$ mas and a relative flux contribution of $f_{\rm CSE} = 0.07 \pm 0.01$. A model of visible nebula (a background source filling the field of view of the interferometer) with the same relative flux contribution is also consistent with our data at small spatial frequencies. However, in both cases, we find discrepancies in the squared visibilities at high spatial frequencies (maximum 2σ) with two different regimes over the pulsation cycle of the star, $\phi = 0.0$–0.8 and $\phi = 0.8$–1.0. We provide several hypotheses to explain these discrepancies, but more observations and theoretical investigations are necessary before a firm conclusion can be drawn.

Conclusions. For the first time we have been able to detect in the visible domain a resolved structure around δ Cep. We have also shown that a simple model cannot explain the observations, and more work will be necessary in the future, both on observations and modelling.

Key words. techniques: interferometric – circumstellar matter – stars: oscillations

1. Introduction

The Baade-Wesselink (BW) method for the distance determination of Cepheids is, in its first version, purely spectro-photometric (Lindemann 1918; Baade 1926; Wesselink 1946). Results by Fouqué et al. (2007) and Storm et al. (2011a,b) illustrate the central and current role of this method in the distance scale calibration, even if recent calibrations of the Hubble constant rely exclusively on the trigonometric parallaxes of a few Galactic Cepheids (Riess et al. 2011; Benedict et al. 2007). The first interferometric version of the BW method was attempted in the visible by Mourard et al. (1997), and soon afterward in the infrared by Kervella et al. (1999, 2001) and Lane et al. (2000). Since then, the infrared interferometric BW method has been applied to a significant number of Cepheids, twelve in total (see Table 1), while among these stars only four have been observed by visible interferometers, and the pulsation could actually be resolved for only one of them, ℓ Car (Davis et al. 2009).

The principle of the interferometric version of the BW method is simple. Interferometric measurements lead to angular diameter estimations over the whole pulsation period, while the stellar radius variations can be deduced from the integration of the pulsation velocity. The latter is linked to the observational velocity deduced from spectral line profiles by the projection factor p (Nardetto et al. 2004; Mérand et al. 2005; Nardetto et al. 2007, 2009).

There are several underlying assumptions to the BW method. First, the limb-darkening of the star is assumed to be constant during the pulsation cycle. This has no impact on the interferometric analysis, at least in the infrared (Kervella et al. 2004), while in the visible Davis et al. (2009) reported the need to take into account a limb-darkening variation from Sydney University Stellar Interferometer (SUSI) observations. On the theoretical side, Nardetto et al. (2006a) found via hydrodynamical simulation that considering a constant limb darkening in the visible leads to a systematic shift of about 0.02 in phase on the angular diameter curve, which basically means that there is no impact on the derived distance (because the amplitude of the angular diameter curve is unchanged). Second, the projection-factor, mostly dominated by the limb-darkening calculated in the visible

⋆ The data are available on the Jean-Marie Mariotti Center OiDB service (http://oidb.jmmc.fr) and at the CDS via anonymous ftp to cdsarc.u-strasbg.fr (130.79.128.5) or via http://cdsarc.u-strasbg.fr/viz-bin/qcat?J/A+A/593/A45

A&A 593, A45 (2016)

Table 1. Cepheids for which an interferometric BW method has been applied.

Cepheids	Reference
visible	
δ Cep*	Mourard et al. (1997)
α UMi*, ζ Gem*, δ Cep*, η Aql*	Nordgren et al. (2000)
δ Cep*, η Aql*	Armstrong et al. (2001)
ℓ Car	Davis et al. (2009)
H band	
ζ Gem	Lane et al. (2000)
ζ Gem, η Aql	Lane et al. (2002)
κ Pav	Breitfelder et al. (2015)
ℓ Car	Anderson et al. (2016)
X Sgr, W Sgr, ζ Gem, β Dor, ℓ Car	Breitfelder et al. (2016)
K band	
ζ Gem*	Kervella et al. (2001)
X Sgr*, η Aql, W Sgr, ζ Gem*, β Dor, Y Oph*, ℓ Car	Kervella et al. (2004)
δ Cep	Mérand et al. (2005)
Y Oph	Mérand et al. (2007)
FF Aql, T Vul	Gallenne et al. (2012)
δ Cep, η Aql	Merand et al. (2015a)

Notes. For some studies corresponding to the first attempts (indicated by asterisks) the pulsation could not be clearly resolved angularly leading to a mean value of the angular diameter of the Cepheid. In the visible domain, the BW method was applied successfully to only one Cepheid, ℓ Car, while in the infrared, among the eleven Cepheids the pulsation could be resolved for all stars, even X Sgr, which is known to be atypical likely owing to shockwaves travelling within the atmosphere (Mathias et al. 2006).

domain, is also assumed to be constant, which seems reasonable, at least in theory (Nardetto et al. 2004). Third, when applying the BW method, visible spectroscopy (e.g. Nardetto et al. 2006b) is often combined with infrared interferometric data, or even – in the recent photometric version of the BW method – with various photometric bands (Breitfelder et al. 2015). In the distance determination, we implicitly assume that the angular and linear diameters correspond to the same physical layer in the star. In this context, testing these hypotheses using visible interferometric observations seems to be of prime importance. This can be done first by simply verifying the internal consistency of the BW distances derived from visible and infrared interferometry, and then comparing them with available precise parallaxes (Benedict et al. 2007; Majaess et al. 2012).

This paper is the first in a series which investigates Cepheids with the Visible spEctroGraph and polArimeter (VEGA) beam combiner (Mourard et al. 2009) operating at the focus of the Center for High Angular Resolution Astronomy (CHARA) array (ten Brummelaar et al. 2005) located at the Mount Wilson Observatory (California, USA). The study focuses on the prototype δ Cep star. The VEGA data are first reduced (Sect. 2) and then analysed in terms of uniform disk angular diameters (Sect. 3). In Sect. 4, we show that δ Cep is clearly surrounded by a resolved structure, while some evidence in our interferometric data point toward an additional physical effect. We explore two hypotheses: a circumstellar reverberation and a strong limb-darkening variation. We draw our conclusions in Sect. 5.

2. VEGA/CHARA observations of δ Cep

The CHARA array consists of six telescopes of 1 m in diameter, spread in a Y-shaped configuration, which offers 15 different baselines from 34 m to 331 m. These baselines can achieve a spatial resolution up to 0.3 mas in the visible. The interferometric observations were secured with the VEGA/CHARA instrument. The journal of observations is presented in Tables A.1 to A.2. Given the large angular size of δ Cep, we used only two short baselines, i.e. S1S2 and E1E2, with projected baselines ranging from about 27 to 31 m for S1S2 and from 52 to 66 m for E1E2. The data were processed using the standard VEGA pipeline (Mourard et al. 2009, 2011; Ligi et al. 2013) considering different spectral bands from 3 nm (in high spectral resolution mode) to 20 nm (in medium spectral resolution mode), and with reference wavelengths ranging from 500 nm to 745 nm (the minimum and maximum wavelengths of these bands are given in Tables A.1 to A.2).

In order to calibrate the squared visibilities, we considered the references stars HD 214734 (C1) and HD 213558 (C2). The first was used to calibrate the data of β Cep presented in Nardetto et al. (2011). Several nights of VEGA observations in 2008 and 2009 were also devoted to controlling the quality of these two calibrators by comparing their transfer functions (defined as the ratio of the actual to expected squared visibility) with those of six other calibrators listed in Table 2 (hereafter C3 to C8). The consistency among the eight calibrators is shown in Fig. A.1, while the general quality of VEGA/CHARA data is illustrated in Fig. A.2.

Cycle-to-cycle variations have never been detected for δ Cep, although they have been for a few other Cepheids (Anderson 2014; Anderson et al. 2016). The data are thus recomposed into a unique cycle and the data corresponding to nights that are close in pulsation phase are merged (see phases 0.180, 0.526, 0.627 in Tables A.1 to A.2). Delta Cephei was finally observed on 20 separate nights corresponding to 17 different pulsation phases. As the observations over a given night can be spread over several hours, we first derive the phase for each observation during the night and then calculate the average and the corresponding standard deviation. The standard deviations of the pulsation phases are rather low and range from 0.001 to 0.017, except for $\phi = 0.999$ where we get an error of 0.025 because the

Table 2. List and properties of calibration stars selected with the *SearchCal* software provided by the Jean-Marie Mariotti Center (JMMC) (Bonneau et al. 2006, 2011).

Calibrator HD	Number	Spectral type	$T_{\rm eff}$ K	log g [cgs]	R	$\theta_{\rm UD}$ (R band) [mas]
HD 214734	C1	A3IV	8600	4.2	5.073	0.327 ± 0.023
HD 213558	C2	A1V	9500	4.1	3.770	0.458 ± 0.033
HD 195725	C3	A7III	8000	3.3	4.050	0.617 ± 0.044
HD 182564	C4	A2IIIs	9380	3.4	4.550	0.377 ± 0.027
HD 211336	C5	F0IV	7300	4.3	3.920	0.714 ± 0.051
HD 214454	C6	A8IV	7500	4.3	4.410	0.581 ± 0.042
HD 3360	C7	B2IV	20 900	3.9	3.740	0.284 ± 0.020
HD 192907	C8	B9III	10 500	3.4	4.410	0.346 ± 0.025

Notes. $T_{\rm eff}$ is the effective temperature, g the gravitation acceleration, R the magnitude of the calibrator in the Johnson R filter, $\theta_{\rm UD}$ the uniform disk angular diameter for the R filter of the Johnson photometric system. These parameters were adopted from Lafrasse et al. (2010) for all calibrators, except HD 195725 (C3) for which we used the *SearchCal* tool itself. C1 and C2 were used in this study to calibrate the δ Cep VEGA/CHARA data (see Fig. A.2), while C3 to C8 were used to test the robustness of the C1 and C2 calibrators (see Fig. A.1).

star was observed at the very beginning and at the very end of the night. The pulsation phases can be found in Table 3 together with their respective errors, the number of visibility measurements (N), and the baseline used. For each calibrated visibility, the statistical and systematic calibration errors are given separately. The systematic calibration errors, owing to the uncertainty on the estimation of the diameter of the reference star, were found to be negligible compared to the statistical values. Therefore, we only considered the statistical uncertainties in the model fitting. In a few cases, the statistical uncertainty was clearly underestimated. Thus, we fixed the uncertainty on the calibrated squared visibility to 0.05 (Mourard et al. 2012) for the following nights: 2012 September 23, 2013 October 26, 2013 November 26, 2014 July 02, 2014 July 05, and 2014 July 09.

3. Uniform disk (UD) angular diameters

In Figs. A.3, the calibrated visibilities corresponding to E1E2 measurements are plotted as a function of the spatial frequency together with the corresponding (u,v) coverage and for each pulsation phase. We fit these calibrated visibilities by a uniform disk using a JMMC[1] tool, *LITpro* (Tallon-Bosc et al. 2008). The results are given in Table 3 and plotted in Fig. 1 with blue crosses. The data corresponding to S1S2 measurements are shown in Fig. 2a. Owing to their low spatial frequencies, these S1S2 measurements are almost not sensitive to the pulsation of the star. This can be seen in Fig. 2b. Moreover, we have only a few S1S2 measurements per pulsation phase (four at most). Consequently, as a point of comparison with the E1E2 data, we merge the S1S2 data and fit them with a uniform disk angular diameter. The result is given in Table 3 and plotted in Fig. 1 by a horizontal dashed zone. For the data of 2014 October 24, which include both E1E2 and S1S2 baselines, we made two fits, one including all the S1S2 data and another with the E1E2 data. We overplot the very precise K-band uniform disk angular diameter curve obtained by Mérand et al. (2005) (magenta dots). To analyse our VEGA/CHARA angular diameter measurements, we consider the Spectroscopy-Photometry-Interferometry for Pulsating Stars algorithm (SPIPS; Merand et al. 2015a). The SPIPS code combines all the available observables of δ Cep: radial velocimetry (Bersier et al. 1994; Storm et al. 2004), interferometry (FLUOR/CHARA data), and photometry in

[1] http://www.jmmc.fr/litpro

Table 3. Pulsation phases, number of visibility measurements (N), resulting uniform disk angular diameters, and reduced χ^2.

ϕ	N	$\theta_{\rm UD}$ [mas]	$\chi^2_{\rm red}$	Baseline
0.300	2	$1.705_{\pm 0.035}$	0.9	S1S2
$0.543_{\pm 0.009}$	4			S1S2
$0.666_{\pm 0.006}$	3			S1S2
$0.821_{\pm 0.012}$	3			S1S2
$0.180_{\pm 0.006}$	15	$1.418_{\pm 0.027}$	1.2	E1E2
$0.192_{\pm 0.015}$	7	$1.400_{\pm 0.010}$	0.1	E1E2
$0.292_{\pm 0.009}$	9	$1.454_{\pm 0.022}$	1.6	E1E2
$0.401_{\pm 0.003}$	4	$1.439_{\pm 0.026}$	4.4	E1E2
$0.526_{\pm 0.001}$	12	$1.425_{\pm 0.012}$	0.6	E1E2
$0.627_{\pm 0.017}$	7	$1.436_{\pm 0.019}$	0.6	E1E2
$0.741_{\pm 0.003}$	8	$1.318_{\pm 0.017}$	2.4	E1E2
$0.783_{\pm 0.002}$	15	$1.316_{\pm 0.010}$	0.9	E1E2
$0.821_{\pm 0.012}$	6	$1.393_{\pm 0.025}$	2.2	E1E2
$0.848_{\pm 0.007}$	24	$1.360_{\pm 0.020}$	3.3	E1E2
$0.893_{\pm 0.005}$	30	$1.405_{\pm 0.019}$	8.1	E1E2
$0.927_{\pm 0.003}$	8	$1.353_{\pm 0.029}$	0.9	E1E2
$0.942_{\pm 0.007}$	13	$1.408_{\pm 0.026}$	1.1	E1E2
$0.999_{\pm 0.025}$	8	$1.337_{\pm 0.016}$	1.4	E1E2

Notes. The baseline used is also indicated. The pulsation phases are calculated using the ephemeris from Kukarkin et al. (1971): T_0 = 2 427 628.86 days and P = 5.3663 days. There is no error on the phase at 0.300 since the two measurements are from the same date but at different reference wavelengths. The S1S2 data were merged in order to derive a mean uniform disk angular diameter.

the V (Berdnikov & Turner 2002; Engle et al. 2014; Kiss 1998; Moffett & Barnes 1984), J, H, and K bands (Barnes et al. 1997) in order to estimate the projection factor, the variation of the effective temperature, and the H and K band excesses. The data used for the fit for δ Cep have been published in digital form (Merand et al. 2015b). In the list of these outputs, we are particularly interested in the uniform disk angular diameter curves, calculated at 2200 nm and 800 nm, and derived directly from the framework of Merand et al. (2015a). The data are given in Table 4 and are shown in Fig. 1 by red crosses and light blue squares, respectively. In the infrared, the K-band UD angular diameter curve of SPIPS is consistent with the FLUOR/CHARA

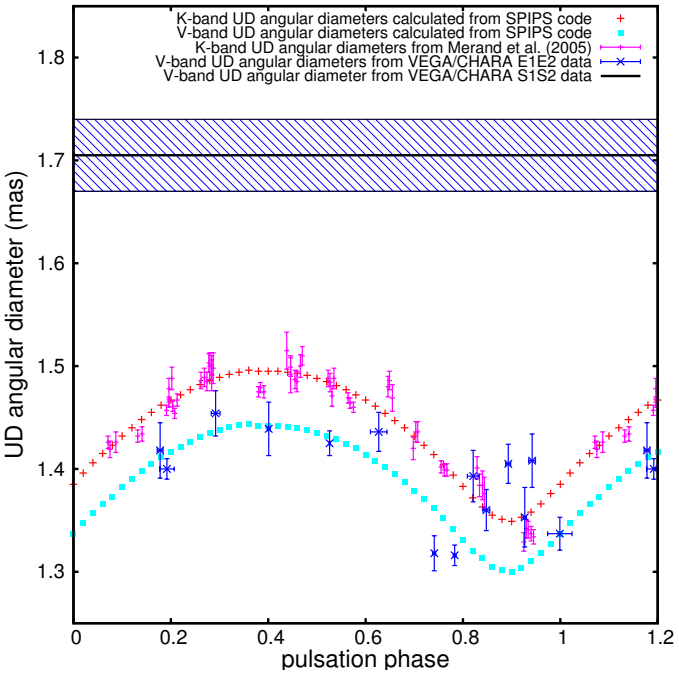


Fig. 1. Uniform disk diameters θ_{UD} derived from the VEGA/CHARA E1E2 data plotted as a function of the pulsation phase (blue crosses). The S1S2 data (corresponding to four different pulsation phases, see Table 3) were merged and the corresponding mean θ_{UD} is represented by a black horizontal line together with the 1σ uncertainty (blue dashed zone). The uniform disk angular diameter curve from FLUOR/CHARA in the K band (Mérand et al. 2005) is also shown for comparison. The red crosses and the light blue squares show the K band and R band UD angular diameter curves, respectively, as predicted from the SPIPS code (Merand et al. 2015a).

measurements. In the visible domain, the reduced χ^2 between the VEGA (E1E2) and SPIPS UD angular diameters is 9, while it increases slightly to 11 when we replace the SPIPS angular diameter variation by a constant corresponding to the average of the VEGA UD angular diameters, i.e. 1.376±0.030 mas. We thus detect a pulsation in the visible band, but make three remarks:

1. The VEGA S1S2 measurements provide a mean θ_{UD} (with a reduced χ^2 of 0.9), which is significantly larger than the E1E2 angular diameter curve by about 10σ. This suggests the presence of a large angular structure around the pulsating Cepheid.
2. The SPIPS predictions are consistent with the VEGA θ_{UD} angular diameters from 0.0 to 0.8 in phase (with a reduced χ^2 of 4). This basically means that δ Cep is pulsating in a quasi-hydrostatic way over this range of pulsation phase, even if the two measurements (at $\phi = 0.741$ and $\phi = 0.783$) are slightly below the SPIPS curve (around 2σ).
3. Five measurements between 0.8 and 1.0 are clearly from 2 to 6σ above the SPIPS curve (with a reduced χ^2 of 8).

4. Detection of a circumstellar environment or a nebulae in the visible

In Fig. 2b, the S1S2 data are fitted with a model (open symbols) composed of the UD derived from the SPIPS UD angular diameter curve at the corresponding phases of VEGA observations and a second static disk describing the circumstellar environment (CSE). The orientation of the S1S2 measurements in the

Table 4. Angular diameters as derived from the application of the SPIPS algorithm to δ Cep, using photometry, interferometry, and the cross-correlated radial velocity curves as inputs (see Merand et al. 2015a).

Phase	θ_{Ross}	$\theta_{UD}[0.8\ \mu m]$	$\theta_{UD}[2.2\ \mu m]$
0.00	1.399	1.337	1.385
0.02	1.409	1.347	1.396
0.04	1.420	1.357	1.406
0.06	1.430	1.366	1.415
0.08	1.439	1.373	1.423
0.10	1.449	1.382	1.432
0.12	1.457	1.390	1.440
0.14	1.465	1.398	1.448
0.16	1.473	1.405	1.455
0.18	1.480	1.412	1.462
0.20	1.487	1.416	1.467
0.22	1.492	1.421	1.472
0.24	1.498	1.426	1.477
0.26	1.502	1.431	1.482
0.28	1.507	1.435	1.486
0.30	1.510	1.438	1.489
0.32	1.513	1.441	1.492
0.34	1.515	1.443	1.494
0.36	1.517	1.444	1.496
0.38	1.518	1.442	1.495
0.40	1.518	1.442	1.495
0.42	1.518	1.442	1.495
0.44	1.517	1.441	1.494
0.46	1.515	1.440	1.493
0.48	1.513	1.438	1.491
0.50	1.511	1.435	1.488
0.52	1.508	1.432	1.485
0.54	1.504	1.429	1.481
0.56	1.499	1.424	1.477
0.58	1.494	1.420	1.472
0.60	1.489	1.414	1.467
0.62	1.482	1.408	1.461
0.64	1.476	1.402	1.454
0.66	1.468	1.395	1.447
0.68	1.460	1.387	1.440
0.70	1.452	1.379	1.432
0.72	1.443	1.371	1.423
0.74	1.433	1.362	1.414
0.76	1.423	1.352	1.404
0.78	1.412	1.342	1.394
0.80	1.401	1.331	1.383
0.82	1.390	1.320	1.372
0.84	1.379	1.313	1.363
0.86	1.370	1.305	1.355
0.88	1.364	1.302	1.351
0.90	1.362	1.300	1.349
0.92	1.365	1.304	1.353
0.94	1.371	1.310	1.358
0.96	1.379	1.318	1.366
0.98	1.389	1.327	1.376
	mas	mas	mas

Notes. θ_{Ross} is the Rosseland angular diameter (provided as an indication, but not used in this paper); $\theta_{UD}[0.8\ \mu m]$ and $\theta_{UD}[2.2\ \mu m]$ are the UD angular diameters calculated at 0.8 and 2.2 μm, respectively. We used a distance d of 274 ± 11 pc (Benedict et al. 2002).

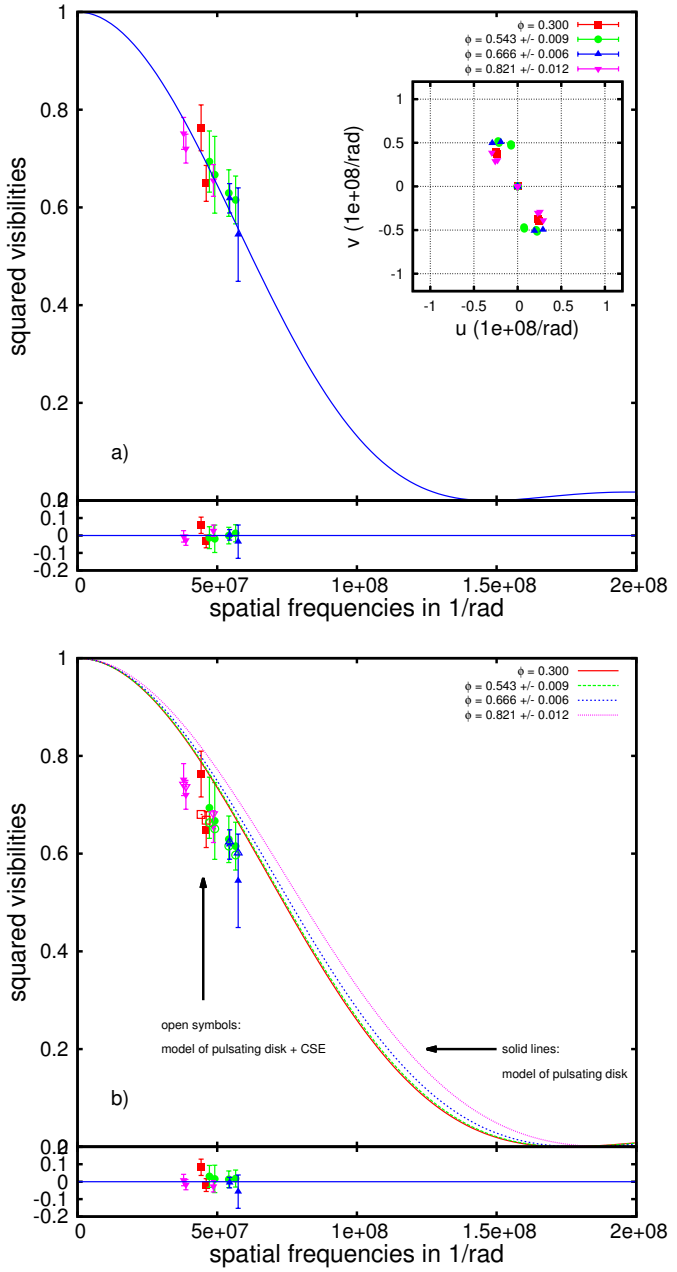


Fig. 2. a) S1S2 observed calibrated squared visibilities secured at four different pulsation phases plotted as a function of the spatial frequency together with the best fit of uniform disk model (solid blue line). In the upper right corner we show the corresponding (u, v) coverage. **b)** Same data fitted with a two-component model (open symbols) including a uniform pulsating disk and a CSE (see text). As a comparison, the solid lines are the corresponding one-component models, i.e. a uniform pulsating disk (in the R band) without the CSE.

(u, v) coverage are between 148 and 171 degrees, preventing us from investigating a non-centrosymmetric CSE. The best-fit parameters are $\theta_{\rm CSE} = 8.9 \pm 3.0$ mas (the size of the CSE) and $\frac{f_{\rm cse}}{f_\star} = 0.07 \pm 0.01$ (the relative flux contribution of the CSE, where $f_{\rm cse}$ and $f_\star$ are the fluxes of the CSE and the star in the R band, respectively) with a reduced χ^2 of 0.6. The two parameters, however, are significantly correlated (0.8) owing to the low number of S1S2 observations. Interestingly, we can also fit the S1S2 data (with the same reduced χ^2 of 0.6) using a model composed of a pulsating disk, as in the previous case, together with a background contribution of 0.07 ± 0.01 in flux filling the field of view of the interferometer. This model physically corresponds to the visible counterpart of the infrared nebulae discovered by Marengo et al. (2010) and the HI nebula found with the Very Large Array (VLA) (Matthews et al. 2012). Unfortunately, our S1S2 data are too scarce to distinguish between these two hypotheses.

We have fitted the S1S2 data with a two-component model without considering the E1E2 data. Hence, we now have to verify whether this two-component model is consistent with our E1E2 data, in particular at minimum radius. In Sect. 3, we find that the E1E2 measurements are not consistent with a quasi-hydrostatic pulsating disk at the minimum radius of the star (between phase 0.8 and 1.0).

In order to address this issue, we plot in panel a) of Fig. 3 all the VEGA visibilities measured as a function of $x = \frac{\pi B_{\rm p}[{\rm m}]\theta_{\rm UD}[{\rm mas}]}{\lambda[{\rm nm}]}$, where $\theta_{\rm UD}$ is fixed and interpolated from the SPIPS UD angular diameter curve at the corresponding pulsation phase of VEGA observations. The data are rescaled in such a way that they can be compared, despite different $\theta_{\rm UD}$ (or pulsation phases) and different wavelengths of observation. This is possible since the reference is the SPIPS $\theta_{\rm UD}$ semi-theoretical curve represented by the solid blue line expressed by $V^2(x) = |\frac{2J_1(x)}{x}|$, where J_1 is the Bessel function of the first order. This concept of pseudo-baseline was first introduced by Mérand et al. (2006). Using this approach, we confirm the three statements found in Sect. 3:

1. The S1S2 measurements, whatever the pulsation phase, are significantly lower than in the rescaled uniform disk model (see the S1S2 measurements, i.e. data with x from approximately 0.5 to 1.4, Fig. 3b). This deviation is removed as soon as we consider a resolved structure around δ Cep (see below).
2. The data with a pulsating phase from $\phi = 0.0$ to $\phi = 0.8$ are consistent with the uniform disk model for E1E2 measurements (blue crosses with x from 1.5 to 2.8 in Fig. 3b).
3. The data with a pulsating phase from $\phi = 0.8$ to $\phi = 1.0$ are not consistent with the uniform disk model for E1E2 measurements (green circles around $x = 1.7$ in Fig. 3b).

In Fig. 3a, we overplot a red dotted line to the squared visibility curve corresponding to a uniform disk surrounded by the CSE using the formula

$$V^2(x) = \left(f_\star \left| \frac{2J_1(x)}{x} \right| + f_{\rm cse} \left| \frac{2J_1(s_{\rm r}x)}{s_{\rm r}x} \right| \right)^2 , \quad (1)$$

where $f_{\rm cse} = 0.065$ and $f_\star = 0.935$ (corresponding to $\frac{f_{\rm cse}}{f_\star} = 0.07 \pm 0.01$ and $f_{\rm cse} + f_\star = 1$), $s_{\rm r}$ is the mean size ratio between the CSE and the pulsating disk. Considering the mean UD angular diameter of the SPIPS curve ($\theta_{\rm mean} = 1.39$ mas), we find $s_{\rm r} = 6.32$. The result is unchanged (i.e. within the width of the line) if we use the 6.75 and 6.07 values corresponding to the minimum and maximum UD angular diameters.

We find that the S1S2 measurements are properly fitted by this two-component model, as expected (Fig. 3c). However, around $x = 1.7$ the E1E2 measurements corresponding to $\phi = 0.0$–0.8 and $\phi = 0.8$–1.0 are respectively above and below the curve (by about 2σ). All the E1E2 measurements are partly above the curve (about 1σ) at larger frequencies ($x > 2.3$).

If we consider the model composed of a uniform disk surrounded by a background, we obtain

$$V^2(x) = \left(f_\star \left| \frac{2J_1(x)}{x} \right| \right)^2 - f_{\rm cse}^2 , \quad (2)$$

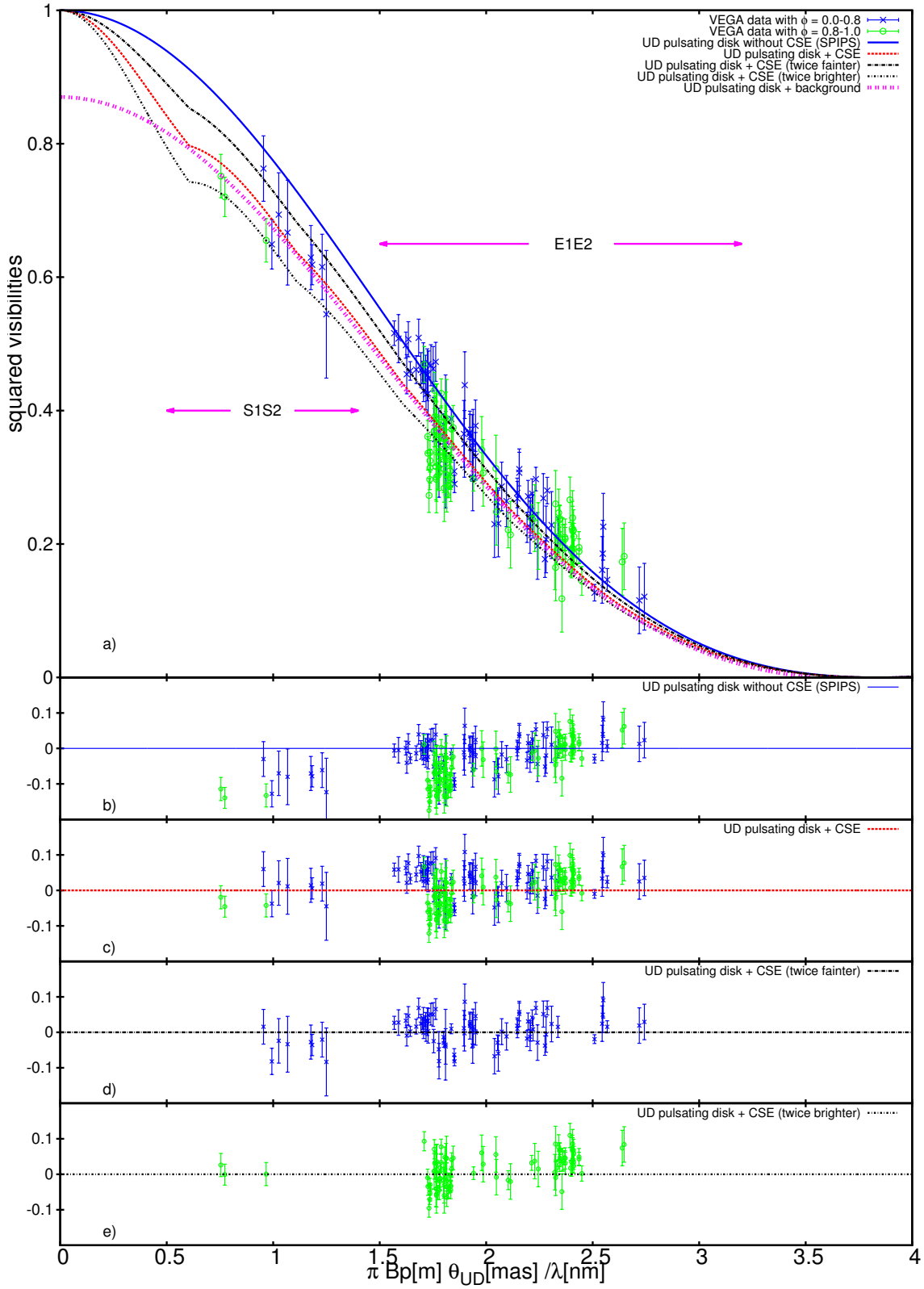


Fig. 3. Panel **a)**, the VEGA squared visibilities plotted as a function of $x = \frac{\pi B_{\rm p}[{\rm m}]\theta_{\rm UD}[{\rm mas}]}{\lambda[{\rm nm}]}$ in order to allow a comparison between data of different phases (i.e. different $\theta_{\rm UD}$) and effective wavelengths. Five models are overplotted: (1) the UD pulsating disk without CSE from the SPIPS algorithm (blue solid line); (2) the SPIPS UD pulsating disk + the CSE from Eq. (1) (red dotted line); (3) the SPIPS UD pulsating disk + the CSE from Eq. (1) but two times brighter (dashed line); (4) the SPIPS UD pulsating disk + the CSE or Eq. (1) but two times fainter (dash-dotted line); (5) the SPIPS UD pulsating disk + a background contribution filling the field of view of the interferometer (magenta dotted line). The residual between the observations and models 1 to 4 are shown in panels **b)**, **c)**, **d)**, and **e)**, respectively. In panels **d)** and **e)** we show only the data corresponding to phases intervals $\phi = 0.0{-}0.8$ and $\phi = 0.8{-}1.0$, respectively.

and the corresponding curve is plotted by a magenta dotted line in Fig. 3a. We arrive at the same conclusions as the model of the pulsating uniform disk surrounded by a CSE. In particular, we find the presence of two regimes in phase, even considering a CSE or a background. We explore two hypotheses.

First, we cannot fit all the VEGA measurements at the same time if we consider a CSE two times fainter or brighter (see black dotted and dot-dashed lines in Fig. 3a). Qualitatively, however, it seems that considering a CSE two times fainter between phase 0.0 and 0.8 is a good compromise to fit the S1S2 and E1E2 measurements together, even if not totally satisfactory (see Fig. 3d). To consider a CSE two times brighter between phase 0.8 and 1.0 (when the size of the star is at a minimum, and is hot and bright) helps to fit the data except at large spatial frequencies (see Fig. 3e). If this hypothesis is correct, then the δ Cep would light up its environment (CSE or background) differently at maximum and minimum radius.

The second possibility is to consider that the CSE (or the background) has a constant brightness and that the discrepancy found for E1E2 measurements comes mainly from an additional structure angularly smaller ($\phi = 0.0-0.8$) or larger ($\phi = 0.8-1.0$) in size than the SPIPS $\theta_{\rm UD}$ stellar pulsating disk, for instance a strong limb-darkening variation. The limb-darkening coefficient, defined as $k = \frac{\theta_{\rm UD}}{\theta_{\rm LD}}$, is used to convert the $\theta_{\rm UD}$ diameters into limb-darkened $\theta_{\rm LD}$ angular diameters. The k coefficient variation in the visible band (at 600 nm) and over the cycle of pulsation of the star is found to be from the hydrodynamical model of 0.015 (Nardetto et al. 2006a), which corresponds to about 1%. Similarly, Marengo et al. (2002, 2003) have found a variation for the k-parameter of about 0.01 and 0.02 for ζ Gem and at 570 nm using quasi-hydrostatic and hydrodynamical models, respectively. Also for comparison, Davis et al. (2009) used a phase-dependent k-parameter to analyse their SUSI data of ℓ Car, and found a variation of 0.012. This means typically a 1% difference in $\theta_{\rm UD}$, and thus a 1% difference in x, which corresponds to 0.02 in absolute value around $x = 1.7$ in Fig. 3. Consequently, the limb-darkening variation of δ Cep is one order of magnitude lower than the discrepancies found for the E1E2 measurements. In the case of δ Cep, the theoretical average value of k is of 0.954 (Nardetto et al. 2006a). So far, the only published direct measurement of the limb-darkening coefficient of a Cepheid (in the visible) has been performed by Pilecki et al. (2013) for a Cepheid ($P = 3.80$ d) in an eclipsing binary system in the LMC. They find the limb-darkening effect to be much stronger than expected for a star of that temperature, giving a possible range for k from 0.91 to 0.93, assuming however no temperature dependence. Recently, Gieren et al. (2015) studied another Cepheid in the LMC ($P = 2.99$ d) and found a similar rather strong limb-darkening effect. If we consider the lower k value found by Pilecki et al. (2013), all the E1E2 measurements in Fig. 3 should translate towards lower values of $x - 4\%$ or about 0.06. The measurements in blue crosses in the figure would be better fitted, while green open circles would not (in particular near $x \simeq 1.7$). The limb-darkening effect is probably not the key issue to explain the discrepancy found for the E1E2 measurements.

5. Discussion

We observed δ Cep intensively on twenty nights. The initial purpose of these observations was to apply the BW method, but instead we detected for the very first time a static resolved structure around δ Cep contributing to about 7% of the total flux in the visible. This is not totally surprising as envelopes around Cepheids have already been discovered by long-baseline interferometry in the K band with VLTI and CHARA (Kervella et al. 2006; Mérand et al. 2006). In addition, four Cepheids have also been observed in the N band with VISIR and MIDI (Kervella et al. 2009; Gallenne et al. 2013) and one with NACO (Gallenne et al. 2011, 2012). Some evidence has also been found using high-resolution spectroscopy (Nardetto et al. 2008). From these observations, the typical size of the envelope of Cepheids seems to be around 3 stellar radii and the flux contribution from 2% to 10% of the continuum in the K band for medium- and long-period Cepheids, respectively, while it is around 10% or more in the N band. However, Mérand et al. (2005) do not mention any contribution from a CSE in the case of δ Cep in their infrared FLUOR data, while Mérand et al. (2006) found an improved agreement with a larger set of data when considering a model with a CSE. They used a ring model 3.54 mas in size, 0.5 mas in width, and with a relative brightness of 1.5%, which is confirmed in Merand et al. (2015a). The processes at work in infrared and in the visible regarding the CSE are different. We expect thermal emission in the infrared and scattering in the visible. It is also worth mentioning that the mid-infrared flux in excess is not necessarily the evidence for mass loss (see e.g. Schmidt 2015) and that the resolved structure we observe around δ Cep, instead of a CSE, could be simply a visible nebulae (also contributing to 7% of the total flux), as reported in the infrared by Marengo et al. (2010) and in the radio domain by Matthews et al. (2012).

Our second result is the presence of an additional second-order discrepancy between the observations and the models (pulsating disk + CSE or pulsating disk + background) at high spatial frequencies, which is not clearly understood. One possibility could be that the star is lighting up its environment differently at minimum ($\phi \simeq 0.8-1.0$) and maximum ($\phi \simeq 0.0-0.8$) radius. This reverberation effect would then be more important in the visible than in the infrared since the contribution in flux of the CSE (or the background) in the visible band is about 7% compared to 1.5% in the infrared. Interestingly, the phase interval from 0.8 to 1.0 is usually disregarded in the infrared surface brightness version of the BW method owing to general poor agreement between spectroscopic and photometric angular diameters (Storm et al. 2011a,b). The other possibility is to consider a *static* environment with a constant brightness in time, but with an additional dynamical effect. However, from the hydrodynamical simulations and observations of Cepheids in eclipsing binary systems, it seems that the limb-darkening effect in the visible band does not vary strongly enough to reproduce the second-order discrepancy found in our interferometric observations. Also possible is a strong compression or shockwave occurring near the photosphere at the minimum radius, which is indeed the layer probed by photometry and interferometry. However, such a shock is not seen in the hydrodynamical code (Nardetto et al. 2004) or in the spectroscopic data, conversely to X Sgr, an atypical Cepheid in which a shockwave has indeed been reported (Mathias et al. 2006). Why this dynamical effect is seen in the visible band and not in the infrared is another pending question in this hypothesis. We also exclude non-radial pulsation, since very accurate space photometry does not support the detection of such modes in Galactic classical Cepheids (e.g. Poretti et al. 2015), and the previous spectroscopic campaigns would have shown up quite easily. Furthermore, Anderson et al. (2015) found the signature of a companion in recent spectroscopic data of δ Cep. The expected flux contribution is supposed to be lower than 1% in the visible, clearly not detectable by VEGA/CHARA. Finally, reverberation seems to be the more

plausible hypothesis. More interferometric data on Cepheids in the visible might shed light on it. In particular, covering the spatial frequencies properly (x from 0.2 to 3) at a unique pulsating phase (maximum and minimum radii) is probably required to go further in the analysis.

Acknowledgements. The authors acknowledge the support of the French Agence Nationale de la Recherche (ANR), under grant ANR-15-CE31-0012- 01 (project UnlockCepheids). We acknowledge financial support from "Programme National de Physique Stellaire" (PNPS) of CNRS/INSU, France. The CHARA Array is funded by the National Science Foundation through NSF grants AST-0606958 and AST-0908253 and by Georgia State University through the College of Arts and Sciences, as well as the W. M. Keck Foundation. W.G. gratefully acknowledges financial support for this work from the BASAL Centro de Astrofisica y Tecnologias Afines (CATA) PFB-06/2007, and from the Millenium Institute of Astrophysics (MAS) of the Iniciativa Cientifica Milenio del Ministerio de Economia, Fomento y Turismo de Chile, project IC120009. We acknowledge financial support for this work from ECOS-CONICYT grant C13U01. Support from the Polish National Science Center grant MAESTRO 2012/06/A/ST9/00269 is also acknowledged. EP and MR acknowledge financial support from PRIN INAF-2014. N.N., P.K., A.G., and W.G. acknowledge support from the French-Chilean exchange program ECOS- Sud/CONICYT (C13U01). This project was partially supported by the Polish Ministry of Science grant Ideas Plus. This research has made use of the SIMBAD and VIZIER databases at CDS, Strasbourg, France (`http://cdsweb.u-strasbg.fr/`), the Jean-Marie Mariotti Center `Aspro` service (`http://www.jmmc.fr/aspro`), and the electronic bibliography maintained by the NASA/ADS system. This research has made use of the Jean-Marie Mariotti Center `SearchCal` service (`http://www.jmmc.fr/searchcal`) co-developed by FIZEAU and LAOG/IPAG, and CDS Astronomical Databases SIMBAD and VIZIER (`http://cdsweb.u-strasbg.fr/`). This research has made use of the Jean-Marie Mariotti Center `LITpro` service co-developed by CRAL, IPAG, and LAGRANGE (LITpro software available at `http://www.jmmc.fr/litpro`). This research has made use of the Jean-Marie Mariotti Center `OiDB` service (`http://oidb.jmmc.fr`).

References

Anderson, R. I. 2014, A&A, 566, L10
Anderson, R. I., Sahlmann, J., Holl, B., et al. 2015, ApJ, 804, 144
Anderson, R. I., Mérand, A., Kervella, P., et al. 2016, MNRAS, 455, 4231
Armstrong, J. T., Nordgren, T. E., Germain, M. E., et al. 2001, AJ, 121, 476
Baade, W. 1926, Astron. Nachr., 228, 359
Barnes, III, T. G., Fernley, J. A., Frueh, M. L., et al. 1997, PASP, 109, 645
Benedict, G. F., McArthur, B. E., Fredrick, L. W., et al. 2002, AJ, 124, 1695
Benedict, G. F., McArthur, B. E., Feast, M. W., et al. 2007, AJ, 133, 1810
Berdnikov, L. N., & Turner, D. G. 2002, VizieR Online Data Catalog J/ApJS/137/209
Bersier, D., Burki, G., Mayor, M., & Duquennoy, A. 1994, A&AS, 108, 25
Bonneau, D., Clausse, J.-M., Delfosse, X., et al. 2006, A&A, 456, 789
Bonneau, D., Delfosse, X., Mourard, D., et al. 2011, A&A, 535, A53
Breitfelder, J., Kervella, P., Mérand, A., et al. 2015, A&A, 576, A64
Breitfelder, J., Mérand, A., Kervella, P., et al. 2016, A&A, 587, A117
Davis, J., Jacob, A. P., Robertson, J. G., et al. 2009, MNRAS, 394, 1620
Engle, S. G., Guinan, E. F., Harper, G. M., Neilson, H. R., & Remage Evans, N. 2014, ApJ, 794, 80
Fouqué, P., Arriagada, P., Storm, J., et al. 2007, A&A, 476, 73
Gallenne, A., Mérand, A., Kervella, P., & Girard, J. H. V. 2011, A&A, 527, A51
Gallenne, A., Kervella, P., & Mérand, A. 2012, A&A, 538, A24
Gallenne, A., Mérand, A., Kervella, P., et al. 2013, A&A, 558, A140
Gieren, W., Pilecki, B., Pietrzyński, G., et al. 2015, ApJ, 815, 28
Kervella, P., Coudé du Foresto, V., Traub, W. A., & Lacasse, M. G. 1999, in Working on the Fringe: Optical and IR Interferometry from Ground and Space, eds. S. Unwin, & R. Stachnik, ASP Conf. Ser., 194, 22
Kervella, P., Coudé du Foresto, V., Perrin, G., et al. 2001, A&A, 367, 876
Kervella, P., Nardetto, N., Bersier, D., Mourard, D., & Coudé du Foresto, V. 2004, A&A, 416, 941
Kervella, P., Mérand, A., Perrin, G., & Coudé du Foresto, V. 2006, A&A, 448, 623
Kervella, P., Mérand, A., & Gallenne, A. 2009, A&A, 498, 425
Kiss, L. L. 1998, in A Half Century of Stellar Pulsation Interpretation, eds. P. A. Bradley, & J. A. Guzik, ASP Conf. Ser., 135, 173
Kukarkin, B. V., Kholopov, P. N., Pskovsky, Y. P., et al. 1971, in General Catalogue of Variable Stars, 3rd edn.
Lafrasse, S., Mella, G., Bonneau, D., et al. 2010, VizieR Online Data Catalog: II/300
Lane, B. F., Kuchner, M. J., Boden, A. F., Creech-Eakman, M., & Kulkarni, S. R. 2000, Nature, 407, 485
Lane, B. F., Creech-Eakman, M. J., & Nordgren, T. E. 2002, ApJ, 573, 330
Ligi, R., Mourard, D., Nardetto, N., & Clausse, J.-M. 2013, J. Astron. Instrum., 2, 40003
Lindemann, F. A. 1918, MNRAS, 78, 639
Majaess, D., Turner, D., & Gieren, W. 2012, ApJ, 747, 145
Marengo, M., Sasselov, D. D., Karovska, M., Papaliolios, C., & Armstrong, J. T. 2002, ApJ, 567, 1131
Marengo, M., Karovska, M., Sasselov, D. D., et al. 2003, ApJ, 589, 968
Marengo, M., Evans, N. R., Barmby, P., et al. 2010, ApJ, 725, 2392
Mathias, P., Gillet, D., Fokin, A. B., et al. 2006, A&A, 457, 575
Matthews, L. D., Marengo, M., Evans, N. R., & Bono, G. 2012, ApJ, 744, 53
Mérand, A., Kervella, P., Coudé du Foresto, V., et al. 2005, A&A, 438, L9
Mérand, A., Kervella, P., Coudé du Foresto, V., et al. 2006, A&A, 453, 155
Mérand, A., Aufdenberg, J. P., Kervella, P., et al. 2007, ApJ, 664, 1093
Merand, A., Kervella, P., Breitfelder, J., et al. 2015a, A&A, 584, A80
Merand, A., Kervella, P., Breitfelder, J., et al. 2015b, VizieR Online Data Catalog: J/A+A/584/A80
Moffett, T. J., & Barnes, III, T. G. 1984, ApJS, 55, 389
Mourard, D., Bonneau, D., Koechlin, L., et al. 1997, A&A, 317, 789
Mourard, D., Clausse, J. M., Marcotto, A., et al. 2009, A&A, 508, 1073
Mourard, D., Bério, P., Perraut, K., et al. 2011, A&A, 531, A110
Mourard, D., Challouf, M., Ligi, R., et al. 2012, in SPIE Conf. Ser., 8445, 0
Nardetto, N., Fokin, A., Mourard, D., et al. 2004, A&A, 428, 131
Nardetto, N., Fokin, A., Mourard, D., & Mathias, P. 2006a, A&A, 454, 327
Nardetto, N., Mourard, D., Kervella, P., et al. 2006b, A&A, 453, 309
Nardetto, N., Mourard, D., Mathias, P., Fokin, A., & Gillet, D. 2007, A&A, 471, 661
Nardetto, N., Groh, J. H., Kraus, S., Millour, F., & Gillet, D. 2008, A&A, 489, 1263
Nardetto, N., Gieren, W., Kervella, P., et al. 2009, A&A, 502, 951
Nardetto, N., Mourard, D., Tallon-Bosc, I., et al. 2011, A&A, 525, A67
Nordgren, T. E., Armstrong, J. T., Germain, M. E., et al. 2000, ApJ, 543, 972
Pilecki, B., Graczyk, D., Pietrzyński, G., et al. 2013, MNRAS, 436, 953
Poretti, E., Le Borgne, J. F., Rainer, M., et al. 2015, MNRAS, 454, 849
Riess, A. G., Macri, L., Casertano, S., et al. 2011, ApJ, 730, 119
Schmidt, E. G. 2015, ApJ, 813, 29
Storm, J., Carney, B. W., Gieren, W. P., et al. 2004, A&A, 415, 531
Storm, J., Gieren, W., Fouqué, P., et al. 2011a, A&A, 534, A94
Storm, J., Gieren, W., Fouqué, P., et al. 2011b, A&A, 534, A95
Tallon-Bosc, I., Tallon, M., Thiébaut, E., et al. 2008, in SPIE Conf. Ser., 7013
ten Brummelaar, T. A., McAlister, H. A., Ridgway, S. T., et al. 2005, ApJ, 628, 453
Wesselink, A. J. 1946, Bull. Astron. Inst. Netherlands, 10, 91

[1] Université Côte d'Azur, Observatoire de la Côte d'Azur, CNRS, Laboratoire Lagrange, UMR7293, Nice, France
e-mail: `Nicolas.Nardetto@oca.eu`
[2] European Southern Observatory, Alonso de Córdova 3107, Casilla 19001, Santiago 19, Chile
[3] Leibniz Institute for Astrophysics, An der Sternwarte 16, 14482 Potsdam, Germany
[4] Departamento de Astronomía, Universidad de Concepción, Casilla 160-C, Concepción, Chile
[5] Millenium Institute of Astrophysics, Santiago, Chile
[6] Observatoire Midi-Pyrénées, Laboratoire d'Astrophysique, UMR 5572, Université Paul Sabatier – Toulouse 3, 14 avenue Édouard Belin, 31400 Toulouse, France
[7] Nicolaus Copernicus Astronomical Center, Polish Academy of Sciences, ul. Bartycka 18, 00-716 Warszawa, Poland
[8] LESIA (UMR 8109), Observatoire de Paris, PSL, CNRS, UPMC, Univ. Paris-Diderot, 5 place Jules Janssen, 92195 Meudon, France

[9] Unidad Mixta Internacional Franco-Chilena de Astronomía, CNRS/INSU, France (UMI 3386) and Departamento de Astronomía, Universidad de Chile, Camino El Observatorio 1515, Las Condes, Santiago, Chile
[10] Department of Astronomy & Astrophysics, University of Toronto, 50 St. George Street, Toronto, ON, M5S 3H4 , Canada
[11] Laboratoire Dynamique Moléculaire et Matériaux Photoniques, UR11ES03, Université de Tunis/ESSTT, Tunisie
[12] Université de Toulouse, UPS-OMP, Institut de recherche en Astrophysique et Planétologie, Toulouse, France
[13] CNRS, UMR5277, Institut de recherche en Astrophysique et Planétologie, 14 avenue Édouard Belin, 31400 Toulouse, France
[14] Université Grenoble Alpes, IPAG, 38000 Grenoble, France
[15] CNRS, IPAG, 38000 Grenoble, France
[16] INAF–Osservatorio Astronomico di Brera, via E. Bianchi 46, 23807 Merate (LC), Italy
[17] Université de Lyon, Université Lyon 1, École Normale Supérieure de Lyon, CNRS, Centre de Recherche Astrophysique de Lyon UMR5574, 69230 Saint-Genis-Laval, France
[18] Georgia State University, PO Box 3969, Atlanta GA 30302-3969, USA
[19] CHARA Array, Mount Wilson Observatory, 91023 Mount Wilson CA, USA

A&A 593, A45 (2016)

Appendix A: VEGA observations: Log, transfer functions, and visibility curves

Table A.1. Observing log with the E1E2 baseline.

	Date [yyyy.mm.dd]	RJD [days]	HA [hour]	λ_{min} [nm]	λ_{max} [nm]	Bp [m]	PA [deg]	S/N	$V^2_{cal\pm stat\pm syst}$
$\phi = 0.180 \pm 0.006$	2013.10.26	56 591.755	2.19	535	555	65.85	–149.17	5	$0.226\ _{\pm 0.050 \pm 0.003}$
	2013.10.26	56 591.755	2.19	710	730	65.85	–149.16	7	$0.352\ _{\pm 0.050 \pm 0.003}$
	2013.10.26	56 591.755	2.19	725	745	65.85	–149.16	9	$0.438\ _{\pm 0.050 \pm 0.003}$
	2013.10.26	56 591.770	2.55	535	555	65.79	–153.92	4	$0.186\ _{\pm 0.050 \pm 0.003}$
	2013.10.26	56 591.770	2.55	710	730	65.79	–153.91	6	$0.300\ _{\pm 0.050 \pm 0.002}$
	2013.10.26	56 591.770	2.55	725	745	65.79	–153.91	7	$0.350\ _{\pm 0.050 \pm 0.003}$
	2013.10.26	56 591.785	2.91	535	555	65.72	–158.70	3	$0.161\ _{\pm 0.050 \pm 0.002}$
	2013.10.26	56 591.785	2.91	710	730	65.72	–158.70	7	$0.344\ _{\pm 0.050 \pm 0.003}$
	2013.10.26	56 591.785	2.91	725	745	65.72	–158.70	7	$0.365\ _{\pm 0.050 \pm 0.003}$
	2014.07.05	56 843.917	–1.27	730	750	62.08	–106.85	6	$0.320\ _{\pm 0.050 \pm 0.002}$
	2014.07.05	56 843.933	–0.87	730	750	63.14	–111.65	4	$0.354\ _{\pm 0.050 \pm 0.002}$
	2014.07.05	56 843.958	–0.17	490	510	64.52	–120.01	2	$0.116\ _{\pm 0.050 \pm 0.002}$
	2014.07.05	56 843.958	–0.16	660	680	64.53	–120.02	5	$0.230\ _{\pm 0.050 \pm 0.002}$
	2014.07.05	56 843.979	0.26	490	510	65.09	–125.08	2	$0.121\ _{\pm 0.050 \pm 0.002}$
	2014.07.05	56 843.979	0.26	660	680	65.10	–125.09	5	$0.231\ _{\pm 0.050 \pm 0.002}$
$\phi = 0.192 \pm 0.015$	2012.09.24	56 194.645	–2.49	547	560	57.61	–91.87	7	$0.241\ _{\pm 0.050 \pm 0.002}$
	2012.09.24	56 194.645	–2.51	710	730	57.53	–91.65	28	$0.457\ _{\pm 0.050 \pm 0.002}$
	2012.09.24	56 194.645	–2.51	730	750	57.53	–91.65	25	$0.498\ _{\pm 0.050 \pm 0.003}$
	2012.09.24	56 194.760	0.26	532	547	65.10	–125.10	9	$0.146\ _{\pm 0.050 \pm 0.002}$
	2012.09.24	56 194.760	0.26	547	560	65.10	–125.10	10	$0.127\ _{\pm 0.050 \pm 0.002}$
	2012.09.24	56 194.760	0.26	710	730	65.09	–125.06	39	$0.366\ _{\pm 0.050 \pm 0.003}$
	2012.09.24	56 194.760	0.26	730	750	65.09	–125.06	28	$0.387\ _{\pm 0.050 \pm 0.003}$
$\phi = 0.292 \pm 0.009$	2014.07.11	56 849.865	–2.14	585	600	59.09	–96.30	12	$0.312\ _{\pm 0.025 \pm 0.003}$
	2014.07.11	56 849.865	–2.14	730	750	59.08	–96.26	12	$0.454\ _{\pm 0.039 \pm 0.002}$
	2014.07.11	56 849.876	–1.87	585	600	60.10	–99.54	10	$0.225\ _{\pm 0.023 \pm 0.002}$
	2014.07.11	56 849.876	–1.88	730	750	60.09	–99.51	12	$0.387\ _{\pm 0.033 \pm 0.002}$
	2014.07.11	56 849.931	–0.57	660	680	63.80	–115.21	12	$0.262\ _{\pm 0.022 \pm 0.002}$
	2014.07.11	56 849.944	–0.24	660	680	64.40	–119.09	8	$0.286\ _{\pm 0.036 \pm 0.002}$
	2014.07.11	56 849.972	0.45	610	630	65.30	–127.45	7	$0.269\ _{\pm 0.037 \pm 0.003}$
	2014.07.11	56 849.984	0.72	610	630	65.52	–130.73	6	$0.177\ _{\pm 0.027 \pm 0.002}$
	2014.07.11	56 849.984	0.72	630	650	65.52	–130.73	6	$0.225\ _{\pm 0.039 \pm 0.002}$
$\phi = 0.401 \pm 0.003$	2012.08.29	56 168.980	3.91	700	720	65.51	–172.09	22	$0.290\ _{\pm 0.013 \pm 0.002}$
	2012.08.29	56 168.980	3.91	720	740	65.51	–172.09	29	$0.362\ _{\pm 0.012 \pm 0.003}$
	2012.08.29	56 169.013	4.70	700	720	65.47	177.14	18	$0.309\ _{\pm 0.017 \pm 0.002}$
	2012.08.29	56 169.013	4.70	720	740	65.47	177.14	24	$0.379\ _{\pm 0.016 \pm 0.003}$
$\phi = 0.526 \pm 0.001$	2013.07.23	56 497.003	1.90	525	540	65.87	–145.43	3	$0.094\ _{\pm 0.036 \pm 0.001}$
	2013.07.23	56 497.003	1.90	540	555	65.87	–145.43	12	$0.133\ _{\pm 0.011 \pm 0.002}$
	2013.07.23	56 497.003	1.90	710	730	65.87	–145.43	11	$0.307\ _{\pm 0.029 \pm 0.002}$
	2014.07.07	56 845.819	–3.51	514	527	52.67	–78.48	9	$0.307\ _{\pm 0.036 \pm 0.003}$
	2014.07.07	56 845.819	–3.51	527	542	52.67	–78.48	7	$0.264\ _{\pm 0.038 \pm 0.002}$
	2014.07.07	56 845.819	–3.51	695	715	52.66	–78.46	14	$0.508\ _{\pm 0.036 \pm 0.003}$
	2014.07.07	56 845.831	–3.26	514	527	53.95	–81.85	8	$0.241\ _{\pm 0.029 \pm 0.002}$
	2014.07.07	56 845.831	–3.26	527	542	53.95	–81.85	10	$0.268\ _{\pm 0.026 \pm 0.002}$
	2014.07.07	56 845.831	–3.26	695	715	53.94	–81.84	15	$0.454\ _{\pm 0.029 \pm 0.002}$
$\phi = 0.627 \pm 0.017$	2013.10.23	56 588.841	4.12	710	730	65.50	–174.91	10	$0.377\ _{\pm 0.039 \pm 0.003}$
	2013.10.23	56 588.841	4.12	725	740	65.50	–174.91	10	$0.361\ _{\pm 0.038 \pm 0.003}$
	2013.10.23	56 588.877	4.91	710	730	65.50	174.27	9	$0.331\ _{\pm 0.036 \pm 0.003}$
	2013.10.23	56 588.877	4.91	725	740	65.50	174.27	14	$0.367\ _{\pm 0.027 \pm 0.003}$
	2014.07.02	56 840.912	–1.51	580	595	61.35	–103.99	4	$0.197\ _{\pm 0.050 \pm 0.002}$
	2014.07.02	56 840.912	–1.51	730	750	61.35	–103.98	7	$0.354\ _{\pm 0.050 \pm 0.002}$
	2014.07.02	56 840.930	–1.13	580	595	62.46	–108.48	4	$0.207\ _{\pm 0.050 \pm 0.002}$
	2014.07.02	56 840.930	–1.13	730	750	62.46	–108.47	7	$0.349\ _{\pm 0.050 \pm 0.002}$

Notes. The columns give, respectively, the date, the RJD, the hour angle (HA), the minimum and maximum wavelengths over which the squared visibility is calculated, the projected baseline length Bp and its orientation PA, the signal-to-noise ratio on the fringe peak; the last column provides the calibrated squared visibility V^2 together with the statistic error on V^2, and the systematic error on V^2 (see text for details). The data are available on the Jean-Marie Mariotti Center `OiDB` service (`http://oidb.jmmc.fr`), and at the CDS.

Table A.1. continued.

	Date [yyyy.mm.dd]	RJD [days]	HA [hour]	λ_{min} [nm]	λ_{max} [nm]	Bp [m]	PA [deg]	S/N	$V^2_{cal\pm stat\pm syst}$
$\phi = 0.741 \pm 0.003$	2012.09.27	56 197.642	–2.40	532	547	58.02	–93.06	11	$0.272\ _{\pm 0.024 \pm 0.003}$
	2012.09.27	56 197.642	–2.40	547	560	58.02	–93.06	12	$0.277\ _{\pm 0.022 \pm 0.003}$
	2012.09.27	56 197.642	–2.42	710	730	57.92	–92.79	33	$0.459\ _{\pm 0.014 \pm 0.003}$
	2012.09.27	56 197.642	–2.42	730	750	57.92	–92.79	28	$0.516\ _{\pm 0.018 \pm 0.003}$
	2012.09.27	56 197.665	–1.79	532	547	60.39	–100.54	14	$0.280\ _{\pm 0.020 \pm 0.003}$
	2012.09.27	56 197.665	–1.79	547	560	60.39	–100.54	17	$0.297\ _{\pm 0.018 \pm 0.003}$
	2012.09.27	56 197.665	–1.80	710	730	60.37	–100.47	30	$0.459\ _{\pm 0.015 \pm 0.003}$
	2012.09.27	56 197.665	–1.80	730	750	60.37	–100.47	19	$0.507\ _{\pm 0.026 \pm 0.003}$
$\phi = 0.783 \pm 0.002$	2013.10.24	56 589.603	–1.61	547	562	61.03	–102.77	12	$0.275\ _{\pm 0.022 \pm 0.003}$
	2013.10.24	56 589.603	–1.61	705	725	61.03	–102.77	18	$0.424\ _{\pm 0.023 \pm 0.003}$
	2013.10.24	56 589.603	–1.61	710	730	61.03	–102.77	26	$0.430\ _{\pm 0.016 \pm 0.003}$
	2013.10.24	56 589.603	–1.61	725	740	61.03	–102.77	18	$0.509\ _{\pm 0.028 \pm 0.003}$
	2013.10.24	56 589.603	–1.61	725	745	61.03	–102.77	22	$0.461\ _{\pm 0.021 \pm 0.003}$
	2013.10.24	56 589.615	–1.35	532	547	61.83	–105.83	5	$0.228\ _{\pm 0.050 \pm 0.003}$
	2013.10.24	56 589.615	–1.35	705	725	61.83	–105.83	15	$0.468\ _{\pm 0.031 \pm 0.003}$
	2013.10.24	56 589.615	–1.35	710	730	61.83	–105.83	24	$0.470\ _{\pm 0.019 \pm 0.003}$
	2013.10.24	56 589.615	–1.35	725	740	61.83	–105.83	15	$0.471\ _{\pm 0.031 \pm 0.003}$
	2013.10.24	56 589.615	–1.35	725	745	61.83	–105.83	18	$0.461\ _{\pm 0.026 \pm 0.003}$
	2013.10.24	56 589.625	–1.07	532	547	62.64	–109.25	7	$0.211\ _{\pm 0.030 \pm 0.002}$
	2013.10.24	56 589.625	–1.07	705	725	62.64	–109.25	16	$0.473\ _{\pm 0.029 \pm 0.003}$
	2013.10.24	56 589.625	–1.07	710	730	62.64	–109.25	14	$0.463\ _{\pm 0.033 \pm 0.003}$
	2013.10.24	56 589.625	–1.07	725	740	62.64	–109.25	13	$0.426\ _{\pm 0.034 \pm 0.003}$
	2013.10.24	56 589.625	–1.07	725	745	62.64	–109.25	17	$0.456\ _{\pm 0.027 \pm 0.003}$
$\phi = 0.821 \pm 0.012$	2014.10.24	56 954.655	–0.29	570	585	64.32	–118.48	11	$0.238\ _{\pm 0.021 \pm 0.003}$
	2014.10.24	56 954.655	–0.29	730	750	64.32	–118.47	13	$0.336\ _{\pm 0.025 \pm 0.002}$
	2014.10.24	56 954.678	0.24	520	535	65.07	–124.85	7	$0.145\ _{\pm 0.022 \pm 0.002}$
	2014.10.24	56 954.678	0.24	695	710	65.07	–124.84	11	$0.374\ _{\pm 0.033 \pm 0.003}$
	2014.10.24	56 954.699	0.75	660	680	65.54	–131.04	17	$0.297\ _{\pm 0.018 \pm 0.002}$
	2014.10.24	56 954.724	1.35	610	630	65.82	–138.49	8	$0.221\ _{\pm 0.027 \pm 0.002}$
$\phi = 0.848 \pm 0.007$	2013.12.17	56 643.578	1.34	532	547	65.81	–138.43	6	$0.224\ _{\pm 0.040 \pm 0.003}$
	2013.12.17	56 643.578	1.34	535	555	65.81	–138.43	11	$0.210\ _{\pm 0.020 \pm 0.003}$
	2013.12.17	56 643.578	1.34	705	725	65.81	–138.41	16	$0.321\ _{\pm 0.020 \pm 0.002}$
	2013.12.17	56 643.578	1.34	725	745	65.81	–138.41	14	$0.388\ _{\pm 0.027 \pm 0.003}$
	2013.12.17	56 643.592	1.65	532	547	65.87	–142.23	6	$0.239\ _{\pm 0.041 \pm 0.003}$
	2013.12.17	56 643.592	1.65	535	555	65.87	–142.23	6	$0.194\ _{\pm 0.031 \pm 0.003}$
	2013.12.17	56 643.592	1.64	705	725	65.87	–142.21	11	$0.274\ _{\pm 0.026 \pm 0.002}$
	2013.12.17	56 643.592	1.64	725	745	65.87	–142.21	14	$0.359\ _{\pm 0.026 \pm 0.003}$
	2013.12.17	56 643.603	1.90	705	725	65.87	–145.54	9	$0.304\ _{\pm 0.034 \pm 0.002}$
	2013.12.17	56 643.614	2.16	532	547	65.86	–148.81	6	$0.220\ _{\pm 0.037 \pm 0.003}$
	2013.12.17	56 643.614	2.16	535	555	65.86	–148.81	7	$0.208\ _{\pm 0.030 \pm 0.003}$
	2013.12.17	56 643.614	2.16	705	725	65.86	–148.77	8	$0.332\ _{\pm 0.040 \pm 0.003}$
	2013.12.17	56 643.614	2.16	725	745	65.86	–148.77	8	$0.300\ _{\pm 0.036 \pm 0.002}$
	2013.12.17	56 643.624	2.42	705	725	65.82	–152.21	6	$0.385\ _{\pm 0.062 \pm 0.003}$
	2013.12.17	56 643.624	2.42	725	745	65.82	–152.21	6	$0.379\ _{\pm 0.060 \pm 0.003}$
	2013.12.17	56 643.644	2.91	532	547	65.72	–158.69	5	$0.190\ _{\pm 0.040 \pm 0.002}$
	2013.12.17	56 643.644	2.91	705	725	65.72	–158.66	9	$0.386\ _{\pm 0.042 \pm 0.003}$
	2013.12.17	56 643.676	3.67	535	555	65.56	–168.84	8	$0.203\ _{\pm 0.026 \pm 0.003}$
	2013.12.17	56 643.676	3.67	705	725	65.56	–168.81	12	$0.357\ _{\pm 0.030 \pm 0.003}$
	2013.12.17	56 643.676	3.67	725	745	65.56	–168.81	13	$0.391\ _{\pm 0.031 \pm 0.003}$
	2013.12.17	56 643.687	3.92	532	547	65.52	–172.21	8	$0.266\ _{\pm 0.034 \pm 0.003}$
	2013.12.17	56 643.687	3.92	535	555	65.52	–172.21	6	$0.207\ _{\pm 0.032 \pm 0.003}$
	2013.12.17	56 643.687	3.91	705	725	65.52	–172.18	13	$0.390\ _{\pm 0.029 \pm 0.003}$
	2013.12.17	56 643.687	3.91	725	745	65.52	–172.18	15	$0.370\ _{\pm 0.024 \pm 0.003}$

Table A.1. continued.

	Date [yyyy.mm.dd]	RJD [days]	HA [hour]	λ_{min} [nm]	λ_{max} [nm]	Bp [m]	PA [deg]	S/N	$V^2_{cal\pm stat\pm syst}$
$\phi = 0.893 \pm 0.005$	2013.07.25	56 498.942	0.64	525	540	65.46	–129.77	8	$0.174\ _{\pm 0.022 \pm 0.003}$
	2013.07.25	56 498.942	0.64	540	555	65.46	–129.77	9	$0.191\ _{\pm 0.021 \pm 0.003}$
	2013.07.25	56 498.942	0.64	690	710	65.46	–129.77	16	$0.287\ _{\pm 0.017 \pm 0.002}$
	2013.07.25	56 498.942	0.64	710	730	65.46	–129.77	15	$0.302\ _{\pm 0.020 \pm 0.002}$
	2013.07.25	56 498.942	0.64	730	750	65.46	–129.77	15	$0.361\ _{\pm 0.024 \pm 0.002}$
	2013.07.25	56 498.961	1.04	525	540	65.71	–134.71	5	$0.194\ _{\pm 0.037 \pm 0.003}$
	2013.07.25	56 498.961	1.04	540	555	65.71	–134.71	7	$0.247\ _{\pm 0.036 \pm 0.003}$
	2013.07.25	56 498.961	1.04	690	710	65.71	–134.70	11	$0.310\ _{\pm 0.027 \pm 0.002}$
	2013.07.25	56 498.961	1.04	710	730	65.71	–134.70	11	$0.307\ _{\pm 0.027 \pm 0.002}$
	2013.07.25	56 498.961	1.04	730	750	65.71	–134.70	11	$0.273\ _{\pm 0.026 \pm 0.002}$
	2013.07.25	56 498.978	1.41	525	540	65.83	–139.32	7	$0.221\ _{\pm 0.031 \pm 0.003}$
	2013.07.25	56 498.978	1.41	540	555	65.83	–139.32	11	$0.236\ _{\pm 0.022 \pm 0.003}$
	2013.07.25	56 498.978	1.41	690	710	65.83	–139.31	17	$0.299\ _{\pm 0.017 \pm 0.002}$
	2013.07.25	56 498.978	1.41	710	730	65.83	–139.31	13	$0.340\ _{\pm 0.025 \pm 0.002}$
	2013.07.25	56 498.978	1.41	730	750	65.83	–139.31	20	$0.297\ _{\pm 0.015 \pm 0.002}$
	2013.07.25	56 498.988	1.67	525	540	65.87	–142.58	9	$0.176\ _{\pm 0.020 \pm 0.002}$
	2013.07.25	56 498.988	1.67	540	555	65.87	–142.58	12	$0.208\ _{\pm 0.017 \pm 0.003}$
	2013.07.25	56 498.988	1.67	690	710	65.87	–142.57	22	$0.299\ _{\pm 0.014 \pm 0.002}$
	2013.07.25	56 498.988	1.67	710	730	65.87	–142.57	15	$0.337\ _{\pm 0.023 \pm 0.002}$
	2013.07.25	56 498.988	1.67	730	750	65.87	–142.57	19	$0.325\ _{\pm 0.017 \pm 0.002}$
	2013.07.25	56 498.999	1.95	525	540	65.87	–146.15	11	$0.211\ _{\pm 0.020 \pm 0.003}$
	2013.07.25	56 498.999	1.95	540	555	65.87	–146.15	12	$0.238\ _{\pm 0.019 \pm 0.003}$
	2013.07.25	56 498.999	1.95	690	710	65.87	–146.14	21	$0.330\ _{\pm 0.015 \pm 0.003}$
	2013.07.25	56 498.999	1.95	710	730	65.87	–146.14	25	$0.369\ _{\pm 0.015 \pm 0.003}$
	2013.07.25	56 498.999	1.95	730	750	65.87	–146.14	18	$0.337\ _{\pm 0.018 \pm 0.002}$
	2013.07.25	56 499.010	2.16	525	540	65.86	–148.78	9	$0.186\ _{\pm 0.020 \pm 0.003}$
	2013.07.25	56 499.010	2.16	540	555	65.86	–148.78	10	$0.197\ _{\pm 0.020 \pm 0.003}$
	2013.07.25	56 499.010	2.16	690	710	65.86	–148.77	12	$0.288\ _{\pm 0.025 \pm 0.002}$
	2013.07.25	56 499.010	2.16	710	730	65.86	–148.77	13	$0.330\ _{\pm 0.025 \pm 0.002}$
	2013.07.25	56 499.010	2.16	730	750	65.86	–148.77	14	$0.314\ _{\pm 0.022 \pm 0.002}$
$\phi = 0.927 \pm 0.003$	2014.07.09	56 847.948	–0.29	580	595	64.33	–118.57	5	$0.239\ _{\pm 0.050 \pm 0.002}$
	2014.07.09	56 847.948	–0.29	735	755	64.33	–118.56	7	$0.368\ _{\pm 0.050 \pm 0.002}$
	2014.07.09	56 847.961	0.03	580	595	64.81	–122.35	4	$0.212\ _{\pm 0.050 \pm 0.002}$
	2014.07.09	56 847.961	0.03	735	755	64.81	–122.33	8	$0.390\ _{\pm 0.050 \pm 0.002}$
	2014.07.09	56 847.978	0.47	490	510	65.32	–127.66	3	$0.173\ _{\pm 0.050 \pm 0.003}$
	2014.07.09	56 847.978	0.47	660	680	65.32	–127.65	7	$0.341\ _{\pm 0.050 \pm 0.003}$
	2014.07.09	56 847.990	0.74	490	510	65.54	–130.97	4	$0.181\ _{\pm 0.050 \pm 0.003}$
	2014.07.09	56 847.990	0.74	660	680	65.53	–130.96	6	$0.307\ _{\pm 0.050 \pm 0.003}$
$\phi = 0.942 \pm 0.007$	2013.11.26	56 622.628	1.23	547	562	65.78	–137.04	4	$0.181\ _{\pm 0.050 \pm 0.002}$
	2013.11.26	56 622.628	1.23	705	725	65.78	–137.03	7	$0.327\ _{\pm 0.050 \pm 0.002}$
	2013.11.26	56 622.628	1.23	725	740	65.78	–137.03	6	$0.316\ _{\pm 0.050 \pm 0.002}$
	2013.11.26	56 622.644	1.58	547	562	65.86	–141.35	5	$0.260\ _{\pm 0.050 \pm 0.003}$
	2013.11.26	56 622.644	1.57	705	725	65.86	–141.26	6	$0.313\ _{\pm 0.050 \pm 0.002}$
	2013.11.26	56 622.644	1.57	725	740	65.86	–141.26	7	$0.363\ _{\pm 0.050 \pm 0.003}$
	2013.11.26	56 622.658	1.90	535	555	65.87	–145.46	2	$0.118\ _{\pm 0.050 \pm 0.002}$
	2013.11.26	56 622.658	1.90	547	562	65.87	–145.46	3	$0.165\ _{\pm 0.050 \pm 0.002}$
	2013.11.26	56 622.658	1.90	705	725	65.87	–145.45	6	$0.284\ _{\pm 0.050 \pm 0.003}$
	2013.11.26	56 622.658	1.90	725	740	65.87	–145.45	6	$0.297\ _{\pm 0.050 \pm 0.002}$
	2013.11.26	56 622.698	2.85	597	617	65.73	–157.82	4	$0.214\ _{\pm 0.050 \pm 0.002}$
	2013.11.26	56 622.698	2.85	617	637	65.73	–157.82	5	$0.248\ _{\pm 0.050 \pm 0.002}$
	2013.11.26	56 622.712	3.17	617	637	65.66	–162.08	6	$0.313\ _{\pm 0.050 \pm 0.003}$
$\phi = 0.999 \pm 0.025$	2013.10.25	56 590.620	–1.09	705	725	62.59	–109.03	16	$0.430\ _{\pm 0.027 \pm 0.003}$
	2013.10.25	56 590.620	–1.09	725	745	62.59	–109.03	17	$0.469\ _{\pm 0.027 \pm 0.003}$
	2013.10.25	56 590.841	4.20	532	547	65.49	–176.10	10	$0.189\ _{\pm 0.019 \pm 0.002}$
	2013.10.25	56 590.841	4.20	705	725	65.49	–176.09	19	$0.372\ _{\pm 0.019 \pm 0.003}$
	2013.10.25	56 590.841	4.20	725	745	65.49	–176.09	20	$0.426\ _{\pm 0.022 \pm 0.003}$
	2013.10.25	56 590.860	4.68	532	547	65.49	177.37	3	$0.195\ _{\pm 0.024 \pm 0.003}$
	2013.10.25	56 590.860	4.68	705	725	65.49	177.37	14	$0.346\ _{\pm 0.024 \pm 0.003}$
	2013.10.25	56 590.860	4.68	725	745	65.49	177.37	18	$0.382\ _{\pm 0.025 \pm 0.003}$

Table A.2. Observing log with the S1S2 baseline.

	Date [yyyy.mm.dd]	RJD [days]	HA [h]	λ_{min} [nm]	λ_{max} [nm]	Bp [m]	Arg [deg]	S/N	$V^2_{cal\pm stat\pm syst}$
$\phi = 0.300$	2008.08.03	54 681.988	2.36	628	632	29.01	148.13	13	$0.649\ _{\pm 0.037\pm 0.003}$
	2008.08.03	54 681.988	2.36	654	658	29.01	148.13	15	$0.763\ _{\pm 0.049\pm 0.003}$
$\phi = 0.543 \pm 0.009$	2008.07.30	54 677.894	–0.19	629	632	30.97	171.02	8	$0.667\ _{\pm 0.079\pm 0.003}$
	2008.07.30	54 677.894	–0.19	654	658	30.97	171.01	11	$0.694\ _{\pm 0.063\pm 0.003}$
	2008.07.30	54 677.958	1.37	530	533	30.08	156.84	12	$0.615\ _{\pm 0.049\pm 0.004}$
	2008.07.30	54 677.958	1.37	553	558	30.08	156.84	13	$0.629\ _{\pm 0.048\pm 0.004}$
$\phi = 0.666 \pm 0.006$	2008.08.05	54 683.928	1.10	554	559	30.29	159.25	12	$0.619\ _{\pm 0.030\pm 0.004}$
	2008.08.05	54 683.974	2.18	507	510	29.24	149.68	6	$0.544\ _{\pm 0.096\pm 0.004}$
$\phi = 0.821 \pm 0.012$	2014.10.24	56 954.792	2.99	570	585	28.10	142.69	20	$0.655\ _{\pm 0.033\pm 0.001}$
	2014.10.24	56 954.792	2.99	730	750	28.10	142.70	23	$0.752\ _{\pm 0.033\pm 0.001}$
	2014.10.24	56 954.812	3.49	695	710	27.25	138.53	24	$0.720\ _{\pm 0.030\pm 0.001}$

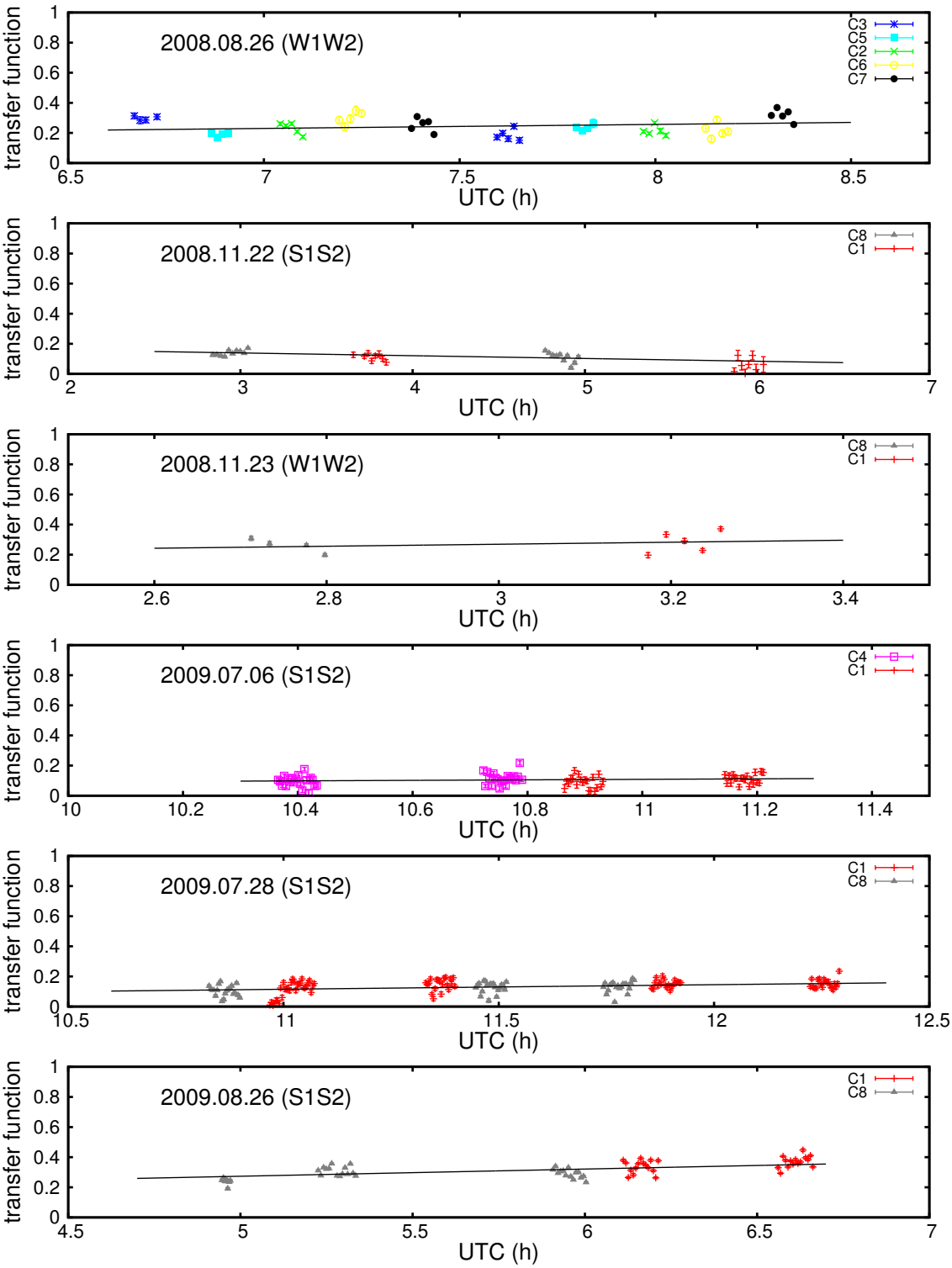


Fig. A.1. Two calibrators, C1 and C2, used to calibrate the VEGA/CHARA data of δ Cep are compared in terms of transfer functions with six other calibrators, C3 to C8 (listed in Table 2), on six different nights during 2008 and 2009. The consistency between the calibrators, which is shown by a linear fit (black line), is independent of the two-telescope baseline considered, S1S2 or W1W2.

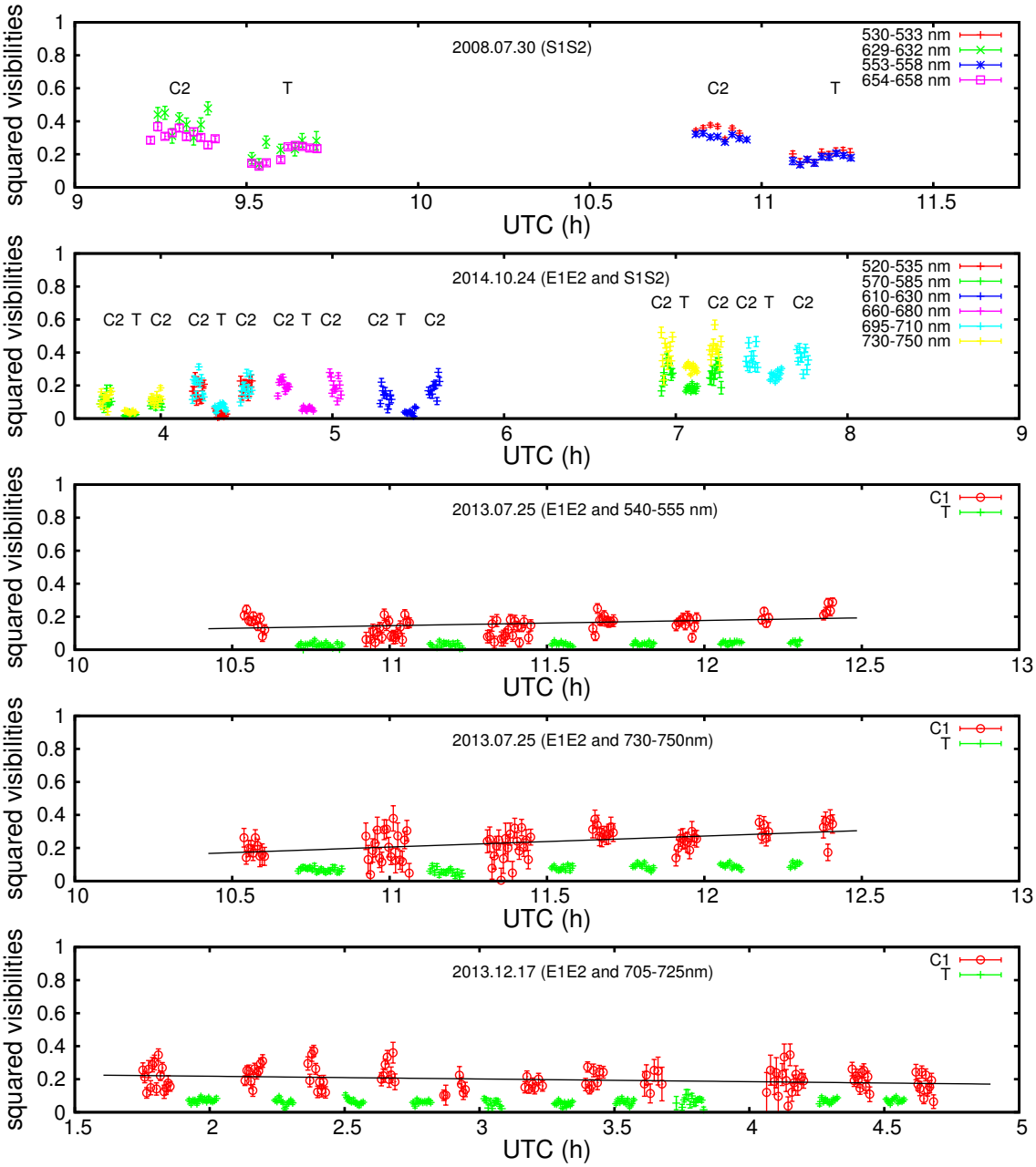


Fig. A.2. Transfer function (calculated either from the C1 or C2 calibrator) is shown together with the raw visibilities of the target (T) for four different nights in our sample, using different spectral configurations and two baselines, E1E2 and S1S2. For nights 2008 July 30 and 2014 October 24, the squared visibilities (or transfer functions) associated with calibrators C1 and C2 cannot be consistently compared as they correspond to different spectral configurations, but they are shown to illustrate the quality of the data. The 2014 October 24 observing night is the only one for which we have successive data from E1E2 (from around 3.5h to 6h in UTC) and S1S2 (from around 6.5h to 8h in UTC). For nights 2013 July 25 and 2013 December 17, the instrument configuration is the same over the entire observing time, and the stability of the transfer function is evident (black line).

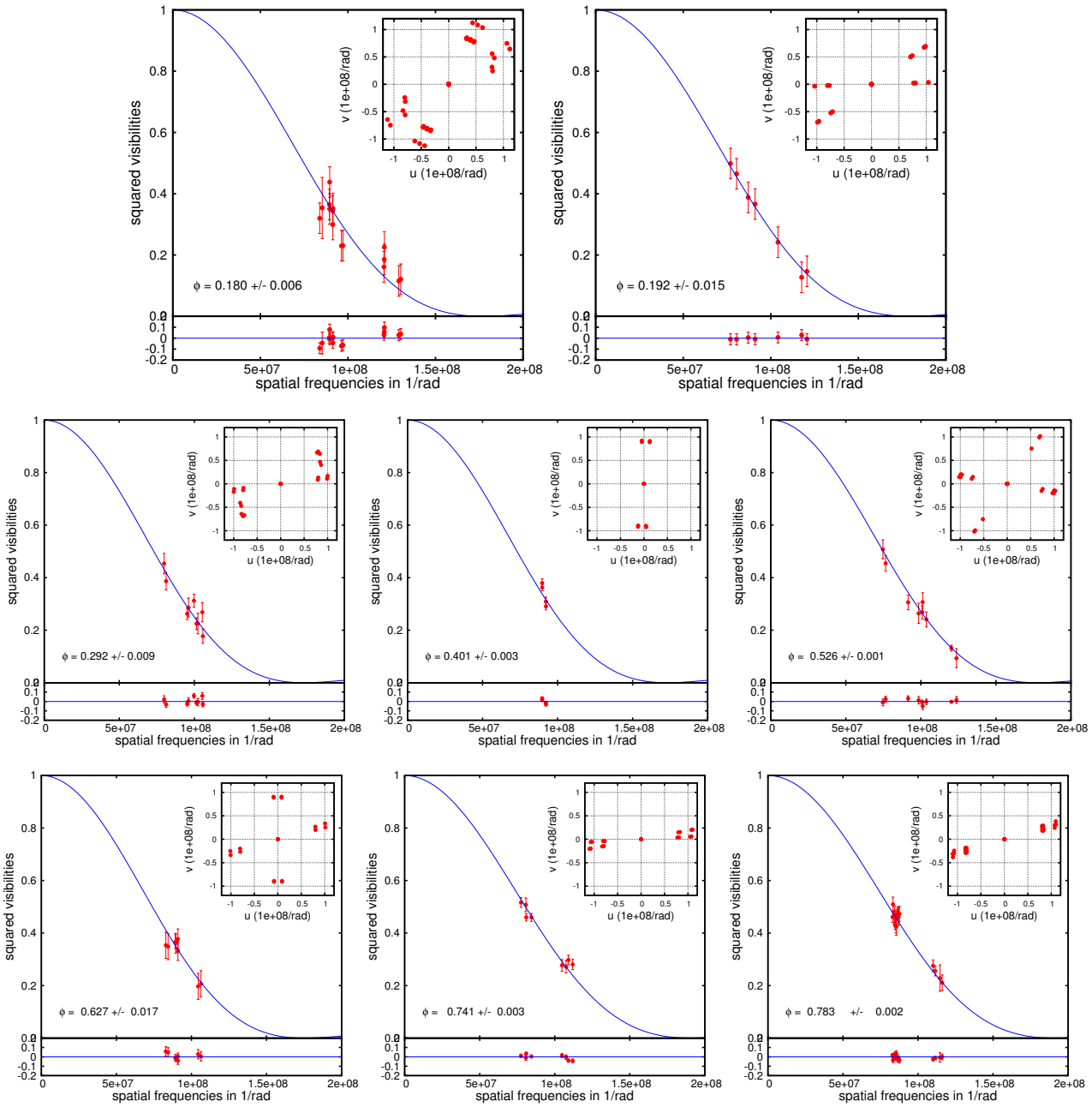


Fig. A.3. Observed calibrated squared visibilities (red dots) are plotted as a function of the spatial frequency for each pulsation phase (indicated in the lower left corner of each panel) together with the best fit of uniform disk model (solid blue line). In the upper right corner (*inset panel*) we show the corresponding (u, v) coverage.

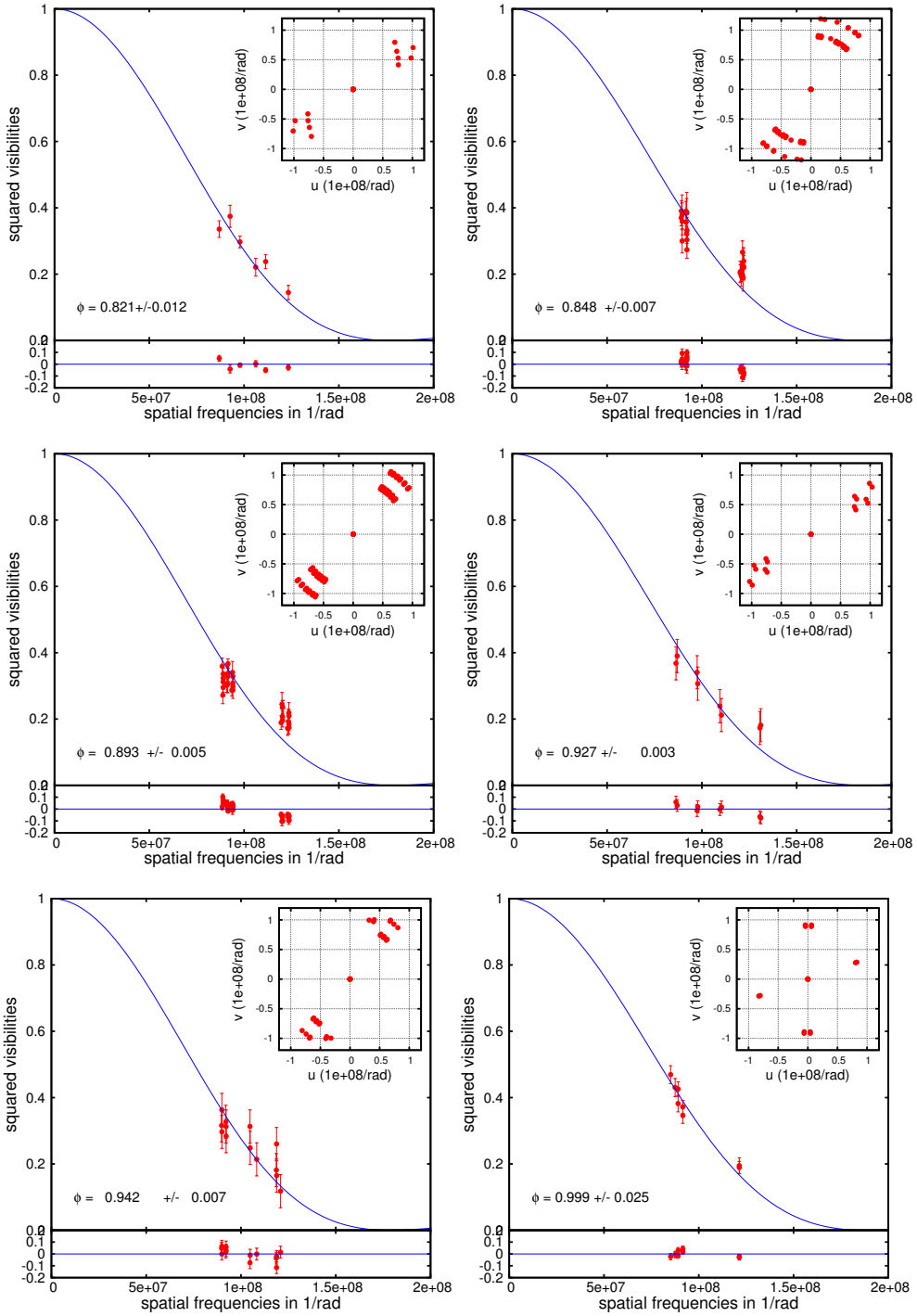


Fig. A.3. continued.

Annexe Q

Understanding the dynamical structure of pulsating stars : The center-of-mass velocity and the Baade-Wesselink projection factor of the β Cephei star α Lupi

A&A 553, A112 (2013)
DOI: 10.1051/0004-6361/201220644
© ESO 2013

Astronomy & Astrophysics

Understanding the dynamical structure of pulsating stars: The center-of-mass velocity and the Baade-Wesselink projection factor of the β Cephei star α Lupi⋆

N. Nardetto[1], P. Mathias[2], A. Fokin[1,3], E. Chapellier[1], G. Pietrzynski[4,5], W. Gieren[4], D. Graczyk[4,5], and D. Mourard[1]

[1] Laboratoire Lagrange, UMR7293, Université de Nice Sophia-Antipolis, CNRS, Observatoire de la Côte d'Azur, Nice, France
e-mail: Nicolas.Nardetto@oca.eu
[2] Institut de Recherche en Astrophysique et Planétologie, CNRS, 14 avenue Edouard Belin, Université de Toulouse, UPS-OMP, IRAP, 31400 Toulouse, France
[3] Institute of Astronomy of the Russian Academy of Sciences, 48 Pjatnitskaya Str., 109017 Moscow, Russia
[4] Universidad de Concepcíon, Departamento de Astronomía, Casilla 160-C, Concepcíon, Chile
[5] Warsaw University Observatory, Al. Ujazdowskie 4, 00-478 Warsaw, Poland

Received 29 October 2012 / Accepted 24 March 2013

ABSTRACT

Context. High-resolution spectroscopy of pulsating stars is a powerful tool to study the dynamical structure of their atmosphere. Lines asymmetry is used to derive the center-of-mass velocity of the star, while a direct measurement of the atmospheric velocity gradient helps determine the projection factor used in the Baade-Wesselink method of distance determination.
Aims. We aim at deriving the center-of-mass velocity and the projection factor of the β Cephei star α Lup.
Methods. We present HARPS high spectral resolution observations of α Lup. We calculate the first-moment radial velocities and fit the spectral line profiles by a bi-Gaussian to derive line asymmetries. Correlations between the γ-velocity and the γ-asymmetry (defined as the average values of the radial velocity and line asymmetry curves respectively) are used to derive the center-of-mass velocity of the star. By combining our spectroscopic determination of the atmospheric velocity gradient with a hydrodynamical model of the photosphere of the star, we derive a semi-theoretical projection factor for α Lup.
Results. We find a center-of-mass velocity of $V_\gamma = 7.9 \pm 0.6$ km s^{-1} and that the velocity gradient in the atmosphere of α Lup is null. We apply to α Lup the usual decomposition of the projection factor into three parts, $p = p_0 f_{\rm grad} f_{\rm og}$ (originally developed for Cepheids), and derive a projection factor of $p = 1.43 \pm 0.01$. By comparing our results with previous HARPS observations of classical Cepheids, we also point out a linear relation between the atmospheric velocity gradient and the amplitude of the radial velocity curve. Moreover, we observe a phase shift (Van Hoof effect), whereas α Lup has no velocity gradient. New HARPS data of a short-period β Cephei star, τ^1 Lup, are also presented in this paper.
Conclusions. By comparing Cepheids and β Cephei stars, these results bring insight into the dynamical structure of pulsating star atmospheres, which helps to better understand the k-term problem and the Baade-Wesselink p-factor for Cepheids.

Key words. stars: oscillations – stars: atmospheres – line: profiles – stars: individual: τ^1 Lup – stars: individual: α Lup – stars: distances

1. Introduction

A member of the β Cephei variable class, α Lupi (HD 129056 = HR 5469, B1.5 III, $V = 2.3$) is characterized by small light variations ($20 < \Delta V < 30$ mmag; Van Hoof 1964, 1965), a radial velocity period of $P = 0.2598$ d or 3.85 d^{-1} (Heynderickx 1992), and a 2K-amplitude of about 20 km s^{-1} (Pagel 1956; Rodgers & Bell 1962; Milone 1962; Van Hoof 1964). Lampens & Goossens (1982) found that both the light variability and the radial velocity variations can be represented by an oscillation with a constant frequency. Then, performing a detailed spectroscopic analysis, Mathias et al. (1994) found, in addition to the main radial mode, a small-amplitude non-axisymmetric mode with degree $1 \leq l \leq 3$. This additional non-radial mode is considered as negligible in first approximation, which makes the comparison with classical Cepheids relevant and extremely interesting for various reasons.

First, the motion of classical Cepheids in the Milky Way is puzzling and has led to disagreements in the literature for decades. If an axisymmetric rotation of the Galaxy is taken into account, Cepheids appear to "fall" towards the Sun with a mean blue-shifted velocity of about 2 km s^{-1}. This residual velocity shift has been dubbed the k-term and was first estimated by Joy (1939). A debate has raged for decades as to whether this phenomenon was truly related to the actual motion of the Cepheids and, consequently, to a complicated rotating pattern of our Galaxy, or if it was the result of effects within the atmospheres of the Cepheids (Camm 1938, 1944; Parenago 1945; Stibbs 1956; Wielen 1974; Caldwell & Coulson 1987; Moffett & Barnes 1987; Wilson et al. 1991; Pont et al. 1994; Butler et al. 1996). In Nardetto et al. (2008), we derived calibrated center-of-mass velocities of eight Cepheids observed with High Accuracy Radial velocity Planetary Search (HARPS) spectrograph using spectral line asymmetry. By comparing these systemic velocities with the ones found in the literature (generally based on the cross-correlation method) and in particular in the Galactic

⋆ Based on observations made with ESO telescopes at the Silla Paranal Observatory under programme IDs 085.C-0614(A).

Cepheid database (Fernie et al. 1995), we obtained an average red-shifted correction of 1.8 ± 0.2 km s^{-1}. This result shows that the k-term of Cepheids stems from an intrinsic property of Cepheids. However, this physical explanation should be generalized to be reinforced. Studying the k-term for other kinds of pulsating stars (if it exists) is extremely interesting to identify its physical origin.

Second, by comparing the dynamical structure of pulsating stars' atmospheres, one can seek interesting relations in the Hertzsprung-Russell (HR) diagram and produce constraints on the physical nature of the pulsation. The β Cephei star α Lup is studied in this paper, while δ Scuti stars are presented in Guiglion et al. (2013).

Third, the Baade-Wesselink (hereafter BW) method of determining the distances of Cepheids was recently used to calibrate the period-luminosity (PL) of Galactic and Large Magellanic Cloud Cepheids (Fouqué et al. 2007; Storm et al. 2011a,b). The basic principle of this method is to compare the linear and angular size variation of a pulsating star in order to derive its distance through a simple division. The angular diameter is either derived by interferometry (e.g. Kervella et al. 2004; Davis et al. 2009) or by using the infrared surface brightness (IRSB) relation (Gieren et al. 1998, 2005a). However, when determining the linear radius variation of the Cepheid by spectroscopy, one has to use a conversion projection factor from radial to pulsation velocity. This quantity has been studied using hydrodynamic calculations by Sabbey et al. (1995) and more recently by Nardetto et al. (2004, 2007, 2009, 2011). Conversely, the period-luminosity relation of β Cephei stars (calibrated through parallax measurements) contains a significant scatter (McNamara & Mathews 1967; Balona & Feast 1975; Waelkens 1981; Sterken & Jerzykiewicz 1992). The scatter is probably due to the finite width of the instability strip (Leung 1967; Jakate 1980; Tian et al. 2003) and the presence of different modes among β Cephei stars (Lesh & Aizenman 1974). Although Sterken & Jerzykiewicz (1979) have concluded on the basis of this scatter that a PL relation does not exist for β Cephei stars, deriving the projection factor is useful for different reasons. First, the projection factor can be used to derive the actual radius of the star and the acceleration in the atmosphere (Mathias et al. 1991, 1994). Moreover, the BW method can be applied to any kind of pulsating star in principle, even if the star pulsates in a non-radial mode (Dziembowski 1977; Balona & Stobie 1979; Stamford & Watson 1981; Hatzes 1996). However, pulsating star with shockwaves should be avoided (Mathias et al. 2006). Deriving the BW distance of β Cephei stars could help in calibrating the PL relation and in better understanding the physical reason for the scatter. This paper is part of the international Araucaria project, whose purpose is to provide an improved local calibration of the extragalactic distance scale out to distances of a few megaparsecs (Gieren et al. 2005b).

In Sect. 2, we present our HARPS observations of α Lup, which is the main interest of this paper, in addition to those of τ^1 Lup. τ^1 Lup (HD 126341 = HR 5395, B2 IV, $V = 4.5$) is a β Cephei star of shorter period ($P = 0.17736934$d or 5.637953 d^{-1}; Cuypers 1987), which we use in the analysis of Sect. 4 only. In Sect. 3, we derive the center-of-mass velocity of α Lup using spectral line asymmetry and compare it with previous estimates. Section 4 is devoted to a comparison of the dynamical structures of the atmospheres of β Cephei stars (α Lup and τ^1 Lup) and classical Cepheids. The results in Sects. 3 and 4 are based on observations only. In Sect. 5, we apply the projection factor decomposition to α Lup. We end with some conclusions (Sect. 6).

2. Observations and analysis

The HARPS spectrometer is dedicated to the search for extrasolar planets by means of radial velocity measurements. It is installed at the Coudé room of the 3.6 meter telescope at La Silla. The resolution is $R = 80\,000$ (in the EGGS mode) and the average signal to noise ratio we obtain over all observations in the continuum is 340 per pixel for α Lup (11 spectra) and 220 for τ^1 Lup (15 spectra). We have used the standard ESO/HARPS pipeline reduction package. Using the Vienna Atomic Line Database[1] (Piskunov et al. 1995; Heiter et al. 2008), we have identified 46 unblended spectral lines in the spectra of α Lup (Table 2). Three lines were rejected in the analysis of τ^1 Lup: Si 3856.02 Å, O 3907.44 Å, and N 3995.00 Å because of blends.

Following the same methods as described in Nardetto et al. (2006a), we derived for each spectral line of α Lup the first moment radial velocity, the full-width at half-maximum, the line depth, and the bi-Gaussian line asymmetry. The pulsation period given in the literature for α Lup is $P = 0.2598466$d (Heynderickx 1992). We decided to take the Julian date of our first observation in our sample as the reference ($T_0 = 2\,455\,430.0553$d). Our 11 observations of α Lup spread over eight pulsating cycles. No significant differences (in radial velocity and in line asymmetry) were found from one cycle to the other, but more spectroscopic observations of this star would be necessary to confirm this statement. Nevertheless, using the FAMIAS software[2] (Zima 2008) and the modes identified by Mathias et al. (1994), we found that the non-radial mode (compared to a pure radial mode) might lead to a systematic change of the amplitude of the radial velocities (and also line asymmetries) by only one percent (this is in principle true for all spectral lines). We consider in the following that the contamination of the data by a weak non-radial mode is negligible for our purposes. Therefore, spectra have been recomposed consistently into a unique cycle.

For τ^1 Lup we obtained 15 observations covering 12 cycles. We considered $P = 0.17736934$d (Cuypers 1987) and $T_0 = 2\,455\,429.8273$d, such that the maximum of the radial velocity curve for α Lup and τ^1 Lup corresponds to the same phase of pulsation ($\phi \simeq 0.3$). Again, no significant differences were found in the radial velocities from one cycle to the other, and the spectra have been recomposed consistently into a unique cycle to derive the radial velocity curve. However, we found that the spectral line asymmetry is probably contaminated by additional modes which are eventually non-radial. While the latter are again negligible in the radial velocity determination (first moment of the spectral line profile), they are significative in the spectral line asymmetry (which can also be considered as the third moment of the spectral line profile). Consequently, we use in this study the radial velocity only and, the detailed analysis of the spectral line asymmetry and mode idenfication for τ^1 Lup will be done in another paper (for this purpose, additional data should be obtained).

Figures 1 and 2 present the typical O 4705.3 Å spectral line variation for α Lup and τ^1 Lup respectively. Table 1 shows the results derived for both stars from the same line.

For α Lup, the RV_c and A quantities for all selected spectral lines are interpolated over the pulsation phase using a periodic

[1] http://www.astro.uu.se/~vald/php/vald.php

[2] Result obtained with the software package FAMIAS developed in the framework of the FP6 European Coordination Action HELAS (http://www.helas-eu.org/)

Table 1. HARPS observations results for α Lup and τ^1 Lup for the O 4705.3 Å spectral line (see also Figs. 1 and 2).

JD$_c$ [d] [a]	Phase [b]	Cy. [c]	RV_c [km s^{-1}] [d]	$FWHM$ [Å] [e]	D [f]	A [%] [g]	S/N [h]	χ^2_{red} [i]
				α Lup				
430.055	0.00	1	3.4 ± 0.6	0.396 ± 0.002	0.18	–10.00 ± 0.81	356	2.2
430.069	0.05	1	1.3 ± 0.4	0.389 ± 0.002	0.18	–9.33 ± 0.76	395	2.7
430.087	0.12	1	1.0 ± 0.5	0.385 ± 0.002	0.17	–12.26 ± 0.92	347	2.6
431.961	0.33	8	9.4 ± 0.7	0.377 ± 0.003	0.17	–13.46 ± 1.34	255	1.4
431.984	0.42	8	14.4 ± 0.5	0.367 ± 0.002	0.18	–10.01 ± 0.82	381	1.9
430.963	0.49	4	20.4 ± 0.8	0.376 ± 0.002	0.18	–4.39 ± 1.00	298	1.6
432.006	0.51	8	19.1 ± 0.6	0.367 ± 0.002	0.18	–7.65 ± 0.80	373	1.6
430.997	0.62	4	23.3 ± 1.0	0.404 ± 0.002	0.17	1.54 ± 1.04	279	1.2
431.025	0.73	4	20.1 ± 0.8	0.400 ± 0.002	0.17	–5.10 ± 0.94	315	1.0
431.060	0.86	4	12.2 ± 0.6	0.383 ± 0.002	0.18	–6.50 ± 0.80	359	2.5
431.084	0.96	4	6.7 ± 0.5	0.389 ± 0.002	0.18	–10.06 ± 0.79	387	2.3
				τ^1 Lup				
431.091	0.12	7	–23.32 ± 1.25	0.388 ± 0.004	0.11	–2.49 ± 2.42	200	0.8
431.981	0.14	12	–22.77 ± 1.18	0.337 ± 0.004	0.12	0.48 ± 2.41	191	0.8
430.049	0.25	1	–20.48 ± 0.90	0.381 ± 0.005	0.11	–9.50 ± 2.23	225	1.3
432.003	0.27	12	–21.07 ± 1.27	0.384 ± 0.005	0.11	–1.91 ± 2.58	187	0.9
430.060	0.31	1	–19.78 ± 1.09	0.378 ± 0.006	0.11	–7.96 ± 2.80	186	0.5
432.017	0.34	12	–19.06 ± 1.01	0.388 ± 0.005	0.10	–7.25 ± 2.53	214	1.4
430.066	0.35	1	–19.25 ± 0.76	0.384 ± 0.004	0.11	–8.73 ± 1.98	269	0.9
430.075	0.40	1	–17.61 ± 0.81	0.392 ± 0.006	0.11	–16.34 ± 2.31	256	0.8
430.969	0.44	6	–18.00 ± 1.14	0.385 ± 0.004	0.11	–4.22 ± 2.26	216	0.8
430.091	0.49	1	–15.44 ± 0.78	0.391 ± 0.005	0.11	–13.26 ± 2.24	247	1.4
430.987	0.54	7	–15.64 ± 0.83	0.359 ± 0.004	0.11	6.46 ± 2.09	233	0.7
431.011	0.67	7	–14.57 ± 0.79	0.333 ± 0.003	0.12	3.38 ± 1.92	235	0.9
431.031	0.79	7	–16.81 ± 0.81	0.309 ± 0.003	0.13	2.79 ± 1.77	244	1.0
431.053	0.91	7	–19.85 ± 1.24	0.340 ± 0.004	0.13	3.61 ± 2.15	196	0.8
431.068	0.99	7	–21.73 ± 1.49	0.351 ± 0.004	0.13	1.83 ± 2.59	168	0.9

Notes. [a] JD$_c$, average Julian date of observation defined by JD$_c$ = JD − 2 455 000 [in days]. [b] Pulsation phase of observation using the ephemeris indicated in the text. [c] Cy., pulsating cycle of the star corresponding to observation. [d] RV_c, heliocentric radial velocity corresponding to the first moment of the spectral line [in km s^{-1}]. [e] $FWHM$, full-width at half-maximum derived from the bi-Gaussian fit [in Angstroms]. [f] D, line depth derived from the bi-Gaussian fit [no dimension]. Errors bars are not indicated but are of the order of 10^{-4}. [g] A, asymmetry derived from the bi-Gaussian fit [in percentage]. [h] S/N, signal-to-noise ratio calculated in the continuum next to the O 4705.3 Å spectral line. [i] χ^2_{red}, reduced χ^2 factor corresponding to the bi-Gaussian fit.

cubic spline function. Then, A_γ and V_γ are calculated by averaging the $A(\phi)$ and $RV_c(\phi)$ interpolated curves, with ϕ the pulsation phase. The uncertainties on A_γ and V_γ are defined as the average values of individual uncertainties on A and RV_c respectively. In Table 2 A_γ and V_γ are given in the case of α Lup. For τ^1 Lup, we made a careful interpolation of the RV_c quantities (used in Sect. 3). The analysis presented in next section, which is based on spectral line asymmetries, is applied to α Lup only.

3. Center-of-mass velocity of α Lup

The aim of this section is to study the γ-velocities (V_γ) defined as the average values of the radial velocity curve and to show that they consist of two components: one related to the space motion of the star itself and one (which we call the k-term) related to the dynamical structure of the star's atmosphere. For an introduction to our methodology (see also Nardetto et al. 2008), we refer to Fig. 3.

Figures 3a and 3b show the interpolated radial velocity and asymmetry curves for three spectral lines: O 4705.3 Å (dashed line), N 5679.5 Å (solid line), and C 6582.9 Å (dot-dashed line). The actual measurements (crosses etc.) are only indicated in the case of the O 4705.3 Å line. From the interpolated curves, we now calculate the γ-velocities and γ-asymmetries corresponding to each spectral line (horizontal lines). An anti-correlation is clearly seen: the larger the γ-velocity, the lower the γ-asymmetry (for a given spectral line).

As a comparison, we show in Fig. 4a the radial velocity curves obtained for τ^1 Lup for the same spectral lines (same legend). Figure 4b shows the O 4705.3 Å spectral line asymmetry as a function of the pulsation phase. As said, we find that the spectral line asymmetry is probably contaminated by a multi-periodicity (or non-radial pulsations), while this is not the case for the radial velocity.

In Fig. 3c, $RV_c - A$ plots and the corresponding (A_γ,V_γ) average values (large crosses) for the three different lines are presented in the case of α Lup. Although the $RV_c - A$ plots have different shapes (confirmed for all spectral lines), which is the result of the dynamical structure of the β Cephei star atmosphere, the average values (large crosses) are aligned, confirming the anti-correlation found in Fig. 3a, b.

Figure 3d is a generalization of diagram (c) for all spectral lines. The $RV_c - A$ curves are not included for clarity. Upper values correspond to residual γ-velocities $V_\gamma(i)$ of the 46 selected spectral lines i. A linear fit is performed, and we find the relation

$$V_\gamma(i) = a_0 A_\gamma(i) + b_0, \quad (1)$$

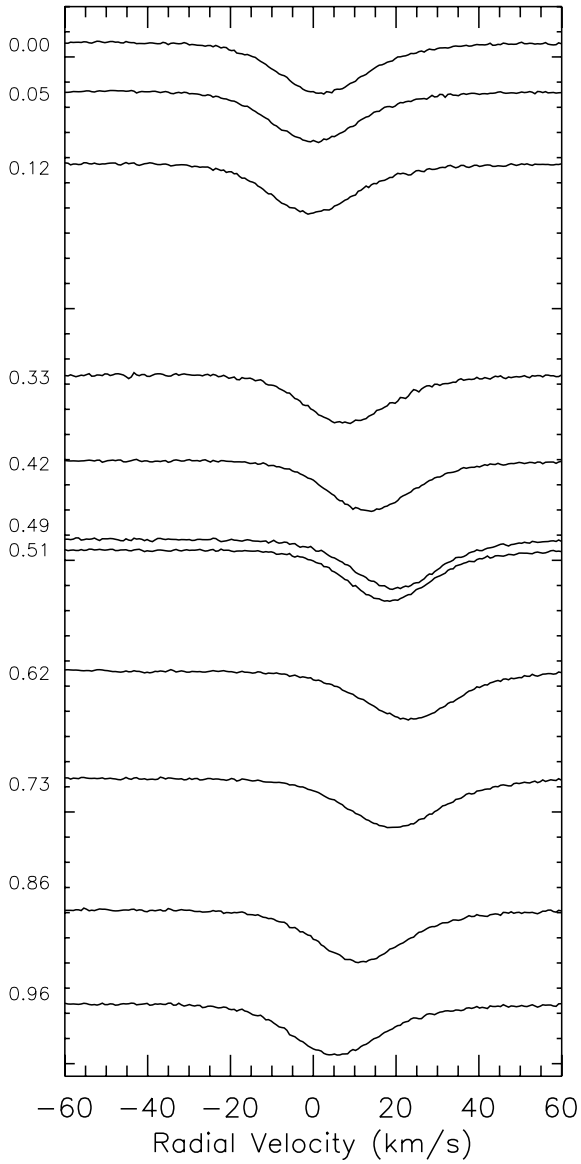


Fig. 1. O 4705.3 Å ($D \simeq 17\%$) spectral line evolution for α Lup. Pulsation phases are given on the left of each profile. Wavelengths have been translated into velocities (positive velocities correspond to a redshift or receding motion).

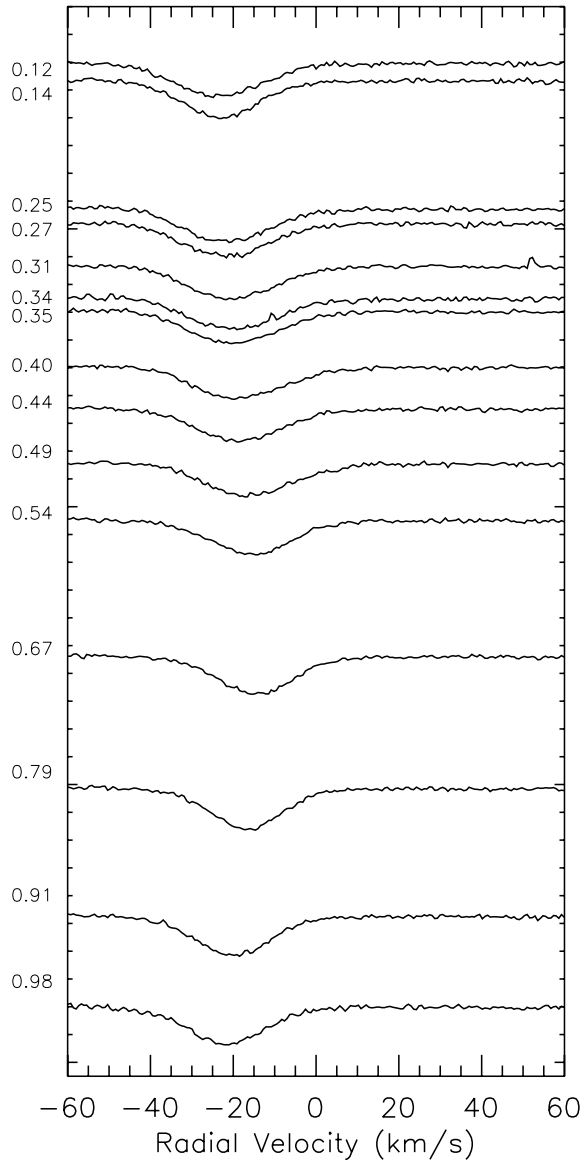


Fig. 2. O 4705.3 Å ($D \simeq 11\%$) spectral line evolution for τ^1 Lup (same legend as in Fig. 1).

with $a_0 = -0.32 \pm 0.08$ km s^{-1} and $b_0 = 7.86 \pm 0.59$ km s^{-1}. The origin of the plot is taken as a reference for the determination of the center-of-mass velocity of the star: the γ-velocity is assumed to be zero when the γ-asymmetry is zero. This means that all points

$$(A_\gamma(i), V_\gamma(i)) \tag{2}$$

are translated into

$$(A_\gamma(i), V_\gamma(i) - b_0), \tag{3}$$

which allows the definition of a physically calibrated center-of-mass velocity for α Lup:

$$V_{\gamma\star} = b_0 = 7.86 \pm 0.59 \text{ km s}^{-1}. \tag{4}$$

This quantity is relatively precise due to the very high S/N and spectral resolution of HARPS data. In Fig. 3d, the dashed line is the resulting $V_\gamma A_\gamma$ line ($a_0 = -0.15 \pm 0.01$) averaged over the eight Cepheids studied in Nardetto et al. (2008). The slopes obtained for Cepheids and α Lup are consistent at the 2σ level.

We now compare our center-of-mass velocity of α Lup to previous estimates, which yields some conclusions concerning the k-term phenomenon. First of all, we have to define several quantities. Originally, the k-term was defined as the difference between the expected systemic velocity of a Cepheid (due to the rotation of the Milky Way) and its measured γ-velocity (i.e. the average value of the interpolated radial velocity curve). Then, Nardetto et al. (2008) estimated the k-term by comparing the measured γ-velocities found in the literature with the center-of-mass velocity of a few Cepheids derived with the method described in this section (based on spectral line asymmetry). They concluded that γ-velocities found in the literature (mainly from the Galactic Cepheid data set; Fernie et al. 1995) were probably biased by the effect of spectral line asymmetry and that a redshift correction of 2 km s^{-1} was necessary. We now apply the same analysis to α Lup. In Table 3, we compare our result $V_{\gamma\star} = 7.9 \pm 0.6$ km s^{-1} with values in the literature. The dispersion of γ-velocities in the literature is too large (from 4.0 to

Table 2. Spectral lines used in this study with corresponding γ-velocity (V_γ) and γ-asymmetry (A_γ) obtained for α Lup.

Elements	λ (Å)	V_γ (km s^{-1})	A_γ (%)
Si	3856.02	11.81 ± 1.36	−7.41 ± 3.52
O	3907.44	10.78 ± 0.96	−6.52 ± 6.92
O	3911.96	11.28 ± 0.98	−11.92 ± 1.52
O	3945.03	10.73 ± 0.95	−8.49 ± 2.00
O	3954.36	9.90 ± 1.33	−8.15 ± 2.69
N	3955.85	9.50 ± 0.85	−7.25 ± 2.49
O	3982.71	9.79 ± 0.70	−4.49 ± 1.73
N	3995.00	9.22 ± 1.44	−5.89 ± 1.07
N	4041.31	9.59 ± 1.11	−6.34 ± 2.03
Si	4128.05	10.32 ± 0.92	−8.21 ± 2.18
Fe	4137.76	10.45 ± 0.62	−11.33 ± 3.16
S	4162.67	8.96 ± 0.87	−3.94 ± 4.82
Fe	4166.84	9.88 ± 0.55	−10.25 ± 4.94
N	4171.60	10.53 ± 0.58	−13.50 ± 4.28
O	4185.44	10.42 ± 1.03	−7.52 ± 2.74
N	4227.74	9.17 ± 0.63	−8.35 ± 2.56
S	4361.53	9.71 ± 0.60	−5.06 ± 3.00
O	4414.88	10.94 ± 0.96	−6.56 ± 0.69
O	4416.97	10.17 ± 1.43	−6.76 ± 1.22
Fe	4419.60	9.56 ± 0.80	−6.76 ± 2.41
Ar	4426.00	9.06 ± 0.42	−1.14 ± 4.44
He	4437.55	11.17 ± 1.04	−5.56 ± 0.88
O	4452.38	9.36 ± 0.58	−6.03 ± 1.48
Al	4512.56	8.97 ± 0.69	−4.77 ± 1.70
Si	4567.84	10.61 ± 0.72	−8.69 ± 0.31
Si	4574.76	10.03 ± 0.74	−8.15 ± 0.51
O	4590.97	10.03 ± 0.60	−8.11 ± 0.72
N	4607.15	9.78 ± 0.54	−6.04 ± 0.93
O	4641.81	10.70 ± 0.88	−8.00 ± 0.69
O	4661.63	10.14 ± 0.64	−6.75 ± 0.67
O	4676.23	10.16 ± 0.98	−7.34 ± 1.31
O	4705.32	11.95 ± 0.64	−8.17 ± 0.91
Si	4813.33	10.68 ± 0.51	−6.50 ± 1.94
S	4815.55	9.52 ± 0.38	−3.91 ± 3.29
N	5005.15	10.19 ± 0.84	−7.90 ± 0.90
He	5015.68	9.49 ± 0.57	−4.38 ± 0.36
N	5666.63	9.12 ± 0.67	−4.21 ± 0.78
N	5676.02	9.42 ± 0.67	−2.92 ± 1.02
N	5679.55	10.06 ± 0.83	−5.94 ± 0.55
N	5686.21	9.92 ± 0.72	−9.75 ± 2.13
Al	5696.60	9.23 ± 0.73	−3.91 ± 0.63
N	5710.77	9.10 ± 0.61	−5.74 ± 1.42
Al	5722.73	9.22 ± 0.83	−3.90 ± 0.95
Si	5739.73	11.75 ± 0.97	−10.07 ± 0.57
C	6578.05	9.31 ± 0.89	−6.99 ± 0.47
C	6582.88	8.95 ± 0.80	−5.02 ± 0.56

10.0 km s^{-1}) to provide any conclusion (we do not find an offset of 2 km s^{-1} as was the case for Cepheids). This result is not surprising: The dispersion in the results presented in Table 3 comes mainly from the method used to derive the radial velocity, the method used to perform the interpolation, the considered spectral lines, or the data quality.

Finally, it seems that the most consistent way to study the k-term (and to proceed to the comparison of Cepheids with α Lup) is to understand the physical nature of the γ-asymmetry (or γ-velocity effects) by considering the following quantity (that we now call the k-term in the remaining paper):

$$k = \langle V_\gamma \rangle - V_{\gamma\star} = 10.1_{\pm 0.8} - 7.9_{\pm 0.6} = 2.2_{\pm 0.8} \text{ km s}^{-1}, \quad (5)$$

where $\langle V_\gamma \rangle$ is defined as the average of the V_γ quantities over all spectral lines in our sample (see Fig. 3d). The value

Table 3. γ-velocities of α Lup derived in the literature.

Reference	Date	N measures	V_γ	Note
Wright	1909	10	7.8	
Campbell	1928	16	7.0	
Wilson	1953	16	7.3	
Pagel	1956	70	4.0 ± 3.0	[a]
Rogers	1962	24	10.0 ± 2.0	[b]
Thackeray	1966	9	10.6	
Mathias	1994	450	7.4 ± 1.7	[c]
Barbier-Brossat	2000	133	5.4 ± 0.6	[d]
This work	2012	12	10.1 ± 0.8	
This work : $V_\gamma\star$		11	7.9 ± 0.6	

Notes. [a] Estimated from their Fig. 6. [b] Estimated from their Fig. 1. [c] Estimated from their Table 1 (average over eight metallic lines). The precision for each individual line is 0.7 km s^{-1}. [d] From the original data set of Evans (1967).

$\langle V_\gamma \rangle = 10.1 \pm 0.8$ km s^{-1} should be comparable with the most recent observations (of good quality) obtained by Mathias et al. (1994), but this is not the case at the 3.5σ level. As mentioned, it probably comes from the methods used. Similarly, we define $\langle A_\gamma \rangle = -6.8 \pm 1.9\%$ as the average of the A_γ a quantities over all spectral lines in our sample.

Figure 5 shows this quantity k and also the γ-asymmetry $\langle A_\gamma \rangle$ for α Lup and for the Cepheids analysed in Nardetto et al. (2008) as a function of the period of pulsation. Surprisingly, α Lup shows a mean negative γ-asymmetry of $-6.8 \pm 1.9\%$, which is significantly lower compared to the positive and period-dependent values found for Cepheids (Fig. 5a). This spectral line asymmetry effect translates directly into a positive γ-velocity of 2.2 ± 0.8 km s^{-1}, while for Cepheids we found values between −1 and 0 km s^{-1} (Fig. 5b).

A first conclusion is that the k-term (as defined above) is correlated to the γ-asymmetry measurements (Fig. 5c), confirming that it reflects an intrinsic property of pulsating stars. Moreover, these spectral line asymmetry effects seem to have different behaviour in α Lup and in classical Cepheids. More observations for stars covering a period between 0.2 and 2.0 days would be extremely interesting. Presently, there is no hydrodynamical model of pulsating stars able to reproduce these physical effects (i.e. A_γ) properly.

4. The dynamical structure of the atmosphere of β Cephei stars compared to classical Cepheids.

Using our HARPS data of β Cephei stars (α Lup and τ^1 Lup) and our previous data obtained for Cepheids, we try to point out some differences in terms of atmospheric velocity gradients and phase shifts.

In Nardetto et al. (2007), we have shown that the line depth (taken at the minimum radius phase, hereafter D) is a good indicator of the line-forming regions. In this case, the photosphere corresponds to a zero line depth. By comparing the 2K amplitude (defined as the amplitude of the first moment radial velocity curve, hereafter ΔRV_c) with the depth of the 46 spectral lines selected (43 for τ^1 Lup), one can directly measure, in principle, the atmospheric velocity gradient. In the case of α Lup, we find the following relation:

$$\Delta RV_c = -[0.24 \pm 1.23]D + [22.46 \pm 0.24] \text{ km s}^{-1}. \quad (6)$$

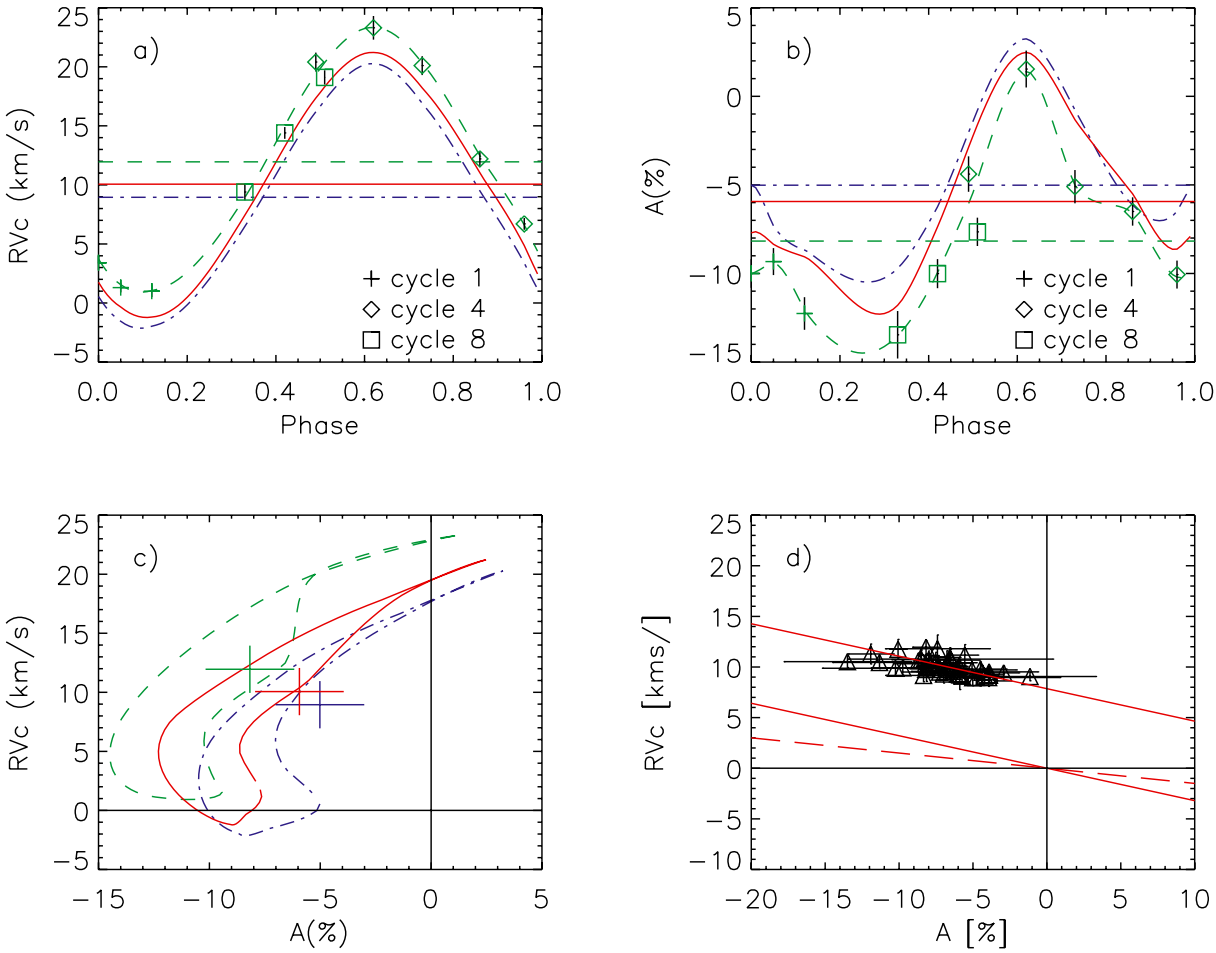


Fig. 3. Illustration of the method applied to derive the center-of-mass velocity of α Lup from the line asymmetries (see text).

The slope is consistent with a lack of velocity gradient within the atmosphere. For τ^1 Lup, we find

$$\Delta RV_c = -[3.77 \pm 2.60]D + [8.50 \pm 0.40]\ \mathrm{km\,s^{-1}}, \quad (7)$$

which is consistent (at the 1.3σ level) with a negative velocity gradient. Surprisingly, the amplitude of the radial velocity curves is larger near the photosphere (spectral lines of low depth) compared to the ones corresponding to the upper part of the atmosphere (spectral lines of large depth).

Figure 6 shows the relation found for α Lup and τ^1 Lup, together with previous results of Cepheids (Nardetto et al. 2007). The larger the 2K-amplitude, the larger the observed velocity gradient. This can also be seen in Fig. 7, where we show the slope a_0 (from the $\Delta RV_c = a_0 D + b_0$ relations for all stars) as a function of the 2K-amplitude (i.e. b_0). We find the following relation:

$$a_0 = [0.25 \pm 0.01]b_0 - [5.79 \pm 3.05]. \quad (8)$$

This trend is interesting and brings intriguing new questions about the atmospheric velocity gradient of low-amplitude pulsating stars ($\Delta RV_c < 20\ \mathrm{km\,s^{-1}}$) for which a negative velocity gradient is expected (as found for τ^1 Lup). Is τ^1Lup a peculiar star? Shall we expect the same result for other kinds of low-amplitude pulsating stars ? Is it due to the presence of non-radial modes in the atmosphere of τ^1 Lup ? More observations are needed to shed light on these questions.

Another interesting approach is to study the Van Hoof effect, which is described in detail in Mathias & Gillet (1993). Figure 8 shows the RV_c curves corresponding to spectral lines N 5679.5 Å (solid line) and O 4705.3 Å (dashed line) as a function of the RV_c curves of C 6582.9 Å in the case of α Lup. The two curves obtained show a loop shape due to the phase shifts between the three spectral lines considered (Van Hoof effect). We find that the two curves are parallel (because there is no velocity gradient observed from the radial velocity amplitudes) and shifted by a few $\mathrm{km\,s^{-1}}$ (because of the difference in γ-velocities). For comparison, Fig. 9 shows the same kind of plot but for the long-period Cepheid RZ Vel (HARPS observations presented in Nardetto et al. 2006a): RV_c curves corresponding to spectral lines N 5082.3 Å (solid line) and Si 6155.1 Å (dashed line) are presented as a function of the RV_c curves of Fe 4896.4 Å. In this case, the Van Hoof effect is significantly larger (larger loops) and the velocity gradient is clearly seen by the difference of slope between both curves. Again, we find a shift of a few $\mathrm{km\,s^{-1}}$ due to the difference between the γ-velocities obtained for the two lines.

These qualitative results show that such plots are extremely useful to synthesize most of the information concerning the dynamical structure of pulsating stars' atmosphere. In particular, in this case we find that a Van Hoof effect is possible even without an atmospheric velocity gradient.

5. The semi-theoretical projection factor

The basic approach used in Nardetto et al. (2004), where we provided a self-consistent projection factor of the Cepheid δ Cep

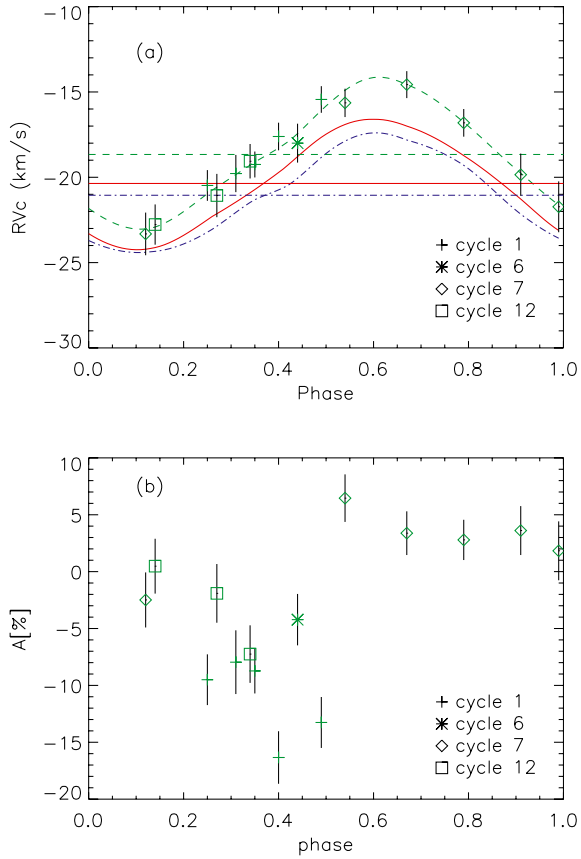


Fig. 4. a) Same as Fig. 3b in the case of τ^1 Lup. **b)** Spectral line asymmetry measurements for the O 4705.3 Å spectral line. The cycles of pulsation are indicated (see Table 2).

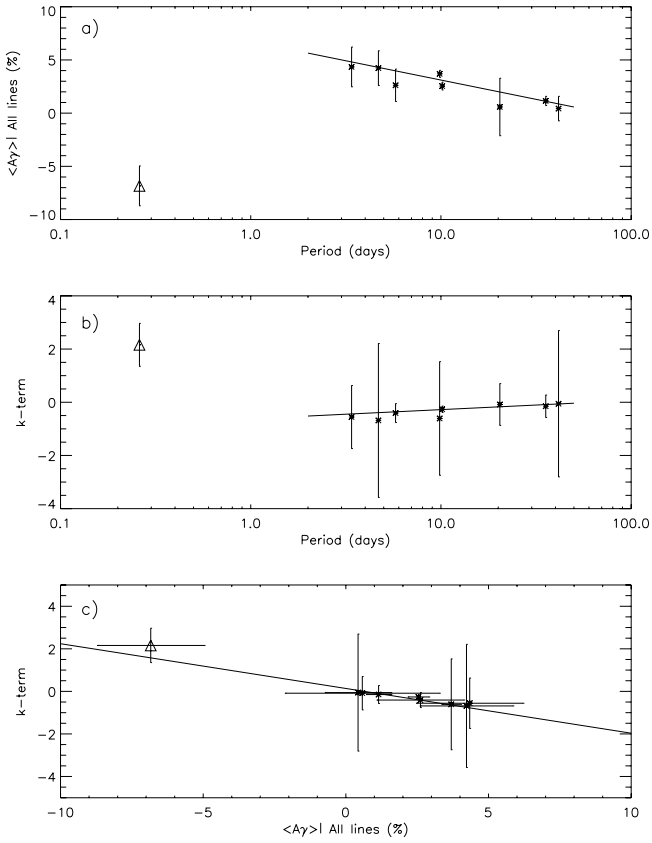


Fig. 5. γ-asymmetry (averaged over all spectral lines) and the k-term (as defined in the text) as a function of the pulsation period of the star (in days). The correlation between the k-term and the γ-asymmetry is presented in panel **c)**. The crosses are for the eight Cepheids studied in Nardetto et al. (2008) and the triangle is for α Lup.

using our non linear hydrodynamical model (Fokin 1990, 1991; Fokin et al. 2004) was not possible for α Lup. The reason is that the best model we obtain for α Lup does not reproduce the HARPS observations satisfactorily. The initial static model requires five input parameters: the luminosity (L), the effective temperature ($T_{\rm eff}$), the mass (M), and the chemical composition (X and Y). The thus built static model is then perturbated, and its dynamic response is improved until the code converges toward a limit-cycle. After that, radiative transfer in the line is solved in the frame of this hydrodynamical model to provide line profiles (Fokin 1991). However, in this study the radiative transfer is not used. For α Lup, Zorec et al. (2009) gave an effective temperature for α Lup of $T_{\rm eff}$ = 23 100 ± 1490 K based on spectrophotometric data, while Heynderickx et al. (1994) found a mass of M = 10.4 $M_{\odot}$. Considering these parameters and the HR diagram by Stankov & Handler (2005, Fig. 5), we find a luminosity of about L = 10 000 $L_{\odot}$. The metallicity is uncertain: Daszynska-Daszkiewicz & Niemczura (2005) provide $[\frac{m}{H}] = Z = 0.04 \pm 0.1$. We consider Y = 0.294 and Z = 0.006. With the input parameters summarized in Table 4, the model converges toward the radial fundamental mode, with a pulsation period of P = 0.25d (consistent at the 4% level with observation), while the amplitude of the radial velocity curve is of about 9.5 km s^{-1}, which is more than twice lower than what we derived from observations (≃22 km s^{-1}). We tried to resolve this discrepancy by computing two other models with L = 18 000 $L_{\odot}$ and L = 25 000 $L_{\odot}$, the other parameters remained as they are in Table 4. Such luminosities increase the amplitude of the radial velocity curve to 12 km s^{-1} and 16 km s^{-1}, respectively. The discrepancy found between the observations and the model (in particular in terms of amplitude of the radial velocity curve) is not sufficient to derive a purely theoretical projection factor of α Lup. The fact that α Lup has an effective temperature and a luminosity about five times larger compared to for instance δ Cep, with an atmosphere five times less extended in percentage (0.4% for α Lup and 2% for δ Cep from our code) might play an important role in explaining this discrepancy. Originally, the code was developed for high-amplitude pulsating stars. The only β Cepheid we successfully modelled was BW Vul, which was presented in Fokin et al. (2004). Improving the model in order to reproduce α Lup observations remains an open problem to be resolved in future studies.

Nevertheless, even if this model of α Lup is imperfect, we can use the same approach as described in Guiglion et al. (2013) for δ Scuti stars and derive a semi-theoretical projection factor. There are, indeed, three separated concepts involved in the decomposition of the BW projection factor: $p = p_0 f_{\rm grad} f_{\rm og}$. This expression has been used for Cepheids (Nardetto et al. 2007, 2011). If we assume that this decomposition is correct for α Lup (which is a conservative approach), we can still provide a semi-theoretical projection factor for α Lup. In this case, our aim here is not to reproduce the spectral line profile or even the radial velocity curve, but to derive a few physical quantities associated with the photosphere of the star, such as p_0 and $f_{\rm og}$. The last quantity, $f_{\rm grad}$, is derived directly from our HARPS observations (as described below). Such an approach is enough to study the projection factor, at least at first order.

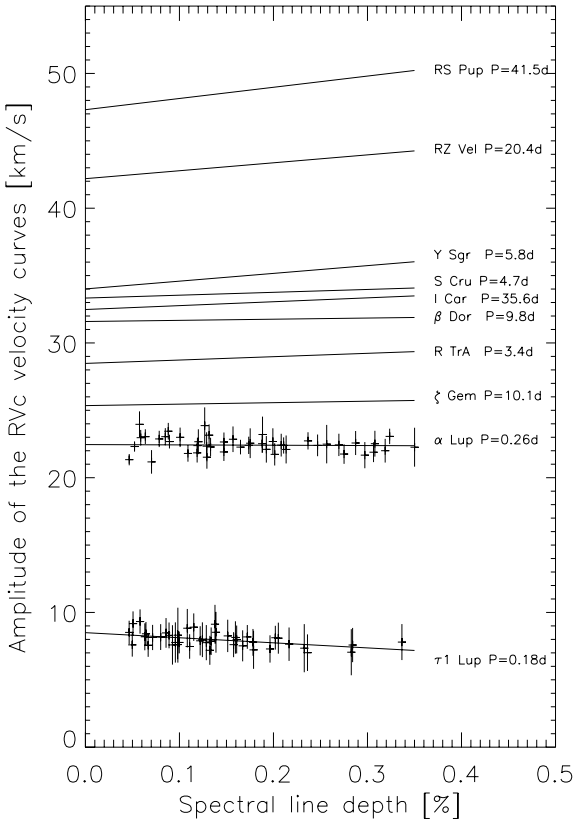


Fig. 6. Amplitude of the RV_c curves as a function of the spectral line depth in the case of the β Cephei stars α Lup and τ^1 Lup (dots are the HARPS measurements presented in this paper with the corresponding uncertainties) and for the eight Cepheids studied in Nardetto et al. (2007).

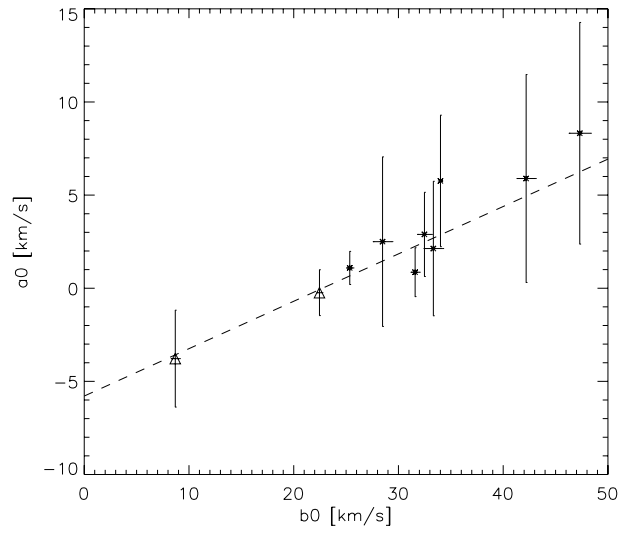


Fig. 7. Velocity gradient in the atmosphere of the stars as a function of the amplitude of the RV_c radial velocity curves. The crosses are for the eight Cepheids and the triangles are for β Cephei stars, α Lup and τ^1 Lup.

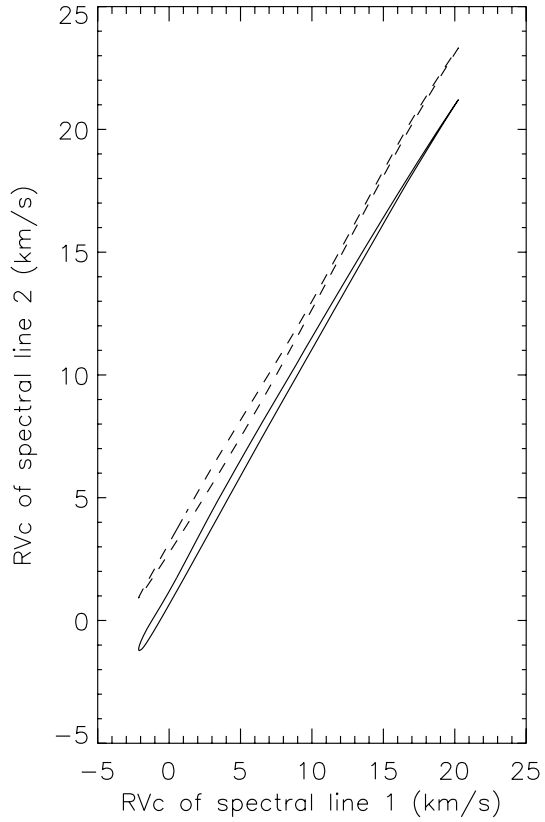


Fig. 8. Van Hoof effect observed in the case of the β Cephei star α Lup.

First, the geometric projection factor, p_0, is mainly related to the limb-darkening of the star. It corresponds to an integration of the pulsation velocity field (associated with the line-forming region) projected on the line of sight and weighted by the surface brightness of the star (including limb darkening within the spectral line). To derive p_o, we consider two models: (1) the intensity distributions in the continuum provided by our hydrodynamical model (using parameters of Table 4) and (2) the corresponding static model of Claret et al. (2011). In both cases, we made the assumption that the limb-darkening variation within the line is negligible. The geometric projection factor derived from the hydrodynamical model varies from 1.435 (when considering the continuum next to the spectral line Si 3856.02 Å) to 1.456 (continuum next to the C 6582.88 Å spectral line). We find a time independent limb darkening, with a mean value of $p_0 = 1.44 \pm 0.01$ (average over the different wavelengths). We use this value in the following. For δ Cep the time-variation of the limb darkening was also found negligible by Nardetto et al. (2006b). Concerning the static model, the linear limb-darkening law of the continuum intensity profile of the star provided by Claret et al. (2000) and Claret & Bloemen (2011) is $I(\cos(\theta)) = 1 - u_V + u_V \cos(\theta)$, where u_V is the limb darkening of the star in V band and θ is the angle between the normal of the star and the line of sight. For Cepheids, u_V is close to 0.7. For α Lup, using the physical parameters described in Table 4, we find $u_V = 0.37$, and using the relation linking p_0 to u_V: $p_0 = \frac{3}{2} - \frac{u_V}{6}$ (Getting 1934; Hadrava et al. 2009), we find $p = 1.44$. We note that this value is consistent with Mathias et al. (1994) and with our hydrodynamical results, but is significantly larger compared to what we generally obtain for Cepheids (typically 1.36 to 1.41).

Second, the correction due to the velocity gradient within the atmosphere, f_{grad}, is a quantity which can be directly derived from spectroscopic observations. Indeed, f_{grad} depends on the spectral line considered: $f_{grad} = b_0/(a_0 D + b_0)$ (Nardetto et al. 2007, their Eq. (3)). Using Eq. (6), we find that f_{grad} is typically the same for all spectral lines ($f_{grad} = 1.00 \pm 0.01$), which is consistent with no correction of the projection factor due to the velocity gradient.

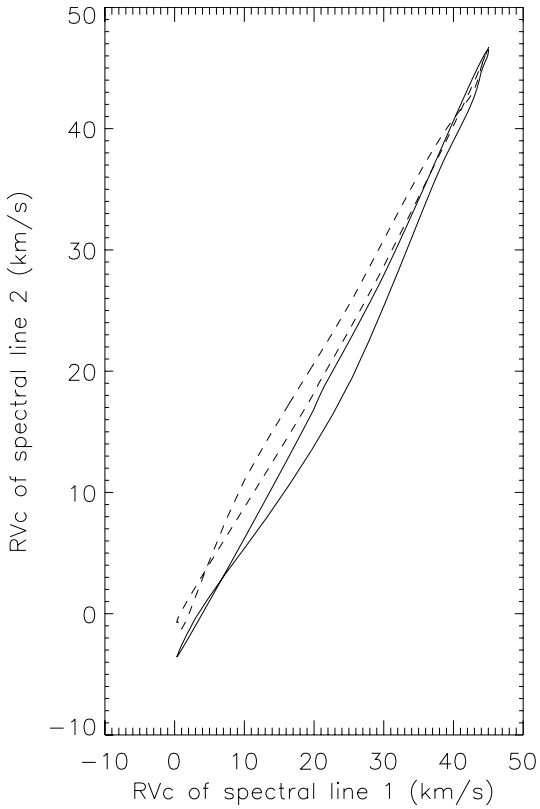


Fig. 9. Van Hoof effect observed in the case of the classical Cepheid RZ Vel.

Table 4. Input parameters for the hydrodynamical modeling of the photosphere of α Lup used to derive p_0 and $f_{\text{o-g}}$.

Input parameters	α Lup
L [$L_\odot$]	10 000
M [$M_\odot$]	12
T_{eff} [K]	23 000
X	0.700
Z	0.006

The $f_{\text{o-g}}$ correction, which is the last component of the projection factor decomposition, cannot be measured from observations. To estimate the differential velocity between the optical and gas layers at the photosphere of the star, we need a hydrodynamic model (for a detailed definition of these two layers, we refer to Eqs. (1) and (3) of Nardetto et al. 2004). For such determination, we use the nonlinear hydrodynamical model described above. We find $f_{\text{o-g}} = 0.99 \pm 0.01$ (numerical uncertainty derived from the model), whatever the model considered ($L = 10\,000\,L_\odot$, $L = 18\,000\,L_\odot$ or $L = 25\,000\,L_\odot$). We note that $f_{\text{o-g}}$ is mainly sensitive to the period (Nardetto et al. 2007). The impact of the amplitude of the radial velocity is negligible, which is confirmed by the fact that we find the same value for our three models.

We can now calculate the projection factor p, using the relation $p = p_0 f_{\text{grad}} f_{\text{o-g}}$. We find $p = 1.43 \pm 0.01$.

6. Conclusion

Like any pulsating star, α Lup shows a cyclic variation of its spectral line asymmetry caused by its pulsation. Nevertheless, on average (i.e. over one pulsation cycle, and over all spectral lines in our sample) the spectral line asymmetry (or γ-asymmetry) is significantly (at the 4σ level) negative ($\simeq -7\%$). For classical Cepheids, the γ-asymmetries are positive and range from about 0 to 5%. This difference between β Cephei stars and classical Cepheids suggests that the different physical mechanisms at work in the atmospheric dynamics are still not all clarified.

However, the β Cephei stars have a dynamical structure of their atmosphere, which seems consistent with classical Cepheids in the sense that we find a clear linear relation between the atmospheric velocity gradient and the amplitude of the radial velocity curve. No velocity gradient has been measured in the atmosphere of α Lup, in contrast to Cepheids. In addition, τ^1 Lup seems to have a negative velocity gradient. More observations of low amplitude pulsating stars are necessary to confirm this result. We also remark that the phase shift due to the Van Hoof effect between two metallic lines forming at different levels in the atmosphere is also possible when the atmospheric velocity gradient is zero (as in the case of α Lup).

Finally, by applying the usual decomposition of the projection factor to α Lup (which remains a conservative assumption), we find a semi-theoretical projection factor for α Lup of $p = 1.43 \pm 0.01$. This value of the projection factor can be used with caution in a BW method of distance determination for this star. The Hipparcos parallax ($\pi = 7.02 \pm 0.17$ mas; Van Leeuwen 2007) and the radius estimate from Lesh & Aizenman (1978), $R = 10.8\,R_\odot$ lead to an expected angular diameter of 0.7 mas. Using our radial velocity curves (in particular, $2K = 22.5$ km s^{-1}), the projection factor $p = 1.43$, and the distance from Hipparcos, we find an absolute angular diameter variation of 4 μas (or 0.6%). Unfortunately, there are no V, $V - K$ photometric observations available for α Lup in the literature to confirm these results.

A comparison of different classes of pulsating stars in which radial modes dominate the pulsations seems an excellent way to gain an improved understanding of their respective dynamical structures, the k-terms, and the BW projection factors appropriate for each class of these variables.

Acknowledgements. W.G. and G.P. gratefully acknowledge financial support for this work from the Chilean Center for Astrophysics FONDAP 15010003 and from the BASAL Centro de Astrofisica y Tecnologias Afines (CATA) PFB-06/2007. Support from the Ideas Plus programme of the Polish Ministry of Science and Higher Education and the TEAM subsidy of the Foundation for Polish Science (FNP) is also acknowledged. This research has made use of the CDS Astronomical Databases SIMBAD. We thank the referee for his useful comments.

References

Balona, L. A., & Feast, M. W. 1975, MNRAS, 172, 191
Balona, L. A., & Stobie, R. S. 1979, MNRAS, 187, 217
Barbier-Brossat, M., & Figon, P. 2000, A&AS, 142, 217
Breger, M. 1967, MNRAS, 136, 51
Butler, R. P., Bell, R. A., & Hindsley, R. B. 1996, ApJ, 461, 362
Buscombe, W., & Morris, P. M., 1960, MNRAS, 121, 263
Caldwell, J. A. R., & Coulson, I. M. 1987, AJ, 93, 1090
Camm, G. L. 1938, MNRAS, 99, 71
Camm, G. L. 1944, MNRAS, 104,163
Campbell, W. W. 1928, Lick Obs., 16, 1
Claret, A. 2000, A&A, 363, 1081
Claret, A., & Bloemen, S. 2011, A&A, 529, A75
Cuypers, J. 1987, A&AS, 69, 445
Daszynska-Daszkiewicz, J., & Niemczura, E. 2005, A&A, 433, 1031
Davis, J., Jacob, A. P., Robertson, J. G., et al. 2009, AnGeo, 27, 2449
Dziembowski, W. 1977, A&A, 27, 203
Evans, D. S. 1967, AUS, 30, 57
Fernie, J. D., Beattie, B., Evans, N. R., & Seager, S. 1995, IBVS No. 4148
Fokin, A. B. 1990, Ap&SS, 164, 95
Fokin, A. B. 1991, MNRAS, 250, 258
Fokin, A., Mathias, Ph., Chapellier, E., et al. 2004, A&A, 426, 687

Fouqué, P., Arriagada, P., Storm, J., et al. 2007, A&A, 476, 73
Getting, 1934, MNRAS, 95, 139
Gieren, W. P., Fouqué, P., & Gómez, M. 1998, ApJ, 496,17
Gieren, W. P., Storm, J., Barnes, T. G., et al. 2005a, ApJ, 627, 224
Gieren, W., Pietrzynski, G., Bresolin, F., et al. 2005b, Msngr, 121, 23
Guiglion, G., Nardetto, N., Mathias, P., et al. 2013, A&A, 550, L10
Hadrava, P., Slechta, M., & Skoda, P. 2009, A&A, 507, 397
Hatzes, A. P. 1996, PASP, 108, 839
Heiter, U, Barklem, P., Fossati, L., et al. 2008, J. Phys. Conf. Ser., 130, 012011
Heynderickx, D. 1992, A&AS, 96, 207
Heynderickx, D., Waelkens, C., & Smeyers, P. D. 1994, A&AS, 105, 447
Jakate, S. M. 1980, A&A, 84, 374
Joy, A. H. 1939, ApJ, 89, 356
Kervella P., Nardetto N., Bersier D., et al. 2004, A&A, 416, 941
Lampens, P., & Goossens, M. 1982, A&A, 115, 413
Lesh, J. R., & Aizenman, M. L. 1974, A&A, 34, 203
Leung, K. C. 1967, ApJ, 150, 233
McNamara, D. H., & Mathews, G. E. 1967, Mod. Astrophys., ed. M. Hack (Paris: Gauthier-Villars), 127
Mathias, P., & Gillet, D. 1993, A&A, 278, 511
Mathias, P., Gillet, D., & Crowe, R. 1991, A&A, 252, 245
Mathias, P., Aerts, C., De Pauw, M., et al. 1994, A&A, 283, 813
Mathias, P., Gillet, D., Fokin, A. B., et al. 2006, A&A, 457, 575
Mérand, A., Kervella, P., Coudé du Foresto, V., et al. 2005 A&A, 438, 9
Milone, L. 1962, Asso. Argent. Astron. Bul., 4, 42
Moffett, T. J., & Barnes, T. G. III 1987, PASP, 99, 1206
Nardetto, N., Fokin, A., Mourard, D., et al. 2004, A&AP, 428, 131
Nardetto, N., Mourard, D., Kervella, P. et al. 2006a, A&A, 453, 309
Nardetto, N., Fokin, A., Mourard, D., et al. 2006b, A&A, 454, 327
Nardetto, N., Mourard, D., Mathias, P., et al. 2007, A&A, 471, 661
Nardetto, N., Stoekl, A., Bersier, D., et al. 2008, A&A, 489, 1255
Nardetto, N., Gieren, W., Kervella P., et al. 2009, A&A, 502, 951
Nardetto, N., Fokin., A., Fouqué, P., et al. 2011, A&A, 534, L16
Pagel, B. E. J. 1956, MNRAS, 116, 10
Parenago, P. P. 1945, Popular. Ast., 53, 441
Piskunov, N. E., Kupka, F., Ryabchikova, T. A., et al. 1995, A&AS, 112, 525
Pont, F., Mayor, M., & Burki, G. 1994, A&A, 285, 415
Reed, B. C. 2003, AJ, 125, 2531
Rodgers, A. W., & Bell, R. A. 1962, Observatory, 82, 26
Sabbey, C. N., Sasselov, D. D., Fieldus, M. S, et al. 1995, ApJ, 446, 250
Stamford, P. A., & Watson, R. D. 1981, Ap&SS, 77, 131
Stankov, A., & Handler, G. 2005, ApJS, 158, 193
Sterken, C., & Jerzykiewicz, M. 1993, Space Sci. Rev., 62, 95
Stibbs, D. W. N. 1956, MNRAS, 116, 453
Storm, J., Gieren, W., & Fouqué, P. 2011a, A&A, 534, A94
Storm, J., Gieren, W., & Fouqué, P. 2011b, A&A, 534, A95
Thackeray, A. D. 1966, MNRAS, 70, 33
Tian, B., Men, H., Deng, L.-C., et al. 2003, Chin. J. Astron. Astrophys., 3, 125
Waelkens, C. 1981, A&A, 97, 274
Van Hoof, A. 1964, Z. Astrophys., 224, 953
Van Hoof, A. 1965, Kl. Verf. d. Remais-Sternwarte Bamberg, 4, 149
Van Leeuwen, F. 2007, A&A, 474, 653
Wielen, R. 1974, A&AS, 15, 1
Wilson, R. E. 1953, General catalogue of stellar radial velocities (Washington: Carnegie Institution of Washington)
Wilson, T. D., Barnes, T. G., Hawley, S. L., & Jefferys, W. H. 1991, ApJ, 378, 708
Wright, W. H. 1909, Lick Obs., 5, 176
Wright, W. H. 1911, Lick Obs., 9, 71
Zima, W. 2008, Commun. Asteroseismol., 155
Zorec, J., Cidale, L., & Arias, M. L. 2009, A&A, 501, 297

Annexe R

Understanding the dynamical structure of pulsating stars : The Baade-Wesselink projection factor of the δ Scuti stars AI Velorum and β Cassiopeiae

A&A 550, L10 (2013)
DOI: 10.1051/0004-6361/201220780
© ESO 2013

Astronomy & Astrophysics

L E

Understanding the dynamical structure of pulsating stars: The Baade-Wesselink projection factor of the δ Scuti stars AI Velorum and β Cassiopeiae⋆

G. Guiglion[1], N. Nardetto[1], P. Mathias[2], A. Domiciano de Souza[1], E. Poretti[3], M. Rainer[3], A. Fokin[4], D. Mourard[1], and W. Gieren[5]

[1] Laboratoire Lagrange, UMR 7293, UNS/CNRS/OCA, BP 4229, 06304 Nice Cedex 4, France
e-mail: guillaume.guiglion@oca.eu
[2] Institut de Recherche en Astrophysique et Planétologie, UMR 5277, 57 avenue d'Azereix, 65000 Tarbes, France
[3] INAF – Osservatorio Astronomico di Brera, via E. Bianchi 46, 23807 Merate, Italy
[4] Institute of Astronomy of the Russian Academy of Sciences, 48 Pjatnitskaya Str., 109017 Moscow, Russia
[5] Departamento de Astronomía, Universidad de Concepción, Casilla 160-C, CL Concepción, Chile

Received 23 November 2012 / Accepted 2 January 2013

ABSTRACT

Aims. The Baade-Wesselink method of distance determination is based on the oscillations of pulsating stars. The key parameter of this method is the projection factor used to convert the radial velocity into the pulsation velocity. Our analysis was aimed at deriving for the first time the projection factor of δ Scuti stars, using high-resolution spectra of the high-amplitude pulsator AI Vel and of the fast rotator β Cas.

Methods. The geometric component of the projection factor (i.e. p_0) was calculated using a limb-darkening model of the intensity distribution for AI Vel, and a fast-rotator model for β Cas. Then, using SOPHIE/OHP data for β Cas and HARPS/ESO data for AI Vel, we compared the radial velocity curves of several spectral lines forming at different levels in the atmosphere and derived the velocity gradient associated to the spectral-line-forming regions in the atmosphere of the star. This velocity gradient was used to derive a dynamical projection factor p.

Results. We find a flat velocity gradient for both stars and finally $p = p_0 = 1.44$ for AI Vel and $p = p_0 = 1.41$ for β Cas. By comparing Cepheids and δ Scuti stars, these results bring valuable insights into the dynamical structure of pulsating star atmospheres. They suggest that the period-projection factor relation derived for Cepheids is also applicable to δ Scuti stars pulsating in a dominant *radial* mode.

Key words. stars: oscillations – stars: atmospheres – stars: variables: δ Scuti – techniques: spectroscopic

1. Introduction

Determining distances in the Universe is not a trivial task. From our Galaxy to the Virgo Cluster, distances can be derived using the period-luminosity relation (PL) of Cepheids (Riess et al. 2009a,b). However, this relation has to be calibrated, using the Baade-Wesselink method of distance determination for instance (Storm et al. 2011a,b). The principle of this method is simple: after determining the angular diameter and the linear radius variations of the star, the distance is derived by a simple ratio. Angular diameter variations can be measured using interferometry (Kervella et al. 2004) or the infrared surface brightness relation (Gieren et al. 1998, 2005). The linear radius variation is measured by integrating the pulsation velocity (hereafter $V_{\rm puls}$) over one pulsating cycle. However, from observations we have only access to the radial velocity ($V_{\rm rad}$) because of the projection along the line-of-sight. The projection factor, used to convert the radial velocity into the pulsation velocity, is defined by $p = V_{\rm puls}/V_{\rm rad}$. There are in principle three sub-concepts involved in the Baade-Wesselink projection factor: (1) the geometric projection factor p_0, which is directly related to the limb-darkening of the star (see Sect. 3), (2) the correction $f_{\rm grad}$ due to the velocity gradient between the spectral-line-forming region and the photosphere of the star; this quantity can be derived directly from observations by comparing different lines forming at different levels in the atmosphere (see Sects. 2 and 4), and (3) the correction $f_{\rm o-g}$ due to the relative motion between the *optical* and *gas* layers associated to the photosphere (see Sect. 4). For a detailed analysis of the p-factor decomposition we refer to Nardetto et al. (2007). The projection factor is then defined by $p = p_0 f_{\rm grad} f_{\rm o-g}$. In the following, we apply this decomposition of the projection factor (originally developed for Cepheids) to the δ Scuti stars AI Vel and β Cas. The impact of non-radial modes of δ Scuti stars on the projection factor is a very difficult question studied previously (Dziembowski 1977; Balona & Stobie 1979; Stamford & Watson 1981; Hatzes 1996). The particular cases of AI Vel and β Cas are discussed in the conclusion. This paper is part of the international Araucaria Project, whose purpose is to provide an improved local calibration of the extragalactic distance scales out to distances of a few megaparsecs (Gieren et al. 2005). In this context, δ Scuti stars are extremely interesting since it has been shown recently that they follow a PL relation (McNamara et al. 2007; Poretti et al. 2008).

⋆ This work uses observations made with the HARPS instrument at the 3.6 m telescope (La Silla, Chile) in the framework of the LP185.D-0056 and with the SOPHIE instrument at OHP (France).

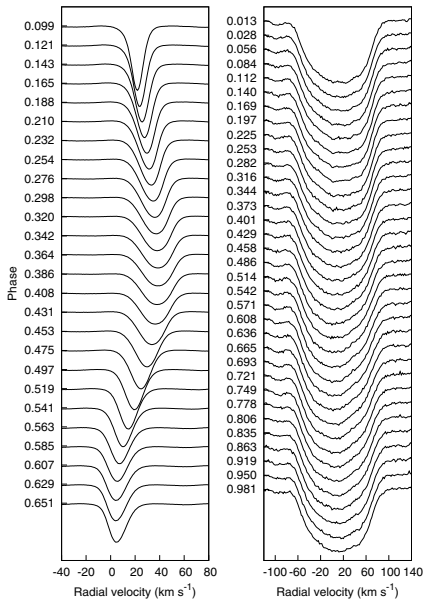


Fig. 1. Mean profiles of the HARPS spectra of AI Vel (*left panel*, T_0 = JD 2 443 176.00) and of the SOPHIE spectra of β Cas (*right panel*, T_0 = JD 2 438 911.88). The pulsation phase is given on the y-axis. A strong broadening is clearly seen for β Cas due to its high rotation velocity. We computed the mean line profiles of AI Vel and β Cas spectra by means of a deconvolution process using the LSD software (Donati et al. 1997).

2. Spectroscopic observations of δ Scuti stars

AI Vel (HD 69213, A9 IV/V) is one of the most often observed double-mode, high-amplitude δ Scuti stars. This star pulsates in the fundamental and first overtone radial modes with a well-constrained period ratio P_1/P_0 of 0.77 (Poretti et al. 2005). In addition to $P_0 = 0.111574$ d and $P_1 = 0.0862073$ d, Walraven et al. (1992) clearly detected two other periods, tentatively identified as the third and fifth radial overtones. We observed AI Vel using the HARPS spectrograph mounted at the ESO 3.6-m telescope. We analysed 26 high signal-to-noise ratio ($S/N \simeq 140$) spectra taken in the high-efficiency mode (EGGS, $R = 80\,000$) on the night of January 9−10, 2011. We identified 53 metallic unblended spectral lines (ranging from 3780 to 6910 Å) relevant for the determination of radial velocities. Figure 1 (left panel) shows the behaviour of the mean spectral line profile along the pulsation phase. The shifts due to the radial modes clearly dominate the line profile variations.

The target β Cas (HD 432, F2 III/IV) is a low-amplitude δ Scuti star. We observed β Cas with the SOPHIE instrument ($R = 75\,000$) at the OHP 1.93-m telescope on the night of September 30, 2011. We collected 241 high-resolution spectra with a mean S/N of 100. We could distinguish only height unblended spectral lines relevant for the spectral analysis because of the strong rotational broadening (Fig. 1, right panel). Riboni et al. (1994) showed that the star is a monoperiodic pulsator at the detection limit of ground-based photometric measurements, with a pulsation period of $P = 0.101036676$ d. The mode identification is unclear (Rodriguez et al. 1992; Riboni et al. 1994). Today, the distance of β Cas is known to be 16.8 pc from the Hipparcos parallax (van Leeuwen 2007). Thus we could obtain the absolute magnitude $M_V = 1.14$ from the apparent magnitude $V = 2.27$. The PL relations (McNamara et al. 2007; Poretti et al. 2008) supply a fundamental radial period of about 0.15 d at this M_V value. Therefore, the observed period is similar to that expected for the second radial overtone. We attempted a mode identification from our spectroscopic data using the FAMIAS[1] software. Since we dealt with a fast rotator, we used the Fourier parameter fit method (Zima 2006). Imposing the frequency $1/P$, the results from spectroscopy point towards an axisymmetric mode, without a clear indication on the ℓ-value. Since β Cas is seen almost pole-on ($i = 19.9 \pm 1.9°$, Che et al. 2011), a low-degree, axisymmetric, nonradial mode mimics the pulsation behaviour of a radial mode very well. On the basis of these considerations, we treated β Cas as a radial monoperiodic pulsator for our purposes. We also used the mean line profiles of β Cas to estimate the $v \sin i$ values from the position of the first zero of their Fourier transforms (Carroll 1933). This approach is possible only for objects where the rotational broadening is dominant with respect to the other sources of line broadening (e.g., instrumental effect, microturbulence), which is always the case for β Cas, but not for AI Vel, where we were unable to use the Fourier transform method on the narrower lines ($v \sin i < 10$ km s^{-1}). The radial velocity values of the observed profiles of β Cas range from 5.3 to 11.6 km s^{-1} and the $v \sin i$ values from 74.0 to 77.5 km s^{-1} (Fig. 1, right panel). We could also determine a mean $v \sin i$ value from the average of all the mean profiles and obtained 75.72 ± 0.14 km s^{-1}. This value is consistent with literature values (Bernacca & Perinotto 1970; Uesugi & Fukuda 1970; Schröder et al. 2009). When considering $i = 19.9°$, this means that β Cas is an intrinsic fast rotator, with a velociy of $v_{\rm rot} \simeq 220$ km s^{-1} which is consistent with Che et al. (2011).

Finally, for both stars, the centroid radial velocity $RV_{\rm c}$ (or the first-moment radial velocity) and the line depth D are derived as a function of the pulsation phase for each selected spectral line. These data are used in Sect. 4.

3. The geometric projection factor p_0

Considering a limb-darkened pulsating star in rotation with a one-layer atmosphere, the projection factor is purely geometric. Thus, $p = \frac{V_{\rm puls}}{V_{\rm rad}} = p_0$. The radial velocity is then defined by

$$V_{\rm rad} = \frac{1}{\pi {\rm R}^2} \int_{x,y \in D_R} I(x,y,\lambda) V_{\rm puls} \sqrt{1 - \frac{(x^2+y^2)}{{\rm R}^2}}\, {\rm d}x{\rm d}y, \qquad (1)$$

where D_R is the surface of the stellar disc of radius R, and $I(x, y, \lambda)$ the limb-darkened *continuum* intensity distribution considered at the wavelength of observation λ defined by $I(x, y, \lambda) = I_0(1 - u_\lambda + u_\lambda \sqrt{1 - (x^2 + y^2)})$, where u_λ is the linear limb-darkening coefficient from Claret & Bloemen (2011). Considering $T_{\rm eff} = 7400$ K and $\log g = 3.5$, we find $u_{\rm R} = 0.474 \pm 0.025$ in the R-band from Claret & Bloemen (2011). Using Eq. (1), we deduce a value of the geometric projection factor for AI Vel of $p_0 = 1.43 \pm 0.01$. p_0 is assumed to be constant with the pulsation phase (Nardetto et al. 2004). This value is higher than what we generally obtain for Cepheids (typically 1.37 to 1.41, see Fig. 2 (top panel)).

The geometrical shape of β Cas and its intensity distribution are distorted by its high rotation rate. The geometric projection factor depends on the inclination of the star's rotation axis compared to the line-of-sight. If the star's rotation axis is along the line-of-sight ($i = 0°$), the star is observed pole-on and is seen as a disc. For $i > 0°$ the star has an ellipsoidal shape.

Using the fundamental parameters of the modified von Ziepel model found by Che et al. (2011) and the rotating stars model by Domiciano de Souza et al. (2002, 2012),

[1] Developed in the framework of the FP6 European Coordination Action HELAS (http://www.helas-eu.org/)

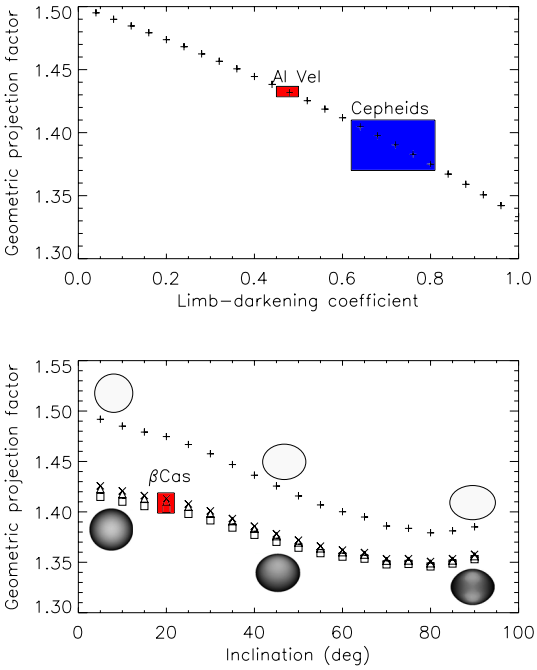


Fig. 2. *Top*: p_0 as a function of the limb-darkening parameter u_λ. The red box indicates the uncertainty on p_0 for the δ Scuti AI Vel. The blue box indicates the typical values of u_λ and p_0 for Cepheids. The dots corresponds to the relation provided by Nardetto et al. (2006). *Bottom*: p_0 as a function of the inclination of the fast rotating star β Cas for three different wavelengths (λ = 6000 Å (□), λ = 6500 Å (△), and λ = 7000 Å (×)). The red box indicates the uncertainty on p_0 for β Cas. The case of an uniform elonged disc is over-plotted (+), and we find that p_0 = 1.5 for i = 0°, as expected for a circular uniform disc.

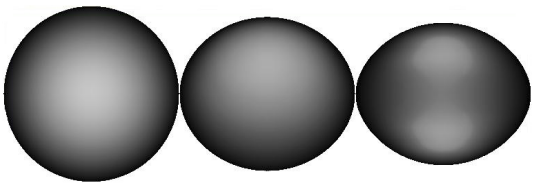


Fig. 3. Modelled intensity distributions of β Cas at 6000 Å for i = 5° (*left*), i = 50° (*middle*), i = 90° (*right*).

we derived the intensity distribution in the continuum for different inclinations of the star (from i = 0° to i = 90° with a step of 5°) and for three wavelengths: λ = 6000, 6500 and 7000 Å. Using these intensity maps, we can easily calculate the geometric projection factor. Indeed, for an ellipsoid, $V_{\rm rad}$ is then defined by

$$V_{\rm rad} = \frac{1}{\pi {\rm R}^2} \int_{x,y \in D_R} I(x,y,\lambda) V_{\rm puls} \sqrt{1 - \left(\frac{x^2}{a^2} + \frac{y^2}{b^2}\right)} {\rm d}x{\rm d}y, \qquad (2)$$

where a and b are the semi-major and semi-minor axis of the ellipse. In Fig. 2 (bottom panel), we show the geometric projection factor (p_0) as a function of i. Fig. 3 presents the modelled intensity distributions for several inclinations. This relation is extremely interesting because it shows that the inclination of a fast-rotating star can have an impact of more than 10% on the projection factor. Of course, it also depends on the rotation velocity of the star: the higher the rotation velocity (for a given inclination), the lower the projection factor. Using the inclination found by Che et al. (2011), i = 19.9 ± 1.9°, we finally find a geometric projection factor for β Cas of p_0 = 1.41 ± 0.02 (averaged over the three wavelengths considered).

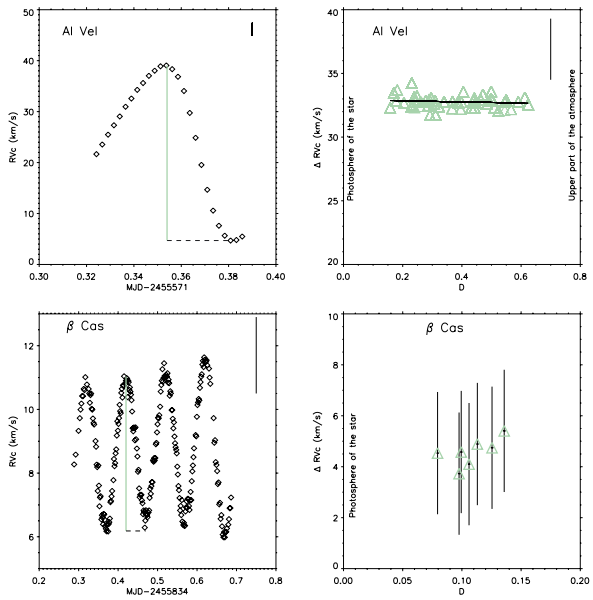


Fig. 4. *Top*: $RV_{\rm c}$ as a function of the MJD in the case of the FeII 5234.625 Å spectral line, and amplitude of the $RV_{\rm c}$ curves as a function of the spectral line depth (D) for AI Vel. Typical error bars are indicated in the upper right of each panel. *Bottom*: the same for β Cas f the FeII 4508.288 Å spectral line.

4. Dynamical structure of the atmosphere

By comparing the 2K-amplitude (defined as the amplitude of the $RV_{\rm c}$ curve, hereafter $\Delta RV_{\rm c}$) with the depth (D) of the 53 spectral lines selected in the case of AI Vel, one can directly measure the atmospheric velocity gradient in the part of the atmosphere where the spectral lines are formed (Fig. 4, top-left). To quantify the impact of velocity gradient on the projection ($f_{\rm grad}$), we do not need to derive the velocity gradient over the whole atmophere, but only at the location of the forming regions of the spectral lines used to derive the distance of the star. We therefore performed a linear regression according to the relation $\Delta RV_{\rm c} = a_0\, D + b_0$. We obtained $\Delta RV_{\rm c} = [-0.40 \pm 0.53]D + [32.87 \pm 0.23]\,{\rm km\,s^{-1}}$ (Fig. 4, top-right). In principle, $f_{\rm grad}$ depends on the spectral line considered (Nardetto et al. 2007): $f_{\rm grad} = b_0/(a_0 D + b_0)$. Here, we find that $f_{\rm grad}$ is typically the same for all spectral lines ($f_{\rm grad}$ = 1.01 ± 0.01), which is consistent with no correction of the projection factor due to the velocity gradient. The uncertainty on $f_{\rm grad}$ is derived from the errors on a_0 and b_0.

Figure 4 (bottom left) presents the interpoled $RV_{\rm c}$ curve of β Cas for the FeI spectral line (λ = 4508.288 Å). We clearly see an increase of the amplitude of the radial velocity curve (~4.6 ± 0.9% per cycle). Moreover, the radial velocity curves have several minima and maxima and we can easily deduce a period of pulsation. We find P = 0.10046 ± 0.00054 d. Our value agrees well with that of Riboni et al. (1994).

In Fig. 4 (bottom right), $\Delta RV_{\rm c}$ is plotted as a function of D for cycle 2 (see the vertical line in the figure). For β Cas, the range of the spectral line depth is eight times lower compared to AI Vel. The velocity gradient is $f_{\rm grad}$ = 0.64 ± 0.82. The large error bar prevents any physical discussion about the exact value of $f_{\rm grad}$. We note that $f_{\rm grad}$ = 0.64 implies a huge velocity gradient in the star's atmosphere, which seems unrealistic. Since it is consistent

with our determination, we assumed $f_{\rm grad} = 1.0$. Considering $a_0 = 0$, we obtained $b_0 = 4.07 \pm 0.25$ with a reduced χ^2 of 1.0, which provides an uncertainty on $f_{\rm grad}$ of 0.14. The $f_{\rm o\text{-}g}$ correction, which is the last component of the projection factor decomposition, cannot be measured from observations. To estimate the differential velocity between the *optical* and *gas* layers at the photosphere of the star, we need a hydrodynamic model.

However, modelling the pulsating atmosphere of δ Scuti stars is not an easy task because of (1) cycle-to-cycle variations (non-radial modes) and (2) fast rotation in some cases (as for β Cas). However, $f_{\rm o\text{-}g}$ have been studied intensively in the Cepheids (Nardetto et al. 2004, 2007, 2011), and it seems that there is a linear relation between $f_{\rm o\text{-}g}$ and $\log P$: $f_{\rm o\text{-}g} = [-0.023 \pm 0.005] \log P + [0.979 \pm 0.005]$. Moreover, we have a theoretical value of $f_{\rm o\text{-}g}$ for the short-period β-Cephei α Lup ($P = 0.2598$ d), $f_{\rm o\text{-}g} = 0.99 \pm 0.01$, which seems to be consistent with the $\log P$–$f_{\rm o\text{-}g}$ relation of Cepheids (Nardetto et al. 2012). For our study, we propose to extend this law for the δ Scuti β Cas and AI Vel. Considering $P = 0.11157$ d for AI Vel and $P = 0.10046 \pm 0.00054$ d for β Cas (from this paper), we find $f_{\rm o\text{-}g} = 1.00 \pm 0.02$ (0.02 is a conservative arbitrary uncertainty) for both stars, which basically means no photospheric correction to the projection factors.

5. Discussion

We can now calculate the projection factor p, using the relation $p = p_0 f_{\rm grad} f_{\rm o\text{-}g}$. We find $p = 1.44 \pm 0.05$ for AI Vel and $p = 1.41 \pm 0.25$ for β Cas. However, the generalisation of this study to any δ Scuti stars is presently limited since we have to study the impact of multi-modes, in particular non-radial ones, on the projection factor. This complicated effect has been studied by several authors for the bisector method of the radial velocity determination (Dziembowski 1977; Balona & Stobie 1979; Stamford & Watson 1981; Hatzes 1996). We assume a star pulsating in two modes, one radial and one non-radial. The projection factor can be defined as $p = \alpha_{\rm r} p_{\rm r} + \alpha_{\rm nr} p_{\rm nr}$, with $\alpha_{\rm r}$ and $\alpha_{\rm nr}$ the relative contributions of the velocity amplitudes of the radial and non-radial modes to the pulsation ($\alpha_{\rm r} + \alpha_{\rm nr} = 1$). $p_{\rm r}$ is our previous decomposition of the projection factor in the case of a purely radial mode $p_{\rm r} = p_0 f_{\rm grad} f_{\rm o\text{-}g}$, while $p_{\rm nr}$ is the projection factor in the case of a purely non-radial mode. Using Eq. (4) of Hatzes (1996), we find that $p_{\rm nr} = p_0 {\rm e}^{+k\ell^2}$, where $k = 0.15$ in the case of a non radial p-mode and $k = 1.2$ in the case of a non-radial g-mode. ℓ is the spherical harmonic degree. This relation is derived for the first moment (i.e. the radial velocity) determination only, which is independent of the star's rotation. This equation can be used when $\ell = m$ only (where m is the spherical harmonic order). Additional work is necessary to derive it when $\ell \neq m$. We emphasize also that the higher $\ell(=m)$, the higher is the non-radial projection factor. This is expected since for high values of ℓ (and this is qualitatively also true when $\ell \neq m$) there are more red- and blue-shifted velocity zones on the star that cancel each other in the integrated line profile, which leads to a lower amplitude of the non-radial velocity curve, and in turn a high value of the non-radial projection factor (see Eqs. (1) and (2) of Hatzes 1996).

We performed our study on AI Vel and β Cas under the assumption of monoperiodic radial pulsation. Our results (without non-radial correction) are consistent (at the 1σ level) with the period-projection-factor (Pp) relation $p = [-0.071 \pm 0.020] \log P + [1.311 \pm 0.019]$ by Laney & Joner (2009) applied for classical and dwarf Cepheids (it corresponds to $p = 1.38 \pm 0.02$ for AI Vel and β Cas). To derive these values, Laney & Joner simply compared the distance of the stars obtained from the PL relation with the distances from the photometric version of the Baade-Wesselink method. This suggests that the eventual non-radial components of β Cas have probably a negligeable impact on the projection factors (which means $\alpha_{\rm nr} \simeq 0$). Interestingly, if we use the Pp relation obtained for classical Cepheids by Nardetto et al. (2007), $p = [-0.064 \pm 0.020] \log P + [1.376 \pm 0.023]$ (derived with the first moment method[2]) to derive the projection factors of the two δ Scuti stars, we find $p = 1.44 \pm 0.01$, which is consistent with our values. This seems to show that the Pp relation provided by Nardetto et al. (2007) for single lines is also applicable to δ Scuti stars pulsating in a dominant *radial* mode. In addition, and as already shown, for fast-rotating δ Scuti stars, an intrinsic dispersion of the Pp relation due to the random orientation of the rotation axis has to be considered.

Acknowledgements. G.G. and N.N. thank J. Monnier for useful discussions. W.G. is grateful for support from the BASAL Centro de Astrofisica y Tecnologias Afines (CATA) PFP-06/2007. E.P. and M.R. acknowledge financial support from the Italian PRIN-INAF 2010 *Asteroseismology: looking inside the stars with space- and ground-based observations*.

References

Balona, L. A., & Stobie, R. S. 1979, MNRAS, 189, 649
Bernacca, P. L., & Perinotto, M. 1970, Contributi dell'Osservatorio Astrofisico dell'Università di Padova in Asiago, 239, 1
Carroll, J. A. 1933, MNRAS, 93, 680
Che, X., Monnier, J. D., Zhao, M., et al. 2011, ApJ, 732, 68
Claret, A., & Bloemen, S. 2011, VizieR Online Data Catalog, 352, 99075
Domiciano de Souza, A., Vakili, F., Jankov, S., Janot-Pacheco, E., & Abe, L. 2002, A&A, 393, 345
Domiciano de Souza, A., Zorec, J., & Vakili, F. 2012, in SF2A, Proc. Annual meeting of the French Society of Astronomy and Astrophysics, eds. S. Boissier, P. de Laverny, N. Nardetto, et al., 321
Donati, J.-F., Semel, M., Carter, B. D., Rees, D. E., & Collier Cameron, A. 1997, MNRAS, 291, 658
Dziembowski, W. 1977, Acta Astron., 27, 203
Gieren, W. P., Fouqué, P., & Gomez, M. 1998, ApJ, 496, 17
Gieren, W., Storm, J., Barnes, III, T. G., et al. 2005, ApJ, 627, 224
Hatzes, A. P. 1996, PASP, 108, 839
Kervella, P., Bersier, D., Mourard, D., Nardetto, N., & Coudé du Foresto, V. 2004, A&A, 423, 327
Laney, C. D., & Joner, M. D. 2009, in Am. Inst. Phys. Conf. Ser. 1170, eds. J. A. Guzik, & P. A. Bradley, 93
McNamara, D. H., Clementini, G., & Marconi, M. 2007, AJ, 133, 2752
Nardetto, N., Kervella, P., Mourard, D., Bersier, D., & Coudé du Foresto, V. 2004, in ASP Conf. Ser. 310, Variable Stars in the Local Group, eds. D. W. Kurtz, & K. R. Pollard,, IAU Colloq., 193, 520
Nardetto, N., Mourard, D., Kervella, P., et al. 2006, A&A, 453, 309
Nardetto, N., Mourard, D., Mathias, P., Fokin, A., & Gillet, D. 2007, A&A, 471, 661
Nardetto, N., Gieren, W., Kervella, P., et al. 2009, A&A, 502, 951
Nardetto, N., Fokin, A., Fouqué, P., et al. 2011, A&A, 534, L16
Nardetto, N., et al. 2012, A&A, submitted
Poretti, E., Suárez, J. C., Niarchos, P. G., et al. 2005, A&A, 440, 1097
Poretti, E., Clementini, G., Held, E. V., et al. 2008, ApJ, 685, 947
Riboni, E., Poretti, E., & Galli, G. 1994, A&AS, 108, 55
Riess, A. G., Macri, L., Casertano, S., et al. 2009a, ApJ, 699, 539
Riess, A. G., Macri, L., Li, W., et al. 2009b, ApJS, 183, 109
Rodriguez, E., Rolland, A., Lopez de Coca, P., Garrido, R., & Gonzalez-Bedolla, S. F. 1992, A&AS, 96, 429
Schröder, C., Reiners, A., & Schmitt, J. H. M. M. 2009, A&A, 493, 1099
Stamford, P. A., & Watson, R. D. 1981, Ap&SS, 77, 131
Storm, J., Gieren, W., Fouqué, P., et al. 2011a, A&A, 534, A94
Storm, J., Gieren, W., Fouqué, P., et al. 2011b, A&A, 534, A95
Uesugi, A., & Fukuda, I. 1970, Memoirs Faculty of Sciences University of Kyoto, 33, 205
van Leeuwen, F. 2007, A&A, 474, 653
Walraven, T., Walraven, J., & Balona, L. A. 1992, MNRAS, 254, 59
Zima, W. 2006, A&A, 455, 227

[2] We remind that using the cross-correlation method, one has to use the Pp relation from Nardetto et al. (2009).

Annexe S

Understanding the dynamical structure of pulsating stars. HARPS spectroscopy of the δ Scuti stars ρ Puppis and DX Ceti

A&A 561, A151 (2014)
DOI: 10.1051/0004-6361/201322356
© ESO 2014

Astronomy & Astrophysics

Understanding the dynamical structure of pulsating stars

HARPS spectroscopy of the δ Scuti stars ρ Puppis and DX Ceti⋆

N. Nardetto[1], E. Poretti[1,2], M. Rainer[2], G. Guiglion[1], M. Scardia[2], V. S. Schmid[3], and P. Mathias[4,5]

[1] Laboratoire Lagrange, UMR7293, Université de Nice Sophia-Antipolis, CNRS, Observatoire de la Côte d'Azur, Nice, France
e-mail: Nicolas.Nardetto@oca.eu
[2] INAF – Osservatorio Astronomico di Brera, via E. Bianchi 46, 23807 Merate (LC), Italy
[3] Instituut voor Sterrenkunde, KU Leuven, Celestijnenlaan 200D, 3001 Leuven, Belgium
[4] Université de Toulouse, UPS-OMP, IRAP, 65000 Tarbes, France
[5] CNRS, IRAP, 57 avenue d'Azereix, BP 826, 65008 Tarbes, France

Received 24 July 2013 / Accepted 5 December 2013

ABSTRACT

Context. High-resolution spectroscopy is a powerful tool to study the dynamical structure of a pulsating star's atmosphere.
Aims. We aim at comparing the line asymmetry and velocity of the two δ Sct stars ρ Pup and DX Cet with previous spectroscopic data obtained on classical Cepheids and β Cep stars.
Methods. We obtained, analysed and discuss HARPS high-resolution spectra of ρ Pup and DX Cet. We derived the same physical quantities as used in previous studies, which are the first-moment radial velocities and the bi-Gaussian spectral line asymmetries.
Results. The identification of $f = 7.098$ d^{-1} as a fundamental radial mode and the very accurate H parallax promote ρ Pup as the best standard candle to test the period–luminosity relations of δ Sct stars. The action of small-amplitude nonradial modes can be seen as well-defined cycle-to-cycle variations in the radial velocity measurements of ρ Pup. Using the spectral-line asymmetry method, we also found the centre-of-mass velocities of ρ Pup and DX Cet, $V_\gamma = 47.49 \pm 0.07$ km s^{-1} and $V_\gamma = 25.75 \pm 0.06$ km s^{-1}, respectively. By comparing our results with previous HARPS observations of classical Cepheids and β Cep stars, we confirm the linear relation between the atmospheric velocity gradient and the amplitude of the radial velocity curve, but *only* for amplitudes larger than 22.5 km s^{-1}. For lower values of the velocity amplitude (i.e., <22.5 km s^{-1}), our data on ρ Pup seem to indicate that the velocity gradient is null, but this result needs to be confirmed with additional data. We derived the Baade-Wesselink projection factor $p = 1.36 \pm 0.02$ for ρ Pup and $p = 1.39 \pm 0.02$ for DX Cet. We successfully extended the period–projection factor relation from classical Cepheids to δ Scuti stars.

Key words. stars: oscillations – stars: atmospheres – line: profiles – stars: individual: rho Puppis – stars: individual: DX Ceti – stars: distances

1. Introduction

The variability of ρ Pup ≡ HD 67523 ≡ HR 3185, one of the brightest ($V = 2.88$) δ Sct stars, was first reported by Cousins (1951) and then clearly demonstrated by Eggen (1956) and Ponsen (1963). An accurate value of the pulsational period ($P = 0.14088143$ d) was determined from photometric data spanning fifty-two years (Moon & van Antwerpen 2009). Atmospheric parameters (effective temperature, surface gravity, and metallicity) were determined from ELODIE spectra by using the MILES library interpolator (Prugniel et al. 2011): $T_{\rm eff} = 6810 \pm 121$ K, $\log g = 3.59 \pm 0.14$, and [Fe/H] $= +0.60 \pm 0.05$. The [Fe/H] value confirms that ρ Pup is a member of the δ Del subgroup, that is, late-A and early-F subgiants showing spectra with enhanced metal-lines (especially the Fe I, Y II, Fe II and Zr II ones) and normal H and Ca II lines (Kurtz 1976, and references therein). ρ Pup is a well-known case where the determinations of the atmospheric parameters by means of Strömgren photometry ($b - y = 0.259$, $m_1 = 0.215$, $c_1 = 0.731$, $\beta = 2.715$) disagree in function of the photometric indices used in the calibrations. This could be ascribed to its particular metallic content. Indeed, the spectroscopic values agree excellently with those obtained from $b - y$ and c_1 indices, that is, 6850 K and $\log g = 3.5$ (Breger 1974; Kurtz 1976). Pioneering IUE spectra show emission features in the Mg II lines throughout the pulsation cycle (Fracassini et al. 1983). Later, detailed spectroscopic investigations of the pulsation properties were performed by Mathias et al. (1997) and Dall & Frandsen (2002). Very recently, the results of a dedicated spectroscopic multisite campaign excluded solar-like oscillations with an amplitude per radial mode larger than 0.5 m s^{-1} (Antoci et al. 2013).

DX Cet ≡ HD 16189 is a bright high-amplitude δ Sct (HADS) star with a period $P = 0.103939529$ d and full amplitude of 0.20 mag in V light (Kiss et al. 1999). Stellar parameters were obtained from *uvbyβ* photometry (Kiss et al. 1999; Stetson 1991): $T_{\rm eff} = 7250 \pm 200$ K, $\log g = 3.6 \pm 0.2$ dex.

Comparing the spectroscopic analysis of these two δ Scuti stars (ρ Pup and DX Cet) with previous results obtained on classical Cepheids and β Cep stars is extremely interesting for various reasons. First, for a given pulsating star, and also when comparing one star to the other, the spectral lines asymmetry show a systematic difference in average (over one pulsation cycle) that is positive or negative, depending on the spectral line considered. This effect is related to the dynamical structure of the star's

⋆ This work is based on observations made with the 3.6 m telescope at La Silla Observatory under the ESO Large Programme LP185.D-0056.

atmosphere and has been investigated in the case of classical Cepheids by means of the k-term (Nardetto et al. 2008, 2009). Since the physical origin of this phenomenon is currently not understood, the comparison of the results obtained for several types of pulsating stars is particularly helpful. Second, Nardetto et al. (2013) found a linear relation between the atmospheric velocity gradient and the amplitude of the radial velocity curve for eight classical Cepheids and two β Cep stars (α Lup and τ^1 Lup). This relation is important in the context of the Baade-Wesselink projection factor (Nardetto et al. 2004, 2007), a quantity that is used to derive the distance to the Milky Way and Large Magellanic Cloud Cepheids (Storm et al. 2011a,b). Improving this relation and generalizing it to other pulsators like δ Sct stars is an interesting roadmap to better understand the Baade-Wesselink projection factor. Finally, the use of pulsating stars located below the horizontal branch as distance indicators requires the mode identification as input parameter, and often this is a challenging task to achieve (Poretti et al. 2008). Therefore, the full characterization of bright, short-period δ Sct stars is a key matter in calibrating their period–luminosity (P–L) relation.

In Sect. 2 we briefly present our spectroscopic data. In Sect. 3, we analyse the pulsating frequencies of the two δ Scuti stars. In Sect. 4, we discuss the implication of our data on the derived distances and on the P–L relations. Section 5 is then devoted to the spectroscopic analysis of the two targets in terms of spectral line asymmetry and velocity. In Sect. 6, we compare our results on δ Sct stars with those on classical Cepheids and β Cep stars. We close with some conclusions in Sect. 7.

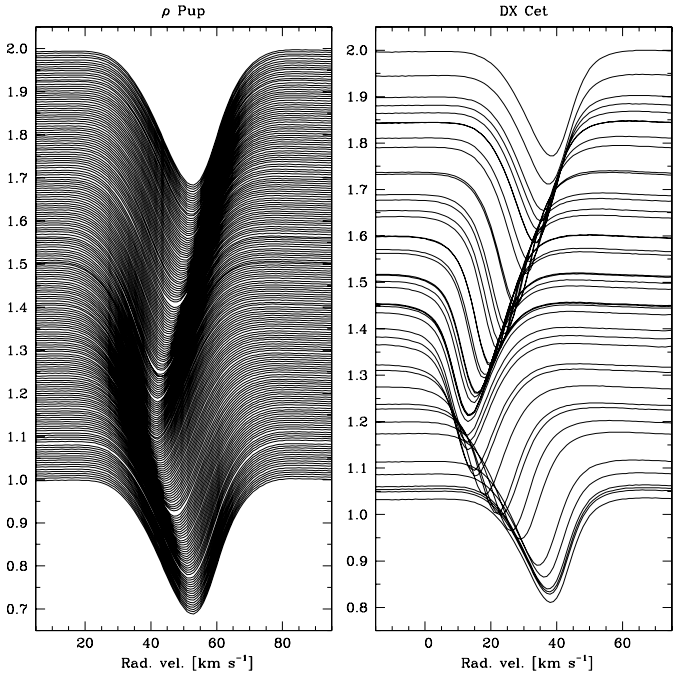


Fig. 1. Mean profiles of ρ Pup *(left panel)* and DX Cet *(right panel)* observed during different nights and folded with the respective pulsation period. Spectral intensities (in continuum units) on the y-axis are arbitrarily shifted to clearly show the profile variations.

2. Spectroscopic observations and physical parameters

We observed ρ Pup and DX Cet as additional targets in the framework of the ESO LP185.D-0056. The observations were planned to extend the physical scenario of the δ Sct stars observed with CoRoT.

Three-hundred and fifty-nine spectra of ρ Pup were obtained with the High-Accuracy Radial-velocity Planetary Searcher (HARPS; Mayor et al. 2003) in the high-resolution mode (HAM, R = 115 000) on five consecutive nights in January 2013. Observations were performed for a few hours at the end of night, as a backup program. The exposure time was set at 30 s and the signal-to-noise ratio (S/N) was typically about 270. Figure 1 (left panel) shows the behaviour of the mean line profile of each spectrum folded with the pulsational period. Forty-three spectra of DX Cet were obtained with HARPS in the high-efficiency mode (EGGS, R = 80 000) on nine consecutive nights in December 2012. Observations were performed for a few hours at the beginning of night, before the rising of CoRoT targets. The exposure time was set at 300 s and the S/N was usually around 200 (see Fig. 1, right panel). The radial velocity values of ρ Pup were obtained from the HARPS pipeline (Mayor et al. 2003), while those of DX Cet were obtained from the mean line profiles of each spectrum, calculated using the least-squares deconvolution method (Donati et al. 1997).

We estimated the physical parameters of both stars by means of a grid of synthetic spectra. For this purpose we selected four HARPS spectra with a high S/N that were taken at intervals of a quarter of a period starting from the maximum of the radial velocity curve. To save computing time, we reconstructed the synthetic spectra in five 200 Å segments in the range 4000–6650 Å by using the ATLAS9 models and the ATC code (Atmospheric Tools Compilation; Stuetz et al. 2006). Temperature, gravity, metallicity, and microturbulence velocity were allowed to vary in the range $6400 \leq T_{\rm eff} \leq 8000$ K, $2.6 \leq \log g \leq 4.8$ dex (cgs units), $-1.0 \leq$ [Fe/H] ≤ 1.0, and $0 \leq v_{\rm mic} \leq 6$ km s^{-1}, respectively. We compared the synthetic 200 Å-segments with the observed ones by computing the χ^2. At the end of this process, each segment supplied a set of physical parameters obtained by averaging its own best 50 least-squares solutions. In turn, these five sets were averaged to give the physical parameters at the pulsation phase of the HARPS spectrum that we were considering. Then, the averages of the four $T_{\rm eff}$, log g, [Fe/H], and $v_{\rm mic}$ values corresponding to the four pulsation phases supplied the mean stellar parameters. The typical uncertainties of the parameters supplied by one spectrum were also adopted as the errorbars of the mean stellar parameters.

The procedure described above supplied $T_{\rm eff}$ = 6650 ± 100 K, $\log g$ = 3.42 ± 0.14 dex, [Fe/H] = +0.20 ± 0.06, and $v_{\rm mic}$ = 4.2 ± 0.7 km s^{-1} for ρ Pup. Moreover, we measured a projected rotational velocity $v_{\rm eq} \sin i$ = 13 ± 1 km s^{-1}. In the case of DX Cet we obtained $T_{\rm eff}$ = 7200 ± 100 K, $\log g$ = 3.58 ± 0.14 dex, $v_{\rm mic}$ = 3.4 ± 0.4 km s^{-1}, [Fe/H] = −0.27 ± 0.06, and $v_{\rm eq} \sin i$ = 7 ± 1 km s^{-1}. Therefore, our spectroscopic analyses yields out that DX Cet has a slight subsolar metallic content, while ρ Pup is confirmed to be a metal-rich star.

To support the [Fe/H] determination of DX Cet in view of the discussion of the P–L relations (see Sect. 4), Fig. 2 shows the agreement between the observed spectrum and the synthetic one calculated with the above parameters.

H parallaxes are available for both stars (van Leeuwen 2007): π = 8.65 ± 0.80 mas for DX Cet and π = 51.33 ± 0.15 mas for ρ Pup. DX Cet is located at 116 ± 5 pc and we obtain M_V = 1.68 ± 0.20 assuming V = 7.00. ρ Pup is much closer, at 19.48 ± 0.02 pc only, and we derive M_V = 1.36 ± 0.01 from the well-established V = 2.81 magnitude. In the case of ρ Pup, the parallax immediately

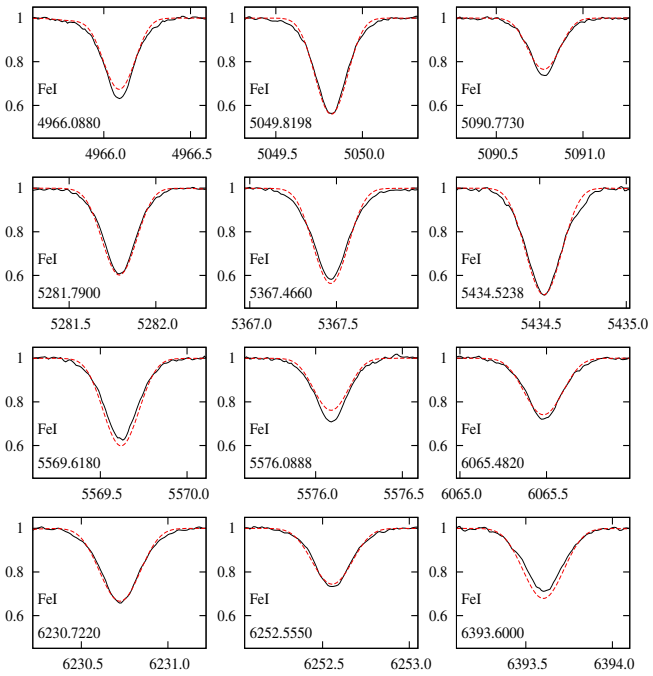


Fig. 2. Fitting of the Fe I lines in the spectrum of DX Cet. The HARPS spectrum (solid black line) is compared with the synthetic spectrum obtained with $T_{\rm eff}$ = 7100 K, $\log g$ = 3.55 dex, $v_{\rm mic}$ = 3.4 km s^{-1}, and [Fe/H] = −0.27 (dashed red). Intensities are normalized to the continuum level.

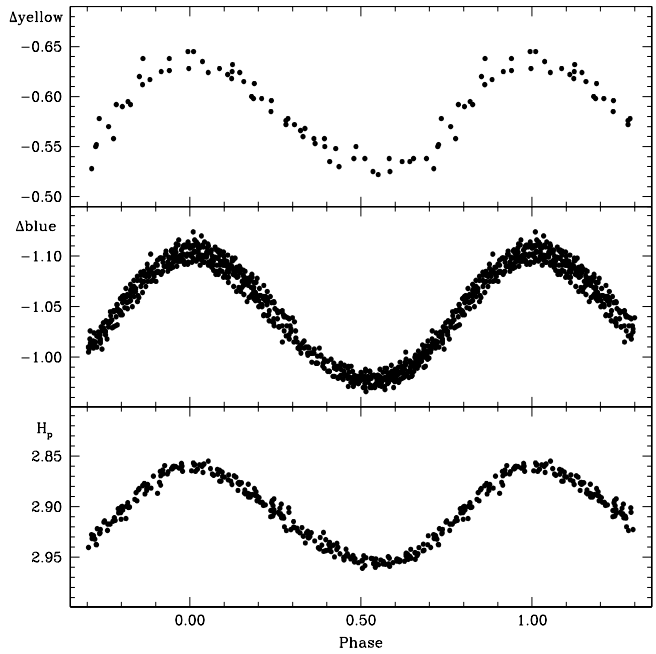


Fig. 3. Light curves of ρ Pup. *Top panel*: Eggen (1956) data, 60 measurements from 19 to 26 March 1956. *Middle panel*: Ponsen (1963) data, 658 measurements from 30 January to 23 April 1961. *Bottom panel*: H data (ESA 1997), 248 measurements from 4 January 1990 to 24 February 1993.

supplied $L = 24.0 \pm 0.2\,L_\odot$. Combined with the interferometric determination of the radius ($R = 3.52 \pm 0.07\,R_\odot$; Antoci et al. 2013), this implies $T_{\rm eff} = 6820 \pm 170$ K, in good agreement with our spectroscopic value. Furthermore, we introduced $T_{\rm eff}$, P, Q = 0.033 d (corresponding to the fundamental radial mode), M_V, and the bolometric correction +0.03 mag (Torres 2010) in the relation (Breger & Bregman 1975)

$$\log Q = -6.456 + \log P + 0.5 \log g + 0.1 M_{\rm bol} + \log T_{\rm eff}, \quad (1)$$

thus obtaining $\log g = 3.70 \pm 0.02$. This latter value agrees within 2σ with ours ($\log g = 3.42 \pm 0.14$) and within 1σ with that of Prugniel et al. (2011) ($\log g = 3.59 \pm 0.14$). When applying the same approach to DX Cet, Eq. (1) can only supply the condition

$$\log g + 2.0 \log T_{\rm eff} = 11.56(\pm 0.04), \quad (2)$$

since we have no radius measurement (see also Poretti et al. 2011). Our spectroscopic values match this condition at about 1σ (11.30 ± 0.16). Since in the case of ρ Pup the $T_{\rm eff}$ value is well constrained, this comparison shows that the $\log g$ determination is the most critical parameter to evaluate.

3. Frequency analyses and nature of pulsations

3.1. ρ Pup

An exhaustive list of photometric measurements of ρ Pup was reported by Moon & van Antwerpen (2009). Ponsen (1963), Eggen (1956), and H (ESA 1997) data are the most suitable for a detailed analysis. Data were obtained in different passbands: Ponsen's measurements were taken through a blue filter, Eggen's through a yellow filter, and those of H in the wide H_p passband. The folded light curves show asymmetric shapes (Fig. 3). The full amplitudes are 0.13, 0.11, and 0.09 mag, respectively. These values fit the sequence observed at 3858, 4310, 4720, and, 5875 Å, that is, 0.17, 0.14, 0.12, and 0.09 mag (Thulassi Doss 1969). Amplitude ratios (R_{21}) and phase shifts (ϕ_{21}) were obtained from a least-squares fit with $f = 1/P$ and $2f$ (P = 0.14088143 d): $\phi_{21} = 3.85 \pm 0.12$ rad and $R_{21} = 0.05 \pm 0.01$ for Ponsen's blue data, $\phi_{21} = 4.26 \pm 0.22$ rad and $R_{21} = 0.14 \pm 0.03$ for Eggen's yellow data, and $\phi_{21} = 4.19 \pm 0.10$ rad and $R_{21} = 0.09 \pm 0.01$ for H data. Taking into account the different passbands, these Fourier parameters agree excellently and suggest significant departure from a perfect sine-shaped light curve. The Fourier parameters of ρ Pup light curves are typical for HADS stars (Figs. 4 and 6 in Poretti 2001). These stars pulsate in a radial mode (typically the fundamental one) and nonradial modes have a much smaller amplitude. However, the amplitude of ρ Pup is not so large that it could be considered as that of a bona-fide HADS star, and more analyses are necessary.

The multiperiodicity of ρ Pup was evident after the detection of clear cycle-to-cycle variations in the radial velocity values obtained with the Coudé Echelle Spectrograph (CES) at the CAT ESO telescope (Mathias et al. 1997). The main oscillation f_1 = 7.098168 d^{-1} was identified as a radial mode and two nonradial modes with frequency 7.8 and 6.3 d^{-1} were also proposed, but the latter is very uncertain. We used the iterative sine-wave least-squares fitting method (Vaníček 1971) to analyse in frequency the radial velocity measurements obtained from the HARPS spectra, determined by the on-line pipeline with an internal error of about 1 m s^{-1}. After the detection of f_1, the power spectrum clearly shows a structure centred at $2f_1$, confirming that the radial velocity curve is asymmetrical, as well. The folded radial velocity curve shows both the asymmetrical shape and cycle-to-cycle variations up to 0.36 km s^{-1} (Fig. 4). Asymmetry can be evaluated from the maximum, which occurs at phase 0.0, while the minimum occurs before phase 0.50 (filled black circles). After introducing f_1 and $2f_1$ as known

Table 1. Least-squares parameters of the HARPS radial velocity curves of ρ Pup (T_0 = BJD 2456293.0056) and DX Cet (T_0 = BJD 2456272.5889).

ρ Pup				DX Cet			
ID	Frequency [d^{-1}]	Amplitude [km s^{-1}]	Phase [0, 2π]	ID	Frequency [d^{-1}]	Amplitude [km s^{-1}]	Phase [0, 2π]
f_1	7.098	4.948	0.129	f_1	9.6197	11.444	0.318
	±0.001	±0.011	±0.008		±0.0001	±0.007	±0.001
$2f_1$		0.297	5.102	$2f_1$		1.890	5.308
		±0.012	±0.007			±0.008	±0.005
$3f_1$		0.039	2.541	$3f_1$		0.377	3.953
		±0.012	±0.364			±0.007	±0.020
$4f_1$		0.022	5.103	$4f_1$		0.092	2.542
		±0.008	±0.651			±0.008	±0.089
f_2	7.900	0.281	2.613	$5f_1$		0.022	0.656
	±0.007	±0.027	±0.149			±0.008	±0.357
Mean rad. vel. [km s^{-1}]		46.739 ± 0.002				25.516 ± 0.004	
Residual rms [km s^{-1}]		0.041				0.023	

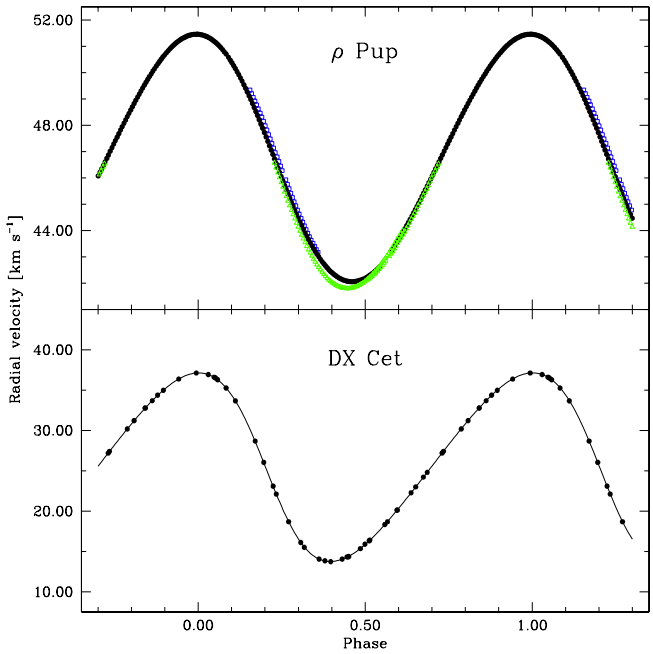


Fig. 4. *Top panel*: HARPS radial velocity values of ρ Pup. Different symbols (colours) denote different nights. Cycle-to-cycle variations are clearly visible around the minimum. *Bottom panel*: HARPS radial velocity values of DX Cet. The solid line is the fit with f_1 and three harmonics (Table 1).

constituents, the highest peak in the power spectrum of HARPS data is at f_2 = 7.900 d^{-1}, in good agreement with the value obtained from CAT data (i.e., 7.815 d^{-1}; Mathias et al. 1997). However, we note that the spectral windows of both datasets are not adequate to perform a very detailed, self-consistent frequency analysis, since these spectroscopic data were acquired with the goal of studying the dynamics of the dominant pulsation mode. The ground-based photometric data are too noisy to supply useful hints about f_2. Even H data are unsuitable to search for a small amplitude, short-period additional mode. However, the spectral window of these data is free from the ±1 d^{-1} aliasing, and we could see, among many others, a peak at 8.860 d^{-1}. Antoci et al. (2013) pointed out 8.82 d^{-1} as a possible additional frequency. Therefore, we calculated the least-squares fit by considering f_2 = 8.860 d^{-1}, but the residual rms (0.067 km s^{-1}) is poorer than that obtained using f_2 = 7.900 d^{-1} (0.041 km s^{-1}). An additional analysis of new data (e.g., Antoci et al., in prep.) may be able to ascertain the true value. We adopted f_2 = 7.900 d^{-1} to describe the dynamical structure of ρ Pup, and the effect of this choice is evaluated at the end of Sect. 5.1.

Table 1 lists the least-squares solution obtained from the HARPS data. The mean value of the radial velocity, 46.74 km s^{-1}, and the $2K$ value (peak-to-peak amplitude of the radial velocity curve), 9.9 km s^{-1}, agree both excellently with all the literature values. The former suggests that ρ Pup is a single star, the latter that the pulsation is very stable over decades (see also Moon & van Antwerpen 2009). The power spectrum of the residuals shows other modes excited around f_1, but the poor spectral window does not allow us to confirm the values proposed by Antoci et al. (2013). In the other parts of the residual power spectrum we were able to observe not only the bunches of peaks related to the higher harmonics of f_1, but also those related to the combination terms between f_1 (and harmonics) and the additional modes. As stressed by Antoci et al. (2013), these patterns affect the same region in which solar-like oscillations are expected to leave their fingerprints. All these unresolved components contribute to increase the residual rms of the solution.

Neither our radial velocity curve nor Ponsen's photometry (blue light should be sensitive to this effect) show the bump provoked by a shock wave crossing the atmosphere (Dravins et al. 1977). The emission features in the Mg II lines and the radial velocity curves in the ultraviolet do not show any particular behaviour either (Fracassini et al. 1983). In the top panel of Fig. 4, cycle-to-cycle variations can be noticed especially at the minimum, which seems to occur at different phases. This strange behaviour is only apparent because ρ Pup was observed more at the minimum that at the maximum. For sake of clarity, we investigated the possibility of transient or particular events in the atmosphere dynamics around maximum compression and subsequent expansion. A close examination of the core of the Ca II K line did not reveal any emission during the observations. Therefore, the cycle-to-cycle variations in radial velocity data are definitely unrelated to the variations in the chromospheric activity.

Dall & Frandsen (2002) investigated the presence of the pulsation in the line indices of the Balmer series using the DFOSC instrument mounted at the Danish 1.54 m telescope in La Silla. Indeed, pulsation effects were found, and the authors calculated a ratio of 0.43 for the ratio between the amplitudes of

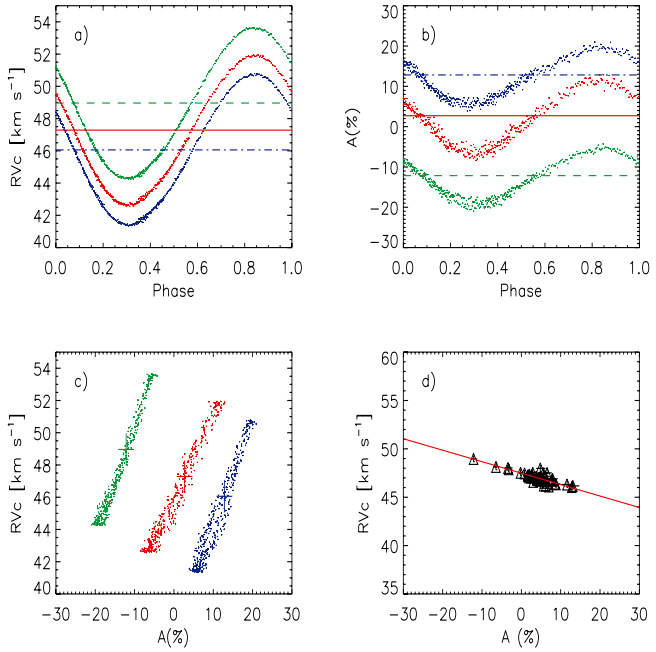


Fig. 5. Illustration of the method applied to derive the centre-of-mass velocity of ρ Pup from the line asymmetries. Points are single observations folded with $f_1 = 7.098$ d^{-1}; the contribution from $f_2 = 7.900$ d^{-1} has been removed.

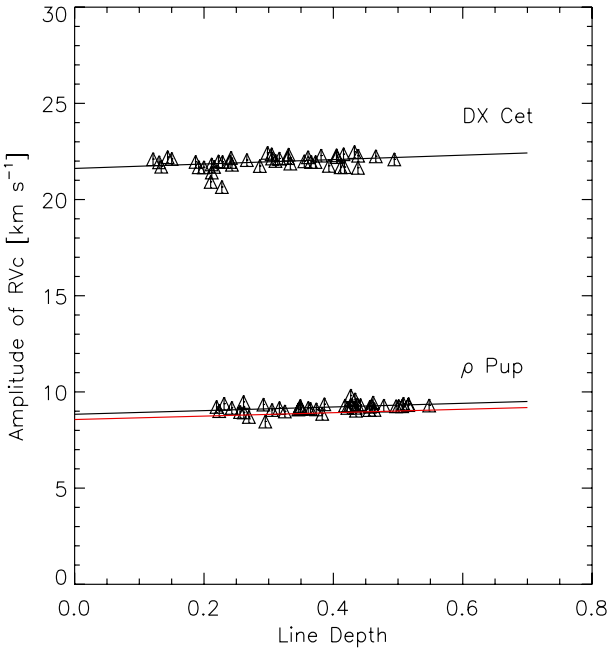


Fig. 6. Amplitude of the RV_c curves as a function of the spectral line depth in the case of the two δ Sct stars ρ Pup (lower values), and DX Cet (larger values). In the case of ρ Pup, the solid red line shows the same relation but after removing the nonradial mode.

variations in the Hα line and photometry. They considered a half-amplitude of 75 mmag from Eggen's measurements, which is that derived from a simple inspection of the light curve. We obtained 0.58 for the yellow data and 0.49 for the blue data from the more accurate values resulting from the least-squares fits. Together with the available radial velocity/magnitude amplitude ratio ($2K/\Delta m_v = 10.0/0.11 = 91$ km s^{-1} mag^{-1}, see Yang et al. 1987, for a review and summary), these results strengthen the identification of f_1 as a radial mode.

3.2. DX Cet

The solution of the radial velocity curve of DX Cet is much simpler than that of ρ Pup. The five components $f_1 = 9.6197$ d^{-1}, $2f_1, 3f_1, 4f_1$ and $5f_1$ are detected in the power spectrum and provide a very satisfactory fit of the radial velocity curve (Table 1 and Fig. 4). The fit of the H data (ESA 1997) supplied the Fourier parameters $R_{21} = 0.24 \pm 0.02$, $\phi_{21} = 3.9 \pm 0.1$, and $\phi_{31} = 1.4 \pm 0.4$ rad. They are typical values for HADS stars (Figs. 4–6 in Poretti 2001). The mean H_p magnitude is 7.077 ± 0.005, which in turn yields $V = 7.00$ for $B_T - V_T = 0.33$ (Bessell 2000). This value and the full amplitude of 0.21 mag as well agree with those reported by Kiss et al. (1999). The $2K/\Delta m_v = 23.1/0.21 = 110$ km s^{-1} mag^{-1} value supports radial pulsation.

4. ρ Pup and DX Cet as distance indicators

The H parallaxes and the identification of the pulsation modes of ρ Pup and DX Cet as the fundamental radial ones allowed us to test the P–L relations of HADS stars. There are two P–L relations:

$$M_V = -1.83(0.08) - 3.65(0.07) \log P \quad (3)$$

(Poretti et al. 2008), and

$$M_V = -1.27(0.05) - 2.90(0.07) \log P - 0.19(0.015)[\mathrm{Fe/H}] \quad (4)$$

(McNamara 2011). Equation (3) was obtained by using all the short-period ($P < 0.20$ d) stars that pulsate in the fundamental radial mode and are located in a wide variety of stellar systems. It provides an excellent fit without knowing any other parameter than the period. The metal-dependent term was introduced in Eq. (4) with the goal to determine the same law for HADS and Cepheids and should only be considered when [Fe/H] < 0.0 (McNamara 2011).

For DX Cet, Eq. (3) supplies $M_V = 1.76 \pm 0.10$ and Eq. (4) $M_V = 1.64 \pm 0.07$ for [Fe/H] = −0.27. Both predictions agree excellently with the H M_V, and hence $P = 0.104$ d can definitely be identified as the fundamental radial mode. For instance, by assuming that the pulsation is in the first overtone mode, the corresponding fundamental mode would be 0.135 d, and the P–L relations would predict $M_V = 1.3$, which does match the H M_V. Due to the relevant error on the parallax, McNamara (2011) applied an LK correction (−0.10 mag, then $M_V = 1.58 \pm 0.20$; Lutz & Kelker 1973), but the star becomes too bright to fit the value predicted by Eq. (4) in a more satisfactory way.

However, because it is a statistical procedure, the LK correction is powerful when applied to a sample of stars (with the same π) and is much more uncertain when applied to a single case (e.g., Oudmaijer et al. 1998).

The period of ρ Pup is among the longest in the δ Sct sample. Equations (3) and (4) predict similar values without the metal-dependent term, that is, $M_V = 1.28 \pm 0.10$ and $M_V = 1.21 \pm 0.07$, respectively. The former agrees excellently with the very accurate H $M_V = 1.36 \pm 0.01$ value, while the latter is slightly outside errorbars. We note that using the [Fe/H] correction in Eq. (4) shifts the calculated value too far ($M_V = 1.09 \pm 0.07$) from the observed one. Therefore, this correction definitely does not have to be applied to stars when [Fe/H] > 0.0. Moreover, assuming that f_1 is the first radial overtone, we derive $M_V = 0.87$ from the P–L relations, a too bright luminosity for

the H parallax. This convinced us that ρ Pup is pulsating in the fundamental radial mode.

This achievement adds an important stellar candle to the sample of galactic δ Sct stars with known parallaxes. The current inventory is composed of nine stars (Table 2 in McNamara 2011). However, the identification of the fundamental radial mode is very reliable only for high-amplitude pulsation, that is, the HADS stars DX Cet, AI Vel, and SX Phe. One can add δ Sct itself, since detailed investigations (Templeton et al. 1997) corrected the previous identification of the dominant mode as a radial overtone (Balona et al. 1981). The remaining five cases are rather uncertain, starting with 1 Mon, whose dominant mode has been identified as an overtone (Balona & Stobie 1980). It is instructive to note that the dominant modes of FG Vir and X Cae are nonradial (Zima et al. 2006; Mantegazza et al. 2000): the fundamental radial mode, if it is indeed excited, has to be searched for in the low-amplitude terms, with a wide margin of uncertainty. α Aql (Altair) is a fast rotating star and the nature of the very weak amplitude variations (<0.001 mag) detected with the WIRE satellite can be generated by a wide variety of modes. In particular, there is no convincing evidence that the observed modes are radial ones (Suárez et al. 2005). Finally, no mode identification has been proposed for the small-amplitude variations (0.02 mag) observed for BS Tuc. Therefore, ρ Pup is by far the most convincing case of a δ Sct pulsating in the fundamental radial mode with an accurate H parallax.

5. Spectroscopic analysis

We performed a detailed analysis of the high-S/N HARPS spectra of ρ Pup and DX Cet following the procedure described in Nardetto et al. (2006a). We selected 45 spectral lines, taking care that they were not blended.

We extracted radial velocity and line asymmetry curves for all selected lines of all stars. The method we use for the radial velocity (that is the best one to use when the S/N allows it) is the first moment of the spectral line, $\mathrm{RV_c}$. The radial velocity curve derived from this method is absolutely independent of the spectral line width and the rotation. This property is extremely valuable for comparing the behaviour of different spectral lines of different pulsating stars. We also derived the spectral line asymmetries A with a very high precision, using an estimator that we call the bi-Gaussian: two analytic semi-Gaussians are fitted to the blue and red part of the spectral line profile. The amount of asymmetry (in percentage) is then given by the comparison of the half-width at half-maximum of each semi-Gaussian (see Nardetto et al. 2006a, their Eqs. (2) and (3)). This definition was well-suited to the data quality.

5.1. ρ Pup

We performed a least-squares fit of the observed values of RV_c and A by means of the Fourier series

$$y(t) = B_0 + \sum_{i=1}^{5} B_i \cos((t - T_0)\ f_i + \phi_i) \quad (5)$$

and by using $f_1 = 7.098\mathrm{d}^{-1}$, $f_2 = 7.900\ \mathrm{d}^{-1}$, $f_3 = 2f_1$, $f_4 = 3f_1$, and $f_5 = 4f_1$. In this way we were able to fold the data on one mode by subtracting the contribution of the other. Figure 5 shows the folded points with f_1 of the radial velocities (panel a) and asymmetries (panel b) for the three following lines, CrII 4634.07 (blue), FeI 5410.91 (green), and FeI 6393.60 Å (red), respectively. The corresponding averages of these curves (or similarly B_0 values obtained from Eq. (5)) are shown as horizontal lines in panels a and b (in dash-dotted, dashed and solid lines), and are called γ-velocities and γ-asymmetries. The residual systematic scatter is caused by the contamination from very small amplitude modes that are still not identified after f_1 and f_2. There is an evident anticorrelation: higher velocities correspond to negative asymmetries, low velocities to positive asymmetries. This behaviour is also shown by the trend in the barycenters (big crosses) of the RV_c–A loops (Fig. 5, panel c). By plotting for each line the γ-velocity and the γ-asymmetry, we can calculate the parameters of the analytic relation

$$V_\gamma(i) = \alpha_0 A_\gamma(i) + \beta_0, \quad (6)$$

thus obtaining $\alpha_0 = -0.12 \pm 0.01\ \mathrm{km\,s^{-1}}$ and $\beta_0 = 47.49 \pm 0.07\ \mathrm{km\,s^{-1}}$ (Fig. 5, panel d). Following Nardetto et al. (2008), the centre-of-mass velocity of the star is defined as $V_{\gamma\star} = \beta_0 = 47.49 \pm 0.07\ \mathrm{km\,s^{-1}}$(i.e., the γ-velocity corresponding to a null γ-asymmetry). We note that the contributions of $f_2 = 7.900\ \mathrm{d^{-1}}$ to the γ-velocity and γ-asymmetry are much less important than those of f_1, which means that they affect the spectral line asymmetries in a marginal way. The k-term, defined as $k = \langle V_\gamma\rangle_\mathrm{i} - V_{\gamma\star} = 47.0_{\pm0.1} - 47.5_{\pm0.1} = -0.5 \pm 0.1\ \mathrm{km\,s^{-1}}$, where $\langle V_\gamma\rangle_\mathrm{i}$ is the γ-velocity averaged over the 45 spectral lines. We briefly discuss the k-term problem in Sect. 5.3.

The next step of the spectroscopic analysis is to measure the velocity gradient within the atmosphere of the star. In Nardetto et al. (2007), we have shown that the line depth (taken at the minimum radius phase) is a good indicator of the line-forming regions. We use this definition of the line depth (hereafter D) in the following. In this case, the photosphere corresponds to a null line depth. By comparing the $2K$ amplitude (defined as the amplitude of the first-moment radial velocity curve, hereafter ΔRV_c) with the depth of the 45 spectral lines selected, one can in principle directly measure the atmospheric velocity gradient (at least in the part of the atmosphere where the lines form). For ρ Pup, we found the following relation (see also Fig. 6):

$$\Delta RV_c = [0.95 \pm 0.49]D + [8.84 \pm 0.19]\ \mathrm{km\,s^{-1}}. \quad (7)$$

This relation (in which we define the slope and the zero-point by a_0 and b_0, respectively) can be used to derive the Baade-Wesselink projection factor following the semi-theoretical approach presented in Guiglion et al. (2013). The projection factor is used to convert the radial velocity into the pulsation velocity in the Baade-Wesselink methods of distance determination. It is composed of three terms: $p = p_0 f_\mathrm{grad} f_{\mathrm{o-g}}$ (Nardetto et al. 2007). First, the geometric projection factor, p_0, is mainly related to the limb-darkening of the star. The linear limb-darkening law of the continuum intensity profile of the star provided by Claret & Bloemen (2011) is $I(\cos(\theta)) = 1 - u_R + u_R \cos(\theta)$, where u_R is the limb darkening of the star in R-band and θ is the angle between the normal of the star and the line of sight. For ρ Pup we found $u_R = 0.484$ (considering the rounded values $T_\mathrm{eff} = 6500$ K, $\log g = 3.5$, $v_\mathrm{mic} = 4\ \mathrm{km\,s^{-1}}$, and $Z = 0.0$). Using the relation linking p_0 to u_R: $p_0 = \frac{3}{2} - \frac{u_R}{6}$ (Getting 1934; Hadrava et al. 2009), we found $p_0 = 1.416$. In this determination of the geometric projection factor, we assumed (as done previously for Cepheids) that the limb-darkening variation within the lines (Nardetto et al. 2007) and that the geometric projection factor time-dependency in the R-band (Nardetto et al. 2006b) are negligible.

Then, f_grad depends on the spectral line considered: $f_\mathrm{grad} = b_0/(a_0 D + b_0)$ (Nardetto et al. 2007, their Eq. (3)). For ρ Pup, it ranges from 0.94 ($D = 0.22$) to 0.98 ($D = 0.55$). For a typical depth in our sample of $D = 0.4$, we find $f_\mathrm{grad} = 0.96 \pm 0.01$.

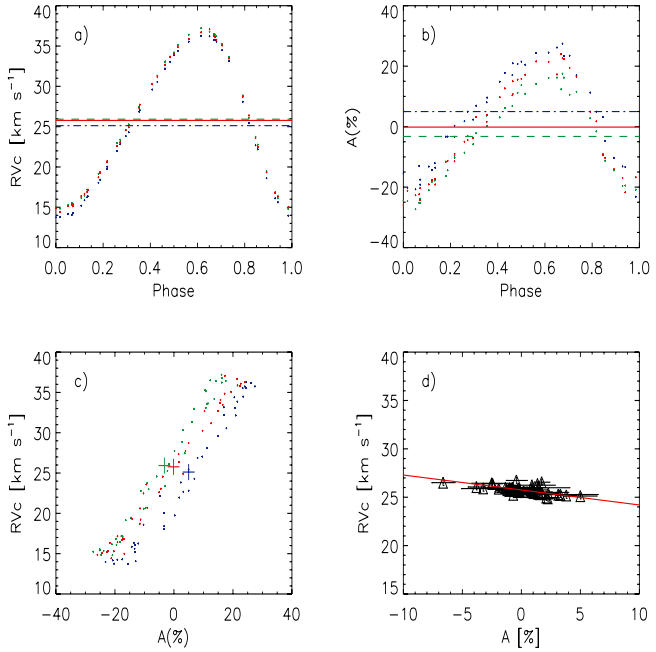


Fig. 7. Same as Fig. 5 for DX Cet.

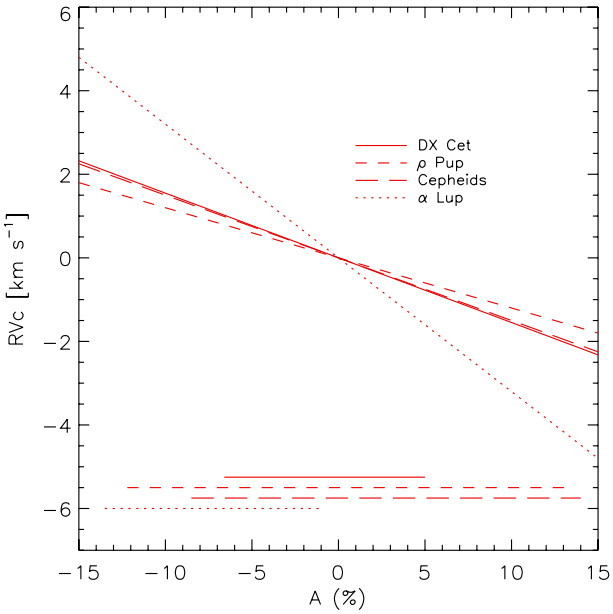


Fig. 8. Same as Figs. 5d and 7d, but including the results obtained for classical Cepheids (averaged over eight stars) and α Lup (β Cep star). The horizontal lines at the bottom show the corresponding γ-asymmetry ranges.

Finally, there is a linear relation between f_{o-g} (correction to the projection factor due to the differential velocity between the *optical* and *gas* layers at the photosphere of the star) and $\log P$: $f_{o-g} = [-0.023 \pm 0.005] \log P + [0.979 \pm 0.005]$ (derived using classical Cepheids; Nardetto et al. 2007). When we apply this relation for ρ Pup as in Guiglion et al. (2013) for the δ Sct stars AI Vel and β Cas, we found $f_{o-g} = 1.00 \pm 0.02$. The final value of the projection factor of ρ Pup is thus $p = p_0 f_{grad} f_{o-g} = 1.36 \pm 0.02$.

From a methodological point of view, it is interesting to note that we find $a_0 = 0.88 \pm 0.49$ and $b_0 = 8.56 \pm 0.19$ (i.e., a decrease of the slope and zero-point of the relation by 8% and 3%, respectively) when fitting the original data with f_1 and harmonics alone. In turn, this increases the value of f_{grad}, and consequently that of p, by only 0.2%. In a similar way, there is no change in the parameters of Eq. (7) and a non-significant decrease of the zeropoint of Eq. (6) (from 8.86 to 8.84 km s^{-1}) when using $f_2 = 8.86$ d^{-1} instead of 7.90 d^{-1} (see Sect. 3.1).

5.2. DX Cet

We applied the same analysis to DX Cet. Figure 7 (panels a and b) shows the radial velocity and line asymmetry curves for the three lines FeI 4213.65, FeI 5393.17, and FeI 6393.60 Å. We found the same anticorrelation between the γ-velocity and the γ-asymmetry:

$$V_\gamma(i) = [-0.15 \pm 0.03] A_\gamma(i) + [25.75 \pm 0.06].$$

The centre-of-mass velocity of the star is then $V_{\gamma\star} = \beta_0 = 25.75 \pm 0.06$ km s^{-1} and the k-term is $k = \langle V_\gamma \rangle - V_{\gamma\star} = 25.7_{\pm 0.1} - 25.7_{\pm 0.1} \simeq 0.0 \pm 0.1$ km s^{-1}.

For the atmospheric velocity gradient we found (Fig. 6)

$$\Delta RV_c = [1.15 \pm 0.48] D + [21.62 \pm 0.14] \text{ km s}^{-1}, \quad (8)$$

which corresponds to a velocity gradient or f_{grad} correction of the projection factor ranging from 0.97 ($D = 0.12$) to 0.99 ($D = 0.49$). The average value $f_{grad} = 0.98 \pm 0.01$ ($D = 0.30$) was used. From the rounded values available in Claret & Bloemen (2011, $T_{eff} = 7000$ K, $\log g = 3.5$, $v_{mic} = 2.0$ km s^{-1} and $Z = -0.3$), we obtained $u_R = 0.474$ and a geometric projection factor $p_0 = 1.421$. Considering, as for ρ Pup, $f_{o-g} = 1.00 \pm 0.02$, we finally found a Baade-Wesselink projection factor $p = 1.39 \pm 0.02$ for DX Cet.

6. Comparing δ Scuti stars with β Cep stars and classical Cepheids

Our HARPS sample is composed of stars with a good phase coverage and for which we were able to measure the spectral line asymmetry properly. We have eight classical Cepheids (R TrA, S Cru, Y Sgr, ζ Gem, β Dor, RZ Vel, ℓ Car, and RS Pup; Nardetto et al. 2008), two δ Sct stars (ρ Pup and DX Cet; this paper), and the β Cep star α Lup (Nardetto et al. 2013). Moreover, we have other cases. AI Vel has an incomplete phase coverage that prevented us from measuring the γ-asymmetry, although we were able to measure the atmospheric velocity gradient and the projection factor. β Cas is rotating too fast to measure the spectral line asymmetry or derive the atmospheric velocity gradient with a good precision. Thus, we determined the projection factor only with a large uncertainty (Guiglion et al. 2013). The classical Cepheid X Sgr shows spectral line splitting due probably to a shockwave in the atmosphere (Mathias et al. 2006). The β Cep τ^1 Lup shows significant nonradial modes (Nardetto et al. 2013) and we were unable to consistently apply the bi-Gaussian method to measure the line asymmetry.

In Fig. 8, we compare $V_\gamma(i) = \alpha_0 A_\gamma(i) + \beta_0$ relations between the γ-velocities and the γ-asymmetries (after correcting for the zero-point) found for ρ Pup and DX Cet, with previous results obtained for the β Cep star α Lup and for the eight classical Cepheids mentioned above. It is remarkable that the results obtained for δ Scuti stars and classical Cepheids are consistent, while α Lup shows a different behaviour (steeper slope of the relation). We also note that α Lup has only negative γ-asymmetries

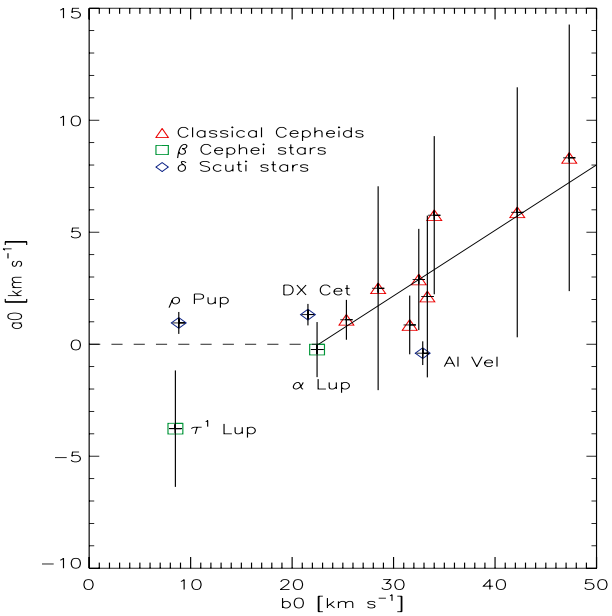


Fig. 9. Velocity gradient in the atmosphere of the stars as a function of the amplitude of the RV_c curves.

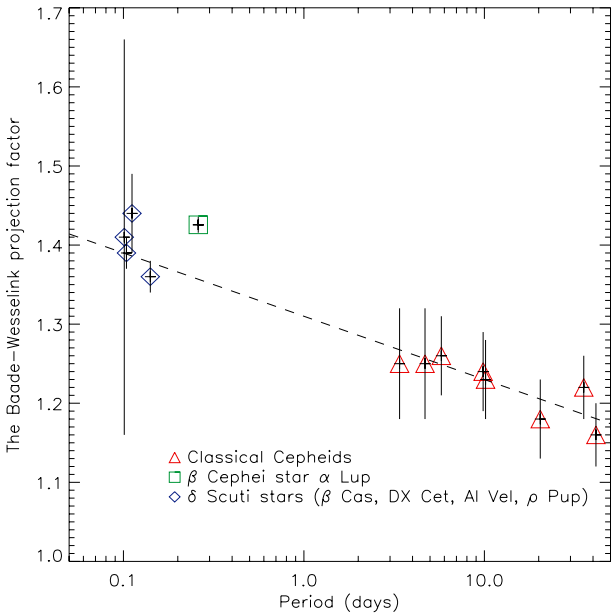


Fig. 10. Baade-Wesselink projection factor as a function of the period for different kinds of pulsating stars. The δ Scuti stars indicated as blue diamonds are, by increasing periods: β Cas, DX Cet, AI Vel and ρ Pup.

(at least over the 55 spectral lines considered in Nardetto et al. 2013). It is currently very difficult to interpret this behaviour, but at least qualitatively, we can conclude that there is a particular physical mechanism that probably affects the α Lup spectral lines asymmetry, while this is not the case for the δ Scuti and Cepheid stars.

For the k-term quantity, we found $k = -0.5$ km s^{-1} and $k = 0$ km s^{-1} for ρ Pup and DX Cet, respectively. These values are consistent with those found for Cepheids (values ranging from 0 to -1 km s^{-1} depending on the period of the star, Nardetto et al. 2013). By using a Cepheid in an eclipsing binary system ($P_{puls} = 3.8$ d, $P_{orb} = 309$ d), Pilecki et al. (2013) independently found a blue-shifted value $k = -0.59$ km s^{-1}. On the other hand, α Lup shows a red-shifted value $k = 2.2$ km s^{-1}.

Figure 9 shows the slope a_0 (from the $\Delta RV_c = a_0 D + b_0$ relation) as a function of the $2K$-amplitude (i.e., b_0). The results obtained for δ Scuti stars, β Cep stars, and classical Cepheids are compared. The case of τ^1 Lup must be considered separately, as previously mentioned in Nardetto et al. (2013). This star indeed shows a reverse atmospheric velocity gradient, which means that a line forming in the upper part of the atmosphere has a $2K$-velocity amplitude lower than a line forming closer to the photosphere. This might be because of the nonradial mode detected in the spectroscopic data. On the other hand, ρ Pup has a null velocity gradient for a similar velocity amplitude of about $b_0 \simeq 10$ km s^{-1}. It has to be confirmed, but it seems that stars with a dominant radial mode and with b_0 lower than 22.5 km s^{-1} have a null atmospheric velocity gradient (dashed line in Fig. 9). Conversely, we can convincingly consider a linear trend (solid line in the figure) for $2K$-amplitudes larger than 22.5 km s^{-1}: $a_0 = [0.29 \pm 0.04] b_0 - [6.61 \pm 1.36]$.

The comparison of the projection factors within our sample is also very interesting. In the framework of our project, we determined the Baade-Wesselink projection factor for four δ Sct stars: ρ Pup ($p = 1.36 \pm 0.02$), DX Cet ($p = 1.39 \pm 0.02$), AI Vel ($p = 1.44 \pm 0.05$), and β Cas ($p = 1.41 \pm 0.25$). Figure 10 shows that all these values excellently fit the extension toward short periods of the relation found for Cepheids, that is, $p = [-0.08 \pm 0.05] \log P + [1.31 \pm 0.06]$ (Nardetto et al. 2009). This result seems more robust than the similar one obtained by Laney & Joner (2009), who used an indirect method based on the comparison of geometric and pulsation parallaxes. On the other hand, the projection factor of the β Cep star α Lup is 8σ higher than the relation (Fig. 10). By omitting α Lup, we can determine the following relation common to δ Sct stars and classical Cepheids:

$$p = [-0.08 \pm 0.01] \log P + [1.31 \pm 0.01], \quad (9)$$

which is similar to the one derived for Cepheids only, but more precise (the reduced χ^2 is 0.97).

However, we have to stress some methodological points. First, in the projection factor decomposition ($p = p_0 f_{grad} f_{o-g}$), the third component, f_{o-g}, was extrapolated for the δ Scuti stars (not for α Lup, for which we used a dedicated hydrodynamical model), while the f_{grad} quantity was derived directly and independently from observations. We also recall that the geometric projection factor, p_0, is directly linked to the limb-darkening and thus to the fundamental parameters of the stars. Second, for the Cepheids, the projection factors are consistent with the cross-correlation method of the radial velocity determination. For DX Cet and ρ Pup, the line depth considered for the f_{grad} correction is typical (i.e., averaged over all lines considered in our sample), which means that the derived projection factors are in principle very close to those to be used in the cross-correlation method. For α Lup, AI Vel, and β Cas, there is no velocity gradient in the atmosphere and the projection factor is the same regardless of the line considered, and thus is consistent with the cross-correlation method. There remains only the fact that in the cross-correlation method a Gaussian is fitted to the cross-correlated spectral line profile, which in principle reduces the value of the projection factor by few percents compared with that based on the first-moment method (Nardetto et al. 2006a). Reducing the projection factor for short pulsators in Fig. 10 by a few per cent will basically not change the relative position of α Lup and our qualitative conclusion that the period–projection factor relation seems to straightly link δ Scuti stars and classical Cepheids. Third, the fast rotation of some δ Scuti stars (as well

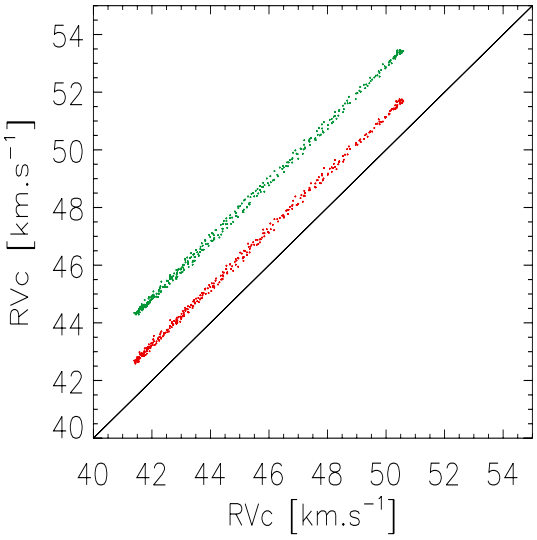


Fig. 11. Van Hoof diagram for ρ Pup. The radial velocity curve associated to the Fe I 5410.91 (green) and Fe I 6393.60 Å (red) spectral line profiles is plotted as a function of the same quantity, but for Cr II 4634.07. The solid line corresponds to the identity function. There is no Van Hoof effect detected (no loops), while the γ-velocity effect is clearly seen (y-axis offsets of the curves).

as the inclination of their rotation axis) can affect the projection factor by 10% or even more (Guiglion et al. 2013). However, the δ Scuti stars in our sample show $v_{\rm eq} \sin i$ values lower than 13 km s^{-1}, except for β Cas with $v_{\rm eq} \sin i \simeq 75$ km s^{-1}.

Even if we were able to derive both the Baade-Wesselink projection factors and the centre-of-mass velocities for the eleven pulsating stars in our sample, an effort (both observational and theoretical) has still to be made to understand the spectral line asymmetry properly. For classical Cepheids, the hydrodynamical models reproduce the observed velocities and even the atmospheric velocity gradient very well (Fokin 1996; Nardetto et al. 2004, 2007). Nevertheless, currently, there is no hydrodynamical model of pulsating stars that can correctly reproduce the γ-velocities and γ-asymmetries. In particular, we emphasize that the k-term quantity cannot be explained by a Van Hoof effect (Mathias et al. 1993, 1995). In Fig. 11, we show the Van Hoof diagram for the three spectral lines of Sect. 5.1 for ρ Pup.

The Van Hoof effect is not detected because there is no phase shift between the radial velocities of the different spectral lines (i.e., no loops). We also find that the two curves have a slope close to one, indicating a null atmospheric velocity gradient, as already mentioned. Nevertheless, the zero-points of the two curves are shifted, as a result from the γ-velocity offsets (Fig. 5, panel a). The possible physical causes of these offsets (e.g., additional modes) are under analysis.

7. Conclusions

We presented HARPS high-resolution spectra of ρ Pup and DX Cet, thus increasing our sample to eleven stars. Among them, the β Cep star α Lup shows an interesting positive value of 2.2 km s^{-1} for the k-term, while other kinds of pulsating stars have negative values (ranging from -1 to 0 km s^{-1}). We also found that ρ Pup shows the same $2K$ velocity amplitude (8.84 ± 0.19 km s^{-1}) regardless of the spectral line considered in our sample (45 lines), while this is not the case for stars with amplitudes larger than 22.5 km s^{-1}, where a trend is indeed found as a function of the the line depth. This behaviour, if confirmed, would mean that the atmospheric velocity gradient correction on the Baade-Wesselink projection factor, $f_{\rm grad}$, is equal to 1.0 for any type of pulsating star as soon as its $2K$ velocity amplitude is lower than 22.5 km s^{-1}. Finally, we found that the period–projection factor relation might be common to classical Cepheids and δ Scuti, while the β Cep star α Lup stands at 8σ above the relation.

The excitation of different pulsation modes (fundamental and overtone radial, pressure and gravity nonradial) usually makes the use of δ Sct stars as distance indicators problematic. For ρ Pup, our analysis of light and radial velocity curves identified the dominant mode as the fundamental radial one. Because it is a very bright star with an accurate H parallax, ρ Pup can be now considered as the best standard candle for the δ Sct class. The H absolute magnitude gives us a luminosity $\log L/L_{\odot} = 1.38$. Combined with $T_{\rm eff} = 6650$–6800 K, this implies that ρ Pup is very close to the red border of the instability strip, probably leaving the central part where most of the HADS stars are located (Pamyatnykh 2000).

Moreover, from the H parallax ($\pi = 7.02 \pm 0.17$ mas), the mean radius of $R = 3.52 \pm 0.07\, R_{\odot}$ (Antoci et al. 2013), and our value of the projection factor $p = 1.36$ together with our radial velocity curve (in particular, $2K = 8.8$ km s^{-1}), we were able to infer an absolute angular diameter variation of 11 μas (or 0.7%). Unfortunately, there are no K photometric observations of ρ Pup that cover a full pulsation cycle to which one might apply the infrared surface brightness relation and confirm these findings.

Acknowledgements. The authors wish to thank the anonymous referee for useful comments. E.P. and M.S. acknowledge financial support from the Italian PRIN-INAF 2010 *Asteroseismology: looking inside the stars with space- and ground-based observations*. M.R. scknowledges financial support from the FP7 project *SPACEINN: Exploitation of Space Data for Innovative Helio- and Asteroseismology*. V.S.S. is an Aspirant PhD fellow of the Fonds voor Wetenschappelijk Onderzoek, Vlaanderen (FWO), Belgium. N.N. and E.P. acknowledge the *Observatoire de la Côte d'Azur* for the one-month grant that has allowed EP to work at OCA in April and May 2013.

References

Antoci, V., Handler, G., Grundahl, F., et al. 2013, MNRAS, 435, 1563
Balona, L., & Stobie, R. S. 1980, MNRAS, 190, 931
Balona, L., Dean, J. F., & Stobie, R. S. 1981, MNRAS, 194, 125
Bessell, M. S. 2000, PASP, 112, 961
Breger, M. 1974, ApJ, 192, 75
Breger, M., & Bregman, J. N. 1975, ApJ, 200, 343
Claret, A., & Bloemen, S. 2011, A&A, 529, A75
Cousins, A. W. 1951, Observatory, 71, 199
Dall, T. H., & Frandsen S. 2002, A&A, 386, 964
Donati, J.-F., Semel, M., Carter, B. D., Rees, D. E., & Collier Cameron, A. 1997, MNRAS, 291, 658
Dravins, D., Lind, J., & Särg, K. 1977, A&A, 54, 381
Eggen, O. J. 1956, PASP, 68, 238
ESA 1997, The Hipparcos and Tycho Catalogues, ESA SP-1200
Fokin, A. B., Gillet, D., & Breitfellner, M. G. 1996, A&A, 307, 503
Fracassini, M., Pasinetti, L. E., Castelli, F., Antonello, E., & Pastori, L. 1983, Ap&SS, 97, 323
Getting, I. A. 1934, MNRAS, 95, 139
Guiglion, G., Nardetto, N., Mathias, P., et al. 2013, A&A, 550, A10
Hadrava, P., Slechta, M., & Skoda, P. 2009, A&A, 507, 397
Kiss, L. L., Csak, B., Thomson, J. R., & Szatmary, K. 1999, IBVS, 4660, 1
Kurtz, D. W. 1976, ApJS, 32, 651
Laney, C. D., & Joner, D. J. 2009, AIPC, 1170, 93
Lutz, T. E., & Kelker, D. H. 1973, PASP, 85, 573
Mantegazza, L., Zerbi, F. M., & Sacchi, A. 2000, A&A, 354, 112
Mathias, Ph., & Gillet, D. 1993, A&A, 278, 511
Mathias, Ph., Gillet, D., Fokin, A. B., & Chadid, M. 1995, A&A, 298, 843
Mathias, Ph., Gillet, D., Aerts, C., & Breitfellner, M. G. 1997, A&A, 327, 1077
Mathias, Ph., Gillet, D., Fokin, A. B., et al. 2006, A&A, 457, 575
Mayor, M., Pepe, F., Queloz, D., et al. 2003, The Messenger, 114, 20

McNamara, D. H. 2011, AJ, 142, 110
Moon, T., & van Antwerpen, C. 1997, JAAVSO, 37, 3
Nardetto, N., Fokin, A., Mourard, D., et al. 2004, A&AP, 428, 131
Nardetto, N., Mourard, D., Kervella, P., et al. 2006a, A&A, 453, 309
Nardetto, N., Fokin, A., Mourard, D., et al. 2006b, A&A, 454, 327
Nardetto, N., Mourard, D., Mathias, P., et al. 2007, A&A, 471, 661
Nardetto, N., Stoekl, A., Bersier, D., et al. 2008, A&A, 489, 1255
Nardetto, N., Gieren, W., Kervella P., et al. 2009, A&A, 502, 951
Nardetto, N., Mathias, P., Fokin, A., et al. 2013, A&A, 553, A112
Oudmaijer, R. D., Groenewegen, M. A. T., & Schrijver, H. 1998, MNRAS, 294, L41
Pamyatnykh, A. A. 2000, in Delta Scuti and Related Stars, eds. M. Breger, & M. H. Montgomery, ASP Conf. Ser., 210, 215
Pilecki, B., Graczyk, D., Pietrzynski, G., et al. 2013, MNRAS, 436, 953
Ponsen, J. 1963, Bull. Astron. Inst. Netherlands, 17, 44
Poretti, E. 2001, A&A, 371, 986
Poretti, E., Clementini, G., Held, E. V., et al. 2008, ApJ, 685, 947
Poretti, E., Rainer, M., Weiss, W. W., et al. 2011, A&A, 528, A147
Prugniel, Ph., Vauglin, I., & Koleva, M. 2011, A&A, 531, A165
Stetson, P. 1991, ApJ, 102, 589
Storm, J., Gieren, W., Fouqué, P., et al. 2011a, A&A, 534, A94
Storm, J., Gieren, W., Fouqué, P., et al. 2011b, A&A, 534, A95
Stuetz, Ch., Bagnulo, S., Jehin, E., et al. 2006, A&A, 451, 285
Suárez, J. C., Bruntt, H., & Buzasi, D. 2005, A&A, 438, 633
Templeton, M. R., McNamara, B. J., Guzik, J. A., et al. 1997, AJ, 114, 1592
Thulassi Doss, A. 1969, Kodaikanal Obs. Bull., 191
Torres, G. 2010, AJ, 140, 1158
van Leeuwen, F. 2007, A&A, 474, 653
Vaniĉek, P. 1971, Ap&SS, 12, 10
Yang, S., Walker, G. A. H., & Bennett, P. 1987, PASP, 99, 425
Zima, W., Wright, D., Bentley, J., et al. 2006, A&A, 455, 235

Annexe T

An investigation of the close environment of β Cephei with the VEGA/CHARA interferometer

A&A 525, A67 (2011)
DOI: 10.1051/0004-6361/201015408
© ESO 2010

Astronomy & Astrophysics

An investigation of the close environment of β Cephei with the VEGA/CHARA interferometer

N. Nardetto[1], D. Mourard[1], I. Tallon-Bosc[2], M. Tallon[2], P. Berio[1], E. Chapellier[1], D. Bonneau[1], O. Chesneau[1], P. Mathias[3], K. Perraut[4], P. Stee[1], A. Blazit[1], J. M. Clausse[1], O. Delaa[1], A. Marcotto[1], F. Millour[5], A. Roussel[1], A. Spang[1], H. McAlister[6,7], T. ten Brummelaar[7], J. Sturmann[7], L. Sturmann[7], N. Turner[7], C. Farrington[7], and P. J. Goldfinger[7]

[1] Laboratoire Fizeau, UNS/OCA/CNRS UMR6525, Parc Valrose, 06108 Nice Cedex 2, France
e-mail: Nicolas.Nardetto@oca.eu
[2] Université de Lyon, 69003 Lyon, France; Université Lyon 1, Observatoire de Lyon, 9 avenue Charles André, 69230 Saint Genis Laval, France; CNRS/UMR 5574, Centre de Recherche Astroph. de Lyon, École Normale Supérieure, 69007 Lyon, France
[3] Laboratoire d'Astrophysique de Toulouse-Tarbes, Université de Toulouse, CNRS, 57 Avenue d'Azereix, 65000 Tarbes, France
[4] Laboratoire d'Astrophysique de Grenoble (LAOG), Université Joseph-Fourier, UMR 5571 CNRS, BP 53, 38041 Grenoble Cedex 09, France
[5] Max-Planck-Institut für Radioastronomie, Auf dem Hügel 69, 53121 Bonn, Germany
[6] Georgia State University, PO Box 3969, Atlanta GA 30302-3969, USA
[7] CHARA Array, Mount Wilson Observatory, 91023 Mount Wilson CA, USA

Received 16 July 2010 / Accepted 21 September 2010

ABSTRACT

Context. High-precision interferometric measurements of pulsating stars help to characterize their close environment. In 1974, a close companion was discovered around the pulsating star β Cep using the speckle interferometry technique, and features at the limit of resolution (20 milli-arcsec or mas) of the instrument were mentioned that may be due to circumstellar material. β Cep has a magnetic field that might be responsible for a spherical shell or ring-like structure around the star as described by the MHD models.
Aims. Using the visible recombiner VEGA installed on the CHARA long-baseline interferometer at Mt. Wilson, we aim to determine the angular diameter of β Cep and resolve its close environment with a spatial resolution up to 1 mas level.
Methods. Medium spectral resolution ($R = 6000$) observations of β Cep were secured with the VEGA instrument over the years 2008 and 2009. These observations were performed with the S1S2 (30 m) and W1W2 (100 m) baselines of the array.
Results. We investigated several models to reproduce our observations. A large-scale structure of a few mas is clearly detected around the star with a typical flux relative contribution of 0.23 ± 0.02. Our best model is a co-rotational geometrical thin ring around the star as predicted by magnetically-confined wind shock models. The ring inner diameter is 8.2 ± 0.8 mas and the width is 0.6 ± 0.7 mas. The orientation of the rotation axis on the plane of the sky is PA $= 60 \pm 1$ deg, while the best fit of the mean angular diameter of β Cep gives $\Phi_{\rm UD}[V] = 0.22 \pm 0.05$ mas. Our data are compatible with the predicted position of the close companion of β Cep.
Conclusions. These results bring additional constraints on the fundamental parameters and on the future MHD and asteroseismological models of the star.

Key words. techniques: interferometric – circumstellar matter – stars: oscillations – stars: individual: β Cephei

1. Introduction

The prototype of the β Cephei class of pulsating stars, β Cep (HD 205021, spectral type B2III, $V = 3.2$), is a massive ($M = 12 \pm 1\ M_\odot$, Donati et al. 2001) pulsating star with a period of approximatively $P = 0.1905$ days (Kukarkin et al. 1971). The radial-velocity variations of this star were first detected by Frost (1902). Five frequencies have been derived from a long-term spectroscopic study of β Cep, two of which were identified as a radial and non radial mode (Telting et al. 1997). The radius of β Cep is $R = 6.5 \pm 1.2\ R_\odot$ (Donati et al. 2001), and its distance is $d = 210 \pm 13$ pc (Van Leeuwen 2007). This corresponds to a limb darkened angular diameter of 0.29 ± 0.06 mas.

The source β Cep is actually known as a tertiary system ("Washington Double Star Catalog"[1]). The pulsating star is a member of a visual pair (STF 2866 AB, $a = 13.4''$, $\Delta m = 5.4$). The primary is a close pair (LAB6 Aa, Ab, $\Delta m = 3.4$), first resolved by speckle interferometry at a separation of approximatively $0.25''$ (Labeyrie 1970; Gezari et al. 1972). Since 1971.48, this system has been extensively observed by speckle interferometry (see the "Fourth Catalog of Interferometric Measurements of Binary Stars"[2]) and has led to the computation of the current orbit with a period of 83 years (Andrade 2006) found in the "Sixth Catalog of Orbits of Visual Binary Stars"[3]. In 1974, Labeyrie et al. noted anisotropic features in the power spectrum of the speckled images, which might indicate a large-scale structure at the limit of resolution (20 mas) of the Palomar 5m telescope. Recently, the technique of spectroastrometry was used to disentangle the component spectra of the speckle binary (Schnerr et al. 2006; Wheelwright 2009). These authors conclude that the Hα emission is certainly due to the

[1] http://ad.usno.navy.mil/wds/
[2] http://ad.usno.navy.mil/wds/int4.html
[3] http://ad.usno.navy.mil/wds/orb6.htm

close companion of β Cep, which appears to be a classical Be star.

A magnetic field strength of 360 G was measured by Henrichs et al. (2000). The magnetic axis is almost 90 degrees from the rotational axis, whose inclination is 60 degrees compared to the line-of-sight (Abt et al. 2002). The rotation period of the star is about 12 days (Donati et al. 2001). If the magnetic field is strong enough the wind can be fully magnetically confined in a region close to the star (Babel & Montmerle 1997). In this case, the stellar wind particles originating in both magnetic poles and forced to follow the magnetic field lines collide at the magnetic equator, creating a decretion ring or circumstellar clouds. The magnetic field could confine the wind of β Cep from 2 $R_\star$ up to a distance of about 8 to 9 $R_\star$ (Donati et al. 2001). Of course, the apparent geometry of the ring will then be modulated by the rotation phase of the star. Later work based on dynamical modeling of the wind-magnetic-field interaction, however, indicates that the thick ring (in the X-ray domain) predicted by Babel & Montmerle (1997) would be unlikely to form around a star such as β Cep (Gagné et al. 2005; ud-Doula & Owocki 2002; Townsend & Owocki 2005). This hypothesis has recently been observationally supported by Favata et al. (2009), who did not find any strong rotational modulation in the X-ray emission as predicted by Donati et al. (2001), which seems to point toward a spherical shell of X-ray emitting plasma around the star located between 5 $R_\star$ to 7 $R_\star$ (for He-like triplets). In this context, long-baseline interferometry is in a unique position to derive the angular diameter of the star and the mas scale geometric structure of its close environment.

The Center for High Angular Resolution Astronomy (CHARA) of Georgia State University operates an optical interferometric array located at Mount Wilson Observatory (ten Brummelaar et al. 2005). It is formed by six telescopes placed in pairs on the arms of a Y-shaped configuration. It yields 15 baselines ranging from 34 to 331 m. The VEGA instrument works in the visible domain and provides a maximum angular resolution of 0.3 mas (Mourard et al. 2009). In Sect. 2, we present the VEGA observations of β Cep and the data reduction process. Then, in Sect. 3, we propose several models of β Cep composed of the star itself and additional geometrical structures such as a Gaussian, a companion, or a ring. The last section is devoted to a discussion and a few conclusions.

2. Observations and data processing

The VEGA instrument works in the visible band [0.45 μm; 0.85 μm] and benefits from three spectral resolutions. The medium (6000) and high (30 000) spectral resolutions are well-suited to kinematic analysis of the interferometric signal, while low (1700) and medium resolutions are well-suited to absolute visibility studies and are also well adapted to the study of binaries or multiple systems. We used the medium spectral resolution to observe β Cep.

We obtained observations on different dates (31/07/08, 08/10/08, 23/11/08, and 26/08/09) and different baselines (S1S2, W1W2) to ensure a good $(u - v)$ plane coverage (Fig. 1). Some of these observations were done remotely from Grasse observatory (Clausse 2008). VEGA is equipped with two photon-counting detectors looking at two different spectral bands (typically 0.55 μm and 0.70 μm, respectively). In medium resolution, the two spectral channels have a typical wavelength range of 30 and 45 nm. We subdivided these spectral domains in 2 parts in order to calculate the raw (or instrumental) visibilities of the science and calibrator stars, by measuring the ratio of the high to low-frequency energy of the averaged Fourier spectrum of the fringes visibility (Mourard et al. 2009).

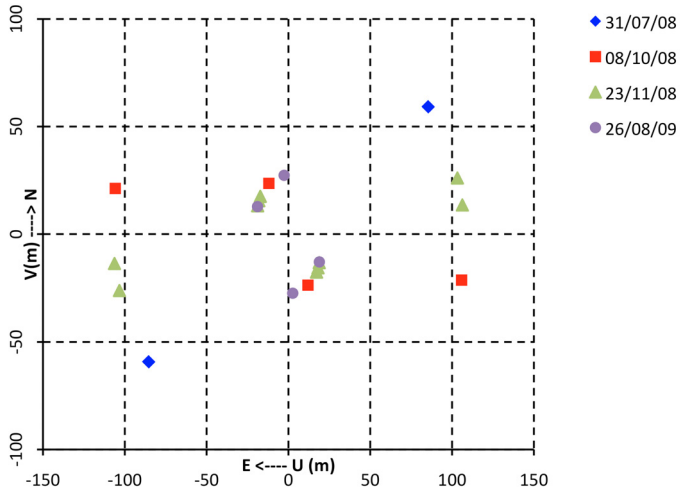


Fig. 1. $(u - v)$ plane coverage of VEGA observations.

An absolute calibration of the science visibilities was performed using references stars HD 192907 and HD 214734 selected with the *SearchCal*[4] software provided by the Jean-Marie Mariotti Center (JMMC), which gives computed photometric angular diameters $\Phi_{\rm LD} = 0.357 \pm 0.025$ mas for HD 192907 and $\Phi_{\rm LD} = 0.340 \pm 0.023$ mas for HD 214734 (Bonneau et al. 2006).

The log and sequence of observations are presented in Table 1. For each calibrated visibility, the statistical and systematic calibration errors are given separately. In most cases, the systematic calibration error is negligible compared to the statistical one. In the model fitting we only consider the statistical uncertainties.

3. Model fitting and strategy

To perform the model fitting we used a tool, *LITpro*, which is currently being developed in the framework of the JMMC[5] (Tallon-Bosc et al. 2008). The fitting engine is based on a modified Levenberg-Marquardt algorithm combined with the trust regions method. The software provides a user-expandable set of geometrical elementary models of the object, able to be combined as building blocks.

All our observations (whatever the baseline, the wavelength, the time, and date of observations) give visibilities ranging from 0.435 to 0.738. It seems to indicate that the instrument is resolving a large-scale feature in the close environment of β Cep. Using the model building blocks provided by *LITpro* we construct a geometrical view of the target step by step. We focus in particular on the relative flux contributions of the star and its close environment, quantities that are indeed strongly constrained by VEGA interferometric observations. Models and fitting results are summarized in Table 2: (1) star + Gaussian, (2) star + circular ring, (3) star + Gaussian + companion at 170 mas (the relative flux contribution of the different geometric components are indicated, respectively) and, (4) star + peculiar ring. The symbol $\star$ indicates that the parameter is fixed.

[4] Available at http://www.jmmc.fr/searchcal

[5] http://www.jmmc.fr/litpro

Table 1. Summary of observations and measured visibilities.

Date dd/mm/yy	JD_c[a] [days]	AH [h]	λ [nm]	Δ_λ [nm]	B_p [m]	Arg. [deg]	S/N	$V^2 \pm V^2_{stat} \pm V^2_{syst}$	CAL[b]	ϕ_{rot}[c]	e_r[d]
31/07/08	4677.5	3.17	635.00	20.00	104	55	15 ± 6	0.684 ± 0.061 ± 0.020	C1-S	0.62	1.37
31/07/08	4677.5	3.18	655.00	20.00	104	55	35 ± 8	0.611 ± 0.083 ± 0.016	C1-S	0.62	1.37
08/10/08	4746.5	–0.03	528.75	12.50	108	101	47 ± 10	0.671 ± 0.064 ± 0.030	C1-S-C1	0.37	1.46
08/10/08	4746.5	1.40	528.75	12.50	26	–27	93 ± 33	0.563 ± 0.048 ± 0.001	C1-S	0.37	1.46
08/10/08	4746.5	–0.03	541.50	13.00	108	101	41 ± 14	0.578 ± 0.049 ± 0.025	C1-S-C1	0.37	1.46
08/10/08	4746.5	1.40	541.50	13.00	26	–27	86 ± 28	0.658 ± 0.050 ± 0.001	C1-S	0.37	1.46
08/10/08	4746.5	-0.03	680.00	20.00	108	101	57 ± 10	0.738 ± 0.065 ± 0.020	C1-S-C1	0.37	1.46
08/10/08	4746.5	1.40	680.00	20.00	26	–27	72 ± 26	0.586 ± 0.028 ± 0.001	C1-S-C1	0.37	1.46
08/10/08	4746.5	–0.03	700.00	20.00	108	101	79 ± 29	0.674 ± 0.051 ± 0.017	C1-S-C1	0.37	1.46
08/10/08	4746.5	1.40	700.00	20.00	26	–27	101 ± 19	0.597 ± 0.029 ± 0.001	C1-S-C1	0.37	1.46
23/11/08	4792.5	3.06	507.50	15.00	25	–44	51 ± 9	0.545 ± 0.049 ± 0.001	C2-S	0.21	4.02
23/11/08	4792.5	3.52	507.50	15.00	24	–49	15 ± 5	0.604 ± 0.107 ± 0.002	C2-S	0.21	4.02
23/11/08	4792.5	4.04	507.50	15.00	23	–55	28 ± 6	0.563 ± 0.050 ± 0.001	C2-S	0.21	4.02
23/11/08	4792.5	1.28	660.00	20.00	107	83	41 ± 10	0.627 ± 0.152 ± 0.017	C1-S	0.21	4.02
23/11/08	4792.5	1.77	660.00	20.00	107	76	58 ± 6	0.489 ± 0.053 ± 0.012	C2-S	0.21	4.02
23/11/08	4792.5	3.06	660.00	20.00	25	–44	108 ± 35	0.590 ± 0.062 ± 0.001	C2-S	0.21	4.02
23/11/08	4792.5	3.52	660.00	20.00	24	–49	34 ± 11	0.639 ± 0.088 ± 0.001	C2-S	0.21	4.02
23/11/08	4792.5	4.04	660.00	20.00	23	–55	47 ± 14	0.585 ± 0.064 ± 0.001	C2-S	0.21	4.02
23/11/08	4792.5	1.28	680.00	20.00	107	83	66 ± 17	0.583 ± 0.055 ± 0.015	C1-S	0.21	4.02
23/11/08	4792.5	1.77	680.00	20.00	107	76	66 ± 18	0.614 ± 0.075 ± 0.014	C2-S	0.21	4.02
23/11/08	4792.5	3.06	680.00	20.00	25	–44	134 ± 31	0.686 ± 0.081 ± 0.001	C2-S	0.21	4.02
23/11/08	4792.5	3.52	680.00	20.00	24	–49	38 ± 15	0.702 ± 0.057 ± 0.001	C2-S	0.21	4.02
23/11/08	4792.5	4.04	680.00	20.00	23	–55	72 ± 9	0.600 ± 0.066 ± 0.001	C2-S	0.21	4.02
26/08/09	5068.5	–0.63	491.25	12.50	27	–6	47 ± 15	0.435 ± 0.033 ± 0.001	C2-S-C2	0.20	3.24
26/08/09	5068.5	–0.63	503.75	12.50	27	–6	51 ± 9	0.468 ± 0.023 ± 0.001	C2-S-C2	0.20	3.24
26/08/09	5068.5	–0.63	660.00	20.00	27	–6	39 ± 10	0.556 ± 0.040 ± 0.001	C2-S-C2	0.20	3.24
26/08/09	5068.5	4.11	660.00	20.00	23	–56	46 ± 8	0.655 ± 0.036 ± 0.001	C2-S-C2	0.20	3.24
26/08/09	5068.5	–0.64	680.00	20.00	27	–5	59 ± 15	0.574 ± 0.019 ± 0.001	C2-S-C2	0.20	3.24
26/08/09	5068.5	4.12	680.00	20.00	23	–56	70 ± 18	0.679 ± 0.034 ± 0.001	C2-S-C2	0.20	3.24

Notes. [a] Julian date of observation defined by $JD_c = JD - 2\,450\,000$. [b] Observation sequence. C1, C2 and S are for calibrator 1 (HD 192907), calibrator 2 (HD 214734) and science star respectively. [c] The reference Julian date (T_0 = 2451238.15 days) and the rotation period (P = 12.00092 days) used to compute the phase are from Donati et al. (2001). The phase 0 is the phase at which the longitudinal magnetic field is at a maximum. [d] The elongation of the ring derived from Fig. 2 of Favata et al. (2009). See also Fig. 3.

3.1. A circumstellar envelope

We consider a model composed of an uniform disk and a Gaussian circumstellar envelope. The best-fit results in an unresolved central object. The envelope flux contributions in the optical range of VEGA is 0.26 ± 0.02. The full-width at half-maximum (hereafter fwhm) of the Gaussian is 4.0 ± 0.4 mas and the reduced χ^2 is 2.5 (Fig. 2). The fit is better than for a single-star model (χ^2 of 37), which indicates that there is indeed a large-scale structure around β Cep.

Following Favata et al. (2009) we tested the hypothesis of a spherical shell around the star by simply considering a circular ring. Our data are consistent with this kind of model with a reduced χ^2 of 1.4. We find the following parameters. The star is again unresolved and the relative flux contribution of the ring is 0.22 ± 0.03; however, the geometry of the ring is not really constrained with an inner angular diameter of 2.7 ± 1.9 mas and a width of 1.3 ± 0.1 mas. We now try to remove the residual discrepancies (especially for the W1W2 baseline), by including the close companion of β Cep in the model.

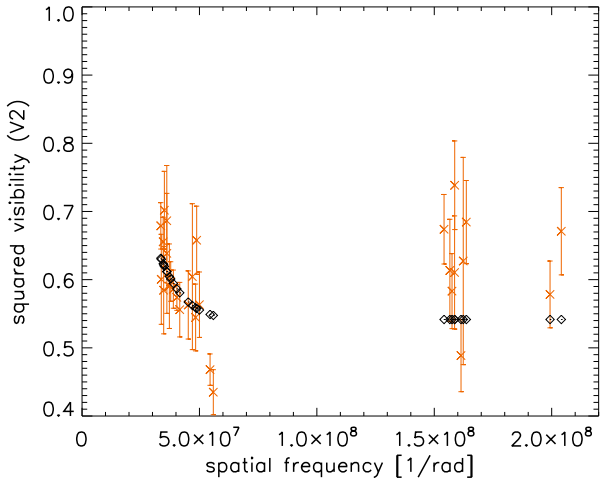


Fig. 2. Visibility of a model composed of β Cep (unresolved) and a gaussian circumstellar envelope (diamonds) together with VEGA observations (crosses). All data are reported in one spatial frequency dimension.

3.2. A close companion at about 170 mas

Using the orbital parameters of the close companion of β Cep presented in Andrade (2006), we added the close unresolved companion of β Cep in our model of the Gaussian circumstellar envelope in order to evaluate its impact on the fitting process. Averaging the four dates of observations, we find x_c = 122.8 mas and y_c = 123.2 mas, where x_c and y_c are the coordinates of the close companion of β Cep. Here, x (resp. y)

is counted positive toward the east (resp. north). A recent determination by Mason et al. (2009) gives $\Delta m = 3.4$, which corresponds to a flux contribution to the total flux of 4%. We found from the best fit that β Cep is still unresolved and an fwhm for the Gaussian of 3.9 ± 0.4 mas, consistent with what was obtained in the previous section. The flux contribution of the Gaussian and the binary (compared to the total flux) are 0.26 ± 0.03 and 0.01 ± 0.01, respectively. The reduced χ^2 is 2.5. The presence of the companion induces a sinusoidal modulation of amplitude about 0.03 in the visibility curve (in the v direction), but it does not help reproduce observations satisfactorily. Our data are thus not really sensitive to the position of the companion. Therefore, the close companion is neglected in the remainder of the analysis.

3.3. A peculiar ring around β Cep

As mentioned in Sect. 1, the hypothesis of a ring surrounding β Cep is supported by MHD codes. In a first approximation we can assume that the ring is rotating about an axis that is in the plane of the sky (Fig. 2 of Favata et al. 2009). Consequently, the ring is modulated by the rotation of the star in such a way that it is alternatively in a pole-on and edge-on geometry. The parameters of the model we use are defined in the *LITpro* software as:

- $\Phi_\star$, the angular diameter of β Cep [in mas];
- f_r, the relative flux contribution of the ring in the optical range of VEGA, compared to the total flux;
- Φ_r, the ring inner diameter [in mas];
- w_r, the width of the ring [in mas];
- the elongation defined as $e_\mathrm{r} = \frac{\Phi_\mathrm{r}}{\Phi_\mathrm{rmin}} = \frac{\omega_\mathrm{r}}{\omega_\mathrm{rmin}}$ where Φ_rmin and ω_rmin are the apparent angular inner radius and width of the ring along the minor axis;
- PA, the orientation of the major axis of the ring on the plane of the sky. It is measured in degrees, from the positive vertical semi-axis (i.e. north direction) towards to the positive horizontal semi-axis (i.e. east direction).

From the ephemeris from Donati et al. (2001), we calculated the rotation phases corresponding to our date of observation (Table 1). Then, using Fig. 2 in Favata et al. (2009), we derived the elongation e_r as a function of the rotation phase (Fig. 3). For the four nights of observation, we obtain the following elongations indicated in Table 1. We basically have two sets of data with an almost similar elongation of the ring. The data corresponding to the nights 23/11/08 and 26/08/09 were analyzed together in the fitting process considering a mean elongation of $e_\mathrm{r} = 3.63$ (ring almost edge-on). Similarly, for nights 31/07/08 and 08/10/08, we consider a mean elongation of $e_\mathrm{r} = 1.42$ (ring almost pole-on). The elongation parameter is fixed in the following, because the data sample is not large enough to constrain all parameters at the same time. We now describe the strategy we used to optimize the fitting process. The parameters $\Phi_\star$, Φ_r, w_r, and PA are supposed to be the same in the edge-on and pole-on geometries, and they are linked during the fitting process (an interesting possibility provided by the *LITpro* software). The relative flux f_r is fitted in both cases, because the brightness of the ring might change with the elongation. We also neglect the radius variation of the star with the pulsation phase (about 1%), which is below the capabilities of the VEGA instrument. The reduced χ^2 is 0.9. Fixed parameters and results are presented in Table 2, while the fitting quality can be appreciated in Fig. 4.

An implicit assumption is that the ring flux contribution is independent of wavelength. For each visibility measurement $V(\lambda)$ of Table 1, the ring flux contribution $f_\mathrm{r}(\lambda)$ is defined as $\frac{V(\lambda)-V_\star}{V_\mathrm{r}-V_\star}$, where $V_\star$ is the modeled visibility of the central star, and V_r of the ring. The values of f_r with the same wavelength are averaged. Results are presented in Fig. 5. The optical emission in the ring-like gaseous structure is mainly due to Rayleigh diffusion at short wavelength ($f_\mathrm{r}(\lambda)$ is decreasing), while the Thomson scattering might be dominant for wavelengths longer than $\lambda > 510$ nm ($f_\mathrm{r}(\lambda)$ is constant).

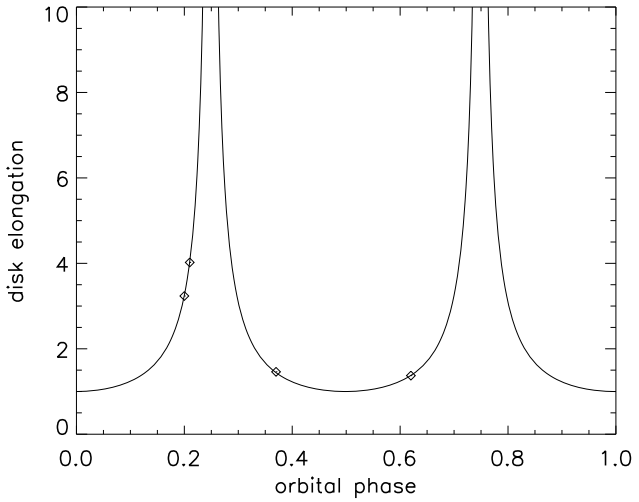


Fig. 3. Elongation of the ring e_r as a function of the orbital phase. Diamond represents the predicted elongation at the observational dates of VEGA (see Table 1). $e_\mathrm{r} = 1$ and $e_\mathrm{r} = \infty$ correspond to a pole-on and edge-on geometry, respectively.

4. Discussion and conclusion

We progressively improved our models by exploring several hypothesis. Models with a large-scale structure of several mas around β Cep have a reduced χ^2 between 15 to 38 times lower than the uniform disk hypothesis. The mean relative flux contribution of this large-scale structure over all the models presented in this paper is 0.23 ± 0.02. This is certainly our most important result.

Our best model (reduced χ^2 of 0.9) points toward a peculiar ring geometry as described by Donati et al. (2001). However, such a ring-model is supposed to be thick in the X-ray band, which implies a strong rotational modulation in the X-ray emission, but it is not observed (Favata et al. 2009). Therefore, if the model of Donati et al. (2001) is valid, the ring should be optically thin even in the X-ray band. In addition, the best-fit geometry we obtain for the ring is somewhat greater than the values provided in Donati et al. (2001): $74 \pm 7\ R_\star$ (compared to $2\ R_\star$) for the inner ring diameter, and $5 \pm 6\ R_\star$ (compared to $6\ R_\star$) for the width.

However, the angular diameter estimate of β Cep we obtain ($\Phi_\star = \Phi_\mathrm{UD}[V] = 0.22 \pm 0.05$ mas) – even if it is indeed model-dependent – is quite precise (23% of relative precision). Considering $T_\mathrm{eff} = 26\,000$ K and $\log g = 4$ for β Cep (Gies & Lambert 1992), we derive the linear limb-darkening coefficient of Díaz-Cordovés et al. (1995) and find $\Phi_\mathrm{LD}[V] = 0.23 \pm 0.05$ mas. This value is consistent with the value ($\Phi_\mathrm{LD}[V] = 0.29 \pm 0.06$ mas) predicted by Donati et al. (2001) when assuming a distance of $d = 210 \pm 13$ pc (Van Leeuwen 2007). In addition, the *LITpro* software provides the correlation matrix for all parameters. It shows that the angular diameter is poorly correlated to other parameters (<0.5), which is a good point. This observational value should be compared to the one provided by

Table 2. Models presented in this paper.

Model	$\Phi_\star$ [mas]	flux contributions	fwhm [mas]	Φ_r [mas]	w_r [mas]	e_r	PA [deg]	x_c [mas]	y_c [mas]	χ^2_{red}
1	0	$0.26_{\pm0.02}$	$4.0_{\pm0.4}$	–	–	–	–	–	–	2.5
2	0	$0.22_{\pm0.03}$	–	$2.7_{\pm1.9}$	$1.3_{\pm1.1}$	1.00⋆	–	–	–	1.4
3	0	$0.26_{\pm0.03}$, $0.01_{\pm0.01}$	$3.9_{\pm0.4}$	–	–	–	–	122.8⋆	123.2⋆	2.5
		$0.22_{\pm0.01}$	–			3.63⋆		–	–	
4	$0.22_{\pm0.05}$		–	$8.2_{\pm0.8}$	$0.6_{\pm0.7}$		$60_{\pm1}$	–	–	0.9
		$0.17_{\pm0.01}$	–			1.42⋆		–	–	

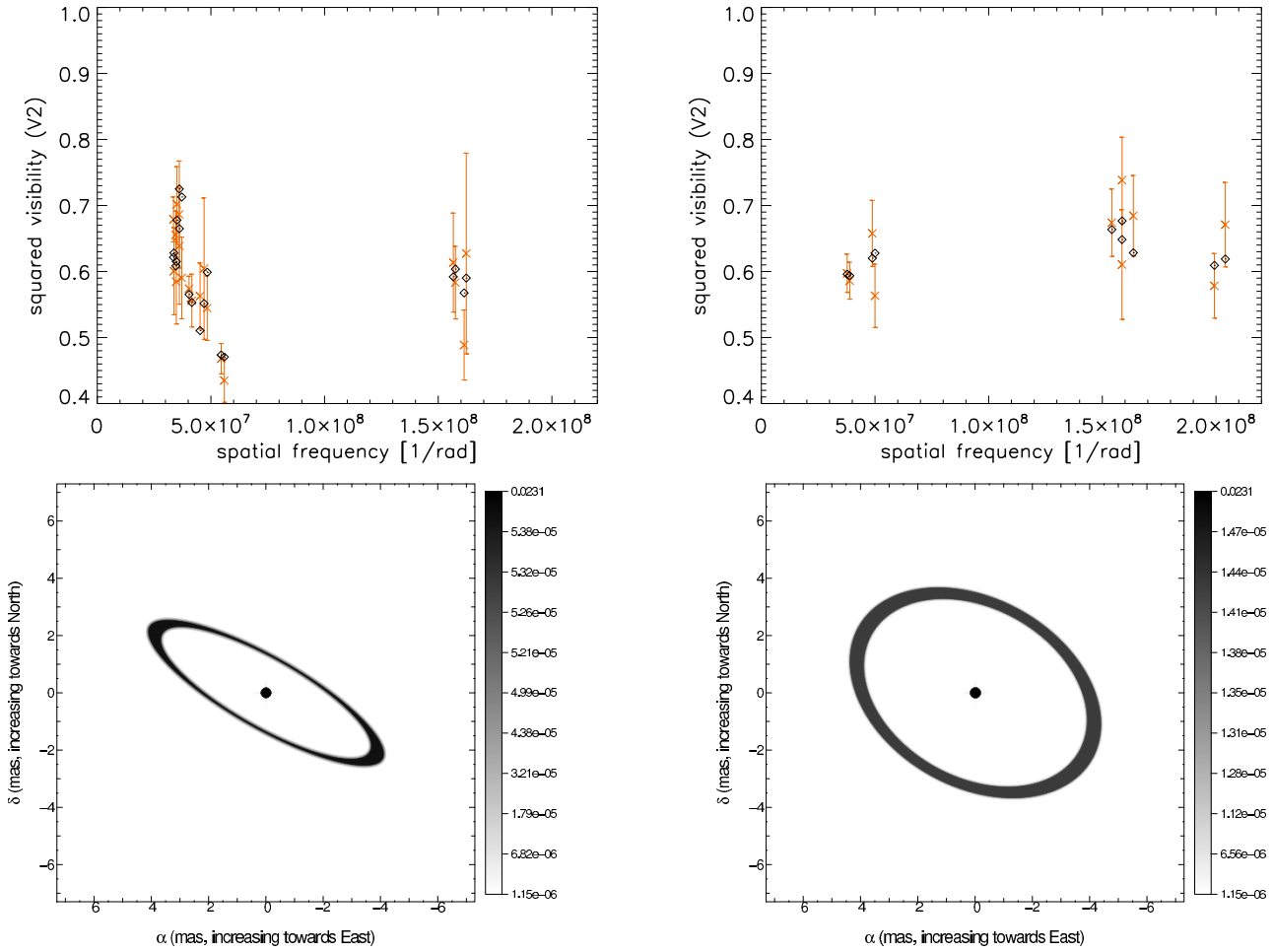


Fig. 4. *Left*: same as Fig. 2 but with a model composed of β Cep and an edge-on ring. Most data are from S1S2 short baseline (see nights 23/11/08 and 26/08/09), which help constrain the geometry of the ring and, in particular, its orientation on the sky. The image of the model is also provided. *Right*: the same but with a model composed of β Cep and a pole-on ring. In this case, we have more data for the W1W2 long baseline (see nights 31/07/08 and 08/10/08), which helps constrain the angular diameter of the β Cep.

classical asteroseismological study, using a method similar to the one performed on the solar-like star α Cen A and B (Thévenin et al. 2002; Kervella et al. 2003).

The hypothesis of a spherical shell of X-ray emitting plasma around the star located between 5 $R_\star$ and 7 $R_\star$ (Favata et al. 2009) is not excluded. Our circular ring model provides a 1.4 reduced χ^2 with only 5 parameters; however, the star is again unresolved, which is not expected (Donati et al. 2001). If we consider the angular diameter derived from the peculiar disk-fitted model (0.22 ± 0.05 mas), the values in stellar radii we obtain for the circular ring geometry are more than in Favata et al. (2009): 24 ± 17 $R_\star$ for the inner ring diameter and 12 ± 1 $R_\star$ for the width.

Additional observations of β Cep in the next years with the VEGA/CHARA instrument will help complete the (u, v) plane coverage and lead to a high-precision determination of the geometrical structure around this star. Moreover, high spectral resolution observations in the metallic lines will help characterize the dynamical structure of the atmosphere of β Cep (Nardetto et al. 2005), and bring constraints on the stellar inclination axis, a parameter that is fundamental to mode identification (Telting et al. 1997).

There are 15 bright β Cephei stars ($V < 7$) with expected angular diameter >0.2 mas that could be observed by long baseline interferometry in the future, and some of them are binaries (Stankov & Handler 2005). Such a survey could constrain the

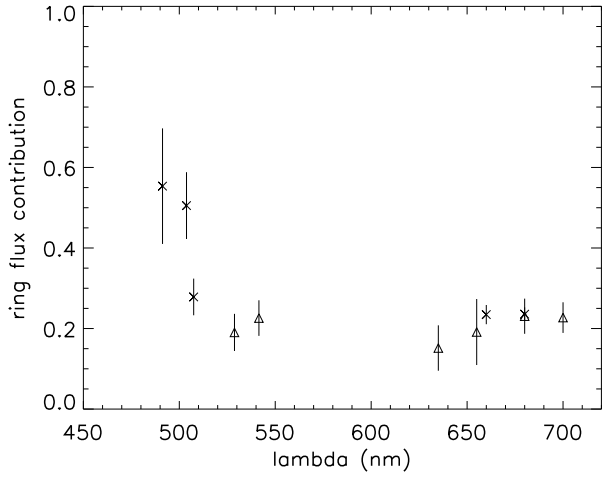


Fig. 5. Ring flux contribution as a function of the wavelength. Crosses and triangles correspond to the edge-on and pole-on ring geometry respectively.

close environment of pulsating stars and help for understanding the close interaction between the pulsation, the mass, and the mass loss (and eventually the magnetic field). This would help the future development of the hydrodynamical codes of pulsating stars (e.g. Fokin et al. 2004), as well as of stellar interior models.

Acknowledgements. VEGA is a collaboration between CHARA and the Laboratoire Fizeau (OCA/UNS/CNRS-Nice), LAOG in Grenoble, CRAL in Lyon, and LESIA in Paris-Meudon. It has been supported by French programs for stellar physics and high angular resolution PNPS and ASHRA, by INSU-CNRS, and by the Région PACA. The project has benefited from the strong support of the OCA and CHARA technical teams. The CHARA Array is operated with support from the National Science Foundation through grant AST-0908253, the W. M. Keck Foundation, the NASA Exoplanet Science Institute, and from Georgia State University.This research has made use of the Jean-Marie Mariotti Center `LITpro`[6] and `SearchCal` services[7] services co-developed by CRAL, LAOG, and FIZEAU, and of CDS Astronomical Databases SIMBAD and VIZIER.

References

Abt, H. A., Levato, H., & Grosso, M. 2002, ApJ, 573, 359
Andrade, M. 2006, Inf. Circ., 158
Babel, J., & Montmerle, T. 1997, ApJ, 485, 29
Bonneau, D., Clausse, J.-M., Delfosse, X., et al. 2006, A&A, 456, 789
Clausse, J.-M. 2008, SPIE Conf. Ser., 7019
Díaz-Cordovés, C., & Gimenez, A. 1995, A&AS, 110, 329
Donati, J.-F., Wade, G. A., Babel, J., et al. 2001, MNRAS, 326, 1265
Favata, F., Neiner, C., Testa, P., et al. 2009, A&A, 495, 217
Fokin, A., Mathias, Ph., Chapellier, E., et al. 2004, A&A, 426, 687
Frost 1902, ApJ, 15, 340
Gagné, M., Oksala, M. E., Cohen, D. H., et al. 2005, ApJ, 628, 986
Gies, D. R., & Lambert, D. L. 1992, ApJ, 387, 673
Gezari, D.Y., Labeyrie, A., & Stachnik, R. V. 1972, ApJ, 173, 1
Henrichs, H. F., de Jong, J. A., Donati, D.-F., et al. 2000, in Magnetic Fields of Chemically Peculiar and Related Stars, ed. Y. V. Glagolevskij, & I. I. Romanyuk, 57
Kervella, P., Thévenin, F., Ségransan, D., et al. 2003, A&A, 404, 1087
Kukarkin, et al. 1971, GCVS3, C, 0
Labeyrie, A. 1970, A&A, 6, 85
Labeyrie, A., Bonneau, D., Stachnik, R. V., et al. 1974, ApJ, 194, 147
Mason, B. D., Hartkopf, W. I., & Gies, D. R. 2009, AJ, 137, 3358
Mourard, D., Clausse, J. M., & Marcotto, A. 2009, A&A, 508, 1073
Nardetto, N., Fokin, A., Mourard, D., et al. 2006, A&A, 454, 327
Schnerr, R. S., Henrichs, H. F., Oudmaijer, R. D., & Telting, J. H. 2006, A&A, 459, L21
Stankov, A., & Handler, G. 2005, ApJS, 158, 193
Tallon-Bosc, I., Tallon, M., & Thiébaut, E., et al. 2008, SPIE, 7013, 44
Telting, J. H., Aerts, C., & Mathias, P. 1997, A&A, 322, 493
Ten Brummelaar, T. A., McAlister, H. A., Ridgway, S. T., et al. 2005, ApJ, 628, 453
Thévenin, F., Provost, J., Morel, P., et al. 2002, A&A, 392, 9
Townsend, R. H. D., & Owocki, S. P. 2005, MNRAS, 357, 251
ud-Doula, A., & Owocki, S. P. 2002, ApJ, 576, 413
Van Leeuwen 2007, A&A, 474, 653
Wheelwright, H. E., Oudmaijer, R. D., & Schnerr, R. S. 2009, A&A, 497, 487

[6] LITpro software available at `http://www.jmmc.fr/litpro`
[7] Available at `http://www.jmmc.fr/searchcal`

Annexe U

Improving the surface brightness-color relation for early-type stars using optical interferometry

A&A 570, A104 (2014)
DOI: 10.1051/0004-6361/201423772
© ESO 2014

Astronomy & Astrophysics

Improving the surface brightness-color relation for early-type stars using optical interferometry⋆,⋆⋆

M. Challouf[1,2], N. Nardetto[1], D. Mourard[1], D. Graczyk[3], H. Aroui[2], O. Chesneau[1], O. Delaa[1], G. Pietrzyński[3,4], W. Gieren[3], R. Ligi[1], A. Meilland[1], K. Perraut[5,6], I. Tallon-Bosc[7,8], H. McAlister[9,10], T. ten Brummelaar[10], J. Sturmann[10], L. Sturmann[10], N. Turner[10], C. Farrington[10], N. Vargas[10], and N. Scott[10]

[1] Laboratoire Lagrange, UMR 7293, UNS/CNRS/OCA, 06300 Nice, France
e-mail: mounir.challouf@oca.eu
[2] Laboratoire Dynamique Moléculaire et Matériaux Photoniques, UR11ES03, Université de Tunis/ESSTT, Tunisie
[3] Departamento de Astronomía, Universidad de Concepción, Casilla 160-C, Concepción, Paraguay
[4] Warsaw University Observatory, AL. Ujazdowskie 4, 00-478 Warsaw, Poland
[5] Univ. Grenoble Alpes, IPAG, 38000 Grenoble, France
[6] CNRS, IPAG, 38000 Grenoble, France
[7] Université Lyon 1, Observatoire de Lyon, 9 avenue Charles André, 69230 Saint Genis Laval, France
[8] CNRS/UMR 5574, Centre de Recherche Astroph. de Lyon, École Normale Supérieure, 69007 Lyon, France
[9] Georgia State University, PO Box 3969, Atlanta GA 30302-3969, USA
[10] CHARA Array, Mount Wilson Observatory, 91023 Mount Wilson CA, USA

Received 7 March 2014 / Accepted 2 September 2014

ABSTRACT

Context. The method of distance determination of eclipsing binaries consists in combining the radii of both components determined from spectro-photometric observations with their respective angular diameters derived from the surface brightness-color relation (SBC). However, the largest limitation of the method comes from the uncertainty on the SBC relation: about 2% for late-type stars (or 0.04 magnitude) and more than 10% for early-type stars (or 0.2 mag).
Aims. The aim of this work is to improve the SBC relation for early-type stars in the $-1 \leq V-K \leq 0$ color domain, using optical interferometry.
Methods. Observations of eight B- and A-type stars were secured with the VEGA/CHARA instrument in the visible. The derived uniform disk angular diameters were converted into limb darkened angular diameters and included in a larger sample of 24 stars, already observed by interferometry, in order to derive a revised empirical relation for O, B, A spectral type stars with a $V-K$ color index ranging from -1 to 0. We also took the opportunity to check the consistency of the SBC relation up to $V-K \simeq 4$ using 100 additional measurements.
Results. We determined the uniform disk angular diameter for the eight following stars: γ Ori, ζ Per, 8 Cyg, ι Her, λ Aql, ζ Peg, γ Lyr, and δ Cyg with $V-K$ color ranging from -0.70 to 0.02 and typical precision of about 1.5%. Using our total sample of 132 stars with $V-K$ colors index ranging from about -1 to 4, we provide a revised SBC relation. For late-type stars ($0 \leq V-K \leq 4$), the results are consistent with previous studies. For early-type stars ($-1 \leq V-K \leq 0$), our new VEGA/CHARA measurements combined with a careful selection of the stars (rejecting stars with environment or stars with a strong variability), allows us to reach an unprecedented precision of about 0.16 magnitude or ≃7% in terms of angular diameter.
Conclusions. We derive for the first time a SBC relation for stars between O9 and A3, which provides a new and reliable tool for the distance scale calibration.

Key words. stars: early-type – techniques: interferometric – stars: distances – binaries: eclipsing – methods: observational – stars: atmospheres

1. Introduction

The distance measurements to extragalactic targets in the last century revolutionized our understanding of the distance scale of the universe. The distance to the Large Magellanic Cloud is a critical rung on the cosmic distance ladder, and numerous independent methods involving, for instance, RR Lyrae stars (Feast 1997; Szewczyk et al. 2008; Pietrzyński et al. 2008), Cepheids (Bohm-Vitense 1985; Evans 1991, 1992; Freedman & Madore 1996; Freedman et al. 2008), or red clump stars (Udalski et al. 1998b,a; Pietrzyński & Gieren 2002; Laney et al. 2012) have been used to derive its distance.

The main goal of the long term program called the Araucaria project is to significantly improve the calibration of the cosmic distance scale based on observations of several distance indicators in nearby galaxies (Gieren et al. 2005). Eclipsing binary systems are particularly important to provide the zero point of the extragalactic distances and study in detail populational dependence on other distance indicators like RR Lyrae stars, Cepheids, red clump stars, etc. Thirteen long period systems composed of late-type giants were analyzed in the Magellanic Clouds so far: eight in the Large Magellanic Cloud (Pietrzyński et al. 2009, 2013), and five in the Small Magellanic Cloud (Graczyk et al. 2012, 2014). For such systems, the linear dimen-

⋆ Partly based on VEGA/CHARA observations.
⋆⋆ Appendix A is available in electronic form at http://www.aanda.org

sion of both components can be measured with a precision up to of 1% from the analysis of high-quality spectroscopic and photometric data (e.g., Torres et al. 2010). The distance to an eclipsing binary follows from the dimensions determined in this way, plus the angular diameters derived from the absolute surface brightness, which is very well calibrated for late-type stars (Di Benedetto 2005). This conceptually very simple technique very weakly depends on reddening and metallicity, and provides the most accurate tool for measuring distances to nearby galaxies (Pietrzyński et al. 2013; Graczyk et al. 2014).

However the heart of this method, the surface brightness-color (SBC) relation, is very well calibrated only for late-type stars which significantly limits its usage. The late-type systems composed of main-sequence stars are usually faint, while those composed of giants have very long periods (several hundred days) that makes them very difficult to find. As a result, only about 45 late-type systems, well suited to precise distance determination have been discovered so far in the Magellanic Clouds by the Optical Gravitational Microlensing Experiment (OGLE; Pawlak et al. 2013; Graczyk et al. 2011). On the other hand, many more relatively bright systems are known in nearby galaxies (Massey et al. 2013; Graczyk et al. 2011; Wyrzykowski et al. 2003, 2004; Bonanos et al. 2006; Macri et al. 2001; Mochejska et al. 2001; Vilardell et al. 2006; Pawlak et al. 2013). Therefore, in order to derive the distance to nearby galaxies and to study the geometry of the Magellanic Clouds, it is imperative to calibrate SBC relation for early-type stars.

The purpose of this paper is to improve the SBC relation for early-type stars by using the resolving power of the Visible spEctroGraph and polArimeter (VEGA) beam combiner (Mourard et al. 2009) operating at the focus of the Center for High Angular Resolution Astronomy (CHARA) Array (ten Brummelaar et al. 2005) located at Mount Wilson Observatory (California, USA). The CHARA array consists of six telescopes of 1 m in diameter, configured in a Y shape, which offers 15 different baselines from 34 m to 331 m. These baselines can achieve a spatial resolution up to 0.3 mas in the visible which is necessary in order to resolve early-type stars. Early-type stars are very small in terms of angular diameter and can be affected by several physical phenomena, like fast rotation, winds, and environment, which can potentially bias the interferometric measurements.

This paper is structured as follows. Section 2 is devoted to a description of the stars in our sample. In Sect. 3, we present the data reduction process and the method used to derive the angular diameters. Section 4 is dedicated to the calibration of the SBC relation, and we discuss our results in Sect. 5. We draw conclusions in Sect. 6.

2. VEGA/CHARA observations of eight early-type stars

We carefully selected eight early-type stars with a $(V-K)$ color index ranging from −0.70 to 0.02. They are north hemisphere main-sequence subgiant and giant stars ($\delta > 4°$) with spectral types ranging from B1 to A1. They are much brighter (with a visual magnitude m_V ranging from 1.6 to 4.7) than the limiting magnitude of VEGA (about $m_V = 7$ in medium spectral resolution). They are also bright in the K band (with a m_K magnitude lower than 5.1) which makes it possible to track the fringes simultaneously with the infrared CLIMB combiner (Sturmann et al. 2010). All the apparent magnitudes in V and K bands that we have collected from the literature are in the Johnson system (Johnson et al. 1966; see also Mermilliod et al. 1997). The accuracy of their parallaxes π spans from 1.5% to 15%. The color excess $E(V-K)$, the visual absorption A_V, the effective temperature $T_{\rm eff}$, the mass M, the radius R, the luminosity L, the surface gravity $\log g$, and the metallicity index [Fe/H] are listed in Table 1. We emphasize that for our purpose (limb-darkening estimates; see end of Sect. 3.1), we do not need very precise estimates of the fundamental parameters of the stars in our sample, which explains why we do not provide any uncertainty on these parameters in the second part of Table 1.

Among the eight early-type stars in our sample, there are six low rotators (λ Aql, γ Ori, γ Lyr, ι Her, 8 Cyg, and ζ Per) and two fast rotating stars (δ Cyg and ζ Peg). In the following, we define fast rotators as stars with $v_{\rm rot} \sin i > 75$ km s^{-1}. A theoretical study which aims at quantifying the impact of fast rotation on the SBC relation for early-type stars is currently in progress and will be published in a forthcoming paper.

We observed our sample stars from July 23, 2011, to August 29, 2013, using different suitable triplets available on the CHARA array. A summary of the observations is given in Table 2.

3. The limb-darkened angular diameters

In this section, we describe how we derive the limb-darkened angular diameter for all the stars in our sample.

3.1. Data reduction and methodology

The first step is to calibrate the visibility measurements of our targets using observations of reference stars. These calibrators (Table 3) were selected using the SearchCal[1] software developed by the Jean-Marie Mariotti Center (JMMC; Bonneau et al. 2006). The way this calibration is done is shown in Fig. 1 in the case of γ Lyr (data obtained on June 21, 2012, with the E1E2W2 three-telescope configuration). We used the standard sequence C6-S-C6 in which S is the target and C6 is the reference star. The light blue dots are the raw visibilities obtained on the science star for the three corresponding baselines: E2E1 (upper panel), E2W2 (middle panel), and E1W2 (bottom panel). Our VEGA measurements are typically divided into 30 blocks of observations, and each block contains 1000 images with an exposure time of 15 millisec. For each block, the raw squared visibility is calculated using the auto-correlation mode (Mourard et al. 2009, 2011). The red dots in the figure represent the transfer function obtained by comparing the expected visibility of the reference star to the one that has been measured. This transfer function is then used to calibrate the visibilities obtained on the science target (blue dots). A cross-check of the quality of the transfer function is usually done for several bandwidths and over the whole night. Under good seeing conditions, the transfer function of VEGA/CHARA is generally stable at the level of 2% for more than one hour. The squared calibrated visibilities $V^2_{\rm target}$ obtained from our VEGA observations are listed in Tables A.1. The systematic uncertainties that stem from the uncertainty on the reference stars are negligible compared to the statistical uncertainties, and are neglected in the rest of this study.

The calibrated visibility curves obtained for each star in our sample (Fig. 2) are then used to constrain a model of uniform disk, that contains only one parameter, the so-called uniform disk angular diameter ($\theta_{\rm UD}$). This is performed using the LITpro[2] software developed by the JMMC (Tallon-Bosc et al. 2008). The following formula of Hanbury Brown et al. (1974b)

[1] Available at http://www.jmmc.fr/searchcal

[2] Available at http://www.jmmc.fr/litpro

Table 1. Physical parameters of the stars in our sample.

	λ Aql HD 177756	γ Lyr HD 176437	γ Ori HD 35468	8 Cyg HD 184171	ι Her HD 160762	ζ Per HD 24398	ζ Peg HD 214923	δ Cyg HD 186882
RA	19:06:14	18:58:56	05:25:07	19:31:46	17:39:27	03:54:07	22:41:27	19:44:58
Dec	+04°52′57″	+32°41′22″	+06°20′58″	+34°27′10″	+46°00′22″	+31°53′01″	+10°49′52″	+45°07′50″
S. Type[a]	B9V	A1III	B2III	B3IV	B3IV	B1Ib	B9IV	A0IV
m_V[mag][b]	3.430	3.248	1.637	4.740	3.794	2.850	3.406	2.868
m_K[mag][b]	3.670	3.240	2.340	5.114	4.228	2.670	3.565	2.810
π[mas][c]	26.37 ± 0.64	5.26 ± 0.27	12.92 ± 0.52	3.79 ± 0.16	7.17 ± 0.13	4.34 ± 0.19	15.96 ± 0.19	19.77 ± 0.48
A_V[d]	0.03 ± 0.01	0.12 ± 0.03	0.00 ± 0.06	0.15 ± 0.11	0.04 ± 0.03	0.87 ± 0.05	0.05 ± 0.01	0.04 ± 0.01
$E(V-K)$[e]	0.03 ± 0.01	0.11 ± 0.03	0.00 ± 0.05	0.12 ± 0.10	0.03 ± 0.03	0.77 ± 0.05	0.04 ± 0.01	0.04 ± 0.01
$T_{\rm eff}[K]$	11 780[a]	10 000[a]	21 840[a]	16 100[m]	17 000[m]	22 580[a]	11 430[a]	10 150[a]
$M[M_\odot]$	2.99[j]	5.76[k]	7.77[j]	6.40[m]	6.30[m]	15.50[l]	3.22[j]	2.93[j]
$R[R_\odot]$	2.24[j]	15.40[k]	5.75[j]	6.50[m]	5.40[m]	26[f]	3.98[j]	5.13[j]
$L[L_\odot]$	78[g]	2430[k]	9211[n]	2512[m]	2138[m]	47039[h]	224[g]	155[n]
log g	4.22[j]	4.06[o]	3.84[o]	3.62[m]	3.77[m]	3.27[o]	3.75[j]	3.49[j]
[Fe/H]	−0.08[o]	0.15[o]	−0.07[o]	0.25[i]	−0.04[o]	−0.08[o]	0.06[o]	–

Notes. [(a)] Zorec et al. (2009); [(b)] magnitudes from the General Catalogue of Photometric Data Mermilliod et al. (1997); [(c)] van Leeuwen (2007); [(d)] derived from Eq. (3) for stars with distances lower than 75 pc (λ Aql, ζ Peg, and δ Cyg), and from Eq. (4) for more distant stars; [(e)] average value based on the literature (Wegner 1994; Pecaut & Mamajek 2013; Ducati 2002; Fitzpatrick 1999), see the text for more explanations; [(f)] Pasinetti Fracassini et al. (2001); [(g)] Zorec & Royer (2012); [(h)] Hohle et al. (2010); [(i)] Gies & Lambert (1992); [(j)] Allende Prieto & Lambert (1999); [(k)] Maestro et al. (2013); [(l)] Tetzlaff et al. (2011); [(m)] Fitzpatrick & Massa (2005); [(n)] McDonald et al. (2012); [(o)] Wu et al. (2011).

Table 2. Summary of the observing log.

Name	3 telescope configurations	N	Reference stars
γ Lyr	E2E1W2	23	C6, C7
γ Ori	E2E1W2, W2W1S2, E2E1W2	8	C1, C2, C3
8 Cyg	W2W1E1	8	C10
ι Her	W2W1E1	8	C4
λ Aql	S2S1W2	45	C5, C9
ζ Per	E2E1W2	6	C12
δ Cyg	E2E1W2	22	C8, C10
ζ Peg	E2E1W2	12	C11

Notes. All the details are given in Table A.1. N corresponds to the number of visibility measurements for each star. The reference stars used are also indicated (cf. Table 3).

Table 3. Reference stars and their parameters, including the spectral type, the visual magnitude (m_V), and the predicted uniform disk angular diameter (in mas) derived from the JMMC SearchCal software (Bonneau et al. 2006).

No.	Reference stars	S.Type	m_V	$\theta_{UD}[R]$ [mas]
C1	HD 34989	B1V	5.7	0.130 ± 0.009
C2	HD 37320	B8III	5.8	0.153 ± 0.011
C3	HD 38899	B9IV	4.8	0.265 ± 0.019
C4	HD 167965	B7IV	5.5	0.150 ± 0.011
C5	HD 170296	A1IV/V	4.6	0.429 ± 0.031
C6	HD 174602	A3V	5.2	0.330 ± 0.024
C7	HD 178233	F0III	5.5	0.399 ± 0.029
C8	HD 184875	A2V	5.3	0.295 ± 0.021
C9	HD 184930	B5III	4.3	0.317 ± 0.022
C10	HD 185872	B9III	5.4	0.200 ± 0.014
C11	HD 216735	A1V	4.9	0.310 ± 0.022
C12	HD 22780	B7Vn	5.5	0.167 ± 0.012

provides an analytical way to convert the equivalent uniform disk angular diameter θ_{UD} into the limb-darkened disk θ_{LD}:

$$\theta_{LD}(\lambda) = \theta_{UD}(\lambda)\left[\frac{(1-\frac{U_\lambda}{3})}{(1-\frac{7U_\lambda}{15})}\right]^{\frac{1}{2}}. \quad (1)$$

For each star, the limb-darkening coefficient U_λ is derived from the numerical tables of Claret & Bloemen (2011). These tables are based on the ATLAS (Kurucz 1970) and PHOENIX (Hauschildt et al. 1997) atmosphere models. The input parameters of these tables are the effective temperature (T_{eff}), the metallicity ([Fe/H]), the surface gravity ($\log g$), and the micro-turbulence velocity. The steps for these quantities are 250 K, 0.5, 0.5, and 2 km s^{-1}, respectively. The three first parameters are given in Table 1 and were rounded, for each star, to the closest value found in the table of Claret. The micro-turbulence velocity has almost no impact on the derived limb-darkened diameter (fifth decimal). We took arbitrarily 8 km s^{-1} for stars with $T_{eft} > 15\,000$ K and 4 km s^{-1} for stars with $T_{eft} < 15\,000$ K. We also consider the limb-darkening coefficient applicable to the R band of VEGA (U_R in the following).

3.2. Results

The uniform disk angular diameter (θ_{UD}), the limb-darkening coefficients (U_R), and the derived limb-darkened angular diameters

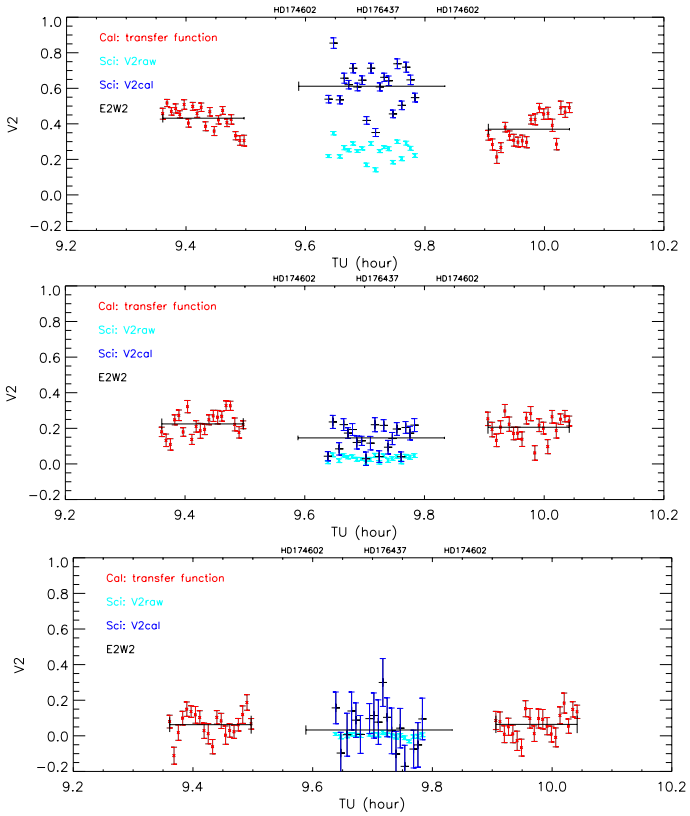


Fig. 1. Time sequences of raw visibilities of the science observations (light blue dots), calibrated (blue dots) using the transfer function (red dots).

(θ_{LD}) are listed in Table 4 for each star in our sample. The value of θ_{LD} ranges from 0.31 mas to 0.79 mas, with a relative precision from 0.5% to 3.5% (average of 1.5%). The reduced χ^2_{red} is from 0.4 to 2.9 depending on the dispersion of the calibrated visibilities. For γ Lyr, our result ($\theta_{UD} = 0.742 \pm 0.010$ mas) agrees at the 1σ level with the measurements from the PAVO/CHARA instrument ($\theta_{UD} = 0.729 \pm 0.008$ mas, Maestro et al. 2013). For γ Ori, our angular diameter ($\theta_{LD} = 0.715 \pm 0.005$ mas) is consistent with the value derived from the Narrabri Stellar Intensity Interferometer (NSII) ($\theta_{LD} = 0.72 \pm 0.04$ mas, Hanbury Brown et al. 1974a). For other stars with angular diameters lower than 0.6 mas (ι Her, λ Aql, 8 Cyg, and ζ Per) and for the two fast rotators (ζ Peg and δ Cyg) there are no interferometric observations available to our knowledge.

For the two rotators, we derive the apparent oblateness using the approximate relation provided by van Belle et al. (2006), their Eq. (A1) $\frac{R_b}{R_a} \simeq 1 - (v \sin i)^2 \frac{R_b}{2GM}$, where R_b, R_a, M, and G are the major and minor apparent radius of the star, its mass, and the gravitational constant. We find $\frac{R_b}{R_a} = 1.07$ for ζ Peg considering $R_b \simeq \overline{R} = 4.03\ R_\odot$ and $M = 3.22\ M_\odot$, where $\overline{R}$ is the mean radius (see Table 1), while the rotational projected velocity $v \sin i$ is set to 140 km s^{-1} (Abt et al. 2002). For δ Cyg, we find similarly $\frac{R_b}{R_a} = 1.06$ considering $v \sin i = 140$ km s^{-1} (Slettebak et al. 1975; Gray 1980; Carpenter et al. 1984; Abt & Morrell 1995; Abt et al. 2002; van Belle 2012). Consequently, our data might be sensitive to the expected gravity darkening intensity distribution and the flatness of the star. However, this also depends on the baseline orientation. For both stars, the three telescopes (Table 2) are aligned. Thus, even if our reduced χ^2_{red} are rather low (1.7 for ζ Peg and 1.2 for δ Cyg), we cannot exclude a bias on our de-

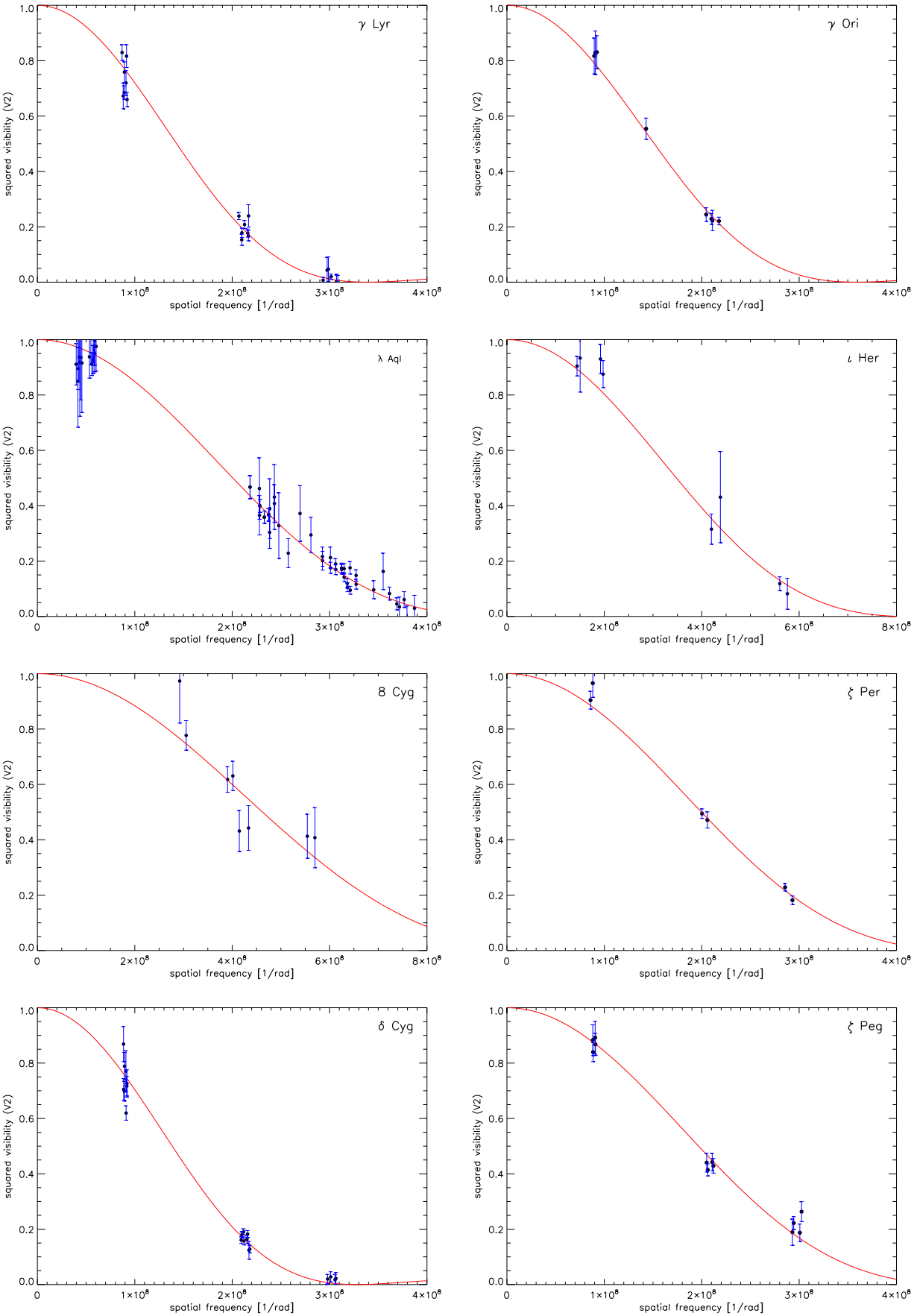


Fig. 2. Squared visibility versus spatial frequency for all stars in our sample with their corresponding statistical uncertainties. The red solid lines indicate the best uniform disk model obtained from the LITpro fitting software.

Table 4. Angular diameters obtained with VEGA/CHARA and the corresponding surface brightness.

Star	$(V-K)_0$	$\theta_{\rm UD}$ [mas]	χ^2	U_R	$\theta_{\rm LD}$ [mas]	S_v[mag]
λ Aql	-0.265 ± 0.055	0.529 ± 0.003	1.0	0.301	0.544 ± 0.003	2.079 ± 0.030
γ Lyr	-0.102 ± 0.072	0.742 ± 0.010	2.9	0.402	0.766 ± 0.010	2.544 ± 0.059
γ Ori	-0.703 ± 0.097	0.701 ± 0.005	0.4	0.269	0.715 ± 0.005	0.909 ± 0.081
8 Cyg	-0.492 ± 0.147	0.229 ± 0.011	1.3	0.299	0.234 ± 0.011	1.456 ± 0.177
ι Her	-0.459 ± 0.076	0.304 ± 0.010	1.2	0.280	0.310 ± 0.010	1.225 ± 0.082
ζ Per	-0.592 ± 0.092	0.531 ± 0.007	1.2	0.343	0.542 ± 0.007	0.652 ± 0.081
ζ Peg	-0.204 ± 0.055	0.539 ± 0.009	1.7	0.442	0.555 ± 0.009	2.076 ± 0.152
δ Cyg	$+0.021 \pm 0.055$	0.766 ± 0.004	1.3	0.408	0.791 ± 0.004	2.318 ± 0.129

Notes. The systematical uncertainties for the two fast rotating stars, ζ Peg and δ Cyg, are of 0.039 mas and 0.047 mas, respectively (see Sect. 3.2).

rived limb-darkened angular diameters. In order to get a rough estimate of this bias, we only consider in first approximation the oblateness of the star while the gravity darkening is set to be negligible. As a consequence, if the orientation of the baseline is aligned with the polar or equatorial axis, we can estimate a maximum systematic error of about 0.039 mas (6%) for ζ Peg, while we find 0.047 mas (7%) for δ Cyg. We translate these uncertainties in terms of S_v magnitude in Sect. 4.

4. The calibration of the surface brightness relation

4.1. Methodology

As already mentioned in the introduction, the SBC relation is a very robust tool for the distance scale calibration. The surface brightness S_V of a star is linked to its visual intrinsic dereddened magnitude m_{V_0} and its limb-darkened angular diameter $\theta_{\rm LD}$ by the following relation:

$$S_V = m_{V_0} + 5 \log \theta_{\rm LD}. \quad (2)$$

Instead of S_V, the surface brightness parameter $F_V = 4.2207 - 0.1 S_V$ is often adopted in the literature to determine the stellar angular diameters (Barnes & Evans 1976). In order to derive m_{V_0}, we first selected the apparent m_V magnitudes for all the stars in our sample (Mermilliod et al. 1997). These magnitudes are expressed in the Johnson system (Johnson et al. 1966) and their typical uncertainty is of about 0.015 mag. In order to correct these magnitudes from the reddening we then use the following formulae $m_{V_0} = m_V - A_V$, where A_V is the extinction in the V band. Determining the extinction is a difficult task. We adopt the following strategy. For stars lying closer than 75 pc we use the simple relation

$$A_V = \frac{0.8}{\pi}, \quad (3)$$

where π is the parallax of the stars [in mas]. This equation is standard in the literature (Blackwell et al. 1990; Di Benedetto 1998, 2005). The corresponding uncertainty is set to 0.01 mag.

For distant stars we derive the absorption using the $(B-V)$ extinction (Laney & Stobie 1993):

$$A_V = 3.1 E(B-V). \quad (4)$$

The difficulty is then to derive $E(B-V)$. We have several possibilities. First, we use the so-called Q method, with $Q = (U-B) - 0.72(B-V)$, which was originally proposed by Johnson & Morgan (1953). The value of Q is derived for each star using observed UBV magnitudes from (Ducati 2002). Then a relation between $(B-V)_0$ and Q can be found in Pecaut & Mamajek (2013), and $E(B-V)$ is finally derived using $E(B-V) = (B-V) - (B-V)_0$.

Second, from the spectral type of the stars in our sample, we can derive their intrinsic colors in different bands using Table 5 of Wegner (1994). We thus obtain $(B-V)_0$, $(V-R)_0$, $(V-I)_0$, $(V-J)_0$, $(V-H)_0$, and $(V-K)_0$. Once compared with the observed colors from Ducati (2002), we derive $E(B-V)$, $E(V-R)$, $E(V-I)$, $E(V-J)$, $E(V-H)$, and $E(V-K)$, and we finally use Table 2 (Col. 4) from Fitzpatrick (1999) and assume total to selective extinction ratio in B-band $\frac{A_B}{E(B-V)} = 4.1447$ (Table 3 from Cardelli et al. 1989) to perform a conversion into $E(B-V)$ using the following equations:

$$E(B-V) = \frac{E(V-R)(A_B - A_V)}{(A_V - A_R)} = 1.2820 E(V-R) \quad (5)$$

$$E(B-V) = \frac{E(V-I)(A_B - A_V)}{(A_V - A_I)} = 0.6536 E(V-I) \quad (6)$$

$$E(B-V) = \frac{E(V-J)(A_B - A_V)}{(A_V - A_J)} = 0.4464 E(V-J) \quad (7)$$

$$E(B-V) = \frac{E(V-H)(A_B - A_V)}{(A_V - A_H)} = 0.3891 E(V-H) \quad (8)$$

$$E(B-V) = \frac{E(V-K)(A_B - A_V)}{(A_V - A_K)} = 0.3650 E(V-K). \quad (9)$$

We finally obtain seven values of the extinction (Q method, and six values derived from Table 5 of Wegner 1994). These quantities are averaged and their statistical dispersion provides a realistic uncertainty (indicated in Table 1 for the VEGA sample). However, the Q method is applicable only for stars of class IV and V, while Table 5 of Wegner (1994) can be used only for spectral types O and B. We thus have in some cases fewer than seven values. And even, in the case of γ Lyr, for instance (which is an A1III star standing at a distance greater than 75 pc), we used other $E(B-V)$ estimates available in the literature (see Table 1). The uncertainty on S_V is finally derived from the uncertainty on m_V (typically 0.015), the angular diameter (see Table 4), and A_V.

In order to mitigate the effects from a somewhat erroneous calibration of the intrinsic colors, we recalculate $(V-K)_0$ from the derived $E(B-V)$ value. First we calculate $E(B-V)$ from averaging via Eqs. (5)–(9). Then using this value and Eq. (9), we derive $E(V-K)$ (given in Table 1). From $E(V-K)$, m_V, and m_K we obtain $(V-K)_0$. The uncertainty on $(V-K)_0$ is derived assuming an uncertainty of 0.015 for m_V, 0.03 for m_K (following Di Benedetto 2005), and the uncertainty on $E(V-K)$, itself derived from the uncertainty obtained on $E(B-V)$. The m_V and

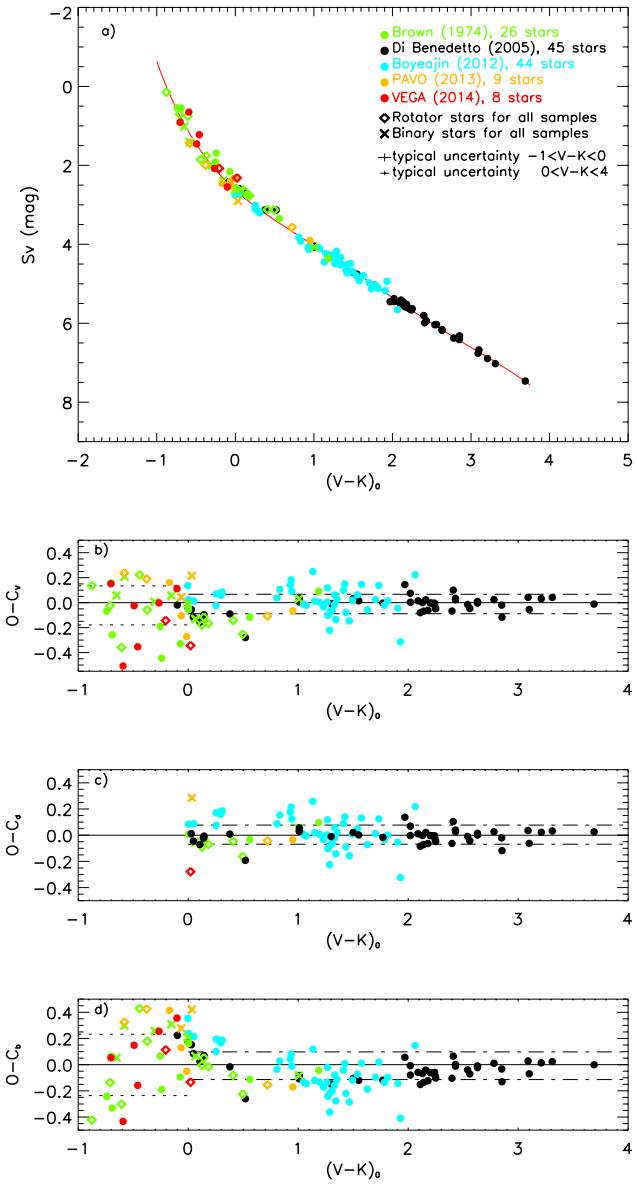


Fig. 3. Relation between visual surface brightness S_V as a function of the color index $(V-K)_0$. The black, light blue, green, brown, and red measurements are from Di Benedetto (2005), Boyajian et al. (2012), Hanbury Brown et al. (1974a), Maestro et al. (2013), and VEGA (this work), respectively. The red line corresponds to our fit when considering all stars. The rms of the difference between the surface brightness computed from our fit and measured surface brightness is presented in the lower panels (see the text for more detail).

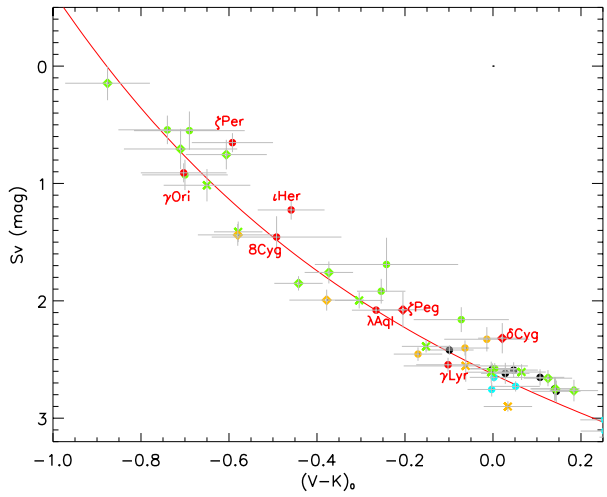


Fig. 4. Same as Fig.3, but with the names of the VEGA/CHARA stars in our sample (in red).

m_K magnitudes for the stars in our sample are given in Table 1 together with π, $E(V-K)$, and A_V. The derived values of the surface brightness for each star are given in Table 4.

In order to calibrate the SBC relation, we also need to combine the eight limb-darkened angular diameters derived from the VEGA observations with different sets of diameters already available in the literature.

4.2. A revised SBC relation for late- and early-type stars

Historically, the SBC was first derived from interferometric observations of 18 stars by Wesselink (1969) using the $(B-V)$ index. Five years later, the apparent angular diameters of 32 stars in the spectral range O5 to F8 have been measured using the NSII (Hanbury Brown et al. 1974a). Based on this sample, Barnes et al. (1976) and Barnes & Evans (1976) calibrated the SBC for late-type and early-type stars, respectively, but this was not done with the $V-K$ color index. In order to constrain the SBC relation as a function of $V-K$ we therefore use these 32 angular diameters (but 6 are rejected, see below). This is the first set of data we have used. We emphasize that the $(V-K)_0$ color index is usually used to calibrated the SBC relation because it provides the lowest rms and it is mostly parallel to the reddening vector on the $Sv-(V-K)$ diagram. Moreover, for all the datasets we have considered, we have recalculated the $(V-K)_0$ and A_V values in a similar way as for the VEGA objects (see Sect. 4.1).

More than ten years later, Di Benedetto (1998) made a careful compilation of 22 stars (with A, F, G, K spectral types) for which angular diameters were available in the literature and calibrated the SBC relation. Moreover, the direct application of the SBC relation to Cepheids was done by Fouque & Gieren (1997) and Di Benedetto (1998). Later, 27 stars were measured by NPOI and Mark III optical interferometers and the derived high precision angular diameters were published by Nordgren et al. (2001) and Mozurkewich et al. (2003), respectively. Finally, using a compilation of 29 dwarfs and subgiant (including the sun) in the $0.0 \leq (V-K)_0 \leq 6.0$ color range, Kervella et al. (2004) calibrated for the first time a linear SBC relation with an intrinsic dispersion of 0.02 mag or 1% in terms of angular diameter. A short time later, Di Benedetto (2005) made the same kind of compilation but with 45 stars in the $-0.1 \leq (V-K)_0 \leq 3.7$ color range (accuracy of 0.04 mag or 2% in terms of angular diameter). We use this larger second data set for our analysis.

One year later, Bonneau et al. (2006) provided a SBC relation (as function of $V-K$ color magnitude) based on interferometric measurements, lunar occultation, and eclipsing binaries. We compare our results with those of Bonneau et al. (2006) and also Di Benedetto (2005) in Sect. 5.

Recently, Boyajian et al. (2012) enlarged the sample to 44 main-sequence A-, F-, and G-type stars using CHARA array measurements. In addition, ten stars with spectral types from B2 to F6 were observed using the astronomical visible observations (PAVO) beam combiner at the CHARA array

(Maestro et al. 2013) and these recent CHARA measurements have been incorporated in our analysis.

However, in order to derive a SBC relation accurate enough for distance determination, one has to perform a consistent selection. Our strategy is the following: we consider all stars in multiple systems (as soon as the companion is far and faint enough not to contaminate interferometric measurements), fast rotators, and single stars. Fast rotating stars should be included as they improve the statistics of the relation (in particular for early-type objects), even if a slight bias is not excluded as discussed in Sect. 3.2 (see also next section). Conversely, we exclude stars with environments (like Be stars with strong wind) or stars with a strong variability. Following these criteria, we found seven stars to reject. The first one is Zeta Orionis (ζ Ori). Its angular diameter, measured by Hanbury Brown et al. (1974a) is most probably biased by a companion which was discovered later and with a separation of 40 mas (Hummel et al. 2000, 2013). Kappa Orionis (κ Ori) shows a P Cygni profile in Hα caused by a stellar wind (Searle et al. 2008; Stalio et al. 1981; Cassinelli et al. 1983). Delta Scorpii (δ Sco) is an active binary star exhibiting the Be phenomenon (Meilland et al. 2013). Gamma2 Velorum (γ^2 Vel) is a binary system with a large spectral contribution from the Wolf-Rayet star (Millour et al. 2007). Zeta Ophiuchi (ζ Oph) is a magnetic star of O_e-type (Hubrig et al. 2011). Alpha Virginis (α Vir) is a double-lined spectroscopic binary (B1V+B4V) with an ellipsoidal variation of 0.03 mag due to tidal distortion (Harrington et al. 2009). The last one, Zeta Cassiopeiae (ζ Cas), is in the PAVO sample (Maestro et al. 2013). It stands at 7σ from the relation. It is a β Cepheid and the photometric contamination by a surrounding environment and/or a close companion is not excluded (Sadsaoud et al. 1994; Nardetto et al. 2011).

We finally end with 26 stars from Hanbury Brown et al. (1974a), 44 stars from Boyajian et al. (2012), 9 stars from Maestro et al. (2013), and 45 values of S_v from Di Benedetto (2005), to which we can add our eight angular diameters obtained with VEGA/CHARA. The total sample is composed of 132 stars (with $-0.876 < V-K < 3.69$), including 32 early-type stars with $-1 < V-K < 0$. Using this sample of 132 stars, we find the relation

$$S_v = \sum_{n=0}^{n=5} C_n (V-K)_0^n \quad (10)$$

with, $C_0 = 2.624 \pm 0.009$, $C_1 = 1.798 \pm 0.020$, $C_2 = -0.776 \pm 0.034$, $C_3 = 0.517 \pm 0.036$, $C_4 = -0.150 \pm 0.015$, and $C_5 = 0.015 \pm 0.002$. Uncertainties on coefficients of the SBC relation do not take into account the X-axis uncertainties on $(V-K)_0$. This relation can be used consistently in the range $-0.9 \leq V-K \leq 3.7$ with $\sigma_{S_v} = 0.10$ mag. This corresponds to a relative precision on the angular diameter of $\frac{\sigma\theta}{\theta} = 46.1\sigma_{S_V} \simeq 4.6\%$ derived from Eq. (5) of Di Benedetto (2005). For stars earlier than A3 ($-0.9 < V-K < 0.0$), we successfully reached a magnitude precision of $\sigma = 0.16$ or 7.3% in terms of angular diameter.

5. Discussion

Figure 3a shows the resulting SB relation as a function of the $(V-K)_0$ color index for the five different data sets we have considered. The VEGA data appear in red in the figure. The residual O−C$_v$, which is the difference obtained between the measured surface brightness (O) and the relation provided by Eq. (10) (C$_v$), is shown in Fig. 3b. In the following, we define σ_+ and σ_- as the positive and negative standard deviation. We obtain $\sigma_+ = 0.07$ and $\sigma_- = 0.09$ for $0 < V-K < 3.7$ (late-type stars, dot-dashed line in the figure) and $\sigma_+ = 0.13$ mag and $\sigma_- = 0.18$ mag for $-0.9 < V-K < 0$ (early-type stars, dotted line in the figure). In Fig. 3c we derive the residual compared to the Di Benedetto (2005) relation (Eq. (2)) which is applicable only in the $-0.1 < V-K < 4$ color domain. We obtain a residual (O−C$_d$) which are similar: $\sigma_+ = 0.08$ mag and $\sigma_- = 0.07$ mag. This basically means that improving the statistics does not improve the thinnest of the relations. For this purpose, a homogeneous set of V and K photometry is probably required.

We also compare our results with those of Bonneau et al. (2006), which is, to our knowledge, the only SBC relation, versus $V-K$, provided for early-type stars in the literature (actually the relation is set from −1.1 to 7, their Table 2), but instead of using Eq. (2), they considered another quantity, $\frac{\theta}{9.306.10^{-\frac{V}{5}}}$. We therefore made a conversion to compare with the S_V quantity. The residual (O−C$_b$) is shown in Fig. 3d. We find $\sigma_+ = 0.10$ mag and $\sigma_- = 0.11$ mag for $0 < V-K < 4$ (or late-type stars) and $\sigma_+ = 0.23$ mag and $\sigma_- = -0.23$ mag for $-1 < V-K < 0$ (or early-type stars). These residuals are significantly larger then the ones obtained when using our Eq. (10) or Eq. (2) from Di Benedetto (2005).

In Fig. 3a we also have indicated the fast rotating stars and binaries. In Fig. 4 we provide a zoom of the SBC relation over the $-1 < V-K < 0.25$ color range. In this zoom we have also indicated the uncertainties and the names of the stars in our VEGA sample. We find that the O−C$_v$ residual in the $(V-K)$ color range −1 to 0 is $\sigma = 0.06$, $\sigma = 0.17$, and $\sigma = 0.18$, for stars in binary systems (6), for fast rotating stars (8), and for single stars (18). We note the following points:

First, we want to emphasize that a careful selection (by rejected stars with environment and stars with companions in contact), in particular in the range of $-1 < V-K < 0$ can significantly improve the precision on the SBC relation. We obtain $\sigma \simeq 0.4$ otherwise.

Second, the dispersion of the O−C residual for stars in binary systems is significantly lower (0.06) than to the one obtained with the whole sample (about 0.16), which indicates that interferometric and photometric measurements are not contaminated by the binarity.

Third, we obtain a large dispersion ($\sigma = 0.17$) for fast rotating stars. Five stars are beyond 1σ, while three are within, including ζ Peg in our VEGA sample (see Fig. 3b). Delta Cygni (δ Cyg) is, in particular, at 2σ. In Sect. 3.2, we estimated the impact of the fast rotation on the angular diameters of ζ Peg and δ Cyg to be 0.039 mas and 0.047 mas, respectively. Using Eq. (2), it translates into a magnitude effect of ±0.150 mag and ±0.127 mag, respectively. As already said, fast rotation modifies several stellar properties such as the shape of the photosphere (Collins 1963; Collins & Harrington 1966) and its brightness distribution (von Zeipel 1924a,b), which should be taken into consideration. However, studying these effects requires dedicated modeling, and this will be done in a forthcoming paper. Finally, in our VEGA sample, four stars are beyond 1σ from the relation, but when also considering the uncertainty in $V-K$, they remain consistent with the relation (see Fig. 4).

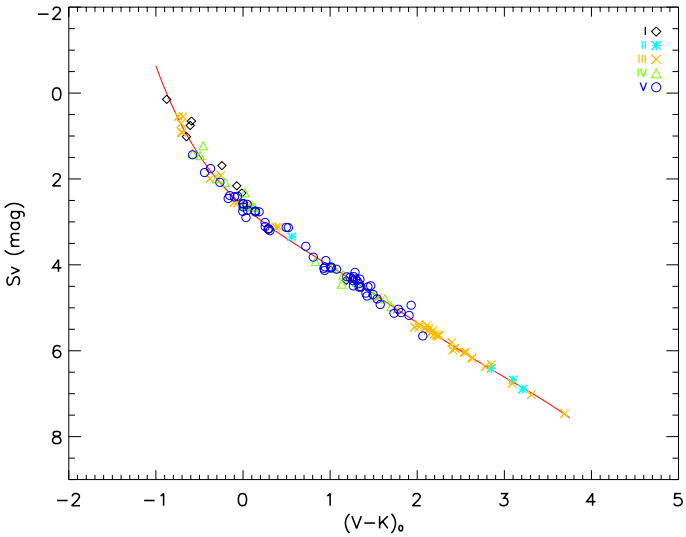


Fig. 5. Relation between the visual surface brightness S_V and the color index $(V-K)_0$ for luminosity class I ($\diamond$), luminosity class II ($*$), luminosity class III ($\times$), luminosity class IV ($\triangle$), and luminosity class V ($\circ$).

Fourth, we calculate the SBC relation for luminosity classes I and II, III, IV, and V (Fig. 5). We obtain the following results:

$$-0.88 \leq (V-K)_0 \leq 3.21$$
$$S_v = 2.291 + 2.151(V-K)_0 - 0.461(V-K)_0^2 + 0.073(V-K)_0^3$$
$$[\sigma_{S_v} = 0.08 \text{ mag}; \sigma_\theta \simeq 3.5\%; 12 \text{ stars}; \text{Class I + II}] \quad (11)$$

$$-0.74 \leq (V-K)_0 \leq 3.69$$
$$S_v = 2.497 + 1.916(V-K)_0 - 0.335(V-K)_0^2 + 0.050(V-K)_0^3$$
$$[\sigma_{S_v} = 0.07 \text{ mag}; \sigma_\theta \simeq 3.4\%; 41 \text{ stars}; \text{Class III}] \quad (12)$$

$$-0.58 \leq (V-K)_0 \leq 2.06$$
$$S_v = 2.625 + 1.823(V-K)_0 - 0.606(V-K)_0^2 + 0.197(V-K)_0^3$$
$$[\sigma_{S_v} = 0.10 \text{ mag}; \sigma_\theta \simeq 4.8\%; 79 \text{ stars}; \text{Class IV + V}] \cdot \quad (13)$$

We find a slight difference in the zero-points of these relations. Their dispersion is, however, similar, about 0.09 mag, which is slightly lower than the global dispersion of 0.16 mag that we obtain when considering the whole sample.

6. Conclusions

Taking advantage of the unique VEGA/CHARA capabilities in terms of spatial resolution, we determined the angular diameters of eight bright early-type stars in the visible with a precision of about 1.5%. By combining these data with previous angular diameter determinations, we provide for the very first time a SBC relation for early-type stars with a precision of about 0.16 mag, which means that this SBC relation can be used to derive the angular diameter of early-type stars with a precision of 7.3%. This relation is a powerful tool for the distance scale calibration as it can be used to derive the individual angular diameters of detached, early-type, and thus bright eclipsing binary systems. It will be used in the course of the Araucaria Project (Gieren et al. 2005) to derive the distance of different galaxies in the Local Group, for exemple M33. As the eclipsing binary method is independent of the metallicity of the star, it can be used as a reference to test the impact of the metallicity on several other distance indicators, in particular the Cepheids. In the course of the Araucaria project, we also aim to test the method consistently on galactic early-type eclipsing binaries using photometry, spectroscopy, and interferometry.

Acknowledgements. This research has made use of the SIMBAD and VIZIER databases at the CDS (http://cdsweb.u-strasbg.fr/), Strasbourg (France), of the Jean-Marie Mariotti Center Aspro service (http://www.jmmc.fr/aspro), and of the electronic bibliography maintained by the NASA/ADS system. The research leading to these results has received funding from the European Community's Seventh Framework Programme under Grant Agreement 312430 and financial support from the Ministry of Higher Education and Scientific Research (MHESR) – Tunisia. The CHARA Array is funded by the National Science Foundation through NSF grants AST-0606958 and AST-0908253 and by Georgia State University through the College of Arts and Sciences, as well as the W. M. Keck Foundation. W.G. gratefully acknowledges financial support for this work from the BASAL Centro de Astrofisica y Tecnologias Afines (CATA) PFB-06/2007, and from the Millenium Institute of Astrophysics (MAS) of the Iniciativa Cientifica Milenio del Ministerio de Economia, Fomento y Turismo de Chile, project IC120009. We acknowledge financial support for this work from ECOS-CONICYT grant C13U01. Support from the Polish National Science Center grant MAESTRO 2012/06/A/ST9/00269 is also acknowledged. We also wish to thank the referee, Dr Puls, for his numerous and precise suggestions for improving the photometric aspects of the paper. This was an enormous help in refining our results. This research has largely benefited from the support, suggestions, advice of our colleague Olivier Chesneau, who passed away this spring. The whole team wish to pay homage to him.

References

Abt, H. A., & Morrell, N. I. 1995, ApJS, 99, 135
Abt, H. A., Levato, H., & Grosso, M. 2002, ApJ, 573, 359
Allende Prieto, C., & Lambert, D. L. 1999, A&A, 352, 555
Barnes, T. G., & Evans, D. S. 1976, MNRAS, 174, 489
Barnes, T. G., Evans, D. S., & Parsons, S. B. 1976, MNRAS, 174, 503
Blackwell, D. E., Petford, A. D., Arribas, S., Haddock, D. J., & Selby, M. J. 1990, A&A, 232, 396
Bohm-Vitense, E. 1985, ApJ, 296, 169
Bonanos, A. Z., Stanek, K. Z., Kudritzki, R. P., et al. 2006, ApJ, 652, 313
Bonneau, D., Clausse, J.-M., Delfosse, X., et al. 2006, A&A, 456, 789
Boyajian, T. S., McAlister, H. A., van Belle, G., et al. 2012, ApJ, 746, 101
Cardelli, J. A., Clayton, G. C., & Mathis, J. S. 1989, ApJ, 345, 245
Carpenter, K. G., Slettebak, A., & Sonneborn, G. 1984, ApJ, 286, 741
Cassinelli, J. P., Myers, R. V., Hartmann, L., Dupree, A. K., & Sanders, W. T. 1983, ApJ, 268, 205
Claret, A., & Bloemen, S. 2011, A&A, 529, A75
Collins, II, G. W. 1963, ApJ, 138, 1134
Collins, II, G. W., & Harrington, J. P. 1966, ApJ, 146, 152
Di Benedetto, G. P. 1998, A&A, 339, 858
Di Benedetto, G. P. 2005, MNRAS, 357, 174
Ducati, J. R. 2002, VizieR Online Data Catalog: II/237
Evans, N. R. 1991, ApJ, 372, 597
Evans, N. R. 1992, ApJ, 389, 657
Feast, M. W. 1997, MNRAS, 284, 761
Fitzpatrick, E. L. 1999, PASP, 111, 63
Fitzpatrick, E. L., & Massa, D. 2005, AJ, 129, 1642
Fouque, P., & Gieren, W. P. 1997, A&A, 320, 799
Freedman, W. L., & Madore, B. F. 1996, in Clusters, Lensing, and the Future of the Universe, eds. V. Trimble, & A. Reisenegger, ASP Conf. Ser., 88, 9
Freedman, W. L., Madore, B. F., Rigby, J., Persson, S. E., & Sturch, L. 2008, ApJ, 679, 71
Gieren, W., Pietrzyński, G., Soszyński, I., et al. 2005, ApJ, 628, 695
Gies, D. R., & Lambert, D. L. 1992, ApJ, 387, 673
Graczyk, D., Soszyński, I., Poleski, R., et al. 2011, Acta Astron., 61, 103
Graczyk, D., Pietrzyński, G., Thompson, I. B., et al. 2012, ApJ, 750, 144
Graczyk, D., Pietrzyński, G., Thompson, I. B., et al. 2014, ApJ, 780, 59
Gray, D. F. 1980, PASP, 92, 771
Hanbury Brown, R., Davis, J., & Allen, L. R. 1974a, MNRAS, 167, 121
Hanbury Brown, R., Davis, J., Lake, R. J. W., & Thompson, R. J. 1974b, MNRAS, 167, 475
Harrington, D., Koenigsberger, G., Moreno, E., & Kuhn, J. 2009, ApJ, 704, 813
Hauschildt, P. H., Baron, E., & Allard, F. 1997, ApJ, 483, 390
Hohle, M. M., Neuhäuser, R., & Schutz, B. F. 2010, Astron. Nachr., 331, 349
Hubrig, S., Oskinova, L. M., & Schöller, M. 2011, Astron. Nachr., 332, 147
Hummel, C. A., White, N. M., Elias, II, N. M., Hajian, A. R., & Nordgren, T. E. 2000, ApJ, 540, L91

Hummel, C. A., Rivinius, T., Nieva, M.-F., et al. 2013, A&A, 554, A52
Johnson, H. L., & Morgan, W. W. 1953, ApJ, 117, 313
Johnson, H. L., Mitchell, R. I., Iriarte, B., & Wisniewski, W. Z. 1966, Communications of the Lunar and Planetary Laboratory, 4, 99
Kervella, P., Thévenin, F., Di Folco, E., & Ségransan, D. 2004, A&A, 426, 297
Kurucz, R. L. 1970, SAO Special Report, 309
Laney, C. D., & Stobie, R. S. 1993, MNRAS, 263, 921
Laney, C. D., Joner, M. D., & Pietrzyński, G. 2012, MNRAS, 419, 1637
Lyubimkov, L. S., Rachkovskaya, T. M., Rostopchin, S. I., & Lambert, D. L. 2002, MNRAS, 333, 9
Macri, L. M., Stanek, K. Z., Sasselov, D. D., Krockenberger, M., & Kaluzny, J. 2001, AJ, 121, 870
Maestro, V., Che, X., Huber, D., et al. 2013, MNRAS, 434, 1321
Massey, P., Neugent, K. F., Hillier, D. J., & Puls, J. 2013, ApJ, 768, 6
McDonald, I., Zijlstra, A. A., & Boyer, M. L. 2012, MNRAS, 427, 343
Meilland, A., Stee, P., Spang, A., et al. 2013, A&A, 550, L5
Mermilliod, J.-C., Mermilliod, M., & Hauck, B. 1997, A&AS, 124, 349
Millour, F., Petrov, R. G., Chesneau, O., et al. 2007, A&A, 464, 107
Mochejska, B. J., Kaluzny, J., Stanek, K. Z., & Sasselov, D. D. 2001, AJ, 122, 1383
Mourard, D., Clausse, J. M., Marcotto, A., et al. 2009, A&A, 508, 1073
Mourard, D., Bério, P., Perraut, K., et al. 2011, A&A, 531, A110
Mozurkewich, D., Armstrong, J. T., Hindsley, R. B., et al. 2003, AJ, 126, 2502
Nardetto, N., Mourard, D., Tallon-Bosc, I., et al. 2011, A&A, 525, A67
Nordgren, T. E., Sudol, J. J., & Mozurkewich, D. 2001, AJ, 122, 2707
Pasinetti Fracassini, L. E., Pastori, L., Covino, S., & Pozzi, A. 2001, A&A, 367, 521
Pawlak, M., Graczyk, D., Soszyński, I., et al. 2013, Acta Astron., 63, 323
Pecaut, M. J., & Mamajek, E. E. 2013, ApJS, 208, 9
Pietrzyński, G., & Gieren, W. 2002, AJ, 124, 2633
Pietrzyński, G., Gieren, W., Szewczyk, O., et al. 2008, AJ, 135, 1993
Pietrzyński, G., Thompson, I. B., Graczyk, D., et al. 2009, ApJ, 697, 862
Pietrzyński, G., Graczyk, D., Gieren, W., et al. 2013, Nature, 495, 76
Sadsaoud, H., Le Contel, J. M., Chapellier, E., Le Contel, D., & Gonzalez-Bedolla, S. 1994, A&A, 287, 509
Searle, S. C., Prinja, R. K., Massa, D., & Ryans, R. 2008, A&A, 481, 777
Slettebak, A., Collins, II, G. W., Parkinson, T. D., Boyce, P. B., & White, N. M. 1975, ApJS, 29, 137
Stalio, R., Sedmak, G., & Rusconi, L. 1981, A&A, 101, 168
Sturmann, J., ten Brummelaar, T., Sturmann, L., & McAlister, H. A. 2010, in SPIE Conf. Ser., 7734, 45
Szewczyk, O., Pietrzyński, G., Gieren, W., et al. 2008, AJ, 136, 272
Tallon-Bosc, I., Tallon, M., Thiébaut, E., et al. 2008, SPIE, 7013
ten Brummelaar, T. A., McAlister, H. A., Ridgway, S. T., et al. 2005, ApJ, 628, 453
Tetzlaff, N., Neuhäuser, R., & Hohle, M. M. 2011, MNRAS, 410, 190
Torres, G., Andersen, J., & Giménez, A. 2010, A&ARv, 18, 67
Udalski, A., Pietrzyński, G., Woźniak, P., et al. 1998a, ApJ, 509, L25
Udalski, A., Szymanski, M., Kubiak, M., et al. 1998b, Acta Astron., 48, 1
van Belle, G. T. 2012, A&ARv, 20, 51
van Belle, G. T., Ciardi, D. R., Ten Brummelaar, T., et al. 2006, ApJ, 637, 494
van Leeuwen, F. 2007, A&A, 474, 653
Vilardell, F., Ribas, I., & Jordi, C. 2006, A&A, 459, 321
von Zeipel, H. 1924a, MNRAS, 84, 665
von Zeipel, H. 1924b, MNRAS, 84, 684
Wegner, W. 1994, MNRAS, 270, 229
Wesselink, A. J. 1969, MNRAS, 144, 297
Wu, Y., Singh, H. P., Prugniel, P., Gupta, R., & Koleva, M. 2011, A&A, 525, A71
Wyrzykowski, L., Udalski, A., Kubiak, M., et al. 2003, Acta Astron., 53, 1
Wyrzykowski, L., Udalski, A., Kubiak, M., et al. 2004, Acta Astron., 54, 1
Zorec, J., & Royer, F. 2012, A&A, 537, A120
Zorec, J., Cidale, L., Arias, M. L., et al. 2009, A&A, 501, 297

Pages 11 to 13 are available in the electronic edition of the journal at http://www.aanda.org

Appendix A

Table A.1. Journal of the observations.

Star	Date obs. [yyyy-mm-dd]	TU [h]	HA [h]	MJD [days]	λ [nm]	Base [m]	Arg [deg]	$V^2 \pm_{stat} \pm_{syst}$
γ Ori	2011-10-12	10.206	−1.707	55 845.5	710	65.574	−114.974	0.830 ± 0.059 ± 0.001
	2011-10-12	10.209	−1.704	55 845.5	731.5	65.578	−114.977	0.817 ± 0.064 ± 0.000
	2011-10-12	10.194	−1.719	55 845.5	731.5	153.578	−110.390	0.228 ± 0.019 ± 0.001
	2011-10-13	9.654	−2.194	55 846.5	710	64.439	−114.627	0.828 ± 0.078 ± 0.000
	2011-10-13	9.708	−2.141	55 846.5	710	149.824	−110.214	0.222 ± 0.036 ± 0.001
	2011-10-13	9.693	−2.155	55 846.5	731.5	149.659	−110.214	0.244 ± 0.024 ± 0.001
	2011-11-22	10.851	1.633	55 886.5	730	104.340	92.583	0.554 ± 0.038 ± 0.001
	2011-12-10	7.745	−0.2984	55 904.5	708.5	154.258	−112.675	0.220 ± 0.012 ± 0.006
γ Lyr	2011-07-27	5.633	−0.916	55 768.5	715	65.4495	−116.028	0.809 ± 0.060 ± 0.008
	2011-07-27	5.633	−0.916	55 768.5	715	154.448	−109.563	0.168 ± 0.020 ± 0.010
	2011-07-27	5.633	−0.916	55 768.5	735	65.4495	−116.028	0.907 ± 0.050 ± 0.009
	2011-07-27	5.633	−0.916	55 768.5	735	154.448	−109.563	0.188 ± 0.014 ± 0.012
	2011-07-27	5.633	−0.916	55 768.5	735	219.605	−111.486	0.002 ± 0.066 ± 0.000
	2011-09-01	5.244	1.060	55 804.5	715	63.897	−133.244	0.699 ± 0.056 ± 0.007
	2011-09-01	5.244	1.060	55 804.5	715	152.073	−126.300	0.190 ± 0.026 ± 0.012
	2011-09-01	5.244	1.060	55 804.5	715	215.640	−128.353	0.016 ± 0.011 ± 0.002
	2011-09-01	5.244	1.060	55 804.5	735	63.897	−133.244	0.784 ± 0.044 ± 0.007
	2011-09-01	5.244	1.060	55 804.5	735	152.073	−126.300	0.222 ± 0.020 ± 0.013
	2011-09-01	5.244	1.060	55 804.5	735	215.640	−128.353	0.005 ± 0.012 ± 0.000
	2012-06-21	7.755	−1.103	56 098.5	707	65.125	−114.643	0.659 ± 0.025 ± 0.005
	2012-06-21	7.755	−1.103	56 098.5	707	153.401	−108.177	0.239 ± 0.040 ± 0.010
	2012-06-21	7.755	−1.103	56 098.5	707	218.236	−110.103	0.026 ± 0.050 ± 0.002
	2012-06-21	7.755	−1.103	56 098.5	730.5	65.125	−114.643	0.684 ± 0.024 ± 0.004
	2012-06-21	7.755	−1.103	56 098.5	730.5	153.401	−108.177	0.178 ± 0.017 ± 0.007
	2012-06-21	7.755	−1.103	56 098.5	730.5	218.236	−110.103	0.046 ± 0.044 ± 0.004
	2012-06-21	9.712	0.858	56 098.5	707.5	64.388	−131.216	0.719 ± 0.044 ± 0.005
	2012-06-21	9.712	0.858	56 098.5	707.5	153.274	−124.351	0.167 ± 0.018 ± 0.007
	2012-06-21	9.712	0.858	56 098.5	707.5	217.337	−126.380	0.003 ± 0.025 ± 0.000
	2012-06-21	9.712	0.858	56 098.5	730.5	64.388	−131.216	0.672 ± 0.046 ± 0.004
	2012-06-21	9.712	0.858	56 098.5	730.5	153.274	−124.351	0.153 ± 0.020 ± 0.006
	2012-06-21	9.712	0.858	56 098.5	730.5	217.337	−126.380	0.043 ± 0.045 ± 0.003
λ Aql	2013-07-24	8.216	1.388	56 496.5	532.5	29.264	−23.993	1.003 ± 0.095 ± 0.002
	2013-07-24	8.216	1.388	56 496.5	532.5	160.270	−35.208	0.205 ± 0.020 ± 0.023
	2013-07-24	8.216	1.388	56 496.5	532.5	189.061	−33.483	0.162 ± 0.088 ± 0.019
	2013-07-24	8.216	1.388	56 496.5	547.5	29.264	−23.993	1.025 ± 0.131 ± 0.005
	2013-07-24	8.216	1.388	56 496.5	547.5	160.270	−35.208	0.201 ± 0.015 ± 0.029
	2013-07-24	8.216	1.388	56 496.5	547.5	189.061	−33.483	0.096 ± 0.024 ± 0.021
	2013-07-24	8.925	2.100	56 496.5	532.5	30.595	−28.275	0.950 ± 0.107 ± 0.002
	2013-07-24	8.925	2.100	56 496.5	532.5	167.700	−37.803	0.142 ± 0.010 ± 0.012
	2013-07-24	8.925	2.100	56 496.5	532.5	197.938	−36.337	0.042 ± 0.061 ± 0.005
	2013-07-24	8.925	2.100	56 496.5	547.5	30.595	−28.275	0.911 ± 0.041 ± 0.002
	2013-07-24	8.925	2.100	56 496.5	547.5	167.700	−37.803	0.169 ± 0.012 ± 0.014
	2013-07-24	8.925	2.100	56 496.5	547.5	197.938	−36.337	0.082 ± 0.021 ± 0.010
	2013-07-24	9.319	2.494	56 496.5	532.5	31.311	−30.138	0.924 ± 0.071 ± 0.0026
	2013-07-24	9.319	2.494	56 496.5	532.5	171.056	−38.738	0.094 ± 0.011 ± 0.008
	2013-07-24	9.319	2.494	56 496.5	532.5	202.070	−37.410	0.005 ± 0.042 ± 0.000
	2013-07-24	9.319	2.494	56 496.5	547.5	31.311	−30.138	0.928 ± 0.050 ± 0.002
	2013-07-24	9.319	2.494	56 496.5	547.5	171.056	−38.738	0.170 ± 0.009 ± 0.014
	2013-07-24	9.319	2.494	56 496.5	547.5	202.070	−37.410	0.045 ± 0.021 ± 0.005
	2013-07-24	9.802	2.979	56 496.5	532.5	32.121	−31.950	0.928 ± 0.105 ± 0.002
	2013-07-24	9.802	2.979	56 496.5	532.5	174.274	−39.432	0.116 ± 0.013 ± 0.011
	2013-07-24	9.802	2.979	56 496.5	532.5	206.164	−38.270	0.028 ± 0.062 ± 0.004
	2013-07-24	9.802	2.979	56 496.5	547.5	32.121	−31.950	0.998 ± 0.090 ± 0.002
	2013-07-24	9.802	2.979	56 496.5	547.5	174.274	−39.432	0.105 ± 0.012 ± 0.009
	2013-07-24	9.802	2.979	56 496.5	547.5	206.164	−38.270	0.068 ± 0.043 ± 0.009
	2013-07-24	8.215	1.388	56 496.5	703.0	29.263	−23.990	0.972 ± 0.235 ± 0.001
	2013-07-24	8.215	1.388	56 496.5	703.0	160.265	−35.206	0.488 ± 0.155 ± 0.037

Table A.1. continued.

Star	Date obs. [yyyy-mm-dd]	TU [h]	HA [h]	MJD [days]	λ [nm]	Base [m]	Arg [deg]	$V^2 \pm_{\rm stat} \pm_{\rm syst}$
	2013-07-24	8.215	1.388	56 496.5	734.0	29.263	−23.990	0.918 ± 0.118 ± 0.002
	2013-07-24	8.215	1.388	56 496.5	734.0	160.265	−35.206	0.467 ± 0.021 ± 0.035
	2013-07-24	8.215	1.388	56 496.5	734.0	189.055	−33.480	0.236 ± 0.068 ± 0.026
	2013-07-24	8.925	2.099	56 496.5	703.0	30.594	−28.272	0.935 ± 0.124 ± 0.007
	2013-07-24	8.925	2.099	56 496.5	703.0	167.695	−37.802	0.293 ± 0.119 ± 0.024
	2013-07-24	8.925	2.099	56 496.5	734.0	30.594	−28.272	0.895 ± 0.075 ± 0.001
	2013-07-24	8.925	2.099	56 496.5	734.0	167.695	−37.802	0.399 ± 0.015 ± 0.017
	2013-07-24	8.925	2.099	56 496.5	734.0	197.932	−36.335	0.434 ± 0.146 ± 0.025
	2013-07-24	9.318	2.494	56 496.5	703.0	31.309	−30.134	0.910 ± 0.269 ± 0.002
	2013-07-24	9.318	2.494	56 496.5	703.0	171.050	−38.736	0.431 ± 0.115 ± 0.020
	2013-07-24	9.318	2.494	56 496.5	734.0	31.309	−30.134	0.895 ± 0.075 ± 0.001
	2013-07-24	9.318	2.494	56 496.5	734.0	171.050	−38.736	0.358 ± 0.015 ± 0.016
	2013-07-24	9.318	2.494	56 496.5	734.0	202.062	−37.408	0.550 ± 0.279 ± 0.062
	2013-07-24	9.801	2.979	56 496.5	703.0	32.120	−31.948	0.936 ± 0.090 ± 0.002
	2013-07-24	9.801	2.979	56 496.5	703.0	174.269	−39.431	0.369 ± 0.189 ± 0.018
	2013-07-24	9.801	2.979	56 496.5	703.0	206.158	−38.269	0.885 ± 0.394 ± 0.054
	2013-07-24	9.801	2.979	56 496.5	734.0	32.120	−31.948	1.122 ± 0.100 ± 0.002
	2013-07-24	9.801	2.979	56 496.5	734.0	174.269	−39.431	0.367 ± 0.015 ± 0.017
	2013-07-24	9.801	2.979	56 496.5	734.0	206.158	−38.269	0.318 ± 0.089 ± 0.036
ι Her	2013-08-29	4.351	1.325	56 532.5	538.5	106.359	−94.209	0.875 ± 0.048 ± 0.006
	2013-08-29	4.351	1.325	56 532.5	538.5	310.123	−120.677	0.081 ± 0.056 ± 0.004
	2013-08-29	4.351	1.325	56 532.5	553.5	106.359	−94.209	0.930 ± 0.052 ± 0.006
	2013-08-29	4.351	1.325	56 532.5	553.5	310.123	−120.677	0.118 ± 0.024 ± 0.007
	2013-08-29	4.350	1.324	56 532.5	707.5	106.361	−94.203	0.933 ± 0.122 ± 0.004
	2013-08-29	4.350	1.324	56 532.5	707.5	310.127	−120.670	0.430 ± 0.164 ± 0.015
	2013-08-29	4.350	1.324	56 532.5	738.5	106.361	−94.203	0.904 ± 0.035 ± 0.004
	2013-08-29	4.350	1.324	56 532.5	738.5	310.127	−120.670	0.315 ± 0.054 ± 0.010
8 Cyg	2013-08-28	6.088	1.130	56 531.5	538.5	216.020	−129.391	0.630 ± 0.053 ± 0.035
	2013-08-28	6.088	1.130	56 531.5	538.5	306.627	−116.749	0.407 ± 0.108 ± 0.049
	2013-08-28	6.088	1.130	56 531.5	553.5	216.020	−129.391	0.617 ± 0.046 ± 0.033
	2013-08-28	6.088	1.130	56 531.5	553.5	306.627	−116.749	0.412 ± 0.079 ± 0.047
	2013-08-28	6.088	1.129	56 531.5	707.5	216.025	−129.386	0.776 ± 0.053 ± 0.024
	2013-08-28	6.088	1.129	56 531.5	707.5	306.634	−116.743	0.442 ± 0.080 ± 0.029
	2013-08-28	6.088	1.129	56 531.5	740.0	216.025	−129.386	0.973 ± 0.151 ± 0.028
	2013-08-28	6.088	1.129	56 531.5	740.0	306.634	−116.743	0.431 ± 0.074 ± 0.025
ζ Per	2011-10-13	8.507	−1.828	55 846.5	715.0	63.035	−109.781	0.965 ± 0.051 ± 0.001
	2011-10-13	8.507	−1.828	55 846.5	715.0	147.169	−103.253	0.471 ± 0.028 ± 0.004
	2011-10-13	8.484	−1.851	55 846.5	715.0	209.574	−105.057	0.181 ± 0.014 ± 0.003
	2011-10-13	8.507	−1.828	55 846.5	734.5	63.035	−109.781	0.904 ± 0.032 ± 0.001
	2011-10-13	8.507	−1.828	55 846.5	734.5	147.169	−103.253	0.494 ± 0.016 ± 0.004
	2011-10-13	8.500	−1.835	55 846.5	734.5	209.811	−105.163	0.228 ± 0.012 ± 0.004

Table A.1. continued.

Star	Date obs [yyyy-mm-dd]	TU [h]	HA [h]	MJD [days]	λ [nm]	Base [m]	Arg [deg]	$V^2 \pm_{\rm stat} \pm_{\rm syst}$
δ Cyg	2011-07-23	7.421	−0.153	55 764.5	715	65.642	−121.782	0.772 ± 0.041 ± 0.002
	2011-07-23	7.425	−0.149	55 764.5	715	155.612	−115.029	0.166 ± 0.011 ± 0.002
	2011-07-23	7.421	−0.153	55 764.5	715	65.642	−121.782	0.772 ± 0.040 ± 0.002
	2011-07-23	7.425	−0.149	55 764.5	715	155.612	−115.029	0.166 ± 0.010 ± 0.002
	2011-07-23	7.421	−0.153	55 764.5	735	65.642	−121.782	0.698 ± 0.035 ± 0.001
	2011-07-23	7.419	−0.155	55 764.5	735	155.596	−114.963	0.147 ± 0.008 ± 0.002
	2011-07-23	9.054	1.484	55 764.5	715	65.146	−139.701	0.708 ± 0.059 ± 0.001
	2011-07-23	9.050	1.480	55 764.5	715	154.249	−132.820	0.127 ± 0.012 ± 0.001
	2011-07-23	9.054	1.484	55 764.5	715	219.055	−134.898	0.011 ± 0.019 ± 0.003
	2011-07-23	9.054	1.484	55 764.5	735	65.146	−139.701	0.684 ± 0.040 ± 0.001
	2011-07-23	9.048	1.478	55 764.5	735	154.256	−132.797	0.160 ± 0.009 ± 0.002
	2011-07-23	9.054	1.484	55 764.5	735	219.055	−134.898	0.016 ± 0.010 ± 0.000
	2011-07-27	8.124	0.815	55 768.5	715	65.744	−132.043	0.726 ± 0.040 ± 0.001
	2011-07-27	8.124	0.815	55 768.5	715	155.931	−125.241	0.128 ± 0.013 ± 0.002
	2011-07-27	8.124	0.815	55 768.5	735	65.7443	−132.043	0.788 ± 0.049 ± 0.002
	2011-07-27	8.124	0.815	55 768.5	735	155.931	−125.241	0.157 ± 0.014 ± 0.002
	2011-07-27	8.124	0.815	55 768.5	735	221.349	−127.257	0.028 ± 0.019 ± 0.000
	2011-07-27	8.917	1.610	55 768.5	715	65.007	−141.195	0.770 ± 0.073 ± 0.001
	2011-07-27	8.917	1.610	55 768.5	715	153.819	−134.361	0.163 ± 0.015 ± 0.002
	2011-07-27	8.917	1.610	55 768.5	715	218.501	−136.390	0.018 ± 0.020 ± 0.000
	2011-07-27	8.917	1.610	55 768.5	735	65.007	−141.195	0.797 ± 0.053 ± 0.001
	2011-07-27	8.917	1.610	55 768.5	735	153.819	−134.361	0.160 ± 0.012 ± 0.002
ζ Peg	2011-07-24	8.586	−1.860	55 765.5	715	65.002	−114.225	0.867 ± 0.039 ± 0.005
	2011-07-24	8.583	−1.863	55 765.5	715	151.533	−109.301	0.428 ± 0.021 ± 0.015
	2011-07-24	8.576	−1.870	55 765.5	715	216.288	−110.765	0.263 ± 0.028 ± 0.022
	2011-07-24	8.586	−1.860	55 765.5	735	65.002	−114.225	0.839 ± 0.034 ± 0.005
	2011-07-24	8.583	−1.863	55 765.5	735	151.533	−109.301	0.414 ± 0.015 ± 0.014
	2011-07-24	8.589	−1.857	55 765.5	735	216.431	−110.787	0.222 ± 0.017 ± 0.015
	2011-07-28	8.236	−1.948	55 769.5	715	64.774	−114.068	0.891 ± 0.059 ± 0.054
	2011-07-28	8.236	−1.948	55 769.5	715	150.724	−109.167	0.442 ± 0.027 ± 0.014
	2011-07-28	8.213	−1.971	55 769.5	715	215.043	−110.606	0.187 ± 0.028 ± 0.013
	2011-07-28	8.240	−1.944	55 769.5	735	64.784	−114.074	0.882 ± 0.055 ± 0.005
	2011-07-28	8.240	−1.944	55 769.5	735	150.760	−109.173	0.440 ± 0.030 ± 0.013
	2011-07-28	8.243	−1.941	55 769.5	735	215.419	−110.650	0.188 ± 0.045 ± 0.012

Annexe V

Theoretical impact of fast rotation on calibrating the surface brightness-color relation for early-type stars

A&A 579, A107 (2015)
DOI: 10.1051/0004-6361/201526240
© ESO 2015

Astronomy & Astrophysics

Theoretical impact of fast rotation on calibrating the surface brightness-color relation for early-type stars

M. Challouf[1,2], N. Nardetto[1], A. Domiciano de Souza[1], D. Mourard[1], H. Aroui[2], P. Stee[1], O. Delaa[1], D. Graczyk[3], G. Pietrzyński[3,4], and W. Gieren[3,5]

[1] Laboratoire Lagrange, UMR7293, UNS/CNRS/OCA, 06300 Nice, France
e-mail: mounir.challouf@oca.eu
[2] Laboratoire Dynamique Moléculaire et Matériaux Photoniques, UR11ES03, Université de Tunis/ESSTT, Tunisie
[3] Departamento de Astronomía, Universidad de Concepción, 2204240 Casilla 160-C, Concepción, Chile
[4] Warsaw University Observatory, AL. Ujazdowskie 4, 00-478 Warsaw, Poland
[5] Millenium Institute of Astrophysics, Cassilla 306, Santiago 22, Chile

Received 1 April 2015 / Accepted 18 May 2015

ABSTRACT

Context. The eclipsing binary method for determining distance in the local group is based on the surface brightness-color relation (SBCR), and early-type stars are preferred targets because of their intrinsic brightness. However, this type of star exhibits wind, mass-loss, pulsation, and rotation, which may generate bias on the angular diameter determination. An accurate calibration of the SBCR relation thus requires careful analysis.

Aims. In this paper we aim to quantify the impact of stellar rotation on the SBCR when the calibration of the relation is based on interferometric measurements of angular diameters.

Methods. Six stars with $V - K$ color indices ranging between –1 and 0.5 were modeled using the code for high angular resolution of rotating objects in nature (CHARRON) with various rotational velocities (0, 25, 50, 75, and 95% of the critical rotational velocity) and inclination (0, 25, 50, 75, and 90 degrees). All these models have their equatorial axis aligned in an east-west orientation in the sky. We then simulated interferometric observations of these theoretical stars using three representative sets of the CHARA baseline configurations. The simulated data were then interpreted as if the stars were non-rotating to determine an angular diameter and estimate the surface-brightness relation. The $V - K$ color of the rotating star was calculated directly from the CHARRON code. This provides an estimate of the intrinsic dispersion of the SBCR relation when the rotation effects of flattening and gravity darkening are not considered in the analysis of interferometric data.

Results. We find a clear relation between the rotational velocity and (1) the shift in zero point (Δa_0) of the SBCR (compared to the static relation) and (2) its dispersion (σ). When considering stars rotating at less than 50% of their critical velocity, Δa_0 and σ have about 0.01 mag, while these quantities can reach 0.08 and 0.04 mag, respectively, when the rotation is larger than 75% of the critical velocity. Besides this, the inclination angle mostly has an impact on the $V - K$ color: $i < 50°$ (resp. $i > 50°$) makes the star redder (resp. bluer). When considering the 150 models, Δa_0 and σ have 0.03 and 0.04 mag, respectively. These values are slightly but not significantly modified (about 0.03 and 0.01 mag in Δa_0 and σ, respectively) when considering different CHARA configurations. Interestingly, these 150 models, regardless of the interferometric configuration, are consistent with the empirical SBCR, which is within its dispersion of 0.16 mag. In addition, if one only considers projected rotational velocity $V_{\rm rot} \sin i$ lower than 100 km s^{-1}, then Δa_0 and σ have 0.02 and 0.03 mag, respectively.

Conclusions. To calibrate the SBCR interferometrically at the 0.02 mag precision (or lower), one should consider (1) a baseline configuration covering all directions of the (u, v) plan; (2) a sample of stars with rotational velocity lower than 50% of their critical velocity or, alternatively, stars with $V_{\rm rot} \sin i$ lower than 100 km s^{-1}; (3) homogeneous visible and infrared photometry precisely at the 0.02 mag level or lower.

Key words. techniques: interferometric – stars: distances – stars: rotation – instrumentation: interferometers – methods: numerical – stars: early-type

1. Introduction

Detached eclipsing double-lined spectroscopic binaries offer a unique opportunity to measure the distance to nearby galaxies directly and very accurately (Graczyk et al. 2011; Wyrzykowski et al. 2003, 2004; Bonanos et al. 2006; Macri et al. 2001). The distance to an eclipsing binary (EB) follows from the combination of the radii of both components determined from spectro-photometric observations with their respective limb-darkened angular diameters derived from the surface brightness color relation (SBCR; Evans 1992, 1991; Paczynski & Stanek 1998; Bohm-Vitense 1985; Stanek & Garnavich 1998; Udalski 2000). By applying this technique to eight long-period eclipsing binaries in the LMC, consisting of G-K type giants, Pietrzyński et al. (2013) obtained a distance to the LMC with 2% precision.

It would be extremely interesting to apply this method to early-type eclipsing binaries (O, B, A), which are much brighter and thus easier to detect (Pietrzyński et al. 2009; Mochejska et al. 2001; Vilardell et al. 2006; Pawlak et al. 2013). The only limitation is currently the precision of the surface-brightness relation. Recently, Challouf et al. (2014b; hereafter Paper I) derived the SBCR (as a function of the $V - K$ color) for the first time and with a precision of about 0.16 mag using interferometric measurements (Challouf et al. 2012, 2014a). However, to achieve 0.02 mag of precision on the SBCR (or 1% in terms of distance), one has to consider the stellar activity in early-type

stars, such as wind, mass-loss, pulsation, and the rotation, which together represent the most important effect on the SBCR.

The surface brightness relation allows the angular diameter of a star to be estimated from its different magnitudes. The usual way to improve the relation is to obtain more direct measurements of angular diameters for a better determination of the empirical relation. The uncertainties in the SBCR stems from the photometry (about 0.03 mag), but also from the angular diameter determination.

One of the limitations in the angular diameter determination is the classical use of a uniform disk model. Indeed, in many cases, the stars are deformed by rotation and thus the determination is biased and generates an additional source of uncertainty in the SBCR calibration. Interpreting the interferometric measurements with a rotating model is possible in principle but requires a very large number of measures (e.g., van Belle et al. 2001; Peterson et al. 2006; Monnier et al. 2007; Zhao et al. 2009). A recent review with several references to interferometric measurements of fast rotators is given by van Belle (2012). Therefore it is not compatible with a survey program. Moreover, the definition of the SBCR relationship including the impact of fast rotation on the surface brightness is something that is very complex so clearly beyond the scope of this paper. We define criteria for the rotational velocity or the projected velocity $V \sin i$ to correctly select the stars considered for the calibration of SBCR (Challouf et al. 2015).

The purpose of this work is thus to quantify the impact of stellar rotation on the SBCR and to determine the corresponding intrinsic dispersion (in magnitude) we could expect. The paper is structured as follows. In Sect. 2, we present the CHARRON code and the six reference non-rotating models we consider. We then apply various values of rotation rates and inclination to these models, which gives us a sample of 150 models. In Sect. 3, we explain our methodology and show, in particular, how the $V-K$ colors and the surface brightness are defined. To derive the surface brightness from the intensity distribution of a star, we simulated interferometric observations and proceed as if the star considered was not rotating. For one model, we show how the $V-K$ color and the surface-brightness quantities are varying as a function of the rotational velocity and the inclination of the star. In Sect. 4 we present the derived SBCR relation and estimate its dispersion. We also clarify how this dispersion varies when considering different sets of stars with different rotational velocities. We discuss the implication of our results in the framework of Paper I in Sect 5.

2. CHARRON model for fast-rotating stars

The numerical model of fast-rotating star used here is the code CHARRON (code for high angular resolution of rotating objects in nature) described by Domiciano de Souza et al. (2012a,b, 2002). The stellar photospheric shape is given by the commonly adopted Roche approximation (rigid rotation and mass concentrated in the stellar center), which is well adapted to non-degenerate, fast-rotating stars.

The effective temperature $T_{\rm eff}$ at the surface for fast rotators is not uniform (depending on the colatitude θ) owing to the decreasing effective gravity $g_{\rm eff}$ (gravitation plus centrifugal acceleration) from the poles to the equator (gravity darkening effect). We model the gravity darkening as a generalized form of the von Zeipel law (von Zeipel 1924):

$$T_{\rm eff}(\theta) = K g_{\rm eff}^{\beta}(\theta), \quad (1)$$

Table 1. Parameters of the non-rotating models we use as a reference.

Model	M1	M2	M3	M4	M5	M6
$V-K$	−0.8	−0.5	−0.3	0	0.3	0.4
$T_{\rm eff}$	23 701	18 418	13 660	9794	8353	7822
$\log g$	3.57	3.78	4.13	4.08	4.08	4.14
$M[M_\odot]$	13.61	5.59	4.11	2.52	2.17	1.99
$R[R_\odot]$	10.00	5.01	2.88	2.39	2.23	1.99
U_R	0.287	0.296	0.315	0.403	0.468	0.456

Notes. The physical parameters are based on Worthey & Lee (2011), Allende Prieto & Lambert (1999).

where β is the gravity darkening coefficient. von Zeipel (1924) derived a theoretical value of 0.25 for early-type stars with radiative external layers and pressure, only depending on the density (barotropic approximation). However, recent interferometric observations have measured somewhat lower values for β (e.g., Che et al. 2011; Domiciano de Souza et al. 2014).

The value of 0.20 seems a good compromise between the theoretical value of von Zeipel and most values measured from interferometric observations of fast-rotating stars and also with recent theoretical models of gravity darkening (e.g., Espinosa Lara & Rieutord 2011; Claret 2012). We thus consider $\beta = 0.20$ for our six models. The K is the proportionality constant between $T_{\rm eff}$ and $g_{\rm eff}$, which depends on the stellar physical parameters. Once $T_{\rm eff}(\theta)$ and $g_{\rm eff}(\theta)$ are defined, we use the spectral synthesis code SYNSPEC (Hubeny & Lanz 2011) and the ATLAS9 stellar atmosphere models (Kurucz 1979) to compute the specific intensity maps of the star.

For this study of the SBCR relation, we define six reference models (non-rotating or static models) covering the range between –0.8 to 0.4 in terms of the $V-K$ color index, which is typical of early-type stars. Using the online data from Worthey & Lee (2011), we find the effective temperature $T_{\rm eff}$ and the surface gravity $\log g$ for each model, corresponding to a specific value of the $V-K$ color. Using these quantities, we derive the corresponding mass and radius from Allende Prieto & Lambert (1999). The color index $V-K$, the effective temperature $T_{\rm eff}$, the surface gravity $\log g$, the mass M, and the radius R are listed in Table 1. These parameters are used as input for the CHARRON code for the six non-rotating stars (M1 to M6). We then apply five values of the rotational velocity (0, 25, 50, 75, and 95% of the critical rotational velocity defined as the value of the rotation velocity at the equator such that the centrifugal acceleration compensates for the net radial attracting force, V_c in the following) and five values of the inclination angle of the rotation axis (0, 25, 50, 75, and 90 degrees). Zero (resp. 90) degrees corresponds to a pole-on (resp. edge-on) star.

3. The derived $V-K$ color and surface brightness

In this section, we explain our methodology, including in particular how the $V-K$ colors are derived from our 150 models and how we simulate interferometric observations in order to derive the calibration of the surface-brightness relation.

3.1. The $V-K$ color

The stellar surface is divided into a predefined grid with nearly identical surface area elements (typically 50 000 surface elements). From $T_{\rm eff}(\theta)$ and $g_{\rm eff}(\theta)$ defined in Domiciano de Souza et al. (2002), a local specific intensity from a plane-parallel

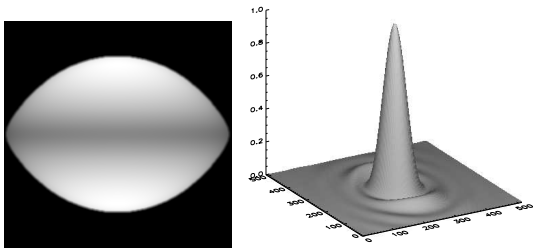


Fig. 1. *Left*: modeled intensity distributions; *Right*: the Fourier transform of the intensity map of M1 at 720 nm for 95% of V_c and $i = 90°$.

atmosphere $I = I(g_{\rm eff}, T_{\rm eff}, \lambda)$ is associated with each surface element, where λ is the wavelength. (Limb darkening is thus automatically included in the model.) The stellar spectral flux in a solid angle dΩ is given by

$$f_\lambda = \int_\Omega I \mathrm{d}\Omega. \quad (2)$$

A surface-averaged $T_{\rm eff}$ can be directly related to the flux f_λ and to the mean angular diameter ϕ (diameter of spherical star having a surface area S) by

$$f_\lambda = \sigma T_{\rm eff}^4 \frac{\phi^2}{4}. \quad (3)$$

We defined the apparent magnitude m_λ, which represents the flux of a star relative to a reference flux at a given wavelength,

$$m_\lambda = -2.5 \log\left(\frac{f_\lambda}{f_{0\lambda}}\right). \quad (4)$$

The color index of our stars is defined as the difference between the apparent magnitude modeled in two different spectral bands,

$$m_{\lambda 2} - m_{\lambda 1} = -2.5 \log\left(\frac{f_{\lambda 1}}{f_{\lambda 2}}\right). \quad (5)$$

We use the V and K bands, therefore $m_{\lambda 2} - m_{\lambda 1} = V - K$.

3.2. From visibilities to surface brightness

3.2.1. The visibilities

The intensity distribution were derived from the CHARRON code for the 150 models we studied. An example is given in the left side of Fig. 1 in the case of M1. We then calculate the fast Fourier transform (FFT) of this intensity distribution following the theorem of Zernike-Van Cittert (van Cittert 1934; Zernike 1938), in which the interferometric visibility is defined as

$$V(u,v) = \frac{\int\int I_{\rm star}(\alpha,\beta) \mathrm{e}^{2\pi(u\alpha+v\beta)} \mathrm{d}\alpha \mathrm{d}\beta}{\int\int I_{\rm star}(\alpha,\beta) \mathrm{d}\alpha \mathrm{d}\beta}, \quad (6)$$

where (α, β) are the angular coordinates in the plane of sky, while (u, v) are the spatial frequencies, defined as $u = \frac{B_u}{\lambda}$ and $v = \frac{B_v}{\lambda}$, with λ the wavelength of the incident radiation, B_u the u-component of the baseline vector $\boldsymbol{B}$, B_v the v-component of the baseline vector $\boldsymbol{B}$. Once the complex visibility is derived, we can determine the squared visibility, which provides the fringe contrast as a function of the spatial frequency (see Fig. 1-right) given by

$$V(u_c, v_c)^2 = V(u_c, v_c) V^*(u_c, v_c), \quad (7)$$

where u_c and v_c are the spatial frequencies.

Table 2. CHARA configuration used in this study.

Configuration	Telescope	Base length
C1*	W2S2	177 m
C2	E2W1	251 m
	E2W2	156 m
	W1W2	108 m
C3	E2W1W2-W2S2	108–251 m

Notes. (*) We used different wavelengths, 750 nm and 545 nm, to slightly improve the (u, v) coverage (as usually done, for instance, with the VEGA/CHARA instrument, Mourard et al. 2009, 2011).

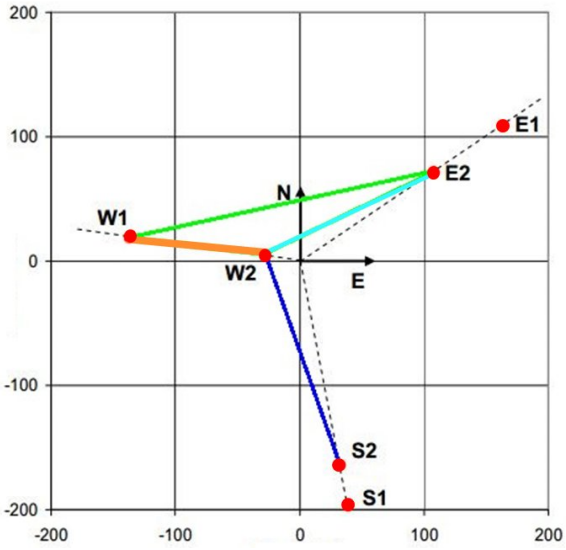


Fig. 2. Configuration of the CHARA array (ten Brummelaar et al. 2005) located at the Mount Wilson Observatory, north of Los Angeles (California, USA). The CHARA array consists of 6 telescopes of 1 meter in diameter, configured in a Y-shape, which offers 15 different baselines from 34 m to 331 m.

For our study we consider three realistic CHARA[1] configurations indicated in Table 2. We decided to use the CHARA case because this interferometer presents the longest baselines and access to the visible wavelength, allowing thus to reach the best angular resolution and the one needed to accurately measure the considered stars. C1 and C2 are mainly oriented north-south and east-west, respectively, while C3 is a combination of C1 and C2 (Fig. 2). We mention here that our 150 models have their rotation axis aligned with the north-south direction.

3.2.2. The angular diameter

The squared visibilities (V^2) obtained from the intensity distribution and the baseline configurations presented in the previous section are then interpreted using a simple uniform disk model. The theoretical visibility of this model is given by $V^2 = (2\frac{J_1(z)}{z})^2$ where $J_1(z)$ is the Bessel function of the first kind and first order, and $z = \pi\theta_{\rm UD}B/\lambda$, where B is the projected baseline, λ the effective wavelength, and $\theta_{\rm UD}$ the apparent UD angular diameter of the star.

In Fig. 3, we present the squared visibility as a function of the spatial frequency in the case of the M1 model (Table 1) and

[1] CHARA: Center for High Angular Resolution Astronomy.

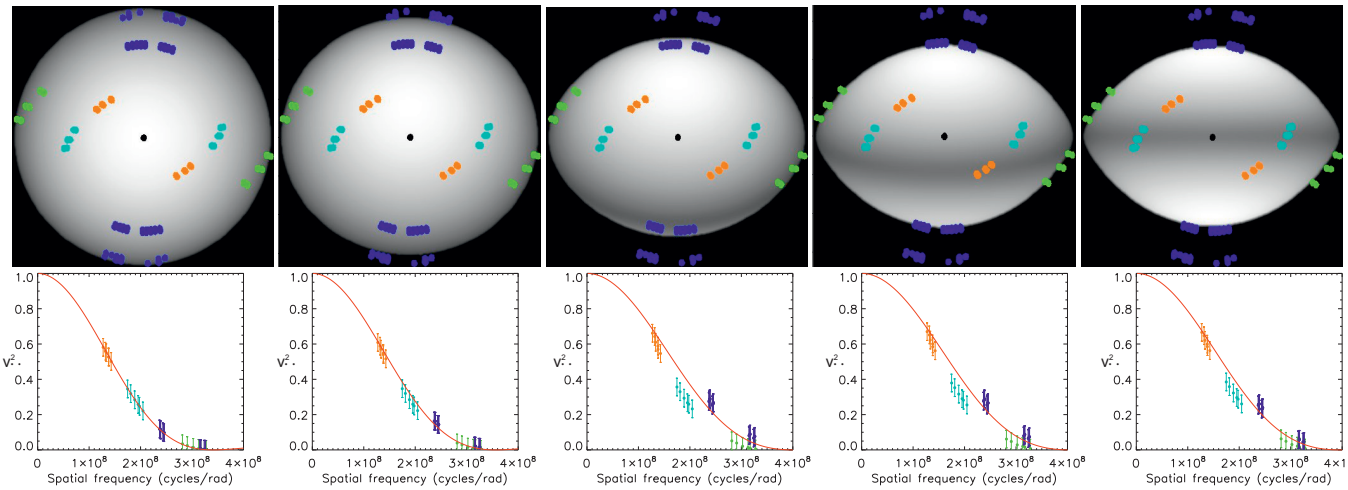


Fig. 3. *Top*: intensity maps are given in units of the equatorial radius (Req) with the project baselines in the sky. *Bottom*: squared visibility versus spatial frequency. The figures calculated for inclination (*from left to right*): 0°, 25°, 50°, 75°, and 90°. The rotational velocity for all inclinations is of 0.95Vc. The visibilities points presented with same color bases of Fig. 2, and the red lines are the best fitted uniform disk. The mean angular diameter $\theta_{\rm UD}$ ranges from 0.635 ± 0.006 mas to 0.736 ± 0.001 mas.

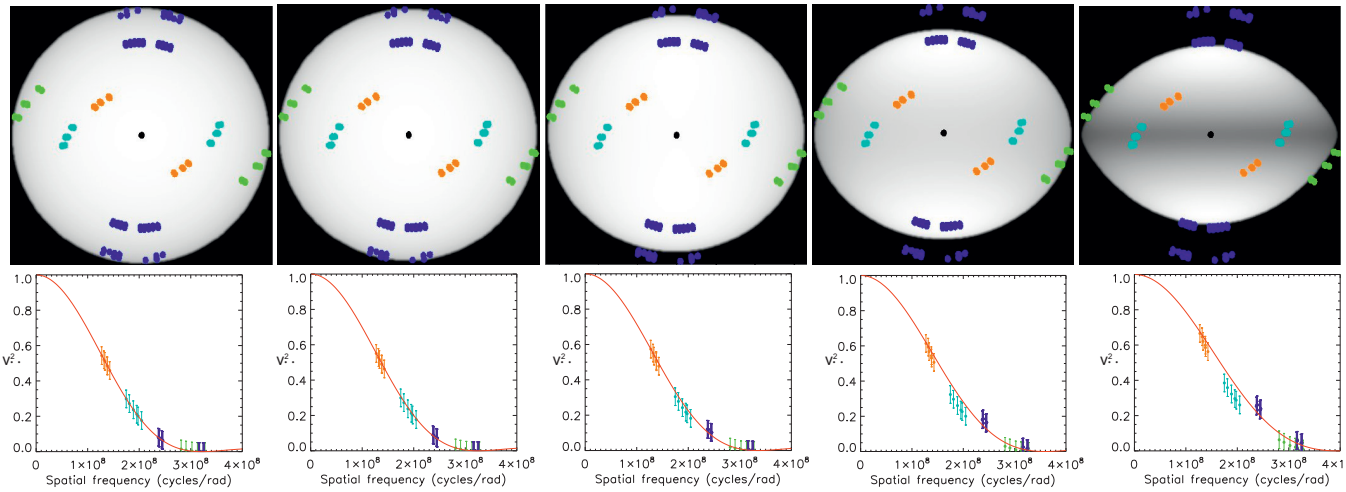


Fig. 4. *Top*: intensity maps given in units of the equatorial radius (Req) with the project baselines in the sky. *Bottom*: squared visibility versus spatial frequency. The figures calculated for rotational velocities (*from left to right*): $0.0Vc$, $0.25Vc$, $0.50Vc$, $0.75Vc$, and $0.95Vc$. The inclination for all rotational velocities is 90°. The visibilities points presented with same color bases as in Fig. 2, and the red lines are the best-fitted uniform disk. The mean angular diameter $\theta_{\rm UD}$ ranges from 0.635 ± 0.006 mas to 0.782 ± 0.001 mas.

the C3 configuration (Table 2). In the upper panel, the M1 model rotates at 95% of its break-up velocity but seen for different inclination angles. In the lower panel, the model is seen edge-on, but for different rotation velocities.Based upon our understanding of the current VEGA limitations (Mourard et al. 2012), we decided to set a conservative lower limit to the absolute uncertainty of the squared visibility measurements at the level of 0.05 [no unit]. From this figure, we interestingly find that a pole-on star rotating close to the breakup velocity (0.95 $V_{\rm c}$) can be fitted by a uniform disk without any large residuals. In contrast, when the star is seen close to edge-on (high value of the inclination angle), the residual is significant, when compared to our uncertainties of 5%. In any case (with low or large residuals), there will be a bias in our estimate of the UD angular diameter of the star.

The equivalent uniform disk angular diameter $\theta_{\rm UD}$ is then converted into a limb-darkened disk, and the relationship incorporating the linear limb-darkening coefficients U_λ (Hanbury Brown et al. 1974) is

$$\theta_{\rm LD}(\lambda) = \theta_{\rm UD}(\lambda)\left[\frac{(1-U_\lambda/3)}{(1-7U_\lambda/15)}\right]^{1/2}. \quad (8)$$

The LD coefficient is derived as if the star was non-rotating, which means from the table of Claret & Bloemen (2011) after adopting the following stellar parameter: effective temperatures ($T_{\rm eff}$), metallicity ([Fe/H]), and surface gravity (log g) values from Worthey & Lee (2011), see also Table 1.

3.2.3. The surface brightness

The surface brightness F, defined by $F = \log T_{\rm eff} + 0.1BC$, is directly related to the effective temperature of the star and thus to its color (Wesselink 1969). According to

Barnes & Evans (1976), the surface brightness in a given spectral band F_λ may be found from its absolute visual magnitude $m_{\lambda 0}$ and true apparent limb-darkened angular diameter $\theta_{\rm LD}$

$$F_\lambda = 4.2207 - 0.1 m_{\lambda 0} - 0.5 \log \theta_{\rm LD}, \quad (9)$$

where the coefficient 4.2207 only depends on the solar bolometric absolute magnitude $M_{\rm bol\odot}$, the solar total integrated flux $f_\odot$, and on the Stefan-Boltzmann constants σ. It is given by

$$4.2207 = 0.1 M_{\rm bol\odot} + 1 + 0.25 \log \frac{4 f_\odot}{\sigma}. \quad (10)$$

Equation (9) can also be written as

$$F_\lambda = 4.2207 - 0.1 S_\lambda, \quad (11)$$

where S_λ is defined by

$$S_\lambda = m_{\lambda 0} + 5 \log \theta_{\rm LD}. \quad (12)$$

Wesselink (1969), Parsons (1970), Barnes & Evans (1976), and Barnes et al. (1976, 1978) demonstrated using known angular diameters of stars, a correlation between S_λ, and color index C $(m_{\lambda 2} - m_{\lambda 1})$ given by

$$S_\lambda = \sum_0^n a_n C^n, \quad (13)$$

where a_n are the polynomial coefficients of the calibration between S_λ and color index C^n.

For all our 150 models, we have thus obtained the surface brightness from Eq. (12) and the $V-K$ color index from Eq. (5). Finally the calibration of these two quantities give the Eq. (13).

3.3. The M3 model as an example

We show in Fig. 5 how the $V-K$ and S_v quantities associated with the M3 model (and C3 interferometric configuration) vary as a function of the rotation, the inclination, and also the projected rotational velocity $V_{\rm rot} \sin i$. We can make several remarks:

1. The higher the rotational velocity, the greater the bias compared to the static model: can be as large as 0.1 mag in $V-K$ color and/or surface brightness.
2. The inclination angle essentially has an impact on the $V-K$ color: $i < 50°$ (resp. $i > 50°$) makes the star redder (resp. bluer). More particularly and very interestingly, regardless of its rotational velocity, as soon as a star is seen edge-on or pole-on, the interferometric bias in $V-K$ and in surface brightness compensate in such a way that the star stands almost on the static SBCR.
3. A model with a given projected rotational velocity $V_{\rm rot} \sin i$ can cover a large domain in $V-K$ and in surface brightness, which introduces a significant bias compared to the static model. The lowest bias is found for stars with $V_{\rm rot} \sin i < 100$ km s^{-1}; in this case, the models stand reasonably close to the static relation.

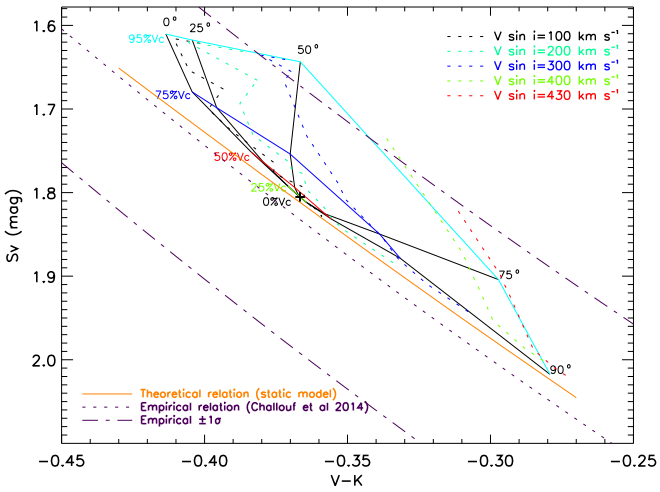


Fig. 5. Surface brightness versus the $V-K$ color for the M3 model (Table 1), considering the C3 interferometric configuration (Table 2). The rotational velocity of the star is indicated in percentage of the critical rotational velocity (V_c), together with the inclination angle (in degrees). The corresponding projected rotational velocity $V_{\rm rot} \sin i$ are also indicated by dotted lines. The orange solid line is the SBCR found for the static models (see next section). The violet dotted line is the empirical SBCR from Challouf et al. (2014b), together with its dispersion (red dot-dashed line).

4. Impact of the interferometric configuration on the SBCR

In this section, we consider the 150 computed models and derive their $V-K$ and S_V following the methodology described in Sect. 3. This is done for the three CHARA configurations C1, C2, and C3. The result is shown in Fig. 6. In this figure we do not show the 150 models for clarity, but only the 50 models corresponding to extreme cases in term of rotational velocity and inclination. In Table 3, we present the coefficients of the SBCR (polynomial fit of degree 3) for the three configurations, along with their dispersion (σ). The relation obtained for the six static models (rotational velocity of zero) is shown for comparison. We also use the difference of the zero points of the three relations for C1, C2, and C3, respectively, compared to the static SBCR, as an indicator of their average shift along the Y-axis: $\Delta a_0 = a_0$ [for C_i] $- a_0$[static] in magnitude. It actually corresponds to the shift obtain at $V-K=0$.

We can make the following remarks:

1. We find that considering a baseline configuration along the polar axis (resp. equatorial axis) produces a statistical bias of −0.05 (resp. 0.00) magnitude (along Y-axis) compared to the static SBCR. These values are extreme cases in the sense that our 150 models have their equatorial axis aligned with the east-west orientation on the sky. If the baseline configuration covers the (u, v) plan properly, then the bias has −0.03 mag.
2. Regardless of the baseline configuration, the expected dispersion in the SBCR due to the rotation (rotational velocity and inclination) ranges from 0.04 (C3 configuration) to 0.06 (C1 configuration) magnitude. Interestingly, no matter what the interferometric configuration is, the large majority of the 150 models lie within the dispersion (0.16 mag) of the empirical SBCR found by Challouf et al. (2014b).
3. When the star is seen edge-on and whatever the rotational velocity, the SBCR is almost on the static relation when we take the best covering (u, v) plane (Fig. 6 below).

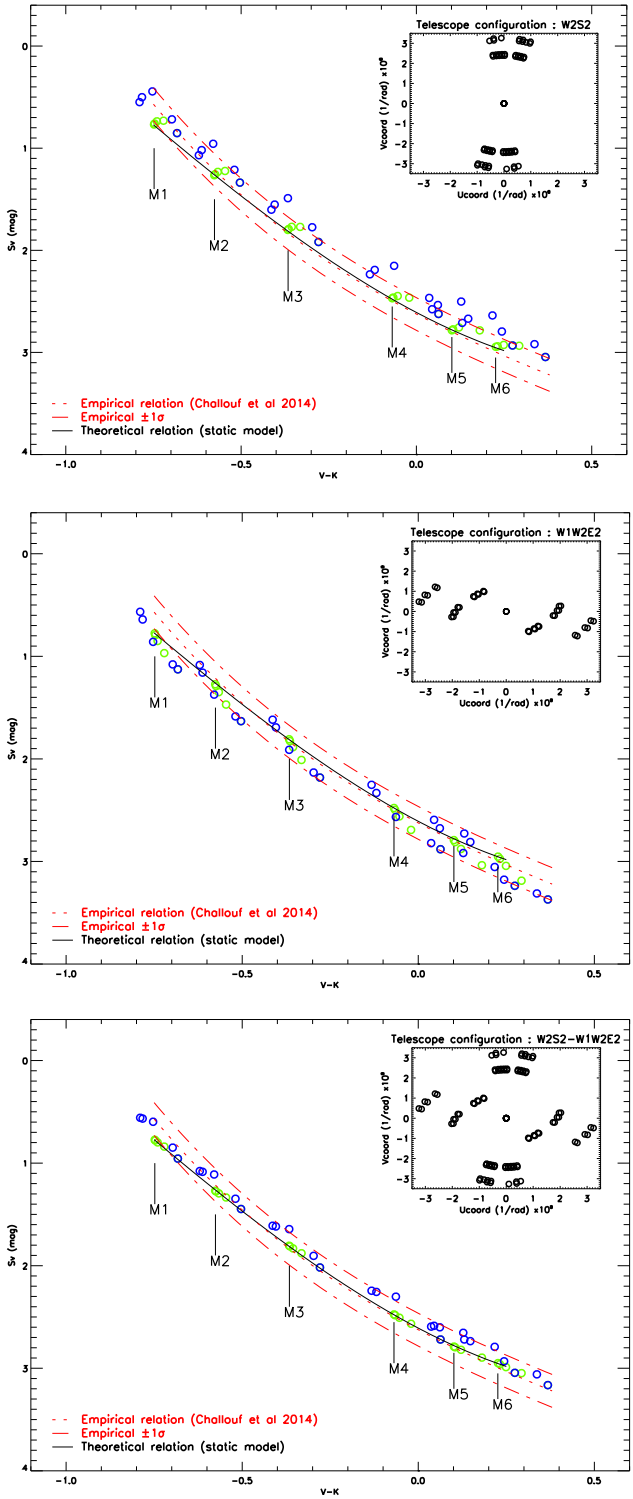


Fig. 6. Sv as function of $V-K$, for the 6 models of Table 1 rotating at 95% of their critical velocity and for different inclination angles: 0°, 25°, 50°, 75°, and 90° (blue points). The same but for edge-on models with different rotational velocity: $0.0Vc$, $0.25Vc$, $0.50Vc$, $0.75Vc$, and $0.95Vc$ (green points). *Top*: W2S2 (C1). *Middle*: W1W2E2 (C2). *Below*: W2S2-W1W2E2 (C3). The SBCR from Challouf et al. (2014b) is shown for comparison.

4. The static SBCR relation is consistent with the empirical one from Challouf et al. (2014b), which is within a $+/-\sigma = 0.16$ mag. empirical uncertainty.

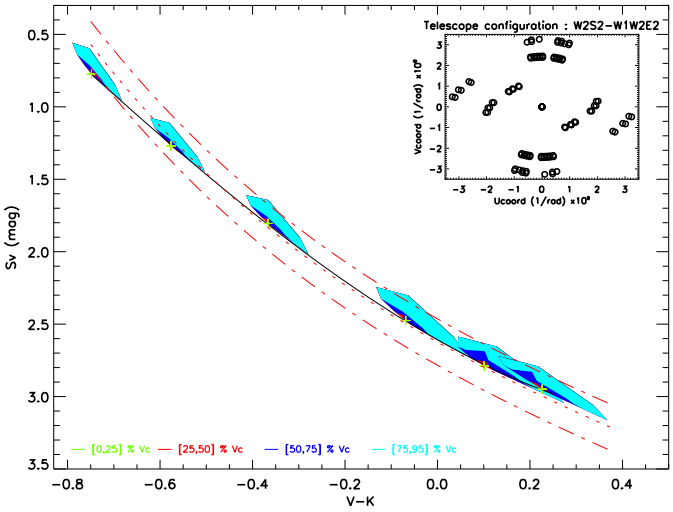


Fig. 7. Surface brightness versus the $V-K$ color considering the C3 interferometric configuration for 150 models. The colors indicate the different velocity intervals. The black solid line is the SBCR found for the static models. The red dotted line is the empirical SBCR from Challouf et al. (2014b), together with its dispersion (red dot-dashed line). The (+) symbol presents the static models.

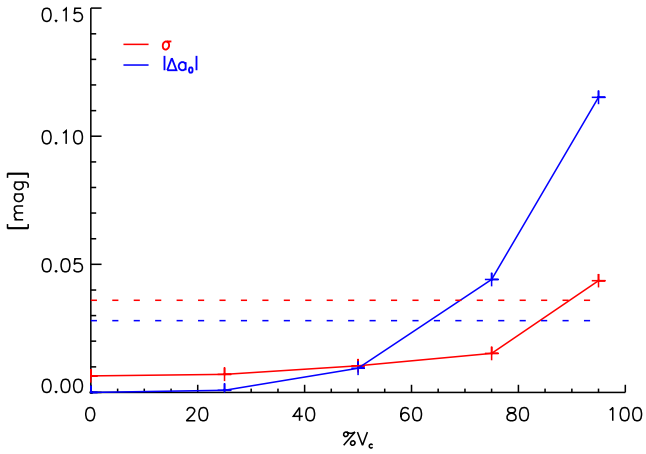


Fig. 8. Relation between the rotational velocity (as a percentage of the critical rotational velocity) and (1) the shift in zero point (Δa_0) of the SBCR (compared to the static relation) and (2) its dispersion (σ). The horizontal red (resp. blue) dotted lines correspond to the average σ (resp. Δa_0) for the 150 models (see Table 3). All the quantities are derived using the C3 interferometric configuration.

We now consider our six samples of models with rotational velocities of 0, 25, 50, 75, and 95% of the critical rotational velocity, respectively (thus 30 models per sample). In Fig. 7, we show the 150 models with their respective rotational velocities, as in Fig. 5 but interpolated for each interval of velocity and illustrated by a color. All models within a given interval of velocity (i.e., one sample of 30 models) is fitted with a polynomial function of degree 3, and the results are given in Table 3. The corresponding Δa_0 values and dispersion of these SBCR relations are indicated in the table and illustrated in Fig. 8. We find a clear relation between the rotational velocity and (1) the shift in zero point (Δa_0) of the SBCR (compared to the static relation) and (2) its dispersion (σ). When considering stars rotating at less than 50% of their critical velocity, Δa_0 and σ have about a 0.01 mag, while

Table 3. 150 models fitted with a polynomial function defined as $Sv = a_0 + a_1(V-K) + a_2(V-K)^2 + a_3(V-K)^3$ for the three interferometric configuration (Table 2).

Config.	C1	C2	C3	Static
a_0	2.555 ± 0.004	2.605 ± 0.004	2.580 ± 0.004	2.609 ± 0.009
a_1	1.800 ± 0.014	1.870 ± 0.014	1.826 ± 0.014	1.805 ± 0.030
a_2	−1.139 ± 0.069	−0.527 ± 0.069	−0.910 ± 0.070	−1.142 ± 0.159
a_3	−0.366 ± 0.084	0.309 ± 0.084	−0.114 ± 0.084	−0.377 ± 0.190
σ	0.064	0.052	0.036	0.006
Δa_0	–0.054	–0.004	-0.029	0.000

Notes. The coefficients are given with the statistical dispersion, and σ is the statistical dispersion on the SBCR relation. The last line provides $\Delta a_0 = a_0$ [for C_i] $- a_0$ [static] in magnitude.

Table 4. Calibration of SBCR for different rates of rotational velocities with the following function $Sv = a_0 + a_1(V-K) + a_2(V-K)^2 + a_3(V-K)^3$.

% Vc	[0–25]	[25–50]	[50–75]	[75–95]
a_0	2.608 ± 0.006	2.603 ± 0.006	2.582 ± 0.007	2.531 ± 0.007
a_1	1.805 ± 0.022	1.807 ± 0.023	1.820 ± 0.024	1.849 ± 0.024
a_2	−1.140 ± 0.114	−1.110 ± 0.118	−0.957 ± 0.120	−0.632 ± 0.102
a_3	−0.374 ± 0.136	−0.338 ± 0.140	−0.164 ± 0.142	0.196 ± 0.127
σ	0.007	0.009	0.018	0.042
Δa_0	0.001	0.005	0.026	0.077

these quantities can reach 0.08 and 0.04 mag, respectively, when the rotation is more than 75% of the critical velocity. The dashed lines are the same quantities but considering the 150 models for C3 (see previous section).

5. Conclusion

In this paper we aimed at theoretically quantifying the impact of fast rotation on the SBCR of early-type stars. After verifying that the static theoretical and empirical (Challouf et al. 2014b) SBCR relations are roughly consistent, we concluded that the rotational velocity and the inclination (compare to the line of sight) of the stars result in a dispersion of the SBCR of about 0.04 mag and a bias of about the same value, 0.03 mag. These values are slightly but not significantly changed (about 0.03 and 0.01 mag in Δa_0 and σ, respectively) when considering different CHARA configurations. Finally, all our models (regardless of the interferometric configuration) are consistent with the 0.16 mag dispersion of the empirical SBCR found by Challouf et al. (2014b). This does not mean that the 0.16 mag of dispersion is entirely due to rotation, but most certainly that rotation is one of the various physical effects (along with mass loss and environment) that is contributing to the dispersion of the SBCR. We also notice that the bias (or zero-point shifts) due to the interferometric configuration (from 0 to 0.05 mag) are lower than the observed dispersion, which explains why rotating stars have been used up to now to calibrate the SBCR: the bias due to rotation was indeed within the uncertainties and not seen in the data analysis.

The aim of this work is to improve the SBCR of early-type stars. In the framework of the Araucaria project, we need a SBCR for early-type stars as precise as 1% or 0.02 mag in order to derive the distance in the local group of bright early-type eclipsing binaries, which are not affected by the rotation in principle. To reach such objective, our suggestion is (1) to use a decent (u, v) coverage; (2) observe a large sample of rotating early-type stars again by interferometry (most preferably in the visible because these stars are generally small angularly) with rotational velocities lower than 50 km s^{-1}; (3) secure new and homogeneous optical and infrared photometry to calibrate the SBCR relation. Alternatively, if one cannot determine the rotational velocity of the stars, our calculations show that considering stars with projected rotational velocity $V_{\rm rot} \sin i$ lower than 100 km s^{-1} result in a zero-point shift of $\Delta a_0 = 0.02$ mag and a dispersion of $\sigma = 0.03$ mag, respectively.

Acknowledgements. This research made use of the SIMBAD and VIZIER databases at the CDS, Strasbourg France (http://cdsweb.u-strasbg.fr/), and of the electronic bibliography maintained by the NASA/ADS system. The research leading to these results has received funding from the European Community's Seventh Framework Program under Grant Agreement 312430 and financial support from the Ministry of Higher Education and Scientific Research (MHESR) – Tunisia. W.G. and G.P. gratefully acknowledge support for this work from the BASAL Centro de Astrofisica y Tecnologias Afines (CATA) PFB-06/2007. W.G. also acknowledges support from the Chilean Ministry of Economy, Development and Tourism's Millenium Science Initiative through grant IC 120009 awarded to the Millenium Institute of Astrophysics (MAS). Support from the Polish National Science Center grant MAESTRO 2012/06/A/ST9/00269 is also acknowledged.

References

Allende Prieto, C., & Lambert, D. L. 1999, A&A, 352, 555
Barnes, T. G., & Evans, D. S. 1976, MNRAS, 174, 489
Barnes, T. G., Evans, D. S., & Parsons, S. B. 1976, MNRAS, 174, 503
Barnes, T. G., Evans, D. S., & Moffett, T. J. 1978, MNRAS, 183, 285
Bohm-Vitense, E. 1985, ApJ, 296, 169
Bonanos, A. Z., Stanek, K. Z., Kudritzki, R. P., et al. 2006, ApJ, 652, 313
Challouf, M., Nardetto, N., Mourard, D., Aroui, H., & Chesneau, O. 2012, in SF2A-2012: Proc. Annual meeting of the French Society of Astronomy and Astrophysics, eds. S. Boissier, P. de Laverny, N. Nardetto, et al., 299
Challouf, M., Nardetto, N., Mourard, D., Aroui, H., & Delaa, O. 2014a, in SF2A-2014: Proc. Annual meeting of the French Society of Astronomy and Astrophysics, eds. J. Ballet, F. Martins, F. Bournaud, R. Monier, & C. Reylé, 471
Challouf, M., Nardetto, N., Mourard, D., et al. 2014b, A&A, 570, A104
Challouf, M., Nardetto, N., Domiciano de Souza, A., et al. 2015, in IAU Symp., 307, 288
Che, X., Monnier, J. D., Zhao, M., et al. 2011, ApJ, 732, 68
Claret, A. 2012, A&A, 538, A3
Claret, A., & Bloemen, S. 2011, A&A, 529, A75
Domiciano de Souza, A., Vakili, F., Jankov, S., Janot-Pacheco, E., & Abe, L. 2002, A&A, 393, 345
Domiciano de Souza, A., Hadjara, M., Vakili, F., et al. 2012a, A&A, 545, A130

Domiciano de Souza, A., Zorec, J., & Vakili, F. 2012b, in SF2A-2012: Proc. Annual meeting of the French Society of Astronomy and Astrophysics, eds. S. Boissier, P. de Laverny, N. Nardetto, et al., 321
Domiciano de Souza, A., Kervella, P., Moser Faes, D., et al. 2014, A&A, 569, A10
Espinosa Lara, F., & Rieutord, M. 2011, A&A, 533, A43
Evans, N. R. 1991, ApJ, 372, 597
Evans, N. R. 1992, ApJ, 389, 657
Graczyk, D., Soszyński, I., Poleski, R., et al. 2011, Acta Astron., 61, 103
Hanbury Brown, R., Davis, J., Lake, R. J. W., & Thompson, R. J. 1974, MNRAS, 167, 475
Hubeny, I., & Lanz, T. 2011, Astrophysics Source Code Library [record ascl:1109.022]
Kurucz, R. L. 1979, ApJS, 40, 1
Macri, L. M., Stanek, K. Z., Sasselov, D. D., Krockenberger, M., & Kaluzny, J. 2001, AJ, 121, 870
Mochejska, B. J., Kaluzny, J., Stanek, K. Z., & Sasselov, D. D. 2001, AJ, 122, 1383
Monnier, J. D., Zhao, M., Pedretti, E., et al. 2007, Science, 317, 342
Mourard, D., Clausse, J. M., Marcotto, A., et al. 2009, A&A, 508, 1073
Mourard, D., Bério, P., Perraut, K., et al. 2011, A&A, 531, A110
Mourard, D., Challouf, M., Ligi, R., et al. 2012, in SPIE Conf. Ser., 8445
Paczynski, B., & Stanek, K. Z. 1998, ApJ, 494, L219
Parsons, S. B. 1970, ApJ, 159, 951
Pawlak, M., Graczyk, D., Soszyński, I., et al. 2013, Acta Astron., 63, 323
Peterson, D. M., Hummel, C. A., Pauls, T. A., et al. 2006, ApJ, 636, 1087
Pietrzyński, G., Thompson, I. B., Graczyk, D., et al. 2009, ApJ, 697, 862
Pietrzyński, G., Graczyk, D., Gieren, W., et al. 2013, Nature, 495, 76
Stanek, K. Z., & Garnavich, P. M. 1998, ApJ, 503, L131
ten Brummelaar, T. A., McAlister, H. A., Ridgway, S. T., et al. 2005, ApJ, 628, 453
Udalski, A. 2000, ApJ, 531, L25
van Belle, G. T. 2012, A&ARv, 20, 51
van Belle, G. T., Ciardi, D. R., Thompson, R. R., Akeson, R. L., & Lada, E. A. 2001, ApJ, 559, 1155
van Cittert, P. H. 1934, Physica, 1, 201
Vilardell, F., Ribas, I., & Jordi, C. 2006, A&A, 459, 321
Von Zeipel, H. 1924, MNRAS, 84, 665
Wesselink, A. J. 1969, MNRAS, 144, 297
Worthey, G., & Lee, H.-c. 2011, ApJS, 193, 1
Wyrzykowski, L., Udalski, A., Kubiak, M., et al. 2003, Acta Astron., 53, 1
Wyrzykowski, L., Udalski, A., Kubiak, M., et al. 2004, Acta Astron., 54, 1
Zernike, F. 1938, Physica, 5, 785
Zhao, M., Monnier, J. D., Pedretti, E., et al. 2009, ApJ, 701, 209

Annexe W

The Surface Brightness–Color Relations Based on Eclipsing Binary Stars : Toward Precision Better than 1% in Angular Diameter Predictions

Draft version February 21, 2017
Preprint typeset using LaTeX style emulateapj v. 12/16/11

arXiv:1611.09976v2 [astro-ph.SR] 20 Feb 2017

THE SURFACE BRIGHTNESS–COLOR RELATIONS BASED ON ECLIPSING BINARY STARS: TOWARD PRECISION BETTER THAN 1% IN ANGULAR DIAMETER PREDICTIONS.

Dariusz Graczyk[1,2,3], Piotr Konorski[4], Grzegorz Pietrzyński[3,2], Wolfgang Gieren[2,1], Jesper Storm[5], Nicolas Nardetto[6], Alexandre Gallenne[7], Pierre F. L. Maxted[8], Pierre Kervella[9,10] and Zbigniew Kołaczkowski[11]

[1]Millennium Institute of Astrophysics (MAS), Chile
[2]Universidad de Concepción, Departamento de Astronomia, Casilla 160-C, Concepción, Chile; darek@astro-udec.cl
[3]Centrum Astronomiczne im. Mikołaja Kopernika (CAMK), PAN, Bartycka 18, 00-716 Warsaw, Poland; darek@ncac.torun.pl
[4]Obserwatorium Astronomiczne, Uniwersytet Warszawski, Al. Ujazdowskie 4, 00-478, Warsaw, Poland
[5]Leibniz-Institut für Astrophysik Potsdam, An der Sternwarte 16, 14482 Potsdam, Germany
[6]Université Côte d'Azur, Observatoire de la Côte d'Azur, CNRS, Laboratoire Lagrange, UMR7293, Nice, France
[7]European Southern Observatory, Alonso de Córdova 3107, Casilla 19001, Santiago 19, Chile
[8]Astrophysics Group, Keele University, Staffordshire, ST5 5BG, UK
[9]Unidad Mixta Internacional Franco-Chilena de Astronomía (CNRS UMI 3386), Departamento de Astronomía, Universidad de Chile, Camino El Observatorio 1515, Las Condes, Santiago, Chile
[10]LESIA (UMR 8109), Observatoire de Paris, PSL Research University, CNRS, UPMC, Univ. Paris-Diderot, 5 place Jules Janssen, 92195 Meudon, France and
[11]Instytut Astronomiczny, Uniwersytet Wrocławski, Kopernika 11, 51-622 Wrocław, Poland

Draft version February 21, 2017

ABSTRACT

In this study we investigate the calibration of surface brightness–color (SBC) relations based solely on eclipsing binary stars. We selected a sample of 35 detached eclipsing binaries with trigonometric parallaxes from *Gaia* DR1 or *Hipparcos*, whose absolute dimensions are known with an accuracy better than 3% and that lie within 0.3 kpc from the Sun. For the purpose of this study, we used mostly homogeneous optical and near-infrared photometry based on the Tycho-2 and 2MASS catalogs. We derived geometric angular diameters for all stars in our sample with a precision better than 10%, and for 11 of them with a precision better than 2%. The precision of individual angular diameters of the eclipsing binary components is currently limited by the precision of the geometric distances (∼5% on average). However, by using a subsample of systems with the best agreement between their geometric and photometric distances, we derived the precise SBC relations based only on eclipsing binary stars. These relations have precisions that are comparable to the best available SBC relations based on interferometric angular diameters, and they are fully consistent with them. With very precise *Gaia* parallaxes becoming available in the near future, angular diameters with a precision better than 1% will be abundant. At that point, the main uncertainty in the total error budget of the SBC relations will come from transformations between different photometric systems, disentangling of component magnitudes, and for hot OB stars, the main uncertainty will come from the interstellar extinction determination. We argue that all these issues can be overcome with modern high-quality data and conclude that a precision better than 1% is entirely feasible.

Keywords: binaries: eclipsing

1. INTRODUCTION

The surface brightness–color (SBC) relations play a fundamental role in predicting angular diameters of stars and serve as an almost perfect tool for deriving precise distances to eclipsing binary stars. They have also been extremely useful in Baade–Wesselink techniques to determine the distances to classical Cepheid stars (e.g. Gieren et al. 1995; Fouqué & Gieren 1997; Storm et al. 2011). The SBC relations are commonly calibrated based on direct stellar angular diameters measured by means of ground-based interferometry (e.g. Kervella et al. 2004; di Benedetto 2005; Challouf et al. 2014; Boyajian et al. 2014). The precision of the SBC relations is gradually improving thanks to the ever-growing number of stars with interferometric angular diameters and to improvements in dealing with the limb darkening.

Eclipsing binaries with known trigonometric parallaxes can also be used to derive the SBC relation. This idea was first formulated and used by Lacy (1977): the combination of a geometric distance and stellar radius immediately provides an angular diameter of a component of an eclipsing binary. This can later be used to derive a dependence of the radiative flux scale on color, expressed in terms of the surface brightness parameter or the effective temperature. Deriving angular diameters of eclipsing binary stars is significantly more complex than determining an angular diameter of a single star with interferometry. However, using eclipsing binaries usually has an important advantage: good control on the limb-darkening uncertainties, at least when the light curves are of sufficient quality (e.g. Popper 1984). Early attempts were constrained to the color $V-R$ (Lacy 1977; Barnes et al. 1978; Popper 1980) and were based on only on three eclipsing binary systems with secure trigonometric parallaxes.

When Hipparcos parallaxes became available, Popper (1998) analyzed 14 well-detached eclipsing binaries with the most accurate parallaxes and absolute dimensions to compare radiative flux scales defined by interferometry and eclipsing binary systems. However, this analysis was

made only for $(B-V)$ color and included eclipsing binaries with a significant amount of chromospheric activity. Nonetheless, Popper (1998) concluded that the SBC relation based on non-active eclipsing binaries seemed to be complementary to that based on interferometric angular diameters. Kruszewski & Semeniuk (1999) developed the idea of using a large number of eclipsing binaries with geometric distances from Hipparcos to precisely calibrate the SBC relations. They compiled an extensive list of promising eclipsing binaries in the solar neighborhood (up to 200 pc). Soon after, Semeniuk (2001) derived the SBC relation from a sample of 13 eclipsing binary stars with *Hipparcos* parallaxes and Strömgren photometry. The calibration was made for the $(b-y)$ color and compared with the relation by Popper (1998), which was mostly based on interferometric and lunar occultation angular diameter measurements. The samples agreed well, but the derived SBC relation had very large scatter.

The usefulness of eclipsing binaries for distance measurements was investigated by Jerzykiewicz (2001) by comparison of corrected trigonometric parallaxes and photometric distances, with the conclusion that EBs are excellent standard candles. Smalley et al. (2002) used 15 eclipsing binary stars with Hipparcos parallaxes to derive a fundamental temperature scale for A-type stars, and Bilir et al. (2008) presented a brief analysis of using eclipsing binary stars to calibrate the absolute magnitudes of stars as a function of some intrinsic colors. The most recent application of eclipsing binaries to derive the SBC relations known to us is the work by Bonneau et al. (2006), where the SBC relation was calibrated against $(V-K)$ color, but these authors used photometric distances to derive angular diameters (see our Sec. 3.6). Recently, Stassun & Torres (2016a,b) used more than 100 eclipsing binaries to investigate possible systematics in recent Gaia DR1 parallaxes (Gaia Collaboration 2016) and concluded that a likely systematic shift of -0.25 mas is presented in Gaia parallaxes. The shift is consistent with the systematic global error of 0.3 mas in the DR1 that was announced by the Gaia team.

The list of eclipsing binary systems reported by Kruszewski & Semeniuk (1999) is the basis for our programme of investigating eclipsing binaries and deriving the SBC relations. The first paper from our program was devoted to the IO Aqr system (Graczyk et al. 2015) and showed that unrecognized triples may bias the derivation of the SBC relations. Although the maximum-light contribution of the third component of IO Aqr is low and relatively well determined, the SBC calibrations would have substantial problems to reach a precision of about 1% for this system. In a following paper (Gallenne et al. 2016) we derived a very precise orbital parallax to TZ For that allowed us to perform a preliminary check of the precision of existing SBC relations. Our parallax measurement to TZ For is in perfect agreement with the photometric distance and the Gaia DR1 parallax. The work on TZ For is a part of our larger effort to determine very precise dynamical parallaxes to a number of long-period eclipsing binaries.

Here we present in detail the method of deriving the SBC relations based on eclipsing binary stars, and for the first time, we publish the precise relations that are based solely on eclipsing binaries. Sect. 2 characterizes a sample of systems and describes the selection criteria and data we used. In Sect. 3 we present the method outline of our analysis. Sect. 4 contains results, and these are discussed in Sect. 5. The last section is devoted to final remarks.

2. THE SAMPLE

For the purpose of our work, we use a volume-limited ($d < 300$ pc) sample of detached eclipsing binaries with published high-quality light curve and radial velocity solutions. The sample is supposed to contain *standard* eclipsing binary systems for the purpose of accurate distance determination/validation and surface brightness calibration. We made an extensive search for suitable systems in the literature using the SIMBAD database (Wenger et al. 2000) and NASA ADS. Useful guidance in this measure is provided by the compilations done by Kruszewski & Semeniuk (1999), Bilir et al. (2008), Torres et al. (2010) and more recently by Eker et al. (2014), Southworth (2015) and Stassun & Torres (2016a). The final sample contains 34 systems and additionally AL Ari, a system for which our new analysis is as-yet unpublished (Konorski et al. 2017). Our intention is that the sample would serve as a reference catalogue for very precise determinations of the photometric distances, the angular diameters and the surface brightness. We put very strict conditions for including an eclipsing binary in our sample. As a part of a selection procedure we did an extensive consistency check of published physical parameters for every candidate system and in some cases recalculated fundamental parameters to make them more concordant with the observables. Table 1 presents the basic information about selected eclipsing binaries. The criteria are described in details below.

2.1. *Proximity effects*

No proximity effects larger than 0.03 mag. Although semi-detached or even contact configuration eclipsing binaries were suggested as good distance indicators (e.g. Wyithe & Wilson 2002; Wilson et al. 2010), our experience shows that their physical parameters are usually much more model dependent and thus less robust than those coming from analysis of detached eclipsing binaries. In fact only well-detached systems offer very simple geometry where both stars can be treated as almost perfect spheres. This simplifies the analysis, as magnitudes and colors of the system are virtually constant outside eclipses.

2.2. *Intrinsic variability*

No intrinsic variability amplitude larger than 0.04 mag. Larger variability (spots, pulsations) over a given threshold may lead to some bias in the estimation of true photometric indices on a level of >2%, so we removed all systems with an active or pulsating component from our sample (e.g. RS CVn stars, chromospheric activity). The only system retained is EF Aqr showing some spot activity on a secondary but only small changes in the combined out-of-eclipse light (Vos et al. 2012).

2.3. *Absolute dimensions*

Precision better than 3%. For the purpose of surface brightness calibration a knowledge of the physical radii is fundamental because combined with a distance it gives the angular diameters. We chose known systems with the most precise absolute dimensions. An average precision of the radii determination in the sample is $\sigma_R/R = 1.2\%$. This sample is useful for utilization of the present Gaia parallaxes. For the future Gaia releases expected to have precision better than 1% for all stars in our sample (de Bruijne et al. 2014) some of the systems will need to be reanalyzed in order to achieve precision better than 2% of radii determination or eventually will have to be removed from the sample i.e. V1229 Tau, FM Leo, FL Lyr, MY Cyg, VZ Cep, V821 Cas.

2.4. *Geometric distance*

Precision better than 10% within 300 pc horizon. We used trigonometric parallaxes from the recent Gaia Data Release 1 (Gaia Collaboration 2016), augmented with Hipparcos parallaxes (van Leeuwen 2007) for some bright and nearby systems. Even so, there are just a few eclipsing binaries in our sample with high precision trigonometric parallaxes (fractional uncertainty $\sigma_\pi/\pi < 2\%$). In the case of one system, TZ For, we utilized the orbital parallax determined by Gallenne et al. (2016) which is by a factor of 5 more precise than the Gaia DR1 parallax.

2.5. *Temperature*

Effective temperatures known to within 5%. We use them to build precise models of the systems and to calculate infrared light ratios. In this work we utilized also temperatures to derive photometric distances (by the flux scaling) as proxies of the true geometric distances. In general temperatures are important for determining auxiliary parameters (e.g. limb darkening) during light curve analysis and thus we preferred systems with well determined radiative properties.

2.6. *Multiplicity*

We excluded systems with confirmed third light in photometry/spectroscopy or known close bright companions affecting photometric indexes. CD Tau has a close K-type companion at a distance of $\sim 10''$. The light of the companion is present in the optical light curves analyzed by Ribas et al. (1999) but it was carefully accounted for in their analysis. The companion is far enough away to not influence the Tycho or 2MASS magnitudes. Also AI Phe has a fainter visual companion ($11''$), the presence of which was accounted for by Kirkby-Kent et al. (2016) in their analysis. The case of AI Phe is actually more complicated as this system has another, even closer, invisible companion inducing acceleration on a main binary system (M. Konacki - priv. com.). At this moment the nature of this companion is uncertain but spectroscopic data suggests an M type dwarf. In that case its luminosity can be completely neglected (even in NIR) and we included this system in our sample. RR Lyn is a proposed triple system with a companion of 0.1 $M_\odot$ (Khaliullin & Khaliullina 2002). Even if the companion will be confirmed with future spectroscopic monitoring at the moment no third light is visible in high quality light curves (e.g. Khaliullin et al. 2001) and we retained this system in our sample.

2.7. *Photometry*

We decided to use homogenous non-saturated optical/infrared photometry from Tycho-2 and the Two Micron All Sky Survey.

2.7.1. *Optical*

We downloaded the optical BV Tycho-2 photometry (Høg et al. 2000) of the eclipsing binaries from Vizier (Ochsenbein et al. 2000)[1]. β Aur, which is by far the brightest star in our sample, is the only star that lacks Tycho photometry. In this case we used Johnson photometry from a compilation by Mermilliod (1991). Tycho photometry was subsequently transformed into the Johnson system using the method outlined by Bessell (2000). For 6 systems Tycho-2 photometry leads to unexplainable shifts in the temperatures and surface brightness parameter derived so and we replaced it by more precise out-of-eclipse optical photometry from the literature.

2.7.2. *Near infrared*

We downloaded NIR JHK_S photometry of the Two Micron All Sky Survey (2MASS) (Skrutskie et al. 2006) from Vizier[2]. Magnitudes were converted onto the Johnson system using equations given in Bessell & Brett (1988) and Carpenter (2001)[3]. The transformation equations are as follow:

$$K_J - K_{2\mathrm{M}} = 0.037 - 0.017(J-K)_{2\mathrm{M}} - 0.007(V-K)_{2\mathrm{M}}$$
$$(J-K)_J = 1.064(J-K)_{2\mathrm{M}} + 0.006$$
$$(H-K)_J = 1.096(H-K)_{2\mathrm{M}} - 0.027$$

2MASS photometry of β Aur is saturated and we used Johnson JK photometry from a compilation by Ducati (2002). A lack of good NIR photometry forced us to remove from the sample the otherwise well suited system ψ Cen.

3. METHOD

3.1. *The Wilson-Devinney model of the systems*

For the purpose of obtaining homogenous parameters for the eclipsing binary sample we decided to create a model of each system. The models were built using the Wilson-Devinney code version 2007 (Wilson & Devinney 1971; Wilson 1979, 1990; van Hamme & Wilson 2007) while parameters of the models were based on solutions published in the literature. None of the eclipsing binaries in our sample has infrared J, H, K light curves suitable for deriving direct light ratios in those bands. Thus, in order to calculate intrinsic infrared colors of the components of each system we employed eclipsing binary models based on optical light curves and we extrapolated them into infrared. Such an approach may introduce some bias which will be discussed later in this paper. All models were checked for internal consistency of the parameters and it turned out that in many cases they had to be fine-tuned. In particular, the temperature ratio and the absolute temperature scale, being crucial for

[1] http://vizier.u-strasbg.fr: I/259/tyc2
[2] http://vizier.u-strasbg.fr: II/281/2mass6x
[3] `http://www.astro.caltech.edu/~jmc/2mass/v3/transformations/`

4

Table 1
Basic data on the selected detached eclipsing binaries

Name	Tycho-2 ID	RA_{2000} h:m:s	DEC_{2000} deg:m:s	V[a] mag	Spectral Type	Ref. SpT	Orbital Period (d)	Ref. OrP	Parallax mas
YZ Cas	4307-2167-1	00:45:39.077	+74:59:17.06	5.653±0.015	A2m+F2V	1	4.4672235	36	10.30±0.49
AI Phe	8032-0625-1	01:09:34.195	−46:15:56.09	8.610±0.019	F8V+K0IV	8	24.592483	40	5.94±0.24
V505 Per	3690-0536-1	02:21:12.964	+54:30:36.28	6.889±0.016	F5V+F5V	2	4.222020	2	15.56±0.32
AL Ari	0645-1107-1	02:42:36.341	+12:44:07.77	9.223±0.034	F5V+G4V	3	3.7474543	3	7.11±0.37
V570 Per	3314-1225-1	03:09:34.944	+48:37:28.69	8.091±0.018	F3V+F5V	4	1.9009382	4	7.85±0.26
TZ For	7026-0633-1	03:14:40.093	−35:33:27.60	6.888±0.016	F7IV+G8III	5	75.66647	37	5.379±0.055[c]
V1229 Tau[d]	1800-1622-1	03:47:29.454	+24:17:18.04	6.807±0.017	A0V+Am	6	2.46113408	38	7.57±0.40
V1094 Tau	1263-0642-1	04:12:03.593	+21:56:50.55	8.981±0.031	G0V+G2V	16	8.9885474	45	8.26±0.25
CD Tau	1291-0292-1	05:17:31.153	+20:07:54.63	6.768±0.016	F6V+F6V	7	3.435137	39	13.56±0.38
EW Ori	0104-1206-1	05:20:09.147	+02:02:39.97	9.902±0.043[e]	F8V+G0V	16,47	6.9368432	47	5.48±0.23
UX Men	9378-0190-1	05:30:03.184	−76:14:55.35	8.251±0.017	F8V+F8V	9, 5	4.181100	41	9.72±0.21
TZ Men	9496-0590-1	05:30:13.886	−84:47:06.37	6.186±0.016	A0V+A8V	10, 5	8.56900	10	8.02±0.49
β Aur	2924-2742-1	05:59:31.723	+44:56:50.76	1.900±0.020[f]	A1mIV+A1mIV	11,57	3.960047	42	40.21±0.23[b]
RR Lyn	3772-2770-1	06:26:25.836	+56:17:06.35	5.558±0.015	A6mIV+F0V	12	9.945074	12	13.34±0.60[b]
WW Aur	2426-0345-1	06:32:27.185	+32:27:17.63	5.832±0.016	A4m+A5m	13	2.5250194	43	11.03±0.50
HD 71636	2489-1972-1	08:29:56.311	+37:04:15.48	7.903±0.018	F2V+F5V	14	5.013292	14	8.40±0.40
VZ Hya	4874-0811-1	08:31:41.413	−06:19:07.56	8.953±0.027[g]	F3V+F5V	21	2.9043002	51	6.94±0.24
KX Cnc	2484-0592-1	08:42:46.211	+31:51:45.37	7.192±0.017	F9V+F9V	15	31.2197874	44	20.54±0.38
PT Vel	7690-2859-1	09:10:57.720	−43:16:02.93	7.027±0.016	A0V+F0	17	1.802008	17	6.15±0.45
KW Hya	4891-1371-1	09:12:26.044	−07:06:35.38	6.100±0.016	A5m+F0V	18	7.750469	46	11.53±0.42[b]
RZ Cha	9422-0104-1	10:42:24.104	−82:02:14.19	8.091±0.018	F5V+F5V	20	2.832084	48	5.68±0.26
FM Leo	0263-0727-1	11:12:45.095	+00:20:52.83	8.460±0.021	F7V+F7V	21	6.728606	49	7.00±0.32
GG Lup	7826-3079-1	15:18:56.376	−40:47:17.60	5.603±0.015	B7V+B9V	23	1.8495927	50	5.96±0.30[b]
V335 Ser	0353-0301-1	15:59:05.756	+00:35:44.55	7.490±0.017	A1V+A3V	19	3.4498837	19	4.74±0.30
WZ Oph	0977-0216-1	17:06:39.042	+07:46:57.78	9.126±0.024	F8V+F8V	24, 25	4.183507	51	6.61±0.24
FL Lyr	3542-1492-1	19:12:04.862	+46:19:26.86	9.366±0.026	F8V+G8V	27	2.1781542	27	7.25±0.22
UZ Dra	4444-1595-1	19:25:55.045	+68:56:07.15	9.601±0.028	F7V+G0V	22	3.261302	52	5.21±0.25
V4089 Sgr	7936-2270-1	19:34:08.486	−40:02:04.70	5.907±0.016	A2IV+A7V	28, 29	4.6270956	29	6.75±0.49
V1143 Cyg	3938-1983-1	19:38:41.184	+54:58:25.65	5.889±0.015	F5V+F5V	30, 31	7.640742	54	24.75±0.35
MY Cyg	2680-1529-1	20:20:03.390	+33:56:35.02	8.341±0.019	F0m+F0m	32	4.0051870	55	3.95±0.24
EI Cep	4599-0082-1	21:28:28.206	+76:24:12.59	7.600±0.017	F3V+F1V	33	8.4393522	33	5.07±0.24
VZ Cep	4470-1334-1	21:50:11.135	+71:26:38.30	9.717±0.009[h]	F3V+G4V	26	1.1833638	26	3.88±0.35
LL Aqr	5236-0883-1	22:34:42.152	−03:35:58.17	9.243±0.037[i]	F8V+G2V	34	20.178321	56	7.75±0.27
EF Aqr	5248-1030-1	23:01:19.088	-06:26:15.35	9.885±0.022[j]	F8V+G8V	15	2.8535721	53	5.06±0.50
V821 Cas	4001-1445-1	23:58:49.175	+53:40:19.81	8.286±0.017	A1V+A4	35	1.7697397	35	3.61±0.30

Note. — **Ref.** to Spectral Type (SpT) and/or Orbital Period (OrP): 1 - Pavlovski et al. (2014); 2 - Tomasella et al. (2008a); 3 - Konorski et al. (2017); 4 - Tomasella et al. (2008b); 5 - Torres et al. (2010); 6 - Abt & Levato (1978); 7 - Popper (1971); 8 - Andersen et al. (1988); 9 - Houk & Cowley (1975); 10 - Andersen et al. (1987a); 11 - Nordström & Johansen (1994b); 12 - Khaliullin et al. (2001); 13 - Kiyokawa & Kitamura (1975); 14 - Henry et al. (2006); 15 - this work; 16 - Nesterov et al. (1995); 17 - Bakiş et al. (2008); 18 - Andersen (1991); 19 - Lacy et al. (2012); 20 - Popper (1966); 21 - Houk & Swift (1999); 22 - Lacy et al. (1989); 23 - Andersen et al. (1993); 24 - Popper (1965); 25 - Batten et al. (1978); 26 - Torres & Lacy (2009); 27 - Popper et al. (1986); 28 - Houk (1978); 29 - Veramendi & González (2015); 30 - Hill et al. (1975); 31 - Andersen et al. (1987b); 32 - Malkov (1993); 33 - Torres et al. (2000); 34 - Griffin (2013); 35 - Çakirli et al. (2009); 36 - Lacy (1981); 37 - Gallenne et al. (2016); 38 - David et al. (2016); 39 - Ribas et al. (1999); 40 - Kirkby-Kent et al. (2016); 41 - Clausen & Grønbech (1976); 42 - Southworth et al. (2007); 43 - Southworth et al. (2005); 44 - Sowell et al. (2012); 45 - Maxted et al. (2015); 46 - Andersen & Vaz (1984); 47 - Clausen et al. (2010); 48 - Jørgensen & Gyldenkerne (1975); 49 - Ratajczak et al. (2010); 50 - Budding et al. (2015); 51 - Clausen et al. (2008a); 52 - Gülmen et al. (1986); 53 - Vos et al. (2012); 54 - Giménez & Margrave (1985); 55 - Tucker et al. (2009); 56 - Southworth (2013); 57 - Lyubimkov et al. (1996)

[a] Tycho-2 V_T magnitudes from Høg et al. (2000) converted onto Johnson V magnitudes using transformation given by Bessell (2000)
[b] Hipparcos parallax (van Leeuwen 2007)
[c] Orbital parallax from Gallenne et al. (2016), Hipparcos value $\varpi = 5.75 \pm 0.51$ mas, Gaia value $\varpi = 5.44 \pm 0.25$ mas
[d] HD 23642, in the Pleiades cluster
[e] Clausen et al. (2010)
[f] Mermilliod (1991)
[g] Clausen et al. (2008a)
[h] Lacy (2002)
[i] Graczyk et al. (2016)
[j] Vos et al. (2012)

precise prediction of infrared light ratios, were inspected carefully.

The procedure was as follows. For each system we collected orbital and photometric parameters from the most recent publications. The input parameters were the radial velocity semi-amplitudes $K_{1,2}$, the orbital period P, three parameters describing the position of the orbit (the orbital inclination i, the eccentricity e and the longitude of periastron ω), the photometric relative radii $r_{1,2}$ and the effective temperatures $T_{1,2}$. Those parameters were transformed into the semi-major axis of the system a, the mass ratio q and into dimensionless Roche potentials $\Omega_{1,2}$ using equations given in Torres et al. (2010) and Wilson (1979), i.e. parameters directly fitted or used within the WD program. We usually fixed the temperature of the primary star T_1 and then, using published light ratios in different photometric bands, we adjusted the temperature of the companion T_2. In some cases however we also re-derived T_1 as it is described later. The rotation parameter $F_{1,2}$ was kept to 1 (synchronous rotation), unless there was a direct spectroscopic determination of F significantly different from unity. The albedo A and the gravity brightening g were set in a standard way for a convective atmosphere cooler than 7200 K and radiative ones for a hotter surface temperature. This was done only for the sake of consistency because the two parameters have negligible effect on the light ratios. The input and derived parameters used to create the appropriate WD models are listed in Table 2.

3.2. *Correction of 2MASS magnitudes taken during eclipses*

KX Cnc, GG Lup and WW Oph have 2MASS observations taken during the secondary eclipses. To account for a light lost during minima we used our models to calculate the appropriate corrections. The corrections are $\Delta J = -0.333$ mag, $\Delta H = -0.331$ mag and $\Delta K = -0.331$ mag for KX Cnc, $\Delta J = -0.277$ mag, $\Delta H = -0.281$ mag and $\Delta K = -0.285$ mag for GG Lup, $\Delta J = -0.392$ mag, $\Delta H = -0.390$ mag and $\Delta K = -0.390$ mag for WZ Oph. For GG Lup we accounted also for the apsidal motion which shifts the position of the eclipses (Wolf & Zejda 2005).

3.3. *Temperature and Reddening*

In some individual cases, described in the Appendix the temperature T_1 or/and color excess E(B−V) were adjusted in order to obtain agreement between intrinsic colors and temperatures. Reddenings to each object were taken from the literature, if available, and also derived independently using the extinction maps by Schlegel et al. (1998) following the prescription given in Suchomska et al. (2015). Dereddened magnitudes and colors were calculated using the mean Galactic interstellar extinction curve from Fitzpatrick & Masana (2007) assuming $R_V = 3.1$. To re-derive temperatures we used a number of calibrations given below:

- $b-y$: Holmberg et al. (2007), Ramírez & Meléndez (2005), Alonso et al. (1996), Napiwotzki et al. (1993).
- $B-V$: Casagrande et al. (2010), González Hernández & Bonifacio (2009), Ramírez & Meléndez (2005), Flower (1996).
- $V-J$: Casagrande et al. (2010), González Hernández & Bonifacio (2009).
- $V-K$: Worthey & Lee (2011), Casagrande et al. (2010), González Hernández & Bonifacio (2009), Masana et al. (2006), Ramírez & Meléndez (2005), Houdashelt et al. (2000), Alonso et al. (1996).

3.4. *Radial velocity semi-amplitudes*

Usually we assumed radial velocity semi-amplitudes from the literature. When two or more orbital solutions were published based on different radial velocity sets and having uncertainties of the same order of magnitude, we used the weighted mean to derive the final parameters, i.e. AI Phe, EW Ori, UX Men, β Aur, GG Lup, UZ Dra, and V1143 Cyg. However, in few cases we redetermined the spectroscopic orbits from source data in order to derive directly $K_{1,2}$ or to check the consistency of the orbital parameters and their errors. The spectroscopic orbits were derived with the Wilson-Devinney code taking into account the full model of a system and all proximity effects. A set of numerical constants used to change from SI units into astrophysical units were chosen after Torres et al. (2010). Individual cases are described in the Appendix.

3.5. *Distances*

3.5.1. *Geometric distances*

The source of parallaxes is almost exclusively the recent release of Gaia parallaxes DR1 (Gaia Collaboration 2016) and in a few cases of close and bright systems where those parallaxes are unavailable we use parallaxes from the latest reduction of the Hipparcos data (van Leeuwen 2007). Distances are calculated through simple inversion of trigonometric parallaxes. It is known that this procedure for larger parallax errors ($\gtrsim 4\%$) is not unequivocal and must include some prior on expected space distribution of an object (e.g. Sandage & Saha 2002; Bailer-Jones 2015). Existence of this prior is necessary to recover a true distribution (distances) from an observed distribution (parallaxes) in the presence of observational errors. In terms of absolute luminosity bias it leads to the so called Lutz-Kelker correction (Lutz & Kelker 1973). However errors given by the Gaia DR1 are preliminary and likely overestimated (e.g. Casertano et al. 2016) and using them for parallax corrections would introduce unknown amounts of systematics. For the purpose of this paper we decided to not apply Lutz-Kelker corrections to the distances, especially as any such correction would be smaller than quoted errors. The resulting distances are summarized in Tab. 3.

3.5.2. *Photometric distances*

We employed the so-called standard method utilizing V-band bolometric corrections to derive photometric distances, known also as the bolometric flux scaling. We calculated distance d to the i-th component of the system using equation:

$$d_i(\mathrm{pc}) = 3.360 \cdot 10^{-8} R_i T_i^2 10^{0.2(BC_i+V_i)}, \qquad (1)$$

where index $i = \{1, 2\}$, R is the radius of a component in solar radii, T is its effective temperature in K, BC is a bolometric correction interpolated from the Flower

Table 2
Parameters of the Wilson-Devinney models

Eclipsing binary	RV semiamplitude K_1(km s^{-1})	RV semiamplitude K_2(km s^{-1})	Orientation of the orbit e	Orientation of the orbit ω (rad)	Orientation of the orbit i (deg)	Fractional radius r_1	Fractional radius r_2	Effective temperature T_1(K)	Effective temperature T_2(K)	Reference	Model parameters Semimajor axis($R_\odot$)	Model parameters Mass ratio	Model parameters Ω_1	Model parameters Ω_2
YZ Cas	73.05(19)	124.78(27)	0.0	0.0	88.33(7)	0.14456(56)	0.07622(33)	9520(120)	6880(240)	2	17.4764	0.5854	7.5141	8.8912
AI Phe[d]	51.128(28)	49.120(19)	0.187(3)	1.933(6)	88.55(5)	0.03845(35)	0.06070(27)	6175(150)	5140(120)	3,4,5,1	47.8850	1.0409	27.290	18.361
V505 Per	89.01(8)	90.28(9)	0.0	0.0	87.95(4)	0.0860(9)	0.0846(9)	6512(21)	6460(30)	6	14.9724	0.9859	12.618	12.665
AL Ari	76.98(13)	98.38(21)	0.051(3)	1.20(2)	89.48(6)	0.1060(4)	0.0696(3)	6300(80)	5412(80)	7	12.9738	0.7825	10.269	12.411
V570 Per[a]	114.09(27)	122.48(28)	0.0	0.0	77.4(3)	0.1675(31)	0.1526(19)	6842(30)	6562(30)	8,1	9.10738	0.9315	6.9200	7.1538
TZ For[b]	40.868(11)	38.900(22)	0.0	0.0	85.66(4)	0.03320(70)	0.06972(92)	6350(70)	4930(30)	9,10	119.650	1.0506	31.416	16.046
V1229 Tau	99.02(27)	140.86(36)	0.0	0.0	78.2(1)	0.1450(23)	0.1262(37)	9950(300)	7640(300)	11,12	11.9214	0.7030	7.6115	6.7280
V1094 Tau[c]	65.38(7)	70.83(12)	0.2677(4)	5.822(3)	88.21(1)	0.06050(24)	0.04744(29)	5850(100)	5720(100)	13,1	23.3292	0.9231	17.792	20.863
CD Tau	96.8(5)	102.1(5)	0.0	0.0	87.7(3)	0.1330(10)	0.1172(13)	6200(50)	6194(50)	14	13.5172	0.9481	8.4785	9.1246
EW Ori[c]	72.48(21)	75.45(25)	0.076(2)	5.40(2)	89.86(9)	0.05786(18)	0.05434(18)	6070(95)	5875(95)	15,16,17,1	20.2258	0.9607	18.325	18.783
UX Men[c]	87.36(17)	90.08(14)	0.003(3)	1.3(6)	89.6(1)	0.0918(9)	0.0868(9)	6200(100)	6127(100)	18,3,1	14.6652	0.9682	11.871	12.196
TZ Men	62.15(12)	102.82(45)	0.035(7)	4.75(2)	88.7(1)	0.0722(7)	0.0513(5)	10400(500)	7240(300)	19	27.9328	0.6045	14.480	13.018
β Aur[c]	108.04(10)	110.93(10)	0.0018(4)	1.579(5)	76.8(1)	0.15694(81)	0.14595(82)	9350(200)	9297(200)	20,21,22,23,1	17.6051	0.9739	7.3643	7.7040
RR Lyn	65.65(6)	83.92(17)	0.079(1)	3.14(1)	87.5(1)	0.0878(5)	0.0541(11)	7570(120)	6980(100)	24,25	29.340	0.7823	12.244	15.657
WW Aur[d]	116.81(23)	126.49(28)	0.0	0.0	87.55(4)	0.1586(9)	0.1515(9)	8180(260)	7872(250)	26,1	12.1546	0.9235	7.2450	7.1487
HD 71636[a]	80.30(18)	94.45(19)	0.0	0.0	85.63(2)	0.0904(5)	0.0784(5)	6950(140)	6440(140)	27,1	17.3682	0.8502	11.917	11.923
VZ Hya	94.92(19)	105.31(34)	0.0	0.0	88.88(9)	0.1143(4)	0.0968(6)	6645(150)	6300(150)	28	11.4972	0.9013	9.6587	10.367
KX Cnc[a,d]	50.039(65)	50.503(65)	0.4667(1)	1.113(1)	89.83(1)	0.01940(4)	0.01913(5)	6050(110)	5995(110)	29,1	54.8787	0.9908	53.405	53.674
PT Vel	117.2(2)	158.5(5)	0.127(6)	5.06(1)	88.2(5)	0.215(2)	0.160(2)	9250(150)	7650(155)	30	9.7457	0.7394	5.5259	5.9125
KW Hya[c]	70.12(21)	93.17(79)	0.0945(1)	3.929(2)	87.65(4)	0.0853(5)	0.0594(8)	8000(200)	6960(210)	31,1	24.9247	0.7526	12.559	13.908
RZ Cha[d]	108.2(6)	107.6(9)	0.0	0.0	82.89(7)	0.1777(20)	0.1893(40)	6580(150)	6530(150)	32,33,1	12.1746	1.0056	6.6545	6.3340
FM Leo	76.62(27)	78.46(28)	0.0	0.0	87.98(6)	0.0798(21)	0.0732(24)	6316(240)	6190(210)	34	20.6392	0.9765	13.505	14.354
GG Lup[c]	125.1(5)	203.4(8)	0.154(5)	2.351(3)	86.8(1)	0.2003(18)	0.1456(14)	14750(450)	11200(500)	35,36,1	11.8871	0.6150	5.7696	5.6076
V335 Ser	106.57(12)	120.07(38)	0.141(2)	1.139(7)	87.2(2)	0.1325(17)	0.1131(22)	9020(150)	8500(150)	37	15.3191	0.8876	8.5918	9.0764
WZ Oph[d]	88.77(19)	89.26(24)	0.0	0.0	89.1(1)	0.0952(8)	0.0964(8)	6232(100)	6212(100)	28,1	14.7240	0.9945	11.505	11.326
FL Lyr[c]	93.5(5)	118.9(7)	0.0	0.0	86.3(4)	0.140(3)	0.105(3)	6150(120)	5270(110)	15,1	9.1640	0.7864	7.9411	8.6028
UZ Dra[d]	93.52(35)	101.55(43)	0.0	0.0	89.1(2)	0.103(2)	0.091(2)	6450(120)	6170(120)	38,39,1	12.5768	0.9209	10.637	11.165
V4089 Sgr[a]	78.48(18)	126.20(24)	0.0	0.0	83.48(6)	0.2104(9)	0.0852(3)	8433(100)	7361(105)	40,1	18.8426	0.6219	5.3991	8.4925
V1143 Cyg	88.02(5)	89.97(10)	0.5378(3)	0.860(1)	87.0(1)	0.059(1)	0.058(1)	6450(100)	6400(100)	41,42	22.6950	0.9783	19.069	19.045
MY Cyg	101.9(8)	103.3(6)	0.010(1)	1.21(4)	88.58(2)	0.138(3)	0.134(3)	7050(200)	7000(200)	43,44,45	16.2482	0.9867	8.2580	8.3912
EI Cep[c]	76.84(13)	81.02(13)	0.0	0.0	87.23(9)	0.1099(20)	0.0884(18)	6750(120)	6977(120)	46,1	26.3649	0.9484	10.056	11.760
VZ Cep[c]	118.88(22)	150.48(67)	0.0	0.0	79.97(5)	0.2398(17)	0.1630(61)	6690(160)	5705(120)	47,1	6.3985	0.7900	4.9955	5.9680
LL Aqr	49.948(13)	57.736(14)	0.3165(1)	2.714(1)	89.55(3)	0.03246(5)	0.02459(8)	6080(50)	5705(60)	48,49	40.7438	0.8651	32.074	36.708
EF Aqr[a]	84.175(66)	110.66(24)	0.0	0.0	88.45(8)	0.1222(9)	0.0876(7)	6150(65)	5185(110)	50,1	10.9940	0.7607	8.9529	9.8076
V821 Cas[a]	120.8(1.7)	152.4(2.0)	0.127(7)	2.71(7)	82.6(1)	0.2434(13)	0.1466(17)	9400(400)	8600(400)	51,1	9.5600	0.7927	5.0538	6.6690

Note. — Reference: 1 - this paper; 2 - Pavlovski et al. (2014); 3 - Hełminiak et al. (2009); 4 - Andersen et al. (1988); 5 - Kirkby-Kent et al. (2016); 6 - Tomasella et al. (2008a); 7 - Konorski et al. (2017); 8 - Tomasella et al. (2008b); 9 - Andersen et al. (1991); 10 - Gallenne et al. (2016); 11 - David et al. (2016); 12 - Groenewegen et al. (2007); 13 - Maxted et al. (2015); 14 - Ribas et al. (1999); 15 - Popper et al. (1986); 16 - Imbert (2002); 17 - Clausen et al. (2010); 18 - Andersen et al. (1989); 19 - Andersen et al. (1987a); 20 - Smith (1948); 21 - Behr et al. (2011); 22 - Nordström & Johansen (1994b); 23 - Southworth et al. (2007); 24 - Tomkin & Fekel (2006); 25 - Khaliullin et al. (2001); 26 - Southworth et al. (2005); 27 - Henry et al. (2006); 28 - Clausen et al. (2008b); 29 - Sowell et al. (2012); 30 - Bakış et al. (2008); 31 - Andersen & Vaz (1984); 32 - Andersen et al. (1975); 33 - Giuricin et al. (1980); 34 - Ratajczak et al. (2010); 35 - Andersen et al. (1993); 36 - Budding et al. (2015); 37 - Lacy et al. (2012); 38 - Imbert (1986); 39 - Lacy et al. (1989); 40 - Veramendi & González (2015); 41 - Albrecht et al. (2007); 42 - Andersen et al. (1987b); 43 - Popper (1971); 44 - Tucker et al. (2009); 45 - Torres et al. (2010); 46 - Torres et al. (2000); 47 - Torres & Lacy (2009); 48 - Southworth (2013); 49 - Graczyk et al. (2016); 50 - Vos et al. (2012); 51 - Çakirli et al. (2009)

[a] We recalculated radial velocity semiamplitudes - see Section 3.4.
[b] We set rotation parameter $F_1 = 18.0$
[c] We adjusted temperature T_2.
[d] We recalculated both temperatures - see Section 3.3

Table 3
Photometric and physical parameters used to derive individual angular diameters and colors.

Eclipsing binary	$E(B-V)$ mag	Ref.	Radius ($R_\odot$) R_1	R_2	Distance (pc) Geom.	Photom.[c]	σ	Unreddened Johnson photometry[a] (mag) B_0	V_0	J_0	H_0	K_0	Light ratio L_2/L_1[b] B	V	J	H	K
YZ Cas	0.015(10)	1	2.526(11)	1.332(6)	97.1(4.6)	99.2(4.0)	0.35	5.657(48)	5.607(34)	5.616(21)	5.652(42)	5.635(22)	0.0610	0.0882	0.1682	0.2004	0.2046
AI Phe	0.012(10)	2,1	1.841(17)	2.907(13)	168.4(6.8)	167.9(6.7)	0.15	9.212(52)	8.573(36)	7.345(25)	6.930(38)	6.832(27)	0.7382	1.0057	1.6394	1.9685	1.9828
V505 Per	0.003(5)	1	1.288(14)	1.267(14)	64.3(1.3)	60.7(9)	2.23	7.287(34)	6.880(22)	6.117(70)	5.791(40)	5.794(21)	0.9244	0.9348	0.9522	0.9584	0.9588
AL Ari	0.012(10)	3	1.375(6)	0.903(4)	140.6(7.3)	137.0(4.0)	0.45	9.696(69)	9.186(46)	8.235(23)	7.933(23)	7.905(27)	0.1646	0.2100	0.3087	0.3571	0.3597
V570 Per	0.070(30)	1	1.525(30)	1.390(19)	127.4(4.2)	118.6(5.4)	1.29	8.270(126)	7.875(94)	7.156(35)	6.921(23)	6.888(22)	0.6567	0.6950	0.7645	0.7916	0.7926
TZ For	0.015(5)	4	3.972(84)	8.34(11)	185.9(1.9)	185.2(3.8)	0.17	7.569(34)	6.842(22)	5.530(21)	5.124(26)	5.007(30)	0.7888	1.2341	2.4644	3.1856	3.2193
V1229 Tau	0.020(10)	5,6	1.729(27)	1.505(45)	132.1(7.0)	133.1(7.5)	0.10	6.784(50)	6.745(35)	6.663(25)	6.644(29)	6.637(25)	0.2628	0.3385	0.5223	0.5800	0.5917
V1094 Tau	0.026(10)	7	1.411(6)	1.107(7)	121.1(3.7)	118.0(3.8)	0.58	9.575(66)	8.901(44)	7.814(23)	7.520(46)	7.437(22)	0.5318	0.5524	0.5851	0.5980	0.5986
CD Tau	0.005(5)	8,1	1.798(17)	1.584(20)	73.7(2.1)	68.6(1.2)	2.22	7.231(34)	6.753(22)	5.894(22)	5.671(34)	5.612(30)	0.7702	0.7724	0.7749	0.7764	0.7760
EW Ori	0.026(14)	9	1.170(5)	1.099(5)	182.5(7.7)	173.8(6.3)	0.88	10.407(94)	9.822(61)	8.837(26)	8.598(69)	8.513(22)	0.7209	0.7595	0.8223	0.8474	0.8486
UX Men	0.027(10)	10	1.346(13)	1.273(13)	102.9(2.2)	100.6(2.9)	0.62	8.692(50)	8.168(35)	7.222(29)	6.966(30)	6.931(25)	0.8318	0.8476	0.8721	0.8818	0.8822
TZ Men	0.000(5)	11	2.017(20)	1.433(15)	124.7(7.6)	117.7(8.2)	0.63	6.166(34)	6.186(22)	6.180(31)	6.128(44)	6.153(27)	0.1150	0.1623	0.3002	0.3508	0.3607
beta Aur	0.000(3)	1	2.763(15)	2.569(15)	24.9(1)	25.0(9)	0.26	1.930(34)	1.900(22)	1.869(42)	—	1.859(41)	0.8462	0.8524	0.8585	0.8597	0.8603
RR Lyn	0.007(5)	1	2.576(20)	1.587(30)	75.0(3.4)	72.6(2.0)	0.50	5.764(33)	5.536(22)	—	5.073(23)	5.021(17)	0.2343	0.2645	0.3298	0.3534	0.3541
WW Aur	0.008(5)	1	1.928(11)	1.841(11)	90.7(4.1)	85.8(4.0)	1.02	5.976(34)	5.807(22)	5.533(22)	5.505(29)	5.513(22)	0.7600	0.7953	0.8607	0.8753	0.8789
HD71636	0.020(10)	12	1.570(9)	1.362(7)	119.0(5.7)	118.6(4.1)	0.07	8.223(51)	7.841(36)	7.104(22)	6.917(24)	6.907(35)	0.4910	0.5442	0.6474	0.6886	0.6911
VZ Hya	0.027(20)	13	1.314(5)	1.113(7)	144.1(5.0)	146.0(7.3)	0.23	9.307(93)	8.870(67)	8.105(29)	7.844(28)	7.801(18)	0.5254	0.5683	0.6439	0.6747	0.6766
KX Cnc	0.001(5)	1	1.065(2)	1.050(3)	48.7(9)	49.0(1.4)	0.19	7.766(35)	7.189(23)	6.223(32)	5.949(30)	5.905(31)	0.9196	0.9330	0.9537	0.9616	0.9621
PT Vel	0.005(5)	14	2.095(20)	1.559(20)	163(12)	164.8(4.9)	0.19	7.062(34)	7.012(22)	6.902(32)	6.861(32)	6.871(30)	0.2395	0.2949	0.4199	0.4580	0.4641
KW Hya	0.006(6)	1	2.126(15)	1.480(22)	86.7(3.2)	86.5(3.6)	0.05	6.308(37)	6.081(24)	5.694(24)	5.642(44)	5.574(22)	0.2249	0.2699	0.3816	0.4221	0.4255
RZ Cha	0.038(20)	1	2.163(20)	2.305(20)	176.1(8.1)	179.4(8.0)	0.37	8.384(87)	7.974(64)	7.148(35)	6.926(40)	6.919(39)	1.0879	1.0988	1.1177	1.1241	1.1250
FM Leo	0.019(10)	1	1.648(43)	1.511(49)	142.9(6.5)	139.6(8.8)	0.27	8.884(53)	8.401(37)	7.554(23)	7.324(56)	7.229(24)	0.7441	0.7681	0.8062	0.8216	0.8222
GG Lup	0.027(10)	15	2.381(22)	1.732(17)	167.8(8.4)	147.3(9.5)	1.61	5.386(48)	5.520(34)	5.861(32)	5.980(38)	5.961(31)	0.3026	0.3236	0.3774	0.3875	0.3964
V335 Ser	0.068(8)	16	2.030(26)	1.733(34)	211(13)	195.2(6.0)	1.15	7.352(43)	7.280(30)	7.127(23)	7.105(36)	7.080(22)	0.5730	0.6109	0.6720	0.6870	0.6901
WZ Oph	0.030(16)	1	1.402(12)	1.420(12)	151.3(5.5)	164.9(5.7)	1.72	9.543(76)	9.033(55)	8.208(34)	7.972(37)	7.894(31)	1.0068	1.0115	1.0188	1.0214	1.0217
FL Lyr	0.010(7)	1	1.283(30)	0.962(30)	137.9(4.2)	131.9(5.2)	0.83	9.875(52)	9.335(34)	8.285(28)	7.983(36)	7.917(21)	0.2065	0.2646	0.3969	0.4623	0.4661
UZ Dra	0.012(7)	17	1.295(25)	1.144(25)	191.9(9.2)	189.7(6.6)	0.20	10.036(54)	9.564(35)	8.653(22)	8.423(22)	8.393(20)	0.5991	0.6411	0.7124	0.7419	0.7431
V4089 Sgr	0.027(15)	1	3.964(20)	1.605(7)	148(11)	145.5(4.3)	0.19	5.889(67)	5.824(49)	5.710(25)	5.627(40)	5.623(25)	0.0776	0.0953	0.1327	0.1452	0.1466
V1143 Cyg	0.000(5)	18,1	1.339(23)	1.316(23)	40.4(6)	39.2(1.1)	1.02	6.347(34)	5.889(22)	5.024(21)	4.845(22)	4.798(21)	0.9233	0.9339	0.9512	0.9577	0.9581
MY Cyg	0.048(30)	19	2.242(50)	2.178(50)	253(15)	229(14)	1.17	8.520(126)	8.193(94)	7.702(51)	7.563(46)	7.538(26)	0.9075	0.9158	0.9312	0.9360	0.9363
EI Cep	0.007(5)	20	2.898(48)	2.331(44)	197.2(9.3)	194.0(5.8)	0.30	7.956(35)	7.578(23)	6.879(21)	6.738(37)	6.696(18)	0.7702	0.7405	0.6891	0.6742	0.6723
VZ Cep	0.044(10)	21	1.534(12)	1.043(39)	258(23)	211.1(8.5)	2.07	10.025(46)	9.581(32)	8.796(23)	8.621(33)	8.606(22)	0.1764	0.2256	0.3308	0.3830	0.3851
LL Aqr	0.018(14)	22	1.323(6)	1.002(5)	129.0(4.5)	132.4(3.6)	0.57	9.748(86)	9.187(57)	8.180(26)	7.864(37)	7.836(24)	0.3848	0.4268	0.4998	0.5306	0.5320
EF Aqr	0.025(15)	23	1.343(10)	0.963(8)	198(20)	169.4(6.0)	1.57	10.385(77)	9.808(51)	8.849(27)	8.511(29)	8.496(24)	0.1678	0.2207	0.3480	0.4141	0.4174
V821 Cas	0.060(30)	1	2.327(29)	1.401(33)	277(23)	306(24)	0.91	8.158(125)	8.101(94)	7.976(29)	7.994(32)	7.975(29)	0.2554	0.2829	0.3231	0.3333	0.3354

Note. — References to reddening: 1 - this work; 2 - Hrivnak & Milone (1984); 3 - Konorski et al. (2017); 4 - Gallenne et al. (2016); 5 - Munari et al. (2004); 6 - Groenewegen et al. (2007); 7 - Maxted et al. (2015); 8 - Ribas et al. (1999); 9 - Clausen et al. (2010); 10 - Andersen et al. (1989); 11 - Andersen et al. (1987a); 12 - Henry et al. (2006), 13 - Clausen et al. (2008b); 14 - Bakiş et al. (2008); 15 - Andersen et al. (1993); 16 - Lacy et al. (2012); 17 - Ammons et al. (2006); 18 - Andersen et al. (1987b); 19 - Popper & Etzel (1981); 20 - Torres et al. (2000); 21 - Torres & Lacy (2009); 22 - Graczyk et al. (2016); 23 - Vos et al. (2012)

[a] Combined, extinction-corrected, out-of-eclipse magnitudes of both components expressed in Johnson photometric system.
[b] Calculated using the WD model.
[c] Photometric distances derived from bolometric flux scaling.

(1996) tables for a given temperature and V is the intrinsic magnitude of a component (corrected for extinction). The distance to a particular system was calculated as the unweighted average distance of the two components. The purposes of introducing photometric distances is to check for consistency of the eclipsing binary model parameters and validation of the Gaia parallaxes used in the analysis. The photometric distances are given in Tab. 3.

3.6. *Angular diameters*

In order to derive surface brightness – color relations we need to calculate individual angular diameters of the stars. Angular diameters are calculated with the formula:

$$\phi(\mathrm{mas}) = 9.3004 \cdot R(\mathrm{R}_\odot)/d(\mathrm{pc}), \qquad (2)$$

where d is a distance, R the radius of the star and the conversion factor is equal to $2000R_\odot/1\mathrm{AU}$ assuming a solar radius $R_\odot = 695660$ km (Habbereiter et al. 2008) and a length of the astronomical unit 1AU = 149597871 km (Pitjeva & Standich 2009).

We emphasize that angular diameter calculated from the photometric distance is a function of *radiative* properties of a star (mainly its effective temperature) and not its *geometric* properties. Indeed, if we combine equations 1 and 2 we derive angular diameter which is only a function of the effective temperature, the V-band bolometric correction (also temperature dependent) and extinction corrected V-band magnitude. Because of this we do not utilize the photometric distances to calculate angular diameters in the present work.

3.7. *Intrinsic magnitudes*

In Table 3 we summarize all parameters used to derive the intrinsic photometric indexes of components. The mean galactic extinction curve with $R_V = 3.1$ (Fitzpatrick & Masana 2007) was used to correct the observed magnitudes for reddening. Next, with the help of our WD models, we calculated light ratios in the Johnson $BVJHK$ bands and use them to derive intrinsic magnitudes and colors of each component. The WD code uses an atmospheric approximation with intensities based on ATLAS9 (Kurucz 1993) model stellar atmospheres which are integrated over a given passband to give emerging flux being expressed as fraction of flux emerging from the black body of the same temperature. For all the systems in our sample B and V light ratios are tuned to published light ratios based on literature light curve solutions. However in order to calculate the light ratios in the infrared JHK bands we need to extrapolate the models as none of the systems has infrared light curves published or analyzed. This is why the temperature ratio needs to be well established in order to minimize systematics due to the extrapolation. Provided the temperature ratio and absolute temperatures are well known such a procedure does not introduce significant bias because the relative fluxes from the atmospheric models are much better constrained than the absolute fluxes. We add also that errors given on unreddened magnitudes in Table 3 do not account for possible systematic shifts on a level of 1% due to transformation of Tycho-2 and 2MASS magnitudes onto the Johnson photometric system.

3.8. *Surface brightness*

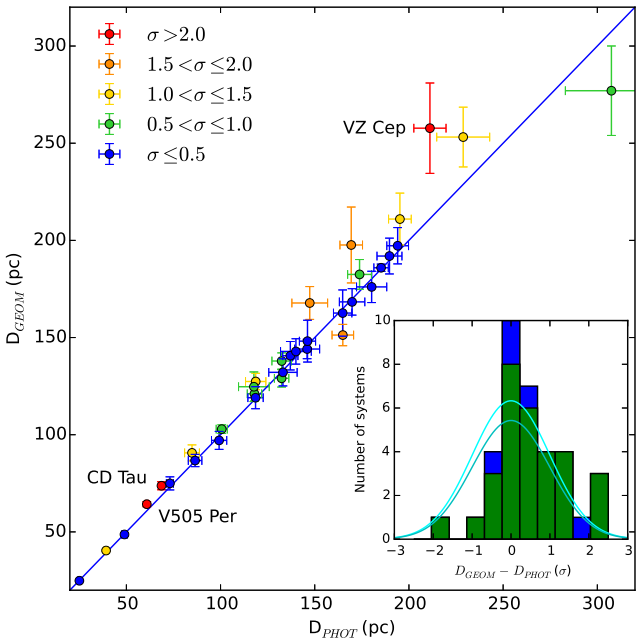


Figure 1. Comparison of geometric and photometric distances for all systems with deviation from a 1:1 relation expressed as fraction of σ and coded with color. Three named systems exhibit offsets larger than 2σ. Systems with $\sigma \leq 0.5$ define the best-fit subsample. *Inset*: the expected distribution of deviations from a 1:1 relation for all systems (upper line) and systems with the Gaia parallaxes (lower line) when random errors dominate. The histogram shows the actual distribution of deviations for the Gaia subsample (green) and the entire sample (green+blue).

We follow Hindsley & Bell (1989) to define the surface brightness parameter S:

$$S_i = m_{i,0} + 5\log\phi, \qquad (3)$$

where i denotes a particular band (B or V) and $m_{i,0}$ is the intrinsic magnitude in a given band. The surface brightness parameter S was then used to obtain the SBC relations by fitting it with first and fifth degree polynomials in a form:

$$S = \sum_{i=0}^{i=1,5} a_i X^i \qquad (4)$$

where X is a given photometric color (see Sect. 4.3 for more details). Use of a higher order polynomial is justified by a strong non-linearity of the SBC relations for the blue-most colors (stellar spectral types earlier than A0).

4. RESULTS

4.1. *Distances*

Stassun & Torres (2016a,b) presented comprehensive comparisons of geometric distances from the Hipparcos and Gaia satellites with photometric distances derived from eclipsing binaries. We underline that we use here a different method to derive photometric distances, and our sample is significantly smaller but on other hand more carefully selected. Figure 1 shows the comparison of geometric and photometric distances, where difference between both distances is expressed in term of the standard deviation of distances σ. Inspection of the

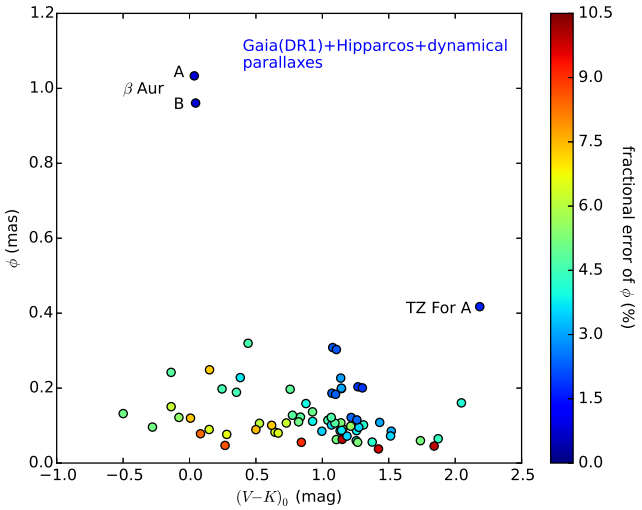


Figure 2. Geometric angular diameters of the eclipsing binary components and their uncertainties calculated from the most recent stellar radii and parallaxes. Three stars that are resolvable by interferometry are named.

figure confirms that detached eclipsing binary stars serve as almost perfect distance indicators, and the photometric distance is a very good proxy of true geometric distance, as long as issues with reddening and temperature are properly handled (e.g. see Section 4 in Torres et al. 2010). Both distances and their σ difference are given in Tab. 3.

The largest deviations from the 1:1 relation between geometric and photometric distance are for V505 Per (2.2σ), CD Tau (2.2σ) and VZ Cep(2.1σ). For the complete sample the reduced $\chi^2 = 0.99$ (34 degrees of freedom) i.e. it is fully consistent with statistical uncertainties dominating the error budget in the distance determination. However if we exclude the three most deviating systems the reduced $\chi^2 = 0.87$ (31 degrees of freedom) suggest that for the majority of systems the errors on the distance determinations are slightly overestimated. We note that the two strongly deviating systems (CD Tau and VZ Cep) also stand out in comparison of photometric and Hipparcos parallaxes (Stassun & Torres 2016a). A possible explanation is wrongly estimated temperatures or/and interstellar extinctions in case of those two systems or the presence of some additional systematics in trigonometric parallaxes. However more work is needed to figure out the source of the discrepancy.

The inset in Figure 1 shows histogram of deviations in terms of the σ from a sub-sample with Gaia parallaxes (30 systems, green) and from the rest of the sample (green+blue). Superimposed are the expected distributions of deviations when errors are uncorrelated and dominated by random uncertainties. We see a clear excess of systems with small deviations signifying that errors on distances are inflated both for the sample and the Gaia sub-sample. This is in agreement with the conclusion by Casertano et al. (2016). We see also that Gaia distances are on average larger than photometric distances, thus corroborating findings by Stassun & Torres (2016b).

4.2. *Angular diameters*

The distances were utilized to calculate geometric angular diameters for all the sample – see Tab. 4. Those angular diameters are direct limb darkened angular diameters and they are complimentary to angular diameters derived from interferometry (e.g. compilations by Boyajian et al. 2014; Challouf et al. 2014). They have an average precision of 4.7% limited by the precision of parallax determinations. The precision is better than 2% for 11 components. Figure 2 shows the derived angular diameters with uncertainties. One can note the clear dependency of uncertainty on angular size and color $(V-K)_0$, with bluer (hotter) stars having angular diameters more poorly determined. From all the sample only one star, the cooler component of TZ For, had its angular diameter measured directly with interferometry (Gallenne et al. 2016), however with much lower precision, and two components of β Aur were barely resolvable (Hummel et al. 1995).

4.3. *SBC relations*

Figure 3 shows the relation between the V-band surface brightness S_V and color $(V-K)_0$ against some interferometric SBC relations (Challouf et al. 2014; Boyajian et al. 2014; di Benedetto 2005; Kervella et al. 2004). Left and right panels correspond to S_V derived from the complete sample and the best-fit subsample, respectively. The best-fit systems were defined as those having their geometrical and photometric distances in agreement to better than 0.5σ – see Tab. 3 and Fig. 1. The V-band surface brightnesses derived from trigonometric parallaxes fits well on the Challouf et al. (2014) calibration with a spread of ∼0.1 mag corresponding to 5% uncertainty in angular diameter, dominated by distance errors. The agreement with the interferometric relation is satisfactory, i.e. both methods of measuring angular diameters, direct from interferometry and semi-direct from eclipsing binary stars, show good consistency. The agreement is even better if we use the best-fit subsample.

In order to quantify the SBC relation we derived it directly. We fitted Eq. 4 to the S_V (see Sect. 3.8) using Orthogonal Distance Regression (Boggs & Rogers 1989) which accounts for the errors on the independent variable, in our case: color $(V-K)_0$. We fitted a fifth-order polynomial to all the data and a first order polynomial to the data from the best-fit systems. The results of the fitting are presented in Figure 4 and coefficients of the derived relations are given in Tab. 5. The precision of the SBC relation based on all systems is rather low (∼ 5%) with the distance errors fully dominating the error budget. However, the use of systems having the best consistency of their geometric and photometric distances results in a remarkable improvement of the precision of the derived SBC relation by a factor of 2. The internal precision of the linear relation in predicting angular diameters of A-, F- and G-type stars is in fact comparable to or even better than published interferometric relations up-to-now, e.g.: Boyajian et al. (2014) – 4.6%, Challouf et al. (2014) – 3.7%, Kervella et al. (2004) – 2.8%[4] and di Benedetto (2005) – 2.1%. The linear SBC relation we derived is almost indistinguishable from the

[4] The precision of S_V-$(V-K)$ calibration by Kervella et al. (2004) is reported to be 1%. We recalculated the unweighted

10

Table 4
Metallicities from literature and derived quantities: masses, gravities and geometric angular diameters of all eclipsing binary components.

ID	[Fe/H]	Ref	Mass		Gravity		Angular Diameter	
			$M_1 \pm \sigma$ $M_\odot$	$M_2 \pm \sigma$ $M_\odot$	$\log g_1 \pm \sigma$ dex	$\log g_2 \pm \sigma$ dex	$\theta_1 \pm \sigma$ mas	$\theta_2 \pm \sigma$ mas
YZ Cas	0.10	1	2.263 ± 0.012	1.325 ± 0.007	3.988 ± 0.004	4.311 ± 0.005	0.242 ± 0.012	0.128 ± 0.006
AI Phe	-0.14	2	1.193 ± 0.004	1.242 ± 0.004	3.985 ± 0.008	3.605 ± 0.004	0.102 ± 0.004	0.161 ± 0.007
V505 Per	-0.12	3	1.272 ± 0.003	1.254 ± 0.003	4.323 ± 0.009	4.331 ± 0.010	0.186 ± 0.004	0.183 ± 0.004
AL Ari	-0.00	4	1.170 ± 0.006	0.916 ± 0.004	4.230 ± 0.004	4.489 ± 0.004	0.091 ± 0.005	0.060 ± 0.003
V570 Per	0.02	5	1.452 ± 0.009	1.352 ± 0.009	4.234 ± 0.017	4.283 ± 0.012	0.111 ± 0.004	0.101 ± 0.004
TZ For	0.02	6	1.957 ± 0.002	2.056 ± 0.002	3.532 ± 0.018	2.909 ± 0.011	0.199 ± 0.005	0.417 ± 0.007
V1229 Tau	0.06	7	2.203 ± 0.013	1.549 ± 0.010	4.306 ± 0.014	4.273 ± 0.026	0.122 ± 0.007	0.106 ± 0.006
V1094 Tau	-0.09	8	1.096 ± 0.004	1.012 ± 0.003	4.179 ± 0.004	4.355 ± 0.006	0.108 ± 0.003	0.085 ± 0.003
CD Tau	0.08	9	1.441 ± 0.016	1.367 ± 0.016	4.087 ± 0.010	4.174 ± 0.012	0.227 ± 0.007	0.200 ± 0.006
EW Ori	0.05	10	1.177 ± 0.009	1.130 ± 0.008	4.373 ± 0.005	4.409 ± 0.005	0.060 ± 0.003	0.056 ± 0.002
UX Men	0.04	11	1.229 ± 0.006	1.192 ± 0.007	4.270 ± 0.009	4.305 ± 0.009	0.122 ± 0.003	0.115 ± 0.003
TZ Men	–		2.482 ± 0.025	1.500 ± 0.010	4.224 ± 0.010	4.302 ± 0.010	0.150 ± 0.009	0.107 ± 0.007
beta Aur	0.15	12	2.365 ± 0.006	2.303 ± 0.006	3.929 ± 0.005	3.981 ± 0.005	1.033 ± 0.008	0.961 ± 0.008
RR Lyn	-0.24	13	1.922 ± 0.026	1.504 ± 0.041	3.900 ± 0.009	4.214 ± 0.020	0.320 ± 0.015	0.197 ± 0.010
WW Aur	–		1.964 ± 0.010	1.814 ± 0.008	4.161 ± 0.005	4.167 ± 0.006	0.198 ± 0.009	0.189 ± 0.009
HD71636	-0.05	14	1.512 ± 0.007	1.285 ± 0.006	4.226 ± 0.005	4.279 ± 0.005	0.123 ± 0.006	0.106 ± 0.005
VZ Hya	-0.20	15	1.271 ± 0.009	1.146 ± 0.006	4.305 ± 0.005	4.404 ± 0.006	0.085 ± 0.003	0.072 ± 0.003
KX Cnc	0.07	16	1.142 ± 0.003	1.132 ± 0.003	4.441 ± 0.002	4.450 ± 0.003	0.203 ± 0.004	0.201 ± 0.004
PT Vel	–		2.199 ± 0.016	1.626 ± 0.009	4.138 ± 0.009	4.264 ± 0.011	0.120 ± 0.009	0.089 ± 0.007
KW Hya	–		1.973 ± 0.036	1.485 ± 0.017	4.078 ± 0.010	4.269 ± 0.014	0.228 ± 0.008	0.159 ± 0.006
RZ Cha	-0.02	17	1.505 ± 0.027	1.513 ± 0.021	3.946 ± 0.011	3.893 ± 0.010	0.114 ± 0.005	0.122 ± 0.006
FM Leo	–		1.318 ± 0.011	1.287 ± 0.010	4.124 ± 0.023	4.189 ± 0.028	0.107 ± 0.006	0.098 ± 0.006
GG Lup	-0.10	18	4.079 ± 0.039	2.508 ± 0.022	4.295 ± 0.009	4.360 ± 0.009	0.132 ± 0.007	0.096 ± 0.005
V335 Ser	–		2.147 ± 0.014	1.905 ± 0.008	4.155 ± 0.011	4.240 ± 0.017	0.089 ± 0.006	0.076 ± 0.005
WZ Oph	-0.27	15	1.227 ± 0.007	1.220 ± 0.006	4.233 ± 0.008	4.220 ± 0.008	0.086 ± 0.003	0.087 ± 0.003
FL Lyr	-0.30	19	1.218 ± 0.016	0.958 ± 0.012	4.307 ± 0.021	4.453 ± 0.028	0.087 ± 0.003	0.065 ± 0.003
UZ Dra	–		1.306 ± 0.012	1.203 ± 0.011	4.330 ± 0.017	4.402 ± 0.019	0.063 ± 0.003	0.055 ± 0.003
V4089 Sgr	–		2.584 ± 0.012	1.607 ± 0.008	3.654 ± 0.005	4.233 ± 0.004	0.249 ± 0.018	0.101 ± 0.007
V1143 Cyg	0.08	20	1.356 ± 0.003	1.328 ± 0.002	4.317 ± 0.015	4.323 ± 0.015	0.308 ± 0.007	0.303 ± 0.007
MY Cyg	–		1.806 ± 0.025	1.782 ± 0.030	3.994 ± 0.020	4.013 ± 0.021	0.082 ± 0.005	0.080 ± 0.005
EI Cep	-0.04	21	1.772 ± 0.006	1.680 ± 0.006	3.762 ± 0.014	3.928 ± 0.016	0.137 ± 0.007	0.110 ± 0.006
VZ Cep	0.06	22	1.402 ± 0.015	1.108 ± 0.008	4.213 ± 0.008	4.446 ± 0.033	0.055 ± 0.005	0.038 ± 0.004
LL Aqr	0.02	23	1.195 ± 0.001	1.034 ± 0.001	4.272 ± 0.004	4.451 ± 0.004	0.095 ± 0.003	0.072 ± 0.003
EF Aqr	0.00	24	1.243 ± 0.006	0.946 ± 0.003	4.276 ± 0.007	4.447 ± 0.007	0.063 ± 0.006	0.045 ± 0.004
V821 Cas	–		2.088 ± 0.064	1.655 ± 0.050	4.024 ± 0.017	4.364 ± 0.024	0.078 ± 0.007	0.047 ± 0.004

Note. — References to metallicities: 1 - Pavlovski et al. (2014); 2 - Andersen et al. (1988); 3 - Tomasella et al. (2008a); 4 - Konorski et al. (2017); 5 - Tomasella et al. (2008b); 6 - Gallenne et al. (2016); 7 - Groenewegen et al. (2007); 8 - Maxted et al. (2015); 9 - Ribas et al. (1999); 10 - Clausen et al. (2010); 11 - Andersen et al. (1989); 12 - Southworth et al. (2007); 13 - Khaliullin et al. (2001); 14 - Holmberg et al. (2009); 15 - Clausen et al. (2008b); 16 - Sowell et al. (2012); 17 - Jørgensen & Gyldenkerne (1975); 18 - Andersen et al. (1993); 19 - Guillout et al. (2009); 20 - Andersen et al. (1987b); 21 - Torres et al. (2000); 22 - Torres & Lacy (2009); 23 - Graczyk et al. (2016); 24 - Vos et al. (2012)

Table 5
Coefficients of polynomial fits to the Surface Brightness parameter S in B- and V-bands.

Band	Color Index	N^a	Color Range (mag)	a_0	a_1	a_2	a_3	a_4	a_5	σ %
Linear fits (best-fit subsample)										
B	$(B-K)$	28	[−0.12:3.15]	2.640(18)	1.252(11)	-	-	-	-	2.5
V	$(B-K)$	28	[−0.12:3.15]	2.625(15)	0.959(9)	-	-	-	-	2.2
V	$(V-K)$	28	[−0.10:2.15]	2.644(19)	1.358(17)	-	-	-	-	2.7
Fifth-order polynomial fits (entire sample)										
B	$(B-K)$	70	[−0.7:3.15]	2.594(31)	1.423(88)	−0.592(164)	0.612(200)	−0.239(93)	0.031(14)	5.1
V	$(B-K)$	70	[−0.7:3.15]	2.579(27)	1.134(85)	−0.598(155)	0.623(187)	−0.245(87)	0.032(13)	5.0
V	$(V-K)$	70	[−0.5:2.15]	2.606(33)	1.526(134)	−0.989(317)	1.498(574)	−0.835(395)	0.156(88)	5.2

Note. — Notes. The S parameter is defined by the Equation 3. Colors are in the Johnson photometric system. The limb darkened stellar angular diameter is expressed in milliseconds of arc and follows from the equation: $\log \theta_{\rm LD} = 0.2*(a_0 - m + a_1*X + ... + a_5*X^5)$, where m is the observed extinction-free magnitude of a star in the B or V band and X is an extinction-free color. The last column gives the precision in predicting the angular diameter of stars in the given color range.

[a] Number of stars used in the fit

relation by Boyajian et al. (2014), it compares well with the relation by Challouf et al. (2014), especially for the bluest colors, and also with di Benedetto (2005) for the reddest colors $(V-K)_0 > 1.0$. This is an important argument in favor of the eclipsing binary method as a fully independent way to derive the SBC calibration.

One of the advantages of using eclipsing binary stars comes from the very precise surface gravities derived for the individual components. This allows, in principle, to determine how a SBC relation might depend on surface gravity (Fig. 4). We see some hints of this dependence where higher surface gravities result in higher surface brightness but the spread is still large and it is premature to draw a conclusion here.

The broadband SBC relations calibrated onto a wide range of colors do not show any statistically significant metallicity dependence with an exception of the bluest colors (e.g. $(B-V)$, see Boyajian et al. 2014). We compiled the metallicity determinations for our sample from the literature (Tab. 4) in order to check the possible dependence. As expected, no clear metallicity dependence is visible for the $V-K$ color – see Figure 5, although the scatter may hide it.

For the SBC relation to be useful it should have small intrinsic scatter and be only weakly dependent on reddening. The SBC relation for the V band and $(V–K)$ has great potential in this respect. This relation is commonly used to predict angular diameters and to determine distances, e.g. to the Magellanic Clouds with accuracy of 2-3% (Pietrzyński et al. 2013; Graczyk et al. 2014). However, for early-type stars (O or B) the relation becomes non-negligibly inclined to the line of reddening and shows significantly larger scatter than for stars with spectral types later than A5 (e.g. Challouf et al. 2014). This reduces its potential for predicting angular diameters of early type stars. Kervella et al. (2004) reported that the SBC relations based on colors with a larger wavelength difference show smaller scatter, i.e. the colors $(B-K)$ and $(V-L)$. However their relations were constrained to intermediate- and late-type stars.

We decided to search for similar relations using our sample. We combined two surface brightness parameters (B- and V-band) with the six colors $(V-J)$, $(V-H)$, $(V-K)$, $(B-J)$, $(B-H)$ and $(B-K)$. We fit the surface brightness parameters for the best-fit and all systems using first- and fifth-order polynomials, respectively. Figure 6 shows the two derived promising SBC relations based on $(B-K)$ color and with the rms minimized. The appropriate polynomial coefficients and the precision of angular diameter prediction are reported in Tab. 5. Both relations give precisions in the predicted angular diameters of 5% for the entire sample, 2-3% for the best-fit subsample, and have the smallest inclination of the relations to the reddening line for bluest colors. We note here that the real precision is lower because of the global systematic uncertainty of Gaia DR1 parallaxes. We estimated that the an upper limit of the systematics is about 3% for our systems.

5. DISCUSSION

The main purpose of the paper is to show that the inverse eclipsing binary method allows for independent and precise calibration of the SBC relations. Results presented in Section 4.3 fully corroborate this premise. Still, the precision of the derived relations is not significantly better than those derived from interferometric measurements of stellar angular diameters. In this section we are going to quantify the necessary steps in order to reach sub-percent precision in predicting angular diameters.

5.1. *Uniform analysis*

We compiled in this work data from numerous papers published by many different groups of researchers. Each group uses different quality photometric and spectroscopic data, different methodology to derive radial velocities, analysis of light and radial velocity curves (separated, simultaneous, single light curve, multi-band light curves), different ways of deriving effective temperatures (color-temperature calibrations, atmospheric model analysis) and finally different sets of astrophysical numerical constants. During this work we made some effort to homogenize existing data on eclipsing binary stars, but it was constrained to the effective temperatures, their ratio and the radial velocity semi-amplitudes.

However, to pin-down systematics a full homogenous re-analysis of each system would be needed using the same methodology and software, and also similar quality observables. That would result in better evaluation of relative precision of each data sets and it would augmented the internal precision of the physical parameters of the whole sample. Significant help in this respect can be expected from using new, high precision numerical codes like *ellc* (Maxted 2016) or Phoebe-2 (Prša et al. 2016), allowing for a very homogenous analysis of the full sample.

Ideally uniform space-based high-precision medium-cadence photometry and homogenous high-resolution, high-stability spectroscopic ground-based data for all the sample would suit best the purpose of the very precise SBC calibration. Such light curves will become available for many of the systems here if the TESS mission is successfully launched. We see this as a long-future next, natural step resulting in additional improvements over internal consistency and precision of derived physical parameters.

5.2. *Sample enlargement*

In order to increase the number of eclipsing binaries with suitable data for this programme, we have selected a number of additional, suitable detached eclipsing binary systems and have collected spectroscopic and photometric data for them. They cover a wide range of spectral classes from B- to early K-type and they are mostly within 300 pc from the Sun (low extinction regime). Besides AL Ari, for which we are already presenting derived physical parameters and a paper describing full analysis will be published soon (Konorski et al. 2017) our ongoing analysis is at an advanced stage for about 20 more systems.

The sample will be expanded in the near future with systems having more precise Gaia parallaxes within and beyond 300 pc horizon. More systems will also join the sample from efforts of other research groups investigating eclipsing binary stars as a large number of high quality light curves from ground based surveys (e.g. SuperWASP, soon the LSST) and space based surveys (e.g. Kepler-2, soon TESS) is registered for both known and

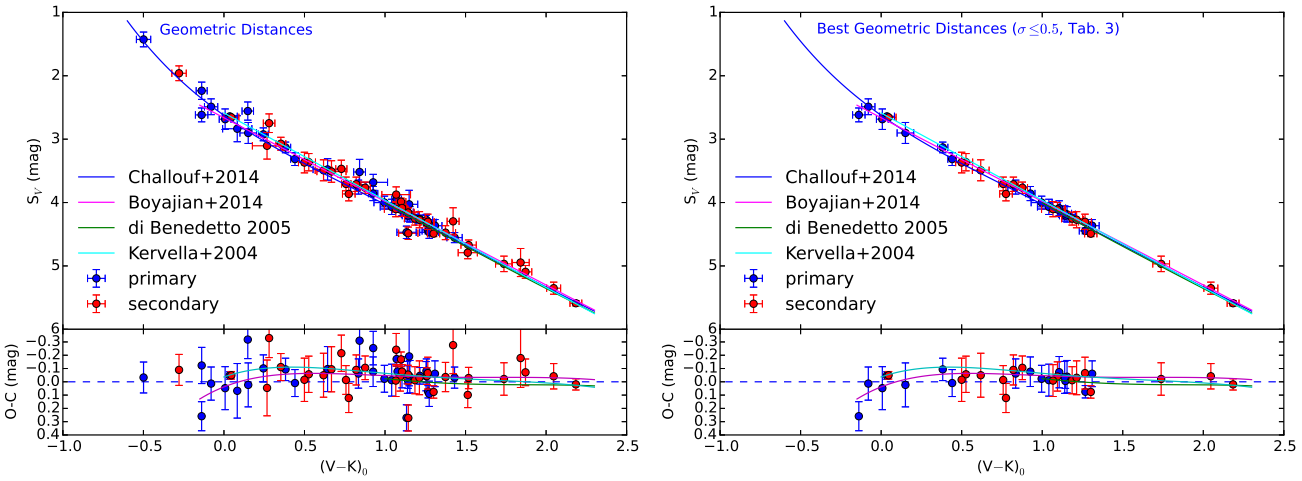


Figure 3. V-band surface brightness vs Johnson color $V-K$ relation. *Left panel*: for all stars based on their geometric distances. *Right panel*: for 14 systems with best agreement between the geometric and the photometric distances. Continuous lines correspond to several published interferometric SBC relations. Lower panels show O–C residuals calculated with respect to SBC relation by Challouf et al. (2014) - dashed line.

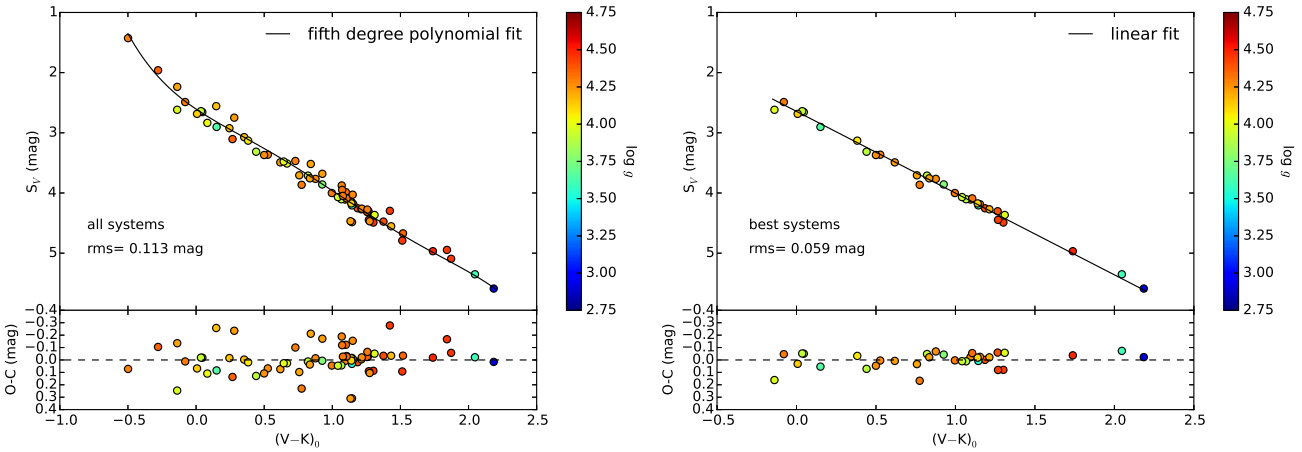


Figure 4. V-band surface brightness vs Johnson color $V-K$ relation with the addition of the surface gravity color scale (right vertical axis). *Left panel*: all the systems. *Right panel*: the systems with the best-fit distances.

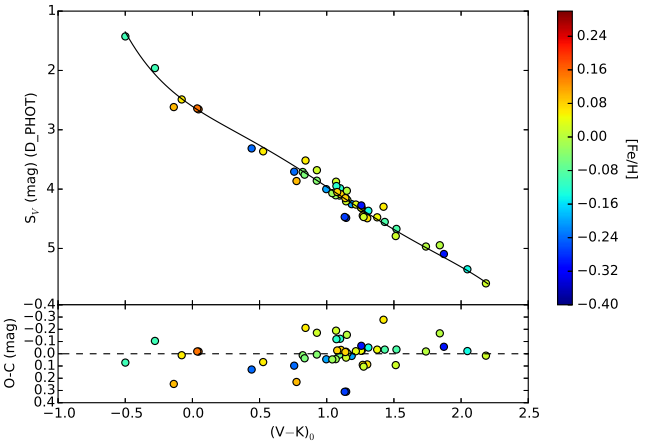


Figure 5. V-band surface brightness vs Johnson color $V-K$ for systems with determined metallicity. The continous line represents a fifth-order polynomial fit to the entire sample.

newly discovered systems. Those efforts will surely result in enlarging significantly the sample to about 100 systems covering B-, A-, F- and G-type stars. More systems will not only help to reduce statistical errors of relations but also to determine the intrinsic spread of the SBC relations.

5.3. *Parallaxes*

Future more precise Gaia parallaxes are fundamental for any significant improvement to SBC relations presented here. We forecast expected precision of Gaia parallaxes for the sample as follows. We assumed conservatively that the precision of astrometry for bright stars (3 mag $< G <$ 12 mag) will be 15 μas and that the photocenter movement of an eclipsing binary will be unequivocally detected and taken into account when it is larger than 35 μas. The resulting expected mean relative precision of Gaia parallaxes will be 0.6% for our sample. Systematic uncertainty introduced into the prediction of angular diameters will likely be smaller but to be conclusive on this point we need to wait for a final

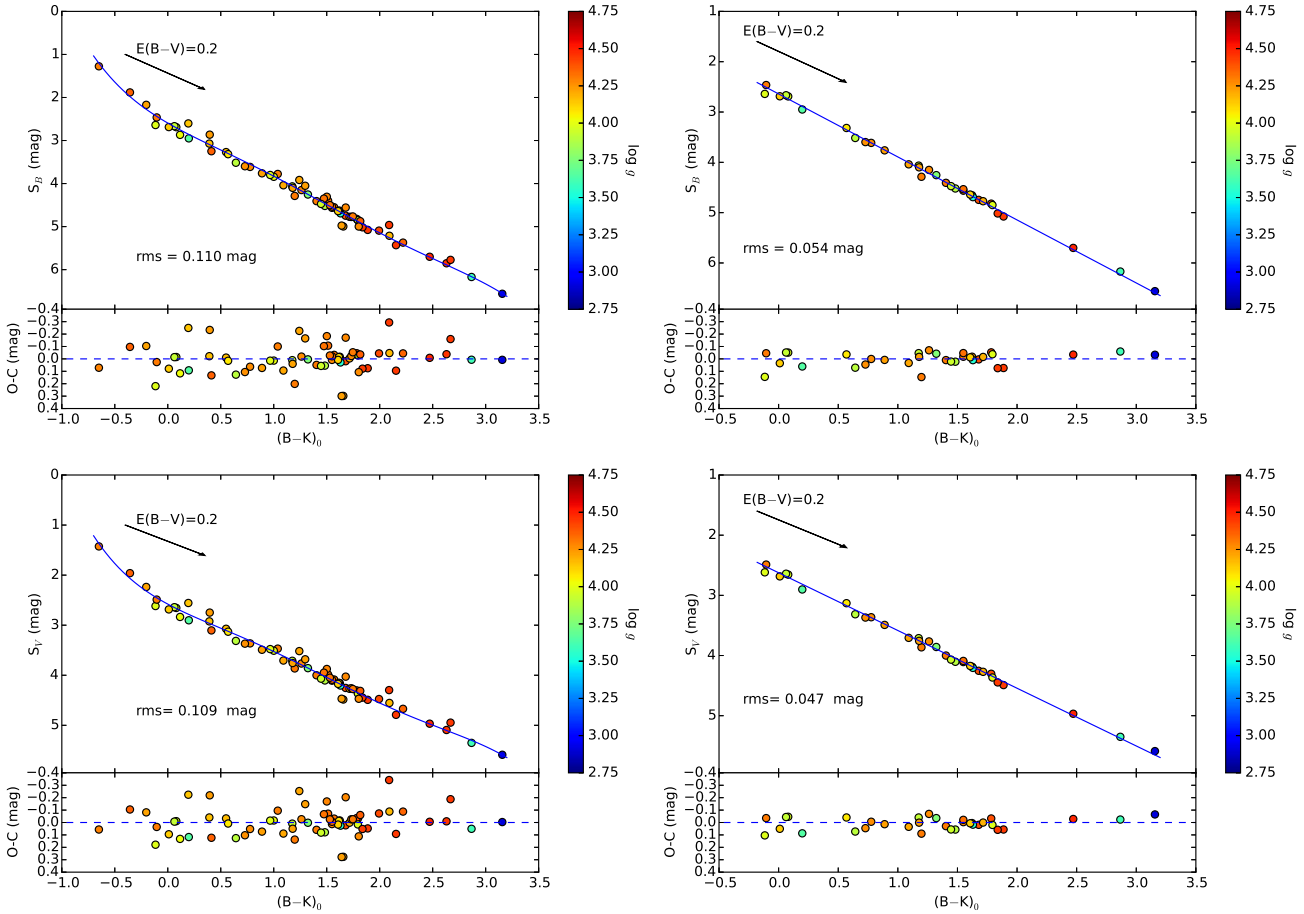


Figure 6. Surface brightness vs Johnson color $B-K$ relations. *Upper panel*: calibrated for the B band. *Lower panel*: calibrated for the V band. The continuous line in the left panels shows fifth-order polynomial fits to all stars in the sample, and in the right panels the line shows linear fits to the best-fit subsample. The reddening vector is denoted as an arrow. The root mean square of the relations is given. The surface gravity in *cgs* units is color coded.

Gaia release quality evaluation. Figure 7 presents the expected angular diameters of stars in our sample after the final Gaia data release, assuming the same radii and uncertainties as in Tab. 3. Inspection of this figure suggests that much improvement is expected, especially for blue stars. Angular diameters with a sub-percent precision will be available for more than half of all components in our eclipsing binary sample. We add that the sample will be augmented by very precise dynamical parallaxes from interferometric orbits for a number of long period eclipsing binary stars.

5.4. *Disentangling of component magnitudes*

It is interesting to estimate to what extent our extrapolation procedure introduce a bias. As was mentioned already in Sec. 3.7, flux ratios are calculated using precomputed intensities based on ATLAS9 atmosphere models which assume a plane-parallel geometry and local thermodynamic equilibrium (LTE). When components have similar effective temperatures to within about 100 K their light ratio changes very little over the optical and NIR range of the spectrum and, regardless of the adopted model atmosphere, the extrapolation leads to negligible errors in comparison with observational photometric uncertainties. However the situation is somewhat different when the temperature difference between the components is much larger, say of the order of 1000 K.

For A-, F- and G-type stars with given atmospheric parameters ($T_{\rm eff}, \log g$, [Fe/H]) and solar-like compositions their absolute spectral energy distributions predicted by various atmospheric models (plane parallel, spherical, LTE and non-LTE) in a range of B and K bands have differences between them of up to 5%, but significantly smaller regarding relative fluxes (i.e. colors) (e.g. Bessell et al. 1998; Martins & Coelho 2007; Edvardsson 2008; Plez 2011). Comparison of model fluxes with empirical fluxes in the aforementioned range of the spectrum gives also very good agreements. As a result, we can expect, on average, a small systematic uncertainty in the derived colors (reaching up to 0.02 mag) even in cases of larger temperature difference between the components. Such an error would be only a fraction of the typical uncertainty of an intrinsic color. This uncertainty can be mitigated even further by using multi-band photometry and carefully determined temperatures derived from disentangled spectra. For hotter stars (O- and B-type) use of plane-parallel and LTE models may lead to much larger systematic shifts (e.g. Aufdenberg et al.

1998; Cugier 2012), however these issues will be addressed in a forthcoming paper.

5.5. *Photometry and transformations into standard system*

5.5.1. *Optical*

The precision of transformation between the Tycho-2 and Johnson photometric systems is about 1% (Bessell 2000) resulting in additional systematic uncertainty in our SBC relations. To mitigate the problem one would use original Tycho-2 B_T and V_T magnitudes and to express the calibration in this system. However we notice that for a few systems in our sample (EW Ori, VZ Hya, VZ Cep, LL Aqr and EF Aqr), Tycho-2 photometry transformed into B, V magnitudes give optical and NIR colors which are inconsistent with each other and with temperatures of the stars. In those cases we used other sources of V-band magnitudes. The source of discrepancy is unclear to us, but we think that although the Tycho-2 photometry is multi-epoch in particular cases mean B_T and V_T magnitudes are affected by the presence of eclipses and/or other kind of systematics (e.g. transformation errors). That strengthens the case for well-calibrated, precise and uniform optical B, V photometry in the standard Johnson system for stars in the sample. In the optical, provided that a photometric system is close to the standard one, it is expected that transformation from instrumental system to the standard one would not produce systematic errors larger than 0.5%.

5.5.2. *NIR*

For the overwhelming majority of eclipsing binary systems, well calibrated photometry NIR comes only from the single-epoch 2MASS survey. We transformed 2MASS magnitudes into the Johnson system which may introduce systematics of up to 1% (0.02 mag), because of poor definition of the Johnson system in NIR. As an example of this fact the transformation equation for $(V-K)$ color used by Holmberg et al. (2007) has an offset of -0.02 mag with respect to the transformation equation we used, of course a non-negligible value when we deal with subpercent precision. Preferentially the future SBC calibration should be expressed in the 2MASS photometric system which is well calibrated (e.g. Cohen et al. 2003) and it is based on all-sky network of standard stars, or eventually by using other NIR system which have similar bandpasses and precisely determined transformation (e.g. SAAO).

Single-epoch photometry is prone to some accidental errors and the statistical uncertainty of one measurement is relatively large. Because of that it would be advisable to carry out new, high quality multi epoch NIR photometry secured for stars in the sample. It would significantly help in reducing statistical uncertainties and in removing any accidental photometric errors. We already started a campaign to secure NIR photometry for southern and equatorial stars from the sample with the plan to derive precise out-of-eclipse magnitudes and later also to provide full NIR light curves for some eclipsing binaries, especially those having large effective temperature difference between components.

5.6. *Quantifying error contributions*

- Radii: the mean precision of stellar radii determination in our sample is 1.2%. By using about 100 systems it would be possible to pin-down the statistical error by a factor of 10, i.e to 0.1-0.2%. Systematics will come mostly from the numerical tools for the analysis of eclipsing binary stars, and it is expected to be of order of 0.1%.

- Parallaxes: taking into account the photocenter movements of the eclipsing binaries, the mean expected precision of Gaia parallaxes would be 0.6%. The systematic error is expected to be significantly smaller.

- Disentangling of magnitudes: up to 0.01 mag of systematics in derived colors and magnitudes translates into a 0.3% mean systematic uncertainty in predicting angular diameters. However, by if we were to use full NIR light curves and/or by using equal-temperature systems, then this error could be almost eliminated because it would be possible to determine the NIR magnitudes directly.

- Photometric zero-points and transformations: in best cases of well-defined photometric systems (Section 5.5) we expect 0.7% systematics in colors and magnitudes.

- Interstellar extinction:
  a) Total extinction: the reddeing is low for almost all our systems. When we assume a standard Galactic exctinction curve with $R_V = 3.1$, it introduces only a little additional uncertainty of about 0.03 mag in the $(V-K)_0$ color. Because the reddening line is largely parallel to the SBC relation, this translates into only a 0.006 mag statistical uncertainty (0.3 %) in predicting the angular diameter.
  b) Reddening law: for about 25% of stars in within 1kpc from the sun (e.g. Fitzpatrick & Masana 2007; Krełowski & Strobel 2012), we expect deviations from the universal law. R_V can vary significantly, but mostly lies between 2.7 and 3.7 (e.g. Gontcharov 2012). When this is not accounted for, it shows as an additional intrinsic scatter in the SBC relation that amounts to about 0.02 mag in some individual cases.

The statistical uncertainty of the future SBC relation is expected to be well below 1% provided the number of suitable systems is sufficient (about 100 systems) and the internal dispersion of a given relation is low. By combining all conservative estimates of errors from the above considerations in quadrature we obtain an upper limit of 0.9% on the systematic uncertainty. This error is dominated by the photometric uncertainties.

6. FINAL REMARKS

New Gaia parallaxes combined with Hipparcos and dynamical parallaxes allow us to derive for the first time the SBC relations based fully on the eclipsing binary stars. The precision of the derived relations for A-, F-, and G-type stars is comparable to the precision of relations derived from interferometric angular diameters, and both types of relations are mutually consistent. The eclipsing binary method has no serious limitations if it based

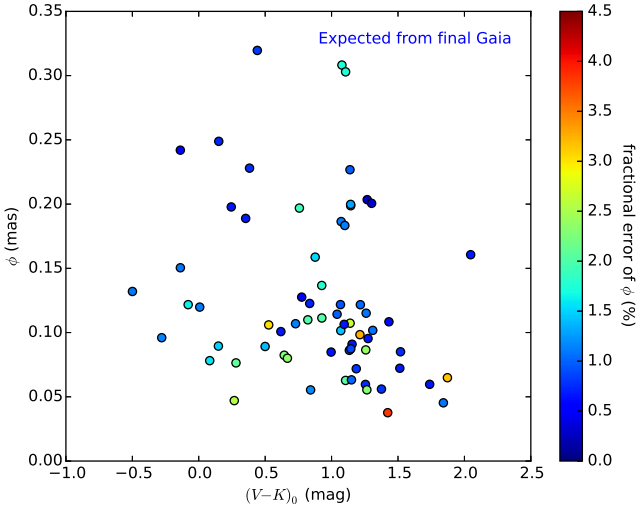


Figure 7. Predicted angular diameter uncertainties for stars in our sample after the final Gaia release. Note the change in scale of the color bar with respect to Fig. 2. The error-bars would be in most cases smaller than the size of the circles.

on a well-selected sample of eclipsing binaries, a self-consistent analysis method, and proper sanity checks. To expand the SBC relation to O- and B-type stars we propose to use the $B-K$ color, which allows reducing interstellar extinction uncertainties. We also discussed all the steps necessary to obtain precise and accurate SBC relations that allow for a precision better than 1% of the angular diameter predictions in the future.

The research leading to these results has received funding from the European Research Council (ERC) under the European Union's Horizon 2020 research and innovation program (grant agreement No 695099).

We are grateful for financial support from Polish National Science Center grant MAESTRO 2012/06/A/ST9/00269. Support from the BASAL Centro de Astrofísica y Tecnologías Afines (CATA) PFB-06/2007, the Millenium Institute of Astrophysics (MAS) of the Iniciativa Cientifica Milenio del Ministerio de Economia, Fomento y Turismo de Chile, project IC120009 and the IdP II 2015 0002 64 grant of the Polish Ministry of Science and Higher Education is also acknowledged. We are also thanks to the staffs in La Silla Observatory (ESO) and Las Campanas Observatory (Carnegie) for their excellent support.

We also thank the anonymous referee for remarks and corrections to the text.

This research has made extensive use of the excellent astronomical SIMBAD database and of the VizieR catalogue access tool, operated at CDS, Strasbourg, France and made also use of NASA's Astrophysics Data System Bibliographic Services (ADS).

This publication makes use of data products from the Two Micron All Sky Survey, which is a joint project of the University of Massachusetts and the Infrared Processing and Analysis Center/California Institute of Technology, funded by the National Aeronautics and Space Administration and the National Science Foundation.

We dedicate this work to Prof. Bohdan Paczyński who encouraged us many years ago to work on this subject.

REFERENCES

Abt, H. A., & Levato, H. 1978, PASP, 90, 201
Albrecht, S., Reffert, S., Snellen, I., Quirrenbach, A., & Mitchell, D. S. 2007, A&A, 474, 565
Alonso, A., Arribas, S., & Martínez-Roger, C. 1996, A&A, 313, 873
Ammons, S. M., Robinson, S. E., Strader, J., et al. 2006, ApJ, 638, 1004
Andersen, J., Gjerløff, H., & Imbert, M. 1975, A&A, 44, 349
Andersen, J., & Vaz, L. P. R. 1984, A&A, 130, 102
Andersen, J., Clausen, J. V., & Nordström, B. 1987a, A&A, 175, 60
Andersen, J., García, J. M., Giménez, A., & Nordström, B. 1987b, A&A, 174, 107
Andersen, J., Clausen, C. V., Gustafsson, B., Nordström, B., & VandenBerg, D. A., 1988, A&A, 196, 128
Andersen, J., Clausen, J. V., & Magain, P. 1989, A&A, 211, 346
Andersen, J. 1991, A&A Rev., 3, 91
Andersen, J., Clausen, J. V., Nordström, B., Tomkin, J., & Mayor, M. 1991, A&A, 246, 99
Andersen, J., Clausen, J. V., & Giménez, A. 1993, A&A, 277, 439
Aufdenberg, J. P., Hauschildt, P. H., & Baron, E. 1998, ASP Conf. Series, Vol. 131, 127
Bailer-Jones, C. A. L. 2015, PASP, 127, 994
Bakiş, V., Bakiş, H., Demircan, O., & Eker, Z. 2008, MNRAS, 384, 1657
Barnes, T. G., Evans, D. S., & Moffett, T. J. 1978, MNRAS, 183, 285
Batten, A. H., Fletcher, J. M., & Mann, P. J. 1978, Publ. Dom. Astrophys. Obs., Victoria, 15, 121
Behr, B. B., Cenko, A. T., Hajian, A. R., et al. 2011, AJ, 142, 6
Bessell, M. S., Brett J. M., 1988, PASP, 100, 1134
Bessell, M. S., Castelli, F., & Plez, B. 1998, A&A, 333, 231
Bessell, M. 2000, PASP, 112, 961
Bilir, S., Ak, T., Soydugan, E., et al. 2008, Astron. Nachr., 117, 393
Boggs, P. T., & Rogers, J. E. 1989, *Orthogonal Distance Regression*, National Institute of Standards and Technology, Gaithersburg, Maryland, Internal Report 89-4197 (Revised 1990)
Bonneau, D., Clausse, J.-M., Delfosse, X., et al. 2006, A&A, 456, 789
Boyajian, T. S., van Belle, G., & von Braun, K. 2014, AJ, 147, 47
Budding, E., Butland, R., & Blackford, M. 2015, MNRAS, 448, 3784
Çakirli, Ö., Ibanoğlu, C., Bilir, S., & Sipahi, E. 2009, MNRAS, 395, 1649
Cannon, A.J., & Pickering, E.C. 1919, *The Henry Draper Catalogue*, Cambridge, Ann. Astron. Obs. Harvard College, Vol. 93
Carpenter J. M., 2001, AJ, 121, 2851
Casagrande, L., I. Ramírez, I., Meléndez, J., Bessell, M., & Asplund, M. 2010, A&A, 512, 54
Casertano, S., Riess, A. G., Bucciarelli, B., & Lattanzi, M. G. 2016, arXiv:1609.05175v1
Challouf, M., Nardetto, N., Mourard, D., et al., 2014, A&A, 570, 104
Clausen, J. V., & Grønbech, B. 1976, A&A, 48, 49
Clausen, J. V., Vaz, L. P. R., García, J. M., et al. 2008a, A&A, 487, 1081
Clausen, J. V., Torres, G., Bruntt, H., et al. 2008b, A&A, 487, 1095
Clausen, J. V., Bruntt, H., Olsen. E. H., Helt, B. E., & Claret, A., 2010, A&A, 511, 22
Cohen, M., Wheaton, Wm., A., & Megeath, S. T. 2003, AJ, 126, 1090
Cugier, H. 2012, A&A, 547, 42
David, T. J., Conroy, K. E., Hillenbrand, L. A., et al. 2016, AJ, 151, 112
de Bruijne, J. H. J., Rygl, K. L. J., & Antoja, T., 2014, The Milky Way Unravelled by Gaia: GREAT Science from the Gaia Data Releases, EAS Publications Series 67-68, N.A. Walton, F. Figueras, L. Balaguer-Nunez and C. Soubiran, 23
Di Benedetto, G. P. 2005, MNRAS, 357, 174
Ducati, J. R. 2002, VizieR Online Data Catalog: 2237, 0
Edvardsson, B. 2008, PhST, Vol. 133, 4011
Eker, Z., Bilir, S., Soydugan, F., et al. 2014, PASA, 31, 24
Fitzpatrick, E. L., & Massa, D. 2007, ApJ, 663, 320
Flower, P. J. 1996, ApJ, 469, 355
Fouqué, P., & Gieren, W. 1997, A&A, 320, 799
Gaia Collaboration: Brown, A. G. A., Vallenari, A., Prusti, T., de Bruijne, J., Mignard, F., et al. 2016, arXiv:1609.04172v1
Gallenne, A., Pietrzyński, G., Graczyk, D., et al. 2016, A&A, 586, 35

Gieren, W., Storm, J., Barnes, T. G., et al. 1995, ApJ, 627, 224
Giménez, A., & Margrave, T. E. 1985, AJ, 90, 358
Giuricin, G., Mardirossian, F., Mezzetti, M., & Predolin, F. 1980, A&A, 85, 259
Gontcharov, G. A. 2012, AstL, 38, 12
González Hernández, J. I. & Bonifacio, P. 2009, A&A, 497, 497
Graczyk, D., Pietrzyński, G., Thompson, I. B., et al., 2014, ApJ, 780, 59
Graczyk, D., Maxted, P. F. L., Pietrzyński, G., et al. 2015, A&A, 581, 106
Graczyk, D., Smolec, R., Pavlovski, K., et al. 2016, A&A, 594, 92
Griffin, R. F. 2013, Observatory, 133, 156
Groenewegen, M. A. T., Decin, L., Salaris, M., & De Cat, P. 2007, A&A, 463, 579
Guillout, P., Klutsch, A., Frasca, A., et al. 2009, A&A, 504, 829
Gülmen, O., Güdür, N., Sezer, C., 1986, IBVS, 2953, 1
Habbereiter, M., Schmutz, W., Kosovichev, A. G. 2008, ApJ, 675, 53
Hełminiak, K. G., Konacki, M., Ratajczak, M., & Muterspaugh M. W., 2009, MNRAS, 400, 969
Henry, G. W., Fekel, F. C., Sowell, J. R., & Gearhart, J. S. 2006, AJ, 132, 2489
Hill, G., Hilditch, R. W., Younger, F., & Fisher, W. A. 1975, MmRAS, 79, 131
Hindsley, R. B., & Bell, R. A. 1989, ApJ, 341, 1004
Holmberg, J., Nordström, B., & Andersen, J. 2007, A&A, 475, 519
Holmberg, J., Nordström, B., & Andersen, J. 2009, A&A, 501, 941
Houdashelt, M. L., Bell, R. A., & Sweigart, A. V. 2000, AJ, 119, 1448
Houk, N., & Cowley, A. P. 1975, *Michigan Spectral Catalog*, Vol. 1, Univ. of Michigan, Ann Arbor, USA
Houk, N. 1978, *Michigan Catalogue of two-dimensional spectral types for HD stars*, Vol. 2, Univ. of Michigan, Ann Arbor
Houk, N., & Swift, C. 1999, *Michigan Catalogue of two-dimensional spectral types for HD stars*, Vol. 5, Univ. of Michigan, Ann Arbor
Høg, E., Fabricius, C., Makarov, V. V., et al. 2000, A&A, 357, 367
Hrivnak, B. J., & Milone, E. F. 1984, ApJ, 282, 748
Hummel, C. A., Armstrong, J. T., Buscher, D. F., et al. 1995, AJ, 110, 376
Imbert, M. 1986, A&AS, 65, 97
Imbert, M. 2002, A&A, 387, 850
Jerzykiewicz, M. 2001, Acta Astron., 51, 151
Jørgensen, H. E., & Gyldenkerne, K. 1975, A&A, 44, 343
Kervella, P., Thévenin, F., Di Folco, E., Ségransan, D., 2004, A&A, 426, 297
Khaliullin, Kh. F., Khaliullina, A. I., & Krylov, A. V. 2001, Astron. Rep., 45, 888
Khaliullin, Kh. F., & Khaliullina, A. I. 2002, Astron, Rep., 46, 119
Kiyokawa, M., & Kitamura, M. 1975, Ann. Tokyo Astron. Obs., second series, 15, 117
Kirkby-Knet, J. A., Maxted, P. F. L., Serenelli, A. M., et al., 2016, A&A, 591, 124
Konorski, P., Graczyk, D., Pietrzyński, G., et al. 2017, in preparation
Krełowski, J. & Strobel, A. 2012, AN, 333, 60
Kruszewski, A., & Semeniuk, I., 1999, AcA, 49, 561
Kurucz R., 1993, ATLAS9 Stellar Atmosphere Programs and 2 km s^{-1} Grid, (Cambridge, MA: SAO) Kurucz CD-ROM No. 13,
Lacy, C. H. S. 1977, ApJ, 213, 458
Lacy, C. H. S. 1981, ApJ, 251, 591
Lacy, C. H., Gülmen, O., Güdür, N., Sezer, C., 1989, AJ, 97, 822
Lacy, C. H. S., 2002, AJ, 124, 1162
Lacy, C. H. S., Fekel, F. C., & Claret, A., 2012, AJ, 144, 63
Lutz, T. E., & Kelker, D. H. 1973, PASP, 85, 573
Lyubimkov, L. S., Rachkovskaya, T. M., & Rostopchin, S. I. 1996, Astron. Rep., 40, 802
Malkov, O. Y., 1993, Bull. Inform. Centr. Donn. Strasb., 42, 27
Martins, L. P., & Coelho, P. 2007, MNRAS, 381, 1329
Masana, E., Jordi, C., & Ribas, I. 2006, A&A, 450, 735
Maxted, P. F. L., Hutcheon, R. J., Torres, G., et al. 2015, A&A, 578, 25
Maxted, P. F. L. 2016, A&A, 591, 111
Mermilliod, J. C. 1991, *Catalogue of Homogeneous Means in the UBV System*, Institut d'Astronomie, Universite de Lausanne, Geneva
Munari, U., Dallaporta, S., Siviero, A., et al. 2004, A&A, 418, L31
Napiwotzki, R., Schoenberner, D., Wenske, V. 1993, A&A, 268, 653
Nesterov, V. V., Kuzmin, A. V., Ashimbaeva, N. T., et al., 1995, A&AS, 110, 367
Nordström, B., & Johansen, K. T. 1994b, A&A, 291, 777
Ochsenbein, F., Bauer, P. & Marcout, J. 2000, A&AS, 143, 23
Olsen, E. H. 1983, A&AS, 54, 55
Pavlovski, K., Tamajo, E., Koubský, et al. 2009, MNRAS, 400, 791
Pavlovski, K., Southworth, J., Kolbas, V., & Smalley, B. 2014, MNRAS, 438, 590
Pecaut, M. J., & Mamajek, E. E. 2013, ApJS, 208, 9
Pietrzyński, G., Graczyk, D., Gieren, W., et al., 2013, Nature, 495, 76
Pitjeva, E. V., & Standish, E. M. 2009, Celest. Mech. Dyn. Astr., 103, 356
Plez, B. 2011, JPhCD, Vol. 328, 2005
Popper, D. M. 1965, ApJ, 141, 126
Popper, D. M. 1966, AJ, 71, 175
Popper, D. M. 1971, ApJ, 169, 549
Popper, D. M. 1980, ARA&A, 18, 115
Popper, D. M., & Etzel, P. B. 1981, AJ, 86, 102
Popper, D. M. 1984, AJ, 89, 132
Popper, D. M., Lacy, C. H., Frueh, M. L., & Turner, A. E. 1986, AJ, 91, 383
Popper, D. M. 1998, PASP, 110, 919
Prša, A., Conroy, K. E., Horvat, M., et al. 2016, ApJS, 227, 29
Ratajczak, M., Kwiatkowski, T., Schwarzenberg-Czerny, A., et al. 2010, MNRAS, 402, 2424
Ramírez, I., & Meléndez, J. 2005, AJ, 626, 465
Ribas, I., Jordi, C., & Jordi, T. 1999, MNRAS, 309, 199
Sandage, A., & Saha, A. 2002, AJ, 123, 2047
Schlegel, D. J., Finkbeiner, D. P. & Davis, M., 1998, ApJ, 500, 525
Semeniuk, I. 2001, AcA, 51, 75
Skrutskie, M. F., Cutri, R. M., Stiening, R., et al. 2006, AJ, 131, 1163
Smalley, B., Gardiner, R. B., Kupka, F., Bessell, M. F. 2002, A&A, 395, 601
Smith, B. 1948, ApJ, 108, 504
Southworth, J., Smalley, B., Maxted, P. F. L., Claret, A., & Etzel, P. B. 2005, MNRAS, 363, 529
Southworth, J., Bruntt, H., & Buzasi, D. L. 2007, A&A, 467, 1215
Southworth, J. 2013, A&A, 557, 119
Southworth, J. 2015, Living Together: Planets, Host Stars and Binaries, ASP Conference Series 496, S. Rucinski, G. Torres, and M. Zejda, San Francisco: Astronomical Society of the Pacific, 164
Sowell, J. R., Henry, G. W., & Fekel, F. C. 2012, AJ, 143, 5
Stassun, K. G., & Torres, G. 2016, AJ, 152, 180
Stassun, K. G., & Torres, G. 2016, ApJ, 831L, 6
Storm, J., Gieren, W., Fouqué, P., et al. 2011, A&A, 534, 94
Suchomska, K., Graczyk, D., Smolec, R., et al. 2015, MNRAS, 451, 651
Tomasella, L., Munari, U., Siviero, A, et al. 2008a, A&A, 480, 465
Tomasella, L., Munari, U., Cassisi, S., et al. 2008b, A&A, 483, 263
Tomkin, J., & Fekel, F. C. 2006, AJ, 131, 2652
Torres, G., & Lacy, C. H. S. 2009, AJ, 137, 507
Torres, G., Andersen, J., Nordström, B., & Latham, D. W. 2000, AJ, 119, 1942
Torres, G., Andersen, J., & Giménez, A. 2010, A&A Rev., 18, 67
Tucker, R. S., Sowell, J. R., Williamon, R. M., & Coughlin, J. L., 2009, AJ, 137, 2949
van Hamme, W., & Wilson, R. E. 2007, ApJ, 661, 1129
van Leeuwen, F. 2007, A&A, 474, 653
Veramendi, M. E., & González, J. F. 2015, New Astronomy, 34, 266
Vos J., Clausen, J. V., Jørgensen, U. G., et al. 2012, A&A, 540, 64
Wenger, M, Ochsenbein, F., Egret, D., et al. 2000, A&AS, 143, 9
Wilson, R. E., & Devinney, E. J. 1971, ApJ, 166, 605
Wilson, R. E. 1979, ApJ, 234, 1054
Wilson, R. E. 1990, ApJ, 356, 613
Wilson, R. E. & van Hamme, W. 2009, ApJ, 699, 118
Wilson, R. E., van Hamme, W., & Terrell. D. 2010, ApJ, 723, 1469
Wolf, M., & Zejda, M. 2005, A&A, 437, 545
Worthey G., Lee H., 2011, ApJS, 193, 1
Wyithe, J. S. B. & Wilson, R. E. 2002, ApJ, 571, 293

APPENDIX

TEMPERATURES AND REDDENING

V570 PER

The temperature of the system V570 Per was determined from a model atmosphere analysis of disentangled spectra (Tomasella et al. 2008b). Although formal errors on the temperatures quoted by the authors are very small (lower than 0.5%), the intrinsic colors of the components $b-y$, $B-V$, $V-J$ and $V-K$, point to much lower temperatures (by about 300 K), unless there is significantly larger interstellar extinction to this object than assumed by Tomasella et al. (2008b): $E(B-V) = 0.07$ mag instead of 0.023 ± 0.007 mag. There are two ways of resolving the problem: (1) the temperatures are indeed lower, or (2) the reddening is indeed higher. The first possibility would force us to assume that some error was made by Tomasella et al. (2008b) during their atmospheric analysis. This seems quite unlikely, however: (a) their atmospheric analysis is standard, (b) the spectra are of good quality, (c) higher temperatures correspond well with the components' spectral types and masses. Thus the more probable explanation of disagreement is possibility (2). However, it was reported that the interstellar potasium line KI (7699 Å) is not detected in the spectra of the system, which would contradict the higher reddening. Because we cannot solve this problem at the moment, for the purpose of this work, we kept the temperatures from Tomasella et al. (2008b) and assumed a reddening of 0.07 ± 0.03 mag to V570 Per. This problem clearly needs some future attention and more detailed investigation.

WW AUR

The temperatures of the components of WW Aur were previously determined by Smalley et al. (2002) and Southworth et al. (2005). However, $b-y$, $B-V$, $V-K$ colors suggest larger temperatures by about ~ 200 K, what was already pointed out by Southworth et al. (2005) in regard of the $b-y$ color. Wilson & van Hamme (2009) used their direct distance estimate (DDE) method and also found the temperatures of both components to be higher by a very similar amount. In our model we employed those higher temperatures.

KX CNC

For the system KX Cnc we determined the temperature from Strömgren uvby photometry ($b-y$=0.378; Olsen 1983) and Johnson's BVJK photometry. The temperature of the primary component derived from the different colors is as follows: $T_{b-y} = 5938$ K, $T_{B-V} = 5985$ K, $T_{V-J} = 6131$ K, $T_{V-K} = 6162$ K. The resulting mean temperature is $T_1 = 6050$ K i.e. larger by 150 K (1.5σ) than the original temperature T_1 derived by Sowell et al. (2012). The larger value is in better agreement with the original HD spectral classification: F8 (Cannon & Pickering 1919). Using the calibration between effective temperature and spectral type for normal main sequence stars (Pecaut & Mamajek 2013) we reclassify the system as F9V+F9V.

RZ CHA

The case of RZ Cha is interesting. Andersen et al. (1975) combined their velocimetry with Strömgren photometry obtained by Jørgensen & Gyldenkerne (1975) to derive "mean" parameters of the components. The reason behind it was their conclusion that the components of the system had very similar physical appearance and thus also parameters. This "indistinguishability" of components was retained by Torres et al. (2010) in their review. However, it is clear from inspection of the light curves that the components have different surface temperatures which was reported already by Giuricin et al. (1980). The difference is small, with the more massive and larger star being cooler by ~ 50 K, but it has an effect on the predicted infrared light ratios.

WZ OPH

The system was quite recently analyzed by Clausen et al. (2008a). They reported the temperature $T_1 = 6165 \pm 100$ K, based on reddening $E(B-V) = 0.044$ mag, intrinsic Strömgren color of the primary $(b-y)_0 = 0.329$ and a calibration by Holmberg et al. (2007). They noted that the temperature derived from atmospheric analysis of the disentangled primary's spectrum is slightly higher, however they did not report how much higher. From unreddened colors b–y, B–V, $V-K$ we derived also a higher temperature of $T_1 = 6301$ K (1.4σ difference). Lower reddening of $E(B-V) = 0.030$ mag resulting from Schlegel et al. (1998) maps leads to the temperature $T_1 = 6232$ K, a value which one would consider "slightly" higher. These values of reddening and temperatures are assumed in this work.

UZ DRA

Using B, V, J, K photometry we redetermined temperatures of both components because the original temperatures given by Lacy et al. (1989) were estimated only from the mean spectral type of the system. Resulting temperatures are higher by about 200 K than those reported by Lacy et al. (1989) and correspond much better with the masses of both components, which seem to be unevolved main-sequence stars.

VZ CEP

There is an inconsistency between the temperatures based on $B-V$, $b-y$ colors and $V-K$, $V-J$ with the NIR colors resulting in temperatures higher by about 300 K. Different values of reddening does not resolve the discrepant temperatures. A possible reason is that 2MASS magnitudes are somehow affected, however they were taken well outside of eclipses and all have an "A" flag. Higher temperatures would be in agreement with relatively massive components of the system, and furthermore the resulting photometric distance would be in perfect agreement with Hipparcos and Gaia parallaxes. However, we have no clue at this moment about the possible source of the discrepancy. We therefore retained in this paper the temperatures from the work by Torres & Lacy (2009), which are based on Strömgren photometry.

RADIAL VELOCITIES

V570 PER

Tomasella et al. (2008b) did not report radial velocity semiamplitudes. We utilized data from their Table 2 to rederive the orbital parameters. Our semi-major axis is larger by 1.5σ than value by Tomasella et al. (2008b) which we attribute mostly to a different choice of astrophysical constants, but our mass ratio q is fully consistent with their value.

HD 71636

Henry et al. (2006) reported two sets of radial velocity semiamplitudes in their Table 3 and Table 5 that contradict each other. Thus we rederived the spectroscopic orbit from the data in their Table 2. Our semiamplitudes are in perfect agreement with the values presented in Table 3 and we accordingly adopted them here.

KX CNC

Sowell et al. (2012) reported two sets of $K_{1,2}$ that contradict each other. Using the data from their Table 2 we determined the spectroscopic orbit that is fully consistent with the solution given in their Table 3.

V4089 SGR

Recently, Veramendi & González (2015) presented light and radial velocity curves solution of the system and they derived its absolute dimensions. However, the semi-major axis a reported in their Table 1 is inconsistent with their radial velocity semiamplitudes $K_{1,2}$ and masses. Our solution to the velocimetry kindly provided by M. Veramendi confirms their masses and $K_{1,2}$, but not their a. Also our K_2 is slightly larger (by 1.2σ); this is probably caused by the fact that we allowed for different systemic velocities for the components. Finally, we recalculated errors on the fundamental parameters which are significantly different from those reported in the Tables 1 and 2 by Veramendi & González (2015).

EF AQR

In paper by Vos et al. (2012) were presented fundamental physical parameters of the system. However, they reported two different sets of radial velocity semiamplitudes $K_{1,2}$ (their Tables 4 and 8). Using their velocimetry we redetermined spectroscopic orbits for this system. Our $K_{1,2}$ are much closer to the values presented in Table 8, but they are still somewhat different. Especially the epoch of spectroscopic conjuction is different in our solution by 0.002 days suggesting some period change in the system. We also recalculated fractional radii from the sum of radii and k given in their Table 6. The resulting radii and errors are again somewhat different from those reported in Table 6. Here we refer only to parameters that we have recalculated.

V821 CAS

Çakirli et al. (2009) reported their radial velocity measurements of the system. Their data in Table 1 are relatively noisy compared to preset-day standards, nevertheless, we rederived the spectroscopic orbits in order to verify the consistency of the orbital parameters and quoted errors. The radial velocity semiamplitudes from our solution are marginally consistent with their values and the overall agreement of the orbit is satisfactory, also regarding the assumed errors.

Annexe X

RR-Lyrae-type pulsations from a 0.26-solar-mass star in a binary system

LETTER

doi:10.1038/nature10966

RR-Lyrae-type pulsations from a 0.26-solar-mass star in a binary system

G. Pietrzyński[1,2], I. B. Thompson[3], W. Gieren[1], D. Graczyk[1], K. Stępień[2], G. Bono[4,5], P. G. Prada Moroni[6,7], B. Pilecki[1,2], A. Udalski[2], I. Soszyński[2], G. W. Preston[3], N. Nardetto[8], A. McWilliam[3], I. Roederer[3], M. Górski[1,2], P. Konorski[1,2] & J. Storm[9]

RR Lyrae pulsating stars have been extensively used as tracers of old stellar populations for the purpose of determining the ages of galaxies, and as tools to measure distances to nearby galaxies[1–3]. There was accordingly considerable interest when the RR Lyrae star OGLE-BLG-RRLYR-02792 (referred to here as RRLYR-02792) was found to be a member of an eclipsing binary system[4], because the mass of the pulsator (hitherto constrained only by models) could be unambiguously determined. Here we report that RRLYR-02792 has a mass of 0.26 solar masses ($M_{\odot}$) and therefore cannot be a classical RR Lyrae star. Using models, we find that its properties are best explained by the evolution of a close binary system that started with $1.4M_{\odot}$ and $0.8M_{\odot}$ stars orbiting each other with an initial period of 2.9 days. Mass exchange over 5.4 billion years produced the observed system, which is now in a very short-lived phase where the physical properties of the pulsator happen to place it in the same instability strip of the Hertzsprung–Russell diagram as that occupied by RR Lyrae stars. We estimate that only 0.2 per cent of RR Lyrae stars may be contaminated by systems similar to this one, which implies that distances measured with RR Lyrae stars should not be significantly affected by these binary interlopers.

Using high-resolution spectra obtained with the MIKE spectrograph at the 6.5-m Magellan Clay telescope at the Las Campanas Observatory in Chile, and the UVES spectrograph attached to the 8.2-m VLT telescope of the European Southern Observatory on Paranal, we confirmed that RRLYR-02792 is a true physical, well detached, double-lined eclipsing binary system very well suited for deriving the masses of its two components with very high accuracy.

Analysis of the spectroscopic and photometric observations (Figs 1 and 2) results in the determination of the astrophysical parameters of our system presented in Supplementary Table 1. Realistic errors of the derived system parameters were determined using Monte Carlo simulations. The resulting masses of the components turned out to be very unexpected. The dynamical mass of the RR Lyrae component, $(0.261 \pm 0.015)M_{\odot}$, is much smaller than the mass required for helium ignition, and therefore completely at odds with the predictions of all theoretical models of RR Lyrae stars[5–7]. Moreover, if the pulsating component of RRLYR-02792 (star 1, temperature T_1) were indeed a classical RR Lyrae star, as suggested by its light curve and pulsation period, the nature of the more massive, cooler (at $T_1 = 6{,}000$ K, $T_2 = 0.68 \times T_1$) and fainter (by some two magnitudes in the V band) secondary component (star 2) would be extremely unusual. Assuming a typical temperature for the RR Lyrae star of 6,000 K, the temperature of the static secondary component (T_2) would be only about 4,100 K, much too cool for a giant star with $M_2 = 1.67M_{\odot}$ (whose temperature is expected to be close to 5,000 K).

A clue comes from the relatively short orbital period of 15.24 days, which suggests that mass exchange between the two components should have occurred during the evolution of this system. Inspired

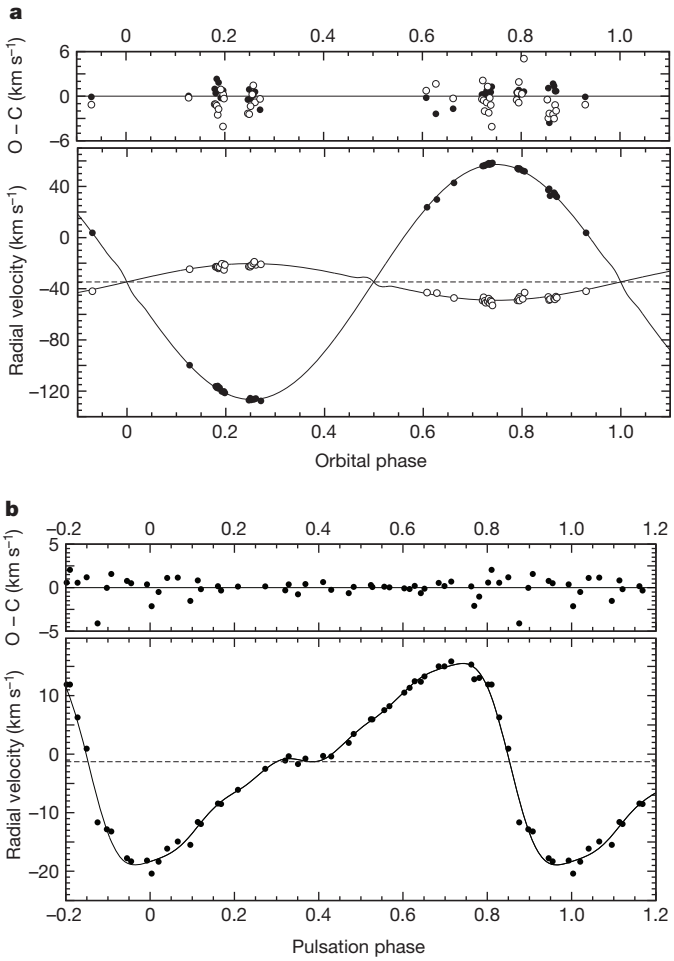


Figure 1 | Orbital motion of the two binary components, and the pulsational motion of the pulsating component of the RRLYR-02792 system. **a**, Main panel, the disentangled orbital radial velocity curves of both components of our binary system. Filled circles and open circles, primary and secondary component, respectively. **b**, The pulsational radial velocity curve of the primary component. The top panel in **a** and **b** shows the residuals of the fits (see below): observed radial velocities (O) minus the computed radial velocities (C). All individual radial velocities were determined by the cross-correlation method using appropriate template spectra and the MIKE and UVES spectra, yielding in all cases velocity accuracies better than 300 m s^{-1} (error bars smaller than the data symbols). Then, the orbit (mass ratio, systemic velocity, velocity amplitudes, eccentricity and periastron passage) plus a Fourier series of order eight approximating the pulsation variations of the primary component was fitted with a least squares method to the measured velocities. The resulting parameters are presented in Supplementary Table 1.

[1]Departamento de Astronomìa, Universidad de Concepción, Casilla 160-C, Concepciòn, Chile. [2]Obserwatorium Astronomiczne Uniwersytetu Warszawskiego, Aleje Ujazdowskie 4, 00-478 Warszawa, Poland. [3]Carnegie Observatories, 813 Santa Barbara Street, Pasadena, California 911101-1292, USA. [4]Dipartimento di Fisica Università di Roma Tor Vergata, via della Ricerca Scientifica 1, 00133 Rome, Italy. [5]Dipartimento di Fisica 'E. Fermi', Università di Pisa, Largo B. Pontecorvo, 3, I-56127, Pisa, Italy. [6]INFN, Sezione di Pisa, Largo B. Pontecorvo, 3, I-56127, Pisa, Italy. [7]INAF–Osservatorio Astronomico di Roma, Via Frascati 33, 00040 Monte Porzio Catone, Italy. [8]Laboratoire Lagrange, UMR7293, UNS/CNRS/OCA, 06300 Nice, France. [9]Leibniz Institute for Astrophysics, An der Sternwarte 16, 14482 Potsdam, Germany.

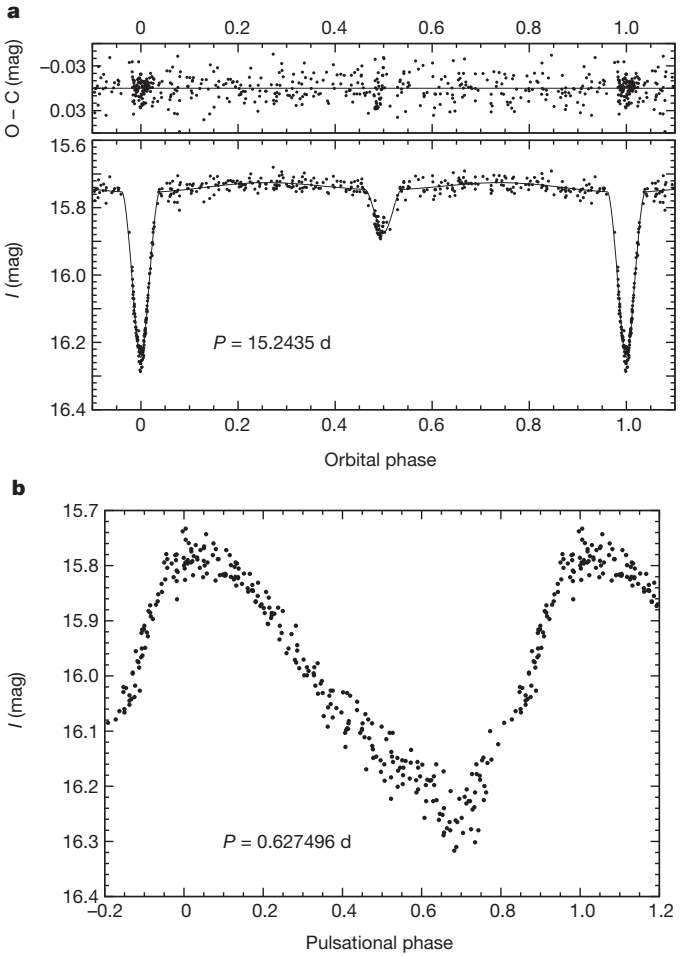


Figure 2 | Change of brightness of the binary system caused by the mutual eclipses, and the intrinsic change of the brightness of the primary component caused by its pulsations. **a**, Main panel, orbital I-band light curve (617 epochs collected over 10 years) of the binary system RRLYR-02792, after removal of the intrinsic brightness variation of the pulsating component (data points), together with the solution (solid line), as obtained with the 2007 version of the standard Wilson-Devinney code[11,12]. Top panel, the residuals of the observed magnitudes from the computed orbital light curve. **b**, Pulsational I-band light curve of the primary component of our binary system, folded on a pulsation period of 0.627496 days. The shape of the light curve is mimicking that of a classical RR Lyrae star. The following final ephemeris for our system was derived from the OGLE photometric data: $P = 15.24340 \pm 0.00021$ d, $T_0 = 2{,}452{,}108.3161 \pm 0.038$ d (orbital); $P = 0.627496 \pm 0.000008$ d, $T_0 = 2{,}455{,}000.355 \pm 0.005$ d (pulsation). Adopting the photometric ephemeris, and the mass ratio obtained from the analysis of the spectroscopic data (Fig. 1), we model our spectroscopic and photometric observations using the Wilson-Devinney code. We accounted for the intrinsic photometric variations of the pulsating star in the system by fitting a Fourier series of order 15 to the observations secured outside the eclipses and then subtract the corresponding variations in the eclipses in an iterative way, scaling the obtained fit according to the obtained Wilson-Devinney model.

by this possibility, we calculated a series of models for Algol-type binary systems[8,9]. We found that a system which initially contained two stars with $M_1 = 1.4M_\odot$ and $M_2 = 0.8M_\odot$ orbiting each other with an initial period of 2.9 days would, after 5.4 Gyr of evolution, have exchanged mass between the components as classical Algols do, and today would form a system very similar to RRLYR-02792 (with $M_1 = 0.268M_\odot$ and $M_2 = 1.665M_\odot$, and orbital period $P = 15.9$ days).

We therefore conclude that the primary component of our observed system is not a classical RR Lyrae star with its well-known internal structure. Rather, it is a star that possesses a partially degenerate helium core and a small hydrogen-rich envelope (undergoing shell burning) that has lost most of its envelope during the previous red giant branch phase to the secondary star due to mass exchange in the binary system. It is now evolving towards the hot subdwarf region on the Hertzsprung–Russell diagram (see Fig. 3 and Supplementary Fig. 2).

The pulsational light curve of such a star very closely resembles that of a classical RR Lyrae star. However, variable stars produced this way are expected to cross the classical pulsational instability region on the Hertzsprung–Russell diagram about 100 times faster than do the RR Lyrae stars. Because the star is moving rapidly at a constant luminosity across the instability strip towards higher temperatures, its radius should become smaller and therefore its pulsation period should steadily decrease. Indeed, using our photometric data we have measured a period decrease of the pulsating component of $(8.4 \pm 2.6) \times 10^{-6}$ d yr^{-1}, which is on average more than two orders of magnitude larger than the period change shown by canonical RR Lyrae stars[10], and therefore strongly supports our interpretation. Moreover, we have detected hydrogen lines in the spectrum of the binary associated with the pulsating primary component (see Supplementary Fig. 1), which

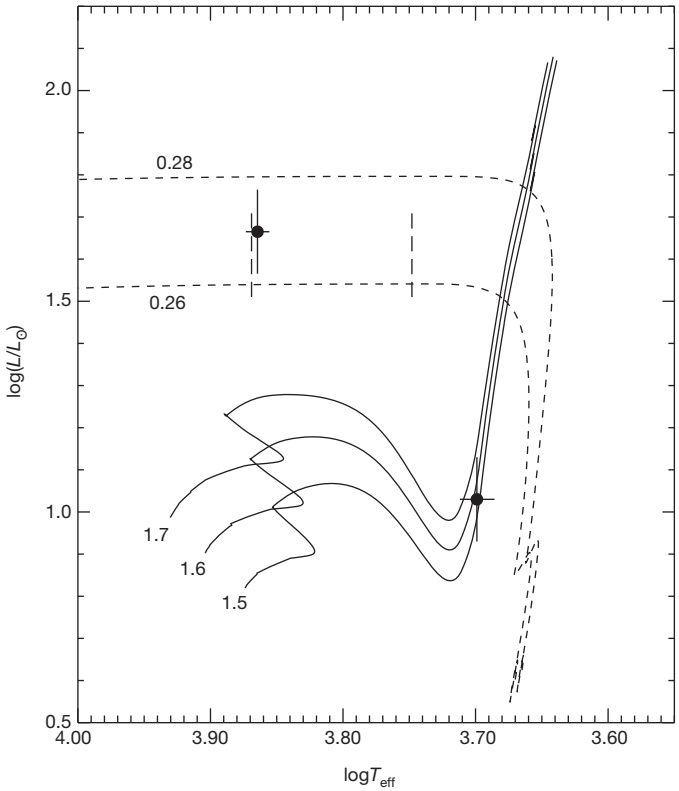


Figure 3 | Positions of the two stars in the RRLYR-02792 binary system on the Hertzsprung–Russell diagram. The two stars are shown by filled circles (error bars, 1σ); L and $L_\odot$, stellar and solar luminosity, respectively; $T_{\rm eff}$, stellar effective temperature. Solid lines show evolutionary models computed for 1.7, 1.6 and 1.5 $M_\odot$ stars with the most recent version of the FRANEC evolutionary code adopting updated input physics[13]. Current evolutionary models were computed assuming a solar chemical composition (metals, $Z = 0.0129$; helium, $Y = 0.274$). We adopted the recent heavy-element solar mixture[14] and a mixing-length value of $\alpha = 1.74$. Dashed lines proceeding horizontally from the luminosity axis show evolution of stellar structures with final masses of $0.26M_\odot$ and $0.28M_\odot$, computed by following the standard evolution of a $1.4M_\odot$ stellar structure from the pre-main sequence up to the beginning of the red giant phase. At $\log(L/R_?) = 0.9$ we applied an enhanced mass loss rate of about 10^{-7} $M_\odot$ yr^{-1} until the final masses (that is, $0.26M_\odot$ and $0.28\ M_\odot$) were approached. We computed the final evolutionary fate of these structures, at constant mass, down to the cooling phase of He-core white dwarfs[15]. The two short vertical dashed lines show the instability strip for typical RR Lyrae stars according to models for a solar chemical composition ($Z = 0.02$, $Y = 0.28$)[16], in which the pulsating component of our binary system is located. We adopted 300 K as the uncertainty of the calculated instability strip. Very good agreement between the evolutionary models and the observations is demonstrated.

Nature nature10966.3d 15/3/12 15:24:43

confirms that the star possesses a hydrogen-rich envelope. In such a scenario, the secondary component is a typical red giant star currently evolving up the red giant branch, increasing its size and luminosity. During its future evolution, our system will turn into a binary system composed of two white dwarfs sharing a common envelope.

We have captured the RRLYR-02792 binary system in a very special and short-lived phase of its evolution, which constitutes just a small fraction (10^{-4}) of its current age. The system provides a number of strong observational constraints that have enabled us to track its past evolution unambiguously and in detail, and so discover a new evolutionary channel for the production of binary pulsating stars—these are inhabitants of the pulsational instability strip on the Hertzsprung–Russell diagram that mimic classical RR Lyrae variables, but have a completely different origin. These low mass pulsating stars could in principle increase the observed spread in luminosity of the RR Lyrae stars, hence affecting distance measurements based on them. Our calculations show that among 1,000 RR Lyrae stars one should expect just 2 such stars, so in practice they should not affect distance determinations to galaxies if these are made with relatively large samples of RR Lyrae stars.

Received 19 October 2011; accepted 10 February 2012.

1. Mateo, M. Dwarf galaxies of the Local Group. *Annu. Rev. Astron. Astrophys.* **36,** 435–506 (1998).
2. Bono, G. & Cignoni, M. in *Proceedings of the Symposium ''The Three-Dimensional Universe with Gaia''* (eds Turon, C., O'Flaherty, K. S. & Perryman, M. A. C.) 659–666 (ESA SP-576, 2005).
3. Szewczyk, O. *et al.* The Araucaria Project. The distance of the Large Magellanic Cloud from near-infrared photometry of RR Lyrae variables. *Astron. J.* **136,** 272–279 (2008).
4. Soszyński, I. *et al.* The Optical Gravitational Lensing Experiment. The OGLE-III catalog of variable stars. XI. RR Lyrae stars in the Galactic Bulge. *Acta Astron.* **61,** 1–23 (2011).
5. Christy, R. F. A study of pulsation in RR Lyrae models. *Astron. J.* **69,** 536–537 (1964).
6. Smith, H. A. *RR Lyrae Stars* (Cambridge Univ. Press, 2004).
7. Bono, G. *et al.* A pulsational approach to near-infrared and visual magnitudes of RR Lyr stars. *Mon. Not. R. Astron. Soc.* **344,** 1097–1106 (2003).
8. Stępień, K. Evolution of cool close binaries — approach to contact. *Acta Astron.* **61,** 139–159 (2011).
9. Stępień, K. Evolutionary status of late-type contact binaries. *Acta Astron.* **56,** 199–218 (2006).
10. Kunder, A. *et al.* Period change similarities among the RR Lyrae variables in Oosterhoff I and Oosterhoff II globular systems. *Astron. J.* **141,** 15–28 (2011).
11. Wilson, R. E. & Devinney, E. J. Realization of accurate close-binary light curves: application to MR Cygni. *Astrophys. J.* **166,** 605–620 (1971).
12. Van Hamme, W. & Wilson, R. E. Third-body parameters from whole light and velocity curves. *Astrophys. J.* **661,** 1129–1151 (2007).
13. Tognelli, E., Prada Moroni, P. G. & Deg'Innocenti, S. The Pisa pre-main sequence tracks and isochrones. A database covering a wide range of Z, Y, mass, and age values. *Astron. Astrophys.* **533,** A109 (2011).
14. Asplund, M., Grevesse, N., Sauval, A. J. & Scott, P. The chemical composition of the Sun. *Annu. Rev. Astron. Astrophys.* **47,** 481–522 (2009).
15. Prada Moroni, P. G. & Staniero, O. Very low-mass white dwarfs with a C-O core. *Astron. Astrophys.* **507,** 1575–1583 (2009).
16. Bono, G., Caputo, F., Cassisi, S., Incerpi, R. & Marconi, M. Metal-rich RR Lyrae variables. II. The pulsational scenario. *Astrophys. J.* **483,** 811–825 (1997).

Supplementary Information is linked to the online version of the paper at www.nature.com/nature.

Acknowledgements We acknowledge financial support from the Chilean Center for Astrophysics FONDAP, the BASAL Centro de Astrofisica y Tecnologias Afines (CATA), NSF, the Polish Ministry of Science (Ideas Plus), the Foundation for Polish Science (FOCUS, TEAM), and the GEMINI-CONICYT found. The OGLE project received funding from the European Research Council 'Advanced Grant' Program. We thank the staff astronomers at Las Campanas and ESO Paranal (program 287.D-5022(A)) who provided support in data acquisition.

Author Contributions G.P., photometric and spectroscopic observations and reductions, and data analysis. I.B.T., spectroscopic observations and reductions, radial velocity measurements, and data analysis. W.G., spectroscopic observations and data analysis. D.G., modelling and data analysis. K.S., theoretical models and analysis. G.B., theoretical models. A.U., photometric observations and reductions, and data analysis. I.S., photometric observations and reductions. B.P. and P.G.P.M., modelling. G.W.P., N.N., M.G., J.S. and P.K., analysis of the data. A.M. and I.R., spectroscopic observations. G.P. and W.G. worked jointly to draft the manuscript, with all authors reviewing and contributing to its final form.

Author Information Reprints and permissions information is available at www.nature.com/reprints. The authors declare no competing financial interests. Readers are welcome to comment on the online version of this article at www.nature.com/nature. Correspondence and requests for materials should be addressed to G.P. (pietrzyn@astrouw.edu.pl).

RESEARCH LETTER

Author Queries

Journal: **Nature**
Paper: **nature10966**
Title: **RR-Lyrae-type pulsations from a 0.26-solar-mass star in a binary system**

Query Reference	Query
1	AUTHOR: When you receive the PDF proofs, please check that the display items are as follows (doi:10.1038/nature10966): Figs 1, 2, 3 (black & white); Tables: None; Boxes: None. Please check all figures (and tables, if any) very carefully as they have been re-labelled, re-sized and adjusted to Nature's style. Please ensure that any error bars in the figures are defined in the figure legends. As part of our commitment to quality, the websum, title and first paragraph will be read by another subeditor before the PDF proofs are produced, and **further changes may have been made**. Please update any 'in the press' or 'submitted' or 'preprint' references if possible.
2	Author: A single sentence summarising your paper, which will appear online on the table of contents and in e-alerts, has been provided below. Please check this sentence for accuracy.
3	AUTHOR: note title revision, after discussion with editor and subeditors
4	AUTHOR: OK?
Web summary	The pulsating star OGLE-BLG-RRLYR-02792 is known to be a member of an eclipsing binary system, and its mass is now determined to be only 0.26 times that of the Sun, meaning that it cannot be a classical RR Lyrae pulsator.

For Nature office use only:

Layout	☐	Figures/Tables/Boxes	☐	References	☐
DOI	☐	Error bars	☐	Supp info (if applicable)	☐
Title	☐	Colour	☐	Acknowledgements	☐
Authors	☐	Text	☐	Author contribs (if applicable)	☐
Addresses	☐	Methods (if applicable)	☐	COI	☐
First para	☐	Received/Accepted	☐	Correspondence	☐
Display items	☐	AOP (if applicable)	☐	Author corrx	☐
				Web summary	☐

Annexe Y

Physical parameters and the projection factor of the classical Cepheid in the binary system OGLE-LMC-CEP-0227

Monthly Notices of the ROYAL ASTRONOMICAL SOCIETY
MNRAS **436,** 953–967 (2013) doi:10.1093/mnras/stt1529
Advance Access publication 2013 October 9

Physical parameters and the projection factor of the classical Cepheid in the binary system OGLE-LMC-CEP-0227

B. Pilecki,[1,2]★ D. Graczyk,[2] G. Pietrzyński,[1,2] W. Gieren,[2,3,4] I. B. Thompson,[5] W. L. Freedman,[5] V. Scowcroft,[5] B. F. Madore,[5] A. Udalski,[1] I. Soszyński,[1] P. Konorski,[1] R. Smolec,[6] N. Nardetto,[7] G. Bono,[8,9] P. G. Prada Moroni,[10,11] J. Storm[12] and A. Gallenne[2]

[1]*Warsaw University Observatory, Al. Ujazdowskie 4, PL-00-478 Warszawa, Poland*
[2]*Departamento de Astronomía, Universidad de Concepción, Casilla 160-C, Concepción, Chile*
[3]*University Observatory Munich, Scheinerstrasse 1, D-81679 Munich, Germany*
[4]*Max Planck Institute for Extraterrestrial Physics, Giessenbachstrasse, D-85748 Garching, Germany*
[5]*Carnegie Observatories, 813 Santa Barbara Street, Pasadena, CA 91101-1292, USA*
[6]*Copernicus Astronomical Centre, Polish Academy of Sciences, Bartycka 18, PL-00-716 Warsaw, Poland*
[7]*Laboratoire Lagrange, UMR7293, UNS/CNRS/OCA, F-06300 Nice, France*
[8]*Dipartimento di Fisica Universit'a di Roma Tor Vergata, viadella Ricerca Scientifica 1, I-00133 Rome, Italy*
[9]*INAF – Osservatorio Astronomico di Roma, Via Frascati 33, I-00040 Monte Porzio Catone, Italy*
[10]*Dipartimento di Fisica E. Fermi, Universit'a di Pisa, Largo B. Pontecorvo 3, I-56127 Pisa, Italy*
[11]*INFN, Sezione di Pisa, Largo B. Pontecorvo 3, I-56127 Pisa, Italy*
[12]*Leibniz-Institut f ur Astrophysik Potsdam (AIP), An der Sternwarte 16, D-14482 Potsdam, Germany*

Accepted 2013 August 10. Received 2013 July 25; in original form 2013 July 3

ABSTRACT

A novel method of analysis of double-lined eclipsing binaries containing a radially pulsating star is presented. The combined pulsating–eclipsing light curve is built up from a purely eclipsing light-curve grid created using an existing modelling tool. For every pulsation phase, the instantaneous radius and surface brightness are taken into account, being calculated from the disentangled radial velocity curve of the pulsating star and from its out-of-eclipse pulsational light curve and the light ratio of the components, respectively. The best model is found using the Markov chain Monte Carlo method. The method is applied to the eclipsing binary Cepheid OGLE-LMC-CEP-0227 ($P_{\rm puls} = 3.80$ d, $P_{\rm orb} = 309$ d). We analyse a set of new spectroscopic and photometric observations for this binary, simultaneously fitting OGLE *V*-band, *I*-band and *Spitzer* 3.6 μm photometry. We derive a set of fundamental parameters of the system significantly improving the precision comparing to the previous results obtained by our group. The Cepheid mass and radius are $M_1 = 4.165 \pm 0.032\,{\rm M}_\odot$ and $R_1 = 34.92 \pm 0.34\,{\rm R}_\odot$, respectively. For the first time a direct, geometrical and distance-independent determination of the Cepheid projection factor is presented. The value $p = 1.21 \pm 0.03({\rm stat.}) \pm 0.04({\rm syst.})$ is consistent with theoretical expectations for a short-period Cepheid and interferometric measurements for δ Cep. We also find a very high value of the optical limb darkening coefficients for the Cepheid component, in strong disagreement with theoretical predictions for static atmospheres at a given surface temperature and gravity.

Key words: binaries: eclipsing – stars: distances – stars: oscillations – stars: variables: Cepheids.

1 INTRODUCTION

Radially pulsating stars like Cepheids, RR Lyrae or Miras stars are important distance indicators in the local Universe. The presence of such a variable star in an eclipsing binary system serves as a unique opportunity to derive fundamental astrophysical parameters of the pulsating component with few model assumptions. Furthermore, eclipsing binaries provide a very good means to independently calibrate distance determination methods based on pulsating stars by comparison with the distance obtained from the binary star analysis. Until now only a few classical Cepheids were identified

★ E-mail: pilecki@astrouw.edu.pl

© 2013 The Authors
Published by Oxford University Press on behalf of the Royal Astronomical Society

Downloaded from http://mnras.oxfordjournals.org/ at :: on February 17, 2014

in eclipsing binaries (Pietrzyński et al. 2010, 2011) and one system with a pseudo-RR Lyrae component was reported (Pietrzyński et al. 2012), there are also candidates for such systems that await confirmation.

The typical eclipsing binary star model consists of fixed-size stars. To account for pulsations, one usually (1) modifies an existing modelling tool, (2) develops a new computer code, (3) removes pulsations from light and radial velocity (RV) curves and solves them with an ordinary eclipsing binary star model. The first approach was used by Wilson & van Hamme (2010) in the case of the well-known Wilson–Devinney code (Wilson & Devinney 1971; hereafter the WD code), but only some phenomenological model was reported. The second approach was employed by the MACHO project to eclipsing binary Cepheids (Alcock et al. 2002; Lepischak, Welch & van Kooten 2004); however, the code was restricted only to a light-curve analysis and a rather simplistic treatment of stellar surfaces was used (e.g. no proximity and reflection effects were accounted for). The third method seems to be the most common and is used in the case of non-radial pulsators like δ-Scuti stars (e.g. Southworth et al. 2011) or γ-Doradus stars (e.g. Maceroni et al. 2013). The drawback of such an approach is that during eclipses pulsations can be removed only approximately from the light curves, which produces some systematic residua in the solution. The way to partly overcome this difficulty is to employ the iterative light-curve solution with the amplitude of the pulsations scaled according to the relative light contribution of a pulsating star during eclipses. This method was applied by Pietrzyński et al. (2010, 2011). To deal fully with changes in the eclipse geometry caused by pulsations, a novel approach is needed where both spectroscopic and photometric data are treated consistently.

We present here a new method of modelling eclipsing binaries with radially pulsating components. Instead of a new code development, we decided to use a well-known and thoroughly tested computer model called JKTEBOP (Popper & Etzel 1981; Southworth, Maxted & Smalley 2004; Southworth, Bruntt & Buzasi 2007) as a core of our method. A PYTHON-based wrapper that we prepared can generate binary light curves with pulsations taken into account using the original JKTEBOP code without any modifications. A similar methodology was proposed by Riazi & Abedi (2006) in the case of the WD code, but only for illustrative purposes.

The method was applied to the case of the eclipsing binary Cepheid OGLE-LMC-CEP-0227 (Soszyński et al. 2008; Pietrzyński et al. 2010) in the Large Magellanic Cloud (LMC). One of the main reasons to develop our approach was to directly determine the projection factor (p-factor) for the Cepheid from an eclipsing binary analysis. The p-factor is defined as the conversion factor between the observed pulsation RVs and the velocity of the pulsating star's photosphere. It plays a crucial role in Baade–Wesselink (Baade 1926; Wesselink 1946) type methods employed to pulsating stars like Cepheids. Its exact value and functional dependence on e.g. pulsation period is currently actively debated – see Section 4.3 for references. In our opinion, the presented method allows for a robust determination of the p-factor for pulsating components of detached eclipsing binary systems.

Three groups were involved in the process of the preparation of this paper, namely the Araucaria project (data, software, analysis), the Carnegie Hubble Project (CHP; data) and the OGLE project (data). The research was based on observations obtained for European Southern Observatory (ESO) programmes 086.D-0103(A), 085.D-0398(A), 084.D-0640(A,B) and time allocation 2010B-059 granted by the Chilean National Time Allocation Committee.

2 DATA

Before starting the analysis, we had to make sure that we have good enough data to obtain reliable results. When the discovery of the object was announced in 2008 by Soszyński et al., the eclipses were rather scarcely covered by the photometry and this analysis would not be possible. Since then as a result of a special observing programme, a strong emphasis was put on the measurement of the brightness change during eclipses.

In total, we acquired 1045 measurements in the I band and 317 in the V band collected with the Warsaw telescope by the OGLE project (Udalski 2003; Soszyński et al. 2012) and during the time granted to the Araucaria project by CNTAC organization. The auxiliary K-band data (only outside eclipses) were acquired by the Araucaria group using the SOFI instrument attached to the New Technology Telescope at La Silla Observatory, which allowed us to use the $V - K$ colour variation to calculate the effective temperature as a function of the pulsation phase. We have also acquired 3.6 and 4.5 μm photometry from the *Spitzer Space Telescope* (114 points) – the observations and data reduction provided by the CHP team. Because in the near-infrared the stellar limb darkening (LD) is low and the amplitude of the pulsations is small, these observations put an important constraint on the geometry of the system. Fig. 1 presents all the photometric data used in our analysis. The *Spitzer* data were collected for two consecutive eclipses, i.e. for one primary and one secondary eclipse, and for one pulsation cycle outside the eclipses to obtain the unaffected pulsational light curve. In the analysis, we used only 3.6 μm photometry because the out-of-eclipse observations in the 4.5 μm band were too scarce and had the signal-to-noise ratio too low to obtain a correct representation of the pulsations (which could subsequently be used in the modelling) at this moment. We plan to complement the data in the future, however. All the photometry used in this paper is provided in Tables 1–3 and in electronic form at http://araucaria.astrouw.edu.pl/p/cep227.

The photometry alone, however, is not sufficient to obtain the absolute values of some important parameters such as mass or scale of the system. Using the MIKE spectrograph at the 6.5 m Magellan Clay telescope at Las Campanas Observatory in Chile, the

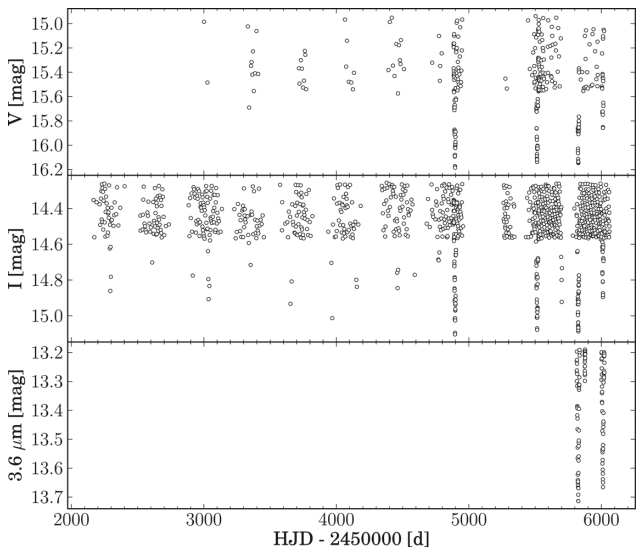


Figure 1. All photometric data collected for OGLE-LMC-CEP-0227. Upper panel: OGLE V-band data, middle panel: OGLE I-band data, lower panel: *Spitzer* 3.6 μm data. Note the difference in the eclipse coverage after the detection of the system at HJD about 245 4900 d.

Downloaded from http://mnras.oxfordjournals.org/ at :: on February 17, 2014

Table 1. OGLE *V*-band photometry sample (the full version is available online). The errors are scaled to match the condition that the reduced χ^2 is equal to 1.

HJD − 245 0000 d	*V* (mag)	Error (mag)
3001.649 90	14.984	0.008
3026.749 85	15.484	0.008
3331.741 55	15.023	0.008
3341.745 43	15.690	0.008
3355.739 41	15.347	0.008
3359.668 48	15.316	0.008
3365.648 74	15.419	0.008
–	–	–

Table 2. OGLE *I*-band photometry sample (the full version is available online). The errors are scaled to match the condition that the reduced χ^2 is equal to 1.

HJD − 245 0000 d	*I* (mag)	Error (mag)
2166.837 48	14.353	0.007
2172.886 23	14.561	0.007
2189.843 43	14.365	0.007
2212.791 65	14.377	0.007
2217.776 57	14.492	0.007
2223.796 86	14.345	0.007
2226.771 67	14.303	0.007
–	–	–

Table 3. *Spitzer* 3.6 μm photometry sample (the full version is available online). The errors are scaled to match the condition that the reduced χ^2 is equal to 1.

HJD − 245 0000 d	3.6 μm (mag)	Error (mag)
5813.541 49	13.229	0.007
5813.999 99	13.264	0.007
5814.570 68	13.299	0.007
5814.908 75	13.262	0.007
5815.557 75	13.197	0.007
5816.058 59	13.225	0.007
5816.580 69	13.239	0.007
–	–	–

HARPS spectrograph attached to the 3.6 m telescope at La Silla Observatory and the UVES spectrograph on VLT at Paranal Observatory, we obtained 123 high-resolution spectra at 116 epochs (49 MIKE + 27 HARPS + 40 UVES) – 76 more than those reported in Pietrzyński et al. (2010). All the observations were performed by the Araucaria project. Using these data we also confirmed the OGLE-LMC-CEP-0227 (hereafter CEP-0227) to be a classical fundamental-mode Cepheid pulsator in a well-detached, double-lined, eclipsing system. The object turned out to have near-perfect properties for deriving the masses of its two components with a very high accuracy.

RVs of both components were measured using the RAVESPAN application (Pilecki, Konorski & Górski 2012). We have used the broadening function formalism (Rucinski 1992, 1999) with templates matching the stars in the temperature–gravity plane. The templates were theoretical spectra taken from the library of Coelho et al. (2005). For deriving RVs, we have analysed the spectra in the range of 4125–6800 Å. The typical formal errors of the derived velocities are $\sim$300 m s^{-1}. In the case of a Cepheid component, the orbital motion had to be extracted from the original RVs by the subtraction of the pulsational RVs. We assumed a mutual Keplerian motion of both components with a constant orbital period, that the stars were point-like sources (i.e. no proximity effects, like star's oblateness, were incorporated at this stage of analysis) and that the pulsation RV curve could be represented by the Fourier series. We fitted simultaneously the orbital period P, eccentricity e, periastron longitude ω, both velocity semi-amplitudes K_1 and K_2, both star systemic velocities γ_1 and γ_2, and a number of Fourier series coefficients (depending on the series order). In Table 4, the orbital radial velocities of both components, RV_1 and RV_2, together with the pulsation radial velocities of the Cepheid RV_p are presented. The original Cepheid radial velocities are simply $\mathrm{RV} = \mathrm{RV}_1 + \mathrm{RV}_p$. The analysis confirmed the presence of the *K*-term effect (Nardetto et al. 2008 and references therein), which affects Cepheid-type stars: the Cepheid systemic velocity is blueshifted in respect to the companion systemic velocity by 0.59 km s^{-1}.

3 METHOD

3.1 Light-curve synthesis

As far as we know, there is no generally available software that allows us to model binary eclipsing stars with pulsating components in a fully consistent physical way. So first, we developed a scheme which was later on followed by the software application that allows the standard modelling tools, such as the WD or JKTEBOP code, to model this kind of systems.

The trick is to generate multiple eclipsing light curves for different stages of a pulsating component while the parameters of the pulsating star remain fixed for every single light curve generated. In this way, we obtain a two-dimensional light curve that depends on both pulsational and orbital phases. Later on for every observation point, both orbital and pulsation phases are calculated and used to obtain a corresponding brightness from the 2D grid. A bilinear interpolation is used to calculate the brightness between the grid points to improve the efficiency and accuracy of the method.

(i) *Generation of the two-dimensional light curve*.

For N uniformly spaced phases ($N = 100$ in our approach) of the pulsation cycle, we calculate the full eclipsing model using the JKTEBOP code. The generated light curve consists of $M = 2000$ points uniformly covering the orbital cycle. This number comes from a compromise between the accuracy of modelling the minima shape and the numerical efficiency of the code. In calculating the N models, we take into account the following pulsation phase-*dependent* parameters: the fractional radius of the primary r_1, the surface-brightness ratio of the components j_{21} and the brightness of the system in a given band (the light scale factor expressed in magnitudes). And the following pulsation phase-*independent* parameters are kept fixed: the fractional radius of the secondary r_2, the eccentricity e, the periastron longitude ω, the orbital inclination i, the mass ratio $q = m_2/m_1$ and the reference time of the primary minimum T_0. The fractional radii are the physical radii, R_1 and R_2, divided by the semimajor axis a. The pulsation period is kept constant and the pulsation phase is calculated according to the following ephemeris:

$$T_{\max}(\mathrm{HJD}) = 245\,4896.285 + 3.797\,086 \times E, \quad (1)$$

where $T_{\max}$ refers to the moment of the Cepheid's maximum optical brightness. The reflection and proximity effects are taken into account internally by the JKTEBOP code, but in the case of CEP-0227

Downloaded from http://mnras.oxfordjournals.org/ at :: on February 17, 2014

Table 4. RV measurements of CEP-0227. HARPS spectra are marked with [a] and UVES spectra are marked with [b].

HJD −245 0000 d	RV_1 (km s^{-1})	RV_2 (km s^{-1})	RV_p (km s^{-1})	HJD −245 0000 d	RV_1 (km s^{-1})	RV_2 (km s^{-1})	RV_p (km s^{-1})	HJD −245 0000 d	RV_1 (km s^{-1})	RV_2 (km s^{-1})	RV_p (km s^{-1})
4810.764 70[a]	288.44	223.94	3.40	5148.726 71	292.06	219.71	3.50	5457.872 58	293.69	220.22	10.72
4811.585 24[a]	288.94	223.57	15.08	5149.701 21	291.62	219.80	17.26	5459.730 87[b]	292.05	219.63	−2.22
4854.608 58	285.72	225.99	−26.84	5149.817 00[b]	292.10	220.04	18.69	5459.822 42	292.77	220.81	0.19
4854.766 34	287.31	226.63	−23.86	5150.660 19[b]	291.49	219.98	−26.65	5459.877 34	292.35	220.74	0.84
4855.628 40	286.57	226.81	−7.73	5150.810 70[b]	290.88	220.03	−26.82	5459.883 46[b]	291.38	219.94	−0.02
4882.543 81	270.06	243.88	−2.23	5151.622 74[b]	291.74	220.89	−12.04	5460.864 28[b]	291.75	220.58	14.85
5129.670 36	292.48	220.78	3.26	5151.726 85[b]	291.48	220.84	−9.99	5461.718 18[b]	291.33	220.31	1.93
5129.686 27	292.43	220.70	3.42	5152.627 06[b]	291.15	220.70	5.38	5461.848 96[b]	291.24	220.97	−17.29
5129.778 28	292.57	220.69	4.90	5152.715 53[b]	290.87	221.07	6.94	5462.749 56[b]	291.19	220.87	−17.54
5129.794 50	292.60	220.68	5.20	5155.609 58	290.48	222.21	−7.87	5463.738 92[b]	290.50	221.10	1.27
5129.852 84	292.72	220.89	6.39	5155.718 77	290.45	222.26	−5.61	5463.876 52[b]	290.72	221.30	3.56
5130.672 81	292.89	220.30	17.69	5155.718 95	290.02	222.31	−6.03	5464.736 57[b]	290.47	221.45	15.64
5130.687 89	292.62	220.38	17.69	5155.840 86	290.82	222.69	−3.35	5464.870 24[b]	290.30	221.44	17.73
5131.677 96	293.56	220.37	−25.20	5167.786 17[b]	285.18	227.84	5.46	5465.705 13[b]	290.12	221.67	−22.52
5131.693 89	293.32	220.18	−25.51	5169.598 89[b]	284.39	228.61	−24.86	5465.819 25[b]	289.79	221.63	−26.61
5131.787 65	292.96	220.14	−25.60	5174.841 69[b]	280.30	231.55	−4.09	5466.708 71[b]	289.60	222.23	−14.11
5131.803 56	292.42	220.19	−26.06	5185.535 22[a]	273.67	237.70	−18.20	5466.811 83[b]	289.54	222.59	−11.69
5131.852 65	293.03	220.25	−25.19	5185.652 59[a]	274.36	239.12	−15.18	5467.753 39[b]	289.34	222.65	4.92
5131.863 98	292.36	220.00	−25.80	5185.799 25[a]	273.48	238.98	−12.38	5468.696 82[b]	288.61	222.95	17.88
5132.679 72	292.99	220.00	−10.91	5187.537 94[a]	273.26	239.88	16.16	5468.850 45[b]	290.13	222.85	20.08
5132.693 56	292.98	220.06	−10.62	5187.686 99[a]	271.54	239.89	16.97	5469.683 92[a]	289.74	224.34	−25.09
5132.693 58	293.54	220.02	−10.05	5187.801 19[a]	272.91	240.05	19.16	5477.793 64[a]	283.78	227.69	−19.80
5132.760 78	293.15	220.21	−9.00	5251.529 15	238.30	273.28	8.94	5477.870 33[a]	284.65	227.85	−18.25
5132.773 22	293.25	220.18	−8.64	5251.529 20	238.60	273.91	9.24	5478.875 48[a]	283.67	228.16	0.45
5132.852 91	293.04	220.14	−7.12	5251.590 65	238.78	274.38	10.58	5479.788 87[a]	283.59	228.98	14.66
5132.866 01	293.05	220.40	−6.84	5251.641 29	238.57	274.67	11.27	5479.876 35[a]	284.03	228.66	15.73
5132.879 16	292.97	220.19	−6.64	5251.641 31	238.84	274.60	11.54	5502.843 68[a]	269.47	243.35	18.43
5141.776 86[b]	293.27	219.22	14.23	5251.694 66	238.54	274.81	12.14	5559.581 84[b]	239.06	272.86	14.74
5144.624 52[a]	292.97	219.09	−1.41	5251.694 69	238.96	274.91	12.56	5560.803 61[b]	238.73	274.02	−26.25
5144.689 58[a]	293.58	219.16	0.46	5251.748 36	238.41	275.08	12.86	5561.811 70[b]	237.77	273.55	−10.43
5144.762 37[a]	293.90	219.11	2.15	5272.502 51	232.83	280.22	−23.32	5582.556 97[b]	232.90	280.11	18.03
5145.646 71[a]	292.38	219.63	13.99	5272.552 69	232.64	280.70	−22.32	5583.560 84[b]	231.99	280.22	−26.60
5145.721 54[a]	294.21	219.98	16.28	5272.634 51	231.82	280.75	−21.27	5584.641 51[b]	232.31	280.73	−8.55
5146.611 50[a]	291.77	220.04	−7.11	5272.634 54	232.47	281.15	−20.61	5588.595 91[b]	231.20	281.25	−5.65
5146.672 62[a]	292.15	220.02	−15.48	5272.682 01	233.08	281.10	−19.19	5590.535 41	231.57	282.04	22.62
5146.736 21[a]	292.75	219.22	−21.43	5272.682 14	233.53	281.42	−18.74	5590.582 81	230.76	281.71	22.36
5146.799 51[a]	293.61	219.38	−24.13	5431.783 59[a]	290.07	223.10	−25.14	5590.638 37	230.56	282.11	21.27
5147.559 95[b]	294.12	220.78	−16.46	5431.825 87[a]	288.39	223.70	−26.60	5590.638 46	230.56	281.51	21.26
5147.699 97[b]	293.16	219.99	−14.64	5431.887 40[a]	290.85	222.81	−23.66	5590.684 03	231.89	282.54	20.08
5147.831 39[b]	292.56	219.89	−12.01	5457.758 68	291.65	220.75	19.98	5590.724 19	232.35	283.02	16.82
5148.633 34[b]	292.19	219.97	2.27	5457.816 26	292.94	220.54	16.88	5598.667 55[b]	230.19	282.81	−25.09

(being of the order of 0.001 mag) they are of minor importance. As a result, we obtain a two-dimensional grid of magnitudes $m = m(\phi_{\rm orb}, \phi_{\rm puls})$ for each photometric band (V, I_C and *Spitzer* 3.6 μm) we use.

The radius of the pulsating component changes during the pulsation cycle. To account for this effect, we use the Cepheid disentangled pulsational RVs and the projected semimajor axis of the system $a \sin i$ – see details in Section 3.3.

The light scale factor is calculated from the out-of-eclipse light curve for a given pulsation phase. To parametrize the pulsations, we use a ninth-order Fourier series for the V and I bands and a sixth-order one for the *Spitzer* data. Next, this fit is used to set the light scale factor for all N pulsation phases in every band. These out-of-eclipse light curves and Fourier fits are presented in Fig. 2.

The method to calculate the actual surface-brightness ratio of the components is presented in Section 3.4. The LD coefficients were treated with special attention and we worked out the methodology to treat them in a consistent way within the model, for details see Section 3.5. Reflection coefficients were calculated from the model geometry. The gravitational brightening was set to 0.32 – a value typical for a convective envelope of a late-type star.

(ii) *Creation of 1D light curve from the 2D one*.

Once all purely eclipsing models (without pulsations) are calculated for a set of different pulsation phases (from 0.0 to 1.0) we are ready to calculate a 1D light curve that exhibits pulsations. For this we need the specific epochs of observation, because the pulsational and eclipsing variabilities are independent. Thus, for each measurement we calculate both the phases and take from the 2D grid the interpolated value that best represents the actual brightness of the system in a given photometric band. This allows us to obtain a direct eclipsing binary light-curve model with a pulsating component like the one in Figs 3 and 4. Note that those figures were simplified to present the idea with more clarity. In reality, we do not use brightness values from where the diagonal lines cross the light curve; we use the brightness values for the exact (calculated) pulsation phases.

Downloaded from http://mnras.oxfordjournals.org/ at :: on February 17, 2014

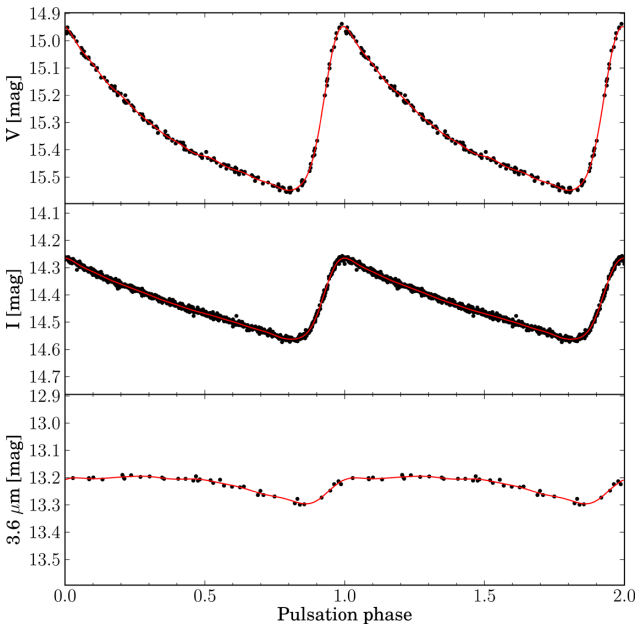


Figure 2. Out-of-eclipse light curves of CEP-0227 folded with the ephemeris given in equation (1). The overplotted ninth (V and I) and sixth (3.6 μm) order Fourier fits (solid lines) are used to calculate the light scale factor expressed in magnitudes for a given pulsation phase which is an input parameter of JKTEBOP.

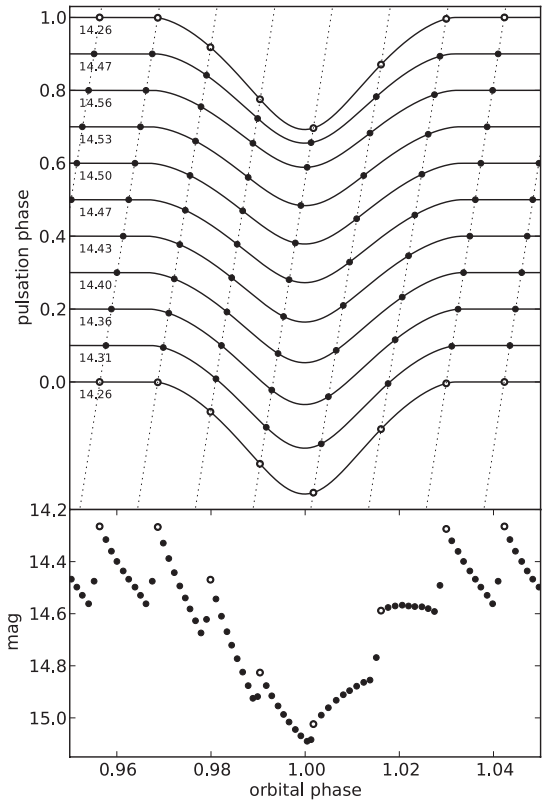


Figure 3. Generation of a 1D light curve (lower panel) from the 2D grid of light curves. Upper panel: this plot shows a small subset (just 10) of fixed-radius eclipsing models for different phases of a pulsating component centred on a primary minimum. The size and shape of the eclipses change as we move through the Y-axis. Small numbers on the left side denote the brightness of the system at the maximum. The pulsation maxima are marked with open circles. The diagonal lines mark the propagation of the pulsation phase as we move through the orbital phase – the pulsation period is many times shorter than the orbital one. Lower panel: the resulting light curve when a pulsating component is obscured by a companion.

As for the pulsation phase, there is also a small correction applied at this moment during the selection of the best model from the grid, due to the light time travel effect (see Section 3.6 for details).

In the way described above, we manage to obtain a light-curve model for a given set of orbital and stellar parameters. In order to find the set of parameters giving the best fit to the observations, we decided to employ the Markov chain Monte Carlo (MCMC) approach (Press et al. 2007). To fully explore the parameter space, we allow for the change of the following parameters: the fractional radius of the pulsating component at phase 0.0 (pulsational), the fractional radius of the second component, the orbital inclination, the orbital period, the reference time of the primary minimum, the eccentricity related parameters ($e\cos\omega$, $e\sin\omega$), the component surface-brightness ratios in all the used bands at phase 0.0 (pulsational), the p-factor and the third light l_3.

3.2 Markov chain Monte Carlo

We decided to use the Monte Carlo (MC) method as it allowed us to realistically estimate errors of the parameters. Specifically, we have used the Metropolis–Hastings algorithm (Hastings 1970) – one of the MCMC random-walk methods, which has an advantage over non-random-walk MC sampling being in general independent of the starting point (unless we start it close to the other deep local minimum) and sampling the χ^2 plane with greater density where the χ^2 values are lower. As the acceptance function, we use the normal distribution function. The method was also modified by the incorporation of simulated annealing (Press et al. 2007) – the probability of jumping away from the χ^2 minimum decreases as the number of calculated models increases. We would like to emphasize here that we fit all the light curves simultaneously, i.e. geometry-related parameters like radii, orbital inclination, p-factor, etc. are common to all bands. The observations are weighted by their observational errors and their modal values are 0.009, 0.007 and 0.008 mag in V, I_C and 3.6 μm, respectively. At the initial stage, all errors were scaled to match the condition that for every single light curve the reduced χ^2 should be equal to unity.

To obtain the well-sampled χ^2 plane for 12 fitted parameters, we need about 50 000 models to be calculated. While 10 000 give a good estimate of the best solution, at least five times more models are needed to reliably estimate the errors.

3.3 Radius change

The radius absolute change of the pulsating component can be found directly from integrating the pulsation RV curve:

$$\Delta R_1(t,p) = B\int p\,(v_{\rm r}(t) - v_{\rm s})\,{\rm d}t = pD(t), \qquad (2)$$

where p is the projection factor, $v_{\rm r}$ is the radial velocity, B is a conversion unit factor and $v_{\rm s}$ is the Cepheid systemic velocity with respect to the system barycentre. If we choose units to be solar radii for length, km s^{-1} for velocity and days for time, we get $B = 0.124\,22$. The systemic velocity $v_{\rm s}$ is selected to give a zero net effect of the radius change after a pulsation cycle, i.e. we require the

Downloaded from http://mnras.oxfordjournals.org/ at :: on February 17, 2014

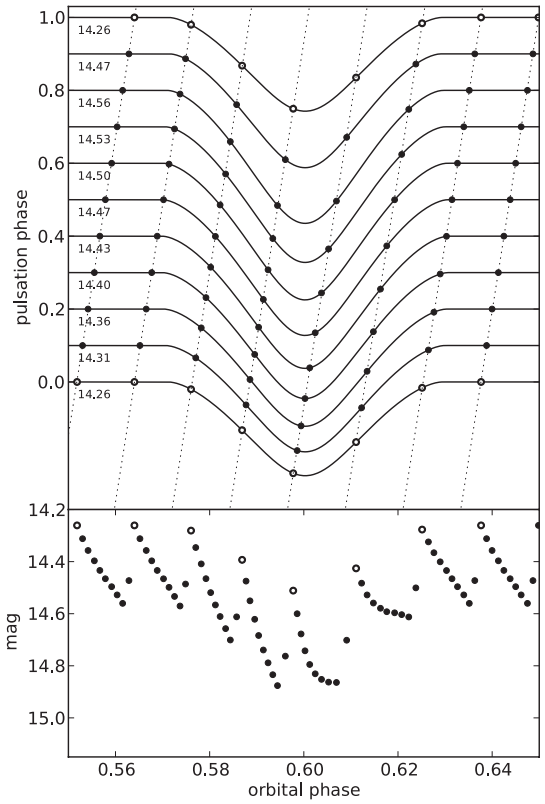


Figure 4. Same plot as in Fig. 3 but for the secondary eclipse. Lower panel: the resulting light curve when a pulsating component passes in front of its companion.

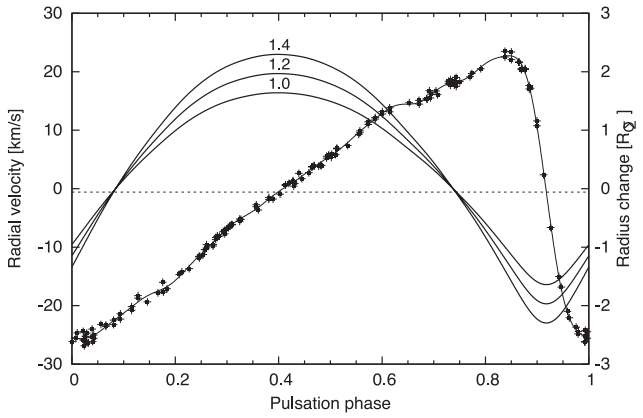


Figure 5. Pulsational RVs of the Cepheid CEP-0227 (crosses) with the overplotted 12th-order Fourier series fit. The dashed straight line corresponds to the Cepheid's systemic velocity of -0.59 km s^{-1} in respect to the barycentre of the system. Three continuous lines correspond to the Cepheid's radius changes, in respect to the mean radius, for the projection factor values of 1.0, 1.2 and 1.4.

star to have always the same radius at a given phase. Fig. 5 shows the pulsational RV curve used in the analysis and the resulting radius changes.

In general, the projection factor can be phase dependent, but as shown by Nardetto et al. (2004) the impact of this dependence is weak (0.2 per cent on the distance determination) and in our analysis we keep it constant for a given model (it is not fixed in regard to the MCMC analysis though). It is convenient to separate the time-independent p-factor and the parameter-independent $D(t)$ term, as the latter can be calculated once for the whole analysis. Let us denote the Cepheid fractional radius and its absolute radius correction at pulsation phase 0.0 by $r_{1,0}$ and $\Delta R_{1,0}$, then the fractional radius of the pulsating component at any time can be found from the relation

$$r_1(t,p) = r_{1,0} + \frac{\Delta R_1(t,p) - \Delta R_{1,0}}{a}, \tag{3}$$

where a is the semimajor axis of the system obtained from the orbital solution – see Section 4.1.

3.4 Surface-brightness ratio

The dimensionless surface-brightness ratio of the components that influences the depth of the eclipses is one of the fitted parameters within the JTKEBOP code. This quantity changes during the pulsation cycle because the effective temperature of the Cepheid is not constant and, what follows, neither is the mean flux emitted from the surface area of the star. To calculate the surface-brightness ratio in a given moment and band, we use an adequate out-of-eclipse pulsation light curve and the fractional radius changes given by equation (3). Let us denote the Cepheid flux, its surface brightness and the total apparent brightness of the system measured in a given band at pulsation phase 0.0 by $F_{1,0}, j_{1,0}$ and m_0, respectively. Their current values during pulsations are $F_1(t), j_1(t)$ and $m(t)$. The radius of the secondary component r_2 and its surface brightness j_2 are constant during the pulsation cycle. Let us now define the surface-brightness ratio at pulsation phase 0.0 and its current value by

$$j_{21,0} = \frac{j_2}{j_{1,0}}$$
$$j_{21}(t) = \frac{j_2}{j_1(t)}. \tag{4}$$

In general, some amount of the third light in the system, being an optical blend or an additional physical stellar companion, may be present. Although it does not affect physically the surface-brightness ratio of the components, it affects the way we derive this quantity from the out-of-eclipse magnitudes. Let us assume that the third light flux is constant in a given band $F_3 = \text{const}$. Then we can define the third light l_3, which is one of the input parameters to the JKTEBOP code, by

$$l_{3,0} = \frac{F_3}{F_{1,0} + F_2 + F_3}$$
$$l_3(t) = \frac{F_3}{F_1(t) + F_2 + F_3}, \tag{5}$$

where F_2 is the flux from the companion and $l_{3,0}$ is the third light at phase 0.0. Note that although we assume constant F_3, the third light l_3 changes during the pulsation cycle because its contribution to the total light changes. By the Pogson equation, we can link the instantaneous and reference apparent brightness $m(t)$ and m_0:

$$m(t) - m_0 = -2.5 \log \frac{F_1(t) + F_2 + F_3}{F_{1,0} + F_2 + F_3}. \tag{6}$$

From equation (5) we derive F_3:

$$F_3 = \frac{l_{3,0}(F_{1,0} + F_2)}{1 - l_{3,0}}. \tag{7}$$

Downloaded from http://mnras.oxfordjournals.org/ at :: on February 17, 2014

The fluxes from both components F_1 and F_2 are proportional to the product of their projected surface area and surface brightness:

$$\begin{aligned} F_1(t) &\sim r_1^2(t)\, j_1(t) \\ F_{1,0} &\sim r_{1,0}^2\, j_{1,0} \\ F_2 &\sim r_2^2\, j_2, \end{aligned} \tag{8}$$

where the r_1 dependence on p is omitted as for any given model, the p-factor is constant across the pulsation cycle. Inserting equations (7) and (8) into equation (6), and after some algebraic manipulations with the help of equation (4), we obtain a pulsation phase-dependent relation for the surface-brightness ratio:

$$j_{21}(t) = \frac{r_1^2(t)\, j_{21,0}}{(r_{1,0}^2 + r_2^2\, j_{21,0})\left(\frac{A(t)}{1-l_{3,0}} - l_{3,0}\right) - r_2^2\, j_{21,0}}, \tag{9}$$

where $A(t) = 10^{0.4(m_0 - m(t))}$. Solving equations (5) and (6) for $l_3(t)$, we obtain an expression for the phase dependence of the third light parameter:

$$l_3(t) = \frac{l_{3,0}}{A(t)}. \tag{10}$$

3.5 LD methodology

The LD of a star surface affects the determination of stellar radii in the case of the eclipsing binary light-curve analysis. Instead of fitting the LD coefficients in all three photometric bands independently, we decided to link them by atmospheric parameters, i.e. the effective temperature $T_{\rm eff}$, the gravity $\log g$ and metallicity [Fe/H] utilizing some theoretical LD predictions. We have tested two sets of stellar LD tables published by Van Hamme (1993) and Claret & Bloemen (2011) and two LD laws, namely a linear and a logarithmic one (Klinglesmith & Sobieski 1970). As the Van Hamme tables lack data for the *Spitzer* 3.6 μm band, equivalent Johnson L-band coefficients were used instead.

Because atmospheric parameters of Cepheids change during the pulsation cycle, we expected that also LD coefficients would change over time. To account for this effect, we need to know how both parameters vary with pulsation phase. The instantaneous surface gravity of the Cepheid is calculated from

$$\log g(t) = 4.438 + \log m_1 - 2\log(r_1(t)\, a),$$

where m_1 is the mass of the Cepheid, a is the orbital semimajor axis and the instantaneous star radius is calculated from equation (3). The masses of both components are adopted from the solution obtained with the WD code.

The effective temperature of the Cepheid can be inferred from the colour indices like $(V-I)$ or $(V-K)$. In practice, temperature calibrations based on $(V-K)$ are much more reliable. In order to obtain intrinsic $(V-K)$ colours of the Cepheid during the pulsation cycle, we have to remove the light contribution of the accompanying red giant in V and K bands, and the same is needed to estimate the amount of interstellar reddening in the direction of CEP-0227. Once the intrinsic $(V-K)$ index is obtained, the effective temperature is estimated using various calibrations. Details of this procedure are described in a separate paper (Gieren et al., in preparation). In Fig. 6, we present how the temperature of the Cepheid changes over one pulsation period. The metallicity [Fe/H] $= -0.5$ was assumed for both components. It is slightly larger than [Fe/H] ~ -0.65 derived by Marconi et al. (2013), but the resulting change in the LD coefficients is insignificant.

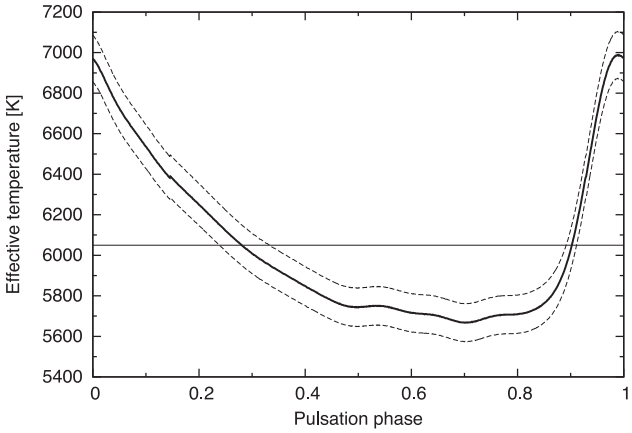


Figure 6. Dependence of the Cepheid effective temperature over the pulsation phase (thick solid curve) with 1σ uncertainties (dashed lines). The temperature variation may be used to calculate LD coefficients for a given phase. The horizontal line represents the mean effective temperature (6050 K) of the star.

In the case of the second component, the effective temperature and gravity are constant; thus, LD coefficients do not need any special treatment. For the secondary component, we set the constant effective temperature $T_{\rm eff,2} = 5120$ K and gravity $\log g_2 = 1.71$.

During our analysis, it appeared that the LD coefficients calculated for a constant average effective temperature gave better results than those for the variable one. Therefore, we tested this option thoroughly and eventually this was the main method that we have used. Note that it does not mean that the Cepheid temperature is constant nor it means that the LD coefficients are such. It only means that the dependence on $T_{\rm eff}$ may be different from the one assumed here. Indeed, Marengo et al. (2003) based on the theoretical considerations found some significant variability of LD between the pulsation phases $\phi = 0.6$ and 0.7 coinciding with a shock-wave passage through the photosphere. However, for most part of the pulsation period LD coefficients were found to change only a little.

3.6 Light time travel effect

A pulsating Cepheid star is a kind of a cosmic clock. When a star orbits another star, we observe that this clock is accelerating when a Cepheid is approaching us and decelerating when a Cepheid is drifting away. This well-known light time travel effect is no doubt present in the binary CEP-0227. The only question is whether the photometry we collected is of the precision good enough to make this effect detectable. The instantaneous distance ρ of the Cepheid star from the system barycentre is given by the equation

$$\rho = \frac{a_1\,(1-e^2)}{1 + e\cos\nu}, \tag{11}$$

where a_1 is the semimajor axis of the Cepheid orbit, e is the eccentricity and ν is the true anomaly. The projection of ρ on to the line of sight passing through the system barycentre equals

$$d = \rho\, \cos(\omega + \nu - \pi/2)\sin i, \tag{12}$$

where ω is the periastron longitude and i is the orbital inclination. The value of d tells us how much the Cepheid is closer to or farther away from us in respect to the system barycentre. The time which light needs to pass this distance is a retardation of the pulsating

Downloaded from http://mnras.oxfordjournals.org/ at :: on February 17, 2014

signal. In other words, the observed pulsation phase ϕ'_p is different from the pulsation phase ϕ_p computed for the constant mean pulsation period P_p, and they are related as follows:

$$\phi'_p = \phi_p - \frac{d}{c P_p}, \tag{13}$$

where c is the velocity of light.

Although the retardation of the pulsation signal in the primary minimum is just ∼0.0014 of the pulsation period, during the most steep part of the pulsation light curve (between phases 0.85 and 1.0), it translates into a 0.003 mag shift in the I band and a 0.005 mag shift in the V band. Such shifts are comparable to the precision of OGLE-IV photometry and, being a systematic effect, can affect our solution. Indeed, after implementation of the effect in our code, we detected it on the 3.5σ significance level. The implementation is made by applying a correction to the calculated pulsation phase while the best model is being taken from the 2D light-curve grid.

4 RESULTS

As the initial parameters for our analysis we used the results from our previous study of this system (Pietrzyński et al. 2010). Because we have gathered a lot of new data and applied a more sophisticated and direct approach, we expect the results to be more reliable and accurate. Some other effects neglected before were also taken into account this time.

First we have obtained a new orbital solution, which was then used as a base for the following analysis of the photometry using the method described above.

4.1 Orbital solution

We analysed disentangled orbital RVs of both components with the WD code (Wilson & Devinney 1971; Wilson 1979; Van Hamme & Wilson 2007) to derive the projected semimajor axis of the system $a\sin i$ and the mass ratio q (see Fig. 7). The reason behind using the WD code is to account for non-Keplerian corrections originating from stars oblateness. These corrections are relatively small (∼0.4 km s^{-1}) but result in the $a\sin i$ different by 3σ from the purely

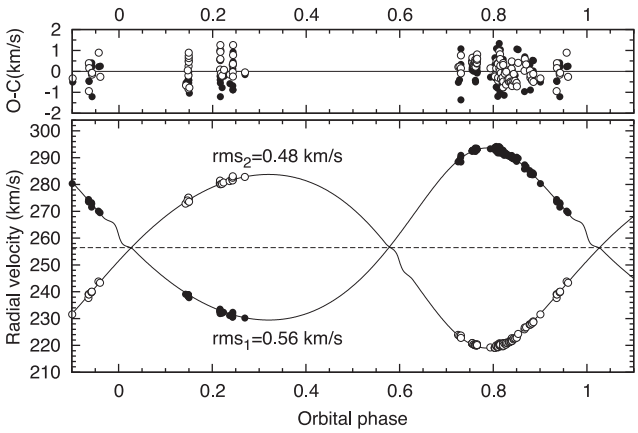


Figure 7. Orbital solution for CEP-0227 (solid lines). Measured RVs of the Cepheid with the pulsations removed (filled circles) and of its constant companion (open circles) are presented. Model residua are shown in the upper panel.

Table 5. Orbital solution for CEP-0227. In RAVESPAN stars are treated as point-like sources, T_0 is HJD − 245 0000 d, and $a\sin i$ is calculated with the rest-frame orbital period $P = 309.404$ d.

Parameter	RAVESPAN	WD	
		Solution 1	Solution 2
γ (km s^{-1})	256.61 ± 0.04	256.48 ± 0.11	256.46 ± 0.09
T_0 (d)		4818.94 ± 0.28	4820.88 ± 0.42
$a\sin i$ (R$_\odot$)	384.24 ± 0.67	389.26 ± 0.44	388.89 ± 0.77
$q = M_2/M_1$	0.993 ± 0.002	0.993 ± 0.003	0.994 ± 0.003
e	0.163 ± 0.002	0.166 (fixed)	0.161 ± 0.003
ω (°)	343.0 ± 1.4	342.0 (fixed)	344.5 ± 1.8
K_1 (km s^{-1})	31.72 ± 0.06	32.14 ± 0.05	32.11 ± 0.07
K_2 (km s^{-1})	31.94 ± 0.06	32.38 ± 0.05	32.31 ± 0.06
rms$_1$ (km s^{-1})	0.54	0.56	0.55
rms$_2$ (km s^{-1})	0.48	0.48	0.44

Keplerian solution (RAVESPAN). The adjusted parameters were the semimajor axis a, the systemic velocity γ, the mass ratio q and the phase shift $\Delta\phi$. The remaining spectroscopic parameters were kept constant during fitting and their values were adopted from the photometric solution – see Section 4.5. The velocity semi-amplitudes were calculated according to

$$K_2[\mathrm{km\,s^{-1}}] = 50.579 \frac{a\sin i[\mathrm{R_\odot}]}{P[d]\,(1+q)\sqrt{1-e^2}} \tag{14}$$

$$K_1[\mathrm{km\,s^{-1}}] = q\,K_2. \tag{15}$$

The results of the preliminary fitting with RAVESPAN and the final fitting with the WD code are summarized in Table 5. We also perform another run of the WD code adjusting the eccentricity e and the periastron longitude ω to check the consistency of the photometric and spectroscopic solutions (Solution 2). The resulting q and a are essentially the same as for the one when e and ω were kept constant. For a later analysis, we adopted the results from Solution 1 with error on the semimajor axis from Solution 2.

4.2 Limb darkening

From the preliminary analysis, we have learned that using the Van Hamme tables and the logarithmic law results in smaller residua than for any other combination of tables and laws used, so they were selected for a later analysis. Also, as described in Section 3.5 for the primary pulsating component, two scenarios have been considered: (1) LD coefficients dependent on $T_{\rm eff}$ and $\log g$ (which change over pulsation phase), (2) LD coefficients calculated for a constant $T_{\rm eff}$ and variable $\log g$. The latter approach gave significantly better results in terms of χ^2 values so we decided to use it to obtain a final solution.

Having set this, we then varied $T_{\rm eff}$ in order to find out how χ^2 of the best solution depends on LD. Surprisingly, we had to lower the Cepheid temperature (what corresponded to larger LD coefficients) to as low as $T_{\rm LD,1} = 3700$ K. The improvement in χ^2 was considerable and significant to the 6σ level – see Fig. 8. The minimum lies well within 1σ from the lower boundary for the tables used, which is 3500 K, but it appears that further decreasing of the temperature (i.e. increasing the LD coefficients) would not improve the fit. The final scaling factor for the temperature is $a_1 = 3700\,\mathrm{K}/6050\,\mathrm{K} \approx 0.61$.

We have also tried to find a better solution varying LD coefficients for the secondary component. In this case, we had to lower the

Downloaded from http://mnras.oxfordjournals.org/ at :: on February 17, 2014

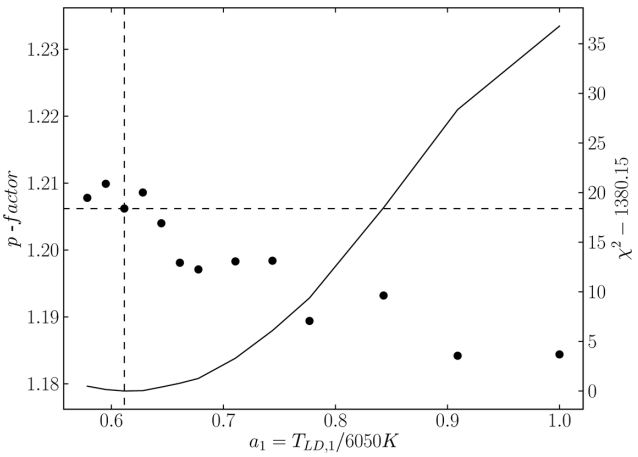


Figure 8. The dependence of the projection factor (filled circles) and χ^2 minimum value (solid line) on the temperature scaling factor $T_{\rm LD,1}/6050$ for the pulsating component. The p-factor and the temperature scaling factor values for the best fit are marked with dashed lines. The y-axis span for the p-factor roughly corresponds to its estimated error (0.03).

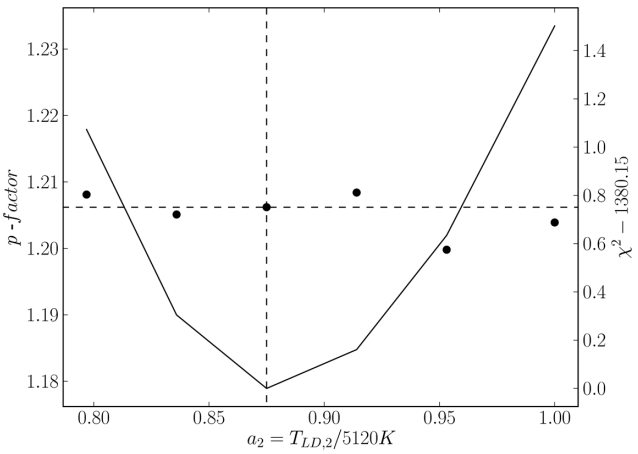


Figure 9. Same plot as in Fig. 8 but for the temperature scaling factor $T_{\rm LD,2}/5120$ for the companion star.

temperature used to evaluate the LD coefficients only moderately to $T_{\rm LD,1} = 4480$ K (scaling factor $a_2 = 4480\,{\rm K}/5120\,{\rm K} \approx 0.88$) and the improvement in the obtained χ^2 was much smaller – see Fig. 9. In fact, the solution obtained for the LD coefficients corresponding to the effective star temperature $T_2 = 5120$ K was only a little more than 1σ inferior to the best one.

4.3 Projection factor

During the last decade, there has been a substantial discussion about the proper projection factor (p-factor) to apply to observed Cepheid RVs to determine pulsational velocities. The issue came up when Gieren et al. (2005) tried to determine direct distances to Magellanic Cloud Cepheids by applying the near-infrared surface-brightness method to LMC Cepheids and found a non-physical period dependence of the derived distances. To correct for this, they inferred, as the most likely explanation, a stronger variation of the p-factor than what had previously been assumed. This period effect has been observationally confirmed recently by Storm et al. (2011),

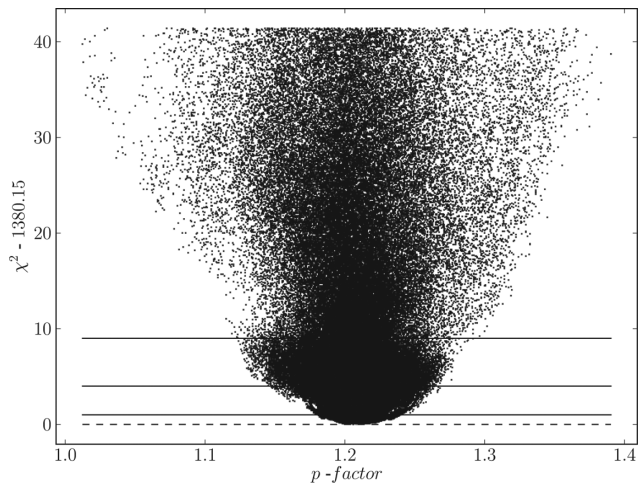


Figure 10. A plot of the p-factor in a χ^2 plane obtained with the MC simulation; 185 000 models are shown. The 1σ, 2σ and 3σ values are marked with solid horizontal lines and the zero level with a dashed one. Each point represents one calculated model. The lowest χ^2 value was obtained for $p = 1.206$, while the central value is $p = 1.208$. The estimated 1σ error is about 0.028.

who applied the surface-brightness method to a much larger sample of Cepheids. Based in large part on these new data, Groenewegen (2013) and Ngeow et al. (2012) confirmed the stronger period dependence of the p-factor. Recent theoretical studies (e.g. Nardetto et al. 2009; Neilson et al. 2012) however do not predict that the p-factor should have a strong period dependence and they found significantly smaller values of the p-factor for short-period Cepheids than inferred by the surface-brightness method studies. CEP-0227 provides a unique opportunity to directly measure the p-factor for a short-period Cepheid.

In our case, the pulsations of the Cepheid star alter the shape of the light curve not only because its flux changes over the pulsation period but also because its radius does. This is manifested during the eclipses as the beginning and the end of the eclipse may be shifted in time and the visible area of the eclipsed star disc depends on the phase of the pulsating component. For any given moment of the eclipse, this area is a function of the star radii and the orbital inclination. As we know the area function from the light-curve solution, we can calculate directly the Cepheid radius and trace its changes for the given constant orbital parameters. Because the amplitude of the radius change scales with the projection factor (i.e. the larger the p-factor, the more profound the radius change), measuring those changes we can directly constrain its value. A conversion from the relative radii (used in the light-curve analysis) to the absolute radii (used in the derivation of the p-factor) is done using the orbital solution previously obtained from the analysis of the RVs.

The value of the projection factor which fits best our data is $p = 1.206 \pm 0.028$, see Fig. 10, and the uncertainty quoted is the statistical error estimated from the MC simulations. This value is different from the value predicted by empirical calibration of Storm et al. (2011) for a Cepheid star with a period of 3.8 d which equals $p = 1.442$. We have tested the p-factor of 1.442 but the χ^2 value was higher by more than 80, i.e. solution was about 9σ away from the best solution. However, such a low value of the projection factor is in good agreement with the theoretical calibrations by Nardetto et al. (2009) and Neilson et al. (2012). The mean wavelength of the

Downloaded from http://mnras.oxfordjournals.org/ at :: on February 17, 2014

spectral region we have used to derive RVs roughly corresponds to the effective wavelength of the Johnson V band. Thus, both calibrations for our Cepheid predict $p = 1.26 \pm 0.03$ and 1.23 ± 0.02, respectively.

It is important to note that the p-factor value does not depend much on the LD coefficients used – see Figs 8 and 9. All the p-factors found for different LD coefficient sets are located within the range of 1.18–1.22, inside the 1σ border. Because of this weak dependence, we use the value and errors derived for the best set of LD coefficients as the final values. Another important thing is the complete independence of our approach to any assumptions on distance to CEP-0227. In fact, our photometric analysis is almost entirely done using only relative radii of the stars, which do not scale with distance. Also a conversion from the RVs to the pulsational ones is distance independent.

To estimate a systematic uncertainty, we compared all the determinations of the projection factor within all sorts of the investigated models (including those with different LD coefficients, the third light neglected, etc.). This tells us how the determined value of the p-factor is sensitive to different model assumptions. In all cases, the resulting p-factor lies within a range of 1.17–1.25. Thus, we assumed the systematic error of 0.04.

4.4 Third light

The presence of the third light was investigated in our analysis. We allowed for its independent presence in each of the photometric bands. In the beginning, the most suspicious was the *Spitzer* 3.6 μm band because some Galactic Cepheids were reported to have near-infrared excess (e.g. Kervella et al. 2006, Mérand et al. 2007) which is usually understood as a result of ongoing mass-loss. The solutions found, however, were consistent with no third light contribution in the *Spitzer* band and the V band as well (being of the order of 0.1 per cent). It turned out, however, that some significant third light was present in the I-band light curve ($l_3 = 0.015$, i.e. 1.5 per cent of the total flux). The detection of the third light only in the I band is a bit surprising. It may indicate a presence of an unaccounted faint red blend in the OGLE photometry or some minor problems with the absolute calibration of the OGLE or *Spitzer* photometry. In fact, Udalski et al. (2008) reported that the uncertainty of the absolute calibration of the OGLE photometry can reach 0.02 mag.

Taking the I-band third light into account results in a considerably smaller χ^2 value with the detection on about 6σ level. A significant (more than 3σ) difference in the obtained parameters between the models with and without the third light was found only in the case of the V-band surface-brightness ratio. For the inclination, the Cepheid radius and 3.6-μm-band brightness ratio, the difference is between 2σ and 3σ, and for the rest of the parameters the results are very consistent between solutions.

4.5 Photometric parameters

The photometric parameters for our best solution, with the third light in the I band taken into account, are summarized in Table 6. The light-curve solution for all three photometric bands is presented in Figs 11–14. The model usually predicts well the brightness of the system during eclipses; however, some small systematic residua are still present. The amplitude of the pulsations during the primary eclipse is smaller because a significant part of the Cepheid disc is covered at this stage and thus, relatively more light comes from the constant component. During the secondary (shallower) eclipse, the Cepheid transits across the companion disc and the observed amplitude of the pulsations grows larger. In the near-infrared, the pulsations become much less prominent and so they affect the shape of the eclipses less. Also the surface-brightness ratio of the components j_{21} changes considerably from the optical to near-infrared. Fig. 15 presents the dependence of j_{21} on the pulsation phase and the photometric band for our best model.

Table 6. Photometric parameters of CEP-0227 from the MC simulations. Values marked with [a] correspond to a pulsation phase 0.0 and T_0 is HJD − 245 0000 d. LD coefficients for the logarithmic law are presented – all of them were adjusted simultaneously using a single parameter (see the text for details). L_{21} is the light ratio of the components in every photometric band.

Parameter	Mean value	Best-fitted value	Error
Adjusted			
$P_{\rm obs}(d)$	–	309.6690	0.0017
T_0 (d)	–	4895.908	0.005
r_1	0.089 57	0.085 32[a]	0.000 25
r_2	–	0.11503	0.000 25
$j_{21}(V)$	0.4566	0.2296[a]	0.0015
$j_{21}(I_C)$	0.5791	0.3881[a]	0.0015
$j_{21}(3.6)$	0.8206	0.7146[a]	0.0045
i (°)	–	86.833	0.016
e	–	0.1659	0.0006
ω (°)	–	342.0	0.6
p-factor	–	1.206	0.030
$l_{3,V}$	–	0.000	0.002
$l_{3,I}$	0.018	0.015[a]	0.002
$l_{3,3.6}$	–	0.000	0.002
$u_{1,V}$		0.805 −0.166	
$u_{1,I}$		0.648 0.129	
$u_{1,3.6}$		0.375 0.218	
Derived quantities			
$L_{21}(V)$	0.7504	0.4174[a]	
$L_{21}(I_C)$	0.9539	0.7054[a]	
$L_{21}(3.6)$	1.357	1.299[a]	

Most of the parameters fitted in our approach are independent and do not exhibit any significant correlation, though some do. We were concerned how the projection factor correlates with the other photometric parameters but in this case we only detected a weak correlation with the surface-brightness ratios. In Fig. 16, the correlation with the I-band surface-brightness ratio is presented, which is the main source of the statistical uncertainty on the determined p-factor value. The strongest correlation among the parameters in our solution was found between the orbital plane inclination i and the sum of the radii $r_1 + r_2$ (same figure) and it is the prime error source of the absolute radius uncertainty. The aforementioned correlation between the inclination and the third light, as well as between the eccentricity and the sum of the fractional radii, is also presented.

4.6 Absolute dimensions

Table 7 presents the physical parameters of both components and some orbital parameters as well. The spectral type is estimated from the effective temperature scale given in table 1 of Alonso, Arribas & Martínez-Roger (1999). The luminosity class is taken from Ginestet, Carquillat & Jaschek (2000). The surface temperatures of the components were calculated according to the dereddened $(V - K)$ colours (Gieren et al., in preparation). The effective

Downloaded from http://mnras.oxfordjournals.org/ at :: on February 17, 2014

temperature of the primary was independently derived by Marconi et al. (2013) as $T_1 = 6100$ K and it is in good agreement with our estimate.

The total error of the absolute radius determination contains statistical uncertainties from the relative radii and the semimajor axis determination. Additionally, we add some systematic uncertainty to the budget error which comes from the presence of the small systematic residua still existing in our photometric solution. During eclipses, the magnitude of these residua reaches 0.01 mag which translates into 0.9 per cent uncertainty of the flux and 0.45 per cent uncertainty of the radii. One must note however that the similar systematic residua are also present *outside* the eclipses and as such may be attributed to some defects of the photometry and not to the model itself. The final error was eventually derived as a sum of all the partial errors in quadrature. The Cepheid is the largest at the pulsation phase $\phi = 0.40$ reaching $R_{\max} = 36.44\,\mathrm{R}_\odot$ and the smallest at the pulsation phase $\phi = 0.92$ shrinking to $R_{\min} = 32.43\,\mathrm{R}_\odot$ (see Fig. 17).

The rotation is derived from the broadening function calculated for all the spectra where the components are well separated. The profile is wide and the instrumental broadening seems to be of secondary importance. We assumed that the rotation axis is perpendicular to the orbital plane. The derived value of the projected rotational velocity of the secondary $v_2 \sin i = 11.1$ km s^{-1} is consistent with its pseudo-synchronous rotation of 10.4 km s^{-1}. The rotational velocity of the primary is strongly affected by the atmospheric turbulence originating from the pulsations, so we do not determine this parameter here.

It is worth mentioning that the new radius, mass and luminosity estimates do agree within one sigma with the recent pulsation and evolutionary prescriptions.

5 CONCLUSIONS

The presented method proved to be a good tool for the analysis of eclipsing binaries with radially pulsating components. It allows for a consistent treatment of the photometric and spectroscopic data – calculating the pulsating component radius change we make use of both of them. As a result, very precise measurements of the physical parameters of a Cepheid variable and its companion were obtained. We fully confirmed the findings of Pietrzyński et al. (2010), especially the reported mass and radius values of the classical Cepheid CEP-0227. Our masses for both components and the radius of the secondary are well within 1σ error bars given by Pietrzyński et al. (2010). A slight difference occurs for the Cepheid mean radius which is about 1.7σ larger in our solution. We do not think that to be significant because we have analysed here a much larger set of observations and the previous analysis was based on the approximate removal of the pulsations from the light curve. Our mean radius is in perfect agreement with the Cepheid period–radius relation of Gieren et al. (1999) and marginally consistent with the Groenewegen (2013) calibration.

The present analysis of the *Spitzer* data excludes the possibility of the additional third light in the near-infrared larger than ∼0.2 per cent. Because the level of the third light detected

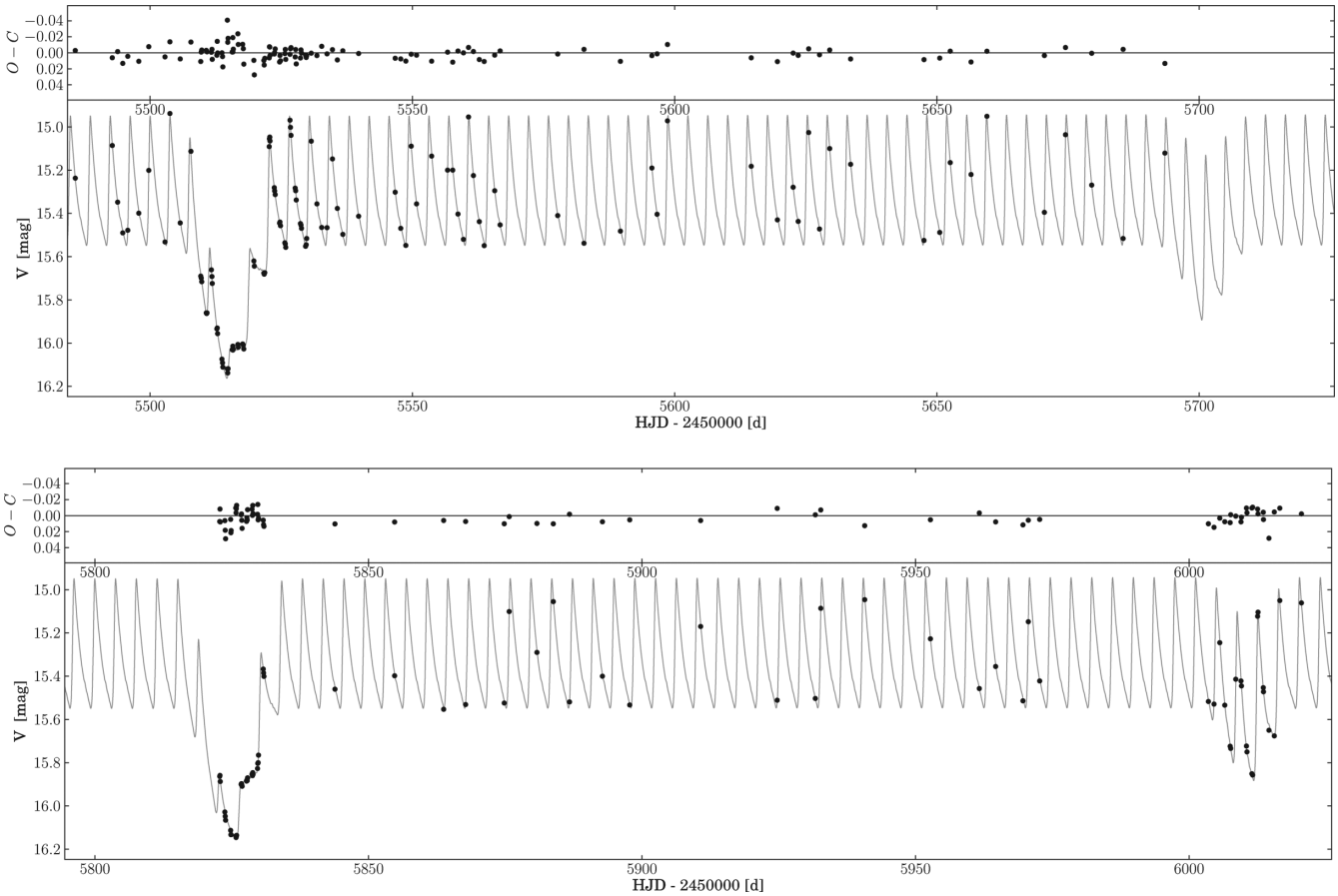


Figure 11. *V*-band model for selected eclipses. Observations are marked by small black circles.

Downloaded from http://mnras.oxfordjournals.org/ at :: on February 17, 2014

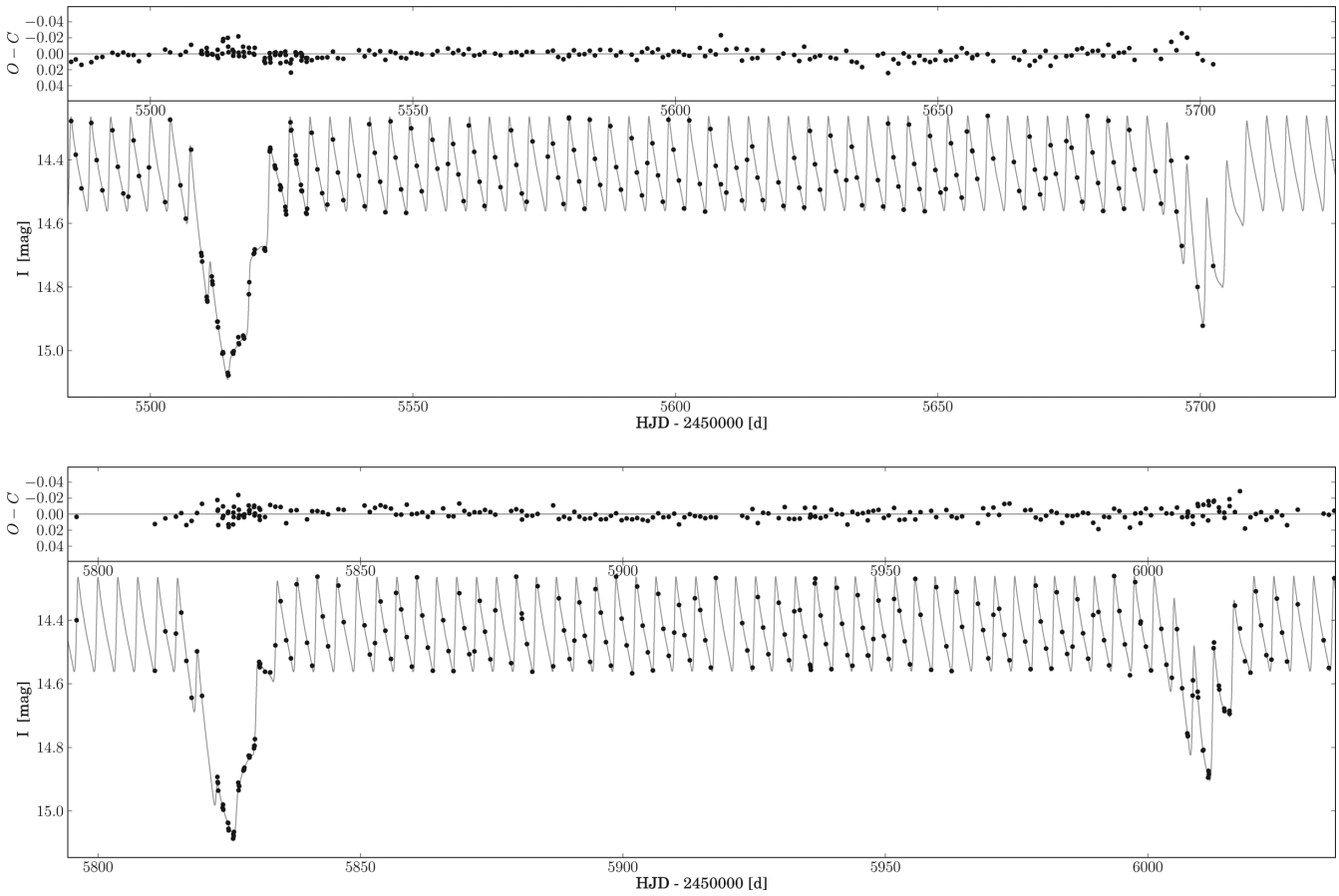


Figure 12. *I*-band model of selected eclipses.

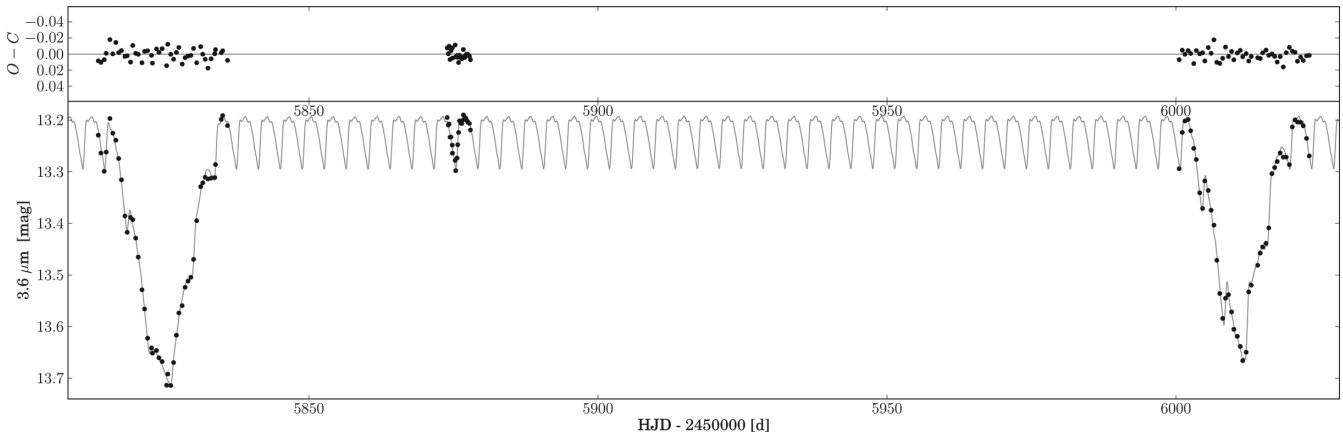


Figure 13. *Spitzer* 3.6-μm-band model.

in the *I* band is also low, we conclude that there is no significant *K*-band excess in this system as well.

The observed disc of the Cepheid surface seems to be heavily darkened, especially in the optical region where the corresponding linear LD coefficient is $u_V \approx 0.9$. It is at odds with the LD coefficient predicted for the static atmosphere at the temperature $T = 6050$ K, the gravity $\log g = 1.97$ and the metallicity $[\mathrm{Fe/H}] = -0.5$, namely $u_V = 0.56$ (van Hamme 1993). Such a strong LD may arise from the high degree of turbulence in the pulsating atmosphere of the Cepheid and from the presence of very deep and profound convective cells more typical for a late-K-type giant.

According to our knowledge, the method we have used for deriving the projection factor is the first one of this kind reported in the literature. It is also a second time, in a general case of short-period Cepheids, that the individual value is precisely determined after the interferometric measurements for δ Cep (Mérand et al. 2005). Our value of the projection factor $p = 1.21 \pm 0.03$ is close to the p-factor determined by Mérand et al. (2005): $p = 1.27 \pm 0.06$. Marconi et al.

Downloaded from http://mnras.oxfordjournals.org/ at :: on February 17, 2014

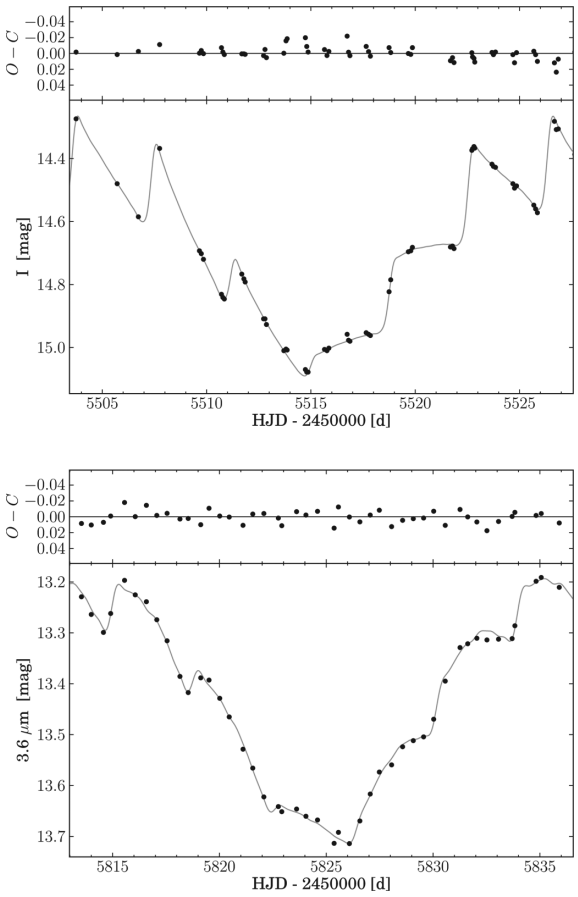


Figure 14. *Spitzer* 3.6 μm and *I*-band models shown for two different primary eclipses.

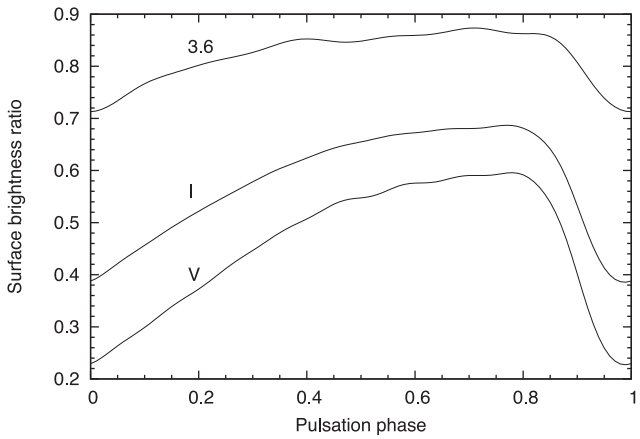


Figure 15. Surface-brightness ratio of the components j_{21} as a function of the pulsation phase for three bands, from up to down: *Spitzer* 3.6 μm, I_C, V.

(2013), based on the hydrodynamic models of CEP-0227, derived the p-factor $p = 1.20 \pm 0.08$, in good agreement with our empirical determination. However, their models were fitted to the pulsation light curves of the Cepheid which were freed from the companion light contribution according to our photometric light-curve solution. Thus, their value of the p-factor is not fully independent.

There are two substantial advantages of our method in comparison with the approach presented by Mérand et al. (2005) making it less prone to systematics. First, our projection factor is distance independent. Secondly, only weak dependence on the LD assumptions is present. In fact, LD coefficients are fitted simultaneously, but independently to the p-factor. Let us emphasize here that in deriving the interferometric angular diameters, one need to convert uniform disc diameters $\theta_{\rm UD}$ into limb darkened ones $\theta_{\rm LD}$. For δ Cep, the conversion was done using the theoretical LD tables for ordinary (non-pulsating) stars. However, in a view of the peculiar LD, we have found that for CEP-0227 such a procedure may be called into question.

Of course, there are some other sources of possible systematics in our solution. First of all, the question whether JKTEBOP can adequately represent the surfaces of giant stars. A comparison made with the WD code (Graczyk et al. 2012), which is still the most elaborated program for the analysis of eclipsing binaries, suggests that for well-detached binaries (as our CEP-0227) the solutions returned by both codes are very similar. If any systematics connected with the use of JKTEBOP exists, most probably it is shared by other computer tools for modelling eclipsing binaries. Some systematics may also arise from the assumptions of constant LD and projection factor during the whole pulsation cycle. The validation of both assumptions is currently under work and will be presented in another paper.

The application of the light travel time effect was important in the analysis. For our object, it barely affected our derived parameters but the overall fit was significantly better removing some systematic residua. For some other objects like CEP-1812, we expect the effect to have an even higher impact on the solution.

In summary, we conclude that themethod presented allowed us not only to improve the precision of the determination of the intrinsic and structural parameters of the binary system and the pulsating component in particular, but also to measure some other characteristics like LD and the p-factor. It has a great potential for the application to other binary systems with radially pulsating components.

ACKNOWLEDGEMENTS

We gratefully acknowledge financial support for this work from the Polish National Science Center grant MAESTRO 2012/06/A/ST9/00269 and the TEAM subsidy from the Foundation for Polish Science (FNP). Support from the BASAL Centro de Astrofísica y Tecnologías Afines (CATA) PFB-06/2007 is also acknowledged. AG acknowledges support from FONDECYT grant 3130361. RS is supported from the Polish NSC grant UMO-2011/01/M/ST9/05914.

This work is based (in part) on observations made with the *Spitzer Space Telescope*, which is operated by the Jet Propulsion Laboratory, California Institute of Technology, under a contract with NASA. Support for this work was provided by NASA. The OGLE project has received funding from the European Research Council under the European Community's Seventh Framework Programme (FP7/2007-2013)/ERC grant agreement no. 246678 to AU.

We would like to thank the support staff at the ESO Paranal and La Silla observatory and at the Las Campanas Observatory for their help in obtaining the observations and the rest of the OGLE team for their contribution in acquiring the data for the object.

This research has made use of NASA's Astrophysics Data System Service.

Downloaded from http://mnras.oxfordjournals.org/ at :: on February 17, 2014

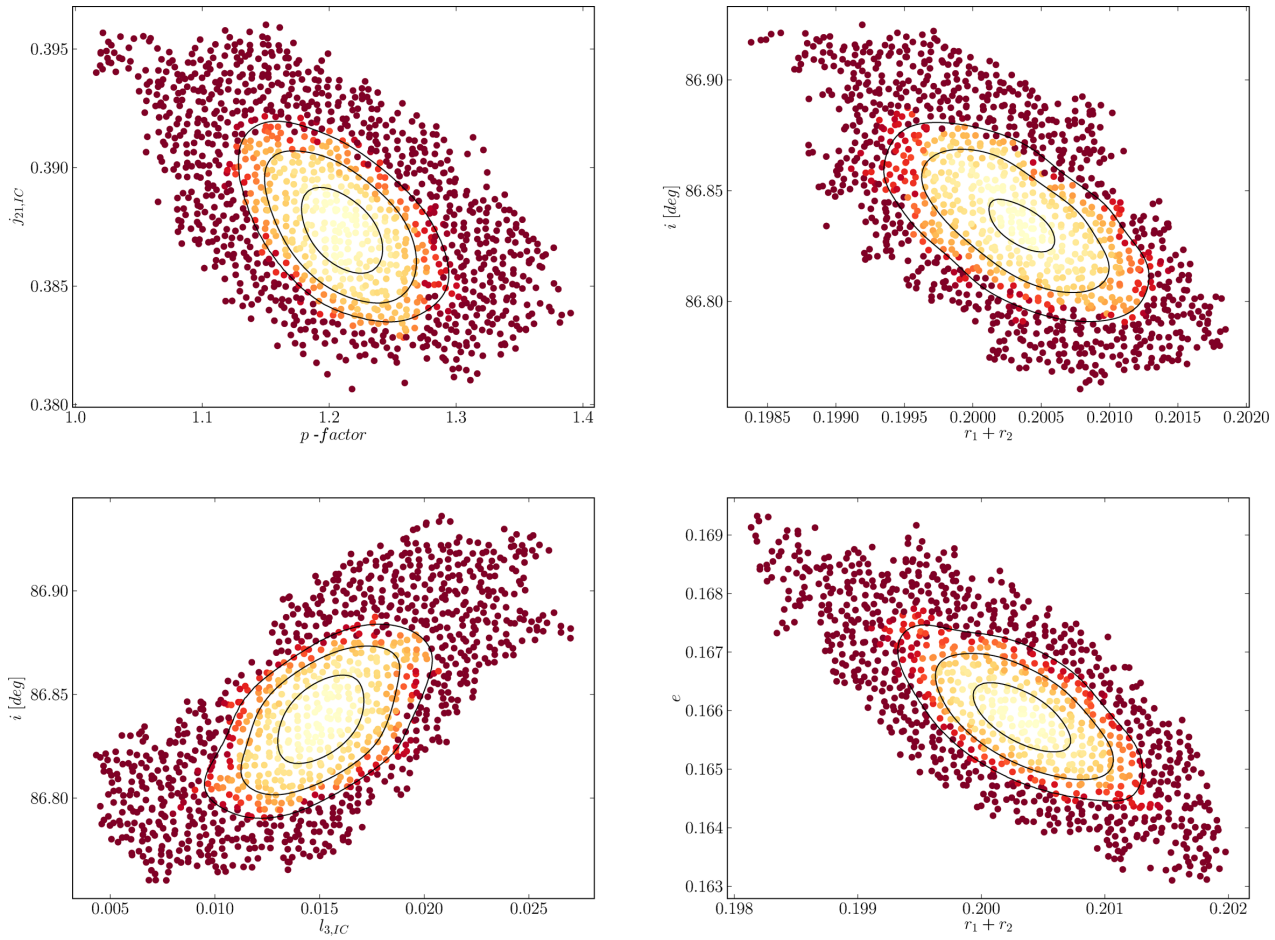


Figure 16. Correlations between the p-factor and the I-band surface-brightness ratio, the inclination and the sum of the star fractional radii, the inclination and the third light in the I band, the eccentricity and the sum of the star radii. The best models for a given pair of the parameters are shown and the χ^2 values are coded with colour (higher values are darker). The solid lines represent the 1σ, 2σ and 3σ levels for the two-parameter error estimation.

Table 7. Physical properties of CEP-0227. The spectral type, radius, gravity ($\log g$), temperature, luminosity ($\log L$) and the observed magnitudes are mean values over the pulsation period. The orbital period is a rest-frame value.

Parameter	Primary (Cepheid)	Secondary
Spectral type	F7 Ib	G4 II
Mass ($M_\odot$)	4.165 ± 0.032	4.134 ± 0.037
Radius ($R_\odot$)	34.92 ± 0.34	44.85 ± 0.29
$\log g$ (cgs)	1.971 ± 0.011	1.751 ± 0.010
Temperature (K)	6050 ± 160	5120 ± 130
$\log L$ ($L_\odot$)	3.158 ± 0.049	3.097 ± 0.047
V (mag)	15.932	16.244
I (mag)	15.178	15.229
K (mag)	14.221	13.903
$v \sin i$ (km s^{-1})	–	11.1 ± 1.2
Orbital period (d)	309.404 ± 0.002	
Semimajor axis ($R_\odot$)	389.86 ± 0.77	

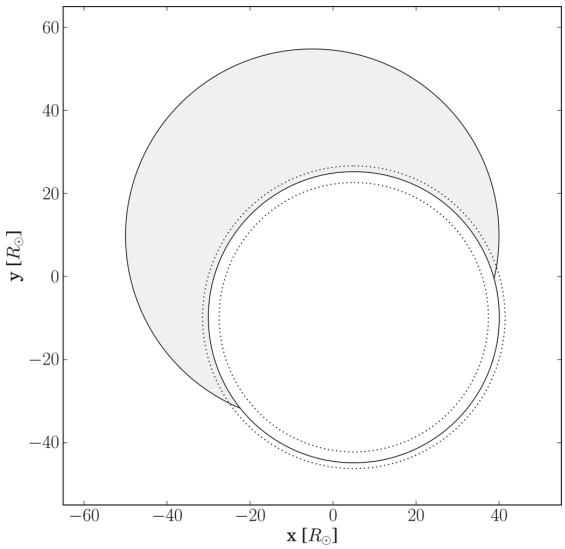


Figure 17. System configuration close to the secondary mid-eclipse. The Cepheid is passing in front of the red giant companion. Star edge line width represents the 1σ formal error in the determination of the radii. The Cepheid radius is a mean value over time, and the dotted lines represent its minimum and maximum radii. Changes in the radial amplitude of the star that correspond to the p-factor error approximately equal the radius error. The distance between the stars at this phase is about 355 $R_\odot$.

Downloaded from http://mnras.oxfordjournals.org/ at :: on February 17, 2014

REFERENCES

Alcock C. et al., 2002, ApJ, 573, 338
Alonso A., Arribas S., Martínez-Roger C., 1999, A&AS, 140, 261
Baade W., 1926, Astron. Nachr., 228, 359
Claret A., Bloemen S., 2011, A&A, 529, 75
Coelho P., Barbuy B., Meléndez J., Schiavon R. P., Castilho B. V., 2005, A&A, 443, 735
Gieren W., Moffett T. J., Barnes T. G., III, 1999, ApJ, 512, 553
Gieren W., Storm J., Barnes T. C., III, Fouqué P., Pietrzyński G., Kienzle F., 2005, ApJ, 627, 224
Ginestet N., Carquillat J. M., Jaschek C., 2000, A&AS, 142, 13
Graczyk D. et al., 2012, ApJ, 750, 144
Groenewegen M. A. T., 2013, A&A, 550, 70
Hastings W. K., 1970, Biometrika, 57, 97
Kervella P., Mérand A., Perrin G., Coudé de Foresto V., 2006, A&A, 448, 623
Klinglesmith D. A., Sobieski S., 1970, AJ, 75, 175
Lepischak D., Welch D. L., van Kooten P. B. M., 2004, ApJ, 611, 1100
Maceroni C., Montalbán J., Gandolfi D., Pavlowski K., Rainer M., 2013, A&A, 552, 60
Marconi M. et al., 2013, ApJ, 768, L6
Marengo M., Karovska M., Sasselov D. D., Papaliolios C., Armstrong J. T., Nordgren T. E., 2003, ApJ, 589, 968
Mérand A. et al., 2005, A&A, 439, L9
Mérand A. et al., 2007, ApJ, 664, 1093
Nardetto N., Fokin A., Mourard D., Mathias Ph., Kervella P., Bersier D., 2004, A&A, 428, 131
Nardetto N., Stoekl A., Bersier D., Barnes T. G., 2008, A&A, 489, 1255
Nardetto N., Gieren W., Kervella P., Fouqué P., Storm J., Pietrzynski G., Mourard D., Queloz D., 2009, A&A, 502, 951
Neilson H. R., Nardetto N., Ngeow C.-C., Fouqué P., Storm J., 2012, A&A, 541, 134
Ngeow C.-C., Neilson H. R., Nardetto N., Marengo M., 2012, A&A, 543, 55
Pietrzyński G. et al., 2010, Nat, 468, 542
Pietrzyński G. et al., 2011, ApJ, 742, 20
Pietrzyński G. et al., 2012, Nat, 484, 75
Pilecki B., Konorski P., Górski M., 2012, in Richards M. T., Hubeny I., eds, Proc. IAU Symp. 282, From Interacting Binaries to Exoplanets: Essential Modeling Tools. Cambridge Univ. Press, Cambridge, p. 301
Popper D. M., Etzel P. B., 1981, AJ, 86, 102
Press W. H., Teukolsky S. A., Vetterling W. T., Flannery B. P., 2007, Numerical Recipes: The Art of Scientific Computing, 3rd edn. Cambridge Univ. Press, Cambridge
Riazi N., Abedi A., 2006, New Astron., 11, 514
Rucinski S. M., 1992, AJ, 104, 1968
Rucinski S. M., 1999, in Hearnshaw J. B., Scarfe C. D., eds, ASP Conf. Ser. Vol. 185, IAU Colloq. 170: Precise Stellar Radial Velocities. Astron. Soc. Pac., San Francisco, p. 82
Soszyński I. et al., 2008, Acta Astron., 58, 293
Soszyński I. et al., 2012, Acta Astron., 62, 219
Southworth J., Maxted P. F. L., Smalley B., 2004, MNRAS, 351, 1277
Southworth J., Bruntt H., Buzasi D. L., 2007, A&A, 467, 1215
Southworth J. et al., 2011, MNRAS, 414, 2413
Storm J. et al., 2011, A&A, 534, 94
Udalski A., 2003, Acta Astron., 53, 291
Udalski A., Szymański M. K., Soszyński I., Poleski R., 2008, Acta Astron., 58, 69
van Hamme W., 1993, AJ, 106, 2096
van Hamme W., Wilson R. E., 2007, ApJ, 661, 1129
Wesselink A. J., 1946, Bull. Astron. Inst. Neth., 10, 91
Wilson R. E., 1979, ApJ, 234, 1054
Wilson R. E., Devinney E. J., 1971, ApJ, 166, 605
Wilson R. E., van Hamme W., 2010, in Prša A., Zejda M., eds, ASP Conf. Ser. Vol. 435, Binaries – Key to Comprehension of the Universe. Astron. Soc. Pac., San Francisco, p. 45

SUPPORTING INFORMATION

Additional Supporting Information may be found in the online version of this article:

Table 1. OGLE *V*-band photometry sample.
Table 2. OGLE *I*-band photometry sample.
Table 3. *Spitzer* 3.6 μm photometry sample (http://mnras.oxfordjournals.org/lookup/suppl/doi:10.1093/mnras/stt1529/-/DC1).

Please note: Oxford University Press is not responsible for the content or functionality of any supporting materials supplied by the authors. Any queries (other than missing material) should be directed to the corresponding author for the paper.

This paper has been typeset from a TEX/LATEX file prepared by the author.

Downloaded from http://mnras.oxfordjournals.org/ at :: on February 17, 2014

Résumé

Pour comprendre la nature de l'énergie noire, il faut mesurer le taux d'expansion de l'univers, c'est-à-dire la constante de Hubble (H_0), avec une bonne précision, soit à mieux que 2%. Les deux principales méthodes qui permettent de faire cela, le rayonnement de fond cosmologique et la détermination des distances dans l'univers présentent des désaccords significatifs, on parle de 'tension'. L'une des clefs pour résoudre cette tension se trouve très probablement dans l'étalonnage de la relation période-luminosité (PL) des Céphéides : quelle est son point-zéro ? Est-il sensible à la métallicité ? Peut-on réduire la dispersion de la relation ? La méthode des binaires à éclipses a permis récemment d'atteindre 2.2% sur la distance du LMC, ce qui permet de contraindre le point-zéro de la relation PL et d'étudier l'effet de la métallicité. Mais cette méthode repose principalement sur l'hypothèse que les étoiles sont de bons corps noirs, ce qui n'est pas toujours le cas comme l'atteste les discordances dans les estimations des relations brillance de surface-couleur pour les étoiles de type O,A,B par exemple, utiles pour la détermination de distances de M31 ou M33. Par ailleurs, appliquer la méthode de Baade-Wesselink de détermination de distance aux Céphéides des nuages de Magellan est maintenant possible, mais la question clef de la valeur du facteur du projection et de sa dépendance avec la période des Céphéides demeure. Il est donc impossible de faire l'impasse sur la compréhension de la dynamique atmosphérique des Céphéides (p-facteur, k-facteur) et de leur environnement pour déterminer les distances dans l'univers. Ceci est d'autant plus vrai que les enveloppes des Céphéides pourraient avoir un effet sur la dispersion de la relation période-luminosité. L'arrivée des nouvelles générations d'interféromètres (MATISSE, SPICA), des parallaxes *Gaia*, dans le contexte du JWST, de PLATO et de l'ELT, permettront de répondre à ces questions fondamentales.

Abstract

Determining the expansion of the universe, i.e. the Hubble constant (H_0) to better than 2% is required in order to understand the nature of dark energy. However, the two most accurate methods to do it, the cosmic microwave background and the distance scale ladder are inconsistent today, which is refereed as the 'tension'. One of the key to resolve this tension is related to the calibration of the period-luminosity (PL) of Cepheids : what is its zero-point ? Is it metallicity dependent ? Can we reduce the dispersion of the PL relation ? The eclipsing binaries method was recently used to determine the distance to LMC with a 2.2% accuracy, which is crucial to constrain the zero-point of the PL relation and to study the impact of metallicity. However, this method is based on the hypothesis that stars are perfect blackbody, which is not always the case as shown by inconsistencies in the surface brightness - color relations of early type stars for instance, that are actually useful for the distance determination of eclipsing binaries in distant galaxies (i.e. M31, M33). On the other hand, it is now possible to apply the Baade-Wesselink method to Cepheids in the Magellanic Clouds, however the value of the projection factor and its dependence with the period of Cepheids remains a key issue. Understanding the dynamical structure of the atmosphere of Cepheids (p-factor, k-factor) and their environment cannot be circumvented in order to determine the distance in the universe. This is even more true that the environment of Cepheids could increase the dispersion of the PL relation. The next generation of interferometers (MATISSE, SPICA), the *Gaia* parallaxes, in the context of JWST, PLATO, and ELT will help to resolve these fundamental issues.